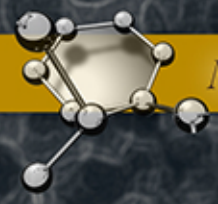

Nanotechnology Science and Technology

Silver Nanoparticles

Properties, Characterization and Applications

Audrey E. Welles
Editor

NOVA

Copyright © 2010, Nova Science Publishers, Incorporated. All rights reserved.

Silver Nanoparticles: Properties, Characterization and Applications : Properties, Characterization and Applications, Nova Science Publishers,

Copyright © 2010. Nova Science Publishers, Incorporated. All rights reserved.

NANOTECHNOLOGY SCIENCE AND TECHNOLOGY

SILVER NANOPARTICLES: PROPERTIES, CHARACTERIZATION AND APPLICATIONS

Copyright © 2010. Nova Science Publishers, Incorporated. All rights reserved.

No part of this digital document may be reproduced, stored in a retrieval system or transmitted in any form or by any means. The publisher has taken reasonable care in the preparation of this digital document, but makes no expressed or implied warranty of any kind and assumes no responsibility for any errors or omissions. No liability is assumed for incidental or consequential damages in connection with or arising out of information contained herein. This digital document is sold with the clear understanding that the publisher is not engaged in rendering legal, medical or any other professional services.

NANOTECHNOLOGY SCIENCE AND TECHNOLOGY

Additional books in this series can be found on Nova's website under the Series tab.

Additional E-books in this series can be found on Nova's website under the E-book tab.

Copyright © 2010. Nova Science Publishers, Incorporated. All rights reserved.

NANOTECHNOLOGY SCIENCE AND TECHNOLOGY

SILVER NANOPARTICLES: PROPERTIES, CHARACTERIZATION AND APPLICATIONS

AUDREY E. WELLES
EDITOR

Copyright © 2010. Nova Science Publishers, Incorporated. All rights reserved.

Nova Science Publishers, Inc.
New York

Silver Nanoparticles: Properties, Characterization and Applications : Properties, Characterization and Applications, Nova Science Publishers,

Copyright © 2010 by Nova Science Publishers, Inc.

All rights reserved. No part of this book may be reproduced, stored in a retrieval system or transmitted in any form or by any means: electronic, electrostatic, magnetic, tape, mechanical photocopying, recording or otherwise without the written permission of the Publisher.

For permission to use material from this book please contact us:
Telephone 631-231-7269; Fax 631-231-8175
Web Site: http://www.novapublishers.com

NOTICE TO THE READER

The Publisher has taken reasonable care in the preparation of this book, but makes no expressed or implied warranty of any kind and assumes no responsibility for any errors or omissions. No liability is assumed for incidental or consequential damages in connection with or arising out of information contained in this book. The Publisher shall not be liable for any special, consequential, or exemplary damages resulting, in whole or in part, from the readers' use of, or reliance upon, this material. Any parts of this book based on government reports are so indicated and copyright is claimed for those parts to the extent applicable to compilations of such works.

Independent verification should be sought for any data, advice or recommendations contained in this book. In addition, no responsibility is assumed by the publisher for any injury and/or damage to persons or property arising from any methods, products, instructions, ideas or otherwise contained in this publication.

This publication is designed to provide accurate and authoritative information with regard to the subject matter covered herein. It is sold with the clear understanding that the Publisher is not engaged in rendering legal or any other professional services. If legal or any other expert assistance is required, the services of a competent person should be sought. FROM A DECLARATION OF PARTICIPANTS JOINTLY ADOPTED BY A COMMITTEE OF THE AMERICAN BAR ASSOCIATION AND A COMMITTEE OF PUBLISHERS.

Additional color graphics may be available in the e-book version of this book.

LIBRARY OF CONGRESS CATALOGING-IN-PUBLICATION DATA

Silver nanoparticles : properties, characterization, and applications /
editors, Audrey E. Welles.
p. cm.
Includes index.
ISBN: 978-1-61728-062-7 (eBook)
1. Silver. 2. Nanoparticles. 3. Metal powder products. 4. Powder metallurgy. I. Welles, Audrey E.
TA480.S5S55 2010
620.1'8923--dc22

2010014091

Published by Nova Science Publishers, Inc. † New York

Copyright © 2010. Nova Science Publishers, Incorporated. All rights reserved.

CONTENTS

Preface		**vii**
Chapter 1	Synthesis, Growth Mechanisms and Tunable Optical and Catalytic Properties of Diverse Silver Nanostructures *Xiangkang Meng, Shaochun Tang and Sascha Vongehr*	**1**
Chapter 2	Low- and High-order Nonlinearities of Silver Nanoparticles *R. A. Ganeev*	**55**
Chapter 3	Laser-Induced Shape Transformation of Silver Nanoparticles Embedded in Glass - Physics and Applications *Andrei Stalmashonak, Heinrich Graener and Gerhard Seifert*	**119**
Chapter 4	Ion-Synthesis of Silver Nanoparticles and Their Optical Properties *Andrey L. Stepanov*	**169**
Chapter 5	Biological Effects of Silver Nanoparticles *Elena M. Egorova*	**221**
Chapter 6	The Study of Silver Nanoparticles Applied on the Photonics Materials Based on the Surface Plasmon Resonance *You Yi Sun*	**259**
Chapter 7	A Biomolecular Approach on the Functionalization of Silver Nanoparticles *Aswathy Ravindran, M. Ashok Raichur, N. Chandrasekaran and Amitava Mukherjee*	**291**
Chapter 8	Applications of Silver Nanoparticles' Surface Plasmon Resonance Effect in the Field of Nonlinear Optical Materials *Xin Chen, Gang Zou, Jun Tao and Yan Deng*	**309**
Chapter 9	Antibacterial Applications of Silver Nanoparticles: Benefits and Human Health Risks *Renat R. Khaydarov, Rashid A. Khaydarov, Yuri Estrin, Svetlana Evgrafova, Seung Y. Cho and Stefanie Wagner*	**327**

Copyright © 2010. Nova Science Publishers, Incorporated. All rights reserved.

Chapter 10 Mass Spectrometry Evaluation of the Improvement of DLC Film Lifetime Using Silver Nanoparticles for Application on Space Devices: Material Review and Etching Experiments **341**
F.R. Marciano, L.F. Bonetti, R.S. Pessoa, J.S. Marcuzzo, M. Massi, L.V. Santos, E.J. Corat and V.J. Trava-Airoldi

Chapter 11 Electrospun Gelatin Nanofibers Functionalized with Silver Nanoparticles **361**
Florentina Tofoleanu, Tudorel Balau Mindru, Florin Brinza, Nicolae Sulitanu, Ioan-Gabriel Sandu, Dan Raileanu, Viorel Floristean, Bogdan Alexandru Hagiu, Cezar Ionescu, Ion Sandu and Vasile Tura

Index **371**

Copyright © 2010. Nova Science Publishers, Incorporated. All rights reserved.

PREFACE

Silver nanoparticles are nanoparticles of silver, of between 1 nm and 100 nm in size. While frequently described as being 'silver' some are composed of a large percentage of silver oxide due to their large ratio of surface to bulk silver atoms. This book explores the properties, characterization and application of silver nanoparticles on topics such as low and high-order nonlinearities of silver nanoparticles; the synthesis, growth mechanisms and tunable optical and catalytic properties of silver nanoparticles; laser-induced shape transformation of silver nanoparticles embedded in glass and others.

Chapter 1- This chapter reviews recent advances in the utilization of various water based synthesis routes towards the shape-controlled synthesis of silver nanoparticles and microstructures in a diverse range of shapes and sizes from several nanometers to micrometers. A variety of very simple one pot methods, at times employing commercial microwave ovens, inexpensive low power ultrasound cleaners, or two- electrode electro-chemistry, can be surprisingly effective in the controlled synthesis of a wide range of nanostructured products, if only parameters are carefully chosen. The many approaches include synthesis of Ag nanostructures with various shapes in solution, doping of Ag nanoparticles on unmodified silica and on/inside carbon spheres; kinetically controlled growth of Ag micro-particles with novel nanostructures on flat substrates, and galvanic replacement towards bimetallic Ag-Au dendrites and carbon composites. Characterizations of shape, composition and microstructure are carried out via scanning and transmission electron microscopy, various spectroscopy methods, N2 absorption measurements and suchlike. The involved growth mechanisms are investigated in order to discover new means towards better control. Size, location and shape control, including micro- and nanostructure features, allows tuning the products' properties towards desired applications. The author focus on the optical properties and catalytic activities, but also the stability of compounds can be an issue of interest.

Chapter 2- The author present the studies of the low-order optical nonlinearities (nonlinear refraction, nonlinear absorption, nonlinear susceptibility) of the silver nanoparticles of various sizes using the probe laser radiation of different pulse duration (100 fs – 50 ps) and wavelength (396, 532, 793, and 1064 nm). The author show that the influence of the surface plasmon resonance of these clusters considerably changes the nonlinear optical response of silver nanoparticle-containing medium. The author analyze the influence of aggregation of silver nanoparticles on the variation of the sign of nonlinear refraction of this

Copyright © 2010. Nova Science Publishers, Incorporated. All rights reserved.

medium. Various methods of nanoparticle formation are analyzed and compared with commercially available samples.

High-order nonlinearities of silver clusters are studied by means of the harmonic generation of laser radiation in laser-produced plasma plumes containing silver nanoparticles. The author show the advantages of the application of nanoparticle-containing plasma plumes as the nonlinear media for radiation conversion compared to the monoparticle-containing plumes. Six to fifteen enhancement factors of conversion efficiency of 800 nm radiation toward the extreme ultraviolet range was achieved in the former case. The author present the results of modification of the morphology of silver nanoparticles before and after laser ablation of nanoparticle-containing targets at different intensities of laser ablation beam.

Chapter 3- Glasses containing metallic nanoparticles show very promising linear and nonlinear optical properties, mainly due to the surface plasmon resonance (SPR) of the nanoparticles. Spectral position (in the visible and near-infrared range) and polarization dependence of the SPR are, besides other parameters, characteristically determined by the nanoparticles' shapes. The focus of this chapter will be on interaction of intense fs laser pulses with silver nanoparticles incorporated in soda-lime glass, and nanostructural modifications in glass-metal nanocomposites induced by such laser pulses. In particular, to give a comprehensive physical picture of the processes leading to laser-induced persistent shape transformation of the nanoparticles, series of experimental results, investigating the dependences of laser assisted shape modifications of Ag nanoparticles on the laser pulse intensity, excitation wavelength, temperature etc. will be considered. In addition, the resulting local optical dichroism allows producing very flexibly polarizing optical (sub-) microstructures with well specified optical properties. The achieved considerable progress towards technological application of this technique will also be discussed.

Chapter 4- Recent results on ion-synthesis by low energy implantation and optical properties of silver nanoparticles in various dielectrics (glasses and polymers) and on the interaction of high power laser pulses with such composite materials are reviewed. One of the features of composites prepared by the low energy ion implantation is the growth of metal particles with a wide size distribution in the thin depth from the irradiated substrate surface. This leads to specific optical properties of implanted materials, partially to difference in reflection measured from implanted and rear face of samples. The excimer laser pulse modification of silver nanoparticles fabricated in silicate glasses are considered. Pulsed laser irradiation makes it possible to modify such composite layer, improving the uniformity in the size distribution of the nanoparticles. The optical absorption of silver nanoparticles fabricated in polymer is also analysed. Unusual weak and broad plasmon resonance spectra of the nanoparticles is studied in the frame of the carbonisation of ion-irradiated polymer. Based on the Mie theory, optical extinction spectra for metal particles in the polymer and carbon matrices are simulated and compared with partical spectra for complex silver core–carbon shell nanoparticles. A new experimental data on nonlinear optical properties of synthesised silver nanoparticles are also presented.

Chapter 5- Silver nanoparticles are widely used now for the creation and production of modified materials with special properties. However, the mode of their action on the living organisms and the conditions providing the safety of their applications for humans and other living beings remain poorly understood. Therefore, of particular interest are studies allowing to reveal the effects of nanoparticles' parameters on various functions of the biological

Copyright © 2010. Nova Science Publishers, Incorporated. All rights reserved.

systems and, in particular, to determine the concentration limits within which the nanoparticles are not toxic for a given plant, animal or human organism..

This chapter presents a review on the biological effects of silver nanoparticles observed in experiments on the living organisms of various types. The nanoparticles used in these studies were obtained by the original method of biochemical synthesis, based on the reduction of metal ions by natural plant pigments (flavonoids) in reverse micelles formed by the anionic surfactant. From micellar solutions of nanoparticles in organic solvent water dispersions are prepared according to the special procedure. Optical spectra and TEM micrographs of silver nanoparticles in solutions are presented. Both water solutions containing silver nanoparticles and solid or polymer materials modified by the nanoparticles are considered. The antimicrobial properties and toxic action of the nanoparticles on slim mold, alga, plant seeds and animals are described. The results are compared with those reported in similar studies using silver nanoparticles obtained by the other methods.

Chapter 6- Recent theoretical progress in understanding the application of silver nanoparticles on the photonics materials based on the surface plasmon resonance (SPR) has been discussed in this chapter. In the first, a novel procedure to enhance the luminescence from Europium complexbased on the surface-enhanced fluorescence of silver nanoparticles, was described. It shows that the noble metal nanoparticles act as enhancer and quencher of Europium complex fluorescence. And then the both interactions strongly depend on noble metal particle diameter, concentration and surrounding medium, the systematic studies have been carried out. Secondly, recent studies about third order nonlinear optical properties of noble metal nanocomposite film were also discussed. It shows that a nonlinear optical response in copper, silver and gold nanocomposite materials with an enhanced third order nonlinear susceptibility, which is particularly useful in their applications as optical switchers with ultrashort time response and optical limiters of intense laser radiation. The crystallite size and concentration of nanoparticles on their nonlinear properties of such systems are discussed. Particularly, the synthesis method of the silver nanocomposite film is also described. Thirdly, the influence of silver nanoparticles on the phase behavior of liquid crystalline polymers was also conclued. A series of polymer films containing liquid crystalline groups and silver nanoparticles were prepared. Local electromagnetic fields near the particle can be many orders of magnitude higher than the incident fields due to hat light at the surface plasmon resonance frequency interacts strongly with metal particles and excites a collective electron motion, or plasmon. As a result, photo-induced reorientation of liquid crystalline polymers was affected by silver nanoparticles. The effect of liquid crystalline polymers structure, size and concentration of silver nanoparticles, polarized light on the photo-induced reorientation of the liquid crystalline group films was systemic studied.

Despite all the studies done so far in this field, the application of silver nanoparticles on the photonics materials here is a relative new physical process first described about 10 years ago. So it is quite usual that most of the work done so far was devoted to the development and optimization of the effect than to a deeper understanding of the mechanism of the physical process. The scope of this chapter is to discuss some mechanistic aspects of the physical process between noble metallic nanoparticles on the photonics materials, which are plausible and in line with earlier and new findings of our group, and to compare them with results of other groups. It may be a help for further discussions and the development of better optical materials based on SPR of noble nanoparticles.

Copyright © 2010. Nova Science Publishers, Incorporated. All rights reserved.

Chapter 7- Nanotechnology involves the production, manipulation and use of materials (nanoparticles) usually in the size range of 1 to 100 nm. Silver nanoparticles offer unusual optical, electronic, and chemical properties due to their ability to effectively interact with photons by virtue of the surface plasmon resonance. Owing to this property, silver nanoparticles are potentially attractive as building blocks for the development of photonic and surface plasmon devices. Silver nanoparticles also exhibit bioactivity and antibacterial properties, which make them attractive for medical and agricultural applications. Moreover the development of nanoparticles for the delivery of therapeutic agents has introduced new opportunities for the improvement of medical treatment. Despite having excellent physical and chemical bulk properties, nanoparticles do not posses suitable surface properties for specific applications like Biomolecular imaging, drug delivery etc. The surface chemistry of the nanoparticles plays a critical role in retaining the biological function of the biomolecules conjugated to nanoparticles. Currently available synthetic methodologies, however, are not satisfactory at providing the appropriate surface chemical properties like water-solubility, biocompatibility and biostability of nanoparticles. There arises the need for surface modification or Biofunctionalization of the nanoparticle where in the author attach suitable organic groups to the nanoparticles. It is a process that also stabilizes the nanoparticles against agglomeration and enables their self-organization. Recent efforts have focused on developing targeted nanoparticles, which are formulated by (for therapeutic delivery) functionalizing nanoparticle surfaces with targeting molecules, such as antibodies, peptides, small molecules and oligonucleotides. Phospholipids derivatives containing disulfide groups were used to modify silver nanoparticle surfaces. The surface modified silver nanoparticles have proved to have improved biocompatibility and intracellular uptake for drug delivery. The biomolecules conjugated with nanoparticles have received the most attention in the field of clinical diagnosis and drug delivery because of their high stability, good biocompatibility and high affinity for biomolecule.

Chapter 8- This Account describes a new strategy for the preparation of nonlinear optical devices based on the silver nanoparticles and the conjugated polymer, polydiacetylene (PDA), owing to the surface plasmon resonance of silver nanoparticles. It is worth nothing that nano metal exhibited the enhancement of NLO properties induced by quantum confinement effect. The large picosecond optical nonlinear of Au and Ag colloids surrounded by water or glass have been reported. For the most part, however, inorganic nonlinear materials are different to modify compared with organic nonlinear materials. So, characteristic interactions between exciton, plasmon and their resonance effect in the hybridized systems between organic microcrystals and inorganic nano fine particles would make it possible to exhibit novel optical properties. In the course of developing composite nonlinear materials, the author discovered that nearly seven times enhancement was observed as a result of localized field enhancement under the surface plasmon resonance of silver nanoparticles at the interface of PDA vesicles. The most importance is that the NLO properties of this PDA/Ag nanocomposite system can be further significantly enhanced and flexibly modulated by three strategies which can tune the surface plasmon resonance of silver nanoparticles: (1) changing the size of Ag nanoparticles (which based on the mediation of a size-dependent light-confinement effect and a size-dependent dielectric constant of Ag particles), (2) varying the array of Ag nanoparticles (which based on the coupling effect of local field between neighboring Ag nanoparticles), (3) altering the concentration of Ag nanoparticles (this based on the particle clusters phenomenon which would reduce the local field). The facile

Copyright © 2010. Nova Science Publishers, Incorporated. All rights reserved.

preparation and modulation of nonlinear optical devices based on the Ag nanoparticles and PDA make a new way for the development of organic/inorganic composite nonlinear optical materials.

Chapter 9- The minimum inhibitory concentrations (MICs) assays conducted for *E. coli*, *S. aureus*, *B. subtilis* and *P. phoeniceum* have shown that the antimicrobial activity of silver ions was superior to that of silver nanoparticles. As silver nanoparticles can be more suitable in some bactericidal applications than silver ions, the efficacy of nanosilver as an antimicrobial agent against a range of microbes on the surface of water paints and cotton fabrics has been studied. The cytotoxicity of silver nanoparticles has been studied using NIH-3T3, HEP-G2, A-549, PC-12, and Colo-320 cells via the MTT ((3-(4,5-dimethylthiazol-2-yl)-2,5-diphenyl-tetrazolium-bromid) test. The MTT test results obtained have shown that silver nanoparticles in concentrations of ~1-10 ppm entering the body from air or liquid suspensions can present a potential risk to human health. However, silver nanoparticles as a commercially viable addition to be used in paint and textile industry are unlikely to present a direct health risk.

Chapter 10- In this chapter, a review of current literature on the improvement of diamond-like carbon (DLC) films lifetime using nanoparticles, in particular, silver nanoparticles, will be presented. Studies carried out in our laboratories will also show the results of incorporating silver nanoparticles in DLC films to improve the solid lubricant's lifetime when submitted atomic oxygen bombardment. For this, etching experiments were performed in oxygen plasma operated at low pressure. The DLC films were deposited on different metallic substrates and on silicon (100) wafer with thin amorphous silicon interlayer by using a pulsed directly current plasma enhanced chemical vapor deposition discharge. During etching experiments, the films were submitted to oxygen ions with energy of ~70 eV in order to evaluate the wear process of the surface in a short period. This evaluation was conducted during and after the etching process through the quadruple mass spectrometry and profilometry techniques, respectively. With the mass spectrometry analysis was possible to monitor in real time the gas effluents during etching process as well as the main volatile compounds resultants of reactions of oxygen with the DLC film surface like atomic carbon, carbon monoxide and carbon dioxide. The results indicate a considerably reduction of the volatile species during the etching process for samples with more concentration of silver nanoparticles. This fact is confirmed by the offline etching profile measurement which indicates a decrease in DLC etching. These results confirm that the DLC films become more wear resistant when silver nanoparticles are incorporated in the film bulk.

Chapter 11- The present chapter deals with gelatin nanofibres functionalized with silver nanoparticles, prepared by electrospinning using solutions of gelatin mixed with silver nitrate. As a common solvent for gelatin and AgNO3 was selected a mixture of formic acid and acetic acid in volume ratio 4:1. In this system, formic acid was used as a solvent of gelatine, but also as reducing agent for silver ions in solution. Silver nanoparticles were stabilized through a mechanism that involves an interaction with oxygen atoms of carbonyl groups of gelatin. The gelatin nanofibres functionalised with silver nanoparticles were characterized by transmission electron microscopy (TEM), scanning electron microscopy (SEM), X-ray diffraction (XRD) and antimicrobial test. The results of investigations by TEM and XRD confirmed the presence of silver nanoparticles with diameters less than 20 nm, uniformly distributed over the surface of smooth nanofibres with an average diameter of 70 nm. The tests demonstrated that gelatin/Ag nanofibers have a good antimicrobial activity against Escherichia coli.

Copyright © 2010. Nova Science Publishers, Incorporated. All rights reserved.

Copyright © 2010. Nova Science Publishers, Incorporated. All rights reserved.

In: Silver Nanoparticles
Editor: Audrey E. Welles, pp. 1-53
ISBN: 978-1-61668-690-1
© 2010 Nova Science Publishers, Inc.

Chapter 1

SYNTHESIS, GROWTH MECHANISMS AND TUNABLE OPTICAL AND CATALYTIC PROPERTIES OF DIVERSE SILVER NANOSTRUCTURES

Xiangkang Meng,*[1] *Shaochun Tang and Sascha Vongehr
National Laboratory of Solid State Microstructures,
Department of Materials Science and Engineering,
Nanjing University, Nanjing 210093 (P. R. China)

ABSTRACT

This chapter reviews recent advances in the utilization of various water based synthesis routes towards the shape-controlled synthesis of silver nanoparticles and microstructures in a diverse range of shapes and sizes from several nanometers to micrometers. A variety of very simple one pot methods, at times employing commercial microwave ovens, inexpensive low power ultrasound cleaners, or two- electrode electro-chemistry, can be surprisingly effective in the controlled synthesis of a wide range of nanostructured products, if only parameters are carefully chosen. The many approaches include synthesis of Ag nanostructures with various shapes in solution, doping of Ag nanoparticles on unmodified silica and on/inside carbon spheres; kinetically controlled growth of Ag micro-particles with novel nanostructures on flat substrates, and galvanic replacement towards bimetallic Ag-Au dendrites and carbon composites. Characterizations of shape, composition and microstructure are carried out via scanning and transmission electron microscopy, various spectroscopy methods, N2 absorption measurements and suchlike. The involved growth mechanisms are investigated in order to discover new means towards better control. Size, location and shape control, including micro- and nanostructure features, allows tuning the products' properties towards desired

[1] Corresponding author: E-mail: mengxk@nju.edu.cn Tel: +86 25 8368 5585. Fax: +86 25 8359 5535.

Copyright © 2010. Nova Science Publishers, Incorporated. All rights reserved.

applications. We focus on the optical properties and catalytic activities, but also the stability of compounds can be an issue of interest.

Keywords: silver, nanostructures, synthetic methods, shape control, crystal growth, electrochemical synthesis, microwave synthesis, ultrasound assisted, growth mechanism, thermal stability, surface plasmon resonance, catalysis.

1. INTRODUCTION

Much attention has been paid to metallic nanoparticles (NPs) and larger nanostructures (NSs) because of their many useful electro-optical, magnetic and catalytic properties [1-5], to name but a few, that find applications in numerous fields such as bio-sensing, surface-enhanced Raman scattering (SERS) detection, optical and micromechanical devices, and magnetic recording [6-12]. Especially silver, an inexpensive noble metal with anti-bacterial action and narrow plasmon resonance has inspired many research projects.

The properties of metal nanostructures strongly depend on the involved sizes and shapes. The synthesis of metal nanostructures with tailored sizes and shapes is thus important already for the research into these properties, not to mention the optimization towards practical applications. The ability to control the size, shape and also distribution of the metal NPs and NSs provides great opportunities to systematically investigate their for example catalytic and electro-optical properties and to discover new applications in form of novel research techniques or consumer oriented medical devices and many things in between.

A myriad of shapes of Ag nanostructures has been already synthesized. A variety of synthesis routes for silver nanostructures have been developed in aqueous and non-hydrolytic media. These approaches include photochemistry,[4] thermo chemistry,[5] sonochemistry, wet-chemistry,[13] biochemistry,[14] and electrochemistry. Among these strategies, electrochemistry, ultrasound assisted reactions and microwave (MW) assisted methods are quite useful, because they can control the driving forces for the reduction of precursor ions, nucleation and growth modes. This is somewhat similar to using different reducers or capping agents to manipulate reduction and growth kinetics, but it is also different in that one can exert control over wide ranges in parameter spaces and allow formation conditions far from thermodynamic equilibrium. As an added advantage, these methods are non-toxic and products are of higher purity if control is exerted via physical rather than chemical means. A mostly water-based system provides the potential for large-scale production [15–22] cost effectively.

The products reviewed here include Ag nanostructures of various shapes from suspension in precursor solutions; Ag micro-particles with novel nanostructures on substrates, Ag NPs on unmodified silica spheres and on as well as inside of carbon spheres; and bimetallic Ag-Au NPs and dendrites to illustrate the application of Ag nanostructures as inexpensive and shaped sacrificial substrates in galvanic replacement reactions (GRR) towards complex, multi metal structures that turn out to be extremely active catalysts.

The characterizations have mainly been a means to investigate the growth mechanisms, as understanding them is important for the progress towards more rational ways of developing new synthesis routes past serendipitous discovery toward predictive discovery and finally materials by design. Characterization of shape, composition and microstructure heavily rely

Copyright © 2010. Nova Science Publishers, Incorporated. All rights reserved.

on scanning electron microscopy (SEM) and transmission electron microscopy (TEM) and related methods like high resolution TEM (HRTEM), energy dispersive spectroscopy (EDS/EDX), selected area electron diffraction (SAED), and fast Fourier transform (FFT), X-ray diffraction (XRD), X-ray photoelectron spectra (XPS), but also sometimes Brunauer-Emmett-Teller (BET) N2 absorption measurements, inductively coupled plasma atomic emission spectroscopy (ICP-AES), and other diverse methods that are applied where appropriate.

Because of the novelty of the nanostructures, large surface areas and sometimes unique interfacial structures towards substrates or added metals, we investigated the UV-visible absorption [surface plasmon resonance (SPR)], SERS enhancement and catalytic activities. The focus of our own work lies on the ability to tune such properties via size, shape, distribution, and partially even location control. Given the novelty of many structures, the thereby often discovered surprisingly great enhancement of desired features is maybe actually unsurprising.

1.1. Ag Nanoparticles in 7 Minutes in Mom's Kitchen

Shape-selective synthesis of metal NPs has resulted in well-defined shapes, e.g. triangular plates, cubes, octahedrons, and bars [13,14,23,24]. Anisotropic crystal growth due to capping agents has initially been the key to such precise control yet is also often presumed to be necessary to avoid coagulation. Less toxic and more facile and cost-effective synthetic strategies are desirable though, especially in the light of eventually desired mass production.

MW assisted synthesis has been demonstrated to be a viable way for the production of metal NPs [25]. To date, NPs of different metals, such as Ag, Pt, Pd and Ru, have been synthesized using MW heating [26]. Its so called "thermal effects" distinguish those effects that are also attainable with conventional heating, for example increased reaction rates. The "non-thermal effects" are for example the overheating of suspended dielectrics and the electro-magnetic field's rotating of molecular dipoles. Usually, MW-assisted synthesis of metal NPs is still carried out in the presence of additional reducers and stabilizers [25, 27-29]. It remains a challenge to develop additive-free methods, but the non-thermal MW effects may open the way towards this goal.

In fact, Ag NPs can be synthesized using MW irradiation without use of reducers or capping agents [30]. MW irradiating an aqueous Ag(NH3)2NO3 precursor solution[2] in a usual kitchen MW oven[3] for 7 minutes at the "warm" level setting obtains a greenish suspension of Ag NPs. The simplicity of this synthesis is characteristic for the kinds of methods this review focuses on: Diligent exploration of the available parameter space can lead to products otherwise only possible with much sophistication and costly devices. In this case, the concentration has to be carefully selected: 5 mM (M = mol/L) is too little and nuclei do not seem to grow sufficiently to result in many NPs, while 50 mM already leads to large

[2] [Ag(NH3)2]+ was in all our here reviewed work freshly prepared by dissolving AgNO3 and adding NH3 solution until intermittently precipitating brown Ag oxides disappear again.

[3] Commercial LG WD700 (MG-5041T) oven with 2450 MHz. Time actually radiating during any 30s cycle is n times 6s where n = 1, 2, 3, 4, and 5 hold for levels warm, defrost/thaw, low, medium, and high. The power we state is always the average power <P> = 700 W n/5 = 140 W, 280 W, etc.

Copyright © 2010. Nova Science Publishers, Incorporated. All rights reserved.

aggregates instead of isolated NPs. 10 mM of Ag ions has optimal results, the yield is large and the method as such scalable. Interestingly, non-thermal MW effects are indeed vital. Conventional heating of equally concentrated silver nitrate solution obtained nothing even after 1 hour at 100 ˚C [30]. This compares to 7 minutes of the MW assisted reaction that also never went above the boiling point of water.

Figure 1a shows a low-magnification TEM image of the Ag NPs. The visible aggregation is two dimensional and thus derives from the surface tension of evaporating fluid in the TEM sample preparation. There is no clumping; hence the as-synthesized NPs are isolated particles in suspension. The inset is a photo of the as-synthesized, greenish suspension. Figure 1b is a high-magnification TEM image of the product. The NPs are mostly nearly spherical in shape. 189 NPs were selected and analyzed (GATAN Digital Micrograph software). The size distribution is reasonably narrow (Figure 1c) with diameters of $d = (20 \pm 10)$ nm.

The formation mechanism of these Ag NPs is as follows: (1) MW irradiation generates highly reductive H radicals from water [31]. Also the NH3 molecules bound to the Ag+ are polar molecules and may as well or instead be activated to form H radicals close to the silver. (2) The Ag+ is reduced by the H radicals in the aqueous environment. (3) Ag atoms nucleate. The nuclei form homogeneously in the solution and the process is fast enough to grow the nuclei into NPs that are too large to mutually attach before they have the chance to meet each other. This results in the well-dispersed particles and a narrow size distribution.

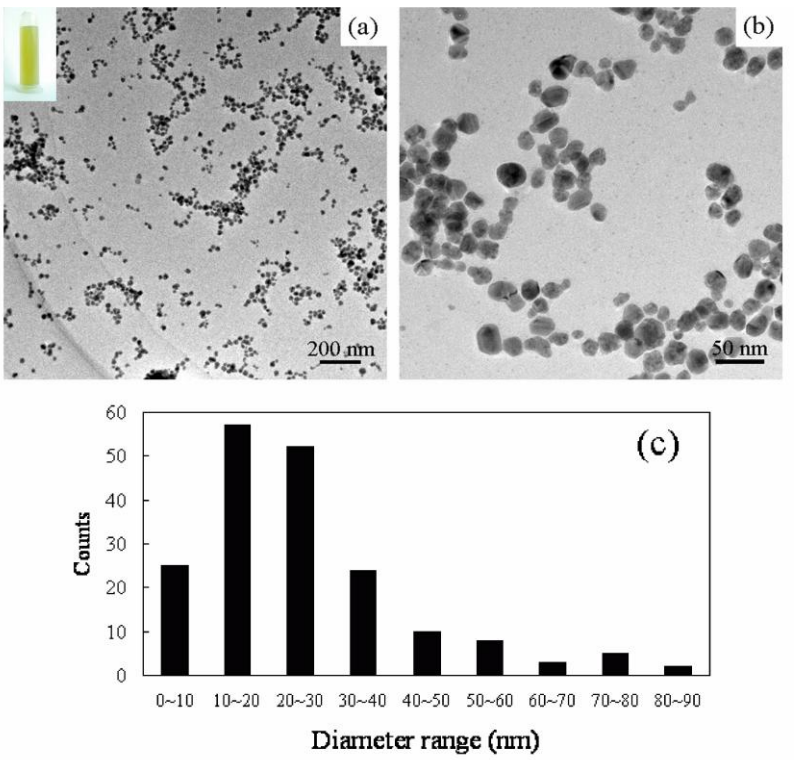

Figure 1. (a) TEM image of Ag NPs synthesized from 10 mM $Ag(NH_3)_2NO_3$ solution by pulsed MW irradiation for 7 min. (b) TEM with higher magnification. (c) Histogram of the diameters of the Ag NPs ($<d> = 20$ nm). This figure is from [30].

Copyright © 2010. Nova Science Publishers, Incorporated. All rights reserved.

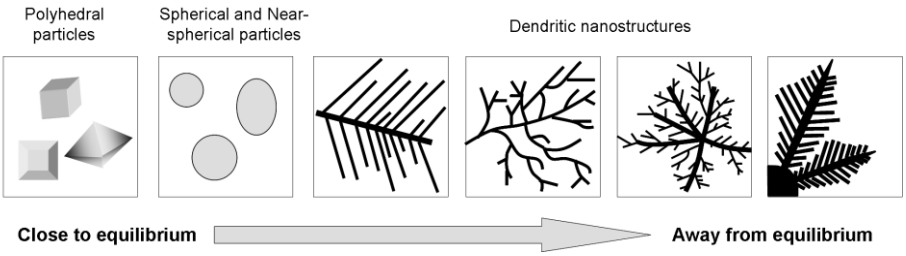

Figure 2. Correlation between the distance of the formation conditions from equilibrium and the morphologies of formed metal NSs. This figure is from [41].

2. SHAPE CONTROLLED SYNTHESIS OF AG NANOSTRUCTURES

2.1. Oriented Attachment Close and Far from Equilibrium

As pointed out above, the properties of metal NSs are highly dependent on size and shape, and so the synthesis of tailored shapes and sizes becomes increasingly important. The morphology of crystals depends on the formation conditions' distance from thermodynamic equilibrium [32,33]. It has been mainly theoretically shown [34,35] that increasing the driving force for crystallization results in the crystals' shapes varying from polyhedrons such as octahedrons, truncated octahedrons, cubes and pyramids, all terminated by thermodynamically stable crystal faces, to various hierarchical structures like dendrites (Figure 2). It is not easy to control a wide range of "distances" from near- to far-equilibrium also experimentally, because strict control over the driving force is difficult. A simple synthesis route accommodating a wide range of conditions is highly desired in order to realize shape control in practice.

Electrochemistry is a simple, low-cost technique. Its driving force, the electrode potential, can be tuned continuously and externally at will. Electrochemistry has been used extensively to generate novel metal NSs with well-defined shapes including wires [15-18], rods [19], cubes [17,20], pyramids [21], plates [22], and dendrites [36]. The electrochemical fabrication of supported metal NPs [20,21] under near-equilibrium conditions forms polyhedrons terminating in thermodynamically stable crystal faces. Far-from-equilibrium, nucleation and growth are fast and result in the instability of the growing surface and formation of hierarchical morphologies [32,33,37].

Some of the benefits of introducing ultrasound to electrochemistry include the continuously ongoing cleaning of electrodes and the acceleration of mass transport and reaction rates [38]. Pulsed ultrasound is often used to prepare silver NPs [39]. Organic capping reagents such as poly(vinyl pyrrolidone) (PVP) [8,39,40] are widely used in the shape-selective synthesis of NSs, because they manipulate growth by selectively adhering to certain crystallographic planes. PVP is a nontoxic food additive (generic name: Povidone) and can be largely washed out after synthesis. With these three ingredients, i.e. simple electro-chemical setup, ultrasound, and PVP, we demonstrated the controllability of the distance from equilibrium over a wide range [41]. Three dimensional (3D) NSs composed of dendritic rod, dendritic sheet, and flower-like dendrites, but also quantum dots with spherical and oval shapes were prepared in this way.

Copyright © 2010. Nova Science Publishers, Incorporated. All rights reserved.

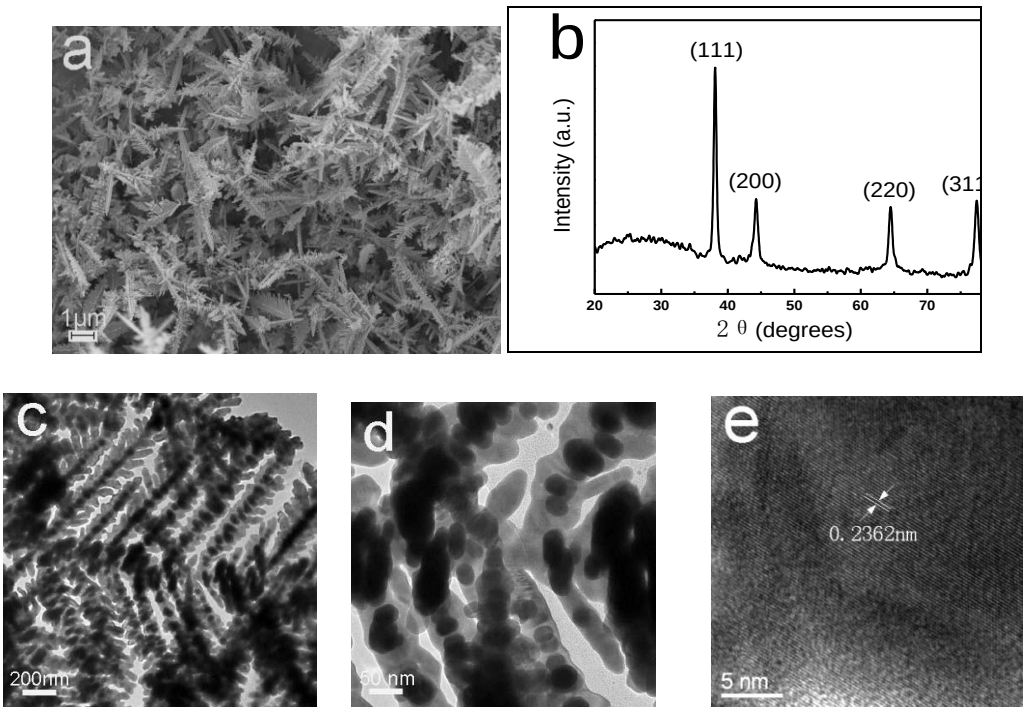

Figure 3. (a) SEM image, (b) XRD pattern, (c)-(d) TEM images with different magnifications, and (e) HRTEM image of the product synthesized by ultrasound electro-deposition. This figure is from [41].

Solutions with a C = 3 mM concentration of silver perchloride AgClO4 were used to investigate whether the distance from equilibrium is also important under ultrasound radiation. Two silver sheets were cleaned with acetone, hydrochloric acid and distilled water to remove all surface contamination. The sheets were fixed on the two opposing sides of a plastic cell 4 cm apart in order to serve as the working cathode and counter anode, both 4cm2 immersed. Electrolysis was conducted at room temperature (r.t.) under continuous 40 kHz ultrasonic vibration at 50 W power and always for 10 minutes. Products were precipitated and purified by five centrifugation/rinsing/re-dispersion steps with deionized water and ethanol. We varied only the current density j and the molar ratio $R = n\text{VP}/n\text{Ag}$ of PVP monomer to Ag+.

Figure 3a shows a SEM image of a typical sample synthesized for 10 min with j and R being 1.25 mA/cm2 and 50. Many fern like dendrites are obtained: long trunks with short side branches terminate in small leaves. Figure 3b is the product's XRD pattern. The four diffraction peaks are indexed as (111), (200), (220) and (311) planes of face-centered cubic (fcc) Ag (a = 4.09 Å, JCPDS No. 4-783). The absence of other peaks indicates high purity silver. A typical TEM image of the product is shown in Figure 3c. All the branches grow sideways from the trunk, forming a flat, almost periodic array. The parallel branches imply that the silver crystals grow along preferred directions. Similarly, each branch seems to be a replica of the main trunk, featuring parallel leaves. A high-magnification TEM image (Figure 3d) displays complex 3D structure on small scales: many dark spots on the side branches are thicker parts, and many bottlenecks are also present on the trunks and junctions. HRTEM (Figure 3e) indicates crystalline dendrites. The distance between lattice planes is 0.236 nm, which is the {111} lattice spacing of fcc Ag (d111 = 0.2359 nm).

Copyright © 2010. Nova Science Publishers, Incorporated. All rights reserved.

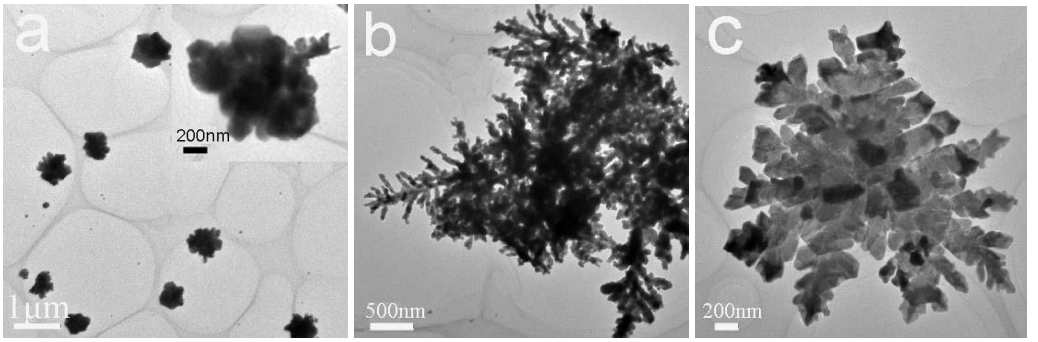

Figure 4. Typical TEM images of the products obtained at various current densities of (a) 0.75, (b) 1.25 and (c) 2 mA/cm^2. This figure is from [41].

The effect of the current density: All samples were prepared with the previous *R*. A large number of irregular agglomerates are observed at *j* = 0.75 mA/cm2 (Figure 4a). The agglomerates consist of closely packed particles (inset). At 1.25 mA/cm2, dendrites with numerous branches are created (Figure 4b). At 2 mA/cm2, the dendrites are more flower-like. Many trunks radiate from the center, and polygonal plates are formed on the ends of the trunks and branches (Figure 4c). High current density promotes formation of hierarchical structures. The change of the driving force of electro-reduction works here similarly to the variation of electrolyte concentration [42]. This is similar to changing the strength of reducing agents in chemical reduction systems [43,44], where for example isotropic silver particles are obtained with a slow reducer, while fast ones induce anisotropic growth with the appearance of dendrites.

PVP is affecting the finer details of the morphology: Figure 5 shows samples prepared with differing *R* while other parameters remained. Coral-like dendrites are formed at *R* = 10 (Figure 5a); the branches' surfaces look smooth, which is different from those in Figure 3. In Figure 5a, some of the trunks diverge gradually at the ends and the distinction between trunk and branches is obscured. When *R* reached 80 (Figure 5b), the structures are composed of several trunks radiating from a center, and most of the trunks diverge into two or more branches at their ends. Microstructures at *R* = 100 are more similar to fern.

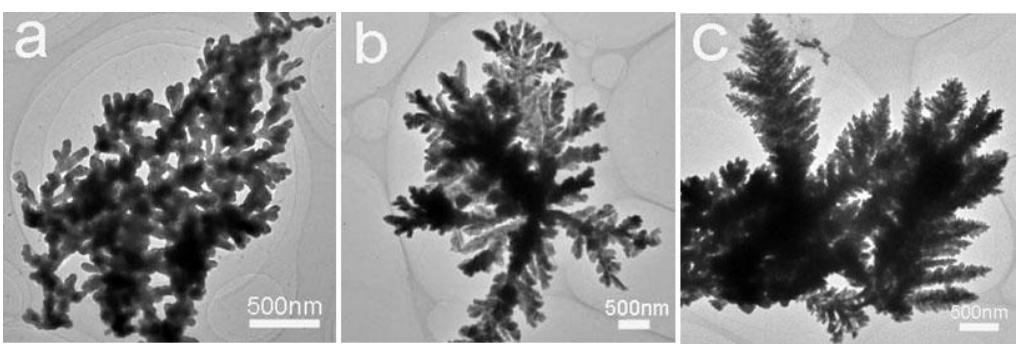

Figure 5. TEM images of the products prepared at different PVP to Ag ratios *R*: (a) 10, (b) 80 and (c) 100. This figure is from [41].

Copyright © 2010. Nova Science Publishers, Incorporated. All rights reserved.

Figure 6 shows samples synthesized at a low j = 0.5mA/cm2 and various PVP concentrations. Spherical silver NPs with a narrow size distribution (d = 7-10 nm) are synthesized at R = 100 (Figure 6a). HRTEM (inset) demonstrates that the NPs are single crystalline. Figure 6b shows spherical NPs of d ~ 15 nm in diameter prepared at R = 50. These NPs have multiple domains, as shown in the HRTEM image of a typical particle (Figure 6c). Figure 6d shows product synthesized with very little PVP (R = 5). These NPs have oval shapes and their size is rather dispersed (Figure 6e).

In summary: spherical silver NPs were obtained at weak driving force, while dendrites were prepared at strong driving force. PVP favors the formation of branches and leaves; it promotes the formation of finer, more hierarchical microstructures. If the initial NPs are sparsely capped by PVP, simple structures with few branches result, while hierarchical structures are formed when the initial NPs are heavily capped.

The role of ultrasound: Ultrasound alone can be an efficient driving force in the synthesis of metal NPs [45] and stratified films [46], but j = 0 yielded only little product. If electro-deposition is performed without ultrasound, all products adhere to the cathode, i.e. only conventional electroplating occurs. Newly formed Ag structures are never shaken from the cathode. Thus, ultrasound is crucial for the formation of the hierarchical Ag nanostructures via attachment of NPs (not ions) in suspension. Ultrasound continues to remove newly grown NPs from the cathode. NPs move continuously around, hit the electrodes, accept the potentials of the electrodes, and travel back into the solution. Differently charged silver particles attach to one another and grow in suspension [36]. Compared with the ultrasonic irradiation by a cathode emitter [45-47], the ultrasound in our experiments is weak. It cannot prevent the particle attachment in the electrolyte. The size cutoff of the hierarchical structures could be directly dependent on the ultrasound power, which should be exploited in future research.

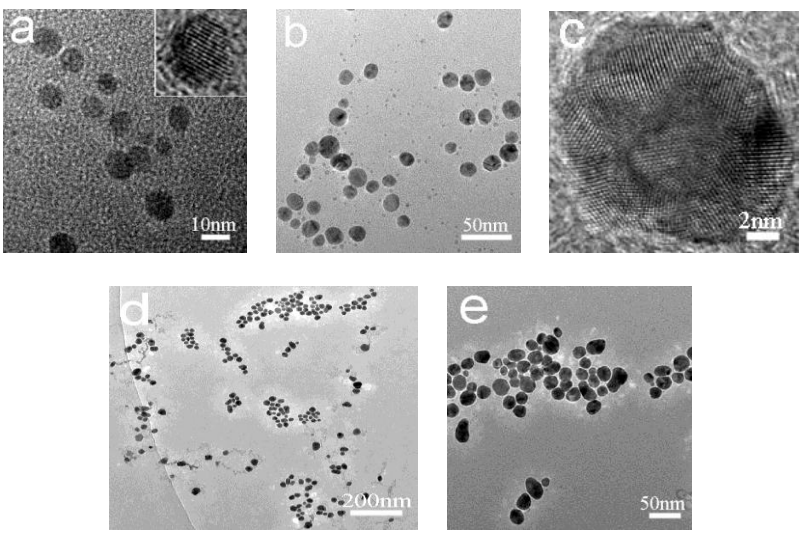

Figure 6. TEM images of Ag NPs obtained at R=100 (a), 50 (b) and 5 (d, e) when j = 0.5 mA/cm^2. The inset in (a) is a HRTEM image of an individual Ag particle. (c) HRTEM image of an Ag nanoparticle in (b). This figure is from [41].

Copyright © 2010. Nova Science Publishers, Incorporated. All rights reserved.

Oriented attachment: The dendritic structures result from oriented attachment of NPs similar to the evolution of silver dendrites in chemical reduction [44]. Oriented attachment of NPs needs firstly NPs that attach (rather than ions), and secondly the fact that they orient while attaching. Let us support these two in detail:

1. From the cathode freed and then suspended NPs (not single ions) mutually attach. The dendrites grow in suspension and none can last on the cathode. Extensive work available on dendrites and established models (for example on the growth mechanism constraining the fractal dimension) deal with "well behaved" mass transport modes like electro migration, diffusion or even electro convection [48,49]. In our case, such research is not directly applicable, because the mass transport is dominated by ultrasonic agitation.
2. The resulting branches are single-crystalline, i.e., the particles orient before they fuse onto the growing dendrite. The size of the many areas investigated at very high resolution (Figure 3e) is comparable to the size of the NPs participating in the attachment process (d ~ 25 nm), yet no domain boundaries are encountered. One must conclude that the branches at least are single crystalline (Branching points could not be imaged at very high resolution). NPs must have oriented themselves while attaching.

2.2. Unusual Growth Mechanisms of Ag Dendrites under Ultrasound

Dendrites are intensively investigated due to their fractal like structures and large surface area [50], both leading to applications in catalysis [51], chemical/biochemical sensors [52] and SERS [53]. Detailed description of the structure is important to understand the underlying growth mechanisms, which in turn is crucial to achieve designable structures (e.g. with well defined branch-stem angles). Particular attention turned to the formation of Ag dendrites by various sono-electrochemical methods with the assistance of organic capping agents such as nitrilotriacetate [54], gelatin [55] and PVP [56]. Many studies focused on the mechanisms of dendrite growth [56-59]. There is a double-interface growth mode of silver where an amorphous phase seems to form first and then crystallizes only below a certain layer thickness of the amorphous phase [61]. As we saw also in section 0, dendrites can emerge from oriented attachment of NPs. Ostwald ripening forms the initial particles and also smoothes the morphology after attachment [62]. Generally, branching angles vary from 15˚ to 90˚ [49]. Many factors affecting structure have been discussed [53,56], but the detailed growth mechanisms are unknown. It remains mostly unclear how the branches emerge from the stems; how the interplay of nucleation and growth at the microscopic scale results in specific densities, branching angles and so on.

In [64], we describe two branch-stem interfacial structures occurring simultaneously in a surfactant-free, constant-current sono-electrochemical process involving silver. Over the whole range of investigated conditions, the reaction always produces two types of dendrites. In Figure 7a, the branches are approximately parallel to each other and attach basically perpendicular to the stem (branching angle is 90˚). The insets magnify the areas inside the white dashed squares and exhibit the angles more clearly. Most branches point towards one

Copyright © 2010. Nova Science Publishers, Incorporated. All rights reserved.

side of the stem. The structure looks 2D although it grew in solution since no large structure can adhere to the electrode under ultrasound.

Without ultrasound, products adhere to the cathode while the electrolyte remains clear, and TEM observation (not shown) evidenced that those products adhering are large conglomerates totally different from the dendrites in Figure 7a. The branches of the dendrite in Figure 7b show angles of 53-61˚ towards the main stem; which agrees with many previous reports [52,65,66]. This slanted branching is commonly observed under non-equilibrium conditions [52,56,66,67] and also happens to be the more prominent in our products. Sometimes, both types of growth even appear on different sections of the same individual dendrite (Figure 7c). The areas representing vertical and slanted growth are denoted as "V" and "S".

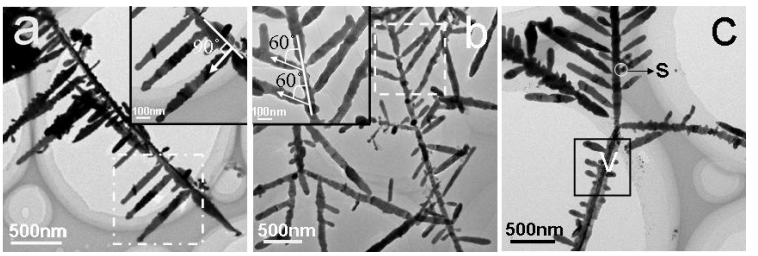

Figure 7. TEM images of silver dendrites: (a) vertical growth and (b) slanted branching. The insets are magnifications of the dashed squares. (c) an individual silver dendrite including both kinds of branching. This figure is from [64].

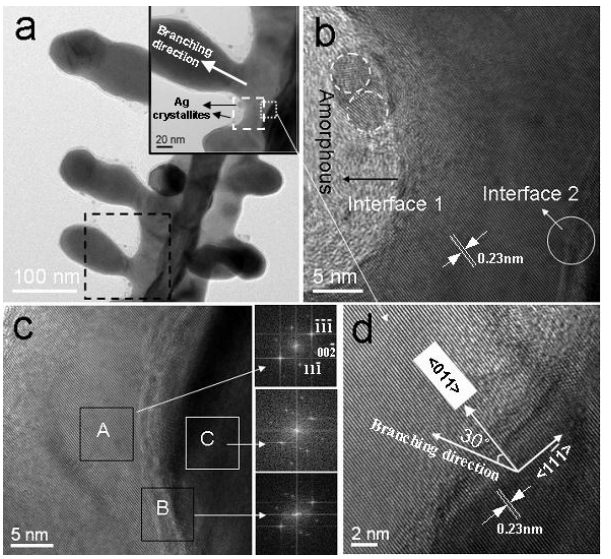

Figure 8. TEM and HRTEM images of vertically branching silver dendrites. (a) local-magnification of area V in Fig. 7c; the inset further magnifies the black dashed square. (b) HRTEM of the area inside the larger dashed square in the inset of 7a. (c) HRTEM of the area of "interface 2" indicated in image b. The right-hand insets are the FFT patterns corresponding to the squared areas labeled A, B, and C. (d) HRTEM with even higher resolution showing the smaller dashed square in the inset of 8a. This figure is from [64].

Copyright © 2010. Nova Science Publishers, Incorporated. All rights reserved.

The branch-stem interfacial structure was analyzed with higher resolution. Figure 8a shows area V, and the inset further magnifies the squared area (black dashed). The strong contrast between the innermost and subsequent outer parts of the stem in area V suggests a core-shell structure. We henceforth call this subsequent shell "transition layer", because there is yet another outermost coating of the dendrite. It has less contrast and is specifically labeled in the inset of Figure 8a. A HRTEM image (Figure 8b) of the area inside the larger dashed square in the inset of Figure 8a reveals that the outermost layer is amorphous. A few small crystallites with different crystallographic orientations are present in the amorphous layer (arrows in the inset of Figure 8a and white dashed circles in 8b). An amorphous layer has been observed in the growth of Ag dendrites by replacement reactions [61]. Similar amorphous regions involve InAs dendrites [68]. The transition layer is single-crystalline (Figure 8b) with an inter-plane spacing of 0.23 nm, i.e. these are (111) planes. The fringes run continuously through both the transition layer and the branch. Both belong to a single crystal and the connection between branch and stem is not simply a physical contact but rather like from an epitaxial growth. The core-shell interface between the transition layer and the inner dark region (labeled "interface 2") is further investigated: 8c shows the FFT of the areas A, B and C. The similarity between all the hexagonal FFT patterns indicates that the transition layer and the inner stem all belong to fcc silver. The electron beam transmits through the whole core-shell structure, and the two types of spots in the FFT corresponding to areas B and C demonstrate the core-shell structure of stem and surrounding transition layer. Figure 8d displays the HRTEM of the smaller dashed square in the inset of Figure 8a. From the FFT pattern one can determine that the direction orthogonal to <11-1> in Figure 8d is <011>. Also the branching direction is indicated in Figure 8d, and it is parallel to the arrow in the inset of Figure 8a (there was no rotation between the images). The branching direction happens to lie at about 30˚ away from <011>, i.e. it is not related to any specific crystallographic direction like, say, a well known fast direction. This implies that the branching angle may still be under the control of global diffusion while the crystal directions had an influence only locally (grain rotation and realignment).

In the slanted branching from the circled area "S" of Figure 7c, the branches have round cross sections (Figure 9a). The dendrite has a bilaterally symmetric structure with branches distributed roughly evenly between the sides of the stem. The HRTEM image in Figure 9b magnifies the squared area in Figure 9a; no transition layer is visible! There are edge dislocations (defined as having a Burgers vector normal to the dislocation line) at the connecting region between the crystal structure of the stem and that of the branch (twinning), which both turn out to be single-crystalline domains. The fringe spacing perpendicular to the twin plane is 0.23 nm, which indicates (111) inter-planar spacing. Another set of fringes in the branch displays the (100) inter-planar spacing of 0.20 nm, but the thereby inferred <100> direction is not quite parallel to the branch. This is expected, because the branching angles are 53-61˚, so they are not equal but close to the angle of 54.7˚ between the <100> and the <111> direction perpendicular to the (111) twin plane (Figure 9b). Such angles indicate that the growth is globally diffusion-controlled, but locally it results from oriented attachment, which is responsible for the dislocations during early crystal growth [69]. Nanoparticle aggregation by oriented attachment has been recognized as an important growth mechanism for dendrites in solution [59,60,70-73]. The formation of dislocations is often a direct consequence of oriented attachment of a nanoparticle, and so marks the occurrence of the initial particle-particle bonding [59, 60,69] that initiates a new branch.

Copyright © 2010. Nova Science Publishers, Incorporated. All rights reserved.

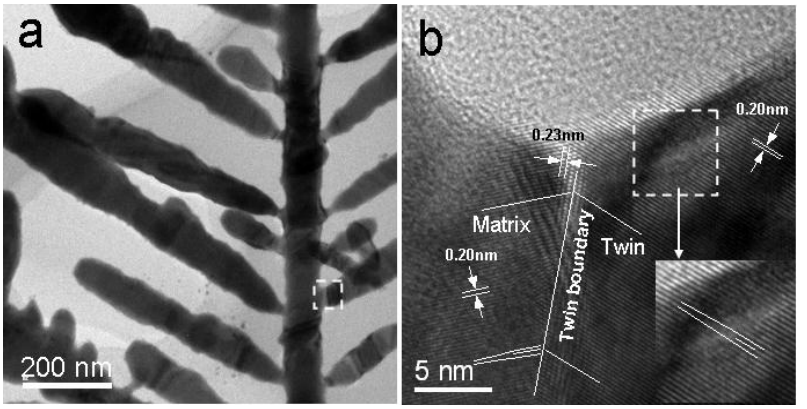

Figure 9. (a) The area S shown in Figure 7c. (b) HRTEM image of the squared area in Figure 9a. This figure is from [64].

Twinning is a common result of two fcc structures joining with their {111} facets to share a crystallographic plane [74]. The inset magnifies the marked square just above to point out another edge dislocation found within the connecting region. Dislocations formed at interfaces due to oriented attachments in other systems have also been reported by Penn and Banfield [60,69]. The formation of defects coincides only with the direct (no transition layer), slanted branching.

Generally, branch formation can involve several growth mechanisms: atom-by-atom crystal growth, amorphous growth with later crystallization, oriented attachment of NPs and grain rotation and realignment, etc. The growth mechanisms for the here observed silver dendrites are still unclear but the following may help further investigations:

In the slanted growth, the attachment of a nanoparticle seed to the stem's surface forms a nucleus for the growth of a side branch. The observed twins and twinning induced dislocations (Figure 9b) are indicative of this. Frequency and angle of branches are consistent with twinning [75]. The branching angles are not exactly 55°, and therefore they are likely affected by the diffusion of Ag precursors [52].

Vertical growth can arise from growth within an amorphous layer, as observed during vapor deposition experiments using catalyst impurities [68]. Such impurities would explain why the amorphous layer has a certain thickness and does not completely crystallize after reaction. An amorphous phase forms and its growth departs orthogonally from the stem. In the area behind the growth front, amorphous Ag spontaneously crystallizes and matures by grain rotation and realignment. The later observable transition layer is the matured part of this deposition process from amorphous Ag. However, it remains the question of why attaching NPs become amorphous and the structure is 2D – such would be both consistent with an on-electrode growth where ions, not NPs are added. Also the origin of possible impurities that hinder crystallization might be less mysterious near the electrode.

Ultrasonic vibration may play an important role because it is very difficult to find vertical branches for electrochemically grown Ag dendrites without ultrasonic vibration [76]. Such strong influence on the growth mechanism has been suggested previously for the case of Ag sono-electrochemical deposition on silica spheres from AgNO3 solution [77].

Copyright © 2010. Nova Science Publishers, Incorporated. All rights reserved.

2.3. Supported Ag Flowers with Flakes as Sub-Units

One can distinguish generally hierarchical micro structures with sub-structure on the nano-scale from true fractal dendrites. All such hierarchical structures (HSs) are promising for catalysis, as SERS active substrates, and for super-hydrophobic coatings (all partially due to large area to surface ratio), but they are also attractive building blocks for advanced nano-technological devices [78,79-81]. There are now many such HSs made from silver with NPs like rods, belts and sheets as sub-units [82,83-86]. Colloid chemistry can synthesize HSs with various morphologies, including coral-like [79], snowflake-like [80], leaf-like [81], dendritic [82,86,87], propeller-like [88] and flowerlike [86,89] structures.

Electrochemistry often allows one-step synthesis of HSs [66,78-81,85]. Such methods have prepared substrate-supported silver HSs with complex geometries such as disk arrays [90], micro islands [91], flowerlike patterns [92], fish bone-like [93] and other dendritic ones [66,93,94]. Most are synthesized in the presence of surfactants [79], templates [90,91,94], or on film-modified electrode surfaces [93]. The surfactants can bind strongly especially on HSs (again due to the large area to weight ratio), limiting their applications [95]. Templates complicate the procedure and limit the synthesis of large quantities [96].

We reported an electrochemical approach to fabricate 3D flowerlike silver HSs on the surface of a Pt film electrode (PFE) [97,98]. A 4 cm x 2 cm Ag sheet served as the anode and a 1 cm × 1 cm PFE substrate as the cathode 4 cm away in a mostly C = 3 mM aqueous AgNO3 electrolyte. The cathode was immersed half into the electrolyte (effective area 0.5 cm2).

Figure 10 shows SEM images obtained from an applied potential of U = 80 mV after t = 10 min. 10±1 μm diameter particles are distributed homogeneously over the substrate. A high-magnification (Figure 10c) reveals the flower like structures' flakes, which seem to intersect mutually sometimes. All of the flakes have smooth surfaces, outwardly wavy edges and uniform thickness. A magnification of the central portion (Figure 10d) of the flower shown in Figure 10c reveals that the average thickness of the flakes is 50 nm.

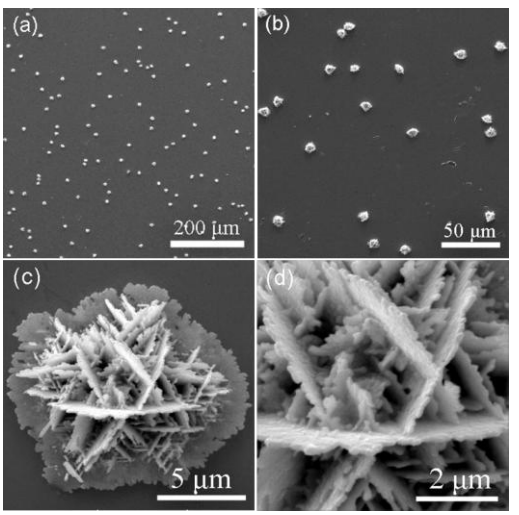

Figure 10. SEM images of HSs grown for 10 min on a PFE substrate (C = 3 mM; U = 80 mV). This figure is from [97].

Copyright © 2010. Nova Science Publishers, Incorporated. All rights reserved.

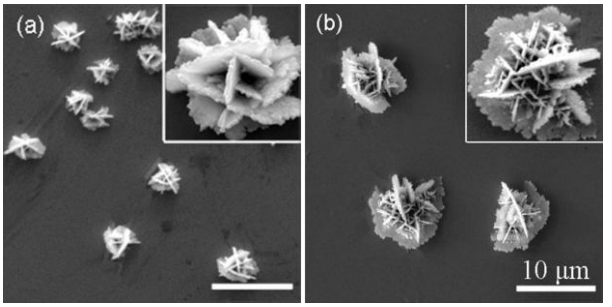

Figure 11. SEM images of HSs after deposition times of 2 min (a) and 5 min (b) (3 mM; 80 mV). The scale bar in (b) is the same as that in (a). This figure is from [97].

Figure 11 shows SEM images obtained from different deposition times while at C = 3 mM and U = 80 mV. When t was 2 min, the results are still flowerlike and they have an average diameter of 5.5 μm (Figure 11a). The HSs are only composed of several flakes. On increasing t to 5 min, the average diameter of the HSs increased to 7.5 μm and a higher density of flakes was observed (Figure 11b). At 10 min (Figure 10c), the average diameter of the HSs is 10 μm and they have a yet higher density of flakes; the inner structure is more compact. There is no number density change on the substrate with t, which is attributed to instantaneous nucleation of silver on the PFE surface. This is different from the electrochemical growth of flowerlike gold on substrates [88,99], where the number density changed with deposition time.

Particle structure also changes with deposition time t at 6 mM and 100 mV. When t was 1 min, the products still exhibit flowerlike structure and they have an average diameter of 1.4 μm (Figure 12a). The particles are only composed of several flakes. On increasing t to 2 min, the average diameter of the flowerlike particles increased to 2 μm and a higher density of flakes was observed (Figure 12b). After 5 min deposition (Figure 13c), $\langle d \rangle$ = 6.5 μm, and the inner structure is even compacter.

As shown in Figure 13, at a low potential (50 mV), the flakes within the particles have a small diameter and thickness, while the number of flakes is high. With increasing the potential, the flakes' thickness and the diameter of the silver particles are getting larger, but the number of flakes within individual particles decreases. Increasing potential does not result in larger particle diameters during the same deposition time, but the number density of Ag particles on the substrate increases. The higher potential increases the number density of silver nuclei.

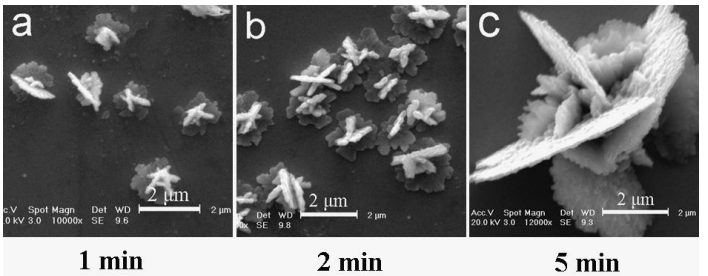

Figure 12. Flowerlike Ag particles grown on PFS from different deposition times. This figure is from [98].

Copyright © 2010. Nova Science Publishers, Incorporated. All rights reserved.

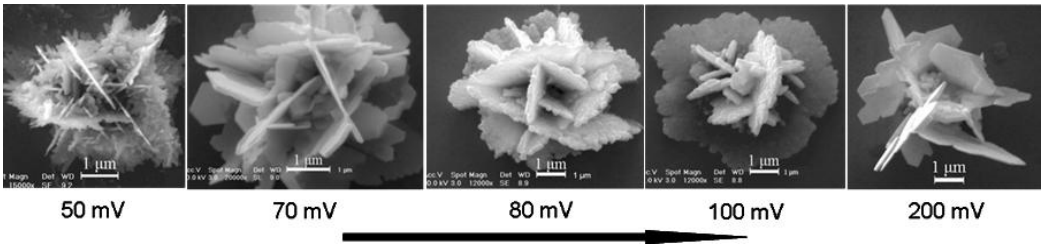

Figure 13. Differing applied potentials have led to different Ag particles after 2 min of deposition. This figure is from [98].

Quite similar HSs composed of flakes were also synthesized using a split galvanic cell method [100]. A copper plate immersed in CuSO4 solution and the same PFE immersed again in AgNO3 solution served as the cathode and anode. The two half-cells were linked by a salt bridge containing saturated KNO3 solution (Figure 14). The replacement reaction is $Cu + 2Ag^{+} \rightarrow Cu^{2+} + 2Ag$ and the total galvanic cell is represented by (−)Cu(s)|CuSO4(aq)||AgNO3(aq)|Pt(s)(+). Without direct contact to the sacrificial electrode and its impurities, a high purity Ag electrode is not necessary. However, the potential is uncontrolled and PVP is necessary to ensure formation of HSs.

The results are very similar to those above. The products grew uniformly dispersed on the substrate (Figure 15a) and have a flower-like morphology (Figure 15b). The mean diameter is 2 μm. They have many seemingly intersecting polygonal flakes again (Figure 15c), now with an average thickness of 40 nm. Figure 15d shows the XRD pattern of the sample, which is very similar to that of the products from above (e.g. shown in Figure 10). The most intensive peak at about $2\theta = 40°$ corresponds to Pt (111) of the substrate. The intense peak at 38.17° is the (111) diffraction of fcc silver (JPCDS card No. 4-783). Lines corresponding to other crystal face types are very weak. The (200) diffraction at 44.30° is barely visible above the noise. The intensity ratio of the (111) to the (200) diffraction line is much higher than the bulk Ag value of 4.7 [101,102], suggesting that the surfaces are mainly bounded by lowest-energy (111) facets [103]. Figure 15e shows the XPS spectrum (again almost equal to the products in Figure 10 for example) of the Ag 3d5/2 and 3/2 doublet binding energy located at 368.0 and 374.1 eV (kinetic energy is ~510.7 eV), which are close to that of pure metallic Ag [81,88]. The XPS results imply high purity and clean surfaces.

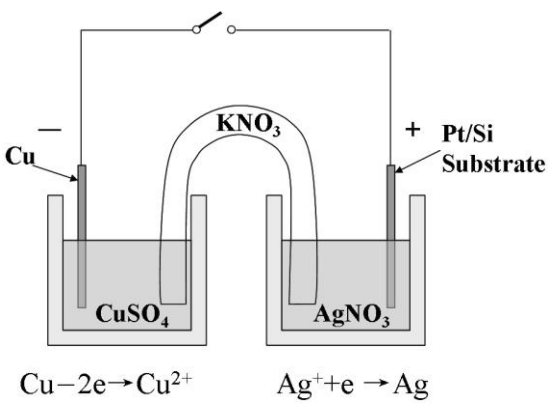

Figure 14. Galvanic cell used to synthesize HSMP. This figure is from [100].

Copyright © 2010. Nova Science Publishers, Incorporated. All rights reserved.

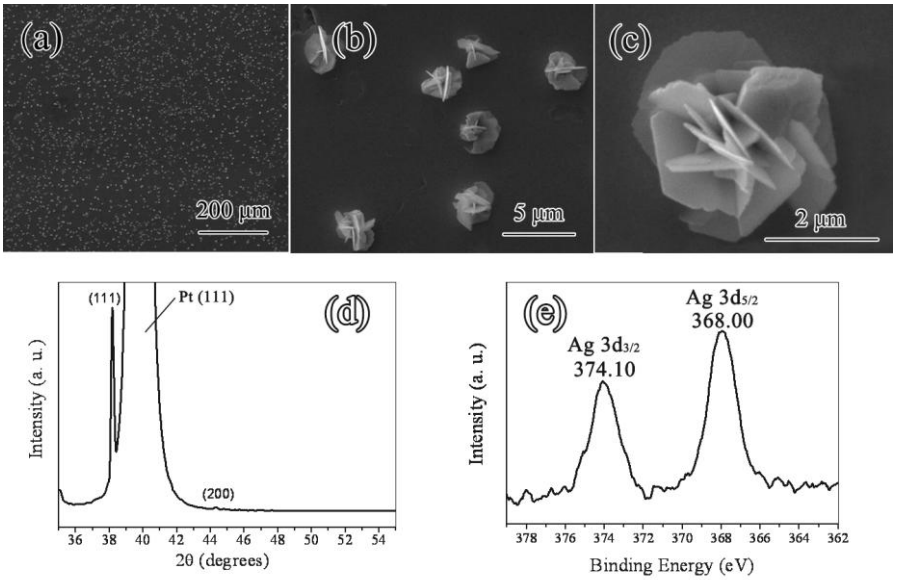

Figure 15. (a-c) SEM images showing the products synthesized in the presence of PVP (100 PVP monomers per Ag ion) at C = 25 mM and t = 3min, (d) XRD pattern and (e) XPS spectrum of the HSs on the Pt substrate. This figure is from [100].

At C = 12.5 mM, the distribution of HSs is sparse and the structures have few flakes (Figure 16a). At 50 mM, only large aggregates of irregular polyhedron like particles can be obtained (Figure 16b). What seems like the remnants of flakes can be found in some of these (inset Figure 3b). When C reaches 100 mM, flakes are absent and only large aggregates of polyhedral particles are observed (Figure 16c).

Silver deposition on the electrode (Figure 17) occurs by diffusion controlled nucleation and growth [104,105]. Silver adatoms are produced by the reduction of Ag ions via electron transfer. Silver nuclei will then be formed at random positions on the bare substrate due to the surface diffusion of atoms. Too low driving forces (U) can not induce silver nucleation, because the formation of a new phase has to go over an energy barrier connected with accumulation of initial atoms to form clusters stable enough to give birth to the new phase [106]. In the subsequent crystal growth, some adatoms join the already formed nuclei by direct transfer from solution. Ag atoms formed on the PFE will diffuse over the substrate and find existing nuclei sooner than other diffusing atoms. Thus, no new silver nuclei will be subsequently created on the bare substrate (similar to "instantaneous nucleation").

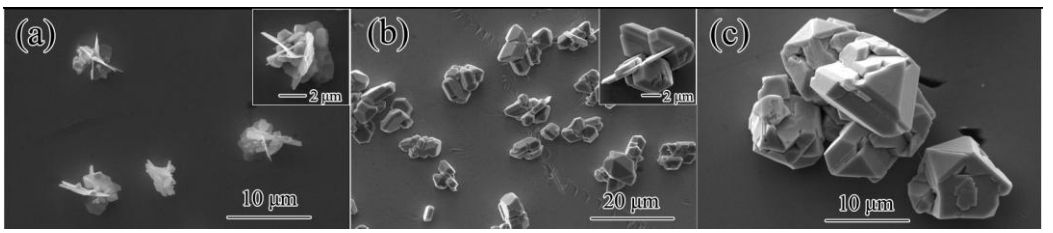

Figure 16. SEM images of the products depositd for 3 minutes in the presence of PVP at C =12.5 (a), 50 mM (b), and 100 mM (c). This figure is from [100].

Copyright © 2010. Nova Science Publishers, Incorporated. All rights reserved.

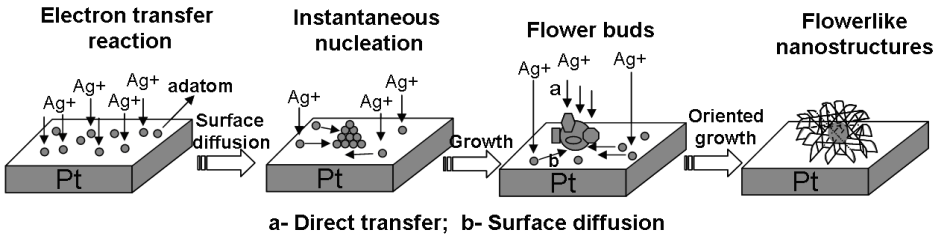

Figure 17. Formation of flowerlike silver on Pt substrate. This figure is from [97].

The nuclei act as a first "step of growth" [106] for subsequent incorporation of new adatoms. The diffusion shield effect [78] favors the Ag+ reduction on already present Ag flakes. Newly arriving atoms are continuously attached onto the surfaces of the silver structures. The driving force determines the growth rate differences due to surface energy differences on different crystallographic directions, leading to geometrical anisotropy. Kinetically-controlled anisotropic crystal growth occurs at small growth rates [107]. The applied potential driving the electrochemical reaction affects the growth in a similar way that additives manipulate the growth of nanostructures from solution [108], e.g. in the synthesis of tetrahexahedral Pt structures by an electrochemical treatment of Pt nano-spheres [109].

In our case, it is slow growth along the <111> orientation and fast growth along the {111} facets. The PVP used in the split-cell method does not select a different direction – it merely slows the process. There inevitably occur some random off-shoots into the slow direction that will grow and lead to the formation of secondary flakes with {111} facet terminations. Together with third and higher level flakes, HSs will finally result.

With the increase of Ag ion concentration, the driving force increases, and at some point, the conditions of kinetic growth can no longer be ensured. The same would likely happen with even higher voltages. A high number density of particles could be obtained by allowing nucleation under a high potential but growth under low ones.

3. Silver Dendrite Based Bimetallic Structures

Noble metal dendrites are widely utilized as catalysts [83,110]. Bimetals often exhibit better catalytic activities than the corresponding monometallic counterparts [111]. Raised interest in bimetallic nanostructures comprised of noble metals such as Au, Ag, Pt, or Pd has been justified by their fascinating optical [112,113], electronic [114], and catalytic [115,116] properties leading to a wide range of applications including as SERS substrates [117], biosensors [118], and of course catalysis [119]. A variety of approaches have been investigated to prepare bimetallic materials, including simultaneous chemical reduction of mixed metal ions [120,121] and electrochemical reduction [122]. Among them, the reduction of metal ions on the surface of sacrificial nanoparticles, also known as galvanic replacement reaction (GRR) [123], is a simple yet versatile tool. GRR has been employed to synthesize bimetallic nanostructures in aqueous [124-127] or organic [128-130] media, among them hollow and porous [125,128] and core/shell particles [125-127,129].

Given all of the above, it is surprising that there are still only few reports on the creation of bimetallic dendrites [131,132]. We immersed Ag dendrites into a HAuCl4 solution. The

Copyright © 2010. Nova Science Publishers, Incorporated. All rights reserved.

GRR resulted in bimetallic Ag/Au nanostructures with a novel morphology having strongly enhanced catalytic activity [133]. The Ag dendrites find here a new application as they serve as a relatively inexpensive, shaped substrate that can lead to novel structures by providing unique starting conditions for the growth of other species.

3.1. Ag Dendrites by GRR from Copper

The Ag dendrites were also synthesized by a GRR with an apparatus similarly used for electro-deposition [134] with some modifications: the electrode was replaced with a thin copper sheet and the lower surface was changed from glass to a silicon wafer in order to facilitate later SEM observation. The replacement reaction needs no counter electrode and uses instead a glass slide for a spacer as illustrated in Figure 18. In a typical procedure, 0.05 M aqueous AgNO3 was placed into the space between a further glass slide on top and the silicon support. Ag dendrites start to grow immediately from the thin edge of the copper sheet exposed to the solution. After four minutes, the solution was drained, the Ag dendrites settle on the Si substrate, which was subsequently immersed in water to remove residual ions.

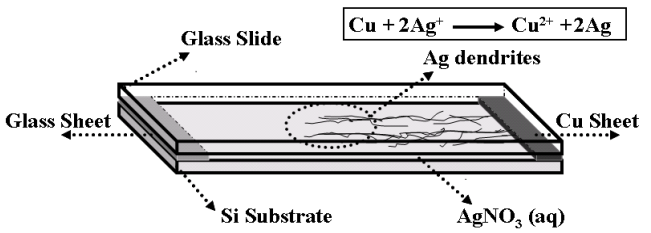

Figure 18. Sketch of apparatus used to synthesize Ag dendrites. This figure is from [133].

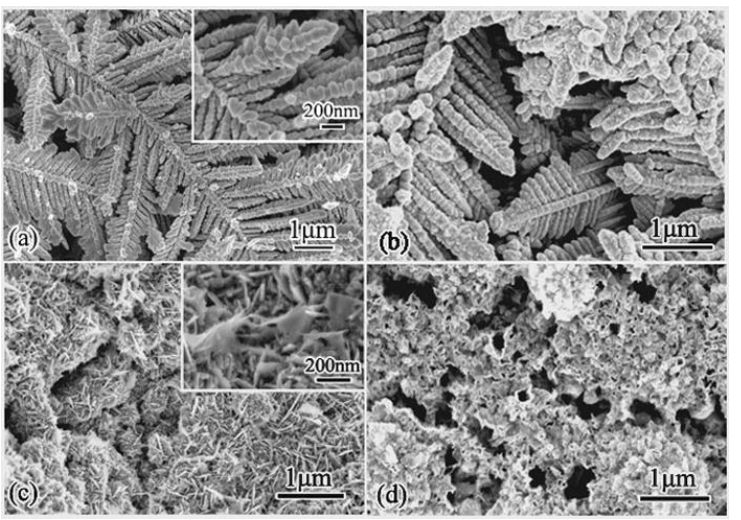

Figure 19. SEM images showing the initial Ag dendrites (a) and Ag/Au structures after t = 4 min (b), 8 min (c), and 12 min (d) of GRR. The insets are corresponding magnified views. This figure is from [133].

Copyright © 2010. Nova Science Publishers, Incorporated. All rights reserved.

Figure 19a is a SEM image of the Ag dendrites. The self-similar (fractal) hierarchical structure expected for a dendrite formed by diffusion limited growth is apparent. The branching angles are all 60°. Trunks and branches mostly consist of almost hexagonal "beads" (inset Figure 19a) of about 100 nm diameter. The EDX spectrum (Figure 20a) shows only the for Ag characteristic peaks. Figure 21a shows TEM images. From the SAED pattern of a region in a tip (inset) we identify the (111), (200), and the (311) planes of fcc Ag. The dendrite is highly crystalline, yet the two sets of diffraction spots also indicate the existence of a twinned structure. From the HRTEM (Figure 21b) we can also detect a lattice spacing of 0.235 nm which is the interplanar spacing of Ag (111).

3.2. Ag/Au Bimetallic Structures via GRR from Silver

Ag dendrites as were described in the previous section were immersed in 5 mM HAuCl4 for a reaction time *t* of up to 12 minutes [133]. Since the electrode potential of the AuCl4-/Au pair (0.99 V vs. standard hydrogen electrode) is higher than that of AgCl/Ag (0.22 V), silver undergoes a GRR: $3Ag + AuCl4^- \rightarrow Au + 3AgCl + Cl^-$. For every three Ag atoms removed, only one Au atom deposits on the remaining Ag dendrite. AgCl byproduct was removed with saturated NaCl solution.

As is shown in Figure 19b, while the overall shape is still that of the initial dendrite, the previously edgy beads quickly evolve into more spherical shapes and protruding flakes can already be identified even when the reaction lasted only $t = 4$ min. If the reaction proceeded for 8 min (Figure 19c), the dendrite is covered with flakes that stand on their edges on top of it. The flakes have a smooth surface and uniform thickness. The flakes also often mutually intersect and overlap (inset); they form the walls of the cavities that are the most recognizable feature of the structures gotten at even longer reaction times. We call Au-wall-build spaces "cavities" to distinguish them from the "pores" due to removal of Ag from the original dendrite. If the reaction proceeds for 12 min, almost all the flakes have disappeared and numerous cavities are visible instead (Figure 19d).

The gradual depression of Ag peaks and development of Au ones (Figure 20b-d) in the EDX profiles evidences the replacement of Ag with Au. The EDX analysis estimates the Au content of the samples to be 33, 60, and 90% for $t = 4$, 8, and 12 min of GRR respectively.

After reacting for 8 min, the Ag dendrites have become porous (Figure 21c) due to the consumption of Ag. The circled region's SAED pattern (top inset Figure 21c) displays discontinuous concentric rings, which implies a polycrystalline bimetallic structure. The generation of Au is re-analyzed by the EDX recorded from the same area (lower inset Figure 21c). The Ag/Au bimetal has an Au atomic percentage of 58.4%. The polycrystalline nature of the bimetallic product is also seen in the HRTEM image (Figure 21d). Various domains with different crystallographic orientations positioned around a pore can be identified. Analyzing the various domains' lattice spacing reveals some that can be assigned to (111) and (200) planes. Since the lattice structures of Au and Ag are too similar, it cannot be established whether these domains are Au, Ag, or mixed regions. Mutual solubility of Ag and Au leads to single crystalline Au/Ag alloys only at high diffusion rates due to high temperatures (e.g. boiling) [135]. Moreover, the surface of the structures here should be all gold. The polycrystalline nature of the obtained nanostructures is thus attributed to Au flakes inter-

Copyright © 2010. Nova Science Publishers, Incorporated. All rights reserved.

growing. The GRR turned almost single-crystalline Ag dendrites (up to twinning) into polycrystalline bimetallic Ag/Au nanostructures.

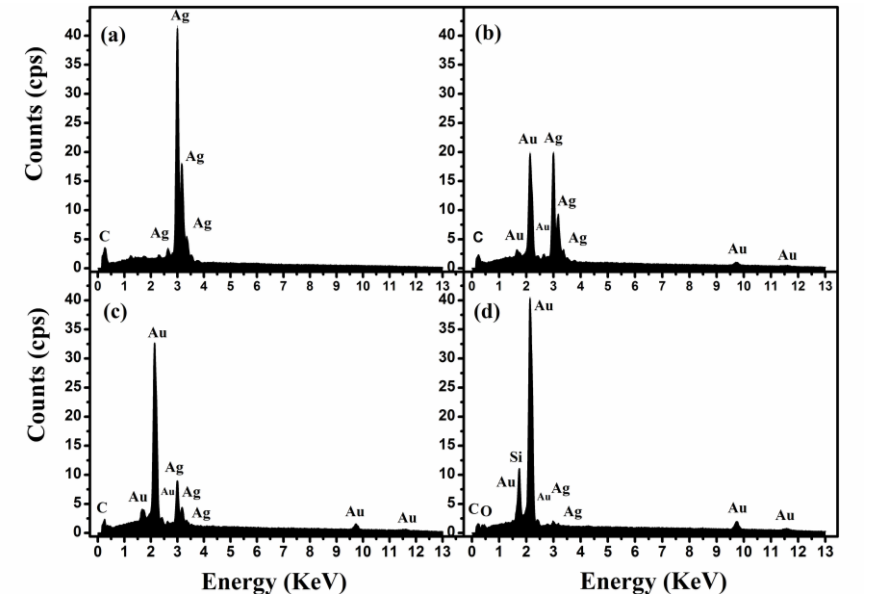

Figure 20. EDX profiles of the initial Ag dendrites (a), and Ag/Au structures after t = 4 (b), 8 (c), and 12 min (d) of GRR. This figure is from [133].

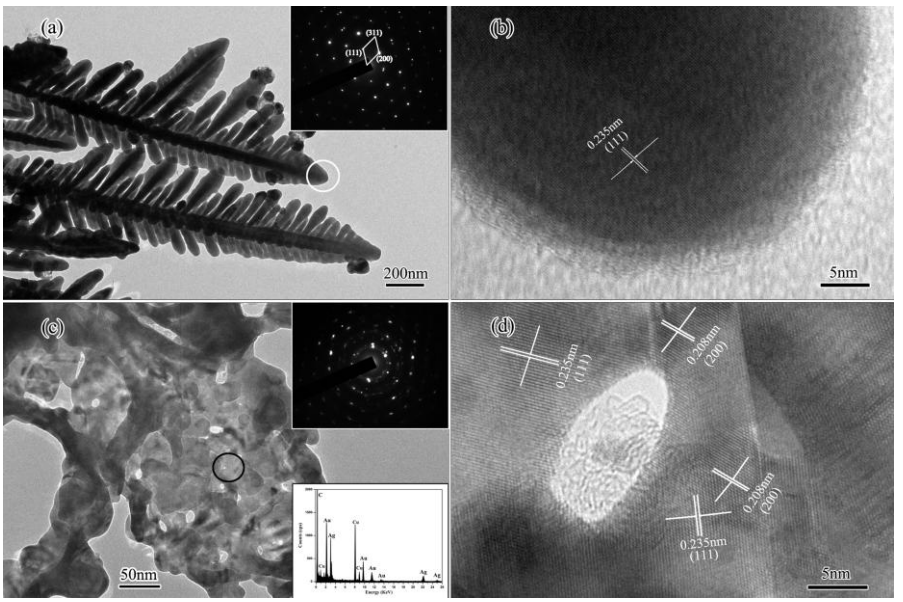

Figure 21. (a) TEM image of a typical Ag dendrite. The inset is the SAED pattern from the circled region; (b) HRTEM image of the circled area in (a); (c) TEM image of an Ag/Au (t = 8 min) sample together with the SAED pattern (top inset) and the EDX profile (lower inset) from the circled region; (d) HRTEM image of the circled area in (c). This figure is from [133].

Copyright © 2010. Nova Science Publishers, Incorporated. All rights reserved.

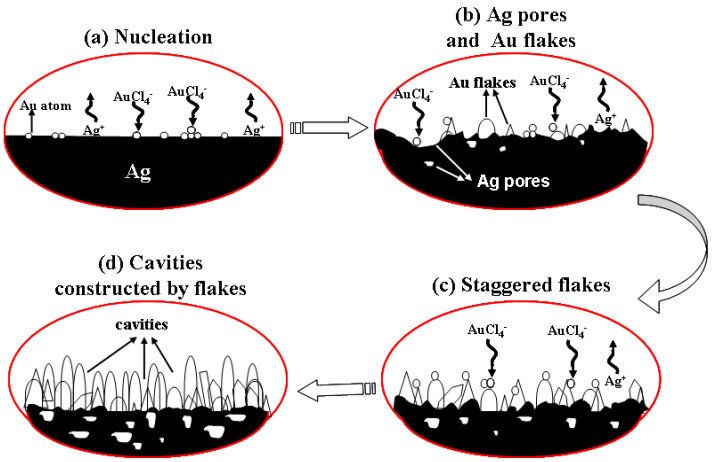

Figure 22. Formation of bimetallic Ag/Au structures in GRR. This figure is from [133].

The GRR unfolds as follows: AuCl4- deposits gold atoms on Ag dendrites while removing Ag (Figure 22a), leading to pores in the Ag dendrite and Au nuclei. The Au nuclei grow into flakes (Figure 22b) while nucleation continues, resulting in different sized flakes later on. The Ag surface is progressively covered with gold and the concentration of AuCl4- decreases, both slowing the GRR so that nucleation is terminated (Figure 22c). Finally, a porous bimetallic structure results from cavities between Au-flakes and pores inside the more and more depleted original Ag dendrite (Figure 22d), where the Ag pores are basically hidden from view by the Au flakes.

4. Ag Nanoparticle Doped Composites via Dielectric Micro Spheres

There are several reasons for putting metal NPs on or into micro sized substrates. Especially optical properties depend not only on the NPs' size [136] and shape [109], but also on their embedding and inter-particle coupling [137,138]. For example, the plasmon resonance band broadens and red-shifts when metal NPs are deposited on the surface of dielectric particles such as silica [139]. Some of this is due to the interaction with the matrix and some of it is attributable to the NPs interacting mutually.

Metal NPs can be produced in high yield using solution based methods, but their subsequent collection and assembly are major challenges [140]. Catalysis requires high particle number density, but NPs tend to aggregate under such conditions. Dispersion of active metal NPs on sub-micro substrates prevents their aggregation without compromising high surface to volume ratios and particle number densities. The composites are more conveniently separated and reused in catalytic applications and may serve as building blocks for functional devices like photonic crystals.

Control over the composites' structure is necessary to tune their properties and optimize them for such applications as catalysis of selected chemical reactions [141] or in the detection

Copyright © 2010. Nova Science Publishers, Incorporated. All rights reserved.

of macromolecules like DNA and antibodies via SPR shifts [142]. Regarding the latter for example, the use of silver NPs has the advantage of an initially relatively narrow plasmon resonance band in comparison with other metals [143,144]. Partially in order to address the problems mentioned above, increasing effort has been aimed towards the introduction of metal NPs on/into small dielectrics like silica, polystyrene and carbon to create composite structures. Such composites exhibit also unexpected properties [137,145-152] and find novel applications in many fields [3, 153-158].

4.1. Silica Spheres Doped with Ag Nanoparticles

Due to the electrostatic repulsion between a silica surface having negative surface charge and silver NPs in aqueous media [159,160], a direct deposition of NPs is quite difficult. In order to form the bonding between silver nuclei and silica, a modification of the silica surface is common in a variety of approaches such as pretreatment steps in electroless plating [161], seeding plating [162], surface functionalization [163] and layer by layer processes [164]. These are all multi step procedures, yet control over silver nuclei distribution and growth to ensure for example dense and uniformly grown yet also mutually isolated NPs are difficult to obtain.

A facile one-step ultrasonic electro-deposition method [165] can deposit silver NPs onto the surface of dielectric silica spheres. The silica spheres used as the substrates were prepared by a modified Stöber method [166]. Typically, a 1:5 mix of ammonia solution and ethanol is kept in a water bath at 35˚C. Then an equal amount of 1:5 mix of Si(OC2H5)4 and ethanol is added drop by drop under vigorous stir. The resulting silica substrates (Figure 23a-b) are spherical with smooth and bare surfaces and a diameter of (760±10) nm.

The setup for the deposition of NPs could again hardly be simpler and utilizes equipment we already introduced in previous sections: A two-electrode setup was partially immersed inside the 400 ml water of an ultrasonic cleaner. Two identical silver slices (effective surface area 2 cm×2 cm) were used as electrodes which were again 4 cm apart from each other. 40 ml of 0.325 μM silver perchlorate solution served as the electrolyte, in which 200 mg pre-prepared silica spheres were suspended by ultrasonic vibration for 10 min prior to the electrochemical reaction. Electrolysis was carried out with 0.75 mA/cm2 current density for half an hour. During the deposition, the electrochemical cell is under the continuous 50 W, 40 kHz ultrasonic radiation. The product was purified by five centrifugation/rinsing/re-dispersion cycles with deionized water and ethanol.

The attentive reader will have noticed that the electrolyte concentration is now in the μM rather than in the mM range as it was in section 0 for example, nevertheless, the current density is again in the mA range. An estimation taking into account the diffusion constant of ions in water will also only lead to a current of a few μA. This should not change by a factor of 1000 due to ultrasound assisted mass transport. In fact, the initial electrolyte cannot support that much current; it only seeds the spheres and gets the reaction started. This will be equally the case with all similar reactions here reported (i.e. the carbon spheres). The majority of the current is partially from the charged micro-spheres movement. They become little traveling capacitors once they have gotten Ag nuclei. Moreover, more positive Ag ions than negative

Copyright © 2010. Nova Science Publishers, Incorporated. All rights reserved.

ions can be in the of course always globally neutral solution once they are compensated for by negatively charged composite spheres.

The resulting Ag/SiO2 composite particles are rather uniform and still spherical (see SEM Figure 23c). The products have a diameter of (780±10) nm (Figure 23d). Higher magnification (Figure 23e-g) indicates that Ag NPs distribute homogeneously on the silica spheres. The NPs look uniform, are 8-10 nm in diameter, and the spaces between them are 2-3 nm. The SAED pattern of an entire composite sphere (Figure 23h) displays several diffraction rings, which emanate from multiple crystals on the silica sphere. The lattice spacing distances are 0.236, 0.144 and 0.123 nm, corresponding to (111), (220) and (311) planes of fcc silver (JCPDS No. 4-783). The crystal lattice of one of the NPs is visible in a HRTEM image (Figure 23i). The lattice spacing is about 0.232 nm, i.e. that of (111) planes of fcc Ag (0.236 nm). The insets are a local magnification (upper corner) and a FFT pattern (lower corner), which confirm the Ag-fcc structure. EDX analysis confirms strong Si, O and Ag peaks next to Cu and C peaks, but no other impurities can be detected. Cu and C result from the sample support. According to the EDX spectrum, the product's Ag/Si ratio is estimated to be 1:54.

Delicate control of reaction conditions is important for obtaining a homogeneous particle coating on the silica substrates. If the reaction rate is too fast, no silver particles will be deposited on the spheres. The silica substrate is dielectric and does not support electro-deposition. Deposition is successful only because silver is initially bonded by surface groups to form nuclei. The nuclei serve as nano-electrodes on which silver ions are attracted and reduced.

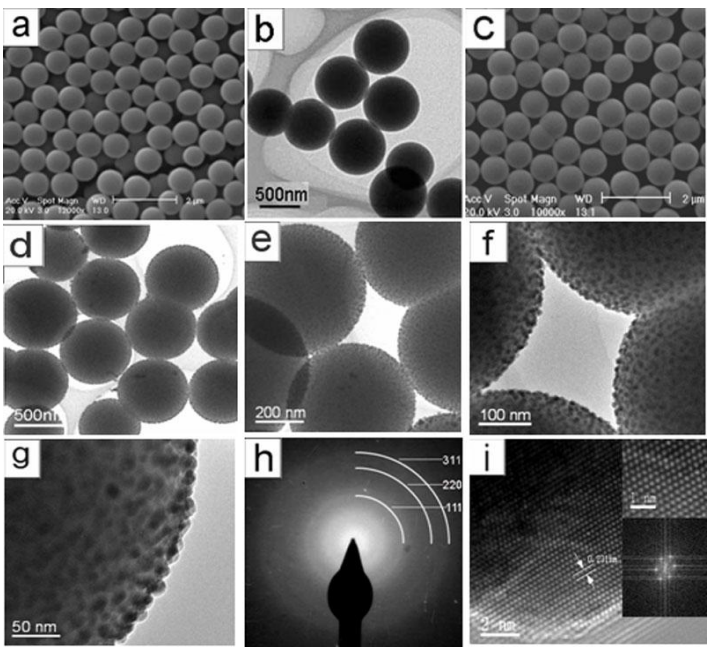

Figure 23. (a) SEM and (b) TEM images of bare silica spheres; (c) SEM, (d)-(g) TEM images, (h) SAED pattern of the Ag-silica compounds; (i) HRTEM image of a single Ag particle on the compound. This figure is from [165].

Copyright © 2010. Nova Science Publishers, Incorporated. All rights reserved.

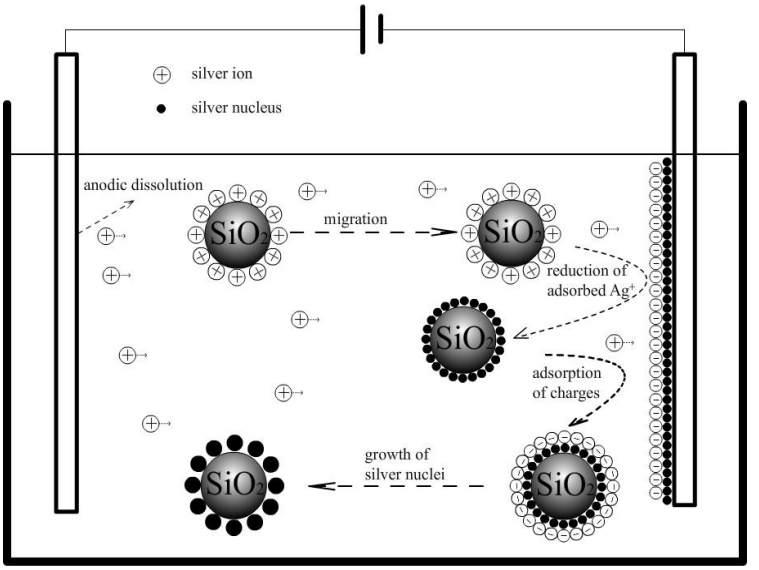

Figure 24. Formation of silver NPs on the surface of silica spheres by means of ultrasonic electro deposition. This figure is from [165].

In more detail, the growth mechanism is as follows (Figure 24): In the initial stage, the positively charged silver ions are attracted to the surface of colloidal silica spheres and form a silver ion layer. The starting pH of the electrolyte solution was 9. The surface of as-synthesized silica colloids is terminated with silanol groups (Si-OH), which are negatively charged at an pH above 7, i.e. Si-O- groups stand out. A moderately strong chemical bond between the siloxane oxygen and elemental Ag (Si-O-Ag) [167] occurs now already or whenever the particle contacts the cathode and the silver ion is reduced. A cluster model and molecular orbital theory [168] show that a direct and primarily covalent bond can be established between elemental metals such as Fe, Ni, Cu, and Ag and the oxygen anions on the surfaces of clean sapphire. The silver ion-silica intermediates migrate to the cathode. When silica spheres collide with the cathode, silver ions bonded to the surface of silica spheres are deoxidized to produce bonded Ag. Subsequently, the bonded Ag serves as a nucleation site for further growth. Due to the ultrasound, the Ag-nuclei loaded silica spheres move ceaselessly in the electrolyte. Whenever they hit the cathode, the silver nuclei take up electrons and afterwards behave like cathodes themselves, which makes it possible to continuously attract and reduce silver ions supplied by the solution and the silver anode.

4.1.1. Thermal stability of Ag NPs on silica spheres

Ag/SiO2 composites have chemical bonds (Si-O-Ag) [165,169-171]. This bonding is expected to fail in a similar temperature regime as the surface groups on SiO2-spheres, namely the Si-OH groups also break [172]. Silica colloids undergo a series of changes when exposed to high temperatures. The absorbed water (ca. 5 wt. %) will be released at 150˚C. Silanol groups crosslink via dehydration in the range of 400-700˚C. The physical and chemical properties of the metal NPs themselves are also temperature-dependent [173-175]. Ag NPs show low-T sintering, for example, Ag NPs of 20 nm diameter sinter at 150˚C [176].

Copyright © 2010. Nova Science Publishers, Incorporated. All rights reserved.

Since many applications involve heat, it is important to investigate the thermal stability of SiO2/metal composite particles.

In situ observation is useful for the study of temperature-induced phase transformations like interfacial diffusion [177,178]. We used a JEM-200CX TEM equipped with a heated sample holder in order to investigate the shape evolution and thermal stability of the SiO2/Ag composites introduced above [179]. The particles were dispersed on an ultrathin amorphous carbon film supported by standard Cu grids. The 0.1 mPa vacuum of the TEM eliminates the effects of extrinsic factors (such as humidity, surface adsorbents, oxygen and so on). Therefore, the thermal stability is here only affected by intrinsic factors such as the size and morphology of Ag NPs, and the interfacial binding between the NPs and the SiO2 substrate.

The heating was commenced at r.t. and ended at values up to 800˚C as measured by a thermocouple in the heater. Above the glass transition temperature of amorphous silica at 800˚C, silica particles will fuse into aggregates. The imaged region of a specimen is heated by the electron beam. This results in errors of 15˚C according to the TEM laboratory's tests. Low electron intensity was also chosen. Specimens annealed at different temperatures in the JEM-200CX microscope were later further analyzed in a high resolution FEI TECNAI F20 microscope.

Figure 25 shows a series of TEM images of a SiO2/Ag composite particles during heating. Below 550˚C, the shape of most Ag NPs in the sample shows no obvious change (Figure 25a-e). Above 550˚C (Figure 25e-f), the NPs changed gradually from semi-spherical into more spherical shapes having a smaller radius of curvature (see also Figure 27). At temperatures around 750˚C, the Ag NPs desquamate gradually from the SiO2 sphere. Figure 25g displays the almost bare SiO2 substrate with only a few Ag NPs after heating to 750˚C. As shown in Figure 25h, the desquamated Ag NPs are spherical with a diameter of 9-12 nm. Note that the sample was firstly annealed for 20 min in the JEM-200CX microscope and then imaged in the FEI TECNAI F20 microscope. Figure 25i is a HRTEM image of one single desquamated Ag nanoparticle. It is a perfect single crystal 9 nm in diameter.

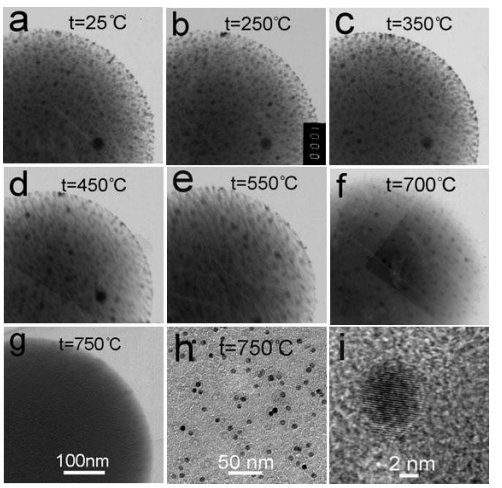

Figure 25. (a)-(g) A series of TEM images of a SiO_2/Ag composite particle heated in situ from 25 to 750˚C, exhibiting shape evolution and desquamation of Ag NPs from the surface of the SiO_2 substrates. The scale bar in (g) is the same as those for (a-f). (h) TEM image of desquamated Ag NPs and (i) HRTEM image of a single Ag nanoparticle in (h). This figure is from [179].

Copyright © 2010. Nova Science Publishers, Incorporated. All rights reserved.

Two sets of samples were further observed with a TECNAI F20 microscope to show the shape evolution more clearly. One is the as-synthesized SiO2/Ag composite particles, and the other is a sample annealed at 650˚C for 20 minutes. With the former, Ag NPs with sizes of 8-11 nm (width at half their height) are dispersed homogeneously on the surface of the spheres (Figure 26a-b). The Ag NPs are hemispherical (Figure 26c-d) with rough surfaces. The average distance between the bottoms of two adjacent particles is 3 nm. The morphology of the annealed Ag NPs on SiO2 sphere is spherical with smooth surfaces and the diameter is in the range of 9-12 nm (Figure 26g). The average space between two adjacent particles is 5 nm. The mutually isolated Ag NPs have not coalesced, as is confirmed by the fact that the volumes of the Ag NPs before and after annealing are equal. The average volume of the hemispheres and the spherical Ag NPs are calculated to be about 1133 nm3 in Figure 26c and 1149 nm3 in Figure 26g.

The Ag NPs are inclined to take on a spherical shape to minimize their surface energy. Surface diffusion increases along with temperature and leads to atomic rearrangement [177]. At some point, surface pre-melting, i.e. the formation of a liquid layer covering solid Ag, occurs. Amorphous SiO2 is not wetted by liquid Ag. The interface tension γ between liquid Ag and SiO2 points tangentially inwards (see also Figure 27). Surface tension compels this liquid layer to circle the solid Ag. As the temperature increases further, the contact area between solid Ag NP and SiO2 shrinks. The Ag NPs experience a shape evolution from semi-spherical to spherical with a smaller radius of curvature and a smoother surface in the temperature range of 550-700˚C, which indeed coincides with the temperature range were silanol groups crosslink via dehydration (400-700˚C). At 700˚C, the particles become spherical and are only in point-contact with the silica sphere. Then, the Ag NPs begin to slide off the surface of the silica support. At 800˚C, almost all NPs fell off the substrates as spherical NPs.

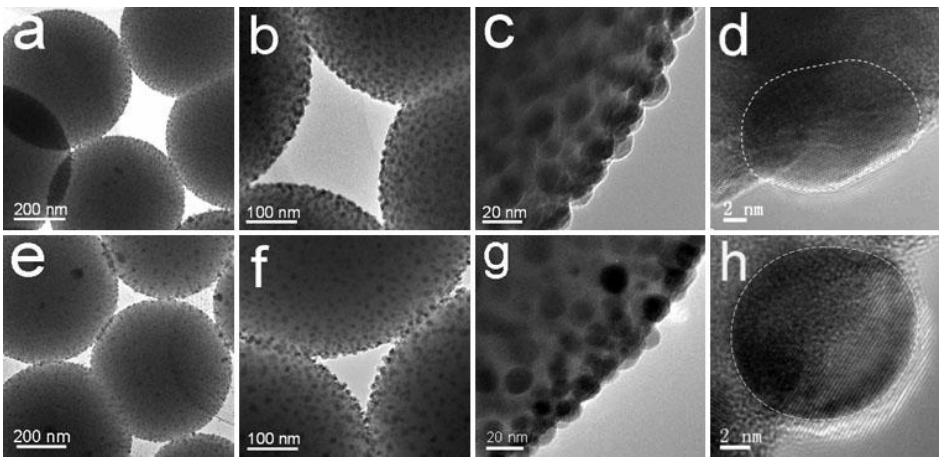

Figure 26. TEM images of SiO_2/Ag composite particles at r.t. (a)-(d) and after heating to 650˚C (e)-(h). To highlight the shape evolution, dashed curves are portrayed along the boundaries of the NPs shown in (d) and (h). This figure is from [179].

Copyright © 2010. Nova Science Publishers, Incorporated. All rights reserved.

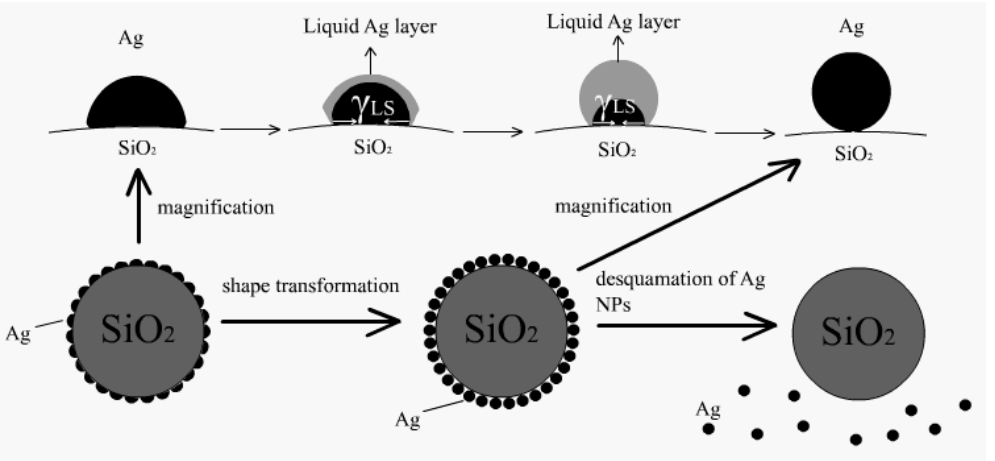

Figure 27. Shape change and desquamation of the Ag NPs. This figure is from [179].

The thermal stability of metal NPs is dependent on their size. SiO2/Ag composite particles with Ag NPs of different sizes were therefore investigated. The average size of Ag NPs shown in Figure 28a is 25 nm. The SAED pattern of an entire composite particle (inset Figure 28a) indicates that the Ag NPs are randomly oriented on the SiO2 surface. The shape of Ag NPs shows no obvious change up to 650˚C (Figure 28a-c). This is expected because the surface pre-melting temperature gets higher with the size increase of metal NPs (they are all of course much below the melting point of bulk Ag at 961˚C). The shape evolution of the 25 nm Ag NPs occurs in the range of 650-750˚C (Figures 28d-e). At 800˚C (Figure 28f), most NPs desquamated, which is confirmed by the SAED pattern (inset Figure 28f).

Also the desquamation of the larger Ag NPs happens at higher temperatures than that of the smaller NPs. This may be a hint as to the metal's properties (size dependent melting transition) and involved interfacial surface tensions being more important for the observed phenomena than the temperature at which the Si-O-Ag bonds break.

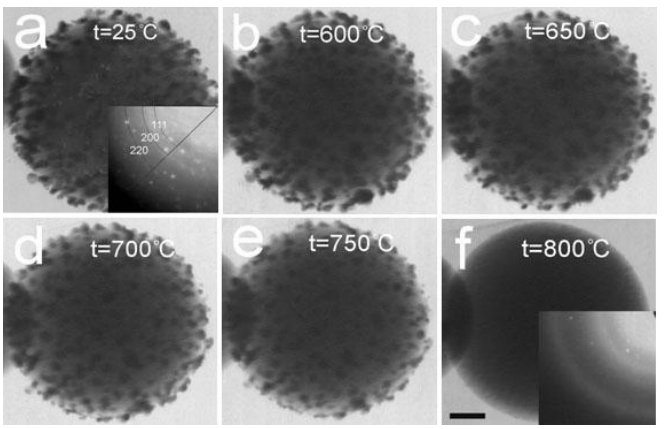

Figure 28. A series of TEM images of a SiO_2/Ag composite particle heated from 25 to 800˚C. The scale bar in (f) is valid also for (a-e). This figure is from [179].

Copyright © 2010. Nova Science Publishers, Incorporated. All rights reserved.

4.2. Carbon Spheres Doped with Ag Nanoparticles

Carbon spheres were prepared by a modified hydrothermal synthesis from sucrose precursor. Typically, 300 mM aqueous sucrose solution filled an 80 ml autoclave half. The autoclave was held at 190˚C for 3 h. The product was purified by repeated centrifugation/re-dispersions cycles with deionized water and ethanol. Figure 29a shows the product. The carbon spheres are narrowly size distributed with an average diameter of 800 nm. The HRTEM image (Figure 29b) shows the nano-pores [180] which seem to be too small for most molecules, however, BET measurements have confirmed that at least N2 can enter the spheres and later experiments showed that one can even dope Ag NPs into the inside of these spherical micro substrates.

When amorphous carbon spheres are used as substrates, silver NPs can be deposited homogeneously on their surfaces [180] just like with the SiO2 spheres above. Preparation of silver perchlorate electrolytes and the equipment for ultrasonic electro-deposition are as before. 40 mL of 3.25 μM silver perchlorate solution served as the electrolyte in which 150 mg carbon spheres were suspended by ultrasonic vibration prior to electro-deposition. Electrolysis of the slurry was carried out with a current density of 2mA/cm2 for half an hour. During the deposition process, the electrochemical cell was continuously radiated by the same ultrasound again. Figure 30 shows TEM images of carbon spheres before (a) and after coating (b). Countless silver NP are uniformly dispersed on the surface of the spheres. The NPs have a narrow size distribution (diameter of 12-16 nm) and are well separated despite their high number density. HRTEM again recognized the NPs as being single crystalline fcc Ag.

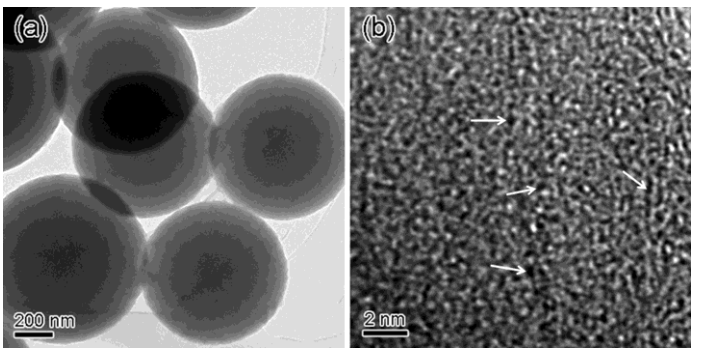

Figure 29. TEM (a) and HRTEM (b) images of carbon spheres synthesized from a hydrothermal reaction of a 300 mM sucrose solution for 3 h at 190˚C. This figure is from [195].

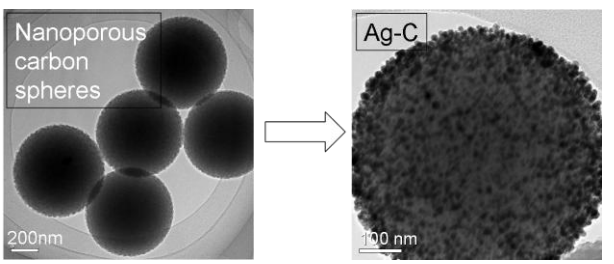

Figure 30. TEM images of (a) porous carbon spheres and (b) a Ag/C composite particle. This figure is from [180].

Copyright © 2010. Nova Science Publishers, Incorporated. All rights reserved.

It should be noted that this deposition was carried out without PVP reducer and that all Ag NPs are outside on the surface of the spheres. FTIR spectra of the carbon spheres before and after deposition of NPs show bands attributed to C–OH stretching and OH bends, which imply the existence of large numbers of hydroxyl groups on the as prepared carbon spheres. After being loaded with silver NP, the intensity of these bands decreases, indicating the rupture of OH bonds and implying the formation of C–O-Ag bonds very similar to what we have met in section 0 before where Si-OH and Si-O-Ag was involved instead.

4.2.1. Ag nanoparticles inside carbon spheres

Depositing metal NPs on the outside of dielectric spheres [145-148, 165] is often characterized by non-uniform distributions, low densities, and poor long-term stability of NPs [138]. Embedding metal NPs inside enhances stability, lowers toxicity and can alter electro-optical properties due to the NPs' differing collective interactions [138] and the matrix embedding. There are few reports on the creation of highly dispersed metal NPs contained inside dielectric spheres [137,181,182]. Methods aimed at silica dielectric for instance all form the NPs in-situ in an ongoing modified Stöber reaction, which makes it difficult to control the size and density of NPs. It remains challenging to introduce NPs into pre-prepared spheres and have the NPs well dispersed with widely controllable sizes and densities.

PVP is often employed as a stabilizer in the preparation of composite spheres [183-186] and to reduce noble metal ions (e.g. Au, Ag, Pd, and Pt) to prepare metallic nanostructures [187-189]. MW heating allows a rapid synthesis of nanostructures [190-193] and matrix deposition of metal NPs [194]. Pre-prepared porous carbon spheres can be doped with Ag NPs internally by micro waving them in aqueous solutions with the assistance of PVP as reducer [195].

250 mg of pre-prepared (section 0) carbon spheres were dispersed in 50 ml 2mM Ag(NH3)2NO3 solution and vigorously stirred for an immersion time of 2 h at r.t. After addition of 50 mg PVP and vigorous stirring for 1 min, the suspension was put into the MW oven for a reaction time of 10 minutes using an average power of $\langle P \rangle = 140$ W. The resulting suspension is opaque and dark black with a yellowish taint that is removed through subsequent washings [195].

The resulting composite spheres (Figure 31) show a large number of Ag NPs that must be inside the spheres as none are visible on the rims of the spheres' 2D projections. The NPs have a high number density yet are still well dispersed as mostly from each other isolated particles. Some NPs overlap only because TEM renders 2D projections of 3D objects. The apparent NPs number density decreases towards the outside of the spheres projections, further corroborating their dispersion inside the sphere. The SAED pattern (inset Figure 31b) of the entire Ag-NPs/C composite sphere displays several diffraction rings due to numerous crystals within the sphere. The inter-planar spacings of 0.23, 0.21, 0.14 and 0.12 nm correspond to the (111), (200), (220) and (311) planes of fcc silver (JCPDS 4-783). Higher magnification (Figure 31c) reveals the NPs to be almost spherical. A sample of 100 NPs resulted in a diameter of $d = (10 \pm 2)$ nm. Still higher magnification (Figure 31d) clearly shows that the NPs are separated from each other.

Copyright © 2010. Nova Science Publishers, Incorporated. All rights reserved.

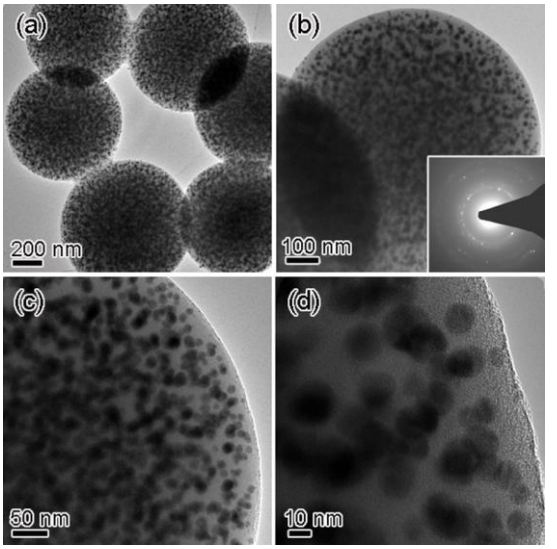

Figure 31. TEM images of Ag-carbon spheres. The inset of b shows the corresponding SAED pattern of a single composite sphere. This figure is from [195].

One may suspect that only the overall energy radiated should be of influence i.e. that using 140 W for 10 min equals maintaining 560 W for 2.5 min. However, this is not the case. At MW power levels above 140 W, the NPs get larger towards the spheres' centre (not shown). This may indicate a higher pressure *p* inside the locally heated dielectric spheres, especially at short warm-up times from r.t. to the boiling point. Solution and heat escaping towards the outside result in pressure and temperature gradients. The higher values towards the middle lead to larger NPs there. The outermost layers may even be free of NPs due to a fast outflow of solution, consistent with the high BET surface after reaction. The BET surface area of the carbon spheres increased from 13 m2/g before doping to 21 m2/g afterwards. The pores have opened up further because of the strong local MW heating [190,194] of the spheres that triggers pressurized expulsion of solution from the inside through the outer layers.

The use of MW may be vital here also in order to have hot spots [190,194] occurring inside the CSs, thereby leading to the short reaction times compared with experiments at or below solvents' boiling temperatures [183], where reduction with help of PVP usually takes on the order of hours. Ultrasound assisted reactions can have local hot spots due to bubble cavitations, too, but such mechanisms cannot work inside the dielectric sphere's pore structure. Ultrasound electro-deposition without PVP grows NPs on the surface of carbon spheres [180] (see section 0). This is consistent with a possible role of bubble cavitations at the surface. Our control experiments also show that no silver NPs form just micro waving in the absence of PVP reducer.

The growth mechanism needs to be investigated further in future research. It seems unlikely that PVP can enter the carbon sphere all the way through the narrow nano-pore network. The PVP chains are on average 360 monomers long and every VP monomer has a carbon ring as big as the average pore. The time between adding PVP and starting the reaction is only a few minutes. This compares to hours that the small precursor ions require to get inside of the sphere. The reduction process itself cuts the PVP chain at random positions,

Copyright © 2010. Nova Science Publishers, Incorporated. All rights reserved.

so the PVP becomes shorter. This however happens too late to allow PVP to enter the spheres' center. One could try to test whether very short reaction times lead to Ag-NPs being absent from the spheres' centers.

What seems clear from the dependence on immersion time (unpublished results) is that precursors initially diffuse into the spheres along interconnected pores. If they all entered during the reaction time, there should be little difference between say 2 or 12 h of immersion time. At no point in time can as many positive ions as there are Ag atoms present in the composite shown in Figure 31 be inside the carbon sphere without the electric charge being compensated by negative charges. Also the NO3- ions enter the sphere. After addition of PVP, the carbon spheres will be covered in PVP. Under MW irradiation, [Ag(NH3)2]+ related ions are reduced by taking up electrons from the carbon. Since carbon is relatively electrically conductive [196], it is sufficient that the PVP is a surfactant and sticks to the sphere's surfaces, in order to be able to replenish the electrons taken up by the reduction. Electrical charge can accumulate only very little of course, and so it is vital to include the NO3+ ions into the description. The negative ions leave the carbon sphere at the same time the PVP's electrons enter the carbon.

5. OPTICAL PROPERTIES

5.1. UV-Visible Absorption

The absorption spectrum of pure Ag exhibits an absorption band at around 420 nm due to the SPR [146]. An absorption minimum appears at 320 nm; it corresponds to a minimum in the imaginary part of the refractive index (about 0.4) for bulk silver [197]. One will find both of these features in almost all the spectra shown in this section. However, the size and shape of metal nanoparticles influences the splitting, positions and widths of plasmon resonances [198]. Thus, absorption spectra can help in understanding the structure of NSs and tuning the morphology of the synthesized products can in turn tune the resulting optical properties.

UV-vis absorption spectroscopy was carried out on a Shimadzu UV-3600 UV-vis-NIR spectrophotometer with wavelength in the range of 300-800 nm. Before measurements, the samples were ultrasonically dispersed in water.

5.1.1. Free Ag NPs

The color of the Ag colloidal suspension obtained from the MW assisted synthesis described in section 0 is dark green (inset Figure 1a) and thus different from the characteristic yellow of silver colloidal solutions from conventional heating. Figure 31a is the UV-vis absorption spectrum of the Ag NPs synthesized by conventional heating. A broad absorption band typical of NPs with irregular shapes and broad size distributions is located around 455 nm. Figure 31b shows the absorption of the MW synthesized Ag NPs (Figure 1a). The main transverse mode [199] plasmon resonance band located at 410 nm is observed. Besides the main band, a shoulder extending to 670 nm is also present, which may correspond to the longitudinal mode [199,200]. The peak absorption is sharper and has less strength in the green range of the spectrum, hence the solutions greenish appearance. The absorption peak's sharpness results from the NPs' narrow size distribution.

Copyright © 2010. Nova Science Publishers, Incorporated. All rights reserved.

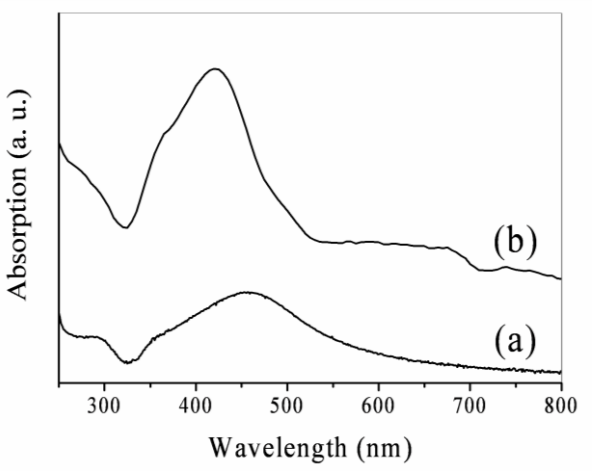

Figure 31. UV-vis absorption spectra of Ag NPs synthesized in 10 mM $Ag(NH_3)_2$ solution reduced by PVP with the PVP-monomer to Ag molar ration being R = 9: Of the sample from a 1 h synthesis at 80˚C (a) and from 7 min of MW irradiation (b). This figure is from [30].

Figure 32d presents the UV-vis absorption spectra of the products shown in Figure 32a-c from ultrasound assisted electro-deposition (section 0). The broad absorption peak around 415 nm is due to the SPR excitation of silver [201]. The fine structure complexity of the silver dendrites increases with the PVP concentration during synthesis (Figure 32a-c), which leads to features with small diameters and also inter-branch couplings similar to the inter-colloidal interactions in the case of NPs [202]. The former leads to the strong increase in UV absorption and the latter may contribute to the red-shifts of the plasmon peak in the visible (from 415 to 420 and 426 nm). The broadness of the bands obtained from high PVP concentrations stems from the broad size distribution of the involved structural features [203].

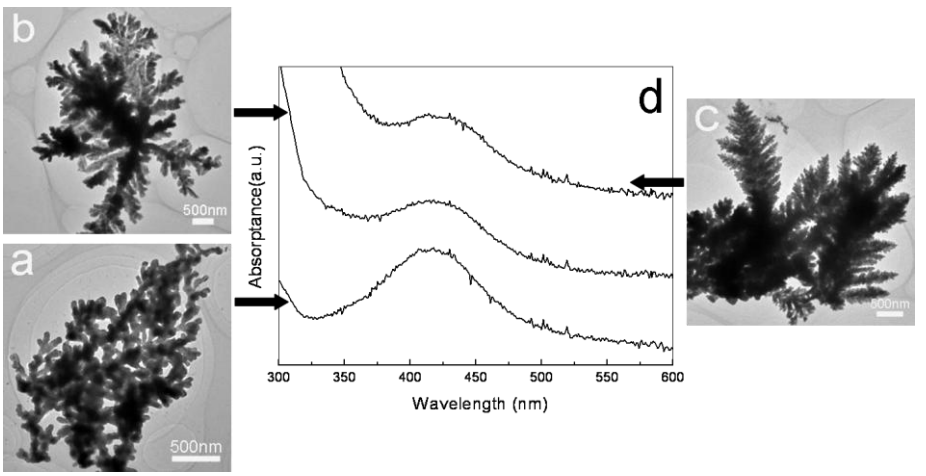

Figure 32. TEM images of the products from 10 minutes of ultrasound assisted electro-deposition in 3 mM of $AgClO_4$ with 1.25 mA/cm2 current density but different PVP-monomer to Ag molar ratios R = 10 (a), 80 (b), and 100 (c). (d) UV-vis absorption spectra corresponding to the products (a)-(c). This figure is from [41].

Copyright © 2010. Nova Science Publishers, Incorporated. All rights reserved.

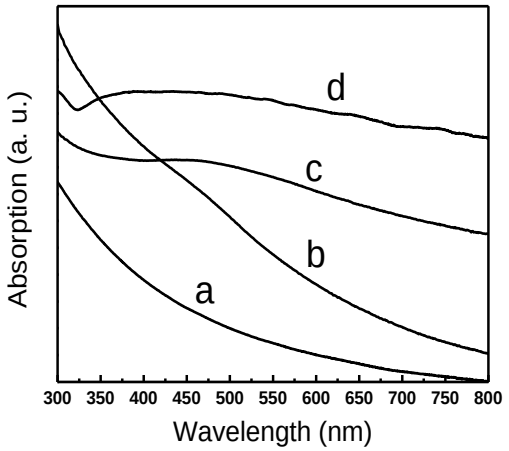

Figure 33. UV-vis absorption spectra of silica spheres before (a) and after deposition of silver NPs: silica spheres coated with isolated silver NPs (b) and coated with a continuous silver layer about 14 nm (c) and 20 nm (d) thick. This figure is from [165].

5.1.2. Ag on silica spheres

No peak in the visible range appears in the spectrum of uncoated silica colloids (Figure 33, curve a). A peak appears at about 480 nm (curve b) after the deposition of discrete silver NPs of 8-10 nm in diameter. With increasing the Ag coating towards a solid, continuous layer, a broad absorption peak near 500 nm (curve c) is established. The dipole-dipole coupling between neighboring NPs and Mie scattering of silver shells promotes red-shift and broadening of plasmon bands [204]. With an increase of the surface roughness and thickness of the silver layer, the extinction band is broadened greatly and covers the wavelength range from 320 to 620 nm (curve d). In addition, silvers' absorption minimum at 320 nm is discernable. The maximum absorption band shifted to shorter wavelengths, which is typically observed when a metal shell becomes completed [205].

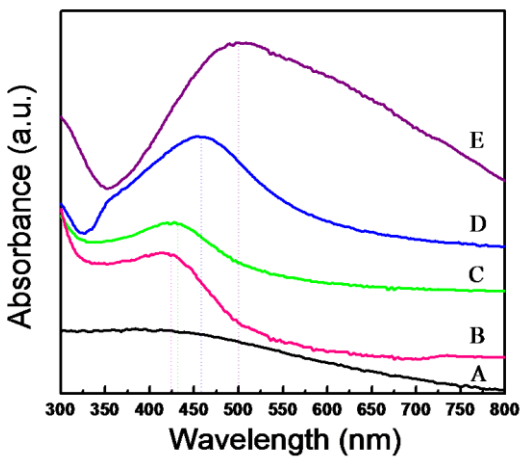

Figure 34. UV-vis absorption spectra of bare carbon spheres (A) and Ag-NPs/C composite particles with increasing Ag particle size and number density (B to E). This figure is from [195].

Copyright © 2010. Nova Science Publishers, Incorporated. All rights reserved.

5.1.3. Ag on carbon spheres

Figure 34 shows UV-vis absorption spectra of pure and doped carbon spheres like in section 0. The bare spheres (Figure 29) have no distinct absorption peak (A). The Ag-carbon composite spheres (like in Figure 30) with small and few NPs have a SPR resonance at 425 nm (B). When increasing the size and number of silver NPs, overall absorption increases, the absorption peaks become broader and stronger and the maxima red-shifts from 429 (C), to 460 nm (D), and to 500 nm (E). These changes are attributed to the dipole-dipole coupling between neighboring metal NPs [137,138,146]. Especially the broadening also results from the in-homogeneity in size and shapes [206]. Since the size and number density of the silver NPs are controlled by the reaction conditions, the optical properties of the composite spheres are tuneable.

5.2. Surface Enhanced Raman Spectroscopy

The intrinsic SERS capability of Ag is quite high [207]. Moreover, intricate structures, especially those with voids having parallel walls, facilitate the near-field coupling among NPs and greatly enhance the local electromagnetic field [208]. Two close metallic surfaces can enhance the electromagnetic field around molecules absorbed in-between, which leads to SERS enhancement [209-211]. High curvature features also can cause large enhancement (lightening rod effect) for molecules adsorbed on the tips of needles or on edges [212].

Closely distributed NPs having a narrow size distribution (monodispersity) may contribute to near-field coupling, because NPs with similar sizes have close SPR frequencies, and resonances will thus be coherently induced among the NPs. This leads not only to effects on the UV-visible absorption, but the fields maintained in between NPs may affect molecules that are adsorbed there. Many of the products discussed in this report are therefore promising SERS substrates.

For SERS investigation, 1 μM aqueous rhodamine B (RhB) solution was dropped on the samples. The samples were then dried in N2 and subjected to Raman scattering measurements using the 514.5 nm line of an argon laser (Jobin-Yvon T64000 triple Raman system).

5.2.1. Flowerlike Ag structures

The SERS signal from the flowerlike Ag nanostructures from section 0 (Figure 35 curve a-c corresponding to the particles shown on the right) is enhanced much over that from smooth platinum film (curve d). Most Raman shifts and the corresponding assignments agree well with the literature [94]. The strong SERS effect is related to the flake structure; the flowerlike particles possess many deep gaps among the flakes. This is consistent with the results from flowerlike gold [213,214] and silver dendrites [215].

5.2.2. Dendritic Ag/Au nanostructures

Figure 36 curve a shows the Raman spectrum when using RhB on a bare Si substrate. It is a featureless spectrum at the resolution chosen. Figure 36 curves b-f are the spectra of RhB adsorbed on Ag dendrites before and after GRR for t = 2, 4, 8, and 12 min, respectively (section 0). Most Raman shifts agree with the literature [216] (left inset), and only a few

Copyright © 2010. Nova Science Publishers, Incorporated. All rights reserved.

Raman shifts (underlined values) have no previous assignment. All curves show a base slope due to the fluorescence extinction effect [217].

From the four right bars that compare the plateau with the intensity of the strongest peak (aromatic C-C stretching at ca. 1649/cm) in curves b through e, we find that the enhancements by the Ag/Au t = 2 and 4 min samples are both higher than that of the pure Ag dendrites, although the SERS effectiveness of Ag is usually better than that of Au or alloys [218]. This SERS enhancement may be related to several factors. Firstly, surfaces of bimetals provide more possibilities for molecules to deposit on the boundaries between Ag and Au domains [117]. Secondly, adequate amounts of Au in homogeneous alloy (solid solution) may intrinsically enhance the SERS activity. However, since the intrinsic activity of Ag is much higher [207], the most important reason may not be related to the added Au directly, but rather the corresponding morphological change of the underlying Ag dendrite: The GRR leaves pores where Ag was depleted. The samples GRR synthesis time increases from 2 min to longer times, SERS enhancement decreases, because SERS-inactive Au covers the active Ag and its pores. Especially the 8 min and 12 min samples also possess rough surfaces and even more parallel flakes. However, as shown in curve e and f, their SERS enhancement is much below that of even the initial unmodified Ag dendrites. This is firstly because compared with the 4 min sample, the content of the SERS inert Au increases further. Again, this is simply due to the fact that deposited Au increasingly starts to hide the rough SERS-active Ag structure beneath. The roughness of Ag increases most strongly at the beginning of the GRR (e.g. t = 2 min).

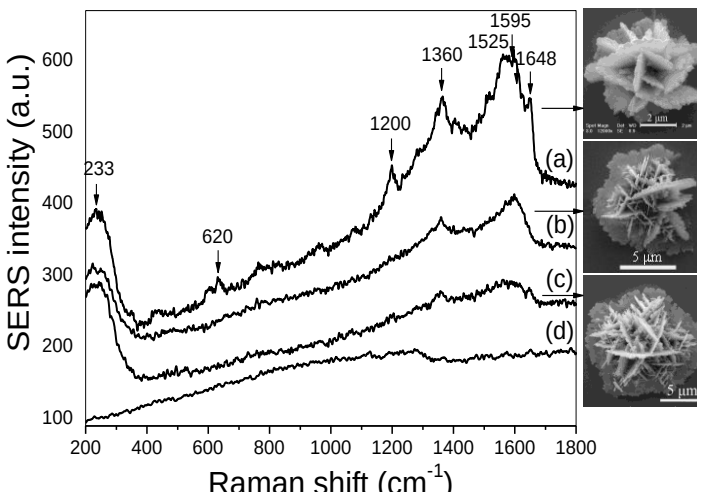

Figure 35. SERS of RhB adsorbed on flowerlike silver. Curves a-c: Ag particles shown on the right. Curve d: bare substrate. This figure is from [97].

Copyright © 2010. Nova Science Publishers, Incorporated. All rights reserved.

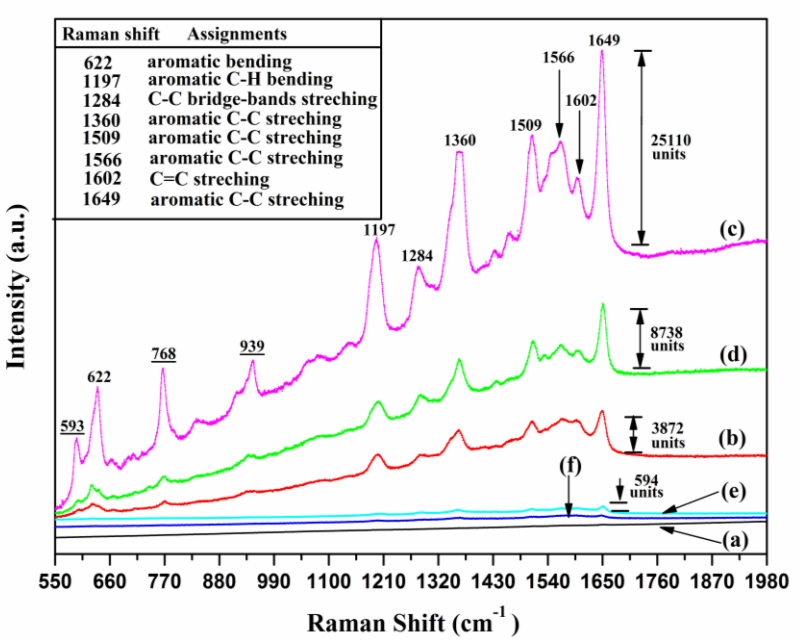

Figure 36. Raman spectra of RhB on a bare Si substrate (a), and on substrates covered by Ag dendrites (b), or (c, d, e, and f) Ag/Au nanostructures (t = 2, 4, 8, and 12 min). This figure is from [133].

6. Catalytic Activities

Many of the above discussed compounds have large active area to volume/weight ratios and moreover present nano-sized structures with selected crystallographic end-faces to the outside. They are therefore suspected to be catalytically active. It indeed turned out that some of the discussed structures are surprisingly active when used in order to promote reductions.

One should not misinterpret such results. The reduction of a molecule like 4-NP by sodium borohydride (NaBH4) is easily monitored and thus has been often reported. By now, that reaction constitutes a convenient standard allowing quantitative comparisons. However, the point of making new catalysts is certainly not in order to reduce 4-NP. A catalyst is supposed to find its own reaction specific niche in some mixture of molecules, in an environment constrained by the specific problematic of the desired application. High activity towards reduction of some benchmark molecule is a convenient hint that provides chemical researchers a promising base set of compounds to start out from. Reduction of a certain molecule is at most a rough hint for the activity towards reduction of a different molecule in a different environment. Moreover, repeatability, being able to resist catalyst poisoning, whether the catalyst can be conveniently retrieved from the reaction mixture, initial cost, environmental and human safety, scalability towards industrial production, and so on are all considerations that are often more important. It is therefore important to keep providing a diverse range of catalysts from scalable reactions and on convenient supports, even if their activity towards the reduction of a certain molecule does not beat all previously reported products.

Copyright © 2010. Nova Science Publishers, Incorporated. All rights reserved.

The discovery and development of new materials capable of efficiently and selectively converting raw oil, coal, and other feedstock into petrochemicals, and especially the isolation and storage of hydrogen in a future hydrogen based economy, require the development of novel catalysts and substrates.

6.1. Ag Nano Structures on Flat Substrates

Catalysts on substrates are very easily separated from the reaction mixture and cleaned for repeated use. To have catalysts directly on a conducting substrate makes them also useful for electrochemical reactions. We therefore decided to test the product as-prepared, i.e. on the Si/Pt substrate, and not scrape the Ag nanostructures first from the substrate in order to test a powder.

The catalytic activity of the flowerlike structures from section 0 was benchmarked via promotion of RhB reduction by NaBH4. 36 mg of NaBH4 was added to 10 ml of 0.01 mM aqueous RhB solution. The mixture was divided into two identical flasks. A Pt/Si plate loaded with the Ag particles was placed into one flask and, as the control, a bare Pt/Si plate into the other. The gradual bleaching of the yellow color in both flasks indicated the reduction of RhB. 0.2 ml samples of the mixtures were taken after 3, 6, 10, and 15 min of reaction time. The samples were immediately diluted with 3 ml of deionized water, and then characterized by an UV-vis spectrophotometer. The absorption and thus RhB content decreases in both samples (Figure 37), but the bare substrate is slightly less active (curve b). This should be mostly due to the presence of the Ag structures since the Pt surface around the Ag structures has not undergone any changes as far as any of the done characterizations can tell.

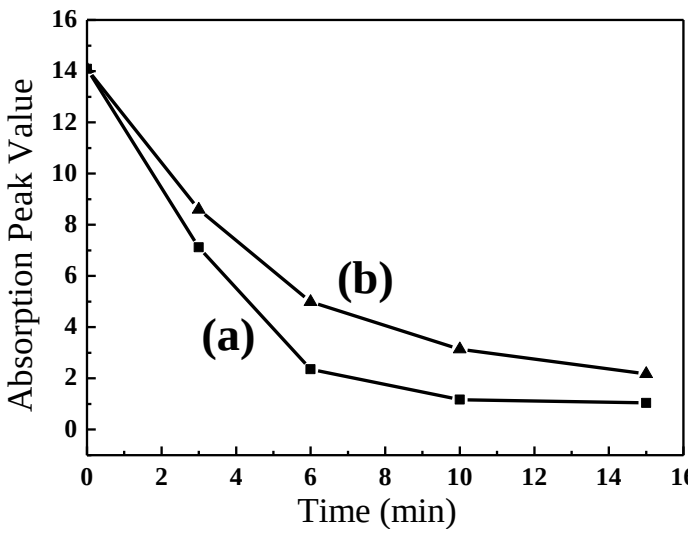

Figure 37. Plot of un-reduced RhB versus time: Reduction of PT substrate with flowerlike hierarchical Ag structures (a) and without (b). This figure is from [133].

Copyright © 2010. Nova Science Publishers, Incorporated. All rights reserved.

6.2. Dendritic Ag/Au Nanostructures

The Ag/Au bimetals are expected to supply significantly enhanced catalytic activity even compared with monometallic dendrites, because they moreover present the newly introduced metal on the surface of the original dendrite and also present metal/metal interfaces.

To study the catalytic activity, 1 mg of the Ag-Au nanostructures from section 0 were added into 2.8 ml of 4-nitrophenol (4-NP, NO2-C6H4-OH) aqueous solution (0.05 mM) under constant stir at r.t. A freshly prepared aqueous solution of (NaBH4) (0.20 ml, 0.1 M) was then added. The mixture was immediately transferred into a quartz cuvette with an optical path length of 1 cm and UV-vis absorption spectra were recorded to monitor changes in the reaction mixture.

The absorption maximum of 4-NP changed from 317 to 400 nm immediately after the addition of NaBH4 solution, which corresponds to a color change of light yellow to yellow-green due to the formation of the 4-nitrophenolate ion NO2-C6H4-O-. Without addition of catalyst, the reduction will not proceed and the mixture maintains a yellow color (inset Figure 38). In case of the reduction of alkaline 4-NP by BH4-, the kinetic barrier between the two negative ions is too high for the reaction to proceed. The presence of a catalyst is important for this redox reaction. When 0.6 mg of the Ag/Au bimetals (t = 8 min) were added, reduction of 4-NP proceeded rapidly as can be seen from the bleaching of the yellow color (inset Figure 38). Time-dependent absorption spectra show the decrease of the absorption peak at 400 nm and concomitant development of a new peak at 300 nm corresponding to 4-aminophenol (4-AP, NH2-C6H4-OH), the reduction product of 4-NP.

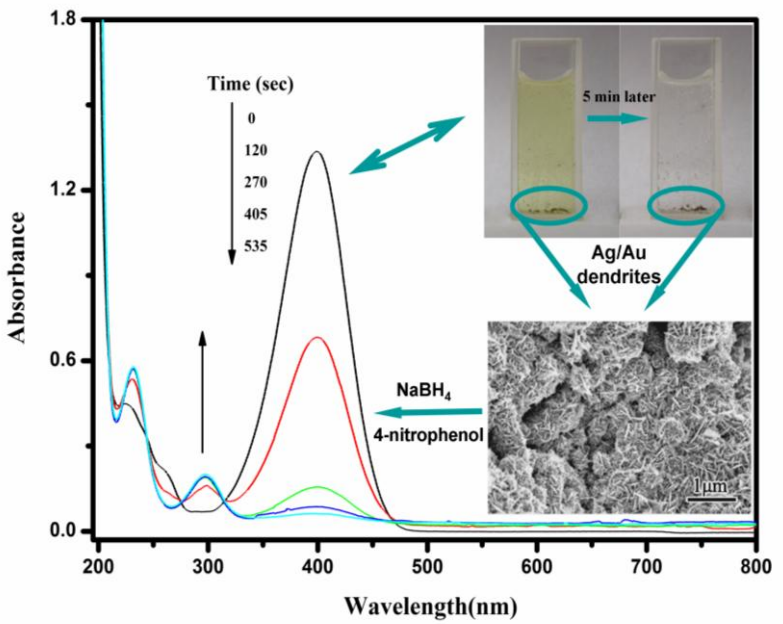

Figure 38. Successive UV-vis absorption spectra of the reduction of 4-NP in the presence of Au/Ag nanostructures. The insets show a typical SEM image of the product and the bleaching of the 4-NP solution. This figure is from [133].

Copyright © 2010. Nova Science Publishers, Incorporated. All rights reserved.

The concentration of BH4- is very high compared with those of 4-NP, and therefore essentially constant during the reaction. This high concentration protects the 4-AP from aerial oxidation [219]. Moreover, pseudo-first-order kinetics with respect to 4-NP can be used to evaluate the catalytic rate. A linear correlation with time in an ln*A* (*A* is the absorbance at 400 nm) plot obtains. The rate constant determined from this plot is 6.07 mHz, which is larger than those of previously reported catalysts [219]. The ratio of rate constant to the amount of the Ag/Au (t = 8 min) dendrites used is 10.1 Hz/g, which is much higher than that (0.35 Hz/g) for spongy gold [220].

Donors like the BH4- ions supply electrons to the catalyst, and thereby allow the 4-NP absorbed on the catalyst to take electrons at their leisure. The high catalytic activity may be firstly related to the number of Ag/Au interfaces. Ag has a lower work function than Au. Therefore, electrons leave the Ag from a thus depleted region near an Au/Ag-interface (Figure 39, region D). The Au ends up with an electron enriched region (E). These surplus electrons facilitate the take-up of electrons by 4-NP molecules that happen to be on top of these regions. The more interfaces there are, the more such regions exist. This in turn increases the chances for randomly absorbed 4-NP to happen to be on top of such regions.

Pure gold particles are generally not catalytic above 5nm diameter and the found rate constant of our t = 12 min sample (90% Au) is larger than that of conventional pure Au catalysts [220]. This suggests that the morphology is mostly responsible for the catalytic activity. The Au structure that is achieved by the GRR seems to be rather unique. Regardless of the as yet largely unknown details, the economical aspect of this bimetallic morphology is certain: Instead of having expensive material also making up parts of the structure that are actually inaccessible to reactive molecules (like stems of dense dendrites), these structures present an expensive catalyst (here Au) precisely where it is needed, namely at the accessible surface, on top of a much less expensive substrate (Ag).

6.3. Ag Nanoparticle Doped Carbon Spheres

When the Ag-NPs/C composite from section 0 was added to a 4-NP/NaBH4 mixture, the time-dependent absorption spectra (Figure 40) show the decrease of the absorption peak at 400 nm and concomitant development of a new peak at 300 nm corresponding to 4-AP as discussed above in section 0. The yellow color has completely disappeared after 25 min. The small amounts of products involved suggest that the Ag-NPs/C composites are effective catalysts for similar reactions. The rate constant k is again determined from the plot of ln*A* vs. reduction time (inset Figure 40). Reported ratios of rate constants k over the weight of catalyst employed are 1.30, 0.41 and 0.09 Hz/g for coral-like dendrite, banana leave like dendrite and spherical Ag nanostructures [55]. These are all lower than the 1.69 Hz/g of the Ag-NPs/C composites, although a substantial part of the weight is actually the carbon in this case. Comparing with other substrate-supported Ag NPs, the rate constant k of Ag-NPs/C composites is much higher than previously reported ratios for silver NPs supported on halloysite nanotubes (0.087 Hz/g) [221] and Ag-NPs-doped hollow poly(N-isopropylacrylamide) spheres (0.014 Hz/g) [222]. We believe that this has to do with the carbon matrix, but the details have to be investigated in further research.

Copyright © 2010. Nova Science Publishers, Incorporated. All rights reserved.

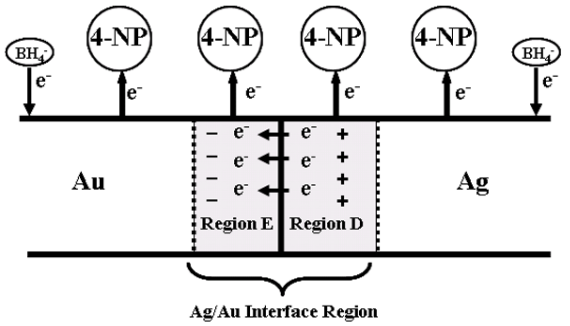

Figure 39. Diagram of bimetallic Ag/Au interface. This figure is from [133].

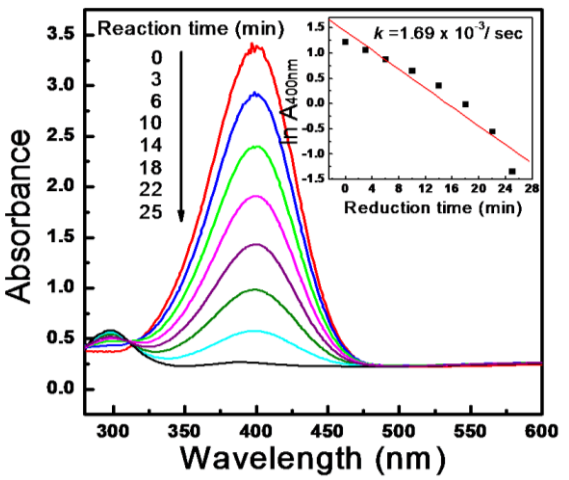

Figure 40. Successive UV-Vis absorption spectra of the reduction of 4-NP by NaBH4 in the presence of Ag-NPs/CSs composites. The inset shows the logarithm of the absorbance at 400 nm vs. reduction time. This figure is from [195].

ACKNOWLEDGMENT

This research was supported by a grant for the State Key Program for Basic Research of China (2004CB619305-2010CB631004), the National Natural Science Foundation of China (50831004), the Innovation Fund of Jiangsu Province (BY2009148), and the Postdoctoral Science Foundation of China (2007410326).

REFERENCES

[1] Maier, S. A., Brongersma, M. L., Kik, P. G., Meltzer, S., Requicha, A. A. G. & Atwater, H. A. (2001). Plasmonics-A Route to Nanoscale Optical Devices. *Adv. Mater. 13*, 1501-1505.

Copyright © 2010. Nova Science Publishers, Incorporated. All rights reserved.

[2] Deng, Z., Chen, M. & Wu, L. (2007). Novel Method to Fabricate SiO2/Ag Composite Spheres and Their Catalytic, Surface-Enhanced Raman Scattering Properties. *J. Phys. Chem. C*, *111*, 11692-11698.

[3] Nie, S. & Emory, S. R. (1997). Probing Single Molecules and Single Nanoparticles by Surface-Enhanced Raman Scattering. *Science*, *275*, 1102-1106.

[4] Kim, Y. H., Lee, D. K., Cha, H. G., Kim, C. W. & Kang, Y. S. (2007). Synthesis and Characterization of Antibacterial Ag−SiO2 Nanocomposite. *J. Phys. Chem. C*, *111*, 3629-3635.

[5] Huang, X., El-Sayed, I. H., Qian, W. & El-Sayed, M. A. (2006). Cancer Cell Imaging and Photothermal Therapy in the Near-Infrared Region by Using Gold Nanorods. *J. Am. Chem. Soc*., *128*, 2115-2120.

[6] Krumeich, F., Mubr, H. J., Niederberger, M., Bieri, F., Schnyder, B. & Nesper, R. (1999). Morphology and Topochemical Reactions of Novel Vanadium Oxide Nanotubes. *J. Am. Chem. Soc*., *121*, 8324-8331.

[7] Tremel, W. (1999). Inorganic Nanotubes. *Angew. Chem. Int. Ed. Engl*., *38*, 2175-2179.

[8] Sun, Y. G. & Xia, Y. N. (2002). Shape-Controlled Synthesis of Gold and Silver Nanoparticles. *Science*, *298*, 2176-2179.

[9] Kijima, T., Yoshimura, T., Uota, M., Ikeda, T., Fujikawa, D., Mouri, S. & Uoyama, S. (2004). Noble-Metal Nanotubes (Pt, Pd, Ag) from Lyotropic Mixed-Surfactant Liquid-Crystal Templates. *Angew. Chem. Int. Ed. Engl*., *43*, 228-232.

[10] Martin, C. R. (1994). Nanomaterials: A Membrane-Based Synthetic Approach. *Science*, *266*, 1961-1966.

[11] Molares, M. E., Buschmann, V., Dobrev, D., Neumann, R., Scholz, R., Schnchert, I. U. & Velter, J. (2001). Single-Crystalline Copper Nanowires Produced by Electrochemical Deposition in Polymeric Ion Track Membranes. *Adv. Mater*, *13*, 62-65.

[12] Sun, Y. G. & Xia, Y. N. (2004). Mechanistic Study on the Replacement Reaction between Silver Nanostructures and Chloroauric Acid in Aqueous Medium. *J. Am. Chem. Soc*., *126*, 3892-3901.

[13] Jin, R. C., Cao, Y. C., Hao, E., Métraux, G. S., Schatz, G. C. & Mirkin, C. A. (2003). Controlling Anisotropic Nanoparticle Growth through Plasmon Excitation. *Nature*, *425*, 487-490.

[14] Sun, Y. & Xia, Y. (2002). Shape-Controlled Synthesis of Gold and Silver Nanoparticles. *Science*, *298*, 2176-2179.

[15] Zhu, J. J., Qiu, Q. F., Wang, H., Zhang, J. R., Zhu, J. M. & Chen, Z. Q. (2002). Synthesis of Silver Nano-wires by a Sonoelectrochemical Method. *Inorg. Chem. Commun*., *5*, 242-244.

[16] Wang, J. G., Tian, M. L., Kumar, N. & Mallouk, T. E. (2005). Controllable Template Synthesis of Superconducting Zn Nanowires with Different Microstructures by Electrochemical Deposition. *Nano Lett*, *5*, 1247-1253.

[17] Singh, D. P., Neti, N. R., Sinha, A. S. K. & Srivastava, O. N. (2007). Growth of Different Nanostructures of Cu_2O (Nanothreads, Nanowires, and Nanocubes) by Simple Electrolysis Based Oxidation of Copper. *J. Phys. Chem. C*, *111*, 1638-1645.

[18] Ramazani, A., Kashi, M. A., Alikhani, M. & Erfanifam, S. (2008). Fabrication of High Aspect Ratio Co Nanowires with Controlled Magnetization Direction Using ac and Pulse Electrodeposition. *Mater. Chem. Phys*., *112*, 285-289.

Copyright © 2010. Nova Science Publishers, Incorporated. All rights reserved.

[19] Chen, C., Wang, L., Yu, H. J., Jiang G. H., Yang, Q., Zhou, J. F., Xiang W. D. & Zhang J. F. (2008). Study on the Growth Mechanism of Silver Nanorods in the Nanowire-seeding Polyol Process. *Mater. Chem. Phys*., *107*, 13-17.

[20] Zhou, X. J., Harmer, A. J., Heinig, N. F. & Leung, K. T. (2004). Parametric study on electrochemical deposition of copper nanoparticles on an ultrathin polypyrrole film deposited on a gold film electrode, *Langmuir*, *20*, 5109-5113.

[21] Ko, W. Y., Chen, W. H., Tzeng, S. D., Gwo, S. & Lin, K. J. (2006). Synthesis of Pyramidal Copper Nanoparticles on Gold Substrate. *Chem. Mater*, *18*, 6097-6099.

[22] Illy, B., Shollock, B. A., MacManus-Driscoll, J. L. & Ryan, M. P. (2005). Electrochemical Growth of ZnO Nanoplates. *Nanotechnology*, *16*, 320-324.

[23] Li, C. C., Shuford, K. L., Park, Q. H., Cai, W. P., Li, Y., Lee, E. J. & Cho, S. O. (2007). High-Yield Synthesis of Single-Crystalline Gold Nano-octahedra. *Angew. Chem. Int. Ed. Engl*., *46*, 3264-3268.

[24] Xiong, Y. J., Cai, H. G., Wiley, B. J., Wang, J. G., Kim, M. J. & Xia, Y. N. (2007). Synthesis and Mechanistic Study of Palladium Nanobars and Nanorods. *J. Am. Chem. Soc*., *129*, 3665-3675.

[25] Tsuji, M., Hashimoto, M., Nishizawa, Y., Kubokawa, M. & Tsuji, T. (2005). Microwave-assisted Synthesis of Metallic Nanostructures in Solution. *Chemistry- A Euro. J*, *11*, 440-452.

[26] Grace, A. N. & Pandian, K. (2007). One pot synthesis of polymer protected Pt, Pd, Ag and Ru Nanoparticles and Nanoprisms under Reflux and Microwave Mode of Heating in Glycerol - A comparative Study. *Mater. Chem. Phys*., *104*, 191-198.

[27] Nadagouda, M. N. & Varma, R. S. (2008). Microwave-Assisted Shape-Controlled Bulk Synthesis of Ag and Fe Nanorods in Poly(ethylene glycol) Solutions. *Cryst. Growth Des*, *8*, 291-295.

[28] Zhu, J. F. & Zhu, Y. J. (2006). Microwave-Assisted One-Step Synthesis of Polyacrylamide-Metal (M = Ag, Pt, Cu) Nanocomposites in Ethylene Glycol. *J. Phys. Chem. B*, *110*, 8593-8597.

[29] Gou, L. F., Chipara M. & Zaleski, J. M. (2007). Convenient, Rapid Synthesis of Ag Nanowires. *Chem. Mater*, *19*, 1755-1760.

[30] Zhu, S. P., Tang, S. T. & Meng, X. K. (2009). Monodisperse Silver Nanoparticles Synthesized by a Microwave-assisted Method. *Chin. Phys. Lett*, *26*, 078101.

[31] Jin, R., Cao Y., Mirkin, C. A., Kelly, K. L., Schatz, G. C. & Zheng, J. G. (2001). Photoinduced Conversion of Silver Nanospheres to Nanoprisms. *Science*, *294*, 1901-1903.

[32] Oaki, Y. & Imai, H. (2003). Experimental demonstration for the morphological evolution of crystals grown in gel media. *Cryst. Growth Des*., *3*, 711-716.

[33] Fukami, K., Nakanishi, S., Yamasaki, H., Tada, T., Sonoda, K., Kamikawa, N., Tsuji, N., Sakaguchi, H. & Nakato, Y. (2007). General Mechanism for the Synchronization of Electrochemical Oscillations and Self-organized Dendrite Electrodeposition of Metals with Ordered 2D and 3D Microstructures. *J. Phys. Chem. C*, *111*, 1150-1160.

[34] Saito, Y. & Ueta, T. (1989). Monte-carlo Studies of Equilibrium and Growth Shapes of Crystal. *Phys. Rev. A*, *40*, 3408-3419.

[35] Bogoyavlenskiy, V. A. & Chernova, N. A. (2000). Diffusion-limited Aggregation: A Relationship between Surface Thermodynamics and Crystal Morphology. *Phys. Rev. E*, *61*, 1629-1633.

Copyright © 2010. Nova Science Publishers, Incorporated. All rights reserved.

[36] Socol Y., Abramson O., Gedanken A., Meshorer Y., Berenstein L. & Zaban A. (2002). Suspensive Electrode Formation in Pulsed Sonoelectrochemical Synthesis of Silver Nanoparticles. *Langmuir*, *18*, 4736-4740.

[37] Tang, S. C., Meng, X. K., Wang, C. C. & Cao, Z. H. (2009). Flowerlike Ag Microparticles with Novel Nanostructure Synthesized by an Electrochemical Approach. *Mater. Chem. Phys*., *114*, 842-847.

[38] Mason, T. J., Lorimer, J. P. & Walton, D. J. (1990). Sonoelectrochemistry. *Ultrasonics*, *28*, 333-337.

[39] Jiang, L. P., Wang, A. N., Zhao, Y., Zhang, J. R. & Zhu, J. J. (2004). A Novel Route for the Preparation of Monodisperse Silver Nanoparticles via a Pulsed Sonoelectrochemical Technique. *Inorg. Chem. Commun*., *7*, 506-509.

[40] Kim, F., Connor, S., Song, H., Kuykendall, T. & Yang, P. D. (2004). Platonic Gold Nanocrystals. *Angew. Chem. Int. Ed*., *43*, 3673-3677.

[41] Tang, S. C., Meng, X. K., Lu, H. B. & Zhu, S. P. (2009). PVP-assisted sonoelectrochemical growth of silver nanostructures with various shapes. *Mater. Chem. Phys*., *116*, 464-468.

[42] Chapman, G. M., Bai, H., Li, C. & Shi, G. Q. (2009). Micro-nanoscale Binary Structured Silver Films Fabricated by Electrochemical Deposition. *Mater. Chem. Phys*., *114*, 120-124.

[43] Zhang, J., Liu, K., Dai, Z. H., Feng, Y. Y., Bao, J. C. & Mo, X. Y. (2006). Formation of Novel Assembled Silver Nanostructures from Polyglycol Solution. *Mater. Chem. Phys*., *100*, 313-318.

[44] Mdluli, P. S. & Revaprasadu, N. (2009). Time Dependant Evolution of Silver Nanodendrites. *Mater. Lett*, *63*, 447-450.

[45] Gedanken, A. (2004). Using Sonochemistry for the Fabrication of Nanomaterials. *Ultrason. Sonochem*, *11*, 47-55.

[46] Perkas, N., Amirian, G., Applerot, G., Efendiev, E., Kaganovskii, Y., Ghule, A. V., Chen, B. J., Ling, Y. C. & Gedanken, A. (2008). Depositing Silver Nanoparticles on/in a Glass Slide by the Sonochemical Method. *Nanotechnology*, *19*, 435604.

[47] Haas, I., Shanmugam, S. & Gedanken, A. (2006). Pulsed Sonoelectrochemical Synthesis of Size-controlled Copper Nanoparticles Stabilized by Poly(N-vinylpyrrolidone). *J. Phys. Chem. B*, *110*, 16947-16952.

[48] Chassaing, E., Rosso, M., Sapoval, B. & Chazalviel, J. N. (1993). Impedance Spectroscopy of Ramified Electrodeposits. *Electrochim. Acta*, *38*, 1941-1944.

[49] Rosso, M., Huttel, Y., Chassaing, E., Sapoval, B. & Gutfraind, R. (1997). Visualization of the Active Zone of an Irregular Electrode by Optical Absorption. *J. Electrochem. Soc*., *144*, 1713-1717.

[50] Rashid, M. H. & Mandal, T. K. (2007). Synthesis and Catalytic Application of Nanostructured Silver Dendrites. *J. Phys. Chem. C*, *111*, 16750-16760.

[51] Selvan, S. T., Hayakawa, T., Nogami, M. & Moller, M. (1999). Block Copolymer Mediated Synthesis of Gold Quantum Dots and Novel Gold-Polypyrrole Nanocomposites. *J. Phys. Chem. B*, *103*, 7441-7448.

[52] Wen, X. G., Xie, Y. T., Mak, M. W .C., Cheung, K. Y., Li, X. Y., Renneberg, R. & Yang, S. H. (2006). Dendritic Nanostructures of Silver: Facile Synthesis, Structural Characterizations, and Sensing Applications. *Langmuir*, *22*, 4836-4842.

Copyright © 2010. Nova Science Publishers, Incorporated. All rights reserved.

[53] Song, W., Cheng, Y. C., Jia, H. Y., Xu, W. Q. & Zhao, B. (2006). Surface Enhanced Raman Scattering Based on Silver Dendrites Substrate. *J. Colloid Interf. Sci*., *298*, 765-768.

[54] Zhu, J., Liu, S., Palchik, O., Koltypin, Y. & Gedanken, A. (2000). Shape-Controlled Synthesis of Silver Nanoparticles by Pulse Sonoelectrochemical Methods. *Langmuir*, *16*, 6396-6399.

[55] Liu, S. W., Huang, W. P., Chen, S. G., Avivi, S. & Gedanken, A. (2001). Synthesis of X-ray Amorphous Silver Nanoparticles by the Pulse Sonoelectrochemical Method. *J. Non-cryst. Solids*, *283*, 231-236.

[56] Tang, S. C., Meng, X. K., Lu, H. B. & Zhu, S. P. (2009). Controllable synthesis of metal particles by a direct current electrochemical approach. *Mater. Chem. Phys*., *52*, 2709-2714.

[57] Ben-Jacob E. & Garik P. (1990). The Formation of Patterns in Non-equilibrium Growth. *Nature*, *343*, 523-530.

[58] Fleury, V. (1997). Branched Fractal Patterns in Non-equilibrium Electrochemical Deposition from Oscillatory Nucleation and Growth. *Nature*, *390*, 145-148.

[59] Lu, L., Kobayashi, A., Kikkawa, Y., Tawa, K. & Ozaki, Y. (2006). Oriented Attachment-Based Assembly of Dendritic Silver Nanostructures at Room Temperature. *J. Phys. Chem. B*, *110*, 23234-23241.

[60] Cheng, Y., Wang, Y. S., Chen, D. Q. & Bao, F. (2005). Evolution of Single Crystalline Dendrites from Nanoparticles through Oriented Attachment. *J. Phys. Chem. B*, *109*, 794-798.

[61] Fang, J. X., Ma, X. N., Cai, H. H., Song, X. P. & Ding, B. J. (2006). Double-interface Growth Mode of Fractal Silver Trees within Replacement Reaction. *Appl. Phys. Lett*, *89*, 173104.

[62] González, G., Rosso, M. & Chassaing, E. (2008). Transition Between two Dendritic Growth Mechanisms in Electrodeposition. *Phys. Rev. E*, *78*, 011601.

[63] Hoyt, J. J., Asta, M. & Karma, A. (2003). Atomistic and Continuum Modeling of Dendritic Solidification. *Mater. Sci. Eng. R*, *41*, 121-163.

[64] Tang, S. C., Vongehr, S. & Meng, X. K. (2009). Two Distinct Branch-stem Interfacial Structures of Silver Dendrites with Vertical and Slanted Branchings. *Chem. Phys. Lett*, *477*, 179-183.

[65] Zhou, Q., Wang, S., Jia, N. Q., Liu, L., Yang, J. J. & Jiang, Z. Y. (2006). Synthesis of Highly Crystalline Silver Dendrites Microscale Nanostructures by Electrodeposition. *Mater. Lett*, *60*, 3789-3792.

[66] Kaniyankandy, S., Nuwad, J., Thinaharan, C., Dey, G. K. & Pillai, C. G. S. (2007). Electrodeposition of Silver Nanodendrites. *Nanotechnology*, *18*, 125610.

[67] Fang, J. X., You, H. J., Zhu, C., Kong, P., Shi, M., Song, X. P. & Ding, B. J. (2007). Thermodynamic and Kinetic Competition in Silver Dendrite Growth. *Chem. Phys. Lett*, *439*, 204-208.

[68] May, S. L., Zheng, J. G., Wessels, B. W. & Lauhon, L. J. (2005). Dendritic Nanowire Growth Mediated by a Self-Assembled Catalyst. *Adv. Mater*, *17*, 598-602.

[69] Penn, R. L. & Banfield, J. F. (1998). Imperfect Oriented Attachment: Dislocation Generation in Defect-Free Nanocrystals. *Science*, *281*, 969-971.

[70] Dougherty, A., Kaplan, P. D. & Gollub, J. P. (1987). Development of Side Branching in Dendritic Crystal Growth. *Phys. Rev. Lett*, *58*, 652.

Copyright © 2010. Nova Science Publishers, Incorporated. All rights reserved.

[71] Pieters, R. & Langer, J. S. (1987). Noise-Driven Sidebranching in the Boundary-Layer Model of Dendritic Solidification, *Phys. Rev. Lett*, *56*, 1948.

[72] Zhang, D. E., Zhang, X. J., Ni, X. M., Song, J. M. & Zheng, H. G. (2006). Fabrication of Novel Threefold Shape CeO_2 Dendrites: Optical and Electrochemical Properties. *Chem. Phys. Lett*, *430*, 326-329.

[73] He, R., Qian, X., Yin, J. & Zhu, Z. K. (2003). Formation of Silver Dendrites under Microwave Irradiation. *Chem. Phys. Lett*, *369*, 454-458.

[74] Wang, Z. L. (2000). Transmission Electron Microscopy of Shape-Controlled Nanocrystals and Their Assemblies. *J. Phys. Chem. B*, *104*, 1153-1175.

[75] Despic, A. R. & Popov K. I. (1972). Transport Controlled Deposition and Dissolution of Metals. *Modern Aspects of Electrochemistry 7*, Ch. 4. (edited by Conway, B. E. and Bockris, J. OM.), New York, Plenum Press.

[76] Ding, B. J. & Song, X. P. (2009). Silver Nanowires Growth via Branch Fragmentation of Electrochemically Grown Silver Dendrites, *Chem. Commun*., 1130-1132.

[77] Pol, V. G., Srivastava, D. N., Palchik, O., Palchik, V., Slifkin, M. A., Weiss, A. M. & Gedanken, A. (2002). Sonochemical Deposition of Silver Nanoparticles on Silica Spheres, *Langmuir*, *18*, 3352-3357.

[78] Guo, S. J., Wang, L. & Wang, E. (2007). Templateless, Surfactantless, Simple Electrochemical Route to Rapid Synthesis of Diameter-controlled 3D Flowerlike Gold Microstructure with "clean" Surface, *Chem. Commun*, 3163-3165.

[79] Duan, G. T., Cai, W. P., Luo, Y. Y., Li, Z. G. & Li, Y. (2006). Electrochemically Induced Flowerlike Gold Nanoarchitectures and Their Strong Surface-enhanced Raman Scattering Effect, *Appl. Phys. Lett*, *89*, 211905.

[80] Zhang, X., Shi, F., Yu, X., Liu, H., Fu, Y., Wang, Z. Q., Jiang, L. & Li, X. Y. (2004). Polyelectrolyte Multilayer as Matrix for Electrochemical Deposition of Gold Clusters: Toward Super-Hydrophobic Surface, *J. Am. Chem. Soc*., *126*, 3064-3065.

[81] Wang, L., Guo, S. J., Hu, X. G. & Dong, S. J. (2008). Facile Electrochemical Approach to Fabricate Hierarchical Flowerlike Gold Microstructures: Electrodeposited Superhydrophobic Surface, *Electrochem. Commun*., *10*, 95-99.

[82] Fang, J. X., You, H. J., Kong, P., Yi, Y., Song, X. P. & Ding, B. J. (2007). Dendritic Silver Nanostructure Growth and Evolution in Replacement Reaction. *Crystal Growth & Design*, *7*, 864-867.

[83] Rashid, M. H. & Mandal, T. K. (2007). Synthesis and Catalytic Application of Nanostructured Silver Dendrites, *J. Phys. Chem. C*, *111*, 16750-16760.

[84] Sun, X. P. & Hagner, M. (2007). Novel Preparation of Snowflake-like Dendritic Nanostructures of Ag or Au at Room Temperature via a Wet-chemical Route, *Langmuir*, *23*, 9147-9150.

[85] Qu, L. T. & Dai, L. M. (2005). Novel Silver Nanostructures from Silver Mirror Reaction on Reactive Substrates, *J. Phys. Chem. B*, *109*, 13985-13990.

[86] Wu, W. T., Pang, W. M., Xu, G. Y., L. Shi, Zhu, Q. R., Wang, Y. S. & Lu, F. (2005). In situ Formation of Ag Flowerlike and Dendritic Nanostructures in Aqueous Solution and Hydrolysis of an Amphiphilic Block Copolymer, *Nanotechnology*, *16*, 2048-2051.

[87] Jing, C. Y. & Fang, Y. (2007). Simple Method for Electrochemical Preparation of Silver Dendrites Used as active and Stable SERS Substrate. *J. Colloid Interf. Sci*., *314*, 46.

Copyright © 2010. Nova Science Publishers, Incorporated. All rights reserved.

[88] Wu, W. T., Wang, Y. S., Shi, L., Pang, W. M., Zhu, Q. R., Xu, G. Y. & Lu, F. (2006). Propeller-like Multicomponent Microstructures: Self-Assemblies of Nanoparticles of Poly (vinyl alcohol)-Coated Ag and/or Cu_2O. *J. Phys. Chem. B*, *110*, 14702-14708.

[89] Lu, L. H., Kobayashi, A., Tawa, K. & Ozaki, Y. (2006). Silver Nanoplates with Special Shapes: Controlled Synthesis and Their Surface Plasmon Resonance and Surface-Enhanced Raman Scattering Properties, *Chem. Mater*, *18*, 4894-4901.

[90] Lombardi I., Cavallotti P. L., Carraro C. & Maboudian R. (2007). Template Assisted Deposition of Ag Nanoparticle Arrays for Surface-enhanced Raman Scattering Applications. S*ensors Actuat. B-Chem.*, *125*, 353-356.

[91] Mazur M., Michota-Kaminska A. & Bukowska J. (2007). Facile Electrochemical Fabrication of Polymeric Templates for Spatially Selective Deposition of Metals. *Electrochem. Commun.*, *9*, 2418-2422.

[92] Fang, J. X., Yi, Y., Ding, B. J. & Song, X. P. (2008). A Route to Increase the Enhancement Factor of Surface Enhanced Raman Scattering (SERS) via a High Density Ag Flower-like Pattern. *Appl. Phys. Lett*, *92*, 131115.

[93] Qian, L. & Yang, X. R. (2008). Dendrimers as "controllers" for Modulation of Electro-deposited Silver Nanostructures. *Colloid Surface A: Physicochem. Eng. Aspects*, *317*, 528-534.

[94] Lin, H. H., Mock, J., Smith, D., Gao, T. & Sailor, M. J. (2004). Surface-Enhanced Raman Scattering from Silver-Plated Porous Silicon. *J. Phys. Chem. B*, *108*, 11654-11659.

[95] He, Y., Wu, X. F., Lu, G. W. & Shi, G. Q. (2006). A Facile Route to Silver Nanosheets. *Mater. Chem. Phys.*, *98*, 178-182.

[96] Huang, S., Ma, H., Zhang, X., Yong, F., Feng, X., Pan, W., Wang, X., Wang, Y. & Chen, S. (2005). Electrochemical Synthesis of Gold Nanocrystals and Their 1D and 2D Organization. *J. Phys. Chem. B*, *109*, 19823-19830.

[97] Tang, S. C., Meng, X. K., Wang, C. C. & Cao, Z. H. (2009). Flowerlike Ag Microparticles with Novel Nanostructure Synthesized by an Electrochemical Approach. *Mater. Chem. Phys.*, *114*, 842-847.

[98] Tang, S. C. & Meng, X. K. (2009). Controllable Synthesis of Metal Particles by a Direct Current Electrochemical Approach. *Science in China Series E-Technological Sciences*, *52*, 2709-2714.

[99] Schulz, J., Roucoux, A. & Patin, H. (2002). Reduced Transition Metal Colloids: A Novel Family of Reusable Catalysts? *Chem. Rev.*, *102*, 3757-3778.

[100] Zhu, S. P., Huang, J. F., Tang, S. C. & Meng, X. K. (2009). Synthesis of Ag Microparticles with Hierarchical Nanostructure on the Anode of a Galvanic Cell. *Mater. Chem. Phys.*, *118*, 442-446.

[101] You, T., Sun, S. X., Song, X. Y. & Xu, S. L. (2009). Simple Extraction-solvothermal Synthesis of Single-crystalline Silver Microplates. *Cryst. Res. Technol.*, *44*, 857- 860.

[102] Bi, Y. & Lu, G. (2008). Morphology-controlled Preparation of Silver Nanocrystals and Their Application in Catalysis. *Chem. Lett.*, *37*, 514-515.

[103] Li, C., Shuford, K. L., Park, Q. H., Cai, W., Li, Y., Lee, E. J. & Cho, S. O. (2007). High-Yield Synthesis of Single-Crystalline Gold Nano-octahedra. *Angew. Chem. Int. Ed.*, *46*, 3264-3268.

[104] Natter, H. & Hempelmann, R. (2008). Nanocrystalline Metals Prepared by Electrodeposition. *Z. Phys. Chem.*, *222*, 319-354.

Copyright © 2010. Nova Science Publishers, Incorporated. All rights reserved.

[105] Gomez, E., Kipervaser, Z. G., Pellicer, E. & Valles, E. (2004). Extracting deposition parameters for cobalt–molybdenum alloy from potentiostatic current transients. *Phys. Chem. Chem. Phys*., *6*, 1340-1344.

[106] Wong, K. P., Chan, K. C. & Yue, T. M. (2001). Modeling of Electrocrystallization for Pulse Current Electroforming of Nickel. *Appl. Surf. Sci*., *178*, 178-189.

[107] Washio, I., Xiong, Y. J., Yin, Y. D. & Xia, Y. N. (2006). Reduction by the End Groups of Poly(vinyl pyrrolidone): A New and Versatile Route to the Kinetically Controlled Synthesis of Ag Triangular Nanoplates. *Adv. Mater*, *18*, 1745-1749.

[108] Feldheim, D. L. (2007). The New Face of Catalysis. *Science*, *316*, 699-700.

[109] Tian, N., Zhou, Z. Y., Sun, S.G., Ding, Y. & Wang, Z. L. (2007). Synthesis of Tetrahexahedral Platinum Nanocrystals with High-Index Facets and High Electro-Oxidation Activity. *Science*, *316*, 732-735.

[110] Zhou, P., Dai, Z. H., Fang, M., Huang, X. H. & Bao, J. C. (2007). Novel Dendritic Palladium Nanostructure and Its Application in Biosensing. *J. Phys. Chem. C*, *111*, 12609-12616.

[111] Liu, J. H., Wang, A. Q., Chi, Y. S., Lin, H. P. & Mou, C. Y. (2005). Synergistic Effect in an Au−Ag Alloy Nanocatalyst: CO Oxidation. *J. Phys. Chem. B*, *109*, 40-43.

[112] Shon, Y. S., Dawson, G. B., Porter, M. & Murray, R. W. (2002). Monolayer-Protected Bimetal Cluster Synthesis by Core Metal Galvanic Exchange Reaction. *Langmuir*, *18*, 3880-3885.

[113] Steinbruck, A., Csaki, A., Festag, G. & Fritzsche, W. (2006). Preparation and Optical Characterization of Core–Shell Bimetal Nanoparticles. *Plasmonics*, *1*, 79-85.

[114] Nishida, N., Shiraishi, Y., Kobayashi, S. & Toshima, N. (2008). Fabrication of Liquid Crystal Sol Containing Capped Ag-Pd Bimetallic Nanoparticles and Their Electro-Optic Properties. *J. Phys. Chem. C*, *112*, 20284-20290.

[115] Li, X. L., Li, B. Z., Cheng, M. H., Du, Y. K., Wang, X. M. & Yang. P. (2008). Catalytic Hydrogenation of Phenyl Aldehydes Using Bimetallic Pt/Pd and Pt/Au Nanoparticles Stabilized by Cubic Silsesquioxanes. *J. Mol. Catal. A: Chem*., *284*, 1-7.

[116] Toshima, N., Harada, M., Yamazaki, Y. & Asakurat, K. (1992). Catalytic activity and structural analysis of polymer-protected gold-palladium bimetallic clusters prepared by the simultaneous reduction of hydrogen tetrachloroaurate and palladium dichloride. *J. Phys. Chem*., *96*, 9927-9933.

[117] Liu, Y. C. & Yang, S. J. (2007). Improved surface-enhanced Raman scattering based on Ag–Au bimetals prepared by galvanic replacement reactions. *Electrochim. Acta*, *52*, 1925-1931.

[118] Ren, X. L., Meng, X. W. & Tang, F. Q. (2005). Preparation of Ag–Au nanoparticle and its application to glucose biosensor. *Sens. Actuators, B-Chem*., *110*, 358- 363.

[119] Lu, L. H., Sun, G. Y., Zhang, H. J., Wang, H. S., Xi, S. Q., Hu, J. Q., Tian, Z. Q. & Chen, R. J. (2004). Fabrication of Core-Shell Au-Pt Nanoparticle Film and its Potential Application as Catalysis and SERS Substrate *J. Mater. Chem*., *14*, 1005-1009.

[120] Link, S., Wang, Z. L. & El-Sayed, M. A. (1999). Alloy Formation of Gold-Silver Nanoparticles and the Dependence of the Plasmon Absorption on Their Composition. *J. Phys. Chem. B*, *103*, 3529-3533.

[121] Kim, M. J., Lee, K. Y., Jeong, G. H., Jang, J. & Han, S. W. (2007). Fabrication of Au-Ag Alloy Nanoprisms with Enhanced Catalytic Activity. *Chem. Lett*, *36*, 1350-1351.

Copyright © 2010. Nova Science Publishers, Incorporated. All rights reserved.

[122] Reetz, M. T. & Helbig, W. (1994). Size-Selective Synthesis of Nanostructured Transition Metal Clusters. *J. Am. Chem. Soc*., *116*, 7401-7402.

[123] Kim, J. H., Chung, H. W. & Lee, T. R. (2006). Preparation and Characterization of Palladium Shells with Gold and Silica Cores. *Chem. Mater*, *18*, 4115-4120.

[124] Sun, Y. G. & Xia, Y. N. (2002). Shape-Controlled Synthesis of Gold and Silver Nanoparticles. *Science*, *298*, 2176-2179.

[125] Zhang, Q. B., Xie, J. P., Lee, J. Y., Zhang, J. X. & Boothroyd, C. (2008). Synthesis of Ag@Ag/Au Metal Core/Alloy Shell Bimetallic Nanoparticles with Tunable Shell Compositions by a Galvanic Replacement Reaction. *Small*, *4*, 1067-1071.

[126] Yang, J. H., Lee, J. Y., Zhang, Q. B., Zhou, W. J. & Liu, Z. L. (2008). Carbon-Supported Pseudo-Core–Shell Pd–Pt Nanoparticles for ORR with and Without Methanol. *J. Electrochem. Soc*., *155*, 776-781.

[127] Shao, M. H., Sasaki, K., Marinkovic, N. S., Zhang, L. H. & Adzic, R. R. (2007). Synthesis and characterization of platinum monolayer oxygen-reduction electrocatalysts with Co–Pd core–shell nanoparticle supports. *Electrochem. Commun*, *9*, 2848-2853.

[128] Selvakannan, P. R. & Sastry, M. (2005). Hollow gold and platinum nanoparticles by a transmetallation reaction in an organic solution. *Chem. Commun*., 1684-1686.

[129] Yang, J., Lee, J. Y., Too, H. P. & Valiyaveettil, S. (2006). A Bis(p-sulfonatophenyl)phenylphosphine-Based Synthesis of Hollow Pt Nanospheres. *J.Phys. Chem. B*, *110*, 125-129.

[130] Lu, X. M., Tuan, H. Y., Chen, J. Y., Li, Z. Y., Korgel, B. A. & Xia, Y. N. (2007). Mechanistic Studies on the Galvanic Replacement Reaction between Multiply Twinned Particles of Ag and $HAuCl_4$ in an Organic Medium. *J. Am. Chem. Soc*., *129*, 1733-1742.

[131] Hu, K. W., Huang, C. C., Hwu, J. R., Su, W. C., Shieh, D. B. & Yeh, C. S. (2008). A New Photothermal Therapeutic Agent Core-Free Nanostructured Au_xAg_{1-x} Dendrites. *Chem. Eur. J*, *14*, 2956-2964.

[132] Hong, Y., Rheem, Y., Lai, M., Cwiertny, D. M., Walker, S. L. & Myung, N. V. (2009). Electrochemical synthesis of Fe_xNi_{1-x} nanostructures for environmental remediation *Chem. Eng. J*, *151*, 66-72.

[133] Huang, J. F., Vongehr, S; Tang, S. C., Lu, H. M., Shen, J. C. & Meng, X. K. (2009). Ag Dendrite-Based Au/Ag Bimetallic Nanostructures with Strongly Enhanced Catalytic Activity *Langmuir*, *25*, 11890-11896.

[134] Fleury, V., Watters, W. A., Allam, L. & Devers, T. (2002). Rapid electroplating of insulators *Nature*, *416*, 716-719.

[135] Skrabalak, S. E., Chen, J. Y., Sun, Y. G., Lu, X. M., Au, L., Cobley, C. M. & Xia, Y. N. (2008). Gold Nanocages: Synthesis, Properties, and Applications. *Acc. Chem. Res*., *41*, 1587-1595.

[136] Mori, K., Kumami, A., Tomonari, M. & Yamashita, H. (2009). A pH-Induced Size Controlled Deposition of Colloidal Ag Nanoparticles on Alumina Support for Catalytic Application. *J. Phys. Chem. C*, *113*, 16850-16854.

[137] Wang W. & Asher, S. A. (2001). Photochemical Incorporation of Silver Quantum Dots in Monodisperse Silica Colloids for Photonic Crystal Applications. *J. Am. Chem. Soc*., *123*, 12528-12535.

Copyright © 2010. Nova Science Publishers, Incorporated. All rights reserved.

[138] Peceros, K. E., Xu, X. D., Bulcock, S. R. & Cortie, M. B. (2005). Dipole-Dipole Plasmon Interactions in Gold-on-Polystyrene Composites. *J. Phys. Chem. B, 109*, 21516-21520.

[139] Mock, J. J., Oldenburg, S. J., Smith, D. R., Schultz, D. A. & Schultz, S. (2002). Composite Plasmon Resonant Nanowires *Nano Lett, 2*, 465-469.

[140] Bansal, V., Jani, H., Plessis, J. D., Coloe P. J. & Bhargava, S. K. (2008). Galvanic Replacement Reaction on Metal Films: A One-Step Approach to Create Nanoporous Surfaces for Catalysis. *Adv. Mater, 20*, 717-723.

[141] Jana, S., Ghosh, S. K., Nath, S., Pande, S., Praharaj, S., Panigrahi, S., Basu, S., Endo, T. & Pal, T. (2006). Synthesis of Silver Nano Shell-coated Cationic Polystyrene Beads: A Solid Phase Catalyst for the Reduction of 4-Nitrophenol. *Appl. Catal. A: General, 313*, 41-48.

[142] Tovmachenko, O. G., Graf, C., van den Heuvel, D. J., van Blaaderen A. & Gerritsen, H. C. (2006). Fluorescence Enhancement by Metal-core/silica-shell Nanoparticles. *Adv. Mater, 18*, 91-95.

[143] Mulvany, P. (1996). Surface Plasmon Spectroscopy of Nanosized Metal Particles. *Langmuir, 12*, 788-800.

[144] Oldenburg, S. J., Averitt, R. D., Westcott, S. L. & Halas, N. J. (1998). Nanoengineering of optical resonances. *Chem. Phys. Lett, 288*, 243-247.

[145] Caruso, F. (2003). Hollow Inorganic Capsules Via Colloid-templated Layer-by-layer Electrostatic Assembly. *Top. Curr. Chem., 227*, 145-168.

[146] Deng, Z. W., Chen, M. & Wu, L. M. (2007). Novel Method to Fabricate SiO_2/Ag Composite Spheres and Their Catalytic, Surface-Enhanced Raman Scattering Properties. *J. Phys. Chem. C, 111*, 11692-11698.

[147] Tamai, T., Watanabe, M., Hatanaka, Y., Tsujiwaki, H., Nishioka, N. & Matsukawa, K. (2008). Formation of Metal Nanoparticles on the Surface of Polymer Particles Incorporating Polysilane by UV Irradiation. *Langmuir, 24*, 14203-14208.

[148] Lee, J. H., Mahmoud, M. A., Sitterle, V., Sitterle, J. & Meredith, J. C. (2009). Facile Preparation of Highly-Scattering Metal Nanoparticle-Coated Polymer Microbeads and Their Surface Plasmon Resonance. *J. Am. Chem. Soc., 131*, 5048-5049.

[149] Esumi, K., Isono, R. & Yoshimura, T. (2004). Preparation of PAMAM-and PPI-Metal (Silver, Platinum, and Palladium) Nanocomposites and Their Catalytic Activities for Reduction of 4-Nitrophenol. *Langmuir, 20*, 237-243.

[150] Guo, D. J. & Li, H. L. (2005). Highly Dispersed Ag Nanoparticles on Functional MWNT Surfaces for Methanol Oxidation in Alkaline Solution. *Carbon, 43*, 1259-1264.

[151] Biella, S., Castiglioni, G. L., Fumagalli, C., Prati, L. & Rossi, M. (2002). Application of Gold Catalysts to Selective Liquid Phase Oxidation. *Catal. Today, 72*, 43-49.

[152] Ishida, T. & Haruta, M. (2007). Gold Catalysts: Towards Sustainable Chemistry. *Angew. Chem. Int. Ed, 46*, 7154-7156.

[153] Averitt, R. D., Westcott, S. & Halas, N. J. (1999). Linear optical properties of gold nanoshells. *J. Opt. Soc. Am, 16*, 1824-1832.

[154] Lu, Y., Yin, Y. D, Li, Z. Y. & Xia, Y. N. (2002). Synthesis and self-Assembly of Au@SiO2 Core-Shell Colloids. *Nano Lett, 2*, 785-788.

[155] Loo, C., Lowery, A., Halas, N., West, J. & Drezek, R. (2005). Immunotargeted Nanoshells for Integrated Cancer Imaging and Therapy. *Nano Lett, 5*, 709-711.

Copyright © 2010. Nova Science Publishers, Incorporated. All rights reserved.

[156] Pető, G., Molnar, G. L., Paszti, Z., Geszti, O., Beck, A. & Guczi, L. (2002). Electronic structure of gold nanoparticles deposited on SiO_x/Si(100) *Mater. Sci. Eng. C*, *19*, 95-99.
[157] Stoeva, S. I., Huo, F. W., Lee, J. S. & Mirkin, C. A. (2005). Three-Layer Composite Magnetic Nanoparticle Probes for DNA *J. Am. Chem. Soc*., *127*, 15362-15363.
[158] Phadtare, S., Kumar, A., Vinod, V. P., Dash, C., Palaskar, D. V., Rao, M., Shukla, P. G., Sivaram, S. & Sastry, M. Direct (2003). Assembly of Gold Nanoparticle Shells on Polyurethane Microsphere Cores. *Chem. Mater*, *15*, 1944-1949.
[159] Westcott, S. L., Oldenburg, S. J., Lee, T. R. & Halas, N. J. **(**1998). Formation and Adsorption of Clusters of Gold Nanoparticles onto Functionalized Silica Nanoparticle Surfaces. *Langmuir*, *14*, 5396-5401.
[160] Hardikar, V. V. & Matijević, E. (2000). Coating of Nanosize Silver Particles with Silica. *J. Colloid Interface Sci*., *221*, 133-136.
[161] Kobayashi, Y., Salgueirinño-Maceira, V. & Liz-Marzán, L. M. (2001). Deposition of Silver Nanoparticles on Silica Spheres by Pretreatment Steps in Electroless Plating. *Chem. Mater*, *13*, 1630-1633.
[162] Zhu' M. W., Qian, G. D., Hong, Z. L., Wang, Z. Y., Fan, X. P. & Wang, M. Q. (2005). Preparation and characterization of silica–silver core-shell structural sub- micrometer spheres. *J. Phys. Chem. Solid*, *66*, 748-752.
[163] Graf, C. & van Blaaderen, A. (2002). Metallodielectric Colloidal Core-Shell Particles for Photonic Applications. *Langmuir*, *18*, 524-534.
[164] Cassagneau, T. & Caruso, F. (2002). Contiguous Silver Nanoparticle Coatings on Dielectric Spheres, *Adv. Mater*, *14*, 732-736.
[165] Tang, S. C., Tang Y. F., Gao, F., Liu, Z. G. & Meng, X. K. (2007). Ultrasonic electrodeposition of silver nanoparticles on dielectric silica spheres. *Nanotechnology*, *18*, 295607.
[166] StÖber, W; Fink, A. & Bohn, E. (1968). Controlled growth of monodisperse silica spheres in the micron size range. *J. Colloid Interface Sci*., *26*, 62-69.
[167] Suslick, K. S., Choe, S. B., Cichowlas, A. A. & Grinstaff, M. W. (1991). Sonochemical synthesis of amorphous iron. *Nature*, *353*, 414-416.
[168] Johnson, K. H. & Pepper, S. V. (1982). Molecular-orbital model for metal-sapphire interfacial strength. *J. Appl. Phys*., *53*, 6634-6637.
[169] Nakanishi, T., Ohtani, B. & Uosaki, K. (1998). Fabrication and Characterization of CdS-Nanoparticle Mono-and Multilayers on a Self-Assembled Monolayer of Alkanedithiols on Gold. *J. Phys. Chem. B*, *102*, 1571-1577.
[170] Pol, V. G., Srivastava, D. N., Palchik, O., Palchik, V., Slifkin, M. A., Weiss, A. M. & Gedanken, A. (2002). Sonochemical deposition. *Langmuir*, *18*, 3352-3357.
[171] Kim , Y. H., Lee, D. K., Kim, C. W., Cha, H. G., Kang, Y. S., Jo, B. G. & Jeong, T. H. (2007). Preparation and Antibiotic Property of Ag-SiO2 Nanoparticle. *Mol. Cryst. Liq. Cryst*., *464*, 665-673.
[172] Badley, R. D., Ford, W. T., McEnroe, F. J. & Assinks, R. A. (1990). Surface Modification of Colloidal Silica. *Langmuir*, *6*, 792-801.
[173] Kim, H. C., Alford, T. L. & Allee, D. R. (2002). Thickness Dependence on the Thermal Stability of Silver Thin Films. *Appl. Phys. Lett*, *81*, 4287-4289.
[174] Seemann, R., Herminghaus, S. & Jacobs, K. (2001). Shape of a Liquid Front Upon Dewetting. *Phys. Rev. Lett*, *86*, 5534-5558.

Copyright © 2010. Nova Science Publishers, Incorporated. All rights reserved.

[175] Zhu, M. W., Qian, G. D., Wang, Z. Y. & Wang, M. Q. (2006). Fabrication of Nanoscaled Silica Layer on the Surfaces of Submicron SiO2-Ag Core-Shell Spheres. Mater. *Chem. Phys*., *100*, 333-336.

[176] Moon, K. S., Dong, H., Maric, R., Pothukuchi, S., Hunt, A., Li, Y. & Wong, C. P. (2005). Thermal Behavior Of Silver Nanoparticles For Low-Temperature Interconnect Applications. *J. Electronic Mater*, *34*, 168-175.

[177] Wang, Z. L. (2003). New Developments in Transmission Electron Microscopy for Nanotechnology. *Adv. Mater*, *15*, 1497-1514.

[178] Wang, Z. L., Petroski, J. M., Green, T. C. & El-Sayed, M. A. (1998). Shape Transformation and Surface Melting Of Cubic and Tetrahedral Platinum Nanocrystals. *J. Phys. Chem. B*, *102*, 6145-6151.

[179] Tang, S. C., Zhu, S. P., Lu, H. M. & Meng, X. K. (2008). Shape Evolution and Thermal Stability of Ag Nanoparticles on Spherical SiO2 Substrates. *J. Solid State Chem.*, *181*, 587-592.

[180] Tang, S. C., Tang, Y. F., Vongehr, S., Zhao, X. N. & Meng, X. K. (2009). Nanoporous Carbon Spheres and Their Application in Dispersing Silver Nanoparticle. *Appl. Surf. Sci*., *255*, 6011-6016.

[181] Chang, S. Y., Liu, L. & Asher, S. A. (1994). Preparation. *J. Am. Chem. Soc*., *116*, 6739-6744.

[182] Chen, D., Li, L. L., Liu, J. S., Qi, S., Tang, F. Q., Ren, X. L., Wu, W., Ren, J. & Zhang, L. (2007). Synthesis and Self-assembly of Monodisperse silver-nanocrystal-doped Silica Particles. *J. Colloid Interf. Sci*., *308*, 351-355.

[183] Deng, Z. W., Chen, M., Zhou, S. X., You, B. & Wu, L. M. (2006). A Novel Method for the Fabrication of Monodisperse Hollow Silica Spheres. *Langmuir*, *22*, 6403-6407.

[184] Chen, M., Wu, L. M., Zhou, S. X. & You, B. (2006). A Method for the Fabrication of Monodisperse Hollow Silica Spheres. *Adv. Mater*, *18*, 801-806.

[185] Graf, C., Vossen, D. L. J., Imhof, A. & van Blaaderen, A. (2003). A General Method to Coat Colloidal Particles with Silica. *Langmuir*, *19*, 6693-6700.

[186] Zhang, J., Liu, J., Wang, S., Zhan, P., Wang, Z. & Ming, N. (2004). Facile Methods to Coat Polystyrene and Silica Colloids with Metal. *Adv. Funct. Mater*, *14*, 1089-1096.

[187] Hoppe, C. E., Lazzari, M., Pardinas-Blanco, I. & Lopez-Quintela, M. A. (2006). One-step Synthesis of Gold and Silver Hydrosols using Poly (N-vinyl-2-pyrrolidone) as a Reducing Agent. *Langmuir*, *22*, 7027-7034.

[188] Xiong, Y. J., Washio, I., Chen, J. Y., Cai, H. G., Li, Z. Y. & Xia, Y. N. (2006). Poly(vinyl pyrrolidone): A Dual Functional Reductant and Stabilizer for the Facile Synthesis of Noble Metal Nanoplates in Aqueous Solutions. *Langmuir*, *22*, 8563-8570.

[189] Washio, I., Xiong, Y. J., Yin, Y. N. & Xia, Y. N. (2006). Reduction by the end groups of Poly (vinyl pyrrolidone): A new and Versatile Route to the Kinetically Controlled Synthesis of Ag Triangular Nanoplates. *Adv. Mater*, *18*, 1745-1749.

[190] Tsuji, M., Hashimoto, M., Nishizawa, Y., Kubokawa, M. & Tsuji, T. (2005). Microwave-Assisted Synthesis of Metallic Nanostructures in Solution. *Chem. Eur. J*, *11*, 440-452.

[191] Tsuji, M., Hashimoto, M., Nishizawa, Y. & Tsuji, T. (2003). Preparation of Gold Nanoplates by a Microwave-Polyol Method. *Chem. Lett*, *32*, 1114-1115.

[192] Harpeness, R. & Gedanken, A. (2004). Microwave Synthesis of Core-Shell Gold/Palladium Bimetallic Nanoparticles. *Langmuir*, *20*, 3431-3434.

Copyright © 2010. Nova Science Publishers, Incorporated. All rights reserved.

[193] Harpeness, R., Gedanken, A., Weiss, A. M. & Slifkin, M. A. (2003). Microwave-Assisted Synthesis of Nanosized MoSe2. *J. Mater. Chem*., *13*, 2603-2606.

[194] Tuval, T. & Gedanken, A. (2007). A Microwave-Assisted Polyol Method for the Deposition of Silver Nanoparticles on Silica Spheres. *Nanotechnology*, *18*, 255601.

[195] Tang, S. C., Vongehr, S. & Meng, X. K. (2009). Carbon Spheres with Controllable Silver Nanoparticle Doping. *J. Phys. Chem. C*, in press (jp-2009-102492).

[196] Banhart, F. (1995). Laplacian Growth of Amorphous-Carbon Filaments in a non-Diffusion-Limited Experiment. *Phys. Rev. E*, *52*, 5156-5160.

[197] Ramesh, S., Koltypin, Y., Prozorov, R. & Gedanken, A. (1997). Sonochemical Deposition and Characterization of Nanophasic Amorphous Nickel on Silica Microspheres. *Chem. Mater*, *9*, 546-551.

[198] Gao, X. L., Gu, G. H., Hu, Z. S., Guo, Y., Fu, X. & Song, J. M. (2005). A Simple Method for Preparation of Silver Dendrites. *Colloids Surf. A*, *254*, 57-61.

[199] Sánchez-Iglesias, A., Pastoriza-Santos, I., Pérez-Juste, J., Rodríguez-González, B., García de Abajo, F. J. & Liz-Marzán, L. M. (2006). Synthesis and Optical Properties of Gold Nanodecahedra with Size Control. *Adv. Mater*, *18*, 2529-2534.

[200] Wiley, B. J., Chen, Y. C., McLellan, J. M., Xiong, Y. J., Li, Z. Y., Ginger, D. & Xia,Y. N. (2007). Synthesis and Optical Properties of Silver Nanobars and Nanorice. *Nano Lett*, *7*, 1032-1036.

[201] Pol, V. G., Srivastava, D. N., Palchik, O., Palchik, V., Slifkin, M. A., Weiss, A. M. & Gedanken, A. (2002). Sonochemical Deposition of Silver Nanoparticles on Silica Spheres. *Langmuir*, *18*, 3352-3357.

[202] Antonietti, M., Wenz, E., Bronstein, L. & Seregina, M. (1995). Synthesis and Characterization of Noble Metal Colloids in Block Copolymer Micelles. *Adv. Mater*, *7*, 1000-1005.

[203] Vorobyova, S. A., Lesnikovich, A. I. & Sobal, N. S. (1999). Preparation of Silver Nanoparticles by Interphase Reduction. *Colloids Surf. A*, *152*, 375-379.

[204] Kalele, S. A., Ashtaputre, S. S., Hebalkar, N. Y., Gosavi , S. W., Deobagkar, D. N., Deobagkar, D. D. & Kulkarni, S. K. (2005). Optical Detection of Antibody Using Silica-Silver Core-Shell Particles. *Chem. Phys. Lett*, *404*, 136-141.

[205] Hucul, D. A. & Brenner, A. (1981). A Strong Metal-Support Interaction Between Mononuclear and Polynuclear Transition-Metal Complexes and Oxide Supports Which Dramatically Affects Catalytic Activity. *J. Phys. Chem*., *85*, 496-498.

[206] Zhu, M. W., Qian, G. D., Ding, G. J., Wang, Z. Y. & Wang, M. Q. (2006). Plasma Resonance of Silver Nanoparticles Deposited on the Surface of Submicron Silica Spheres. *Mater. Chem. Phys*., *96*, 489-493.

[207] Freeman, R. G., Hommer, M. B., Grabar, K. C., Jackson, M. A. & Natan, M. J. (1996). Ag-clad Au Nanoparticles: Novel Aggregation, Optical, and Surface-Enhanced Raman Scattering Properties. *J. Phys. Chem*., *100*, 718-724.

[208] Chu, Y. E., Schonbrun, E., Yang, T. & Crozier, K. B. (2008). Experimental Observation of Narrow Surface Plasmon Resonances in Gold Nanoparticle Arrays. *Appl. Phys. Lett*, 93, 181108.

[209] Xu, M. L. & Dignam, M. J. (1994). Raman-Scattering by High-Density Dispersion. 3. Calculation of Raman Intensities for Molecules Physisorbed on Linear-Chains of Spherical-Particles. *J. Chem. Phys*., *100*, 197-203.

Copyright © 2010. Nova Science Publishers, Incorporated. All rights reserved.

[210] Liver, N., Nitzan, A. & Gersten, J. I. (1984). Local-Fields in Cavity Sites of Rough Dielectric Surfaces. *Chem. Phys. Lett*, *111*, 449-454.

[211] He, Y., Wu, W. F., Lu, G. W. & Shi, G. Q. (2006). A Facile Route to Silver Nanosheets. *Mater. Chem. Phys*., *98*, 178-182.

[212] Zou, X. Q., Ying, E. B. & Dong, S. J. (2007). Preparation of Novel Silver-Gold Bimetallic Nanostructures by Seeding With Silver Nanoplates and Application in Surface-Enhanced Raman Scattering. *J. Colloid Interface Sci*., *306*, 307-315.

[213] Huang, S. X., Ma, H. Y., Zhang, X. K., Yong, F. F., Feng, X. L., Pan, W., Wang, X. L., Wang, Y. & Chen, S. H. (2005). Electrochemical Synthesis of Gold Nanocrystals and Their 1D and 2D Organization. *J. Phys. Chem. B*, *109*, 19823-19830.

[214] Natter, H. & Hempelmann, R. (2008). Nanocrystalline Metals Prepared by Electrodeposition. *Z. Phys. Chem*., *222*, 319-354.

[215] Gomez, E., Kipervaser, Z. G., Pellicer, E. & Valles, E. (2004). Extracting Deposition Parameters for Cobalt-Molybdenum Alloy From Potentiostatic Current Transients. *Phys. Chem. Chem. Phys*., *6*, 1340-1344.

[216] Zhang, J. T., Li, X. L., Sun, X. M. & Li, Y. D. (2005). Surface Enhanced Raman Scattering Effects of Silver Colloids with Different Shapes. *J. Phys. Chem. B*, *109*, 12544-12548.

[217] Hayazawa, N., Tarun, A., Inouye, Y. & Kawata, S. (2002). Near-Field Enhanced Raman Spectroscopy using Side Illumination Optics. *J. Appl. Phys*., *92*, 6983-6986.

[218] Rivas, L., Sanchez-Cortes, S., Garcia-Ramos, J. & Morcillo, G. (2000). Mixed Silver/Gold Colloids: A Study of Their Formation, Morphology, and Surface-Enhanced Raman Activity. *Langmuir*, *16*, 9722-9728.

[219] Hayakawa, K., Yoshimura, T. & Esumi, K. (2003). Preparation of Gold-Dendrimer Nanocomposites by Laser Irradiation and their Catalytic Reduction of 4-Nitrophenol. *Langmuir*, *19*, 5517-5521.

[220] Rashid, M. H., Bhattacharjee, R. R., Kotal, A. & Mandal, T. K. (2006). Synthesis of Spongy Gold Nanocrystals with Pronounced Catalytic Activities. *Langmuir*, *22*, 7141-7143.

[221] Liu, P. & Zhao M. F. (2009). Silver Nanoparticle Supported on Halloysite Nanotubes Catalyzed Reduction of 4-nitrophenol (4-NP). *Appl. Surf. Sci*., *255*, 3989-3993.

[222] Xie, L., Chen, M. & Wu, L. M. (2009). Fabrication and Properties of Hollow Poly-(N-isopropylacrylamide)-Ag Nanocomposite Spheres. *J. Polym. Sci.: Pol. Chem*., *47*, 4919-4926.

Copyright © 2010. Nova Science Publishers, Incorporated. All rights reserved.

Copyright © 2010. Nova Science Publishers, Incorporated. All rights reserved.

In: Silver Nanoparticles
Editor: Audrey E. Welles, pp. 55-117
ISBN: 978-1-61668-690-1
© 2010 Nova Science Publishers, Inc.

Chapter 2

LOW- AND HIGH-ORDER NONLINEARITIES OF SILVER NANOPARTICLES

R. A. Ganeev*
Institute of Electronics, Uzbekistan Academy of Sciences, Akademgorodok,
33, Dormon Yoli Street, Tashkent 100125, Uzbekistan.

ABSTRACT

We present the studies of the low-order optical nonlinearities (nonlinear refraction, nonlinear absorption, nonlinear susceptibility) of the silver nanoparticles of various sizes using the probe laser radiation of different pulse duration (100 fs – 50 ps) and wavelength (396, 532, 793, and 1064 nm). We show that the influence of the surface plasmon resonance of these clusters considerably changes the nonlinear optical response of silver nanoparticle-containing medium. We analyze the influence of aggregation of silver nanoparticles on the variation of the sign of nonlinear refraction of this medium. Various methods of nanoparticle formation are analyzed and compared with commercially available samples.

High-order nonlinearities of silver clusters are studied by means of the harmonic generation of laser radiation in laser-produced plasma plumes containing silver nanoparticles. We show the advantages of the application of nanoparticle-containing plasma plumes as the nonlinear media for radiation conversion compared to the monoparticle-containing plumes. Six to fifteen enhancement factors of conversion efficiency of 800 nm radiation toward the extreme ultraviolet range was achieved in the former case. We present the results of modification of the morphology of silver nanoparticles before and after laser ablation of nanoparticle-containing targets at different intensities of laser ablation beam.

Copyright © 2010. Nova Science Publishers, Incorporated. All rights reserved.

* Corresponding author: E-mail: rashid_ganeev@mail.ru

INTRODUCTION

The investigation of nonlinear optical processes connected with the self-focusing and self-defocusing of various media is of current interest. The optical nonlinearities of such media are attractive for potential applications in nonlinear optical signal processing, optical limiting and optical devices [1]. In recent years, nonlinear optical characteristics of nanoparticle suspensions (NS) have been under active investigation. These materials demonstrate high nonlinearities and fast response [2,3], especially in the frequency region of surface plasmon resonance (SPR). In [3,4], it has been shown that the nonlinear refractive index of the copper colloidal solution has a considerable value. The same results have been shown for silver [2,5] and gold [6] NS. Optical limiting characteristics of colloidal aggregates were studied in [7] at the wavelength of λ = 532 nm of picosecond and nanosecond lasers. It was shown that at certain conditions the optical limiting (OL) in these media can surpass that of C_{60}. The size effects of OL were observed for gold clusters [8]. These colloidal structures possess fast (<360 fs) nonlinear optical response and high nonlinearity in the femtosecond range ($\chi^{(3)} = 1.5\times10^{-7}$ esu for Ag clusters) [9,10]. At the same time, we should note that there have been few OL studies of NS despite their high self-action and nonlinear absorption properties in picosecond and nanosecond ranges.

Silver nanoparticles have attracted interest due to their potential applications. Silver nanoparticles have an advantage over other metal nanoparticles (i.e., gold and copper) since the SPR energy of Ag is located far from the interband transition energy. This means that in the silver nanoparticle-contained compound, we can investigate the nonlinear optical effects solely based on surface plasmon contribution. Both chemical and laser ablation techniques were previously used for the preparation of Ag nanoparticles in liquids. These techniques can be distinguished from each other through their different nanoparticle size distributions. Laser ablation produces silver colloids that do not require the use of stabilizers. The application of laser ablation in liquids has a number of advantages in comparison with an ion implantation technique in solids (e.g., simplicity, low cost, variability, etc). The analysis of optical studies of Ag nanoparticles prepared by laser ablation was presented by Brause *et al* [11]. The nonlinear optical studies of colloidal Ag nanoparticles in various aggregated states were reported in [12]. These colloidal structures demonstrate fast nonlinear optical response and high nonlinear optical susceptibility ($\chi^{(3)} = 1.5\times10^{-7}$ esu for Ag clusters [10]). The dynamics of the spatial parameters of aggregated Ag nanoparticles lead to the variation of their nonlinear optical characteristics. At the same time the mechanisms of these variations have yet to be determined. The location of SPR of silver nanoparticles (400–430 nm) depends on preparation conditions [11]. The enhancement of nonlinear susceptibility responsible for nonlinear absorption and refraction in this spectral range was reported in [13]. The quantum confinement in the case of small-sized Ag nanoparticles can also lead to the growth of nonlinear optical properties of these structures.

The dynamics of spatial parameters of aggregated particles leads (together with the optical characteristics changes) to the nonlinear optical characteristics variations. At the same time, the physical nature of the variation of the nonlinear refractive indices of NS for different pulse durations remains unresolved. Note also the absence of frequency conversion studies in such media.

Copyright © 2010. Nova Science Publishers, Incorporated. All rights reserved.

In this chapter we report the studies of low- and high-order optical nonlinearities of the silver nanoparticles:

(a) The nonlinear optical parameters of silver NS are investigated by the Z-scan method. We measure nonlinear refractive indices (γ or n_2), nonlinear susceptibilities ($\chi^{(3)}$ ($-\omega$; ω, $-\omega$, ω)) and nonlinear absorption coefficients (β) of such solutions on the wavelengths of Nd:YAG laser radiation and its second harmonic (λ = 1064 nm and 532 nm, τ = 35 ps and 28 ns). We study the OL of picosecond and nanosecond radiation (λ = 1064 nm and 532 nm) in NS. The influence of aggregation of colloidal clusters on OL in these media was considered. We show that the appearance of the long-wave wing of absorption at the final stages of aggregation leads to the nonlinear absorption of picosecond pulses. We report on investigations of nonlinear susceptibilities and nonlinear refractive indices of colloidal silver at different stages of aggregation.

(b) Investigations of nonlinear optical characteristics (nonlinear refractive indices, nonlinear absorption coefficients and third-order nonlinear susceptibilities) of silver nanoparticles implanted in glasses are presented using picosecond Nd :YAG laser radiation (λ = 1064 nm) and its harmonics (532 nm, 355 nm) and the *Z*-scan technique. The variations of the sign of the nonlinear refractive indices depending on matrix properties are analyzed. The optical limiting properties of these materials are discussed in the framework of two-photon absorption. The mechanisms responsible for saturated absorption and nonlinear refraction are discussed.

(c) We present our studies of optical, structural, and nonlinear optical properties of Ag nanoparticles prepared by laser ablation in various liquids. We analyze nonlinear refraction and nonlinear absorption of these media using the radiation of different wavelength, pulse repetition rate, and pulse duration. In particular, the optical, structural, and nonlinear optical properties of silver nanoparticles prepared by laser ablation in various liquids were investigated at 397.5, 532, and 795 nm. The TEM and spectral measurements have shown temporal dynamics of size distribution of Ag nanoparticles in solutions. The thermal-induced self-defocusing dominated in the case of high pulse repetition rate as well as in the case of nanosecond pulses. In the case of low pulse repetition rate, the self-focusing ($\gamma = 3\times10^{-13}$ cm^2 W^{-1}) and saturated absorption ($\beta = 1.5\times10^{-9}$ cm W^{-1}) of picosecond and femtosecond radiation were observed in these colloidal solutions. The nonlinear susceptibility of Ag nanoparticles ablated in water was measured to be 5×10^{-8} esu (at λ = 397.5 nm).

(d) A study of silver thin films and nanoparticles prepared by subnanosecond laser deposition in vacuum is reported. We compare the laser ablation in vacuum at the weak- and tight-focusing conditions of a Ti:sapphire laser beam and analyze the nanoparticles synthesized in the latter case using absorption spectroscopy, x-ray fluorescence, atomic force microscopy, and scanning electron microscopy. Our results show that the silver nanoparticle formation can be accomplished using long laser pulses under tight-focusing conditions.

(e) Nanoparticle-containing media can be used for efficient high-order harmonic generation (HHG) of laser radiation. We present the results of studies of the high-order harmonics generated in the laser-produced plasmas containing Ag

Copyright © 2010. Nova Science Publishers, Incorporated. All rights reserved.

nanoparticles. These results are compared with the harmonics generated in the plasma produced on the surface of bulk targets at different delays between the subnanosecond heating prepulse and femtosecond pulse and different intensities of prepulse on the target surface. We discuss the harmonic enhancement, which was observed in the case of nanoparticle-containing plumes with regard to the monoparticle-containing plasmas. Morphological studies of plasma debris confirmed the presence and integrity of Ag nanoparticles in the plumes. High-order harmonic generation up to the 55th order was achieved using 15 nm and 110 nm silver nanoparticle-containing plumes, when femtosecond radiation propagated through the preformed plasma. These results are compared with the high-order harmonics generated from the plasma produced on the surface of bulk silver at different delays between the subnanosecond prepulse and the femtosecond pulse.

(f) We apply the technique of high-order harmonic generation from laser-produced plasma to investigate the harmonics generated from a medium that contains an abundance of micron- and sub-micron-sized structures. We compare harmonic efficiencies from the plasma plumes containing silver nanoparticles (110 nm spherical) and colloidal silver (blocks of 100–1000 nm). We compare these results with those obtained using solid bulk targets. We show that plasma media that are abundant with small-sized structures have higher harmonic generation efficiencies. Results also reveal that the harmonic cutoff is not affected significantly by using the nanostructured targets. The maximum conversion efficiency we observe is 4×10^{-5} using silver nanoparticles.

(g) Highly efficient harmonic generation in the range of 9^{th} order to 19^{th} order was observed for Ag nanoparticles. The stability of harmonic generation is enhanced by utilizing special target fabrication techniques and through optimizing the conditions of plasma plume formation. Broadband harmonic generation was observed through the optimization of femtosecond laser intensity and through the use of spectrally broadened laser pulses. The harmonic generation was compared for various target materials (nanostructured and bulk) and for Ag nanoparticle targets prepared from different fabrication techniques. Efficient generation of even and odd order harmonics was observed through the use of two-color pulses. The observations can be explained qualitatively from symmetry breaking of HHG through the introduction of second harmonic pulses. The spectral broadening and shift of harmonic radiation can be understood from the self-modulation of the laser and harmonic radiation in the plasma.

Copyright © 2010. Nova Science Publishers, Incorporated. All rights reserved.

1. LOW-ORDER NONLINEARITIES OF SILVER NANOPARTICLES AND THEIR CHARACTERIZATION

1.1. Basic Relations

1.1.1. Nonlinear refractive indices, nonlinear absorption coefficients, and nonlinear susceptibilities

The change of a medium's refractive index in an electromagnetic field (when only third-order nonlinear optical processes are taken into consideration) can be determined as follows:

$$\Delta n = \gamma I = 0.5 n_2 |E|^2, \tag{1}$$

where I and E are the intensity and electric field of the electromagnetic wave, respectively. The nonlinear refractive indices (n_2 and γ) describe the same process in different measurement units and are related by the following relation: n_2 [esu units] = $(c \times n_0/40\pi)\gamma$ [SI units]. Here c is the light velocity, and n_0 is the linear term of the refractive index of the medium.

In the general case, the refractive index can be written as follows:

$$n = n_0 + \gamma I + \eta I^2 + \cdots, \tag{2}$$

where η is the fifth-order nonlinear refractive index.

In the case of linear dependence of the absorption coefficient on the laser radiation intensity one can use the following equation:

$$\alpha(I) = \alpha_0 + \beta^{(2\omega)} I, \tag{3}$$

where α_0 is the linear term of the absorption coefficient of the medium, and $\beta^{(2\omega)}$ is the two-photon absorption coefficient. In the case of three-photon absorption, the dependence of the absorption coefficient on the laser radiation intensity can be represented as follows:

$$\alpha(I) = \alpha_0 + \beta^{(2\omega)} \mathrm{I} + \beta^{(3\omega)} I^2 = \alpha_0 + \beta_{\mathrm{eff}} I, \tag{4}$$

where $\beta^{(3\omega)}$ is the three-photon absorption coefficient, and $\beta_{\mathrm{eff}} = \beta^{(2\omega)} + \beta^{(3\omega)} I$ is the 'effective' nonlinear absorption coefficient.

Our calculations of the real and imaginary parts of the nonlinear susceptibility were carried out using the relations

$$\mathrm{Re}\ \chi^{(3)} = 10^{-6} c (n_0)^2 \gamma / 480\pi^2 \tag{5}$$

and

$$\mathrm{Im}\ \chi^{(3)} = 10^{-7} c^2 (n_0)^2 \beta / 96\pi^2 \omega, \tag{6}$$

Copyright © 2010. Nova Science Publishers, Incorporated. All rights reserved.

where c is the light velocity in cm s^{-1}, ω is the laser radiation frequency in cycles s^{-1}, β is the nonlinear absorption coefficient in cm W^{-1}, and γ is the nonlinear refractive index in cm^2 W^{-1}.

1.1.2. The transmission Z-scan

The analysis of nonlinear optical characteristics of different materials using nonlinear interferometry, the degenerate four-photon method, and nondegenerate three-wave frequency mixing is sufficiently precise and versatile. However, the study of nonlinear optical characteristics with these methods requires rather complex instrumentation, and the interpretation of results is often complicated because of the simultaneous presence of two or more nonlinear mechanisms. In most cases, these techniques are insufficiently sensitive for separating the contributions of several nonlinear optical mechanisms.

The Z-scan technique [14,15] shows some advantages compared to the above-mentioned methods. There are several modifications of the Z-scan technique such as the conventional transmission Z-scan ('*TZ*-scan') [14,15], eclipsing Z-scan [15], two-color Z-scan [16], time-resolved Z-scan [17], and reflection Z-scan [18]. In our studies we used the *TZ*-scan schemes. One of the advantages of the *TZ*-scan technique is the possibility of defining the contribution of several nonlinearities when they are present simultaneously. In general, when both nonlinear refraction and absorption are present, the normalized transmittance T can be written as follows [19]:

$$T = 1-4x[(x2 + 9)(x2 + 1)]^{-1}\Delta\Phi_0 -2(x2 + 3)[(x2 + 9)(x2 + 1)]^{-1}\Delta\Psi_0, \quad (7)$$

where $x = z/z_0$, $z_0 = 0.5k(w_0)^2$ is the diffraction length, $k = 2\pi/\lambda$ is the wavenumber, w_0 is the beam waist radius, $\Delta\Phi_0$ and $\Delta\Psi_0$ are the parameters, which determine the phase shift near the focus as a result of nonlinear refraction and absorption, $\Delta\Phi_0 = k\gamma I_0 L_{eff}$, $\Delta\Psi_0 = \beta I_0 L_{eff}/2$, I_0 is the laser radiation intensity in the focus, $L_{eff} = [1 - \exp(-\alpha_0 L)]/\alpha_0$ is the effective length of the sample, and L is the sample length.

Writing the following expression: $\rho = \beta/2k\gamma$, one can get the relation between $\Delta\Phi_0$ and $\Delta\Psi_0$ ($\Delta\Psi_0 = \rho\Delta\Phi_0$). Equation (7) can in this case be rewritten in the following form:

$$T = 1 -2(\rho x2 + 2x + 3\rho)[(x2 + 9)(x2 + 1)]^{-1}\Delta\Phi_0. \quad (8)$$

The best fitting of theory and experiment can be observed at specific values of ρ and $\Delta\Phi_0$. Using ρ and $\Delta\Phi_0$ as parameters, the $\Delta\Psi_0$ value can be determined. Further, by subtracting the nonlinear absorption from equation (7), one can calculate the nonlinear refraction of samples.

1.2. Experimental Arrangements

In our studies we used three lasers operating at different lasing conditions. A picosecond Nd:YAG laser at a 2 Hz pulse repetition rate was used in most of our experiments. A single pulse (t = 55 ps, or in some cases 35 ps) was amplified up to the energy of E = 2 mJ. The nonlinear optical characteristics of nanoparticles were investigated at the wavelengths of this laser (λ = 1064 nm) and its second harmonic (λ = 532 nm, E = 0.2 mJ). We also used a

Copyright © 2010. Nova Science Publishers, Incorporated. All rights reserved.

Ti:sapphire laser delivering femtosecond pulses (t = 110 fs, λ = 795 nm, E = 10 mJ) at a 10 Hz pulse repetition rate. The variation of the distance between the gratings of the compressor of this laser allowed generation of pulses with variable duration (from 110 fs to 1.6 ps). This laser also operated at a *Q*-switching regime producing 8 ns pulses. 80 MHz, 100 fs, 300 mW pulses were also available from the seeding oscillator (Tsunami) of this laser for the investigation of thermally induced self-defocusing of various media. The third laser was a hybrid Nd:glass–Ti:sapphire laser generating 475 fs, 1054 nm, 0.1 mJ pulses at a 1 Hz repetition rate. The laser radiation was focused by a 30 cm focal length lens *FL* (Figure. 1). The objects under study *S* were moved using a translating stage *TS* along the optical *Z*-axis through the focusing area. The maximum radiation intensity was varied in the range of 4×10^{8} – 4×10^{10} W cm^{-2}. Its value depended on the optical breakdown and multiphoton ionization thresholds of the materials investigated. The energy of the laser pulses was measured using a calibrated photodiode *PD1* and recorded by a stroboscopic voltage converter *SVG1*. Calibrated neutral filters varied the laser radiation energy. A 1 mm aperture *A* transmitting 2% of laser radiation was set at a distance of 150 cm from the focusing area (the closed-aperture scheme). A photodiode *PD2* was placed behind the aperture and the propagated radiation was recorded by a stroboscopic voltage converter *SVG2*. In order to exclude the influence of the instability of the laser radiation on the measurement of the nonlinear optical parameters of the samples, a signal detected by the *SVG2* was normalized by a signal detected by the *SVG1*.

The closed aperture scheme was capable of determining both the sign and magnitude of the γ of the materials from the normalized transmittance dependences *T(z)*. The nonlinear absorption coefficient was measured using the open aperture scheme, when the sample's transmission was measured without the aperture. In this case, a detector measuring the energy of the propagated beam had a sufficiently broad aperture and was placed at such a distance from the sample that the transmitted radiation was entirely detected.

A personal computer *PC* collected the measured signals from the stroboscopic voltage converters. The translation system consisted of a micrometer and step motor and provided a step movement of 20 μm/cycle. The data processing procedure included the averaging of measurements over the software-specified number of laser shots at a given coordinate *Z* and the exclusion of certain measurements at significant intensity fluctuations of incident radiation. Twenty separate measurements were performed at a fixed position of the sample. This allowed a decrease in the total error of transmission measurements (to 2%). The *PC* carried out general control over the experimental set-up.

1.3. Characterization of Nonlinear Optical Parameters of Silver-Doped Silica Glasses at λ = 1064 nm

Composite materials based on insulator matrices doped with metal nanoparticles took the attention more than two decades ago [20]. These investigations are of great interest nowadays [21,22] due to the perspectives of using such materials as ultra-fast optical switching systems and optical limiters. These composite materials with metal nanoparticles possess high values of third-order nonlinear susceptibilities, especially in the spectral range of the SPRs [20,22].

Copyright © 2010. Nova Science Publishers, Incorporated. All rights reserved.

SPRs of metal nanoparticles are situated in a broad spectral range depending on metal type, particle shape, structure and size, as well as on the properties of the surrounding insulator.

Nonlinear optical coefficients of ellipsoidal silver nanoparticles in the longitudinal surface plasmon absorption region (800 nm) were analyzed in [23]. It has been observed that the nonlinear absorption and nonlinear refractive indices of silver nanorods embedded in borosilicate glass differ remarkably from those of spheroids. Third-order nonlinearities of glasses doped with a large number of copper or silver particles were studied by Uchida *et al* [4] using degenerate four-wave mixing with an emphasis on particle-size dependence. They observed the growth of $\chi^{(3)}$ at a wavelength of the absorption peak (up to 10^{-7} esu). The increase of the $\chi^{(3)}/\alpha$ value (α is the linear absorption coefficient) with the growth of particle radius was explained by the size dependence of the imaginary part of the dielectric constant of metal particles and the local-field factor. Analogous size dependence of the third-order susceptibility was reported by Yang *et al* [24] in their experiments with copper nanoparticles embedded in fused silica. Osborne *et al* [25] reported laser-induced sign reversal of the nonlinear refractive index of silver-doped glass. The mechanism of this change appears to be a photochemical reaction that produces a silver-oxide layer on the surface of nanoclusters.

All these measurements were carried out using UV [26], visible (532 nm [24], 570 nm [25], 420 nm [4]) or 800-nm radiation [23]. At the same time it is interesting to analyze the behavior of such nanoparticle-doped glasses in the infrared range using photons with an energy far below the SPRs of these materials. The attention to this spectral range can be explained by potential applications of such media in optical limiting and optical switching devices.

In this subsection, the studies of nonlinear optical characteristics of the silver nanoparticles implanted in glass matrices are presented using the *Z*-scan technique and infrared laser radiation (λ = 1064 nm). The optical limiting properties of these materials are discussed in the framework of two-photon absorption [27].

The silica glasses (Heraeus) containing 100% SiO_2 and soda-lime silicate glasses (Societa Italiana Vetro) containing 70% SiO_2, 20% Na_2O and 10% CaO were used for the preparation of composite materials. The linear refractive indices of silica glasses (SGs) and soda-lime silicate glasses (SLSGs) were 1.5 and 1.54, respectively. The glasses were prepared as 2×2 cm^2 plates with a thickness of 1 mm (SG) and 3 mm (SLSG). The energy used for implantation was 60 keV at dose of 4×10^{16} ions cm^{-2} in case of Ag^+. The current density of the ion beam was 10 μA cm^{-2}. The depth of the location of metal nanoparticles in the surface glass layer was 60 nm [28]. X-ray reflectometry was used in order to estimate the density and thickness of thin layers [29]. Composite materials were also analyzed by the grazing incidence small-angle X-ray scattering (GISAXS) technique. Optical transmission measurements were carried out using a spectrophotometer (Perkin Elmer Lambda 19).

The Z-scan technique was used for the determination of nonlinear optical characteristics of the investigated samples. We used a home-made Nd:YAG laser operated in the mode-locked regime. Output characteristics of Nd:YAG laser radiation (λ = 1064 nm) were as follows: pulse duration 35 ps, pulse energy 1 mJ and 2-Hz pulse repetition rate. The maximum laser intensity at the focal point was 3×10^{10} W cm^{-2}, whereas the intensity of optical breakdown was 8×10^{10} W cm^{-2} for the glasses with silver nanoparticles.

Copyright © 2010. Nova Science Publishers, Incorporated. All rights reserved.

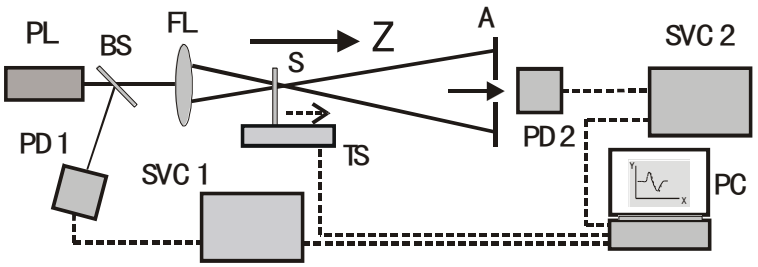

Figure 1. Experimental set-up for Z-scan measurements. PL: picosecond laser; FL: focusing lens; S: sample; PD1 and PD2: photodiodes; SVC1 and SVC2: stroboscopic voltage converters; TS: translation stage; PC: personal computer; A: aperture; BS: beam splitter.

In our studies, the ion-implantation technique was applied for preparation of metal-doped glasses [30]. However, this technique, being capable of sensitizing nanoparticles with a high filling factor, forms in some cases layers with a broad distribution of particle sizes [31]. The growth of metal nanoparticles in glasses during ion implantation occurs when the concentration of metal atoms becomes larger than the solubility level, which is determined by an ionic dose of 1×10^{16} ion cm^{-2} at the ion energy of 60 keV [32]. X-ray and optical spectroscopic measurements proved the formation of metal nanoparticles in our studies. These studies (GISAXS, X-ray reflectometry) have shown a broader size distribution of nanoparticles (from 2 to 18 nm) that was also observed in the transmission electron microscopy (TEM) measurements. The depth of the location of nanoparticles in glasses was 60 nm. The formation of metal nanoparticles was also proven by the appearance of selective absorption lines in optical transmission spectra with the transmission minima in the ranges of 400–450 nm (for silver-doped glasses), corresponding to the SPR of silver nanoparticles (Figure. 2). Radiation defects stimulate additional light absorption in glasses in the short-wavelength spectral range. However, it should be noted that our nonlinear optical studies were performed using 1064-nm radiation, which lies far from both SPRs and intra-band transitions.

Copyright © 2010. Nova Science Publishers, Incorporated. All rights reserved.

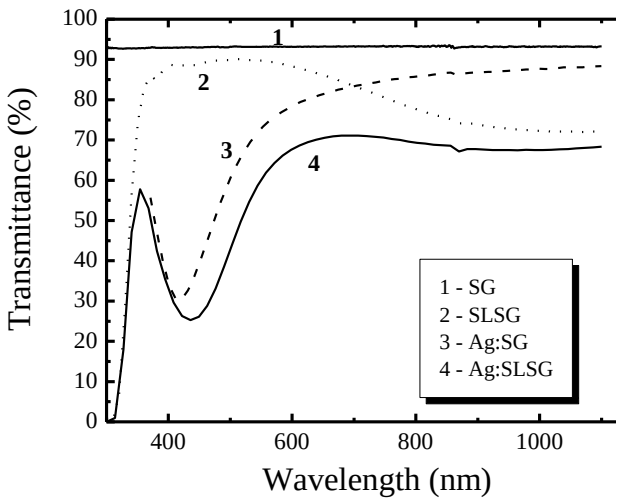

Figure 2. The transmission spectra of (1) SG, (2) SLSG, (3) Ag:SG, and (4) Ag:SLSG.

No considerable differences in normalized transmittance dependences measured both from implanted and non-implanted sides were observed. In fact, as the quantum dots are not uniformly implanted but occupy only a thin layer of the glasses, it can be guessed that the linear refractive indices of the implanted and non-implanted surfaces are different. This variation could induce a small difference in the reflection losses and hence in the net intensity of the laser beam entering the sample.

The value of the nonlinear refraction index can be varied in a large range depending on interaction type (resonant or non-resonant). Non-resonant contributions to the refractive index are usually positive [33]. In the case of quasi-resonant (one- or two-photon) interaction, the sign of the nonlinear refraction index is determined by a correlation between fundamental frequency, doubled frequency (in the case of two-photon quasi-resonance) and resonant frequency of the investigated medium.

A considerable nonlinear contribution to the refractive index can also be due to the thermal effect caused by heat transfer from metal nanoparticles to the lattice. The nonlinear thermal effect is due to matter density changing after local heating. The rise time (τ) of refractive-index variations is determined by $\tau = R/V_s$ (R is the beam-waist radius and V_s is the sound velocity in the lattice). At our experimental conditions (R =75 μm, $V_s \sim 5500$ m s^{-1}) $\tau \approx$ 14 ns, i.e. three orders larger than the laser pulse duration (35 ps), so that the thermal effect can be excluded from the consideration.

The optical properties of nanoparticles can be considered in the framework of an effective medium [34] because the wavelength of the laser radiation used in these studies was larger than the sizes of metal nanoparticles. Such method allows us to consider the composite materials as quasi-homogeneous media. One can consider the simple two-level model for homogeneous condensed matter [13], from which the nonlinear refractive index can be presented as follows:

$$n_2 = -2\pi N \left| \mu_{i0} \right|^4 \{n_0[\hbar(\omega_{i0} - \omega_p)]^3\}^{-1}. \quad (9)$$

Here ω_p and ω_{i0} are the frequencies of SPR and laser radiation. Index i determines one- or two-photon processes, N is the concentration of nanoparticles and μ_{i0} are the transition dipole moments at the frequencies ω_{i0}. The sign of the nonlinear refractive index is determined by the sign of detuning of the laser radiation frequency (or their harmonics) from SPRs of metal nanoparticles. The real part of the third-order nonlinear susceptibility has a linear dependence on n_2 [13]. The spectral dependence of $\chi^{(3)}$ can be written as follows:

$$\mathrm{Re}\chi^{(3)} \propto -(\omega_{i0} - \omega_p)^{-3}. \quad (10)$$

Self-defocusing from a two-photon resonance has been reported by Lehmberg *et al* [35]. The two-photon energy of their laser radiation (1064 nm, 30 ps) was 250 cm^{-1} above the 7*s* level of Cs vapors, giving a two-photon enhancement and a negative contribution to the refractive index.

In the general case, when both nonlinear refraction and nonlinear absorption are present in the material, the third-order susceptibility can be considered as a complex value

$$\chi^{(3)} = \mathrm{Re}\chi^{(3)} + i\,\mathrm{Im}\chi^{(3)}, \quad (11)$$

Copyright © 2010. Nova Science Publishers, Incorporated. All rights reserved.

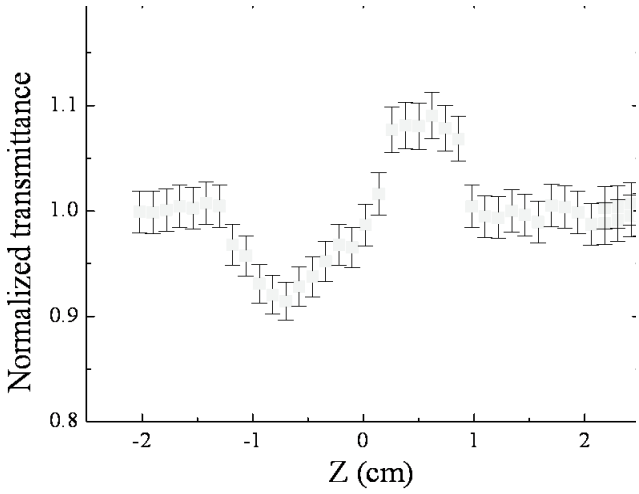

(a)

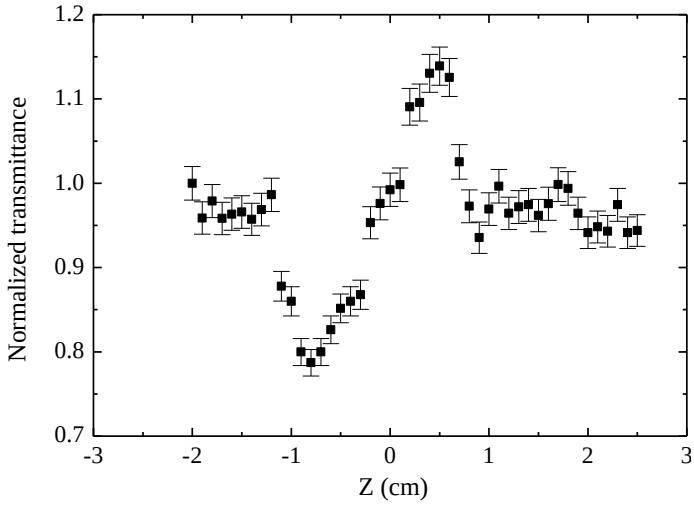

(b)

Figure 3. The normalized transmittance dependences for Ag:SG (a) and Ag:SLSG (b) in closed aperture scheme. λ = 1064 nm.

where the real part is connected with the nonlinear refraction and the imaginary part is connected with the nonlinear absorption. The nonlinear absorption of pure SLSG was negligible, and $\chi^{(3)}$ of SLSG was determined only by the real part as [13]

$$\mathrm{Re}\chi^{(3)} = n_0 n_2 / 3\pi. \tag{12}$$

The following equation was used for the measurements of the nonlinear absorption coefficient:

Copyright © 2010. Nova Science Publishers, Incorporated. All rights reserved.

$$T(z) \approx q(z) - 1/\ln(1 + q(z)), \quad (13)$$

where $q(z) = \beta I(z) L_{\text{eff}}$, $I(z)$ being the laser intensity. Figure 3 presents the dependences of the normalized transmittance in the closed aperture scheme for Ag:SG and Ag:SLSG samples. As one can see from the figure, the positive nonlinearity (self-focusing effect) was observed for both kinds of samples. The composites containing silver nanoparticles are characterized by different locations of SPR maxima depending on substrate type. SPRs of Ag:SG and Ag:SLSG were located at 415 nm (ω = 24096.4 cm^{-1}) and 440 nm (ω = 22727.3 cm^{-1}), respectively. The doubled frequency of the laser radiation is smaller than SPRs of Ag nanoparticles in both matrices, that corresponds to the positive sign of the refractive nonlinearity. The corresponding n_2 and $\text{Re}\chi^{(3)}$ for Ag:SG were measured to be 1.5×10^{-8} esu and 3×10^{-9} esu, while in the case of Ag:SLSG these parameters were measured to be 3.5×10^{-8} esu and 6×10^{-9} esu. Our studies of silver-doped samples in the open aperture scheme have shown no nonlinear absorption in these media at λ = 1064 nm.

The normalized transmittance curves presented in Figure 3 show some instability. These rough curves were especially pronounced in the case of silver-doped glasses. We attribute this phenomenon to the broad size distribution of Ag nanoparticles. Inhomogeneous distribution of nanoparticles in the area of the focal volume can also play an important role in the observed instabilities of the $T(z)$ dependences.

1.4. Saturated Absorption and Nonlinear Refraction of Silicate Glasses Doped with Silver Nanoparticles at 532 nm

The metal nanoparticles demonstrate high values of nonlinear susceptibility in the vicinity of SPR. The resonance occurs at the frequency where the local electric field inside of metal nanoparticle becomes maximal. The SPR maximum is determined by the following equation [34]:

$$\varepsilon_1(\omega_{\text{spr}}) + 2\varepsilon_{\text{m}}(\omega_{\text{spr}}) = 0 \quad (14)$$

where ε_1 and ε_{m} are real dielectric constants of metal nanoparticles and matrix glass, and ω_{spr} is the SPR frequency. The SPR of silver nanoparticles is located in the visible range (400–425 nm). The $\chi^{(3)}$ of silver nanoparticles at the wavelength of second harmonic radiation of Ti:sapphire laser (λ = 400 nm) was measured to be 1.5×10^{-7} esu [10], which is one of the highest values among the reported results of nonlinear susceptibility measurements.

It should be noted that previous studies of nonlinear optical parameters of silver nanoparticles-doped glasses were mostly focused on determination of $\chi^{(3)}$. In this subsection, we present the results of study of the saturated absorption and nonlinear refraction in silicate glasses doped with Ag nanoparticles at λ = 532 nm and their dependence on laser radiation intensity [36].

Silver nanoparticles were implanted in 1 mm thick silicate glass and soda lime silicate glass plates using ion implantation technique (see previous subsection). The output characteristics of second harmonic radiation of Nd:YAG laser were as follows: pulse duration t = 55 ps, pulse energy E = 0.26 mJ, and wavelength λ = 532 nm.

Copyright © 2010. Nova Science Publishers, Incorporated. All rights reserved.

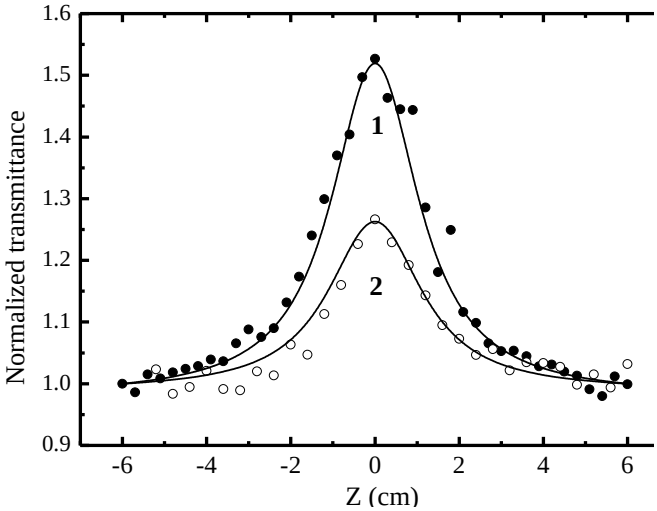

Figure 4. The normalized transmittance dependences of (1) Ag:SLSG, and (2) Ag:SG in the case of open aperture Z-scan scheme at laser radiation intensity of $I_0 = 2.5\times10^9$ W cm^{-2}. The solid lines show theoretical fits.

It was shown previously that silver-doped glasses possess by saturated absorption. Hamanaka *et al* have analysed the spectral dispersion of the imaginary part of third-order susceptibility of silver-doped glass matrices [37]. It was shown that Im $\chi^{(3)}$ was negative in the range of 385–436 nm.

The dependence of absorption coefficient (α) on laser radiation intensity (I) can be written as

$$\alpha(I) = \alpha_0 + \beta I \tag{15}$$

where α_0 is the linear absorption coefficient, and β is the nonlinear absorption coefficient. β is negative in the case of saturated absorption.

Figure 4 shows the normalized transmittance dependences of Ag:SLSG and Ag:SG measured using open aperture Z-scan scheme at $I_0 = 2.5\times10^9$ W cm^{-2}. The transmission of samples was increased due to saturated absorption as they approached close to the focal plane.

The normalized transmittance in the case of open aperture scheme can be determined by Eq. (13). After fitting of Eq. (13) with experimental data the nonlinear absorption coefficients of Ag:SLSG and Ag:SG were calculated to be -6.7×10^{-5} and -3.6×10^{-5} cm W^{-1}, respectively. Parameter β can be presented as $\beta = -\alpha_0/I_s$ that is a ratio between linear absorption coefficient and saturated intensity. The I_s were evaluated for two our samples to be 1.1×10^9 W cm^{-2} (Ag:SLSG) and 1.4×10^9 W cm^{-2} (Ag:SG). The Im$\chi^{(3)}$ of Ag:SLSG and Ag:SG at $I_0 = 2.5\times10^9$ W cm^{-2} were calculated to be -2.4×10^{-8} and -1.3×10^{-8} esu, respectively.

Copyright © 2010. Nova Science Publishers, Incorporated. All rights reserved.

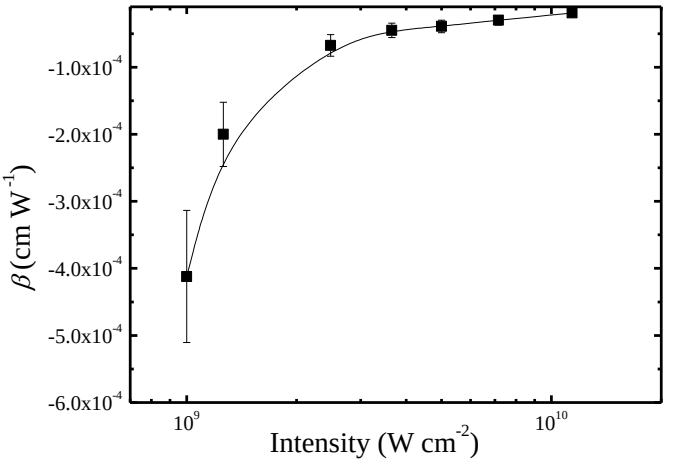

(a)

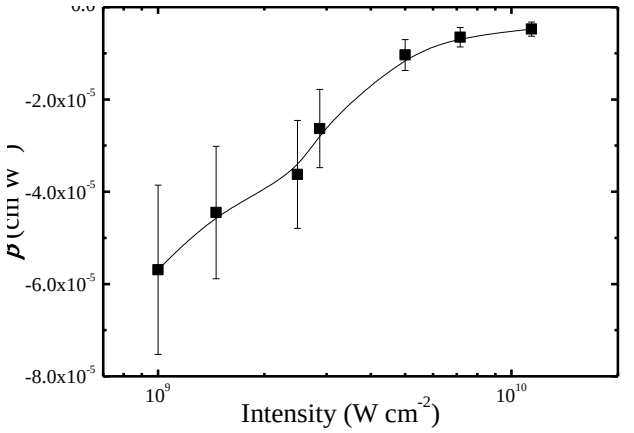

(b)

Figure 5. The $\beta(I_0)$ dependences in the cases of (a) Ag:SLSG, and (b) Ag:SG.

The saturated absorption has been observed from various materials such as dyes [38], polythiophene thin films [24], semiconductor-doped glasses [39], etc. The saturated absorption of Ag nanoparticles embedded in silica glass matrices has been observed as far as 355 nm [40]. Such process was also observed in silver-doped glasses in the vicinity of SPR of Ag nanoparticles [37,41]. Analogous features of silver-contained glasses were reported in [2,39,42,43]. The saturated absorption was also observed previously in the modified LiNbO3 crystals containing Ag nanoparticles close to plasmon band shifted to 550 nm after heat treatment [44].

We observed the intensity-dependent variations of β of our samples. These measurements were carried out at laser intensity varied from 10^9 to 2×10^{10} W cm^{-2}. The $\beta(I_0)$ dependences of Ag:SLSG and Ag:SG are presented in Figure. 5. We observed a decrease of β for higher intensities. In particular, a 21- and 12-fold decrease of β was measured at $I_0 = 1.15\times10^{10}$ W cm^{-2} for Ag:SLSG and Ag:SG, respectively, compared to β measured at $I_0 = 1\times10^9$ W cm^{-2}.

Copyright © 2010. Nova Science Publishers, Incorporated. All rights reserved.

The variations of transmission and nonlinear refraction in such structures were attributed in some cases to the fragmentation [45-47], or fusion [48] of nanoparticles following the photothermal melting. Osborne *et al* [25] reported the alteration of the sign of nonlinear refractive index of small silver clusters embedded in soda-lime glass. They noted that thermal effects could change the properties of nanoclusters. The transparency in these samples was associated with oxidation of Ag nanoparticles. However, no irreversible changes of transmittance were observed in our experiments. These measurements were repeated at several times to ensure reproducibility, and were also performed in pure silica glasses, which showed no measurable nonlinear response under the same conditions.

The reverse saturated absorption can be responsible for the decrease of negative nonlinear absorption of Ag nanoparticles. The common feature of the dispersion curve of $\mathrm{Im}\chi^{(3)}$ of different metal nanoparticle-contained compounds near their SPRs is a negative sign of nonlinear absorption [37]. We can assume that in the case of picosecond pulses the reverse saturated absorption starting to play an important role in the overall dynamics of nonlinear optical transmittance of metal nanoparticles-contained compounds, taking into account the saturation of intermediate transitions responsible for saturated absorption.

We fitted the theoretical dependences (Eq. (8)) with our experimental data obtained in the case of closed aperture Z-scans. The best correlation between theory and experiments was observed at $\Delta\Phi_0 = 0.8$ and 1.08 for Ag:SLSG and Ag:SG, respectively. From these data, the values of γ and $\mathrm{Re}\chi^{(3)}$ were calculated to be -4.1×10^{-10} cm^2 W^{-1} and -2.4×10^{-8} esu for Ag:SLSG, and -6.2×10^{-10} cm^2 W^{-1} and -3.5×10^{-8} esu for Ag:SG. We observed the variation of these parameters with growth of laser intensity leading to the change of the sign of nonlinear refractive index from negative to positive (Figure 6). The maximum positive values of γ and $\mathrm{Re}\chi^{(3)}$ of these samples were observed the laser intensity of 1.4×10^{10} W cm^{-2} and were calculated to be 1.7×10^{-10} cm^2 W^{-1} and 9.6×10^{-9} esu for Ag:SLSG, and 7×10^{-11} cm^2 W^{-1} and 4×10^{-9} esu for Ag:SG. The measurements of nonlinear optical parameters of samples are summarized in Table 1.

Table 1. Nonlinear optical parameters of silicate glasses doped with Ag nanoparticles

Sample	I_0, 10^9 W cm^{-2}	β, 10^{-5} cm W^{-1}	$\mathrm{Im}\chi^{(3)}$, 10^{-8} esu	γ, 10^{-10} cm^2 W^{-1}	$\mathrm{Re}\chi^{(3)}$, 10^{-8} esu
Ag:SG	2.5	-3.6	–1.3	-6.2	-3.5
	11.5	0.48	-0.17		
	14			0.7	0.4
Ag:SLSG	2.5	-6.7	–2.4	-4.1	-2.4
	11.5	-1.7	-0.6		
	14			1.7	0.96

Copyright © 2010. Nova Science Publishers, Incorporated. All rights reserved.

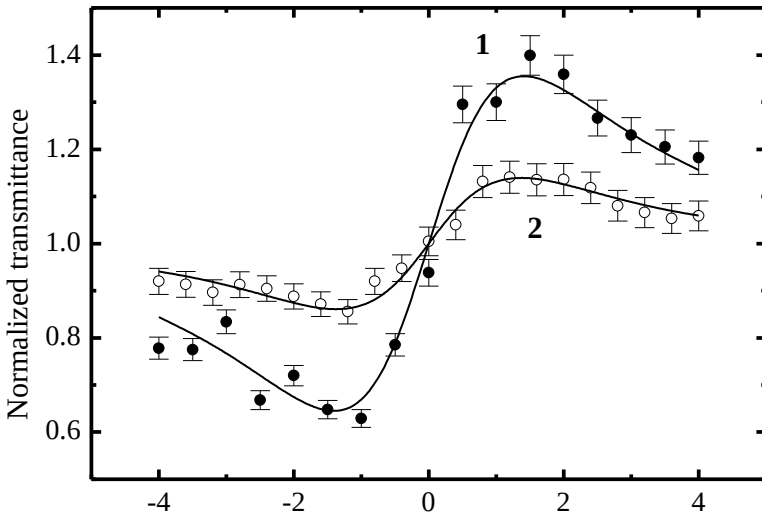

Figure 6. The normalized transmittance dependences of (1) Ag:SLSG, and (2) Ag:SG in closed aperture Z-scan scheme at I_0=1.4×10^{10} W cm^{-2}. λ = 532 nm.

The possible mechanism of the decrease of Im$\chi^{(3)}$ is the influence of nonlinear optical processes with opposite dependences on laser intensity, such as reverse saturated absorption and two-photon absorption [49,50]. The wavelength range corresponded to the interband transitions in silver is located below 320 nm, so the two-photon absorption connected with interband transitions can be involved in the case of 532 nm radiation. The possibility of two-photon absorption due to interband transition of photoexcited electrons was previously demonstrated for silver [51] and copper [52] nanoparticles. The three-photon absorption connected with interband transition for silver nanoparticles was analyzed in [23]. At the same time the reverse saturated absorption can also be involved into the consideration. The only contribution to the nonlinear refraction and absorption processes was caused by metal nanoparticles since no variations in the normalized transmittance dependences of pure substrates were observed in our experiments. However, the defects in matrix can also play an important role in overall change of optical and nonlinear optical properties of metal-doped glasses. The doping of accelerated ions into the glass substrates leads to the appearance of defects, which can stimulate the reversible and irreversible changes in material structure [30]. Different types of defects were registered in previous studies of metal-implanted glasses. Among them are the prolonged and dotted defects, local crystalization and amorphization, etc. In particular, the growth of metal nanoparticles leads to the increase of volume of implanted layer and appearance of internal tension.

Note that the negative value of Re$\chi^{(3)}$was previously observed in Ag-doped materials at the wavelength range of $\lambda > \lambda_{spr}$ [37]. The observed sign change of Re$\chi^{(3)}$ can be caused by several processes:

(1) The influence of interband transitions taking into account the possibility of two-photon process. The decrease of the imaginary part of $\chi^{(3)}$ confirms such assumption.

Copyright © 2010. Nova Science Publishers, Incorporated. All rights reserved.

(2) The influence of thermal effect ($dn/dT > 0$ for glasses). Positive contribution to the nonlinear refractive index can be caused by thermal effect, which can be considered as a result of energy transfer from heated metal nanoparticles to surrounding dielectric matrix [6]. However, the time, which is necessary for this process to be important equal to a few nanoseconds, whereas the pulse duration was three orders shorter (55 ps), that diminishes the influence of the thermal effect causing the acoustic-induced variation of density and refractive index of matrix.

(3) The irreversible change of γ caused by laser radiation. This opportunity was analyzed in several studies of composite materials doped with copper [53] and silver [25] nanoparticles. The sign change of both refractive and absorptive nonlinearities was observed in Cu-doped glass with the growth of laser intensity, and the mechanism of modification was found to be a thermally activated enlargement of Cu nanoparticles [53]. The sigh change of nonlinear refractive index from positive to negative was observed also in Ag-doped glasses [25]. The mechanism responsible for sign change was a photochemical reaction, which produced a silver-oxide layer on the surface of nanoclusters. The irreversible changes in both these studies were caused by a thermal influence produced by high pulse repetition rate radiation (3.8 MHz). In our case, the Z-scans had a good reproducibility, so the influence of irreversible changes can be easily excluded.

Based on above-mentioned analysis we can attribute both nonlinear absorptive and refractive changes observed at the growth of laser intensity to the influence of interband transitions.

In order for a third-order nonlinear material to be useful in optical switching processing devices it must simultaneously satisfy the following conditions [54]:

(1) The excitation time of the nonlinear effect must be less than the pulse width. In our case the nonlinear refraction is caused by Kerr-related phenomenon characterized by femtosecond range excitation time.

(2) The effect of linear absorption must be weak compared to the effect of nonlinearity. This condition quantified in terms of Stegeman figure of merit W:

$$W = n_2 I/\alpha_0 \lambda > 1. \tag{16}$$

In our case $W = 0.7$ (for Ag:SLSG sample), i.e., close to chosen limit.

(3) The effect of two-photon absorption must be weak compared to the nonlinear effect. This condition quantifies in terms of Stegeman figure of merit T:

$$T = 2\beta\lambda/n_2 < 1 \tag{17}$$

In our case $T = 40$ (for Ag:SLSG sample), that is quite far from chosen limit.

Based on above-presented estimations, these samples fell short to the conditions of effective application as optical switching devices at 532 nm. The comparison of observed processes in Ag nanoparticles-contained glasses with those in other nonlinear optical

Copyright © 2010. Nova Science Publishers, Incorporated. All rights reserved.

materials seems important in spite of difference in physical mechanisms playing an appropriate role in each of these particular cases. Such a comparison is valuable when aimed estimating the practical applicability of investigated material in visible range compared to other materials.

1.5. Nonlinear Optical Susceptibilities of Silver-Doped Silicate Glasses in the Ultraviolet Range

In this subsection, nonlinear optical response of silver nanoparticles synthesized by ion implantation in silicate glasses was investigated in ultraviolet range (354.7 nm). The real and imaginary parts of the third-order nonlinear susceptibility $\chi^{(3)}$ of composite materials were measured. It was shown that $\mathrm{Im}\chi^{(3)}$ was connected with saturated absorption whereas $\mathrm{Re}\chi^{(3)}$ was due to self-defocusing of laser radiation in materials.

As it was mentioned earlier, the interest in metal nanoparticles (MN) embedded in dielectric materials is connected with their applications as optical switchers with ultrashort time response [10], and optical limiters of intense laser radiation [55,56]. The saturated absorption observed in such structures makes them perspective mode-lockers [57]. Analogous studies were generally carried out in visible and near IR ranges. At the same time such structures can possess interesting nonlinear optical properties in the UV range. There are only few studies of nonlinear optical properties of nanoparticle composites in that spectral range. In particular, Si nanoparticles were investigated at the wavelength of the Nd:YAG laser third harmonic radiation (λ = 355 nm, τ = 8 ns) and the giant value of nonlinear susceptibility was measured to be 2.28×10^{-5} esu [58].

Below, we investigate the nonlinear optical properties of Ag nanoparticles embedded in silicate glasses in the near UV range using the Z-scan technique [40]. The parameters of third harmonic radiation of the Nd :YAG laser were as follows: pulse duration 55 ps, pulse energy 0.1 mJ, wavelength λ = 354.7 nm. The laser beam waist radius at the focal plane was 42 μm. The intensity of laser radiation I_0 was varied in the range of 10^9 to 5×10^9 W cm^{-2}, whereas the optical damage threshold of samples was measured to be ~10^{10} W cm^{-2}. The closed aperture Z-scan technique was used to determine the value of the nonlinear refractive index n_2 of the samples. The glasses without MN did not shown any changes in transmission experiments at the intensities used. In Figure. 7, the normalized transmittance dependence $T(z)$ in the closed aperture Z-scan scheme is shown for Ag:SG indicating the negative sign of nonlinear refraction. An observed asymmetry of this dependence, when peak exceeds valley, characterizes the saturated absorption in the sample. When nonlinear refraction and nonlinear absorption are simultaneously present in the sample, the $T(z)$ dependence in the closed aperture scheme can be described by Eq. (8). Using Eq. (8), the numerical calculations of $T(z)$ dependencies were carried out for the experimental curve presented in Figure. 7. The best fit was obtained at ρ = –0.07 and $\Delta\Phi_0$ = –0.75. From this fit the nonlinear optical parameters were found to be $n_2 = -2.7\times10^{-7}$ esu, and $\beta = -1.4\times10^{-5}$ cm W^{-1} for Ag:SG.

Copyright © 2010. Nova Science Publishers, Incorporated. All rights reserved.

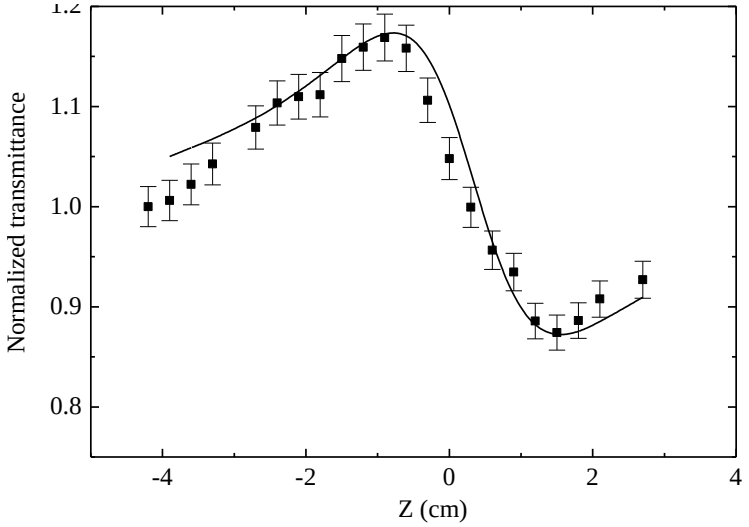

Figure 7. Normalized transmittance dependence for Ag:SG in closed aperture Z-scan scheme. The solid line is the theoretical fit. λ = 355 nm.

In the general case, when nonlinear absorption and nonlinear refraction appear simultaneously, the nonlinear susceptibility can be considered as a complex value $\chi^{(3)} = \mathrm{Re}\chi^{(3)} + i\mathrm{Im}\chi^{(3)}$, where the real and imaginary parts of $\chi_{(3)}$ are connected with n_2 and β by the relations $\mathrm{Re}\chi^{(3)} = (n_0/3\pi)n_2$ and $\mathrm{Im}\chi^{(3)} = (n_0\varepsilon_0 c^2/\omega)\beta$, where ω is the circular frequency of laser radiation, and ε_0 is the dielectric constant. In our case $\mathrm{Re}\chi^{(3)}$ and $\mathrm{Im}\chi^{(3)}$ of Ag:SG were calculated to be -6×10^{-8} and -6.1×10^{-9} esu, respectively.

We consider our composite materials as effective homogeneous media. The legitimacy of this approach proves to be true by the fact that the sizes of MN are much smaller than the wavelength used in experiment. For an effective homogeneous medium described by the presence of resonant transitions one can apply the standard two-level model [13]. The sign of n_2 is determined by the sign of the frequency detuning from resonance $\Delta = \omega_{i0} - \omega_p$ (see Eq. (9)). Let us consider Eq. (10) for frequency $\omega_{10} \sim 28193$ cm^{-1} (λ = 354.7 nm) that was used in these experiments and SPR frequency of Ag:SG ($\omega_p \sim 24096.4$ cm^{-1}, λ = 415 nm). In this case $\mathrm{Re}\chi^{(3)} < 0$, thus predicting the self-defocusing in Ag:SG that was observed experimentally.

1.6. Characterization of Optical and Nonlinear Optical Properties of Silver Nanoparticles Prepared by Laser Ablation in Various Liquids

In this subsection, we present our studies of the optical, structural, and nonlinear optical properties of the Ag nanoparticles prepared by laser ablation in various liquids. We analyze nonlinear refraction and nonlinear absorption of these media using the radiation of different wavelength, pulse repetition rate, and pulse duration. In particular, the optical, structural, and nonlinear optical properties of silver nanoparticles prepared by laser ablation in various liquids were investigated at 397.5, 532, and 795 nm [59]. The TEM and spectral measurements have shown temporal dynamics of size distribution of Ag nanoparticles in

Copyright © 2010. Nova Science Publishers, Incorporated. All rights reserved.

solutions. The thermal-induced self-defocusing dominated in the case of high pulse repetition rate as well as in the case of nanosecond pulses. In the case of low pulse repetition rate, the self-focusing and saturated absorption of picosecond and femtosecond radiation were observed in these colloidal solutions.

1.6.1. Experimental

Laser ablation of silver in various liquids was performed using second harmonic radiation of Nd:YAG laser (Spectra-Physics, LAB 150). Laser radiation (wavelength: λ = 532 nm, pulse duration: t = 9 ns, pulse energy: E = 30 mJ, 10 Hz pulse repetition rate) was focused by a 50 mm focal length lens at normal incidence to the surface of silver block (Nilaco, 99.99%) placed inside 10 mm thick cell filled with liquid of different viscosity (ethylene glycol, water, or ethanol). The fluence of 532 nm radiation at target surface was measured to be 20 J cm^{-2}. The ablation was carried out during 15–30 min. The ablated solution was constantly stirred during interaction of laser radiation with Ag target. The prepared solutions were analyzed by TEM and absorption spectroscopy to confirm the appearance of Ag nanoparticles.

The ablated silver solutions were then studied using Z-scan technique to measure their nonlinear optical characteristics. The 2, 5, and 10 mm thick silica glass cells filled with investigated solutions were used in these studies. The Ti:sapphire laser (Spectra-Physics, CPA TSA-10F; t = 110 fs, λ = 795 nm, E = 10 mJ, 10 Hz pulse repetition rate) was used in these Z-scan studies. The output radiation with variable pulse duration (from 110 fs to 1.6 ps) was also available from this laser. The laser also operated at Q-switched regime delivering 8-ns pulses. The 795 nm, 80 MHz, 100 fs, 300 mW pulses from the seeding oscillator (Spectra-Physics, Tsunami) were used for the investigation of thermal-induced self-defocusing in solutions. We also used the 1054 nm, 100 MHz, 280 fs, 100 mW radiation (Time Bandwidth, GLX-200) for the investigation of thermal-induced nonlinear optical processes caused by IR radiation. Second harmonic radiation of Nd:YAG laser (Continuum, Surelite I; λ = 532 nm, t = 8 ns, 1 Hz pulse repetition rate) was used in Z-scan measurements using long pulses. The beam waists of 795 and 532 nm radiation focused by a 200 mm focal length lens were measured to be 42 and 60 lm, respectively.

The appearance of stable Ag nanoparticles was confirmed by TEM studies of these solutions. These observations have shown a variation of nanoparticle size distribution that was changed for a period of first 10 days and then appeared to be stable. The sedimentation of Ag nanoparticles led to the narrowing of their size distribution. The nanoparticles' sizes were inspected using a transmission electron microscope JEM-201OF. The Ag solutions were dissolved in ethanol. A drop of solution was placed on a carbon-coated copper grid that was left to dry before transferring into the TEM sample chamber. The micrographs were taken at an acceleration voltage of 200 kV. Figure 8 presents the TEM image of silver nanoparticle in ethylene glycol (Ag:EG). The TEM measurements conducted just after laser ablation have shown the appearance of nanoparticles with size distribution ranging from 4 to 200 nm. After half month this distribution was considerably narrowed with only small nanoparticles (ranging from 5 to 10 nm) dominating in ablated solution. We analyzed the shape of Ag nanoparticles using TEM images.

Copyright © 2010. Nova Science Publishers, Incorporated. All rights reserved.

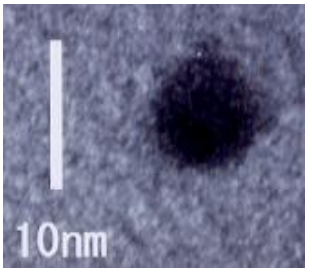

Figure 8. TEM image of single Ag nanoparticle from the Ag:EG suspension.

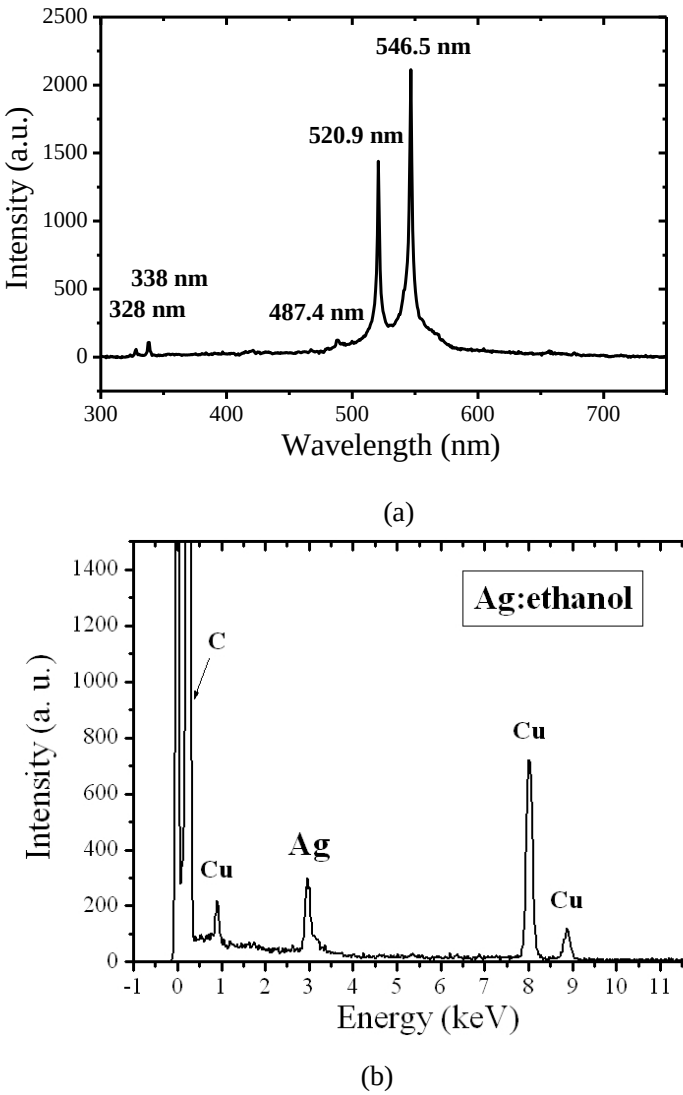

Figure 9. (a) Emission spectrum of ablated silver, and (b) energy dispersive X-ray spectrum of Ag:ethanol solution.

Copyright © 2010. Nova Science Publishers, Incorporated. All rights reserved.

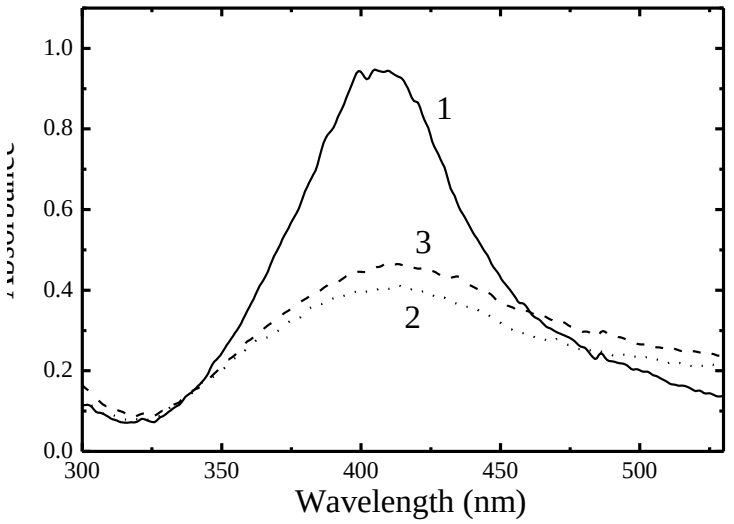

Figure 10. The absorption spectra of Ag:EG solution (1: initial spectrum after ablation; 2: after one week; 3: after three weeks).

Both size and shape of nanoparticles (in particularly, elliptical, spherical, and linear) were varied in a broad range at initial stage after ablation. However, after some time, probably due to sedimentation, the shape of observed TEM images of Ag nanoparticles became predominantly spherical. The emission spectrum of ablated metal has shown spectral lines belonged exclusively to silver (Figure 9(a)). An elemental analysis of silver nanoparticles using energy dispersive X-ray spectroscopy have also confirmed the presence of silver in observed solutions (Figure. 9(b); the copper and carbon lines are originated from grid material).

It was previously shown in various studies that the absorption spectrum of Ag nanoparticles considerably varies depending on preparation technique. The SPR location for mostly often used chemical technique of Ag nanoparticles preparation is centered in the vicinity of 415–425 nm, whereas the absorption spectra of such structures prepared by laser ablation show that this resonance shifting toward a short-wavelength range (between 400 to 410 nm) due to the influence of small-sized nanoparticles. Our observations confirmed this shift. Figure. 10, curve 1 shows the absorption spectrum of silver ablated in ethylene glycol. The absorption curve was centered in the vicinity of 405 nm that indicated the appearance of small nanoparticles. A detailed analysis of the variations of absorption spectra of Ag nanoparticles prepared by laser ablation using radiation of different wavelengths was presented by Tsuji *et al* [60,61].

The variations of absorption spectra of ablated nanoparticles were observed during one month (see Figure 10). The spectral broadening was connected with morphological variations of colloids. Our analysis of TEM images has shown considerable decrease of long-sized nanoparticles after half month due to their sedimentation. Analogous features of Ag:water solution were reported in [60] where the nanoparticles_ size distribution became broadened for the samples possessing narrow plasmon band. The spectral variations observed in our experiments with colloidal silver can be explained by the particle aggregation. Similar peculiarity was previously reported in the case of irradiation of colloidal silver prepared by

Copyright © 2010. Nova Science Publishers, Incorporated. All rights reserved.

chemical methods [62,63]. The aggregation led to the shift of SPR frequency toward long-wavelength range. The initial absorption spectra of silver ablated in different liquids (water, ethylene glycol, and ethanol) were similar. However, the absorption of Ag:water and Ag:ethanol solutions was weakened after two weeks as compared to Ag:EG, probably due to higher value of viscosity of ethylene glycol that prevented nanoparticles from sedimentation.

1.6.2. Nonlinear optical studies at high pulse repetition rate

Previously observed influence of thermal accumulative effects on the behavior of nonlinear optical refraction in various media at high repetition rates of femtosecond pulses (of order of 10 MHz [64,65]) has shown the importance of heat accumulation between pulses due to various (linear and/or nonlinear) mechanisms of optical losses. There are different mechanisms of absorption of 795 nm radiation in Ag-contained medium. The first one is associated with Mie scattering and absorption and the second one can be caused by two-photon absorption due to the closeness of the energy of two photons and SPR of silver nanoparticles. We used the radiation of Ti:sapphire oscillator (Spectra-Physics, Tsunami; λ = 795 nm, W = 300 mW, t =100 fs, 80 MHz pulse repetition rate) to analyze the influence of thermal-induced nonlinearities on the propagation of laser radiation through Ag-contained solutions. The Z-scan studies using the analysis of CCD images in the case of Kerr-induced nonlinearities were previously reported by Marcano *et a*l. [66]. Here we show the application of CCD images for the analysis of thermal-induced self-defocusing.

Figure 11 shows the beam shape variations in far field in the case of Ag:ethanol solution using Z-scan-like configuration. The arrows show the positions of 5 mm thick cell filled with this solution and CCD images in far field, respectively. A strong thermal-induced self-defocusing caused by absorbed radiation clearly seen in these images. The self-defocusing caused by thermal lens concentrates radiation in the far field (position $z = z_1$, CCD image No. 2) relative to the reference beam when the cell was placed far from the focal plane (Nos. 1 and 4). At $z = z_2$, the self-defocusing leads to the appearance of ring structure (No. 3). The positions z_1 and z_2 correspond to the maximum and minimum of normalized transmittance in the case of closed-aperture measurements.

The thermal-induced nonlinear refractive index of Ag:EG solution in the case of high pulse repetition rate was measured to be $\gamma = -8\times10^{-12}$ cm^2 W^{-1}. The pure ethylene glycol has also shown self-defocusing properties caused by thermal lens appearance due to the nonlinear, probably three-photon, absorption of radiation. In that case the thermal-induced self-defocusing was considerably weaker in comparison with silver nanoparticles-contained solution. Our observations have also shown the insignificant influence of accumulative thermal effects on the variations of refractive index in the cases of pure water and ethanol. The observation of similar variations of beam shape in the case of 1054 nm radiation (Time Bandwidth, GLX-200; t = 280 fs, W = 100 mW, 100 MHz) propagated through silver-contained solutions confirmed a decisive role of the first mechanism of absorption. No absorption and beam shape variation was observed in the case of pure ethylene glycol, ethanol, and water at λ = 1054 nm [67].

Copyright © 2010. Nova Science Publishers, Incorporated. All rights reserved.

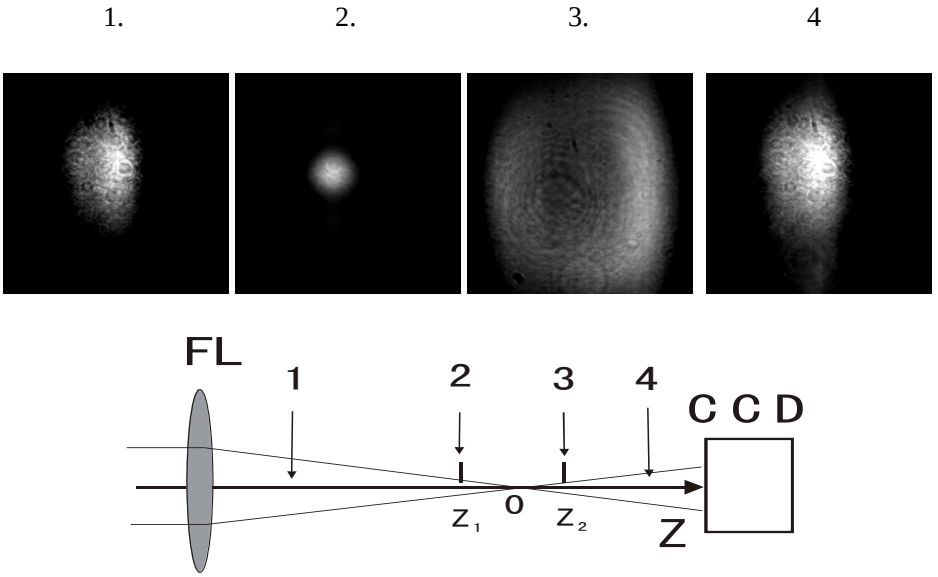

Figure 11. The CCD images of beam shapes of 795 nm radiation operated at high pulse repetition rate and propagated through Ag:EG solution at different positions of cell in Z-scan-like configuration.

1.6.3. Nanosecond pulses

In the next set of nonlinear optical studies we used the radiation operated at 1 and 10 Hz pulse repetition rates in order to exclude the influence of thermal accumulative processes. In the case of nanosecond pulses of Nd:YAG laser second harmonic radiation (λ = 532 nm, t = 8 ns, E = 2 mJ, 1 Hz pulse repetition rate) we did not observe the fast Kerr-induced nonlinear optical processes in Ag nanoparticle-contained solutions up to maximum intensities of I_0 = 8×10^9 W cm^{-2}. These studies were carried out using closed-aperture Z-scan configuration and time-integrated photodiodes. However, the self-defocusing was observed when we analyzed the time waveform of propagated pulses using fast p–i–n diodes. The idea of this method is based on the analysis of oscilloscope traces of the pulse propagated through nonlinear medium in closed aperture Z-scan scheme.

The avalanche photodiode with a rise-time of 1 ns was used as a detector in these studies. The detected signal was displayed on a 10 GHz bandwidth sampling oscilloscope (LeCroy 9362). We observed the variations of the trailed part of laser pulse registered in the far field after the propagation of limiting aperture depending on cell position.

Figure 12(a), curve 1 presents the oscilloscope trace of such a pulse after propagation through the sample placed just behind focal point (at $z = z_2$). One can see a suppression of the trailing part of pulse as compared with initial pulse shape (Figure. 12(a), curve 2). Such a variation of temporal waveform points out on the influence of time-dependent self-defocusing in medium. Analogous observations were previously reported in various liquid-contained media (methyl nitroaniline solutions [68], aqueous colloidal metals [62], CS2 [69]).

Copyright © 2010. Nova Science Publishers, Incorporated. All rights reserved.

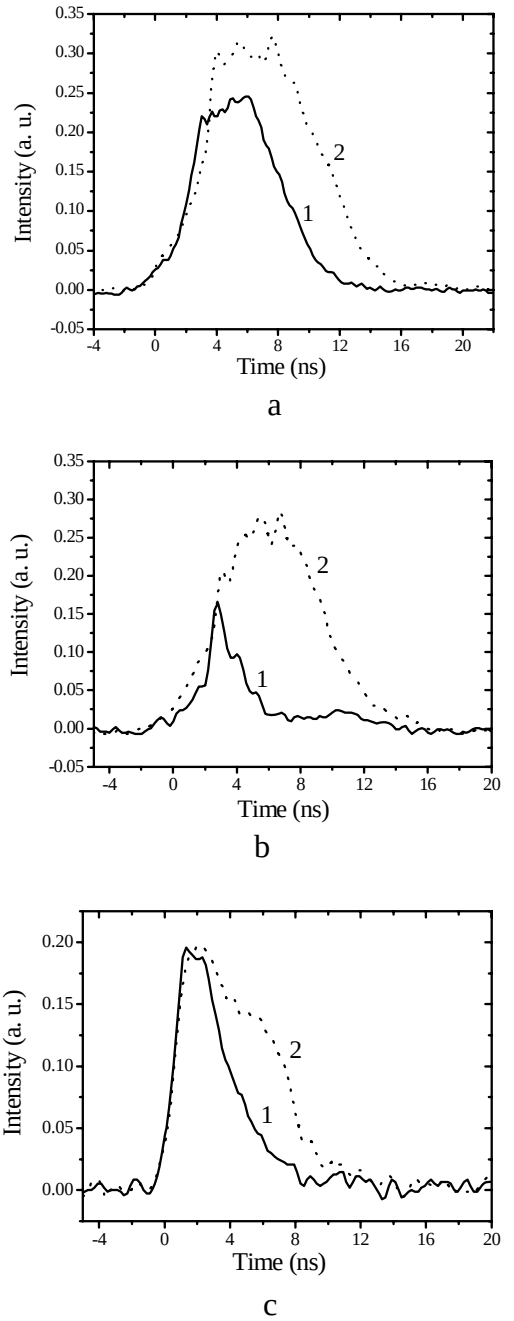

Figure 12. The oscilloscope traces of nanosecond pulses propagated through the aperture in Z-scan-like configuration in the cases of (a) 532 nm radiation, 2 mm thick Ag:EG-contained cell, (b) 532 nm radiation, 10 mm thick Ag:EG-contained cell, and (c) 397.5 nm radiation, 2 mm thick Ag:water-contained cell. 1: the oscilloscope traces in the case when the cells were placed behind focal point, close to z_2 position; 2: the oscilloscope traces in the case when the cells were placed far from focal point (the initial waveforms of laser pulses). z_2 corresponds to the minimum of normalized transmittance in closed aperture scheme.

Copyright © 2010. Nova Science Publishers, Incorporated. All rights reserved.

The origin of observed self-interaction process is a thermal-induced negative lens appearance. However, this process was caused by the physical mechanisms other than those that were observed in the case of high pulse repetition rate. In the latter case the appearance of negative lens was caused by slow heat accumulation, whereas in the former case the self-defocusing was caused by acoustic wave propagation through the beam waist area.

The acoustic wave was generated as a result of optical absorption of laser radiation. The influence of absorption was clearly seen in the case of 10 mm thick cell filled with Ag:EG. In that case we observed the optical breakdown of solution at high intensity of laser radiation (Figure 12(b), curve 1). We carried out analogous studies of waveform variations using 795 and 397.5 nm, 8 ns radiation. In that case we also observed the narrowing of pulse duration of the radiation propagated through limiting aperture. However, in the case of 397.5 nm radiation this process was observed only when the single pulses were interacted with Ag nanoparticles contained solutions (Figure 12(c), curve 1). In the case of 10 Hz repetition rate, the pulse shape after first 3–5 shots became the same as initial one (curve 2). No changes of pulse shape were observed in these studies in the case of Ag nanoparticle-free solutions.

As in subsection 2.4, we attribute the observed peculiarity to the fragmentation, or fusion of nanoparticles following the photo-thermal melting. Such processes lead to the change of particle size and decrease of thermal-induced self-interaction processes. Another process that accompanied the laser irradiation of colloidal solutions is a formation of nanowires, as was reported by Tsuji *et al* [60] in their studies of spherical silver colloids in water.

Below we discuss the thermal-induced self-interaction process in the case of nanosecond pulses. As it was mentioned above, our observation of the temporal behavior of self-defocusing of nanosecond pulses in colloidal silver is based on the assumption of the thermal nature of lensing. The thermal lens appears with energy absorption growth. Because of the time delay of this process due to the transfer of energy to the solvent and temperature rise of solution, this lensing is more effective for the trailing part of pulse.

The heating of host dielectric has a rise-time consisting on the time (t_1) required for energy transfer from nanoparticles to solvent and time (t_2) required for temperature rise of solvent to be transformed into the change of refractive index via density reduction. t_1 is a function of nanoparticles' sizes. For 10 nm particles this time is of order of 25 ps [70]. t_2 is equal to w_o/v, where w_o is the laser beam waist radius, and v is the velocity of acoustic wave in liquid. In our case (w_o = 21 μm, v = 1500 ms^{-1}) this parameter is equal to t_2 = 14 ns. It means that, at least for the central part of focused beam, there are some conditions of self-defocusing in Ag nanoparticle solution during propagation of nanosecond radiation through the sample. It takes between 4 and 6 ns to achieve the density variations in the central part of focal volume. These estimations of self-defocusing start-up time are qualitatively coincide with experimental results (Figure 12).

The open aperture Z-scans of Ag-contained solutions were carried out using 397.5 nm, 8 ns radiation (Figure 13(a)). In that case the reverse saturated absorption can be responsible for the nonlinear absorption of Ag nanoparticles. The common feature of the dispersion curve of $\mathrm{Im}\chi^{(3)}$ of different MN-contained compounds near their SPRs is a negative sign of nonlinear absorption [37] that was also confirmed in our studies using short laser pulses. However, in the case of long laser pulses we registered positive nonlinear absorption in Ag-contained samples. We assume that in the case of long pulses the reverse saturated absorption plays an important role in the overall dynamics of nonlinear optical transmittance of nanoparticles-

Copyright © 2010. Nova Science Publishers, Incorporated. All rights reserved.

contained compounds, taking into account the saturation of intermediate states responsible for saturated absorption in the case of femtosecond and picosecond pulses.

After fitting of Eq. (13) with experimental data (Figure 13(a), solid curve) the nonlinear absorption coefficient of Ag:water solution was calculated to be 3×10^{-9} cm W^{-1}. The imagine part of nonlinear susceptibility of Ag nanoparticles was estimated to be $\mathrm{Im}\chi^{(3)} = 3\times10^{-8}$ esu taking into account the small volume ratio of silver nanoparticles in water solution ($p \approx 4\times10^{-5}$).

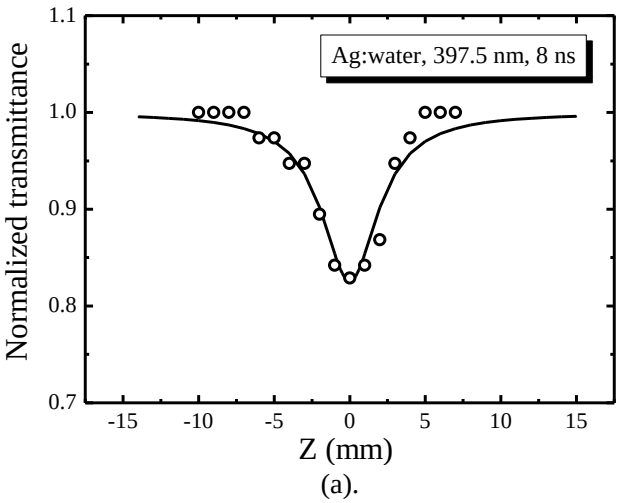

(a).

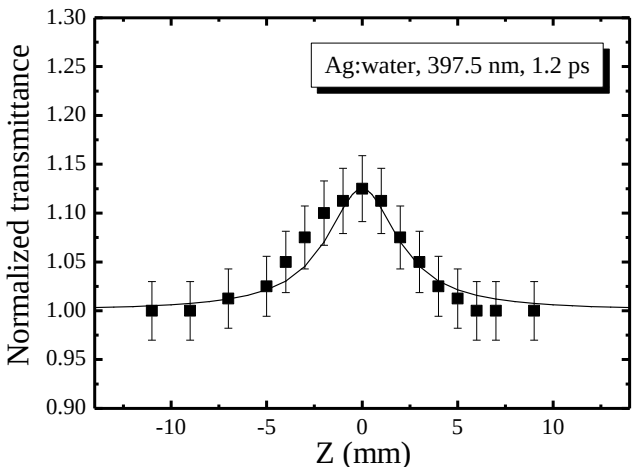

(b).

Figure 13. The normalized transmittances of Ag:water solution in the cases of (a) long pulses (8 ns), and (b) short pulses (1.2 ps). Open aperture scheme, λ = 397.5 nm. The solid lines show theoretical fits.

Copyright © 2010. Nova Science Publishers, Incorporated. All rights reserved.

1.6.4. Picosecond and femtosecond pulses

The application of short laser pulses in Z-scan studies allows excluding the influence of slow thermal-related nonlinear optical processes and analyzing the self-interaction mechanisms caused by electronic response of Ag nanoparticles. Our Z-scan scheme was calibrated using carbon disulfide. The nonlinear refractive index of carbon disulfide was measured to be $(3.5\pm0.7)\times10^{-15}$ cm^2 W^{-1} [69] using 300 fs pulses that was close to previously reported data measured in femtosecond range (2.3×10^{-15} cm^2 W^{-1} [64], $(3.1\pm1)\times10^{-15}$ cm^2 W^{-1} [65]). Our studies using 795-nm radiation were performed at laser intensities up to 1×10^{11} W cm^{-2}. However, we did not register the influence of Ag nanoparticles on nonlinear refractive properties of Ag:liquid solutions, probably due to small volume ratio of Ag nanoparticles. The influence of positive refractive nonlinearities of silica glass and water was observed at the intensities exceeding 4×10^{10} W cm^{-2}, that eclipsed the influence of those of silver nanoparticles. The only nonlinear optical process observed at 795 nm in silver nanoparticles-contained liquids was a nonlinear absorption caused by two-photon processes in these compounds. The nonlinear absorption coefficient of nanoparticles in Ag:water solution using 795 nm, 800 fs radiation was measured to be 8×10^{-9} cm W^{-1}.

In the case of 397.5 nm, 1.2 ps radiation, a positive nonlinear refraction induced by the influence of silver nanoparticles was registered in closed aperture Z-scans. No nonlinear optical processes were observed in this case in silica glass cells filled with pure water at the intensities up to 8×10^9 W cm^{-2}. γ and Re$\chi^{(3)}$ of Ag:water solution were calculated to be 3×10^{-13} cm^2 W^{-1} and 2×10^{-12} esu, respectively. In the case of quasi-resonant interaction the sign of nonlinear refractive index determines by a relation between the fundamental and doubled frequencies of laser radiation and SPR frequency of investigated medium [41]. Our analysis of the sign of γ was based on this consideration and confirmed the positive value of this parameter, in agreement with experimental data.

The normalized transmittance in that case is given by Eq. (8) with negative value of β. The nonlinear absorption coefficient in that case can be presented as $\beta = \alpha/I_s$ that is a ratio between linear absorption coefficient and saturated intensity. The solid line fitted to our data in Figure. 13(b) was calculated by setting β equal to -1.5×10^{-9} cm W^{-1}. I_s was consequently evaluated to be 6×10^8 W cm^{-2}. Our studies of Ag:water solution have shown the dominance of Re$\chi^{(3)}$ over Im$\chi^{(3)}$ at λ = 397.5 nm ($|\text{Re}\chi^{(3)}| = 2\times10^{-12}$ esu, $|\text{Im}\chi^{(3)}| = 6\times10^{-13}$ esu).

The third-order susceptibility of MN-contained dielectrics can be written as [71]

$$\chi^{(3)} = p\,|f_e|^2 f_e^2 \chi^{(3)}_{np}, \tag{17}$$

where $\chi^{(3)}_{np}$ is the intrinsic third-order nonlinear optical susceptibility of nanoparticles, and p is the filling factor (i.e., volume ratio). Factor f_e is the local field enhancement of polarization. The electric field that actually polarizes nanoparticle can be much larger than the external applied electric field. This effect is known as dielectric confinement. The most conspicuous manifestation of confinement in the optical properties of MN is the appearance of the SPR that strongly enhances their linear and nonlinear optical characteristics in the vicinity of SPR wavelength. This resonance is a direct consequence of dielectric confinement and can be interpreted in term of a collective motion of the electrons in MN. Therefore the impact of dielectric confinement on the nonlinear optical response of MN has been extensively studied using different technique in the vicinity of SPR.

Copyright © 2010. Nova Science Publishers, Incorporated. All rights reserved.

We observed a variation of normalized transmittance in the case of 397.5 nm, 800 fs pulses operated at 10 Hz repetition rate. This regime of laser-colloids interaction at high irradiation leads to the fragmentation of Ag nanoparticles. As a result, the saturated absorption presented by a normalized $T(z)$ dependence in the case of open aperture configuration (analogous to Z-scan trace presented for single pulses in Figure 13(b)) was less pronounced at 10 Hz pulse repetition rate compared with single-shot interaction.

1.7. Role of Aggregation in Variations of Nonlinear Optical Parameters of Silver Nanoparticle Suspensions

Now we come to the studies of the role of aggregation rate on the nonlinear optical response of Ag clusters. Colloidal silver is of interest due to the perspectives of its application in OL, optoelectronics, etc [20,72-74]. Aggregation of such samples leads to the increase of nonlinear optical response, in particular, in processes of degenerate four-wave mixing due to the growth of local field amplitude in fractal clusters with high polarizability [75]. The optical characteristics of aggregated silver are determined by the variations of surface plasmon frequency located near the region of 415 nm (in the case of non-aggregated silver) and long-wave absorption wing with the growth of aggregation rate [76]. This parameter was announced in [77] and was based on a variety of theoretical and experimental studies [78-80]. It connects the dynamics of colloidal silver absorption spectrum with the spatial parameters of clusters. Thus, the aggregation rate (A) allows us to determine the sizes of clusters without electron microscopic methods.

Here we analyze and compare the mechanisms of self-action in colloidal silver for various aggregation rates using laser pulses (λ = 1064 nm) of different durations (picosecond and nanosecond) [12]. Figure 14 shows the set of measurements of $T(Z)$ dependences under the action of picosecond pulses for different aggregation rates of colloidal silver. It is worth noting the sign change of n_2 (from the positive (Figure 14, curve 1) to the negative (Figure 14, curves 2–4)). The aggregation rate was an alternating parameter of the investigated medium.

This parameter was determined using the absorption spectra of the colloidal solution [77]. For this purpose, we took the difference of integral absorption in the long-wave wing region between aggregated and non-aggregated solutions and normalized this parameter with respect to the spectrum of maximally aggregated colloidal silver. The variations of absorption spectra for each of the aggregated states are shown in Figure 15. One can see that the growth of the aggregation rate leads to the broadening of absorption spectra and the appearance of the long-wave wing near the surface plasmon resonance of silver. The linear absorption coefficients were increased (from 0.8 cm^{-1} to 2 cm^{-1}) with the growth of the aggregation rate, so it was necessary to decrease the power density of picosecond radiation to prevent an optical damage of the sample. These changes have been taken into account for $\chi^{(3)}(-\omega; \omega,-\omega,\omega)$, n_2, and β calculations. The nonlinear absorption value has reached its maximum ($\beta = 3.8\times10^{-11}$ cm W^{-1}) for maximal aggregation rate (A = 0.8). It should be noted that we did not detect nonlinear absorption for non-aggregated colloidal silver. The dependences between aggregation rates of colloidal silver and nonlinear susceptibilities and nonlinear refractive indices for picosecond pulses are presented in Table 2.

Copyright © 2010. Nova Science Publishers, Incorporated. All rights reserved.

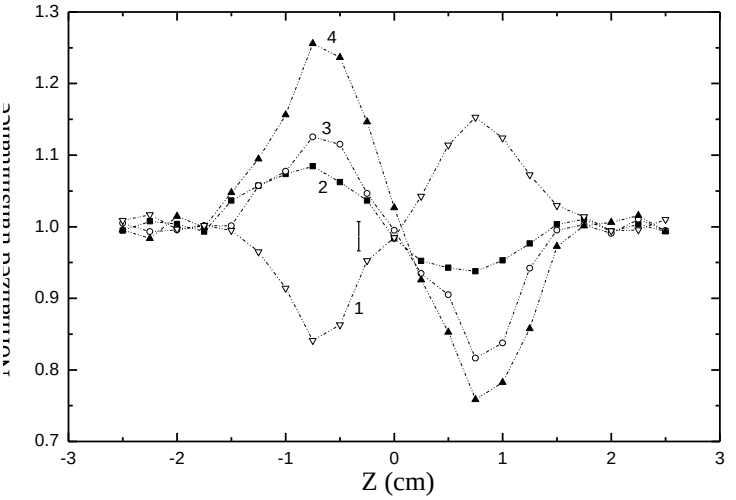

Figure 14. Normalized transmittance as a function of cell position in closed aperture scheme for different aggregation rates (A) of colloidal silver. 1 – A = 0; 2 – A = 0.16; 3 – A = 0.54; 4 – A = 0.80.

Table 2. The dependencies between aggregation rates of colloidal silver and its nonlinear susceptibilities and nonlinear refractive indices for picosecond and nanosecond radiation (λ = 1064 nm)

Aggregation rate	Picosecond pulses		Nanosecond pulses	
	n_2, esu	$\chi^{(3)}$, esu	n_2, esu	$\chi^{(3)}$, esu
0	1.43×10^{-14}	1.97×10^{-15}	1.1×10^{-11}	1.5×10^{-12}
0.16	-3.81×10^{-14}	-5.2×10^{-15}	-4.65×10^{-11}	-6.4×10^{-12}
0.54	-5.69×10^{-14}	-7.85×10^{-15}	-15.9×10^{-11}	-2.19×10^{-11}
0.80	-11×10^{-14}	-1.5×10^{-14}	-31.9×10^{-11}	-4.4×10^{-11}

Maximum values of $\chi^{(3)}(-\omega; \omega,-\omega,\omega)$ and n_2 were found to be -1.5×10^{-14} esu and -1.1×10^{-13} esu, respectively. Here, the Z-scan measurements of the self-defocusing of nanosecond pulses, which is due to the thermal energy transition from MN to the surrounding solvent (water), are presented. It should be noted that this nonlinearity has a 'slow' character which plays a negligible role in experiments with picosecond pulses. Our experiments have shown that the nonlinear optical response of a colloidal structure has a 'slow' component, due to the thermal nonlinearity of surrounded dielectric, and a 'fast' component, due to the Kerr-induced nonlinearity of aggregated particles [81].

The same measurements as for picosecond pulses were performed for nanosecond pulses (see Table 2). The dynamics of nonlinear optical parameters with the growth of aggregation rate remained the same as for picosecond pulses. It should be noted that in the case of nanosecond pulses we did not observe nonlinear absorption up to the maximum intensity used ($I_{max} = 8\times10^9$ W cm^{-2}) which was much smaller than the maximal intensity of picosecond pulses ($I = 4\times10^{11}$ W cm^{-2}). Maximum values of n_2 and $\chi^{(3)}(-\omega; \omega,-\omega,\omega)$ in this case were found to be -32×10^{-11} esu and -44×10^{-12} esu, respectively. The characteristic peculiarity of

Copyright © 2010. Nova Science Publishers, Incorporated. All rights reserved.

these studies was the sign change of n_2 with the growth of the aggregation rate for both nanosecond and picosecond pulses. Electron microscopy analysis of silver fractals at different stages of aggregation has shown that particle sizes varied from 10 nm (for the non-aggregated state) to 40–100 nm (for the aggregated state ($A = 0.8$)).

For the determination of the physical mechanisms of nanosecond pulse' self-defocusing in colloidal silver, we have investigated the dynamics of laser pulses passed through the cell in closed aperture experiments for different cell positions with respect to the focal point ($Z = 0$). Part of the radiation was defocused inside the cell when the energy density reached its definite value. As a result of this, a smaller part of the whole radiation passed through the aperture and was registered by the photodiode. The temporal trace of input radiation passed through the cell and aperture had reached its maximal value before the pulse maximum which was detected in the case when a cell was placed far from the focal point. Such behavior characterizes the thermal nature of self-defocusing [82].

Now we discuss the thermal mechanism of self-defocusing in the nanosecond regime (heat transfer to the water, characteristic times, comparison with others results). As was mentioned, our observation of the temporal behavior in the nanosecond regime is based on the assumption of the thermal nature of lensing. The thermal lens is built-up with the energy absorption growth. Because of the delay of this process due to the transfer of energy to the solvent, this lensing is more effective for the trailing part of the pulse. It is seen in temporal traces of propagated pulses that its trailing part changes depending on sample position with respect to the focal point. The defocusing effect is more distinctly seen in the cases when the cells were placed close to the $T_{\min}$ position (for the closed aperture Z-scan scheme). An important parameter of self-defocusing in that case is $M = 1/C\rho(\mathrm{d}n/\mathrm{d}T)$, which is equal to -1.04×10^{-4} cm^3 cal^{-1} for water [83]. Here, C is the specific heat and ρ is the density of the solvent. This parameter is crucial for determining the variations of refractive index as a function of absorbed energy per unit volume ($\Delta n = M\Delta E$).

Usually, the Z-scan experiments are performed in homogeneous and long-term stable samples which can be characterized by some refractive index. Colloidal systems, in particular when they are aggregated, are inhomogeneous on the λ-scale and, hence, require 'effective medium' models to introduce some effective refractive index n_{eff}. This holds true, both for linear and nonlinear contributions. As we mentioned earlier, the sizes of the investigated nanoparticles have changed from four to ten times (from 10 nm to 40–100 nm). Further growth of particle size led to the increase of absorption and sediment of nanoparticles. These changes do not influence the propagation of laser beam near the focal point due to variations of n_{eff}. It follows from our studies that the nonlinear refractive index in the case of thermal contribution (nanosecond pulses) depends on the aggregation rate (or in other words, on particle size) but not on the beam size. Our studies of colloidal solutions, in the cases of different beam waists, have shown the same values of nonlinear optical parameters within the accuracy of our measurements.

It is worth noting the principal role of the energy density parameter for nanosecond pulses (in comparison with the power density) on the process of thermal defocusing. We explain our results as a thermal self-defocusing, which is due to the transfer of energy absorbed by colloidal fractals to water molecules. The thermal self-defocusing can be considered as a function of absorbed energy. So, radiation energy density plays a more important role in this process in comparison with radiation power density.

Copyright © 2010. Nova Science Publishers, Incorporated. All rights reserved.

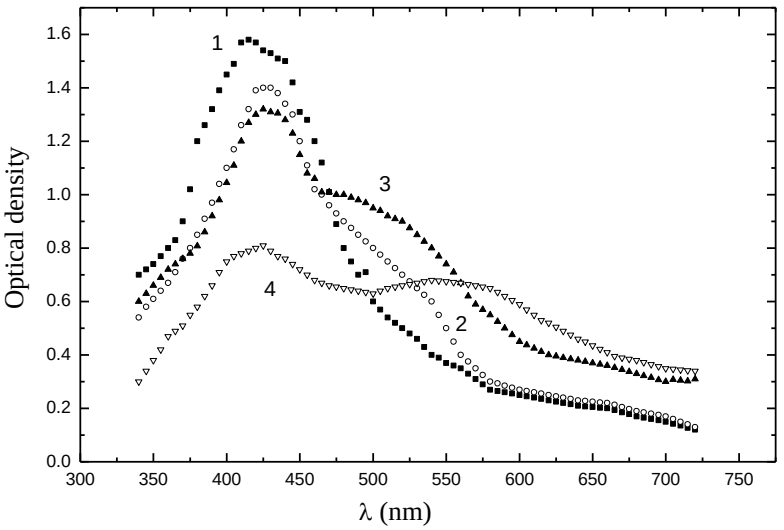

Figure 15. Absorption spectra of colloidal silver for different aggregation rates. (1) A = 0; (2) A = 0.16; (3) A = 0.54; (4) A = 0.80.

1.8. Pulsed Laser Deposition of Silver Films and Nanoparticles in Vacuum Using Subnanosecond Laser Pulses

Past studies on nanoparticles prepared using metal vapor deposition [84], reduction of some salts by alkalides [85], and solution dispersion method [86] have revealed many interesting structural and optical properties of these materials. The laser ablation of metals in vacuum and liquids is among the perspective techniques, which can also be successfully applied for the preparation of nanoparticle-containing media. The application of laser ablation in liquids for the preparation of semiconductor and metal colloids has been demonstrated in [87,88].

It is known that metal ablation in air is significantly less efficient than that in vacuum due to re-deposition of the ablated material. The ablation rates in vacuum can be calculated using a thermal model, which also allows estimating the ablation rates for other metals from basic optical and thermal properties [89]. A comparison of the morphology of deposition after nanosecond and picosecond ablation shows unequivocally the advantages of short-pulse ablation for the preparation of nanoparticles [90]. The most interesting and new features of laser ablation and nanoparticle formation during irradiation of the solid targets have been recently observed in the case of shortest laser pulses (100 fs to 1 ps). To prove the generality of the vacuum deposition method and its potential use for preparing nanoparticles, we considered various metals and analyzed this process at different focusing conditions of the laser radiation [91].

The ablation of silver was carried out in vacuum using uncompressed pulses (of 300 ps duration) from a chirped-pulse amplification-based Ti:sapphire laser system (Thales Lasers). The samples were placed inside a vacuum chamber. Uncompressed pulses from the Ti:sapphire laser (λ = 793 nm, t = 300 ps, E = 30 mJ, 10 Hz pulse repetition rate) were focused on a bulk target at two regimes of focusing. In the first case (referred to as tight

Copyright © 2010. Nova Science Publishers, Incorporated. All rights reserved.

focusing), the intensity of laser radiation was in the range of 2×10^{12} W cm^{-2}, and in the second case (referred to as weak focusing), the intensity was considerably lower (4×10^{10} W cm^{-2}). Float glass, silicon wafer, and various metal strips (Ag, Cu, and aluminum) were used as the substrates, and were placed at a distance of 50 mm from the targets.

The deposition was carried out in oil-free vacuum ($\approx1\times10^{-4}$ mbars) at room temperature. The structure of the deposited films of ablated metals was analyzed using different techniques. The nature of the nanoparticles is governed by the thermodynamic conditions at the target surface. The presence of nanoparticles was inferred by analyzing the spatial characteristics of the deposited material and the spectral absorption of the deposited material. The absorption spectra of the deposited films were analyzed using a fiber-optic spectrograph (USB2000). The analysis of the sizes of deposited nanoparticles was carried out using total reflection x-ray fluorescence (TXRF). Details of the TXRF are described in Ref. [92]. The structural properties of the deposited films were analyzed using a scanning electron microscope [(SEM), Philips XL30CP], an atomic force microscope [(AFM), SOLVER PRO, NT-MDT], and a transmission electron microscope (Philips CM200).

The absorption spectra of the materials deposited on transparent substrates (float glass) were used to determine the presence or absence of nanoparticles. The presence of nanoparticles was inferred from the appearance of strong absorption bands associated with SPR. Figure 16 presents the absorption spectra of Ag films deposited on float glass substrates. Here, we observed a variation of the position of the SPR absorption of Ag deposition, which depended on the conditions of excitation and evaporation of bulk targets by the 300 ps pulses. However, in all these cases, the peaks of SPR were centered in the range from 440 to 490 nm (Figure. 16, curves 1–3). In the case of the deposition of Ag film at the weak-focusing conditions, no absorption peaks were observed in this region, indicating the absence of nanoparticles.

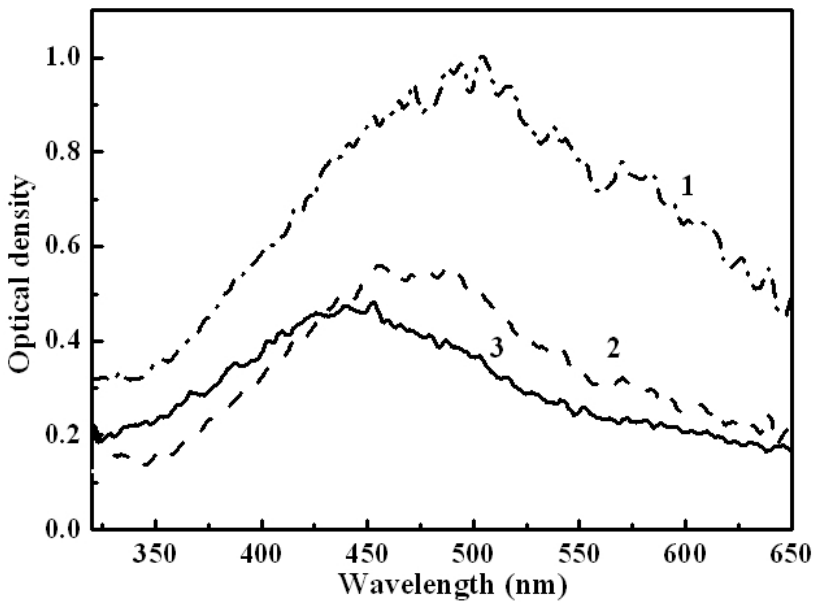

Figure 16. Absorption spectra (curves 1-3) of the silver films deposited at different tight focusing conditions. The corresponding intensities of laser radiation on the surface of Ag target were (1) 2×10^{12}, (2) 8×10^{11}, and (3) 5×10^{11} W cm^{-2}.

Copyright © 2010. Nova Science Publishers, Incorporated. All rights reserved.

Much attention has been devoted during the past few years to precisely determining the spatial arrangement in 2D and 3D structures of metals. However, the ordering and use of the nanomaterials necessitate synthesis of monodispersed individual nanoparticles, for which no general method is presently available. We describe, later in this subsection, the analysis of synthesized nanoparticles by laser ablation of bulk silver at two different conditions of ablation. The structure of the ablated Ag was analyzed by studying the films deposited on silicon substrates.

One of the aims of this study was to investigate whether the plumes contain nanoclusters. The presence of the latter could be responsible for the enhancement of the nonlinear optical characteristics of laser plasma. In particular, high-order harmonic conversion efficiency may be affected due to the quantum confinement effect during the propagation of a femtosecond laser pulse through a nanoparticle-containing plasma. Harmonic generation using single atoms and multiparticle aggregates has been reported for argon atoms and clusters [93]. It was demonstrated that a medium containing intermediate-sized clusters of a few thousand atoms of an inert gas is much better at generating the higher harmonics than a medium of isolated gas atoms of the same density. The reported enhancement factor for the third through ninth harmonics was approximately 5. Also, the dependence of the efficiency of harmonic generation on the intensity of the laser radiation was much more pronounced for clusters than for isolated atoms. The highest harmonic number for clusters was reported in [94], which was higher than that for the isolated atoms.

Total reflection x-ray fluorescence measurements were performed using an in-house-developed TXRF [95] for the analysis of the structural properties of the deposited material. The angular dependence of the fluorescence intensity in the total reflection region [96,97] can be successfully used to identify the presence of nanoparticles on a flat surface. The structure of the nanoparticles prepared by the laser ablation process was analyzed using TXRF, which identified the presence of nanoparticles. This was done for the deposition in tight-focusing conditions. In the case of weak focusing, it showed a thick filmlike deposition of metal, without any inclusion of nanoparticles.

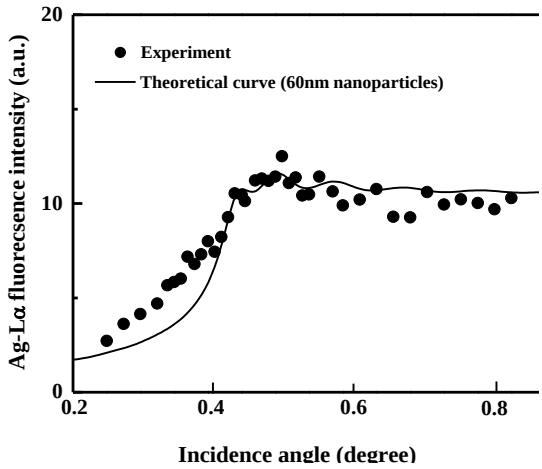

Figure 17. Recorded x-ray fluorescence profile of silver nanoparticles prepared by the laser ablation in vacuum and deposited on a float glass substrate. The dots show experimental data, while the solid line shows a fitted profile.

Copyright © 2010. Nova Science Publishers, Incorporated. All rights reserved.

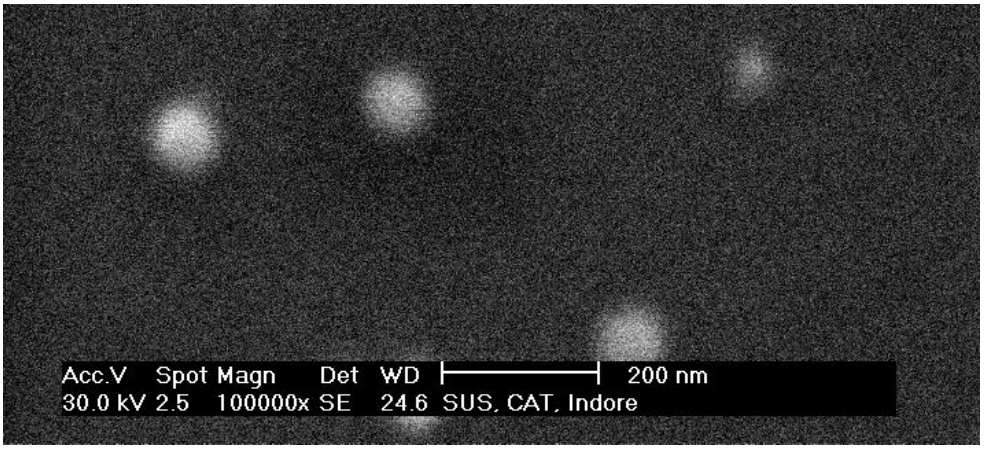

Figure 18. SEM image of the silver nanoparticles deposited on silicon wafer as substrate. The average size of the spherical clusters was measured to be 60 nm.

Figure 17 shows the x-ray fluorescence trace recorded in the case of Ag nanoparticles deposited on a glass substrate at tight-focusing conditions. It can be seen from this figure that the angle-dependent fluorescence profile of the Ag film shows the presence of nanostructure on the flat surface, as well as indicates a monoatomic layer. The average size of the Ag nanoparticles was determined by fitting the recorded fluorescence profile using the CATGIXRF program. The solid curve presents the best theoretical fit, from which the average size of the nanoparticles was estimated to be 60 nm. The TEM measurements also confirmed the presence of Ag nanoparticles in these deposited films.

Our SEM studies of the structural properties of the deposited films showed that, in tight-focusing conditions, these films contain a lot of nanoparticles with variable sizes. In weak-focusing conditions, the concentration of nanoparticles was considerably smaller compared to the tight-focusing condition. In the case of weak focusing, the deposited film was almost homogeneous with a few nanoparticles appearing in the SEM images, while in tight-focusing conditions, plenty of nanoparticles ranging from 30 to 100 nm appeared in the SEM images. The average size of these nanostructures was estimated to be 60 nm. An enlarged SEM image of the Ag nanoparticles prepared in tight-focusing conditions is presented in Figure. 18. The average size of these spherical clusters was also measured to be 60 nm.

Further studies on the characteristics of nanosized structures of the deposited materials were carried out using atomic force microscopy. AFM measurements were carried out in noncontact mode under an ambient environment. Silicon cantilever tips of resonant frequency 180 kHz and spring constant 5.5 N m^{-1} were employed. Figure 19(a) shows the AFM image of the Ag nanoparticles deposited on the surface of a copper strip. The average size of Ag nanoparticles was 65 nm. In contrast to this, the AFM images obtained from the deposited films prepared at weak-focusing conditions showed a considerably smaller number of nanoparticles. Figure 19(b) shows an AFM picture of Ag deposition prepared at these conditions. The image indicates the presence of very few nanoparticles.

Copyright © 2010. Nova Science Publishers, Incorporated. All rights reserved.

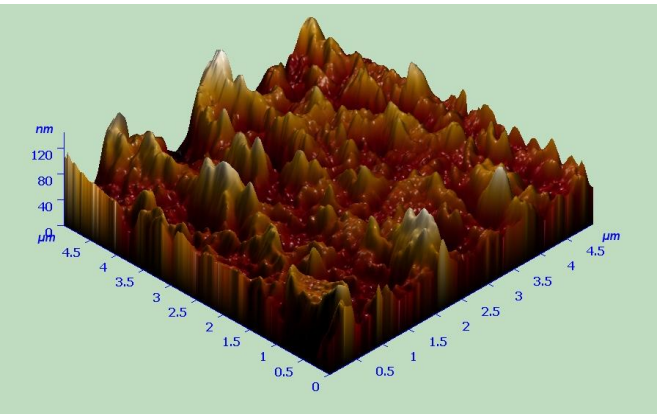

(a)

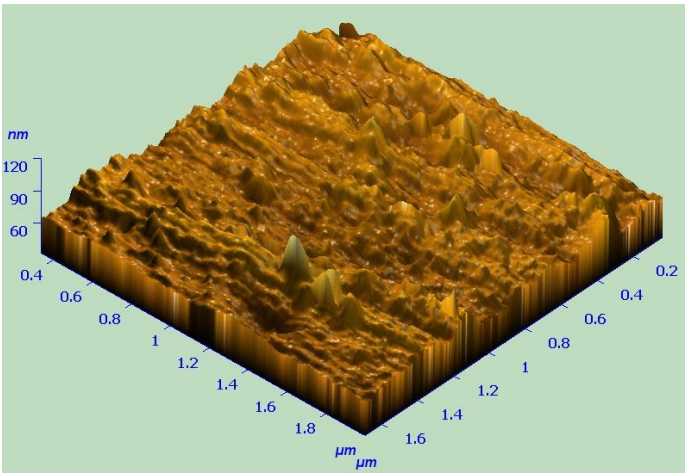

(b).

Figure 19. AFM images of (a) the silver nanoparticles deposited on a copper strip in the tight focusing condition, and (b) the silver nanoparticles deposited in the weak focusing condition. Very few nanoparticles are seen in the case (b) of weak focusing condition compared to the case (a) of tight focusing condition.

To characterize the ablation process, the temporal and spectral characteristics of the light emitted by the plume were also studied. The oscilloscope traces showed a considerable increase in the duration of the plasma emission in the case of tight focusing that could be expected considering the excitation conditions. A combined analysis of the spectra and oscilloscope traces in the cases of two different regimes of the excitation of surface plasma revealed that the structureless continuum appearing in the spectrum in the case of tight focusing is due to the emission from hot nanoparticles produced during laser ablation. Such hot nanoparticles behave like black-body radiators emitting for a longer time, until they get cooled down.

It is well accepted that when a solid target is ablated by laser radiation, the ablating material is in the form of atoms, ions (and electrons), and clusters. These atoms and clusters tend to aggregate during the laser pulse or soon afterward leading to the formation of larger clusters. The reported results (see, for example, [98]) also indicate that the ablation processes in the picosecond and femtosecond time scales are very different compared with the

Copyright © 2010. Nova Science Publishers, Incorporated. All rights reserved.

nanosecond one. In addition to the early experimental observations, several theoretical studies have suggested that rapid expansion and cooling of the solid-density matter heated by short laser pulses may result in nanoparticle synthesis via different mechanisms. Heterogeneous decomposition, liquid phase ejection and fragmentation, homogeneous nucleation and decomposition, and photomechanical ejection are among those processes that can lead to nanoparticle production [99-101]. Short pulses, contrary to the nanosecond pulses, do not interact with the ejected material, thus avoiding complicated secondary laser interactions. Further, short pulses heat a solid to a higher temperature and pressure than do longer pulses of comparable fluence since the energy is delivered before significant thermal conduction can take place.

The model developed in Ref. [102] for laser ablation predicts that, for short laser pulses at intensities in the range from 10^{12} to 10^{13} W cm^{-2}, the adiabatic cooling drives the system into a metastable region of its phase diagram, resulting in the production of a relatively large fraction of nanoparticles. At much larger intensities ($\geq 10^{14}$ W cm^{-2}), the system can never reach the metastable region, resulting in an almost atomized plume. Pulsed laser deposition using short pulses has gained some interest because of a number of advantages over other processes, such as the possibility of producing materials with a complex stoichiometry and a narrowed distribution of nanoparticle sizes with reduced porosity. Typically, laser deposition is carried out in an ambient gas, which quenches the ablated plume, thus controlling the mean particle size [103]. However, some previously reported studies [90,104], as well as the present study, suggest that nanoparticles are generated as a result of some relaxation processes of the extreme material state reached by the irradiated target surface. This stands in stark contrast to the formation of nanoparticles during nanosecond laser ablation in a background gas, where vapor condensation is considered to be an important mechanism.

2. Application of Silver Nanoparticle-containing Laser Plasmas for Optical High-Order Harmonic Generation

Various studies reported during the last decade pointed out the peculiarities of interaction of the strong laser pulses with atomic/ionic media, which in particular allowed for the shift of laser radiation wavelength toward the shorter wavelength range [105]. In the meantime, the enhanced nonlinear optical response of multiatomic particles induced by the quantum confinement has attracted much interest, with novel applications in optoelectronics, optical switchers and limiters, as well as in optical computers, optical memory, and nonlinear spectroscopy. High values of third-order nonlinear susceptibility, especially near the surface plasmon resonances of nanostructured materials, are the trademark of these media, in particular metal nanoparticles. MN subject to intense laser pulses produce strong low-order nonlinear optical response (e.g., nonlinear refraction and nonlinear absorption), as well as can emit the coherent radiation through the low-order harmonic generation [106,107]. These and other studies have shown that one can expect improvement of the harmonic efficiency by switching to the nanoparticle media. In the meantime, previous studies of harmonic generation in such objects were limited to exotic nanoclusters (Ar, Xe), which are formed in high-pressure gas jets due to rapid cooling by the adiabatic expansion. The physical origin of this process in the gas clusters [93,94,108-115] is mostly attributed to standard atomic

Copyright © 2010. Nova Science Publishers, Incorporated. All rights reserved.

harmonic generation, modified by the fact that in clusters the atoms are disposed to each other.

Only a few high-order harmonic generation studies using 10^3–10^4 atoms/cluster media (with the cluster sizes between 2 and 8 nm) have been reported, while some theoretical simulations predicted a growth in the harmonic intensity with regard to the monoatomic media. It may be noted that a pronounced resonant enhancement for nanoparticles is found only for yields of the low-order harmonics, while the high-order harmonics completely disappear from the harmonic spectra in the simulations [116]. Clustered plasma was proposed as a nonlinear medium in which both the phase matching [109] and resonantly enhanced growth of the nonlinear susceptibility for low-order harmonics [112] could be achieved at selected cluster sizes and densities.

One of the approaches to achieve the efficient high-order harmonics is the application of commercially available nanoparticles in the pump-probe HHG experiments using the laser ablation of the targets containing Ag nanoparticles [115,117]. An important issue in the case of nanoparticles ablation is their integrity during evaporation from the target surface. One can expect the fragmentation, melting, or aggregation of nanoparticles during interaction of the strong laser radiation with the target surface. To achieve the harmonic generation from nanoparticles, one should not overexcite the nanoparticle-containing targets to produce the plasma where these species are presented in their indigenous neutral (or ionized) conditions.

2.1. Harmonic Generation of Laser Radiation in the Plasma Plumes Containing Large-Sized Silver Nanoparticles

In this subsection, we analyze the HHG in various commercially available nanoparticles with mean sizes of approximately 100 nm. These studies were carried out using the ablation of nanoparticle media by subnanosecond laser prepulse with further probing of nanoparticle-containing plasma by the femtosecond pulse. The presence of nanoparticles in the plumes was carefully studied by analyzing the morphology of the debris of ablated material deposited on nearby substrates. We show that, at the conditions of optimal ablation, the nanoparticles maintain their integrity in laser plumes, which allows for the enhancement of HHG yield in the case of nanoparticle-containing plumes with regard to the monoparticle-containing plasmas.

Experiments were carried out using the chirped pulse amplification 10 Hz, 10 TW Ti:sapphire laser. To create the ablation, a subnanosecond prepulse (t_{pp} = 210 ps) was split from uncompressed radiation of Ti:sapphire laser and focused on a target placed in the vacuum chamber (see inset in Figure. 20). The intensity of subnanosecond prepulse (I_{pp}) on the target surface was varied between 2×10^9 and 3×10^{10} W cm^{-2}. After some delay (6–74 ns), the femtosecond main pulse (t_{fp} = 35 fs, λ = 800 nm) was focused on the plasma from the orthogonal direction. Our HHG experiments were carried out using the laser intensities (I_{fp}) up to $I_{fp} = 2\times10^{15}$ W cm^{-2}, above which the HHG efficiency considerably decreased due to some restricting processes in the laser plasma. The harmonics were spectrally dispersed by an extreme ultraviolet spectrometer, detected by a micro-channel plate, and recorded using a charge-coupled device camera.

Copyright © 2010. Nova Science Publishers, Incorporated. All rights reserved.

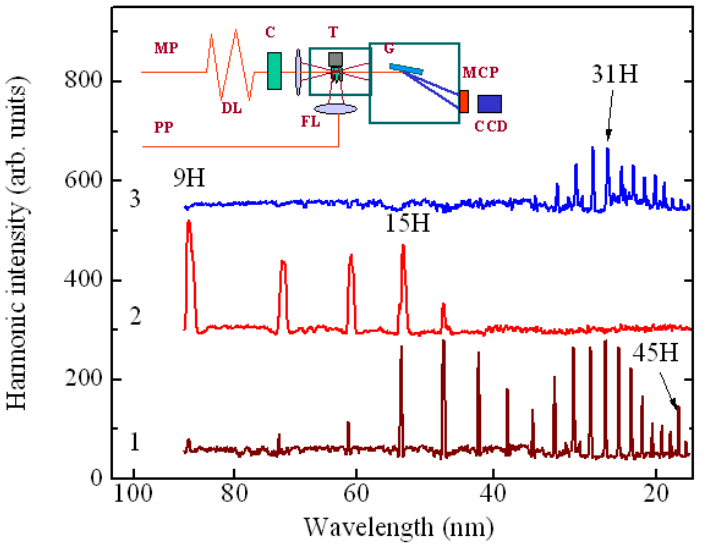

Figure 20. Harmonic spectra obtained from the plasmas produced on the surfaces of (1) bulk silver, and (2,3) silver NP-containing target. The intensities of prepulse on the target surfaces were (1) 3×10^{10} W cm^{-2}, (2) 7×10^{9} W cm^{-2}, and (3) 2×10^{10} W cm^{-2}. $I_{fp} = 4\times10^{14}$ W cm^{-2}. The delay between the prepulse and femtosecond pulse in these experiments was maintained at 20 ns. Inset: Experimental setup. MP: main pulse; PP: prepulse; DL: delay line; C: grating compressor; FL: focusing lenses; T: target; G: gold-coated grating; MCP: micro-channel plate; CCD: charge-coupled device.

In these studies, we used various nanosized silver powders (Alfa Aesar). The sizes of nanoparticles were varied in the range of 30–200 nm. These powders were glued on the glass substrates by mixing with superglue. We also used the bulk materials of the same origin as nanoparticles to compare the HHG from the nanoparticle-containing and atom/ion-containing plumes [118].

These studies were concentrated on (a) comparison of the harmonic spectra generated in the plasmas containing single atomic/ionic particles and nanoparticles, and (b) morphological characterization of the plasma components. Initially, we confirmed the harmonic generation in the plasmas produced on the surfaces of bulk materials. In particular, the plasma produced on the silver solid surfaces showed the harmonics up to the 47th order. Note that the harmonic spectrum generated in silver plasma mostly consisted of the high-order components belonging to the high-energy part of plateau, while the low-wavelength harmonics of plateau were considerably suppressed due to the optimal phase matching conditions for shorter-wavelength harmonics (Figure 20, curve 1). The harmonic cutoff was shifted toward the longer wavelengths when we ablated the silver nanoparticle-containing targets and generated the harmonics in the produced plumes. At the same time, these harmonics were considerably stronger compared with those generated in the single particle-containing plasma created on the surface of bulk silver (Figure 20, curve 2). Moreover, the spectral widths of harmonics were three to four times broader compared with the narrow lines of the harmonics generated in monoparticle-containing plasma. The enhancement factor of the harmonics generated in nanoparticle-containing plumes was varied between 5 and 12 compared with monoparticle plume, depending on the harmonic order and the conditions of excitation. Note that this enhancement of low-order harmonics was observed in the case of moderate excitation of the silver nanoparticle-containing targets ($I_{pp} = (5–7)\times10^{9}$ W cm^{-2}). At the same time, HHG from

Copyright © 2010. Nova Science Publishers, Incorporated. All rights reserved.

plasma produced on bulk surface at these intensities of heating radiation was inefficient. Further growth of prepulse intensity at the target surface containing nanoparticles led to a dramatic change of harmonic spectra, which showed the disappearance of strong low-order harmonics and the appearance of high-order ones (Figure 20, curve 3). The intensity of these harmonics was considerably weaker than the intensity of low-order harmonics in the case when low excitation was applied to the targets. The delay between the prepulse and femtosecond pulse in these experiments was 20 ns.

We carried out the studies of the availability of HHG during propagation of the femtosecond pulse through the glue molecules-containing plasmas, when no nanoparticles were mixed in this organic. No harmonics were generated in that case. The same can be said about the influence of substrates.

The growth of intensity of the femtosecond pulse did not lead to extension of the harmonics generated in the nanoparticle-containing plumes, which is a sign of saturation of the HHG in these media. Moreover, at relatively high intensities of probe femtosecond pulse, we observed a decrease in harmonic conversion efficiency due to some restricting factors (appearance of abundance of free electrons, self-defocusing, phase mismatch, etc). The same can be said about the increase in prepulse intensity on the surface of nanoparticle-containing target over some optimal value. In that case the deterioration of harmonic generation was attributed to the increase in free electron concentration and phase mismatch.

Our experiments show that the optimum delay between the prepulse and femtosecond pulse was 12–50 ns (in the case of nanoparticle-contained plasma) and 40–60 ns (in the case of the plasma produced on the surface of Ag bulk target). These observations demonstrate the dynamics of harmonic generation and point out the particles responsible for this process. At moderate prepulse intensities, the plasma contains predominantly neutral nanoparticles. In that case the harmonic cutoff is defined by interaction of the femtosecond pulse with the neutral nanoparticles. The increase in prepulse intensity led to both the increase in nanoparticle concentration and their ionization. The abundance of free electrons restricted generation of low-order harmonics, while the conditions for higher-order harmonics became more favorable.

We can assume that, in the case of small nanoparticles, the ejected electron, after returning back to the parent particle, can recombine with any of atoms in the nanoparticles due to enhanced cross section of the recombination with parent particle compared with single atom, which considerably increases the probability of harmonic emission in the former case. Thus the enhanced cross section of the recombination of accelerated electron with parent particle compared with single atom can be a reason of observed enhancement of the HHG yield from the nanoparticle-containing plume compared with monoparticle-containing plasma.

At the same time note that, for nanoparticles with the linear sizes higher than the harmonic radiation wavelength, the effective recombination of the ejected electron for the harmonic radiation cannot be with any of ions in the nanoparticles but only with part of ions, for which the phase difference between the initial and the final state of the electron is less than 2π. This feature, probably, points out the optimal sizes of nanoparticles for efficient enhancement of HHG. Accelerated electron can be effectively recombined with the part of the whole nanoparticle, which has the dimensions in the range of generated harmonics' wavelength (i.e., about few tens of nanometers). Further increase in nanoparticle sizes does not lead to enhancement of HHG.

Copyright © 2010. Nova Science Publishers, Incorporated. All rights reserved.

Since nanoparticles are smaller than the laser wavelength, they contain many equivalent, optically active electrons at effectively the same point in the laser field. This leads to the possibility that each of these electron oscillators may contribute coherently to a global nanoparticle dipole. However, this statement is true only for very low harmonics. For high harmonic generation, the dipole approximation is inapplicable because the harmonic radiation wavelength is shorter than the size of nanoparticles (of the order of 100 nm). At these conditions we point out the involvement of the part of nanoparticles in the HHG, which is quite large (of order of 10^5 atoms) and can give the enhancement of harmonics.

In addition, these nanoparticle electrons see a binding potential, which is modified from the single-atom case by the proximity of neighboring ions. At the same time note that the enlargement of nanoparticles above the optimum sizes can lead to a decrease in high-order nonlinear optical response of the medium due to the losses caused by recombination of the electrons before ejection from the nanoparticles, reabsorption of the harmonics inside the high-sized structures, etc. Also, bound and free electrons in the nanoparticles can result in shielding of the laser field inside the nanoparticle.

The presence of nanoparticles in the plumes was confirmed by analyzing the spatial characteristics of the ablated material deposited on nearby glass and aluminum substrates. It was shown that, at optimal excitation conditions, the nanoparticles remain intact in the plasma plume until the main femtosecond pulse arrives in the area of interaction. The SEM images of deposited nanostructures in most cases when we maintained the optimal excitation of targets revealed that they remain approximately the same as the initial powders. The sizes of deposited nanoparticles were in the range of 40–250 nm. The intensity of laser pump pulse at nanoparticle-containing targets was kept in the range of $3\times10^9 - 8\times10^9$ W cm^{-2}. The increase in prepulse intensity above certain level led to the appearance of aggregated clusters.

These SEM studies have demonstrated that the harmonics generated at the optimal conditions of target excitation are the result of interaction of the femtosecond pulse with nanoparticles. Some additional supporting confirmation of this statement is as follows. In most cases of the HHG in the nanoparticle-containing plasma created at moderate intensities of prepulse, we did not observe the extension of high-order harmonics that could be associated with the involvement of ionized particles in the process of harmonic generation, as it was observed in the case of the plasma produced on the surface of bulk materials of the same origin (Figure 20). The harmonic cutoff for the nanoparticle-containing plumes should be in the range of 13th–17th harmonics, taking into account the saturation intensity at which the neutral nanoparticles ionize (~1×10^{14} W cm^{-2}). In most cases these harmonics decreased or even disappeared with the growth of excitation and ionization of plasma, since the phase mismatch of HHG prevented stable generation of low-order harmonics above the cutoffs defined from the three-step model for the neutral particles.

These studies have shown that, for any nanoparticle-containing plume, no improvements in the extension of the harmonic cutoff were observed. At the same time, an enhancement of the harmonic yield in the low-energy plateau range in the case of nanoparticle-containing plumes was achieved. These conclusions are true for the smaller-sized nanoparticles as well. The value of the enhancement factor could be attributed to rather different concentrations of nanoparticles and monoparticles in the plume at different excitation conditions, enhanced cross section of the recombination with parent nanoparticles compared with single atom, as

Copyright © 2010. Nova Science Publishers, Incorporated. All rights reserved.

well as to the processes related with the quantum confinement-induced growth of the nonlinear optical response of such medium.

A comparison of the low-order harmonic generation using the single atoms and multiparticle aggregates has previously been reported for Ar atoms and clusters. It was demonstrated that a medium of intermediate-sized clusters with a few thousand atoms of an inert gas has a higher efficiency for generating the harmonics, compared with a medium of isolated gas atoms of the same density. The reported enhancement factor for the third–ninth harmonics from gas jets was about five. In our HHG experiments with the laser-ablated nanoparticles, these observations were extended toward the higher-order harmonics and stronger enhancement for the harmonics up to the 25th order was achieved. These results have also shown that the dependence of the HHG efficiency on the prepulse and main pulse intensity is much more prominent for nanoparticles than for monoparticles.

2.2. Comparison of High-order Harmonic Generation in Large- and small-Sized Ag Nanoparticle-containing Plasma

The Ag nanoparticle suspension was purchased from the Wako Pure Chemical Industries, Ltd (Japan) and used in experiments without further purification. The molar concentration of the Ag nanoparticles protected by polyethyleneimine in the aqueous solution was 10 mM. This suspension was dried on the surface of a glass plate and further used as a target for laser ablation. Another sample under investigation was silver nanoparticle powder.

Prior to HHG experiments, these nanoparticles were analyzed using scanning electron microscopy and transmission electron microscopy. The nanoparticle's sizes are of crucial importance when one considers the nonlinear optical processes, since the influence of quantum confinement on the nonlinear optical properties of medium strongly depends on the shape and spatial extension of such structure. Figure 21(a) shows the SEM image of silver nanoparticle powder. The mean size of the Ag nanoparticles was defined to be 110 nm, with the particle sizes varying in a broad range between 20 and 180 nm. The TEM images of the Ag nanoparticles in suspension and dried Ag nanoparticles showed considerably smaller sizes, with the mean size of 6 nm in the former case, and narrow size distribution (between 3 and 12 nm, Figure 21(b)), while in the latter case, we observed an increase of particle sizes (up to the mean size of 15 nm, Figure 21(c)). The aggregation probably was responsible for the enhancement of particle sizes after the drying of the nanoparticle-containing suspension. The shape of the nanoparticles was close to spherical. An elemental analysis of the nanoparticles under investigation using energy dispersive x-ray spectroscopy confirmed the presence of Ag particles in these suspensions and films.

The change in the particle sizes was followed by a shift of the SPR of nanoparticle-contained media. Figure 21(d) presents the absorption spectra of an Ag suspension and dried Ag film. One can clearly see the red-shift of the SPR from 360 nm towards 430 nm, when one compares the absorption properties of the suspension and film.

Copyright © 2010. Nova Science Publishers, Incorporated. All rights reserved.

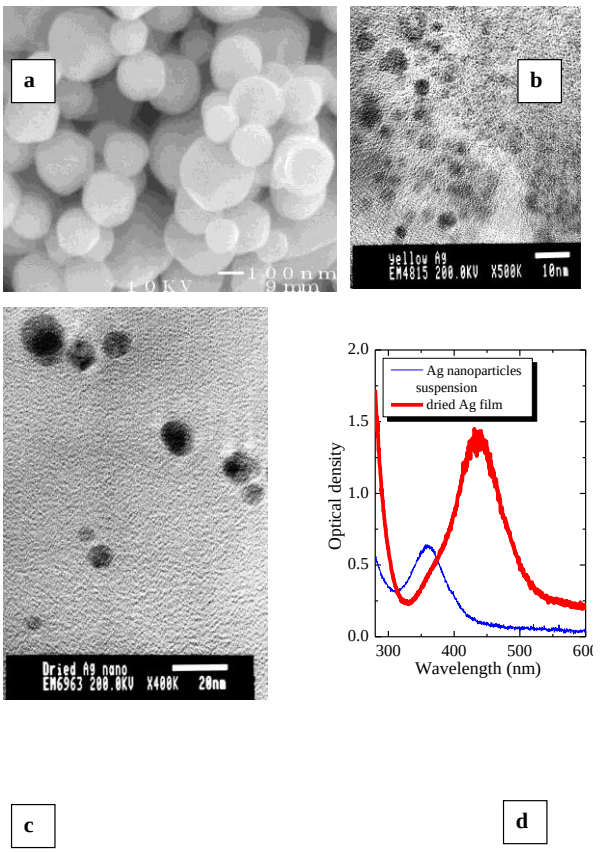

Figure 21. (a) SEM micrograph of the Ag powder, (b) TEM micrograph of the Ag nanoparticles suspension, (c) TEM micrograph of the nanoparticles from Ag dried film, and (d) optical absorption spectra of Ag nanoparticles suspension (thin line) and dried Ag film (thick line).

These structural measurements suggest that only 6 nm particles contained in suspensions could exhibit to some extent the quantum-effect-related enhancement of nonlinear optical properties, due to their relatively small sizes. However, since the harmonic generation occurs in the laser plasma produced on the surface containing nanoparticles (i.e., dried nanoparticle film), we compared the nonlinear optical response from the particles with the mean sizes of 110 nm and 15 nm [119].

To study the high-order nonlinearities through HHG, the Ag nanoparticle powder was glued on various substrates (drop of glue, tape and glass) and placed inside the vacuum chamber to ignite the plume by the laser ablation of these structures. The dried silver film prepared by the evaporation of the aqueous suspension containing silver nanoparticles was also used as the target for the HHG experiments. The pump source was a commercial, chirped pulse amplification Ti:sapphire laser system (Spectra Physics: TAS-10F), whose output was further amplified using a homemade three-pass amplifier operating at a 10 Hz pulse repetition rate. A 210 ns prepulse was split from the amplified laser beam by a beam splitter before a main pulse compressor. A spherical or cylindrical lens focused the prepulse on a target comprising the silver nanoparticle contained film or the silver powder glued on different matrices. We also used the Ag bulk plate as a target to compare the HHG in the cases of the plasma plumes containing clusters or monoparticles (atoms and ions) of the same origin. A

Copyright © 2010. Nova Science Publishers, Incorporated. All rights reserved.

main pulse at a centre wavelength of 790 nm had an energy of 12 mJ with a pulse duration of 120 fs after the propagation of the compressor. After a proper delay with regard to the prepulse irradiation, this pulse was focused by a spherical lens (*f*/10) on the ablation plume from the orthogonal direction. The main pulse intensity at the plasma area was varied between 5×10^{14} and 3×10^{15} W cm^{-2}. The spectrum of generated high-order harmonics was analyzed by a grazing incidence XUV spectrometer with a gold-coated flat-field grating. The XUV spectrum was detected using a micro-channel plate (MCP) with a phosphor screen read-out, and the optical output from the phosphor screen was recorded using a charge-coupled device (CCD) camera. The details of the absolute calibration of XUV registration system are reported in [120].

HHG from bulk silver targets has recently been optimized by various groups using Ti:sapphire lasers generating pulses of different durations (150, 48, and 35 fs). This medium (Ag plasma) still remains the best one from the point of view of highest conversion efficiency at the plateau region (8×10^{-6}). Those studies provided the information about the silver plasma ingredients and conditions measured by both the time-integrated [121] and time-resolved [122] techniques. Previous work revealed that, at the 'optimal plasma' conditions, which means the best output characteristics of generated harmonics, no nanoparticles existed in the laser plume [123]. Our studies confirmed all these properties of silver monoparticle plasma harmonics. Below we compare the harmonic generation using the Ag nanoparticle and monoparticle-containing plumes.

The initial experiments were carried out with the Ag powder nanoparticles. We verified that the harmonics generated from the substrates and glues itself (drop of glue, tape and glass), without nanoparticles, were negligible compared with those from the silver nanoparticle-containing plasmas. Figure 22 shows three sets of the comparative measurements of the harmonic yield from the silver plasmas containing mono-atoms and mono-ions (thin lines) and nanoparticles (thick lines). These measurements were performed at three different delays between the heating prepulse and femtosecond pulse. At small delay (5 ns), the harmonic output from the nanoparticle-containing plume exceeded that from the monoparticle plasma (Figure 22(a)).

Another pattern was observed for a longer delay (17 ns). The harmonics from the plasma produced on the surface of bulk silver prevailed over the HHG from the nanoparticle-containing medium (Figure 22(b)). This feature remained unchanged up to the maximum delays (150 ns) used in these studies (see the harmonic distribution in the case of 88 ns delay, Figure. 22(c)). We found that the HHG from the plume containing Ag multi-atomic particles became more efficient at considerably smaller prepulse intensities (4×10^{9} W cm^{-2}) compared to the case of bulk silver target (1×10^{10} W cm^{-2}). We attribute this tendency to the lower ablation threshold and lower cohesive energy of the host substrate that contains nanoparticles, compared to those of bulk material. The material directly surrounding nanoparticles is a polymer (epoxy glue), which has a considerably lower ablation threshold than the metallic materials. Therefore, the polymer carrying nanoparticles begins to ablate at relatively low intensities resulting in the lower prepulse intensity required for the preparation of the appropriate nonlinear medium for the HHG. This feature allowed for easier creation of the optimal plasma conditions, which resulted in a better HHG conversion efficiency from the nanoparticle-containing plume compared to the plume from the bulk target. Polymer also has a lower melting temperature than metals. Therefore, the repetitive irradiation of the target

Copyright © 2010. Nova Science Publishers, Incorporated. All rights reserved.

leads to the melting and change in the properties of the target. This repetitive irradiation causes the change in conditions of the plasma plume, resulting in a rapid reduction in the harmonic intensity for next laser shots. The different shot-to-shot harmonic intensities for different substrates observed in these studies can be explained by the different adhesion properties of nanoparticles.

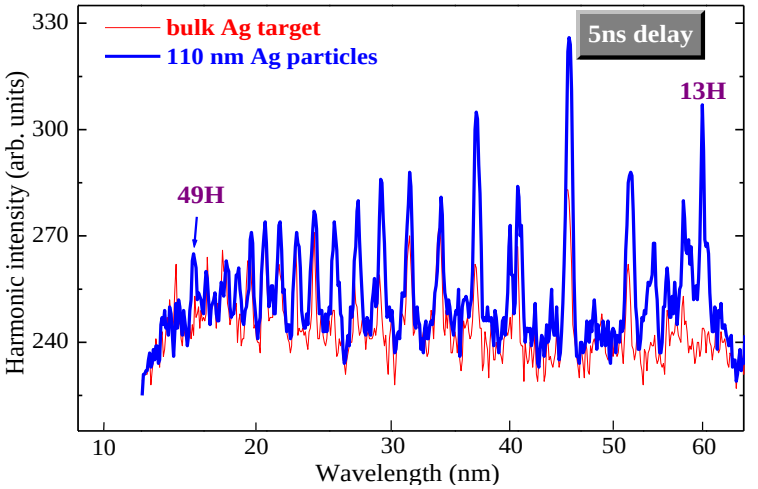

(a)

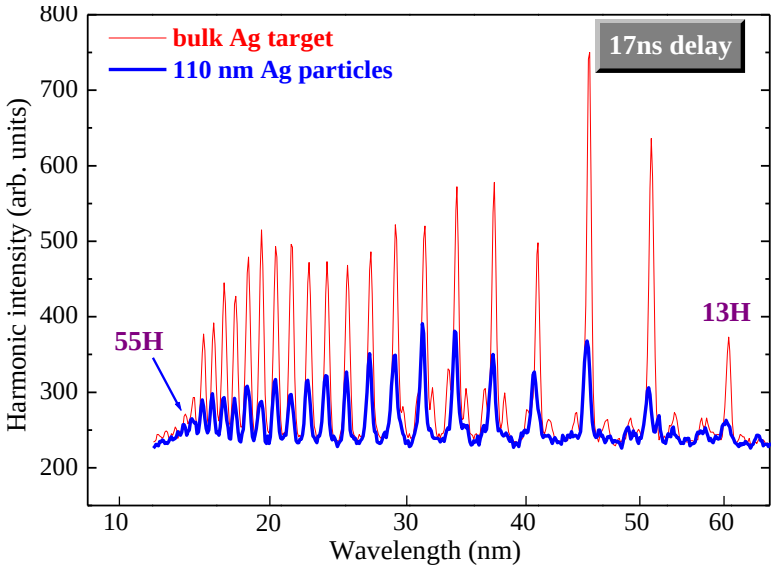

(b)

Copyright © 2010. Nova Science Publishers, Incorporated. All rights reserved.

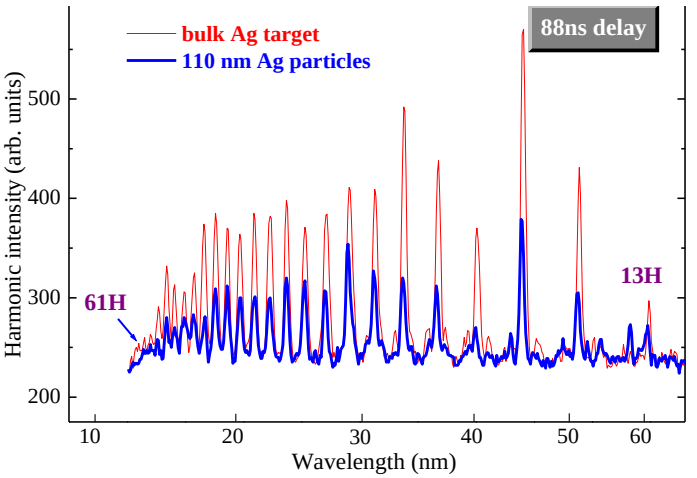

(c)

Figure 22. Harmonic spectra from the plasma containing 110 nm Ag particles (thick lines) and plasma created on the bulk Ag surface (thin lines) at (a) 5 ns, (b) 17 ns, and (c) 88 ns delay between the subnanosecond prepulse and main femtosecond pulse. Prepulse intensity in these experiments was maintained at the level of 1×10^{10} W cm^{-2}.

The presence of rather large nanoparticles caused by very broad size distribution makes it difficult to expect the influence of quantum confinement effect on the nonlinear optical response of the plume containing silver multi-atomic particles. For Ag nanoparticle-containing laser plumes, we were able to generate the harmonics as high as up to the 55th order (Figure 22(b)). The harmonic cutoff for the plume created on the surface of bulk Ag target was approximately the same compared to that obtained from the plasma created on the silver powder-containing substrates. This equality of harmonic cutoffs and efficiencies points out on the absence of the influence of the quantum confinement-induced processes during the HHG from the 110 nm nanoparticle-contained plumes. The prevailing of harmonic yield from the nanoparticle-containing medium over the monoatomic one in the case of short delays can be attributed to the more favorable conditions of evaporation of the nanoparticle-containing medium, which allowed achieving higher particle concentration at the area of femtosecond beam waist compared to the laser ablation of the bulk target.

The influence of the distance between the target surface and femtosecond beam axis (d) on the harmonic yield (I_h) in the case of 110 nm Ag nanoparticles showed two ranges of d, which demonstrated a drastic difference in the $I_h(d)$ dependence (Figure 23). For relatively long distances above the surface (1 mm and longer), the slope of this dependence corresponded to −4.2, while at the distance close to the target, this slope was relatively gradual (−0.7). One can expect a decrease of particle concentration at longer distances from the surface as $N_p \propto d^{-2}$, due to spherical spreading of the laser plasma. Taking into account the quadratic dependence of the harmonic yield on the concentration of the active particles participating in HHG, one can expect the $I_h \propto d^{-4}$ dependence, which was close to the observed experimental results at longer distances ($I_h \propto d^{-4.2}$). It is not clear why this dependence was changed so drastically for shorter distances ($I_h \propto d^{-0.7}$). Probably some

Copyright © 2010. Nova Science Publishers, Incorporated. All rights reserved.

saturation processes in the nanoparticle-containing plasma play an important role, as well as the enhanced absorption of plasma plume and the electron-induced phase mismatching and self-defocusing, at small distances from the surface.

The prepulse intensity used to create the plume is a very sensitive factor that has to be carefully investigated before one can make statements about the integrity of nanoparticles in the plasma area after the ablation. One could expect the aggregation or melting of nanoparticles during the interaction of the laser prepulse with the target surface. The appearance of nanoparticles in laser plasma is governed by the thermodynamic conditions at the target surface. We confirmed the presence of nanoparticles in the plumes by analyzing the spatial characteristics of the deposited material. However, further studies of plasma components during ablation of the nanoparticle-containing targets will benefit the statement about the presence and integrity of nanoclusters in the plumes during the propagation of the femtosecond pulse through the plasma area. The absence of the enhancement of harmonic yield from the nanoparticle-containing plasma (at equal experimental conditions, when the optimal Ag plasma was generated) in our case was probably caused by relatively high sizes of silver nanoparticles. The problem of choosing the appropriate sizes of nanoparticles for the HHG experiments from plasma plumes is related to the competing processes, which can both decrease or increase the nonlinear optical response of the medium. The increase of nanoparticle sizes from a few nanometres to 20 nm (that is, for the particles containing 10^2 to 10^4 atoms) can enhance the ionization potential of such nanostructure [124]. This will lead to the enhancement of cutoff energy and increase in conversion efficiency. Further increase in the cluster size can lead to the decrease of quantum confinement properties.

Our HHG experiments with a dried film of 15 nm particles demonstrated the considerable difference compared to the bulk Ag targets (Figure 24). The results presented in Figure. 24 were obtained at 88 ns delay. One can see that the harmonics from the plume produced on the bulk target exceeded almost 12 times those generated from the 15 nm nanoparticle-containing plume. The reason for such a difference was the same as in the case of silver nanopowder. The concentration of particles at long delay was diminished due to faster plasma formation and spreading away from the target surface for the long delays between the prepulse and main pulse. In the case of shorter delay, the difference between harmonic yields was not so pronounced, though the conversion efficiency from the plasma containing monoparticles prevailed that from the nanoparticle-containing plume. The absence of the influence of the quantum confinement induced enhancement on the overall pattern of harmonic generation in this case can be explained by the small concentration of nanoparticles in the plume. Note that one has to find better conditions for the interaction configuration between the laser pulse and the nanoparticles of appropriate sizes to enhance the harmonic yield. A thin layer of 15 nm particles can be easily evaporated during few shots resulting in a considerable decrease of harmonic yield during further irradiation of the target. The change of target position can considerably improve the conditions of nanoparticle-induced HHG at a 10 Hz pulse repetition rate. A debate is still open as to whether the generation efficiency can be enhanced by the use of a nanoparticle target or not. This paper aimed at providing the reader with experimental evidence on the issue. Even though many factors might be poorly controlled in the experiment (for instance, fragmentation/condensation phenomena occurring during laser ablation of nanoparticle-containing targets), the presented results serve as an experimental test on the role eventually played by the state of aggregation of the matter involved in harmonic generation.

Copyright © 2010. Nova Science Publishers, Incorporated. All rights reserved.

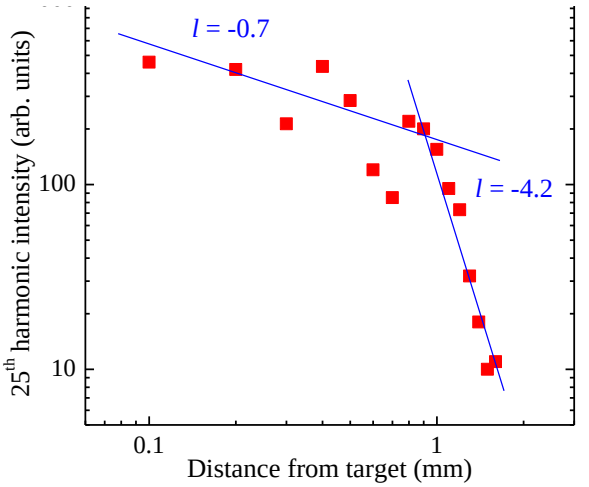

Figure 23. 25th harmonic intensity as a function of the distance between the target surface and the femtosecond beam axis in the case of 110 nm nanoparticle-contained plasma. The beam size of the femtosecond radiation at the plasma area was 60 μm.

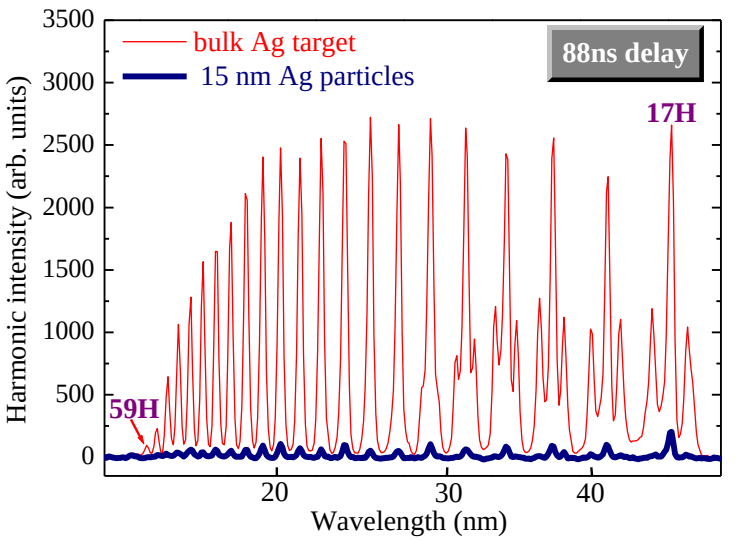

Figure 24. Harmonic spectra from the plasma containing 15 nm Ag particles (thick line) and plasma created on the bulk Ag surface (thin line) at 88 ns delay between the subnanosecond prepulse and main femtosecond pulse.

2.3. Improvements in High-order Harmonic Generation from Silver Nanoparticles

In this subsection, we present the peculiarities of the HHG from silver nanoparticles. We describe the methods of preparation of silver colloids, nanoparticle-contained targets, and the

Copyright © 2010. Nova Science Publishers, Incorporated. All rights reserved.

morphology of nanoparticles. Main aim of this study was to improve the conversion efficiency and stability of harmonic emission. Highly efficient harmonic emission in the range of 9^{th} to 19^{th} harmonic order was generated from the plasmas containing nanoparticles. The HHG is quite stable and the intensity of the HHG does not change appreciably for ~150 shots. Spectral broadening of harmonic radiation through the optimization of the intensity of the femtosecond laser pulse was observed. The spectral broadening of harmonics can be attributed to the spectral broadening of laser pulse due to self-phase modulation effects inside the plasma containing silver nanoparticles. HHG has also been generated using laser pulses spectrally broadened in an external glass medium. Harmonics generated from these pulses are seen to be shifted toward red wavelengths, and are also spectrally broadened. To explore the possibility of increasing the overall conversion efficiency of HHG process, we have also used the two-color pump in the experiment. Orthogonally polarized fundamental and second harmonic pulses were used for HHG in nanoparticle-contained plasma. Both, even and odd harmonic orders, with comparable intensity were observed in the spectrum. Although, the conversion efficiency of the second harmonic pulse in the experiment was small (~2%), it was enough to break the inversion symmetry of HHG and result in efficient odd-even harmonic generation in clustered plasma.

The laser used in this study was a chirped-pulse amplification based Ti:sapphire laser system (Thales Lasers S.A., France) operating at a 10 Hz repetition rate. The repetition rate could be lowered to 1 Hz to avoid excess target depletion. A part of uncompressed laser beam (pulse energy of ~ 20 mJ, pulse duration of 300 ps, central wavelength at 798 nm) was split from the main beam by a beam splitter. This beam was focused at normal incidence by a 500 mm focal length spherical lens on the surface of nanoparticle target kept in a vacuum chamber evacuated to 10^{-5} mbar. This beam (referred to as the "prepulse" beam) created a plasma plume to serve as the medium for harmonic generation. The peak laser intensity of the prepulse beam on the target was varied in the range of 5×10^{9} - 1×10^{10} W cm^{-2}. The prepulse intensity was kept low so that the nanoparticles do not disintegrate in plasma plume, and the free electron density remained low. After a time delay of ~60 ns, the "main" laser pulse, compressed to 45 fs (energy: 120 mJ), propagating in parallel to the target surface, was focused in the above pre-formed plasma plume at a distance of ~100 μm away from the target surface, using a spherical lens of 500 mm focal length. The intensity of main laser pulse inside plasma plume was varied in the range of 1×10^{15} W cm^{-2} and 4×10^{15} W cm^{-2} by adjusting the position of focusing lens.

The high-order harmonics were focused in vertical direction using a grazing incidence cylindrical mirror to increase the collection efficiency. The harmonics were dispersed horizontally by a flat-field grazing-incidence 1200 groves/mm variable line spacing XUV grating (Hitachi). The spectrum was recorded on a multi-channel plate (MCP) detector, and output of MCP was imaged onto a CCD camera connected to a PC. To study the effect of laser spectral broadening and two-color laser pump, a 10 mm thick glass plate and 1 mm thick second harmonic generation crystal (KDP) were mounted on two independent motorized translational stages. The positions of the glass plate and the KDP were chosen to have the laser intensity on the surface of these optical elements high enough to produce these nonlinear effects but below the threshold of white light generation or damage in the optical elements. The bandwidth of laser pulse after passing thorough the glass plate is increased from its initial value of ~ 20 nm to ~ 32 nm. The second harmonic conversion efficiency of the laser pulse

Copyright © 2010. Nova Science Publishers, Incorporated. All rights reserved.

was ~ 2%. This small conversion efficiency was mainly due to lack of phase matching conditions for all components of the converging laser beam.

2.3.1. Preparation and characterization of nanoparticle-contained targets

The study of HHG was mainly performed using the Ag nanoparticles having an average size of 10 nm. A comparison of HHG intensity from Ag nanoparticles with other bulk targets such as Ag and In, and various other nanoparticle targets, such as Au, $SrTiO_3$, and C_{60}, was carried out. Colloidal solutions of silver nano-platelets in water were prepared chemically by a method similar to that described in [125]. A silver salt was reduced with sodium borohydrate and hydrogen-peroxide in the presence of tri-sodium citrate. A capping agent polyvinyl pyrrolidone was used to prevent aggregation. The reaction took place at room temperature. At the end of the reaction, the solution turned blue in color. Absorption spectrum of the sample showed a peak at 638 nm. The TEM images of the samples confirmed that the particles were of triangular cross section. Some of these colloidal solutions demonstrated the SPR at 430 nm, which corresponded to the presence of spherical nanoparticles of diameter of 10 nm.

For comparison of HHG from the Ag nanoparticle targets formed by different methods, the Ag nanoparticle targets were prepared by three methods. In the first method, Ag nanoparticles were dissolved in polyvinyl alcohol (PVA) and then the solution was coated on a glass plate. When the solution got dried, another layer was applied over it. The process was repeated many times such that ~ 2 mm thick layer was formed. In the second method, the target was prepared by same method as explained above, except that the sample was dried in oven at 60 ^oC. This process increased the density of Ag nanoparticles. In the third method, the nanoparticles were mixed with a fast drying glue and spread on the glass plate. This was the easiest method to create the nanoparticle targets, but surface irregularities, and density variation of the nanoparticles was large in these targets.

The ablation-induced nanoparticle formation in laser plumes has carefully been documented in several experiments. However, no study has been reported when nanoparticles already exist at the surface of ablated targets. The comparison of the size and structure characteristics of initial nanoparticles and the deposited debris becomes a versatile approach for definition of the changes of nanoparticle morphology during laser ablation. The maintenance of the original properties of nanoparticles allows one to analyze the optical and nonlinear optical properties of nanoparticle-containing laser plasma at well-defined conditions. Below we report the experimental studies of the morphology of ablated material before and after laser heating of the nanoparticle-containing targets. We have investigated the morphology of initial material and ablated clusters by analyzing the debris deposited on nearby substrates. This technique allowed optimization of laser ablation parameters for maintaining the nanoparticles in the laser plumes. These plumes were used as the nonlinear media for studies of the HHG in the nanoparticle-rich plasma media.

To create the ablation, only the prepulse beam was focused on a target placed in the vacuum chamber. The spot size of this beam on the target surface was maintained in the range of 0.5 – 0.8 mm. The laser energy density during ablation was kept at 0.4 - 1 J cm^{-2}. The chamber was maintained at a pressure of 8×10^{-6} mbar. The debris was deposited from plasma plume on Si substrate and copper grids with carbon films, placed nearby, which were analyzed using the transmission electron microscopy.

Copyright © 2010. Nova Science Publishers, Incorporated. All rights reserved.

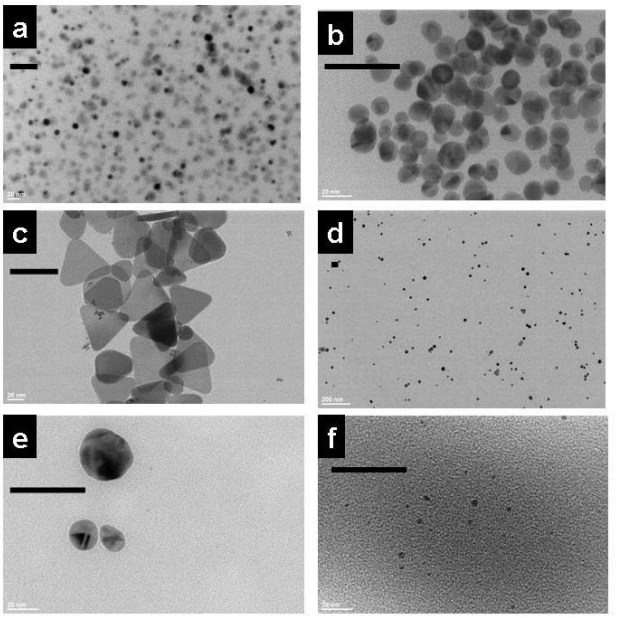

Figure 25. TEM images of (a) commercially purchased Ag nanoparticles, (b) commercially purchased Au nanoparticles, (c) chemically prepared Ag triangle platelets, (d) chemically prepared Ag nanoparticles, (e) deposited Ag nanoparticles obtained at low intensity of prepulse ($\leq 7\times10^{9}$ W cm^{-2}) and (f) deposited disintegrated Ag nanoparticles obtained at high intensity of prepulse ($\geq1\times10^{10}$ W cm^{-2}). The sizes of black lines on the images are 50 nm.

Targets containing various clusters were ablated. Among them were: (a) commercially purchased Ag nanoparticles, and (b) Ag nanoparticles prepared by the methods described in this subsection. Initially, the structure of the nanoparticles used in these studies was analyzed with a transmission electron microscope. It consisted of the clusters in the shape of spheres and triangles (Figure 25). Sample preparation for TEM observation was performed by preparing a suspension of the sample in methanol that was then dropped onto the copper-supported carbon film. To reduce agglomeration, the dilute nanoparticle emulsion was subjected to ultrasonic dispersion for approximately 10 minutes. The transmission electron microscope (Philips CM200) was operated at 200 kV accelerating voltage for micro-structural study. The sizes of nanoparticles covered a range from 10 - 20 nm (in the case of commercially available Ag nanoparticles) to 40 – 50 nm Ag triangle platelets and nano-spheres prepared by chemical methods (Figure 25a-25d).

The TEM images of deposited nanoparticles showed almost identical morphological patterns at moderate intensities of the heating prepulse radiation ($\leq 7\times10^{9}$ W cm^{-2}, Figure. 25e). A different pattern of TEM of the debris of ablated nanoparticles appeared at prepulse intensities above 10^{10} W cm^{-2}. In that case, we observed different patterns of disintegrated (or in some cases aggregated) particles (Figure 25f). These studies revealed the range of prepulse laser intensities, which could be useful for maintaining the nanoparticles in the laser plumes after laser ablation of nanoparticle-containing targets.

Copyright © 2010. Nova Science Publishers, Incorporated. All rights reserved.

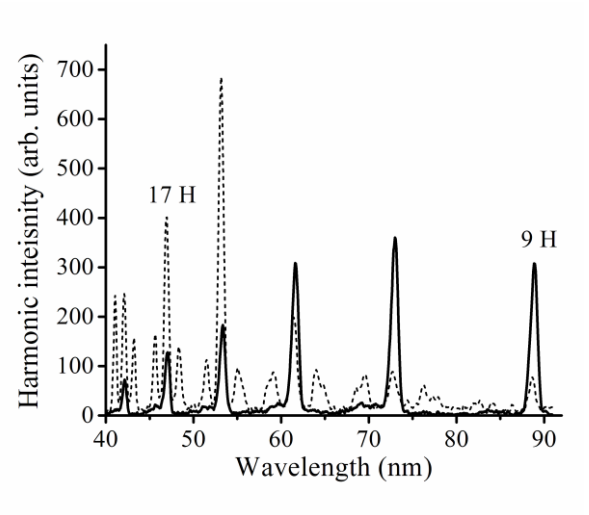

Figure 26. Typical HHG spectra from silver nanoparticles (solid line) and bulk silver target (dashed line). It may be noted that the intensity of HHG spectrum from bulk Ag target is 10× multiplied for better visibility. The intensity of the 9th H from Ag nanoparticles is ~ 40 times higher compared to the 9th H from bulk silver.

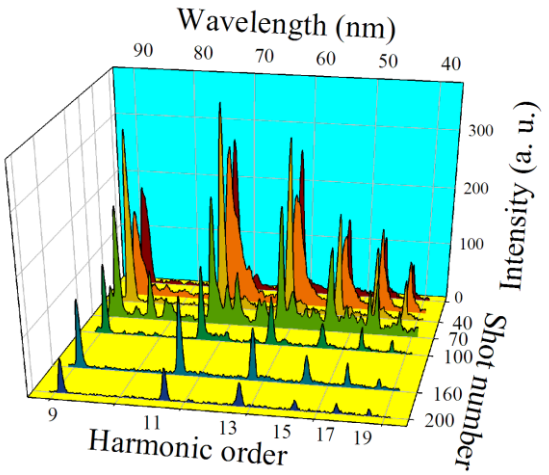

Figure 27. Variation of the harmonic intensity with number of laser shots in the case of nanoparticle-contained target. The target is irradiated at same place. The HHG efficiency does not fall appreciably for ~150 shots.

2.3.2. Harmonic generation from nanoparticles

We found that the HHG from multi-atomic particles started to be efficient at relatively small prepulse intensities ((3–7)×10^9 W cm^{-2}), which were considerably lower compared with those required in the case of bulk graphite target ((1–3) ×10^{10} W cm^{-2}). HHG from silver nanoparticles is shown in Figure. 26. The typical harmonic emission from silver nanoparticles (solid line) is compared with the harmonic emission from bulk silver (dashed line) in this figure. For better visibility, the intensity of HHG from bulk silver is multiplied by 10. It can

Copyright © 2010. Nova Science Publishers, Incorporated. All rights reserved.

be clearly seen that lower order harmonics (9H – 17H) from Ag nanoparticles are very strong compared to the corresponding harmonics from the plasma produced from bulk silver. For example, the 9^{th} H from Ag nanoparticles is ~40 times stronger than that from bulk silver. At the same time, the HHG cutoff is higher for bulk silver. The lower intensity for lower harmonics in the case of bulk Ag (9^{th} to 13^{th} H) has been observed in multiple studies. The higher harmonic intensities on the plateau range (>15^{th} H) could be due to better phase matching conditions for the higher orders. Also, the lower intensity for the lower orders (<13^{th} H) are more likely to be due to decrease in the spectrograph (MCP and grating) response expected for longer wavelengths. This trend has been observed in the spectra of other elements also. In these experiments, the cutoffs from bulk silver and silver nanoparticles corresponded to the 61^{st} and 29^{th} harmonics.

It may be noted that the cutoff for Ag nanoparticles (29^{th} H) is still higher than the cutoff reported in C_{60} (19^{th} H [126]). We believe that the phenomenon which leads to the enhancement of the harmonics from the nanoparticles in the 50-80 nm region by some sort of phase matching in this region, leads to extinction of the harmonics in the region below 50 nm due to phase mismatching. This may be the reason why the nanoparticles have much lower cutoff than that for the bulk material. Strong harmonic yield from fullerene plasma plume can be explained from the enhancement of nonlinear dipole moment at plasmon resonance, while some other mechanisms were offered in Ref [127]. Field enhancement inside the nanoparticle through Mie resonance is especially promising explanation for the increase of harmonic conversion efficiency. Mie resonance plays an important role in cluster dynamics. Various properties of laser-cluster interaction, such as high absorption of laser energy, production of highly energetic ions from small clusters through Coulomb explosion, etc, are explained from the enhancement of laser field inside the cluster [125]. One can expect the enhancement of HHG both in the vicinity of SPR (as in the case of C_{60}, $\lambda_{SPR} \approx 60$ nm) and far from the Mie resonances (as in the case of Ag nanoparticles, $\lambda_{SPR} \approx 430$ nm and 640 nm). Another mechanism of enhanced harmonics can be attributed to the enhanced recombination cross-section of accelerated electron with parent particle in the three-step model. The conversion efficiency using nanoparticles is higher compared to that reported previously [117,119,128,129]. In particular, we have observed a 10 to 100 times enhancement in HHG for nanoparticle plasma plumes compared to plasmas plumes produced using the same element/compound in bulk form. In the previous studies, this enhancement factor was in the range of 3 – 8 only. We attribute the improvement in HHG efficiency using nanoparticles in our experiments to the improvements of target preparation, making the concentration of nanoparticles in plasma plume larger compared to that in previous studies.

We have studied the stability of HHG from silver nanoparticles. The variation of harmonic intensity with laser shots on the same place of nanoparticle-contained target is shown in Figure 27. It can be seen that there is no significant fall in the intensity of HHG up to ~150 laser shots. The stability of HHG process is greatly improved in present study compared to the previous reports on harmonic generation using ablated nanoparticles [117,119,129]. Special target fabrication techniques described in previous section were used to increase the stability of the HHG from silver nanoparticle targets. The new fabrication techniques enable one to grow thicker nanoparticle targets while preserving their nanostructure. The higher thickness of targets is a dominating factor in the enhanced stability of HHG. However, the intensity of the laser prepulse is another very important factor

Copyright © 2010. Nova Science Publishers, Incorporated. All rights reserved.

concerning the stable harmonic generation from these targets. It was observed that, as we increase the laser prepulse intensity, the harmonic intensity increases due to higher concentration of ablated particles. This also results in the rapid degradation of target material followed by rapid fall of the intensity of the harmonics. It is also observed that the stability of HHG can be increased by optimizing the prepulse intensity without any appreciable loss in the HHG intensity. Moreover, stable HHG can be realized for a very long time by laterally shifting the target after few tens of laser shots.

A comparison of relative intensity of HHG in various bulk and nanoparticle targets was also made, which is shown in Figure 28. It can be seen that bulk targets such as Ag and In have very small conversion efficiency for low-order harmonics compared with nanoparticles, except resonantly enhanced 13^{th} H of indium. This is an important observation which shows that materials in their nanoparticle form give much higher harmonic intensity compared to that in bulk form. This implies that nano-size plays some crucial role in harmonic enhancement. This may be due to Mie resonance taking place in the nanoparticles, which is absent in bulk material, is responsible for high conversion efficiency of HHG process in nanoparticles.

2.3.3. Broadening of harmonic spectra in nanoparticle-containing plasma at two-color pump

The harmonic yield was optimized by varying the different laser and plasma parameters. During these optimizations, it was observed that the bandwidth of harmonics could be increased by optimizing the femtosecond laser intensity inside the plasma plume (Figure 29). It was observed that, as the intensity of laser pulse inside the plasma plume containing silver nanoparticles was increased from 1.8×10^{15} W cm^{-2} to 3.5×10^{15} W cm^{-2}, the spectral width of HHG increased. In particular, the spectral width of 11^{th} H is increased from ~1 nm to ~5 nm. It can also be seen from Figure 29 that the spectral broadening of harmonics occurs only towards the blue side. The spectrally broadband harmonics can be useful in spectroscopy experiments due to easier matching of harmonic wavelengths with plasma transitions. The spectral width of harmonics is related to the bandwidth of the laser. For example, the bandwidth of n^{th} harmonic order ($\Delta\lambda_n$) should be equal to ($\Delta\lambda_L/n$) where $\Delta\lambda_L$ is the bandwidth of the laser pulse. The spectral broadening in laser can be achieved through SPM effects inside the plasma. As the laser pulse interacts with nanoparticles, it initiates heating of the nanoparticles and the size of the nanoparticle starts increasing. As a result, the electron density inside the nanoparticle starts decreasing. Due to this decrease in electron density, the polarizability of the nanoparticle starts changing from a large negative value to zero. During this evolution, when the polarizability crosses the value of -2 (i.e. when the electron density becomes equal to 3 n_{cr}) the nanoparticles experience strong Mie resonance. Here n_{cr} is the critical concentration of electrons corresponding to the critical plasma density. It was observed [130] that as a nanoparticle crosses through the Mie resonance, its nonlinear polarizability changes rapidly. Due to rapid change in the polarizability of nanoparticles, the refractive index changes rapidly and additional frequencies are generated in laser spectrum through SPM. Only blue broadening and absence of red broadening of laser spectrum is a salient feature of this process [130]. The spectral broadening in harmonics toward blue side only indicates that the blue broadening of the input laser pulse in nanoparticle-containing plasmas leads to the observed blue broadening of harmonic radiation. Since the SPM effect

Copyright © 2010. Nova Science Publishers, Incorporated. All rights reserved.

increases with laser intensity, the harmonic broadening is observed to increase with laser intensity.

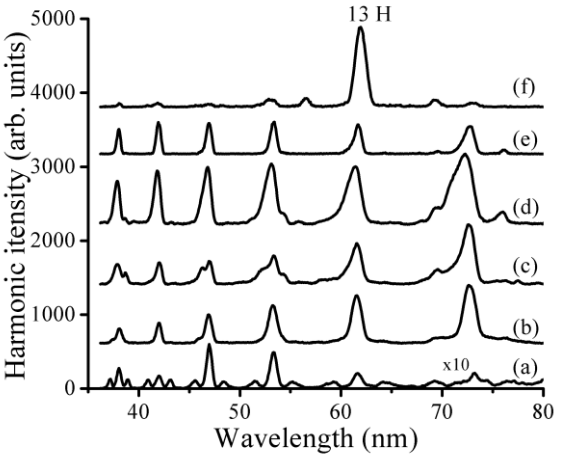

Figure 28. Comparison of relative intensities of harmonics for (a) bulk Ag, (b) Ag nanoparticles, (c) C_{60} targets, (d) $SrTiO_3$ nanoparticles, (e) Au nanoparticles, and (f) bulk In. The intensity of bulk Ag harmonics is multiplied by 10 for better visibility. The intensity of harmonics from nanoparticles is of the order of the enhanced 13^{th} harmonic from indium plasma. The spectra are sequentially shifted up for visual clarity.

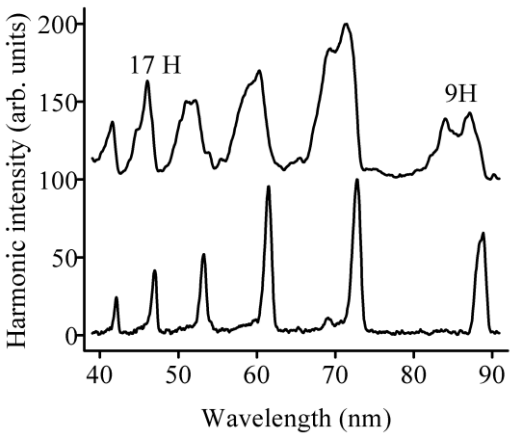

Figure 29. Broadening of harmonic spectrum from nanoparticles with the increase of laser intensity. The bandwidth of 11^{th} H changed from ~1 nm to ~5 nm, when laser intensity was increased from 1.8×10^{15} W cm^{-2} to 3.5×10^{15} W cm^{-2}. The harmonic spectrum for higher laser intensity has been shifted up for visual clarity.

Another objective of the present study was see if one could increase the overall conversion efficiency of HHG process from Ag nanoparticles using two-color pump, as observed in gas targets. The two-color laser pulses were generated by inserting a KDP crystal

Copyright © 2010. Nova Science Publishers, Incorporated. All rights reserved.

in the converging laser beam between the focusing lens and plasma plume. This resulted in orthogonally polarized second harmonic pulse with a conversion efficiency of ~2%. Both, even and odd harmonics were generated by the two-color pump, as seen in Figure 30. The cutoff of harmonic spectrum did not increase, and no enhancement in the intensity of odd harmonics was observed with two-color laser pulses. Although the conversion efficiency of the second harmonic pump was low, the intensity of even harmonics was comparable to that of odd harmonics. The intensity of even harmonics decreased more rapidly compared to that of odd harmonics, with increasing harmonic orders. Utilization of two color pump results in slight increase in overall conversion efficiency of the HHG process, since the conversion of even harmonic orders is now added with odd harmonic orders. No harmonic generation was observed by blocking the fundamental radiation and using only second harmonic pump, indicating that the intensity of the second harmonic pulse by itself was not sufficient for the HHG. This behavior indicated that even a small amount of second harmonic mixing was sufficient to break the inversion symmetry and cause both even and odd harmonic generation. In the previous studies of gas targets, ~50× enhancement in the harmonic conversion efficiency was reported [131]. In the latter, the conversion efficiency of second harmonic pulse was ~20% which was ten times higher than the second harmonic conversion efficiency obtained in our case. It was reported that the harmonic generation only from second harmonic pulse also had high conversion efficiency, comparable to HHG from both pulses. This observation can perhaps be seen as converse of our observation, as in this case, the HHG comes from second harmonic pulse and the symmetry is broken by the fundamental laser pulse, resulting in harmonic spectrum having same intensity of both even and odd orders of harmonics.

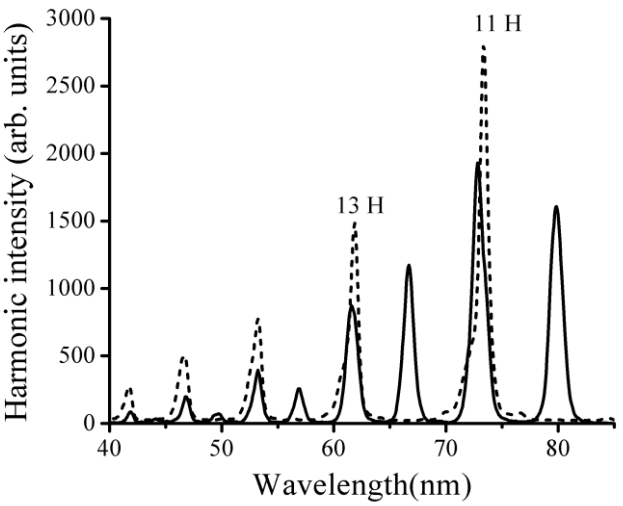

Figure 30. Harmonic generation from two-color laser pulse (solid line) and only fundamental laser pulse (dashed line). Both even and odd orders of harmonics are generated from two-color laser pulse.

Copyright © 2010. Nova Science Publishers, Incorporated. All rights reserved.

3. CONCLUSION

In this chapter, we presented recent results of studies of the low- and high-order nonlinearities of silver nanoparticles. The following conclusions can be derived from these studies:

(a) Nonlinear optical characteristics of silver nanoparticles doped in silica glasses by ion implantation were investigated using 1064, 532, and 355 nm laser radiation. The third-order nonlinear susceptibilities responsible for nonlinear refraction and nonlinear absorption were measured. We analyzed the nonlinear optical characteristics of silicate glasses contained silver nanoparticles at λ = 532 nm. The real and imaginary parts of third-order nonlinear susceptibility of samples at different laser intensities were measured. It was shown that saturated absorption in Ag:SLSG and Ag:SG was dominated at small intensities and decreased with the growth of intensity due to influence of competing effects, whereas the self-defocusing at low intensities was changed to self-focusing at high intensities. The nonlinear absorptive and refractive variations at high intensity were attributed to the influence of interband transitions.

(b) We investigated the optical, structural, and nonlinear optical properties of silver nanoparticles prepared by laser ablation in various liquids using radiation of different wavelength, pulse duration, and pulse repetition rate. TEM and spectral measurements have shown temporal dynamics of Ag nanoparticles_ size distribution. Slow thermal-induced self-defocusing processes dominated in the case of high pulse repetition rate as well as in the case of nanosecond pulses. In the case of short laser pulses, the self-focusing, two-photon absorption, and saturated absorption were observed in these colloidal solutions depending on spectral range. These studies have shown the dominance of $\mathrm{Re}\chi^{(3)}$ over $\mathrm{Im}\chi^{(3)}$ close to the SPR of silver ($|\mathrm{Re}\chi^{(3)}| = 2\times10^{-12}$ esu, $|\mathrm{Im}\chi^{(3)}| = 6\times10^{-13}$ esu). Assuming a small volume ratio of silver in liquid solutions (~4×10^{-5}) we estimated the third-order susceptibility of nanoparticles to be $|\chi^{(3)}| \sim 5\times10^{-8}$ esu. Our observations have also shown that the viscosity of surrounding liquid plays important role in the stabilization of structural and nonlinear optical properties of Ag-contained solutions. The nonlinear refractive index and nonlinear absorption coefficient of these solutions were measured to be 3×10^{-13} cm^2 W^{-1} and -1.5×10^{-9} cm W^{-1}, respectively (at λ = 397.5 nm, t = 1.2 ps).

(c) A study of the metal deposition by laser ablation in vacuum has been performed using subnanosecond laser pulses under different focusing conditions. It is shown that nanoparticles can be formed using long laser pulses under tight-focusing conditions. The average size of Ag nanoparticles was ~60 nm.

(d) Our studies have shown that, for nanoparticle-containing plumes, no improvements in the extension of harmonic cutoff were observed. At the same time, a considerable enhancement of harmonic yield in the lower-wavelength range in the case of nanoparticle-containing plumes was achieved. The enhancement factor of the harmonics generated in nanoparticle-containing plumes compared with monoparticle-containing plasma up to 12 was achieved, depending on the harmonic order and the conditions of excitation. The observed enhancement of harmonics

Copyright © 2010. Nova Science Publishers, Incorporated. All rights reserved.

could be attributed to the difference between the cross sections of recombination of the ejected electron with single ions and nanoparticles and some other processes discussed in this paper. These studies have also shown the presence and integrity of nanoparticles in the plumes at the moment when the femtosecond pulse propagated through the area of interaction.

(e) We demonstrated harmonic generation (up to the 55th order) in a laser plume containing silver nanoparticles of different sizes. We observed a decrease of harmonic yield at small distances from the target compared to the expected dependence between the HHG conversion efficiency and position of femtosecond beam axis. The origin of this phenomenon is discussed. Best conditions were found for 110 nm Ag powder, while in the case of 15 nm particles, the small concentration of the nanoparticles in the plasma did not allow observation of the quantum-confinement-induced enhancement of high-order harmonics. It is important to find the appropriate experimental configuration for the application of small nanoparticles for the HHG, while maintaining a high concentration of nanoparticles in the laser plume.

(f) We studied the influence of particle size in laser ablation plasma on the high-order harmonic generation efficiency. We compared harmonic efficiencies from the laser plumes containing 110 nm spherical Ag particles and 100–1000 nm blocks of colloidal silver. We also compared these results with those from the monoatomic plumes produced on the surfaces of bulk materials. We showed that small-sized structures are favorable for high-order harmonic conversion efficiency. The maximum conversion efficiency observed (for 110 nm Ag nanoparticles) was estimated to be 4×10^{-5}.

There was little difference in the harmonic cutoff order for the plumes that contain small multi-atomic particles and those produced from bulk targets. In particular, the plasma with 110 nm Ag nanoparticles demonstrated 67th harmonic cutoff, compared to the 63rd and 61st harmonic cutoffs for colloidal silver and bulk silver, respectively. Our studies have shown that, to obtain the maximum HHG conversion efficiency, it is essential to define the maximum tolerable particle size that can be used, since particles with larger dimensions have higher polarizability. Some additional studies such as the influence of dipole moment of the nanoparticles and cluster concentration on the phase-matching, Z-scans of the cluster-containing plasma, intensity scaling, etc, will benefit the understanding of the peculiarities of the application of nanostructured media for the HHG.

(g) Highly efficient harmonic generation has been observed from Ag nanoparticles in the range of 9^{th} to 19^{th} harmonic orders. The harmonic generation was moderately stable, and the intensity of HHG did not fall appreciably for ~150 shots fired at the same place. Stability of harmonic generation was enhanced through the use of improved target fabrication techniques and through the optimization of prepulse intensity. Blue spectral broadening of harmonic radiation through the optimization of the intensity of fs laser pulse was observed and explained from SPM generated by rapid change in nanoparticle polarizability. HHG from spectrally broadened femtosecond laser pulses was observed. Spectral broadening in laser pulses, generated by passing it through a 10 mm thick glass slab, produced the harmonics which were red shifted and spectrally broadened. A comparison of harmonic intensity among various

Copyright © 2010. Nova Science Publishers, Incorporated. All rights reserved.

nanoparticle targets and among silver nanoparticle targets prepared from different target fabrication methods was carried out. HHG intensity for different nanoparticle targets was almost same but was much higher (~10 - 100 times) compared to the harmonic intensity from bulk targets for lower harmonic orders. The intensity of HHG from nanoparticle targets was comparable to the intensity of resonantly enhanced 13^{th} H of indium. The intensity of the HHG is more or less same for different target preparation methods, however the higher particle density in targets prepared from the Ag-PVA solution dried in oven resulted in slightly higher intensity of harmonics. Finally, broad bandwidth HHG from two-color pump was also studied. Orthogonally polarized fundamental and second harmonic pulses were used for HHG. Both even and odd harmonic orders with comparable intensities were observed. Enhancement in the intensity of odd harmonics or extension of cutoff harmonic order was not observed, but the even harmonic orders were of intensity comparable to that of the odd harmonic orders, despite very small conversion efficiency (~2%) of the fundamental laser pulse to the second harmonic pulse.

ACKNOWLEDGMENT

The author is indebted to T. Usmanov, I. A. Kulagin, R. I. Tugushev, and S. R. Kamalov from Institute of Electronics, Tashkent, Uzbekistan, H. Kuroda, M. Baba, and M. Suzuki from the Institute for Solid State Physics, University of Tokyo, Japan, P. D. Gupta, P. A. Naik, and H. Singhal from the Raja Ramanna Centre for Advanced Technology, India, T. Ozaki and L. B. Elouga Bom from the Institut National de la Recherche Scientifique, Canada for collaboration. I would especially like to thank A. I. Ryasnyansky for his assistance in these studies. I also thank A. L. Stepanov, N. V. Kamanina, G. Priebe, K. Fostiropoulos, M. K. Kodirov, A. A. Ishchenko, N. A. Derevyanko, and M. Morita for providing the samples for these studies.

REFERENCES

[1] Ganeev, RA. *J. Opt. A*, 2005, 7, 717.
[2] Hache, F; Ricard, D; Flytzanis, C; Kreibig. U. *Appl. Phys. A*, 1988, 47, 347.
[3] Yang, L; Becker, K; Smith, F. M; Marguder, R. H; Haglund, R. F; Yang, L; Dorsinville, R; Alfano, R. R; Zuhr, R. A. *J. Opt. Soc. Am. B*, 1994, 11**,** 457.
[4] Uchida, K; Kaneko, S; Omi, S; Hata, C; Tanji, H; Asahara, Y; Ikushima, AJ. *J. Opt. Soc. Am. B*, 1994, 11**,** 1236.
[5] Hache, F; Ricard, D; Flytzanis, C. *J. Opt. Soc. Am. B*, 1986, 3**,** 1647.
[6] Mehendale, SC; Mishra, SR; Bindra, KS; Laghate, M; Dhami, TS; Rustagi, KS. *Opt. Commun*, 1997, 133**,** 273.
[7] Song, YL; Zhang, C; Zhao, XL; Wang, YX; Fang, GY; Jin, GS; Qu, SL; Wu, SP; Xin, XQ; Ye, HY. *Chem. Lett*, 2000, 9**,** 323.
[8] Francois, L; Mostafavi, M; Belloni, J; Delouis, JF; Delaire, J; Feneyrou, P. *J. Phys. Chem. B*, 2000, 104**,** 6133.

Copyright © 2010. Nova Science Publishers, Incorporated. All rights reserved.

[9] Inouye, H; Tanaka, K; Tanahashi, J; Hirao, K. *Phys. Rev. B*, 1998, 57**,** 11, 334.
[10] Inouye, H; Tanaka, K; Tanahashi, J; Hattori, T; Nakatsuka, H. *Japan. J. Appl. Phys*., 2000, 39**,** 5132.
[11] Brause, R; Moltgen, H; Kleinermanns, K. *Appl. Phys. B*, 2002, 75, 711.
[12] Ganeev, RA; Ryasnyansky, AI; Kamalov, SR; Kodirov, MK; Usmanov, T. *J. Phys. D*, 2001, 34, 1602.
[13] Reintjes, JF. *Nonlinear Optical Parametric Processes in Liquids and Gases*, Academic Press, New York, US, 1984.
[14] Sheik-Bahae, M; Said, AA; Wei, TH; Hagan, DJ; Van Stryland, EW. *IEEE J. Quantum Electron*, 1990, 26**,** 760.
[15] Xia, T; Hagan, DJ; Sheik-Bahae, M; Van Stryland, EW. *Opt. Lett*, 1994, 19**,** 317.
[16] Ma, H; Gomes, ASL; de Araujo, CB. *Appl. Phys. Lett*, 1991, 59**,** 2666.
[17] Kawazoe, T; Kawaguchi, H; Inoue, J; Haba, O; Ueda, M. *Opt. Commun*, 1999, 16**,** 125.
[18] Petrov, DV; Gomes, ASL; de Araujo, CB; *Appl. Phys. Lett*, 1994, 65**,** 1067.
[19] Lui, X; Guo, S; Wang, H; Hou, L. *Opt. Commun*, 2001, 197**,** 431.
[20] Ricard, B; Raussignol, P; Flytzanis, C. *Opt. Lett*, 1985, 10, 511.
[21] Staromlynska, J; McKay, TJ; Wilson, P. *J. Appl. Phys*., 2000, 88, 1726.
[22] Olivares, J; Requejo-Isidro, J; Del Coso, R; De Nalda, R; Solis, J; Afonso, CN; Stepanov, AL; Hole, D; Townsend, PD; Naudon, A. *J. Appl. Phys*., 2001, 90, 1064.
[23] Kyoung, M; Lee, M. *Opt. Commun*, 1999, 171, 145.
[24] Yang, L; Dorsinville, R; Wang, QZ; Alfano, RR. *Opt. Lett*, 1992, 17, 323.
[25] Osborne, DH; Haglund, RF; Gonella, F; Garrido, F. *Appl. Phys. B*, 1998, 66, 517.
[26] Ganeev, RA; Ryasnyansky, AI; Stepanov, AL; Usmanov, T. *Phys. Stat. Sol. B*, 2003, 238, R5.
[27] Ganeev, RA; Ryasnyansky, AI; Stepanov, AL; Usmanov, T. *Phys. Stat. Sol. B*, 2004, 241, 935.
[28] Stepanov, AL; Hole, DE. *Recent Res. Devel. Appl. Phys*., 2002, 5, 1.
[29] Nadon A; Thaiaudiere, D. *J. Appl. Crystallogr*, 1997, 30, 822.
[30] Townsend, PD; Chandler, PJ; *Zhang, L. Optical Effects of Ion Implantation*, Cambridge University Press, London, UK, 1994.
[31] Centora-Gonzalez, O; Muller, D; Estournus, C; Richard-Plouet, M; Poinsot, R; Grob, JJ; Guille, J. *Nucl. Instrum. Meth. B*, 2001, 178, 144.
[32] Stepanov, AL; Hole, DE; Townsend, PD. *J. Non-Cryst. Solids*, 1999, 260, 65.
[33] Owyoung, A. *IEEE J. Quantum Electron*, 1973, 9, 1064.
[34] Kreibig, U; Vollmer, M. *Optical Properties of Metal Clusters*, Springer, Berlin, GE, 1995.
[35] Lehmberg, RH; Reintjes, J; Eckardt, RC. *Phys. Rev. A*, 1976, 13, 1095.
[36] Ganeev, RA; Ryasnyansky, AI; Stepanov, AL; Usmanov, T. Opt. *Quantum Electron*, 2004, 36, 949.
[37] Hamanaka, Y; Hayashi, H; Nakamura, A; Omi. S. *J. Luminesc*, 2000, 859, 87-89.
[38] Ganeev, RA; Tugushev, RI; Ishchenko, AA; Derevyanko, NA; Ryasnyansky AI; Usmanov, T. *Appl. Phys. B*, 2003, 76, 683.
[39] Hwang, LC; Lee, SC; Wen, TC. *Opt. Commun*, 2003, 228, 373.
[40] Ganeev, RA; Ryasnyansky, AI; Stepanov, AL; Usmanov, T. *Solid State Phys*., 2004, 46, 351.
[41] Hamanaka, Y; Nakamura, A; Hayashi, H; Omi, S. *J. Opt. Soc. Am. B*, 2003, 20, 1227.

Copyright © 2010. Nova Science Publishers, Incorporated. All rights reserved.

[42] Smith, DD; Fisher, G; Boyd, RW; Gregory, DA. *J. Opt. Soc. Am. B*, 1997, 14, 1625.
[43] Sarkisov, SS; Williams, E; Curley, M; Ila, D; Venkateswarlu, P; Poker, DB; Hensley, DK. *Nucl. Inst. and Meth. B*, 1998, 141, 294.
[44] Pincon, N; Palpant, B; Prot, D; Charron, E; Debrus, S. *Eur. Phys. J. D*, 2002, 19, 395.
[45] Kurata, H; Takami, A; Koda, S. *Appl. Phys. Lett*, 1998, 72, 789.
[46] Link, S; Mohamed, MB; Nikoobakht, B; El-Sayed, MA. *J. Phys. Chem*., 1999, 103, 1165.
[47] Mafune, F; Kohono, J; Takeda, Y; Kondow, T. *J. Phys. Chem. B*, 2002, 106, 8555.
[48] Chandrasekharan, N; Kamat, PV; Hu, J; Jones II, G. *J. Phys. Chem. B*, 2000, 104, 11103.
[49] Unnikrishnan, KP; Nampoori, VPN; Ramakrishnan, V; Umadevi, M; Vallabhan, CPG. *J. Phys. D*, 2003, 36, 1242.
[50] Sheik-Bahae, M; Hutchings, DC; Hagan, DJ; Van Stryland, EW. IEEE *J. Quantum Electron*, 1991, 27, 1296.
[51] Magruder, RH; Osborne, DH; Zuhr RA. *J. Non-Cryst. Solids*, 1994, 176, 229.
[52] Haglung, RF; Yang, L; Magruder, RH; Whrite, JE; Becker K; Zuhr, RA. *Opt. Lett*, 1993, 18, 373.
[53] Serna, R; Ballesteros, JM; Solis, J; Afonso, CN; Osborne, DH; Haglung, RF; Petford-Long, AK. *Thin Solid Films*, 1998, 318, 96.
[54] Brzozovski, L; Sargent, EH. *J. Mater. Sci. Mater. Electron*, 2001, 12, 483.
[55] Sun, YP; Riggs, JE; Rollins, HW; Guduru, R. *J. Phys. Chem. B*, 1999, 103, 77.
[56] Ganeev, RA; Ryasnyansky, AI; Kodirov, MK; Kamalov, SR; Li, VA; Tugushev, RI; Usmanov, T. *Appl. Phys*., *B*, 2002, 74, 47.
[57] Wundke, K; Potting, S; Auxier, J. *Appl. Phys. Lett*, 2000, 76, 10.
[58] Vijayalakshmi, S; George, MA; Grebel, H. *Appl. Phys. Lett*, 1997, 70, 708.
[59] Ganeev, RA; Baba, M; Ryasnyansky, AI; Suzuki, M; Kuroda, H. *Opt. Commun*, 2004, 240, 437.
[60] Tsuji, T; Iryo, K; Watanabe, N; Tsuji, M. *Appl. Surf. Sci*., 2002, 202, 80.
[61] Tsuji, T; Watanabe, N; Tsuji, M. *Appl. Surf. Sci*., 2003, 211, 189.
[62] Ganeev, RA; Ryasnyansky, AI; Kodirov, MK; Kamalov, SR; Usmanov, T. *Opt. Spectrosc*, 2001, 90, 568
[63] Slabko, VV; Karpov, SV; Zaitsev, VI; Popov, AK. *J. Phys.: Condens. Matter*, 1993, 5, 7231.
[64] Falkonieri, M; Salvetti, G. *Appl. Phys. B*, 1999, 69, 133.
[65] Couris, S; Renard, M; Faucher, O; Loverel, B; Chaux, R; Koudoumas, E; Michaut, X. *Chem. Phys. Lett*, 2003, 369, 318.
[66] Markano, A; Maillotte, OH; Gindre, D; Metin, D. *Opt. Lett*, 1996, 21, 101.
[67] Ganeev, RA; Baba, M; Ryasnyansky, AI; Suzuki, M; Kuroda, H. *Opt. Spectrosc*, 2005, 99, 668.
[68] Toda, H; Verber, CM. *Opt. Lett*, 1992, 17, 1379.
[69] Ganeev, RA; Baba, M; Ryasnyansky, AI; Suzuki, M; Turu, M; Kuroda, H. *Appl. Phys. B*, 2004, 78, 433.
[70] Bloemer, MJ; Haus, JW; Ashley, PR. *J. Opt. Soc. Am. B*, 1990, 7, 790.
[71] Cattaruzza, E; Battaglin, G; Calvelli, P; Gonella, F; Mattei, G; Maurizio, C; Mazzoldi, P; Padovani, S; Sada, C; Scremin, BF; Acapito, FD. *Comp. Sci. Technol*., 2003, 63, 1203.

Copyright © 2010. Nova Science Publishers, Incorporated. All rights reserved.

[72] Lepeshkin, NN; Kim, W; Safonov, VP; Zhu, JG; Armstrong, RL; White, CW; Zuhr, RA; Shalaev, VM. *J. Nonlinear Opt. Phys. Mater*, 1999, 8**,** 191.
[73] Rautian, SG; Safonov, VP; Chubakov, PA; Shalaev, VM; Shtokman, MI, *JETP Lett*, 1988, 47**,** 200.
[74] Ji, W; Du, HJ; Tang, SH; Shi, S. *J. Opt. Soc. Am. B*, 1996, 12, 876.
[75] Butenko, AV; Shalaev, VM; Shtokman, MI. *JETP*, 1988, 94**,** 107.
[76] Karpov, SV; Bas'ko, AL; Koshelev, SV; Popov, AK; Slabko, VV. *Colloidal J*, 1997, 59**,** 765.
[77] Karpov, SV; Popov, AK; Slabko, VV. *JETP Lett*, 1997, 66**,** 97.
[78] Slabko, VV; Karpov, SV; Zaitsev, VI; Popov, AK. *J. Phys.: Condens. Matter*, 1993, 5**,** 7231.
[79] Shalaev, VM; Shtokman, MI. *JETP*, 1987, 92**,** 509.
[80] Markel, VA; Muratov, LS; Shtokman, MI. *JETP*, 1990, 98**,** 819.
[81] Ganeev, RA; Ryasnyansky, AI. *Appl. Phys. B*, 2006, 84, 295.
[82] Ganeev, RA; Baba, M; Ryasnyansky, AI; Suzuki, M; Kuroda, H. *Appl. Phys. B*, 2005, 80, 595.
[83] Stone, J; *J. Opt. Soc. Am*, 1972, 62**,** 327.
[84] Chen, Q; Tanaka, M; Furuya, K. *Surf. Sci*., 1999, 440**,** 398.
[85] Tsai KL; Dye, JL. *J. Am. Chem. Soc*., 1991, 113**,** 1650.
[86] Zhao, Y; Zhang, Z; Dang, H. *J. Phys. Chem. B*, 2003, 107**,** 7574.
[87] Ganeev, RA; Ryasnyansky, AI; Usmanov, T. *Opt. Commun*., 2007, 272, 242.
[88] Ganeev, RA; Ryasnyansky, AI. *Opt. Commun*., 2005, 246**,** 163.
[89] Anisimov, SI; Imas, YA; Romanov, GS; Khodyko, YV. *High Power Radiation Effect in Metals*, Nauka, Moscow, RU, 1970.
[90] Amoruso, S; Ausanio, G; Bruzzese, R; Vitiello, M; Wang, X. *Phys. Rev. B*, 2005, 71**,** 033406.
[91] Ganeev, RA; Chakravarty, U; Naik, PA; Srivastava, H; Mukherjee, C; Tiwari, MK; Nandedkar, RV; Gupta, PD. *Appl. Opt*., 2007, 46, 1205.
[92] Tiwari, MK; Sawhney, KJS; Gowri Sankar, B; Raghuvanshi, VK; Nandedkar, RV. *Spectrochim. Acta B*, 2004, 59**,** 1141.
[93] Donnelly, TD; Ditmire, T; Neuman, K; Perry, MD; Falcone, RW. *Phys. Rev. Lett*, 1996, 76**,** 2472.
[94] Tisch, JWG; Ditmire, T; Fraser, DJ; Hay, N; Mason, MB; Springate, E; Marangos, JP; Hutchinson, MHR. *J. Phys. B*, 1997, 30, L709.
[95] Tiwari, MK; Gowrishankar, B; Raghuvanshi, VK; Nandedkar, RV; Sawhney, KJS. *Bull. Mater. Sci*., 2002, 25, 435.
[96] Bedzyk, MJ; Bommarito, GM; Schildkraut, JS. *Phys. Rev. Lett*, 1989, 62**,** 1376.
[97] de Boer, DKG. *Phys. Rev. B*, 1991, 44**,** 498.
[98] Teghil, R; Alessio, LD; Santagata, A; Zaccagnino, M; Ferro, D; Sordelet, D. J. *Appl. Surf. Sci*., 2003, 210**,** 307.
[99] Glove, TE. *J. Opt. Soc. Am. B*, 2003, 20**,** 125.
[100] Jeschke, HO; Garsia, ME; Bennemann, KH. *Phys. Rev. Lett*, 2001, 87**,** 015003.
[101] Perez, D; Lewis, LJ. *Phys. Rev. B*, 2003, 67**,** 184102.
[102] Amoruso, S; Bruzzese, R; Spinelli, N; Velotta, R; Wang, X; Ferdeghini, C. *Appl. Phys. Lett*, 2002, 80**,** 4315.
[103] Sturm, K; Fahler, S; Krebs, HU. *Appl. Surf. Sci*., 2000, 462, 154-155.

Copyright © 2010. Nova Science Publishers, Incorporated. All rights reserved.

[104] Amoruso, S; Bruzzese, B; Spinelli, N; Velotta, R; Vitiello, M; Wang, X; Ausanio, G; Iannotti, V; Lanotte, L. *Appl. Phys. Lett*, 2004, 84**,** 4502.
[105] Corkum, PB; Krausz, F. *Nat. Phys*., 2007, 3, 381.
[106] Liao, HB; Xiao, RF; Fu, JS; Wong, GKL. *Appl. Phys. B*, 1997, 65, 673.
[107] Shim, B; Hays, G; Zgadzaj, R; Ditmire, T; Downer, MC. *Phys. Rev. Lett*, 2007, 98, 123902.
[108] Hu, SX; Xu, ZZ. *Appl. Phys. Lett*, 1997, 71, 2605.
[109] Tajima, T; Kishimoto, Y; Downer, MC. *Phys. Plasmas*, 1999, 6, 3759.
[110] Tisch, JWG. *Phys. Rev. A*, 2000, 62, 041802.
[111] Vozzi, C; Nisoli, M; Caumes, JP; Sansone, G; Stagira, S; De Silvestri, S; Vecchiocattivi, M; Bassi, D; Pascolini, M; Poletto, L; Villoresi, P; Tondello, G. *Appl. Phys. Lett*, 2005, 86, 111121.
[112] Fomichev, SV; Zaretsky, DF; Bauer, D; Becker, W. *Phys. Rev. A*, 2005, 71, 013201.
[113] Pai, CH; Kuo, CC; Lin, MW; Wang, J; Chen, CY; Lin, JY. *Opt. Lett*, 2006, 31, 984.
[114] Véniard, V; Taïeb, R; Maquet, M. *Phys. Rev. A*, 2001, 65, 013202.
[115] Ganeev, RA; Elouga Bom, LB; Ozaki, T. *J. Phys. B*, 2009, 42, 055402.
[116] Kundu, M; Popruzhenko, SV; Bauer, D. *Phys. Rev. A*, 2007, 76, 033201.
[117] Ganeev, RA; Suzuki, M; Baba, M; Ichihara, M; Kuroda, H. *J. Appl. Phys*., 2008, 103, 063102.
[118] Ganeev, RA; Elouga Bom, LB; Ozaki, T. *J. Appl. Phys*., 2009, 106, 023104.
[119] Ganeev, RA; Suzuki, M; Baba, M; Ichihara, M; Kuroda, H. *J. Phys. B*, 2008, 41, 045603.
[120] Ganeev, RA; Baba, M; Suzuki, M; Kuroda, H. *Phys. Lett. A*, 2005, 339**,** 103.
[121] Ganeev, RA; Singhal, H; Naik, PA; Chakravarty, U; Arora, V; Chakera, JA; Khan, RA; Raghuramaiah, M; Kumbhare, SR; Kushwaha, RP; Gupta, PD. *Appl. Phys. B*, 2007, 87, 243.
[122] Elouga Bom, LB; Kieffer, JC; Ganeev, RA; Suzuki, M; Kuroda, H; Ozaki, T. *Phys. Rev. A*, 2007, 75, 033804.
[123] Ganeev, RA; Chakravarty, U; Naik, PA; Srivastava, H; Mukherjee, C; Tiwari, MK; Nandedkar, RV; Gupta, PD. *Appl. Opt*., 2007, 46, 1205.
[124] Vazquez de Aldana, JR; Roso, L. *J. Opt. Soc. Am. B*, 2001, 18**,** 325.
[125] Metraux, GS; Mirkin, CA. *Advanced Mater*, 2005, 17, 412.
[126] Ganeev, RA; Elouga Bom, LB; Abdul-Hadi, J; Wong, MCH; Brichta, JP; Bhardwaj, V. R; Ozaki, T. *Phys. Rev. Lett*, 2009, 102**,** 013903.
[127] Faria, CFM; Rost, JM. *Phys. Rev. A*, 2000, 62, 051402 (R).
[128] Saalmann, U; Siedschlag, C; Rost, JM. *J. Phys. B*, 2006, 39, R39.
[129] Ganeev, RA; Suzuki, M; Baba, M; Ichihara, M; Kuroda, H. *J. Opt. Soc. Am. B*, 2008, 25, 325.
[130] Singhal, H; Arora, V; Naik, PA; Gupta, PD. *Phys. Rev. A*, 2005, 72, 043201.
[131] Kim, IJ; Kim, CM; Kim, HT; Lee, GH; Lee, YS; Park, JY; *Phys. Rev. Lett*, 2005, 94, 243901.

Copyright © 2010. Nova Science Publishers, Incorporated. All rights reserved.

Copyright © 2010. Nova Science Publishers, Incorporated. All rights reserved.

In: Silver Nanoparticles
Editor: Audrey E. Welles, pp. 119-168
ISBN: 978-1-61668-690-1
© 2010 Nova Science Publishers, Inc.

Chapter 3

LASER-INDUCED SHAPE TRANSFORMATION OF SILVER NANOPARTICLES EMBEDDED IN GLASS - PHYSICS AND APPLICATIONS

Andrei Stalmashonak*[*], *Heinrich Graener and Gerhard Seifert
Physics Department, Martin-Luther-University
Halle-Wittenberg, D-06099 Halle, Germany

ABSTRACT

Glasses containing metallic nanoparticles show very promising linear and nonlinear optical properties, mainly due to the surface plasmon resonance (SPR) of the nanoparticles. Spectral position (in the visible and near-infrared range) and polarization dependence of the SPR are, besides other parameters, characteristically determined by the nanoparticles' shapes. The focus of this chapter will be on interaction of intense fs laser pulses with silver nanoparticles incorporated in soda-lime glass, and nanostructural modifications in glass-metal nanocomposites induced by such laser pulses. In particular, to give a comprehensive physical picture of the processes leading to laser-induced persistent shape transformation of the nanoparticles, series of experimental results, investigating the dependences of laser assisted shape modifications of Ag nanoparticles on the laser pulse intensity, excitation wavelength, temperature etc. will be considered. In addition, the resulting local optical dichroism allows producing very flexibly polarizing optical (sub-) microstructures with well specified optical properties. The achieved considerable progress towards technological application of this technique will also be discussed.

Copyright © 2010. Nova Science Publishers, Incorporated. All rights reserved.

[*] Corresponding author: E-mails: andrei.stalmashonak@physik.uni-halle.de, gerhard.seifert@physik.uni-halle.de.

INTRODUCTION

Glasses and other dielectrics containing metal nanoparticles are very promising materials for photonic applications owing to their unique linear and nonlinear optical properties. These properties are dominated by the strong surface plasmon resonance (SPR) of the metal nanoparticles. The SPR occurs when the electron and light waves couple with each other at a metal-dielectric interface, and they are simply regarded as the collective oscillation of the nanoparticle (NP) electrons. The spectral position of the SPR in the compound materials can be designed within a wide spectral range covering the visible and near-infrared spectra by choice of the electronic properties of the metal and the dielectric matrix [1, 2], or by manipulation of size [1, 3], shape [3, 4], and spatial distribution [5] of the metal clusters. This makes the composite materials very promising candidates for some applications in the field of photonics [6, 7]. One of the main issues in this context is to structure the optical properties of such materials on a micro- or even submicron scale. This aspect, in fact, occupies many researchers within the scientific community. The scientific interest comprises the study of optical sub-wavelength structures such as plasmonic waveguides based on metal nanoparticles [8, 9], as well as larger (micrometer) scale optical structures; for the latter, nanocomposite materials are very appropriate for production of a number of standard and advanced optical elements such as: gratings, segmented filters, polarizers, etc.

Recently, it was shown that laser-induced techniques represent a very powerful and flexible tool for (local) structuring of the optical properties of composite materials with metal nanoparticles [10-18]. Particularly, it was discovered that initially spherical silver nanoparticles embedded in soda-lime glass experience a persisting transformation of their shape when irradiated with intense fs laser pulses at a wavelength near to the SP resonance [14-18]. The results can be macroscopically observed as optical dichroism, i.e., polarization dependent colour changes. This review is intended to give a comprehensive overview of the various physical processes leading to permanent nanostructural alterations in glass-silver nanocomposites initiated by irradiation with intense, ultrashort laser pulses. The studies reported here were aiming to understand the details of the mechanism of NP shape transformation, and to use this knowledge for optimization of the achievable optical parameters such as polarization contrast or as broad as possible tuning range of dichroism. The latter is a necessary prerequisite to exploit the full range of potential applications of this novel technology.

For the sake of compactness, we do not give a comprehensive review of the optical properties of nanocomposites with metal particles, which can be found elsewhere [1, 2, 19], but restrict the discussion in Section 2 to the most important properties needed for easy comprehension of this review. After this, an overview of the possible processes initiated by interaction of the laser pulses with metal nanoparticles will be given. Taking into account experimental results as well as numerical temperature modeling and semi-quantitative descriptions of electron and ion emission into the glass matrix, we arrive at a model for the permanent structural change, which allows us a self-consistent description of all experimental observations. In the next sections, the influence on the achieved dichroism (mainly governed by the NP aspect ratio) of a number of laser and irradiation parameters such as laser pulse intensity, excitation wavelength, temperature etc., are discussed presenting pertinent series of experimental results. Based on the conclusions from these studies we are now in a position to

Copyright © 2010. Nova Science Publishers, Incorporated. All rights reserved.

produce polarizing optical micro-structures with unprecedented properties. First examples of such polarizing micro-patterns will be given at the end.

2. Optical Properties of Nanocomposites Containing Metal Nanoparticles

Interaction of light with nanocomposites reveals novel optical phenomena indicating unrivalled optical properties of these materials. The linear and nonlinear optical response of metal nanoparticles is specified by oscillations of the surface electrons in the Coulomb potential formed by the positively charged ionic core. This type of excitations is called Surface Plasmon (SP). In 1908 Gustav Mie [20] proposed a solution of Maxwell's equations for spherical particles interacting with plane electromagnetic waves, which explains the origin of the SP resonance in extinction spectra and coloration of the metal colloids.

During the last century optical properties of nanoparticles have extensively been studied and metalo-dielectric nanocomposites found various applications in different fields of science and technology [2, 21-24]. Since the optical properties of metal nanoparticles are governed by the surface plasmon resonance, they are strongly dependent on material, size, shape, concentration and distribution of the particles as well as on the properties of the surrounding matrix. Control over these parameters enables such metal-dielectric nanocomposites to become promising media for development of novel nonlinear materials, nanodevices and optical elements.

Thus, in this section the SP resonance and main optical properties of the metal nanoparticles embedded in a dielectric medium will be considered. Complete and excellent review of optical properties of nanostructured random media can be found in Refs. 1 and 19.

Copyright © 2010. Nova Science Publishers, Incorporated. All rights reserved.

2.1. Surface Plasmon Resonance of Isolated Metal Nanoparticles

Exposure of a metal nanoparticle to an electric field results in a shift of the free conduction electrons with respect to the particles' metal ion-lattice. The resulting surface charges of opposite sign on the opposite surface elements of the particles (see Figure 1) produce a restoring local field within the nanoparticle, which rises with increasing shift of the electron gas relative to the ion background. The coherently shifted electrons of the metal particle together with the restoring field consequently represent an oscillator, whose behavior is defined by the electron density and the geometry of the particle. Throughout this text its resonances are called surface plasmons on metal nanoparticles.

An exact analytical theoretical description of surface plasmons of spherical metal nanoparticles is the part of Mie's theory for the scattering and absorption of light by spheres [1, 25]. According to Mie-theory, the different eigenmodes of the spherical particles are dipolar or multipolar in character. For particles which are small compared to the local variations of the involved electromagnetic fields, the quasistatic approximation [1] is valid. It assumes the exciting field to be homogeneous and not retarded over the particle's volume. Under these assumptions, the results of electrostatics can be applied by using the

corresponding frequency dependent dielectric function. In this case, the polarizability α and induced dipole moment p of a metal sphere embedded in dielectric can be given as [26]:

$$\alpha = 4\pi R^3 \frac{\varepsilon_i(\omega) - \varepsilon_h}{\varepsilon_i(\omega) + 2\varepsilon_h}, \tag{1}$$

$$\vec{p}(\omega) = \alpha\varepsilon_0 \vec{E}_0(\omega) = 4\pi\varepsilon_0 R^3 \frac{\varepsilon_i(\omega) - \varepsilon_h}{\varepsilon_i(\omega) + 2\varepsilon_h} \vec{E}_0(\omega), \tag{2}$$

where R is the radius of the nanoparticle, E_0 the electric field strength of an incident electromagnetic wave, ε_0 the electric permittivity of vacuum, $\varepsilon_i(\omega)$ and ε_h are the relative complex electric permittivity of metal and host matrix, respectively.

In turn, the absorption cross section of a spherical metal inclusion placed in a transparent dielectric matrix, where the imaginary part of the relative complex electric permittivity approaches zero ($\mathrm{Im}[\varepsilon_h] \to 0$) is then given as:

$$\sigma(\omega) = 12\pi R^3 \frac{\omega}{c} \varepsilon_h^{3/2} \frac{\varepsilon_i''(\omega)}{\left[\varepsilon_i'(\omega) + 2\varepsilon_h\right]^2 + \varepsilon_i''(\omega)^2}, \tag{3}$$

where $\varepsilon_i'(\omega)$ and $\varepsilon_i''(\omega)$ are real and imaginary part of the electric permittivity of the metal, which in turn can be described by the Drude-Sommerfeld formula:

$$\varepsilon_i(\omega) = \varepsilon_b + 1 - \frac{\omega_p^2}{\omega^2 + i\gamma\omega}. \tag{4}$$

Here, γ is a damping constant of the electron oscillations and ε_b is the complex electric permittivity associated with interband transitions of the core electrons in atom. The free electron plasma frequency is given by:

$$\omega_p = \sqrt{\frac{Ne^2}{m\varepsilon_0}}, \tag{5}$$

where N is the density of the free electrons and m is the effective mass of an electron.

As it can be seen from the Eqs. 1–3, the well known Mie resonance occurs at the SP frequency ω_{SP} under the following conditions:

$$\left[\varepsilon_i'(\omega) + 2\varepsilon_h\right]^2 + \varepsilon_i''(\omega)^2 \to Minimun. \tag{6}$$

If the imaginary part of the metal electric permittivity is small in comparison with $\varepsilon_i'(\omega)$ or it has small frequency dependence, then Eq. 6 can be written as:

Copyright © 2010. Nova Science Publishers, Incorporated. All rights reserved.

$$\varepsilon_i'(\omega_{SP}) = -2\varepsilon_h . \tag{7}$$

Thus, if the condition Eq. 7 is complied with, the dipole moment and local electric field in the vicinity of the nanosphere grow resonantly and can achieve magnitudes in many orders overcoming the field of the incident wave. This phenomenon is responsible for the SP enhanced nonlinearities of the metal colloids.

Eq. 7 requires the real part of the dielectric function of metals to be negative. This is indeed the case for noble metals in the visible spectral region (as an example see Figure 2 for Ag). For a dielectric environment having $\varepsilon_h = 2.25$ surrounding the silver nanoparticle, the resonance condition is observed to occur at around 400 nm. A consequence of this is the bright colours exhibited both in transmitted and reflected light.

Using Eq. 7 and by substituting the real part of the metal electric permittivity from Eq. 4, the position of the SP resonance can be expressed as follows:

$$\omega_{SP}^2 = \frac{\omega_p^2}{\mathrm{Re}[\varepsilon_b] + 1 + 2\varepsilon_h} - \gamma^2 \tag{8}$$

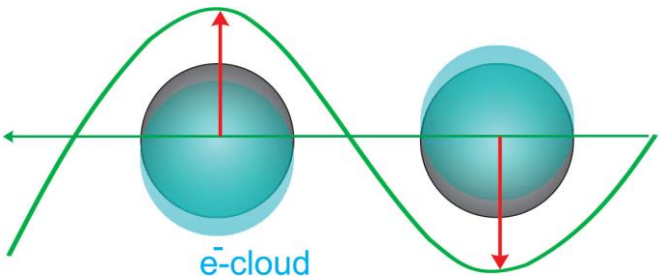

Figure 1. Plasmon oscillations in metal sphere induced by electromagnetic wave.

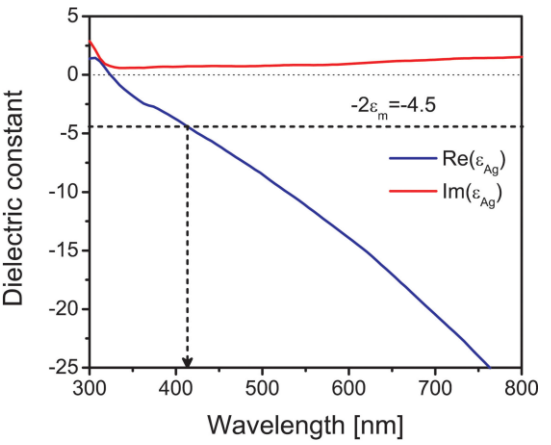

Figure 2. The dielectric function of silver (solid and dashed lines) and the negative of the dielectric constant of a dielectric media (n=1.5, ε_m=2.25) fulfilling the surface plasmon resonance condition (blue line), where ε_m is assumed to be frequency independent. The data are adapted from Ref. 27.

Copyright © 2010. Nova Science Publishers, Incorporated. All rights reserved.

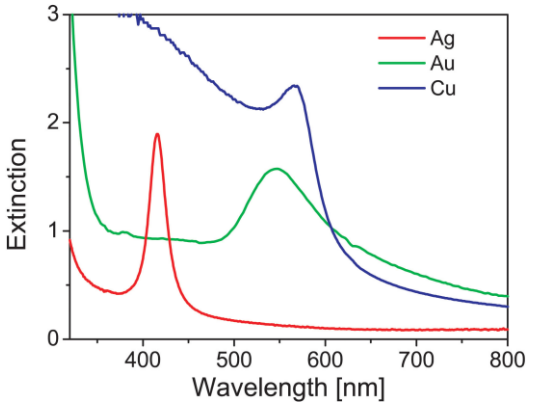

Figure 3. Extinction spectra of glass containing spherical silver, gold and copper nanoparticles.

The core electrons have a significant influence on the surface plasmon and define obviously the position of the SPR in extinction spectra (Figure 3) for different noble metals. For instance, silver nanoparticles embedded in glass matrix exhibit their SP band at about 415 nm. In turn, the SP for Au and Cu nanoparticles is shifted in the red spectral range and peaked at 528 nm and 570 nm, respectively. The broad absorption bands below 500 nm for both Au and Cu containing nanocomposite glasses are associated with interband transitions, namely from *d*- to *s*-shell, of the core electrons in the metal atoms. However, for silver the interband resonance is peaked at 310 nm (4 eV) far away from the SP resonance [28].

On the other hand, Eq. 8 qualitatively describes a dependence of the SP resonance on the dielectric properties of the host matrix, which the metal nanoparticles are incorporated in. An increase of dielectric constant (refractive index) evokes the shift of absorption maximum towards long wavelengths [1, 29, 30] (as it could be expected from Figure 2). Figure 4 represents the spectral positions of surface plasmon resonances of silver nanoparticles embedded in vacuum (ε_h=1) and glass (ε_h=2.25). It is clearly seen that the SPR maxima are more red-shifted for nanocomposites with higher dielectric constant of the matrix.

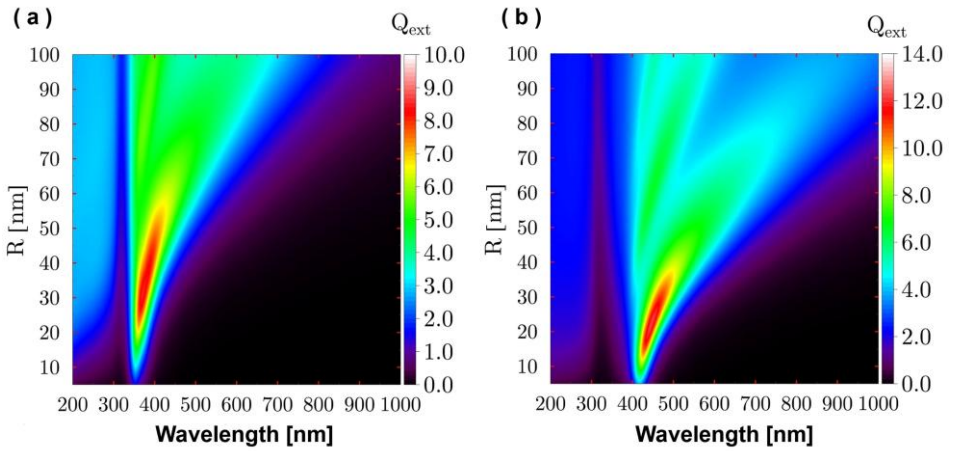

Figure 4. Extinction efficiency spectra of spherical silver nanoparticles in (a) vacuum and (b) glass as a function of particles size.

Copyright © 2010. Nova Science Publishers, Incorporated. All rights reserved.

This Figure 4 also shows that the position of the SP resonance depends on the size of metallic nanoparticles. In fact, its position remains quasi-constant for the nanoparticles with radius smaller than 10-15 nm, while the band halfwidth for these clusters differs by the factor of 4. This is often described as an intrinsic size effect [1, 31, 32]. If the particle size is below the dimension of the mean free path of the electrons in the metal (≈ 10-15 nm) [33], the electron scattering at the particle surface increases mainly the imaginary part of the dielectric function. For the smaller particles (> 1 nm) the spill-out of electrons from the particle surface should be taken into account, which results in an inhomogeneous dielectric function. As a result, very broad plasmon bands are observed for small nanoparticles (not included in Figure 4).

Increase in the radius of the nanosphere larger than 15 nm leads to the shift of the SP resonance towards longer wavelengths with simultaneous increase in the band halfwidth (Figure 4). This effect for the larger particle is referred as the extrinsic size effect [1, 31, 34-36]. Here, higher-order (such as quadrupolar) oscillations of conduction electrons become important.

From the size dependence of the SP it is quite obvious that metal nanoparticle with nonspherical shape will show several SP resonances in the spectra. For instance, the ellipsoidal particles with axes a ≠ b ≠ c own three SP modes corresponding to polarizabilities along principal axes given as:

$$\alpha_k(\omega) = \frac{4\pi}{3} abc \frac{\varepsilon_i(\omega) - \varepsilon_h}{\varepsilon_h + (\varepsilon_i(\omega) + \varepsilon_h)L_k}, \tag{9}$$

where L_k is the geometrical depolarization factor for each axis ($\sum L_k = 1$). Moreover, increase in the axis length leads to minimization of the depolarization factor. For the spherical particle $L_a = L_b = L_c = \frac{1}{3}$.

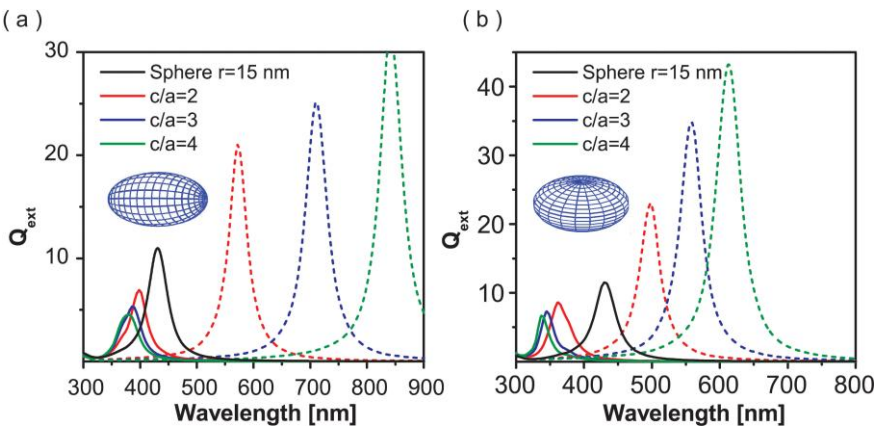

Figure 5. Calculated using the Mie theory for spheroids [38] polarized extinction efficiency spectra of prolate (a) and oblate (b) silver spheroids with different aspect ratios, which are embedded in glass. The volume of spheroids is equal to the volume of a nanosphere with radius of 15 nm. Dashed curves – polarization of the light is parallel to the long axis; solid line – parallel to the short axis. In insets, the shapes of spheroids are shown schematically.

Copyright © 2010. Nova Science Publishers, Incorporated. All rights reserved.

Thus, if the propagation direction and polarization of the electromagnetic wave do not coincide with the axes of the ellipsoid, the extinction spectra can demonstrate three separate SP bands corresponding to the oscillations of free electrons along axes [1]. For spheroids a ≠ b = c the spectra demonstrate two SP resonances. However, if the light is polarized parallel to one of the axes, only one single SP band corresponding to appropriate axis is seen (Figure 5). Moreover, the band lying at higher wavelengths is referred to the long axis, while the small axis demonstrates resonance at shorter wavelengths compared to the single resonance of a nanosphere of the same volume. The spectral separation of the two surface plasmon bands of the ellipsoidal nanoparticle depends strongly on its aspect ratio [37, 38], which is defined as the ratio of the long to the short axes. However, at the same time, it is clearly seen that for prolate and oblate spheroids having the same aspect ratio, the positions of SP resonances are different. Namely, the spectral separation between SP bands is higher for the nanoparticles having zeppelin-like shape.

For many years now, the dichroic property of elongated metallic nanoparticles has been used for manufacturing of broad-band high-contrast polarizers [39]. This became possible owing to the fact that by appropriate choice of aspect ratio between the axes of the nanoparticles, the position of the SP resonance can be designed within a broad spectral range. This aspect will be discussed in more detail in the next sections.

2.2. Optical Properties of Nanocomposites with High Fraction of Metal Nanoparticles

Increasing fraction of metal nanoparticles in a medium leads to the decrease of average particle distances. Thus, enhancement of the dipole moment of spherical metal NPs by excitation near to the SP resonance results in strong collective dipolar interactions between nanoparticles, which affect the linear and nonlinear optical properties of a nanocomposite material. For the purpose of this work it is sufficient to describe this effect in the approximation of the well known Maxwell-Garnett theory, which is widely applied to describe the optical properties of metal particles in dielectric matrices [19, 25, 40, 41]. Although it does not correctly take into account the multipolar interactions between nanoparticles considered in other works [42, 43], the Maxwell-Garnett theory can be used in the following because it describes quite well the position and shape of the SP resonance and its dependence on the metal filling factor [19].

Thus, the effective dielectric constant $\varepsilon_{\text{eff}}(\omega)$ of a composite material with spherical metal inclusions having a filling factor f (volume of the silver inclusions per unit volume of the composite material $f = V_{\text{Ag}}/V_{\text{total}}$) is given by the expression:

$$\varepsilon_{eff}(\omega) = \varepsilon_h \frac{(\varepsilon_i(\omega) + 2\varepsilon_h) + 2f(\varepsilon_i(\omega) - \varepsilon_h)}{(\varepsilon_i(\omega) + 2\varepsilon_h) - f(\varepsilon_i(\omega) - \varepsilon_h)}, \tag{10}$$

where $\varepsilon_i(\omega)$ and ε_h are complex electric permittivities of the metal (given by the Eq. 4) and host matrix. Based on this description, complex index of refraction of a composite medium can be defined as:

Copyright © 2010. Nova Science Publishers, Incorporated. All rights reserved.

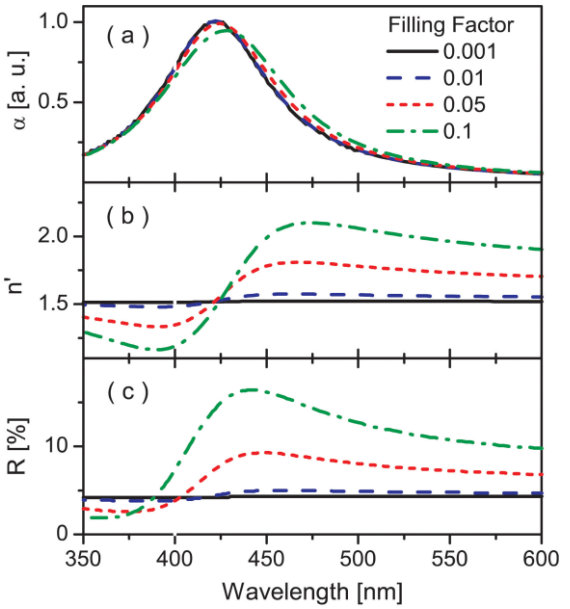

Figure 6. (a) – Absorption cross-section, (b) – dispersion and (c) – reflection spectra of composite glass containing Ag nanoparticles calculated according to the Maxwell–Garnett theory.

$$n(\omega) = n' + in'' = \sqrt{\varepsilon_{eff}(\omega)}\,. \tag{11}$$

Hence, the absorption coefficient α and refractive index n' of the medium with dielectric constant $\varepsilon_{\text{eff}}(\omega)$ can be expressed as:

$$\alpha = \frac{2\omega}{c}\,\mathrm{Im}\sqrt{\varepsilon_{eff}(\omega)}\,, \tag{12}$$

$$n'(\omega) = \mathrm{Re}\sqrt{\varepsilon_{eff}(\omega)}\,, \tag{13}$$

where c is the light velocity. Using Eqs. 10–13, the absorption cross-section and dispersion spectra [Figure 6 (a-b)] of glass with spherical silver nanoparticles can be calculated as a function of the volume filling factor of metal clusters in the glass matrix: ε_h=2.3, ω_p=9.2 eV, γ=0.5 eV [44], ε_b=4.2 [41].

It is seen that the collective dipolar interactions between nanoparticles cause a broadening and red shift of the absorption band with increasing filling factor of silver inclusions in the glass matrix [Figure 6 (a)]. Also the effective refractive index of the composite glass changes with growing filling factor [Figure 6 (b)]: while at low content of silver nanoparticles in glass (f = 0.001) the refractive index is actually identical with that of clear glass (n' = 1.52), higher filling factor results in significant modifications of dispersion dependences of the composite glass. For f = 0.1, the refractive index varies between ~ 1.2 and 2.1 on the different sides of the SP resonance. Finally, as shown in Figure 6 (c), also the sample reflectivity R, given for normal incidence by:

Copyright © 2010. Nova Science Publishers, Incorporated. All rights reserved.

$$R(\omega) = \left| \frac{n(\omega) - 1}{n(\omega) + 1} \right|^2 \tag{14}$$

changes upon increasing the volume filling factor. In particular, in the visible range the main effect is an increase of reflectivity of the composite medium with increasing content of spherical Ag nanoparticles.

2.3. Preparation and Characterization of Glass Samples Containing Silver Nanoparticles

The samples were prepared from soda-lime float glass (72.5 SiO_2, 14.4 Na_2O, 0.7 K_2O, 6.1 CaO, 4.0 MgO, 1.5 Al_2O_3, 0.1 Fe_2O_3, 0.1 MnO, 0.4 SO_3 in wt%) by Ag^+-Na^+ ion exchange. For the ion exchange process glass substrate is placed in a mixed melt of $AgNO_3$ and KNO_3 at 400°C [29, 45]. The thickness of the glass substrate, time of the ion exchange process and weight concentration of $AgNO_3$ in the melt determine the concentration and distribution of Ag^+ ions in the glass. Following thermal annealing of the ion exchanged glass in H_2 reduction atmosphere, typically at 400-450°C, results in the formation of spherical silver NPs [29]. As could be expected, size and distribution of Ag nanoparticles in the depth of the glass sample depend strongly on temperature and time of Na-Ag ion exchange as well as on the annealing time. In our case, the spherical Ag nanoparticles of 30-40 nm mean diameter [Figure 7(a)] are distributed in a thin surface layer of approximately 6 µm thickness (total thickness of glass plate 1 mm).

Figure 7(b) shows an SEM picture of the cross section of the sample, where silver particles are reproduced as white spots. To obtain an information about the distribution of silver NPs in the depth of the glass, surface layers of various thicknesses from the sample were removed by etching in 12% HF acid for different retention times. After this procedure SEM images were recorded for all etched surfaces [examples given in Figure 8(a), increasing etching time from (i) to (iv)], as well as optical extinction spectra [see Figure 8(b)]. The area fraction of silver derived from the SEM pictures was then converted to a volume fill factor assuming a typical electron penetration depth of 500 nm. The result is given as superimposed curve in Figure 7(b), showing the highest silver content of f=0.028 directly below the glass surface. Within a few micrometers the fill factor then decreases strongly with increasing distance from the surface.

Figure 8(b) depicts the corresponding extinction spectra with the same lettering as in Figure 8(a). However, it should be noticed that the optical spectra integrate over the whole particle-containing layer. Thus, for the original sample the absorption around SP resonance is very high, discouraging any detailed analysis of the spectral band shape. The same holds for extinction after the shortest etching time [Figure 8(b), curve (i)]; however at least, one can estimate for this case an extinction peak wavelength in the range of 420-440 nm. Further etching of the sample results in fading of the extinction band caused by the decrease of thickness of the silver-containing layer. Additionally, spectrum (i) indicates that the upper most metal-rich layers are responsible for a shift of the red wing of the SP band towards longer wavelengths.

Copyright © 2010. Nova Science Publishers, Incorporated. All rights reserved.

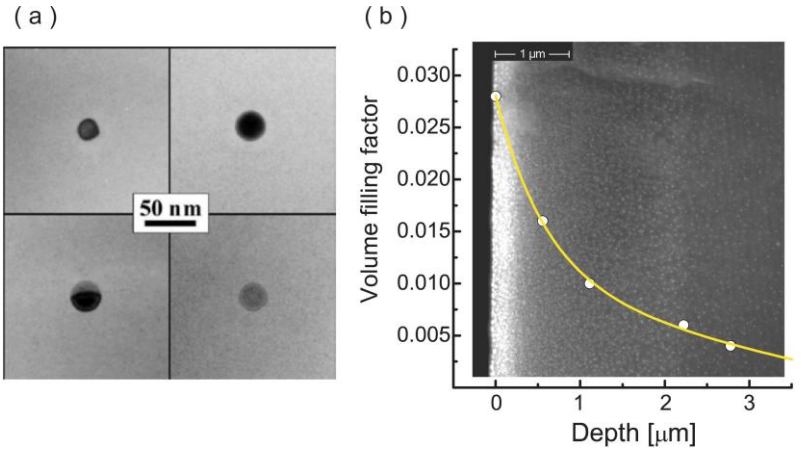

Figure 7. (a) TEM picture of typical spherical silver nanoparticles in nanocomposite glass. (b) SEM picture of the cross section of glass sample containing spherical silver nanoparticles (Ag particles are reproduced as white spots). The gradient of the volume filling factor of Ag nanoparticles is shown in superimposition (The x-axis was adjusted to the length scale of the picture).

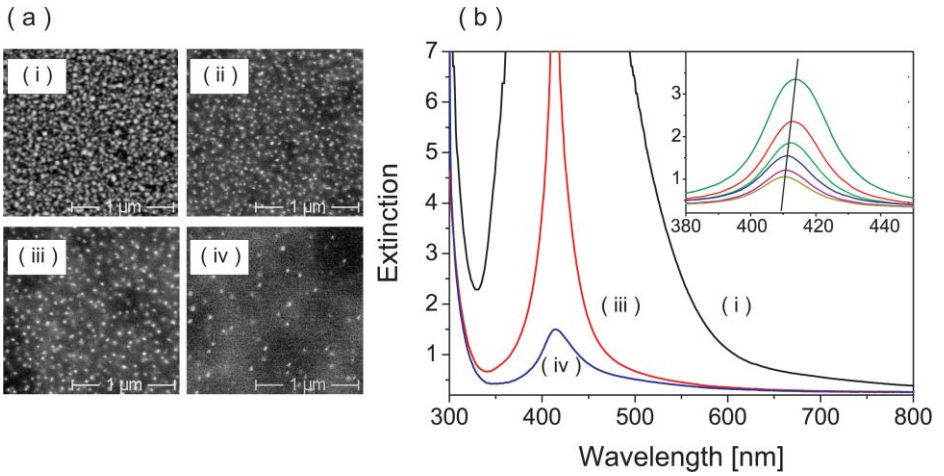

Figure 8. (a) SEM pictures of etched samples with Ag nanoparticles (volume fill factor: i – 0.01; ii – 0.006; iii – 0.004; iv – 0.001). (b) Extinction spectra of samples with spherical silver nanoparticles after different time of etching in 12% HF acid. Lettering of the spectra is according to the SEM pictures shown in Figure 8(a). The samples with lower fill factor have lower extinction.

Etching the samples for longer times, so that one ends up at a residual filling factor of less than 0.004, leads to easily measurable extinction spectra. The corresponding evolution of the spectra with etching time is shown in more detail in the inset of Figure 8(b). It is seen that a decrease of filling factor (by longer time of etching) leads to a slight shift of the SP band maxima to shorter wavelengths. This is well compatible with the Maxwell–Garnett theory, which predicts a red-shift of the SP band for the samples with higher filling factors [1, 19, 46].

It should be mentioned here that for the study of the basic physical processes of nanoparticles shape transformation, etched samples with maximum Ag filling factor of 10^{-3} were used, where the NPs can in good approximation be understood as non-interacting

Copyright © 2010. Nova Science Publishers, Incorporated. All rights reserved.

(isolated nanoparticles). However, the experiments related to maximization of polarization contrast were performed on samples with considerably higher filling factor (f~0.01).

3. Processes Arising by Interaction of Ultrashort Laser Pulses with Metal Nanoparticles Incorporated in Dielectric Media

This section is dedicated to the general understanding of laser pulse interaction with metal nanoparticles. The aim is to collect all physical processes, which may occur when the laser pulse starts to interact with the nanoparticle, as well as all later events and mechanisms, which are triggered by it.

Depending on the laser parameters (e.g. weak and strong excitation regimes) and nanoparticle properties, one can expect various kinds of physical phenomena. Recent investigations of the laser pulse interaction with metal nanoparticles are mostly concentrated on the SP dynamics and the energy exchange (relaxation) mechanisms arising by it (see Refs. 47-52 for a review). These studies employ weak laser pulses to excite the nanoparticles, thereby ensuring only weak electronic perturbations to the nanoparticle. In this low perturbation regime, the changes induced to the surface plasmon bands of the nanoparticles are transient and totally reversible. For the strong excitation as used in this work, however, the energy absorbed by the nanoparticle becomes very high, which creates big perturbation for the nanoparticle electrons resulting in persistent (irreversible) changes to the nanoparticle. In this regime the processes related to the heating and cooling of nanoparticles (e.g. e-e, e-ph scattering, etc.) have to be modified. At the same time, this strong excitation can open up additional channels of the energy relaxation in the form of e.g. hot electron and ion emissions (see for example Refs. 11, 53-55). Although it is currently impossible to account for all the complicated many-body interactions among electrons, phonons, ions, etc., in this regime in detail, some theoretical estimations will be presented.

3.1. Energy Relaxation Following the Excitation of the Nanoparticle: Weak Perturbation Regime

The absorption of a fs laser pulse produces a coherent collective oscillation of the nanoparticle electrons [Figure 9(a)]. During this quasi-instantaneous process, the phase memory is conserved between the electromagnetic field and the electronic states, and the density of excited states depends on the spectral shape of the laser pulse. The corresponding electron distribution is non-thermal [56-58] and lasts for few femtoseconds [47, 48]. Electrons having energies between $E_F-\hbar\omega$ and E_F are excited above the Fermi energy with final energies between E_F and $E_F+\hbar\omega$. The excitation is sketched with rectangular-shaped boxes, whose dimensions are determined by the energy of the exciting laser pulse $\hbar\omega$ as the length and the absorbed energy density as the width.

The next step of the energy relaxation corresponds to a thermalization of the electrons. The occupied electronic states tend to a Fermi–Dirac distribution with a well defined temperature which depends on the laser pulse intensity. The phase coherence is lost and the

Copyright © 2010. Nova Science Publishers, Incorporated. All rights reserved.

collective modes have decayed into quasi-particle pairs. Figure 9(b) shows the equilibrated thermal Fermi distribution following the e-e scattering processes. The excited electrons possess high energies above the Fermi level, and the resulting temperature of the electronic system is much higher compared with the equilibrium temperature before the laser excitation.

Several time-resolved photoemission experiments, performed in noble metal films, have shown that the temporal scale of this thermalization process is a few hundred femtoseconds [57, 59-62]. For small particles, with a diameter typically less than a few tens of nanometers, the scattering time of the electrons at the particle surface is also around a few hundred femtoseconds. Voisin et al. [63] report an internal electron thermalization time of ≈ 350 fs for 12 nm radius Ag nanoparticles in a $BaO\text{-}P_2O_5$ matrix, which is comparable to the one determined from Ag films [51]. The time needed for the internal thermalization decreases for smaller nanoparticles, for example, it is around 150 fs for 2 nm radius Ag nanoparticles embedded in an Al_2O_3 matrix. For the internal electron thermalization of Au nanoparticles of 9 nm and 48 nm radius in solution, decay lifetimes of 500 and 450 fs were found, respectively [48]. The size dependence of the thermalization time is in good agreement with a simple model which phenomenologically introduces surface induced reduction of the Coulomb interaction screening due to the spillout and *d*-electron wave function localization effects [63, 64].

Another important mechanism in the electron dynamics, which is shown in Figure 9(c), is the energy transfer to the lattice. The hot electrons cool externally by electron-phonon (e-ph) interactions until the temperatures of the electron gas and the lattice are equilibrated. The resulting electronic temperature is lower than its peak value, but higher than the equilibrium temperature. Since the e-ph interactions occur on a time scale comparable with the internal electron thermalization, the e-e and e-ph relaxation can actually not be understood as separated processes occurring in sequential order. It means that the non-thermal electrons of Figure 9(a) already interact with the phonons during the same time they scatter with themselves to achieve the Fermi distribution of Figure 9(b). This simultaneous e-ph coupling is an important channel of electron relaxation, heating the nanoparticle lattice.

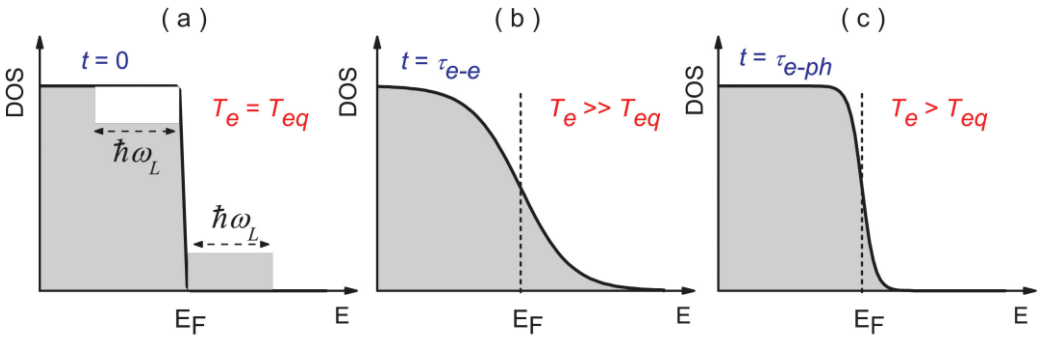

Figure 9. Laser excitation and the subsequent electron dynamics: (a) the electronic distribution is at an equilibrium temperature T_{eq}. Absorption of a laser pulse energy density with photon energy of $\hbar\omega_L$ creates a non-thermal electronic distribution represented by the rectangles. (b) The electrons thermalize to a hot Fermi distribution ($T_e >> T_{eq}$) through electron-electron scatterings within several hundred femtoseconds. (c) Electrons cool down by sharing their energy with the lattice through electron-phonon coupling processes, reaching a temperature which is equal to the lattice temperature $T_e = T_l > T_{eq}$.

Copyright © 2010. Nova Science Publishers, Incorporated. All rights reserved.

In the last years, many groups attempted to define the time scale of this thermalization process in different combination of metals and matrixes [65-72]. Normally one can expect that the lattice heating needs more time than heating of electrons, and the maximum lattice temperature cannot reach temperatures as high as the electron temperatures since the electronic heat capacity is about 2 orders of magnitude smaller than the lattice heat capacity. In addition, Hartland et al. showed that the thermalization time depends on the laser intensity [53, 73]. In the next section we will consider in more detail the two temperature model (2TM, in literature also called TTM) which describes the thermal situations of electrons and phonons and the heat transfer between these two systems. This model will be extended to very high electronic temperatures in order to account for the conditions of strong excitation regime.

The last step in the relaxation is the energy transfer to the dielectric matrix. This transfer corresponds to the heat diffusion from the metal to the environment. It is therefore sensitive to the thermal conductivity of the surrounding medium and, as will be shown later, plays an important role for the mechanism of nanoparticles shape transformation. Therefore, this process will be also considered more deeply in the next sections.

3.2. Electron-Phonon Coupling and Electron Heat Capacity of Silver under Conditions of Strong Electron-Phonon Nonequilibrium

Upon pulse interaction with the nanoparticle, the electrons heat up gradually to a hot electronic distribution. During and after their heating, the electrons couple with the nanoparticle lattice vibrations (the phonons) and heat up the nanoparticle. The heat gained by the nanoparticle lattice can be found from the heat lost by the electrons using the two-temperature model (2TM) [47, 74], where the heat flow between two subsystems (electrons and lattice) is defined by two coupled differential equations. 2TM is the commonly accepted theory to describe the energy relaxation mechanisms between electrons and lattice. The electronic system is characterized by an electron temperature T_e and the phononic system by a lattice temperature T_l. The electron-phonon coupling factor $G(T_e)$ is responsible for the energy transfer between two subsystems. The heat equations describing the temporal evolution of T_e and T_l are given as follows:

$$C_e(T_e)\frac{\partial T_e}{\partial t} = -G(T_e)(T_e - T_l) + S(t), \tag{16}$$

$$C_l\frac{\partial T_l}{\partial t} = G(T_e)(T_e - T_l), \tag{17}$$

where $C_e(T_e)$ and C_l are the electronic and lattice heat capacities, respectively; $S(t)$ in Eq. (16) is a source term describing the absorbed laser pulse energy per nanoparticle, which can be given as:

$$S(t) = \frac{I\sigma_{abs}}{V_{NP}} \cdot \exp\left[-4\ln 2 \cdot (t/\tau_{FWHM})^2\right]. \tag{18}$$

Copyright © 2010. Nova Science Publishers, Incorporated. All rights reserved.

Here I is the peak pulse intensity, σ_{abs} is the absorption cross section of a single nanoparticle (≈3000 nm^2 for a silver nanoparticle in a dielectric environment with refractive index of n = 1.52 [75]); V_{NP} is the nanoparticle volume, and τ_{FWHM} determines the full width at half maximum of the temporal pulse profile.

For any models based on 2TM intended to yield a quantitative description of the kinetics of energy redistribution in the irradiated target it is crucial to use adequate, temperature dependent thermophysical properties of the target material. Looking at the 2TM equation for the electron temperature (Eq. 16), this problem concerns the electron-phonon coupling factor, the electron heat capacity, and the heat conductivity. Due to the small heat capacity of the electrons in metals and the finite time needed for the electron-phonon equilibration, irradiation by a short laser pulse can transiently bring the target material to a state of strong electron-lattice nonequilibrium, in which the electron temperature can rise up to some ten thousand Kelvins (comparable to the Fermi energy) while the lattice still remains cold. At such high electron temperatures, the thermophysical properties of the material can be affected by the thermal excitation of the lower band electrons, which, in turn, can be very sensitive to the details of the spectrum of electron excitations specific for each metal. Indeed, it has been shown for Au that in the range of electron temperatures typically realized in femtosecond laser material processing applications, thermal excitation of *d*-band electrons, located around 2 eV below the Fermi level, can lead to a significant increase (up to an order of magnitude) of the electron-phonon coupling factor and positive deviations of the electron heat capacity from the commonly used linear dependence on the electron temperature [76, 77]. These deviations clearly have to be regarded for a quantitative description of material response to a strong ultrafast laser excitation of a given material. However, for the heat capacity of the nanoparticle lattice (C_l) the room temperature values remain under the same conditions still reasonable approximations, as C_l does not change much as the temperature increases. For the case of silver, it is known that the change of C_l upon lattice temperature increase by 1500 K is less than 20% compared with its room temperature value of 3.5×10^6 $Jm^{-3}K^{-1}$ [78].

For the electron heat capacity the commonly used linear relationship $C_e(T_e) = \gamma T_e$, with $\gamma = \pi^2 k_B^2 g(\varepsilon_F)/3$, ($g(\varepsilon_F)$: electron density of states (DOS) at the Fermi level) is no more valid regarding the very high electron temperatures reached in the strong perturbation regime. Instead, C_e should include the full spectrum of the electron DOS by taking the derivative of the total electron energy density with respect to the electron temperature [79], as given by the expression:

$$C_e(T_e) = \int_{-\infty}^{\infty} \frac{\partial f(\varepsilon, \mu, T_e)}{\partial T_e} g(\varepsilon) \varepsilon d\varepsilon \,, \tag{19}$$

where $g(\varepsilon)$ is the electron DOS at the energy level ε, μ the chemical potential at T_e, and $f(\varepsilon,\mu,T_e)$ the respective Fermi distribution function.

Also the electron-phonon coupling is expected to be no longer a constant (typical *G* values used for silver range between 3×10^{16} to 3.5×10^{16} $Wm^{-3}K^{-1}$ [47, 80, 81]), but to show a considerable temperature dependence for strong excitation. The reason for this is that high electronic temperatures should trigger thermal excitation of the *d*-band electrons located below the Fermi level, leading to dramatic changes for the rate of the electron-phonon energy

Copyright © 2010. Nova Science Publishers, Incorporated. All rights reserved.

exchange. Therefore, the correct treatment of the G factor in the strong perturbation regime requires again the consideration of the full spectrum of electron DOS (as it was done above for C_e). The resulting expression for the temperature dependent electron-phonon coupling factor can be given by [82]:

$$G(T_e) = \frac{\pi\hbar k_B \lambda\langle\omega^2\rangle}{g(\varepsilon_F)} \int_{-\infty}^{\infty} g^2(\varepsilon)\left(-\frac{\partial f}{\partial \varepsilon}\right)d\varepsilon\,, \tag{20}$$

where λ denotes the electron-phonon coupling constant, and the value of $\lambda\langle\omega^2\rangle$ is 22.5 for silver.

Taking into account the above given theory, it is possible to calculate the dependences of electron heat capacity and electron-phonon coupling factor on the electronic temperature [66, 83]. The resulting temperature dependence of electronic heat capacity C_e and electron-phonon coupling term G turns out to be important when T_e values above ~5000 K are achieved, as in the experiments discussed in this work. The enhancement of the electron-phonon coupling at high electron temperatures implies a faster energy transfer from the hot electrons to the lattice. A consequence of this temperature dependent electron-phonon coupling term is that the electron-phonon relaxation times ($\tau_{e\text{-}ph}$) will increase with increasing electron temperatures and hence the applied laser pulse energy [66, 73, 83]. Therefore, slightly different electron-phonon relaxation results presented in the literature could be explained by the temperature dependence of the electron-phonon relaxation.

3.3. Two Temperature Model for the Strong Excitation Regime

We are now going to solve the coupled heat equations (Eqs. 16 and 17) for a quantitative modeling of the energy relaxation dynamics occurring after the very strong excitation of silver nanoparticles by the femtosecond laser pulses applied in this work. As an illustration to this regime, Figure 10(a) depicts the results of 2TM calculations for the case of a single silver nanoparticle excited by a 150 fs pulse with an intensity of 0.5 TW/cm^2 (above the threshold for permanent nanoparticle shape modification [84]) and a central wavelength of 400 nm ($\hbar\omega$ = 3.1 eV), close to the surface plasmon resonance. It is easily seen that, upon absorbing the laser pulse energy, the conduction electrons of the nanoparticle gain very high temperatures (~10^4 K) already during the pulse. Reaching the maximum T_e, the hot electronic system heats the cold silver lattice to a region of temperatures above the melting point of (bulk) silver within a few picoseconds. The electronic and lattice temperatures meet at a value near 2000 K at ~40 ps after the pulse interaction. This suggests the plausibility of the melting of nanoparticles in such a short time. Plech et al. observed by time-resolved X-ray scattering studies the melting of gold nanoparticles suspended in water within 100 ps after a strong laser pulse excitation [85, 86]. However, it should be noticed here that these calculations do not take into account the energy transfer to the matrix and losses due to possible electron emission processes from the nanoparticle, which are additional cooling mechanisms of the electronic sea. The details of these cooling processes will be considered below.

Copyright © 2010. Nova Science Publishers, Incorporated. All rights reserved.

Figure 10(b) shows the dependences of electronic and lattice temperature maxima on a wide range of applied energy densities. The weak regime (up to T_e values of 5000 K) shows a rapid increase in electronic temperature owing to the very low electronic heat capacity C_e in this interval. However, these electrons do not heat up the lattice efficiently due to the relatively low e-ph coupling factor G. Further increases in the energy density of the pulses cause higher T_e values, but the rise of electronic temperature slows down due to the increasing C_e value. The lattice temperatures are observed to increase with a higher slope in this regime as a result of the increasing efficiency of the G factor. If, for comparison, one would employ standard linear values for C_e (i.e. $C_e(T_e) = \gamma T_e$) at an energy density of 20 mJ/cm^2 (used in the presented 2TM calculations) the 2TM would yield a rise of the electronic temperature to more than 10^5 K, and the resulting T_l values would be much higher than the Ag evaporation temperature.

3.4. Heat Transfer from the Nanoparticle to the Glass Matrix

The above given 2TM describes only the heat transfer between the electrons and the nanoparticle lattice. To get the complete "thermodynamical" picture of the nanoparticle and the surrounding glass system, this 2TM has to be extended by the heat transfer from the NP to the glass matrix. The excess energy of the nanoparticle is released to the surrounding matrix via phonon couplings across the nanoparticle-glass interface [87, 88]. Therefore, cooling of the nanoparticle (and heating of the glass matrix) can be calculated considering energy flow from the hot particle to the glass through a spherical shell of infinitesimal thickness. Heat transfer from this first heated glass shell is then described by ordinary heat conduction. Because of the huge difference in thermal diffusivities of Ag (123 nm^2/ps) and glass (0.5 nm^2/ps), any temperature gradient within the NP can be neglected when calculating the transient temperatures in the glass around the nanoparticle (Figure 11). The temporal and spatial evolution of temperature within the glass can then be calculated by the radial heat equation, where the rate of temperature change ($\partial T(r,t)/\partial t$) is proportional to the curvature of temperature density ($\partial^2 T(r,t)/\partial r^2$) through the thermal diffusivity (χ) of the glass medium:

$$\frac{\partial T(r,t)}{\partial t} = \frac{\chi}{r}\frac{\partial^2 [rT(r,t)]}{\partial r^2}. \tag{21}$$

The time scales for the particle cooling range from tens of picoseconds to nanoseconds, depending on the laser excitation strength, the size of the nanoparticle and surrounding environment [88].

Figure 11 shows the radial temperature distribution in NP-glass system calculated numerically in the limit of the above-described 'three temperature model' (3TM) for two different times after irradiation. After ≈ 50 ps, i.e., when within a spherical NP with radius of 15 nm (red disk in Figure 11) an equilibrated high temperature of ≈ 2000 K has been established, the temperature of the surrounding glass matrix is still equal to room temperature (green line). It takes a few nanoseconds to establish by energy dissipation into the glass a heat-affected zone (light magenta circular ring) of the order of 5 nm around the NP (blue line).

Copyright © 2010. Nova Science Publishers, Incorporated. All rights reserved.

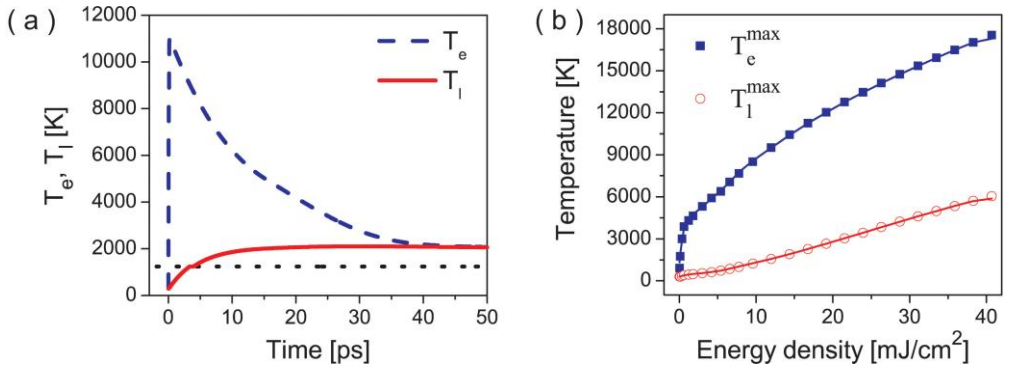

Figure 10. (a) Time evolution of electronic and lattice temperatures of a silver nanoparticle following the absorption of an intense fs laser pulse (around 20 mJ/cm^2 of energy density). The dotted line at 1235 K marks the melting temperature of bulk silver; (b) The dependences of electronic (blue squares) and lattice (red circles) temperature maxima on a wide range of laser energy densities.

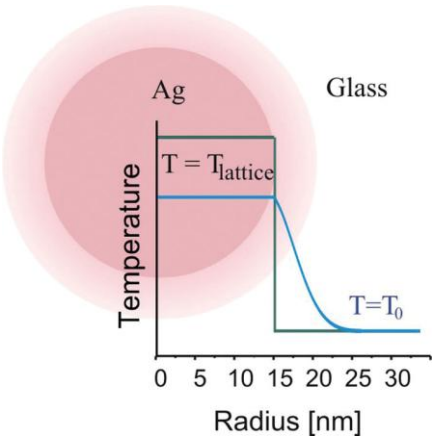

Figure 11. Temperature distribution in NP-Glass system for different times after irradiation; green line – ~50 ps, blue line – a few ns.

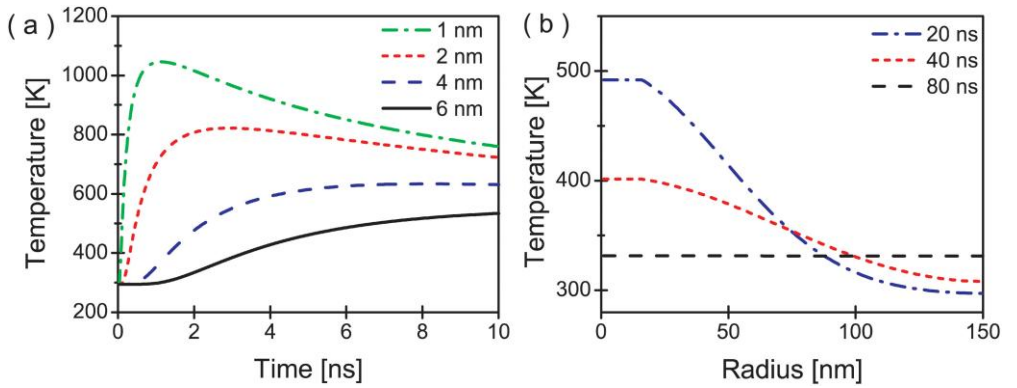

Figure 12. (a) Time evolution of glass temperatures in different shells away from nanoparticle calculated by 3TM. (b) Temperature distribution for longer times (more then 20 ns) after irradiation calculated by 3TM.

Copyright © 2010. Nova Science Publishers, Incorporated. All rights reserved.

More details about the first ten nanoseconds of the time evolution of glass temperatures in different distances away from the nanoparticle are given in Figure 12(a). In a distance of 1 nm from the NP surface the glass is heated up to $T_{max} \approx 1050$ K within approximately 1 ns after irradiation, then slowly cools down again. With increasing distance of the shells, the maximum temperature decreases and is reached considerably later. For instance, in a distance of the 6 nm a peak value of $T_{max} \approx 500$ K is reached only after ≈ 10 ns. The further evolution of the heat dissipation is shown by some characteristic radial temperature profiles in Figure 12(b); here the NP is included, i.e., r = 0 denotes the center of an Ag nanoparticle. At 20 ns the temperatures of nanoparticle and nearest shells are around 450-500 K, while the temperature in a distance of 150 nm is still equal to room temperature. After only 80 ns, however, the total energy is nearly homogeneously distributed and the temperature of the layer containing NPs is ≈ 330 K. These calculations have been done for a single metallic nanoparticle of 15 nm radius being surrounded by glass and irradiated by the pulses at 400 nm, with intensities of 0.5 TW/cm^2. Remembering that our samples used for fundamental investigations had an Ag volume filling factor of $\leq 10^{-3}$, which corresponds to an average glass sphere of 150 nm radius around each Ag NP, it is reasonable to regard this model as a well-suited description for this case.

Summarizing the above results one can conclude the following: (i) In the first few ns after the laser pulse the temperature of the NPs is above 1000 K, and the matrix temperature in the nearest shell up to a distance of 3 nm from the NP can reach or exceed the glass transition temperature [17]; this will cause softening of the glass, which is needed for NP shape transformation [84]. (ii) After ≈ 80 ns the system has come to a steady state within the focal volume; from then on heat transfer into the rest of the sample has to be taken into account. It should be mentioned here that this model neglects any glass heating by laser-driven electron and ion emission (which can take place by strong excitation). However, such contributions will only be present within the first few picoseconds after the laser pulse, and will only affect a shell of few nanometers around the NP [89]. Thus, due to energy conservation the temperature evolution on the time-scale of several nanoseconds or slower discussed here should not be affected by this simplification.

3.5. Photoemission from Nanoparticles Incorporated in Dielectric Media

In the previous sections the thermophysical processes arising by interaction of laser pulses with nanocomposites were discussed. Now we will proceed to possible electrophysical processes such as photoemission of electrons and ions from the nanoparticles, which can take place in the strong excitation regime. We will not discuss here the general processes of nonlinear ionization which can be observed in any kind of material at sufficiently high intensities [90]. Instead, we will concentrate our discussion on the question if and how the well-known electric field enhancement in the vicinity of metallic nanoparticles in combination with the strong laser field and the achieved very high temperatures can cause electrons and ions to be released into the glass matrix. Since these processes can have a strong influence on the energy (re-)distribution among nanoparticles and surrounding dielectric, they are very important for a final understanding of the laser-induced shape transformation of Ag nanoparticles.

Copyright © 2010. Nova Science Publishers, Incorporated. All rights reserved.

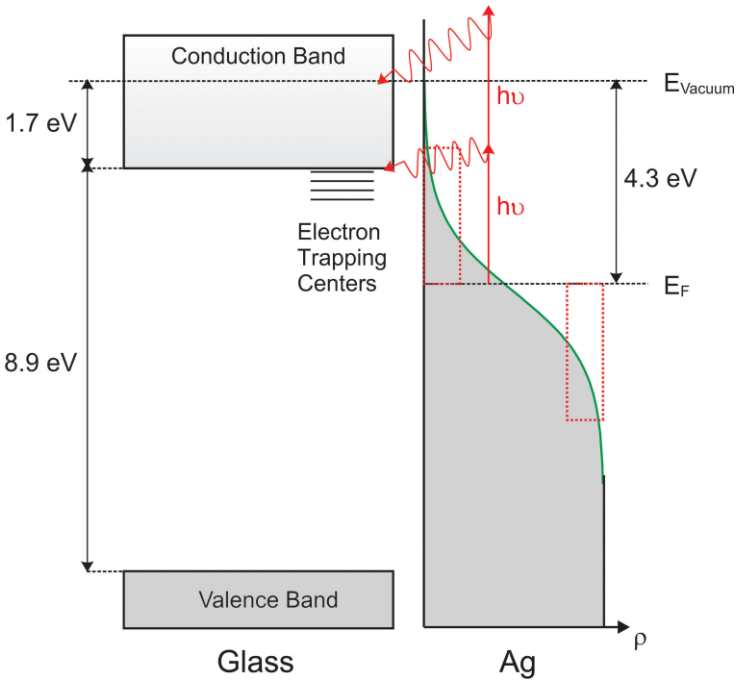

Figure 13. Energy level scheme of the electrons in the composite glass containing silver inclusions. The red dotted line indicates a non-thermal distribution of the electrons in Ag nanoparticle caused by excitation of SP resonance. The green one –distribution of the electrons after thermalization.

In the last years the SP assisted photoelectron emission from supported Ag nanoparticles has been extensively studied upon excitation with intense ultrashort laser pulses [54, 91-97]. The electron work function from the silver clusters defined as an energy gap between the Fermi level and the energy of the free electron in the vacuum is about 4.3 eV [1, 93, 96]. Moreover, it was demonstrated that excitation near to the SP resonance extremely enhances the two-photon photoemission yield from the Ag nanoparticles [54].

In composite glass containing metal nanoparticles, the probability of surface plasmon assisted photoemission can be strongly affected by the structure of the electron energy manifold in the host matrix. In turn, an energy level scheme of the soda-lime glass with embedded Ag nanoparticles can be represented as a junction of the dielectric with a metal (Figure 13). The valence band maximum of the glass lies 10.6 eV below the vacuum level. The lowest energy level of the conduction band in the glass is placed 1.6-1.7 eV below the energy of the free electron in vacuum. Thus, an energy gap between the Fermi level in the silver inclusion (4.3 eV) and conduction band in the glass is about 2.7 eV and consequently any radiation with photon energy >2.7 eV could evoke a tunnel transition of electrons from the silver inclusion into the conduction band of the surrounding glass matrix, even by single photon absorption.

Excitation of the Ag nanoparticles near to the SP resonance (~3 eV) by the fs laser at 400 nm (3.1 eV) leads to a non-thermal distribution of the electrons in the conduction band of the metal (Figure 13, red dotted line). Since the maximal electron energy in this case exceeds the bottom of the conduction band of the matrix by 0.4 eV, the electron injection in the conduction zone of the glass could be possible. At the same time, upon the two-photon

Copyright © 2010. Nova Science Publishers, Incorporated. All rights reserved.

plasma excitation the electrons can overcome the ionization energy level and without any obstacles penetrate in the glass matrix. In turn, the injection of the electrons from metal inclusions in the conduction band of the surrounding matrix is obviously the origin of a rise of conductivity in the composite glass with Ag nanoparticles upon fs laser irradiation near to the SP resonance [98].

Electrons being emitted during the laser pulse interaction will be driven by the strong, oscillating electric field and therefore generate an anisotropic distribution of emission directions, obviously given by the electric field oscillations (polarization) of the laser pulse. The anticipated 100 fs pulses at λ = 400 nm correspond to 75 full oscillation cycles with mostly very high amplitudes. A simple estimation shows that a conduction band electron of the nanoparticle can gain a linear acceleration of around 10^{20} m/s^2 upon encountering a linear-polarized pulse of 0.3 TW/cm^2 intensity (corresponding to an electric field amplitude of 10^8 V/m) within the half plasmon period. This is indeed a huge electric field amplitude on the nanoparticle. In the absence of any damping, the above acceleration can push the electron approximately 0.1 nm away from the nanoparticle surface. However, in the case of SP excitation, the oscillation amplitudes of the surface plasmon waves can overcome the excitation amplitude by few orders of magnitude [3, 99, 100]. This means a strong enhancement of the local electromagnetic field in the vicinity of the nanoparticle. By excitation with polarized light the E-field enhancement (Figure 14) occurs in special points on the surface. Namely, in the case of spherical nanoparticles, the field is enhanced on the poles of the nanoparticle [Figure 14(a)], depending on the polarization direction of the exciting light. However, in the case of non-spherical particles [e.g. Figure 14(b)], it is induced mostly at the tips and corners of the particles [1, 2, 3]. It should be also mentioned here that the local E-field enhancement (EFE) depends on the wavelength (Figure 15); and as it can be seen [Figure 15(a)], for spherical NPs of radius 15 nm the EFE increases very rapidly to the maximum at resonance wavelength and then again decreases, but for longer wavelengths its value remains higher than in UV spectral region. In the case of non-spherical (spheroids) particles [Figure 15(b)] the full spectrum of electric field enhancement factor (as well as extinction spectrum) is shifted to the long wavelength region; and the behavior for the longer and shorter wavelengths stays the same.

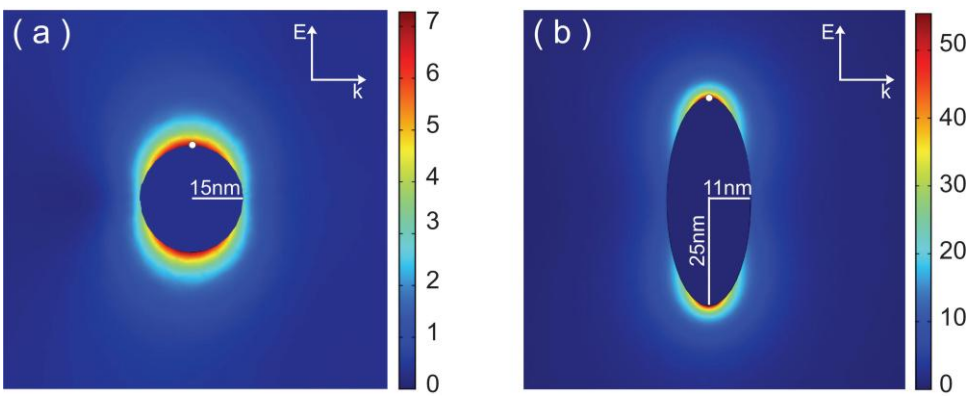

Figure 14. E-field contours for (a) spherical (radius 15 nm); (b) prolate spheroid Ag NPs in a glass. Labeled white points illustrate locations for Figure 15.

Copyright © 2010. Nova Science Publishers, Incorporated. All rights reserved.

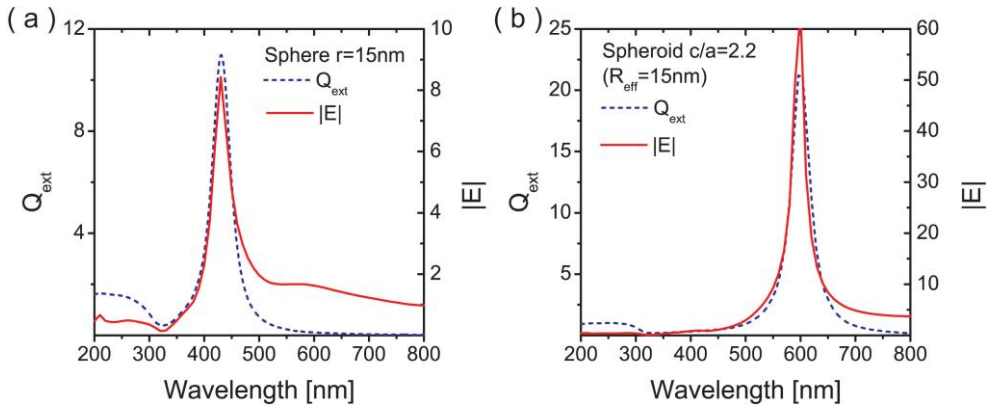

Figure 15. Extinction efficiency and electric field enhancement factor along the polarization direction (in points shown in Figure 14) vs wavelength for (a) spherical NPs with r=15 nm and (b) a prolate spheroids having a major axis of 25 nm and an aspect ratio of 2.2:1.

As a result of the enhanced electric field at the particle-glass interface, the conduction band electrons (discussed above) can move away from the nanoparticle surface up to few nm. Electrons driven far away from the nanoparticle have left the region of the strongest field enhancement, will thus experience a weaker backward force due to the reversed field of the next half plasmon period, and may finally be trapped in the glass matrix. These numbers make plausible that under the specified conditions there is a non-negligible probability for emission of even 'cold' electrons. Increase of the electric field in the vicinity of the nanoparticle could strongly suppress energy levels on the metal-dielectric junction and induce effective electron carrier flow from the nanoparticle surface parallel to the laser polarization. The anisotropy in this case is determined by the anomalous distribution of the local electric field over the nanosphere (Figure 14). On the other hand, the electric field in the vicinity of the metal cluster could overcome a breakdown threshold of the glass resulting in the high density electron plasma formation and even ablation of the glass matrix on the poles of the nanosphere.

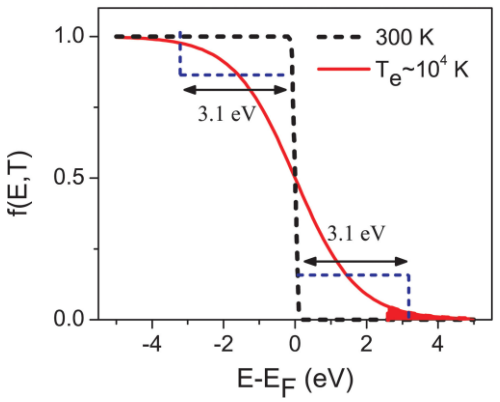

Figure 16. Changes in the Fermi distribution of the electronic system following an ultrashort laser pulse irradiation at an energy of 3.1 eV, which excites electrons below the Fermi level to high energies (represented by the arrows). The resulting hot electronic distribution is shown with the solid curve.

Copyright © 2010. Nova Science Publishers, Incorporated. All rights reserved.

The thermalization of the electrons with a characteristic time of a few hundred femtoseconds obviously restricts the photoemission processes. However, in the case of strong excitation the energy of some electrons could be high enough to jump in the conduction band of the glass [101]. As it was shown above, the maximal electronic temperature after e-e scattering can be higher than 10^4 K. The electrons are thermalized to form a hot Fermi distribution (Figure 16, red solid curve). As it can be seen, the high energy tail of the high T_e Fermi distribution exceeds the energy needed for nanoparticle electrons to penetrate into the glass conduction band (red area, >2.6 eV). As long as the pulse is still present, these electrons can be driven by the electric field of the laser along the direction of its polarization. After this time, i.e., even when the pulse is gone, there is still a probability of 'hot' electron emission. However, as the directionality of the pulse is no more there, this thermal emission of electrons is isotropic.

As a result, irradiation of the silver nanoparticles embedded in glass by the strong laser pulses can lead to two different types of electron emission processes, which could be classified as 'pulse-enhanced' or 'purely thermal'. The first one is accordingly anisotropic, the second one isotropic. The isotropic, purely thermal, electron emissions start after the pulse has gone away and continue to happen as long as the electrons possess high temperatures (few ps). The pulse-enhanced electron emission processes, on the other hand, comprise a 'direct' and a 'pulse-enhanced thermal' electron emission component. The direct electron emission processes are the fastest that happen within the first few plasmon oscillation periods. The second component of the pulse-enhanced electron emissions is thermal in nature, owing to the increased electron temperatures along the plasmon oscillation directions. Therefore, at the end, when the emitted electrons will be trapped in the conduction band of the glass, the pulse-enhanced ionization will lead to a non-homogenous electron concentration along the poles of the nanoparticle (along laser polarization), while the purely thermal electron emission homogeneously spreads the electrons into the surroundings of a nanoparticle. It will be shown below that this anisotropic ionization is one of the key processes in the laser-induced nanoparticle shape transformation.

The ionization process leaves the nanoparticles positively-charged (due to the emitted electrons), and due to e-ph scattering their temperatures rise within a few ps to values of more than 1000 K (see section 3.3), making the NPs unstable electrically and thermally. So it is obvious that after a few picoseconds electric potential and thermal energy can overcome the binding energy of Ag ions, which are being emitted into the surrounding glass matrix [55, 102, 103]. By way of an experimental luminescence study, Podlipensky et al. [103] have proven the presence of Ag ions in the glass matrix emitted upon femtosecond laser irradiation. Additionally, using transmission electron microscopy (TEM) after fs laser irradiation small Ag aggregates around the shape-transformed nanoparticle [15, 104] could be observed indicating that this ion emission leads to partial dissolution of the nanoparticles.

The physical concept behind these ion emission processes is mainly the so called Coulomb explosion [102], which is a direct consequence of the nanoparticle charging. The repulsive Coulomb forces among the accumulated charges lead to the dissolution (destruction) of the nanoparticle. Even extreme cases of nanoparticle dissolution mechanisms were observed for nanoparticles in aqueous medium [53], where not only the ions but also some small fragments could leave the nanoparticle because of the soft surrounding. Nevertheless, independent of the way it happens, the total volume of the nanoparticle is reduced over time due to material ejections. In the case of a glass matrix isotropically emitted

Copyright © 2010. Nova Science Publishers, Incorporated. All rights reserved.

ions can meet the already trapped electrons (result of NPs ionization) and recombine with them to atoms or small silver clusters; the latter can be seen in the TEM images [15, 104]. It is obvious that this process of ion ejection will also lead to changes in the energy relaxation (temperature distribution) of the NP-glass system. Some part of the energy will be taken from the nanoparticle and, via kinetic energy of the ions, be transferred to the glass when the ions are trapped there. This will cause much faster heating (compared to merely heat conduction as discussed above) of the first few nanometer shell around a NP.

All the processes discussed so far for the strong excitation regime are in some respect relevant to the fs laser induced NP shape transformation. We will now develop a self-consistent model for this phenomenon, using all the above ingredients, which are an outcome of a number of experimental studies and in-depth analysis of the obtained results.

3.6. Mechanism of the Shape Transfomation of Spherical Ag Nanoparticles in Soda-Lime Glass upon fs Laser Irradiation

To arrive at a reliable and self-consistent model of the SP assisted shape modifications of spherical Ag nanoparticles embedded in soda-lime glass by excitation with intense ultrashot laser pulses, we start with a brief summary of instructive experimental results. The following experimental facts can be stated:

- The process has a threshold [84], i.e., laser assisted modifications occur only when the laser pulse intensity is sufficiently high (≥ 0.2 TW/cm^2, for excitation at 400 nm).
- Only intensity defines the principal shape of the transformed particles: below ≈ 2 TW/cm^2, the NPs have prolate, above this "second threshold" oblate shapes; the number of laser pulses plays mostly an accumulative role, in particular seen as increase of the aspect ratio of prolate NPs with increasing number of pulses [84].
- The anisotropy of shape modifications is strongly correlated with the laser polarization [104, 105]. This indicates that the processes defining the NP shape are occurring already during the presence of the laser field; so obviously the directed electron emission from the nanoparticle is an important ingredient of the mechanism.
- Applying too high peak pulse intensity or number of pulses, the extinction SP band bleaches and finally disappears completely [84]; this indicates that partial destruction or dissolution of silver NPs is involved in the modification mechanism.
- Modification of the NP shapes stops when the wavelength of irradiation is lying in the blue wing of SPR [106]. However, subsequent irradiation by the pulses at longer wavelength (or simultaneous two wavelengths irradiation) causer further shape transformation. Therefore one may presume that the EFE determines the directional ionization and plays a key role in the mechanism of NP shape transformation.
- Preheating of the sample up to 150-200°C frustrates controlled shape transformation; instead total dissolution of the Ag nanoparticles is observed upon laser irradiation [107]. It is anticipated that this effect is due to the increased mobility of silver cations at higher temperature, which prevents the formation of a cation shell in close vicinity to the NP; in other words, the positively charged shell of silver cations seems to be crucial for the shape modifications.

Copyright © 2010. Nova Science Publishers, Incorporated. All rights reserved.

These conclusions drawn from various experiments show that fs laser assisted modifications of Ag nanoparticles incorporated in glass is accomplished by a rather complex mechanism. We will therefore first give a general discussion of the anticipated sequence of processes after intense laser excitation, and then specify different cases, i.e. below or above the second threshold, and linear or circular polarization.

The two central effects initiated by the incoming laser pulse are photoionization of a silver nanoparticle and strong heating of NP and surroundings. Starting with the latter, we recall that immediately after excitation, the SP relaxes rapidly (within several hundreds of femtoseconds [47, 51]) into a quasi-equilibrated hot electron system via electron-electron scattering. Next, the hot electrons cool down by sharing their energy with the nanoparticle lattice via electron-phonon (e-ph) couplings [47], thereby heating up the particle. The estimations of maximal electronic and lattice temperature, based on the 2TM (section 3.3), give values in the range of 10^4 K for the electron system and a lattice temperature above melting temperature for bulk silver. Although the real temperature of a nanoparticle is expected to be much lower (because of the nanoparticle energy losses caused by the electron and ion emission, see section 3.5), one can conclude that in the course of dissipation of the absorbed laser energy the nanoparticles and as a result its immediate surroundings experience a strong transient 'temperature' increase, which is at least connected with strongly enhanced local mobility of electrons, ions and atoms.

Parallel to heating, photoionization of the silver nanoparticles will occur during exposure to intense fs laser pulses. The physical idea is that the SPR enhances the electric field of the laser pulse close to an Ag particle by a few orders of magnitude, with the highest fields located at the poles (with respect to laser polarization) of the nanospheres [3]. This can lead to enhanced directed emission of (already hot) electrons from the particle surface [54, 98], preferentially parallel to the laser polarization. But also an isotropic, thermal electron emission has to be regarded in the time of the electron-phonon system thermalization. The anisotropy of the direct, laser-driven electron ejection is thought to provide the preferential direction for the following particle shape transformation. Possibly the high electric field in the vicinity of the metal nanoparticle can even exceed the breakdown threshold of glass resulting in high-density electron plasma formation and even ablation of the glass matrix on the poles of the nanosphere. Regardless whether this happens, the free electrons in the matrix will lead to formation of colour centers (trapped electrons) in the surroundings of the Ag nanoparticle [103], which also play an important role for the particle shape modifications. The free electrons as well as the color centers have strong absorption at the SP resonance [18] which might result in resonant coupling of SP oscillations to the matrix [108]. Finally, the ionized positively charged core of the Ag nanoparticles is unstable and the Coulomb forces will eject silver cations, which form a cationic shell in the vicinity of the nanoparticle [103]. Clearly the radius of such a cationic shell is determined by the diffusion length of the silver cations and thus strongly depends on the local temperature.

All those effects are transient phenomena, being controlled either directly by the electric field of the laser pulse or indirectly by the temperature rise induced by it. Thus the pulse intensity is doubtless the decisive parameter for the shape transformation of the metal nanoparticles, and it is obvious to assume that the prevalence of individual processes, due to their different intensity dependence, leads to the characteristic intensity regions yielding prolate or oblate shapes. Our investigations strongly suggest the following picture.

Copyright © 2010. Nova Science Publishers, Incorporated. All rights reserved.

Using linear polarization in the low intensity region (i.e. 0.2 - 2 TW/cm^2) [84], SP field enhancement stimulates the fastest process, field-driven electron emission from the surface of the metal particles [Figure 17(a)]. The emission process happens within a few fs [55], i.e. without delay against the laser pulse. The ejected electrons will then be trapped in the matrix forming color centers close to the poles of the sphere. The ionized nanoparticles are likely to emit Ag ions in statistical directions, in particular when after a few picoseconds electron thermalization and heat transfer to the silver lattice is finished. The resulting positively charged shell of silver cations [103] around the particle meets trapped electrons which are mostly concentrated at the poles [Figure 17(b)]. After some picoseconds they can recombine to Ag atoms [Figure 17(c)], which finally diffuse back to the nanoparticle and precipitate mainly at the poles. Silver atoms which are situated relatively far away from the main NP can locally precipitate to each other forming very small clusters (halo). In multi-shot mode, remaining silver ions may also act as trapping centers for the electrons being emitted by the next laser pulse [Figure 17(d-f)]. Possibly also the fact that electrons are favourably being trapped close to the poles, while ions which are mostly concentrated around equator (because the purely thermal emission of electrons leads to less electrons available for ion annihilation there), may cause local electric field distributions which influence the directional properties of electron and ion emission for following laser pulses. All these processes lead obviously to a step-by-step growth of the Ag particles along the laser polarization, explaining the finally observed prolate spheroidal shape [104] [Figure 17(g, h)]. Especially, in the growing process most of the very small silver clusters having precipitated above the poles (defined by the laser polarization) become closer to the main nanoparticle and can be incorporated in it again, while the clusters situated around the equator contribute only to the halo formation [104]. At the same time, it is obvious that in the case of circular polarization the rotating electric field should lead to precipitation around the equator of a NP rather than at the (no longer defined) poles resulting in oblate spheroidal shape [105]; and the halo is forming in perpendicular direction (direction of propagation). Figure 18 illustrates this case in analogy to Figure 17.

With increasing peak pulse intensity we expect higher temperature, thus larger radius of the cationic shell. In this case, the farthest clusters located even in direction of laser polarization can not diffuse back to the main nanoparticle, and in consequence a larger halo region can be observed [84]. It should be mentioned that all the processes discussed require the presence of a rigid, ionic matrix. This may explain why up to now the laser-induced transformation of metal nanoparticles has only been observed in glass nanocomposites.

In the high intensity range (above 2 TW/cm^2) [84] using linear polarization again, we suggest that, in addition to the processes already discussed, the very high local electric field at the poles of the sphere along the laser polarization can accelerate the free electrons so strongly that they induce a high density plasma by avalanche ionization of the glass [Figure 19(a)]. The following plasma relaxation transfers energy from electrons to the lattice (e-ph interaction) on a time scale much faster than the thermal diffusion time. This can finally result in ablation of the material on the interface between glass and metal inclusion leading to partial destruction of the nanoparticle on the poles [Figure 19(b)], or direct emission of the plasma components further away into the matrix. In any case that process produces oblate rather than prolate particle shapes. It seems very plausible to anticipate that the characteristic intensity ($I_2 \approx 2$ TW/cm^2) marks the balance between (i) the processes leading to particle growth along the laser polarization and (ii) the beginning plasma formation at the particle/matrix interface counteracting this growth.

Copyright © 2010. Nova Science Publishers, Incorporated. All rights reserved.

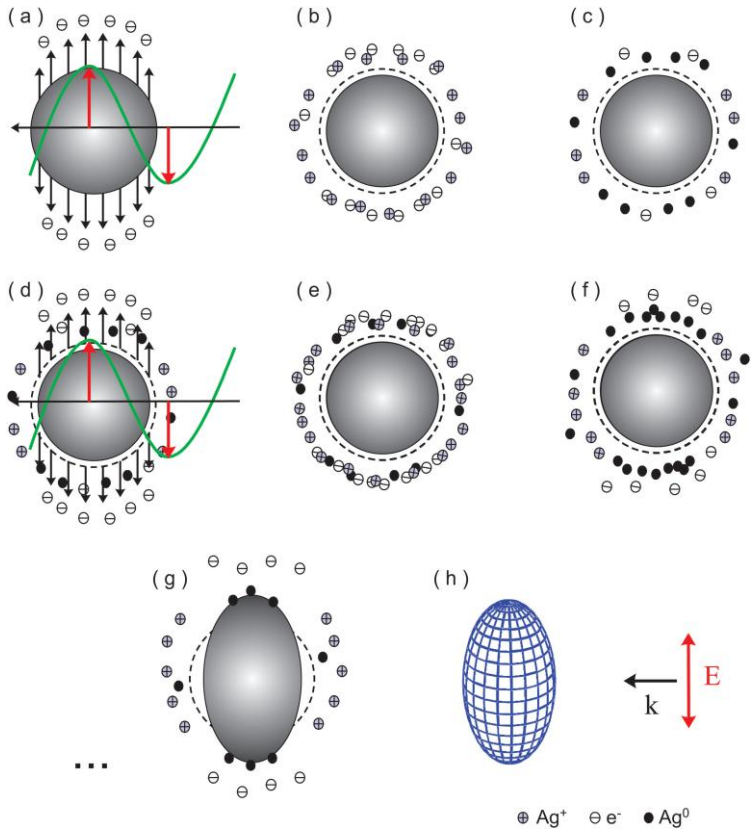

Figure 17. Laser assisted shape transformation of the metal nanospheres in the case of irradiation by linearly polarized laser pulses in low intensity, multi-shot mode.

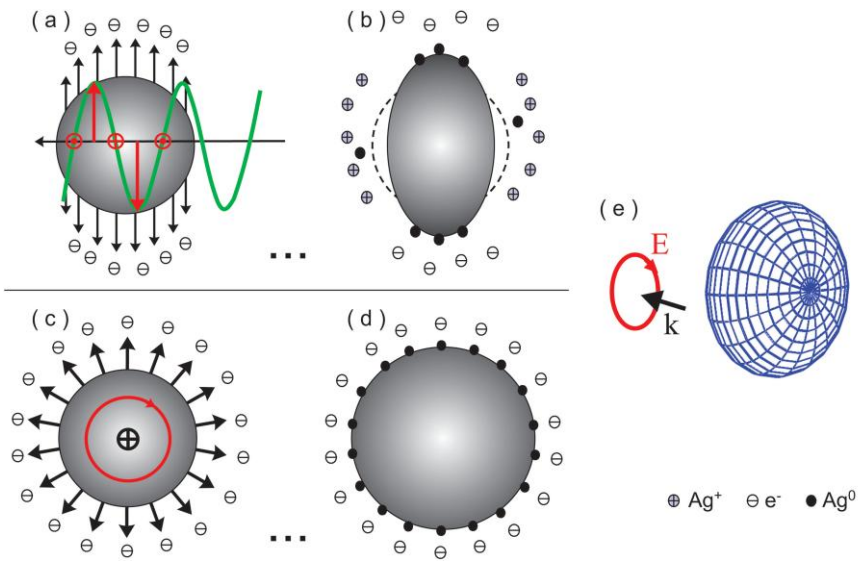

Figure 18. Laser assisted shape transformation of the metal nanospheres in the case of irradiation by circularly polarized laser pulses.

Copyright © 2010. Nova Science Publishers, Incorporated. All rights reserved.

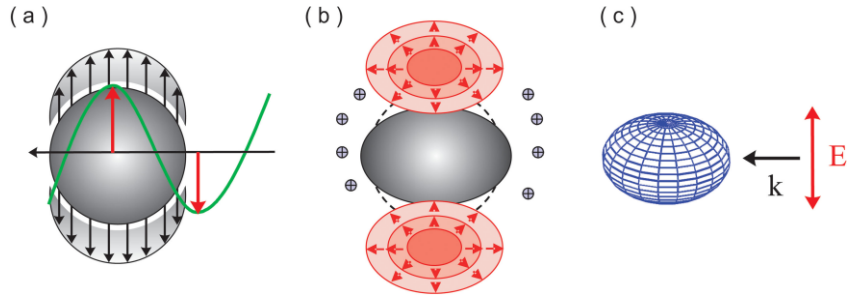

Figure 19. Laser assisted shape transformation of the metal nanospheres in the case of irradiation by linearly polarized laser pulses, high intensities.

We point out that for any type of shape transformation of spherical Ag nanoparticles embedded in soda-lime glass induced by fs laser pulses, the main point of the proposed scenario is the SP assisted (field-driven) photoelectron emission from the metal surface, which defines the particle symmetry. The next steps of the mechanism 'only' decide via the applied laser pulse intensity and the resulting local heating if the nanoparticles can develop their final shape in an accumulative process (multi-shot mode) or if, at too high intensity, a few or even one laser pulse is sufficient to destroy the particle completely.

After having elaborated the physical model for NP shape transformation we will in the following sections describe in some detail several irradiation and sample parameters with respect to their effect on the degree of nanoparticle deformation. This discussion will, on the one hand, confirm the proposed mechanism and, on the other hand, pave the route how our innovative technology can be optimized towards production of optically micro-structured elements with tailored local dichroism.

4. Effect of Pulse Intensity and Writing Density on the Nanoparticles' Shape

We start this discussion with results obtained applying laser pulses of quite different peak intensities and 'writing density'; the latter refers to the question how many pulses are on average hitting one position on the sample. In particular, the following questions will be addressed: (i) Is there a single pulse intensity threshold for deformation, or can lower intensity be compensated by irradiating more pulses? (ii) At which intensity / number of pulses applied does the transition from prolate to oblate shape occur, and which particle shapes are produced there? (iii) What happens with the particles going to very high irradiation intensity and/or large number of pulses applied to one spot?

For measurements of the intensity dependences we used a technique of space resolved transmission spectra, which has been described in details previously [18]. In combination with laser beam profile measurements the space resolved spectra were correlated with local laser pulse intensities. We have produced various dichroic areas on the sample by irradiating different numbers of laser pulses (ranging from 1 to 5000) to the same spot. The huge number of spectra resulting from the described analysis can only be shown here in a parametrized form (see below). Nonetheless, to demonstrate the quality of the spectra and explain the parametrization, a few examples are shown in Figure 20.

Copyright © 2010. Nova Science Publishers, Incorporated. All rights reserved.

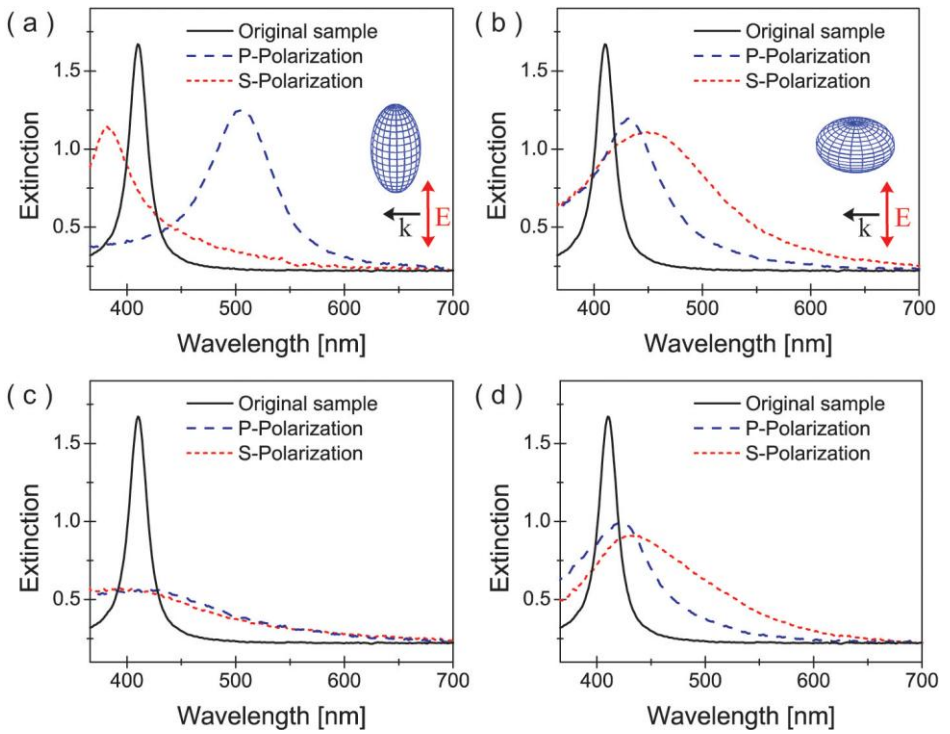

Figure 20. Polarized extinction spectra of original and irradiated samples: a) multi-shot regime (1000 pulses per spot), peak pulse intensity I_p = 0.6 TW/cm^2; b) single shot regime, I_p = 3 TW/cm^2; c) multi-shot (5000 pulses per spot), I_p = 1.2 TW/cm^2; d) single shot, I_p = 3.5 TW/cm^2.

Figures 20(a, c) represent the case of multi-shot, Figure 20(b, d) that of single shot irradiation. In general, the original SPR band peaked at λ = 413 nm splits into two polarization dependent bands upon irradiation, but with significant dependence on peak pulse intensity and number of pulses applied. Figure 20(a) shows multi-shot irradiation (1000 pulses at 0.6 TW/cm^2), which produces bands on different sides of the original SPR band: for polarization parallel to that of the laser (p-polarized, blue line), the peak position is shifted to longer wavelengths, while for perpendicular polarization (s-polarized, red line) the band is observed at a shorter wavelength.

This can be explained on the nanoscale by prolate silver spheroids with their symmetry axes oriented along the laser polarization (see previous section) [inset in Figure 20(a)]. In the single-shot case [Figure 20(b), referring to 3 TW/cm^2], the s-polarized band has a larger red-shift than the p-polarized band. Additionally, both bands are red-shifted in this case. These spectra are due to oblate Ag particles [inset in Figure 20(b)], again with their symmetry axes oriented along the laser polarization [104]. At even higher intensities and, in particular, in the multi-shot regime, the spectral shifts are becoming smaller and the band integrals decrease. These effects, which are obviously indicating – at least partial – destruction of the silver nanoparticles, are most clearly seen in Figure 20(c) (representing 5000 pulses at 1.2 TW/cm^2), but tentatively also in the single-shot regime [Figure 20(d), 3.5 TW/cm^2].

The extreme cases of single- and multi-shot compared in Figure 20 pose the question how a continuous variation of peak intensity and number of applied pulses affect the resulting spectral parameters such as orientation of dichroism, peak position and integrated extinction

Copyright © 2010. Nova Science Publishers, Incorporated. All rights reserved.

of the SPR bands. Figure 21 presents a selection of pertinent results in a parametrized form: the peak positions of the two SP bands observed with polarization perpendicular to each other ('p' referring to parallel with respect to laser polarization) are given as a function of intensity, with increasing number of applied pulses from (a) to (f). It is seen that generally laser-induced spectral changes start at intensities of 0.2-0.3 TW/cm^2. For single-shot irradiation [Figure 21(a)], increase of pulse intensity above this threshold leads to a shift of both SP bands towards longer wavelengths. First, in the region of ~0.4 TW/cm^2 one observes a rather weak dichroism, where the p-polarized SP band has the stronger red-sift. At approximately 2 TW/cm^2 the extinction is becoming isotropic again, seen as crossing of the curves for s- and p-polarization at λ = 427 nm. Above 2 TW/cm^2 a reversed dichroism is observed, i.e. the s-polarization band is now more red-shifted than the p-band. The maximum spectral gap between p- and s-polarized SP bands (peaks at 430 nm and 450 nm, respectively) is found at ~3.2 TW/cm^2. At still higher intensity beyond 3.2 TW/cm^2 (not shown in the Figure 21) the SP bands move back towards shorter wavelengths and the integrated band extinction decreases, indicating (partial) destruction of the silver nanoparticles.

Irradiating 25 pulses to one spot [Figure 21(b)] we find in general a similar peak pulse intensity dependence of the induced dichroism with the two characteristic intensity ranges. There are, however, some important differences compared to the single-shot case: (i) the dichroism (spectral spacing between the polarization dependent bands) is much larger in the low intensity range (below 2 TW/cm^2); (ii) between 0.3 and 1.3 TW/cm^2 the s-polarized SP band is blue-shifted relative to the original SP peak at 413 nm; (iii) the region of reversed dichroism has shrunk considerably, because already from ~2.3 TW/cm^2 on bleaching of the extinction (particle destruction) starts. In such cases the analysis of the SP peak central wavelengths was halted (grey regions in Figure 21).

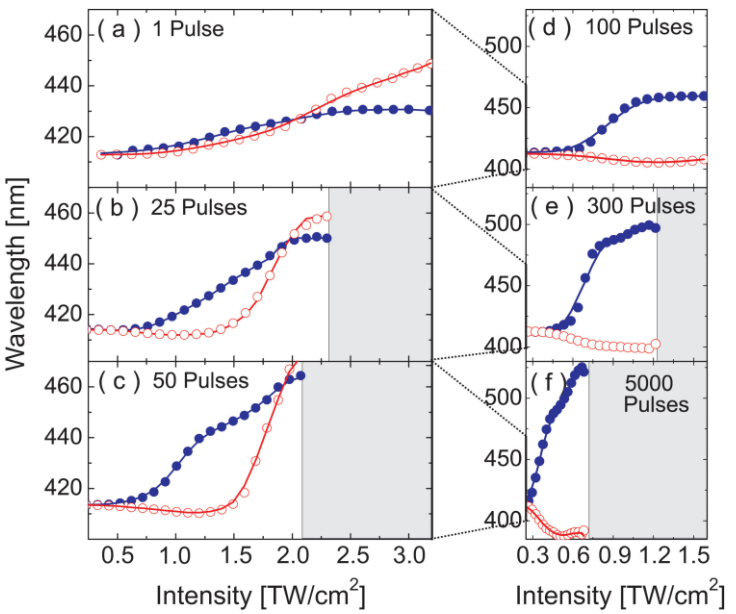

Figure 21. Dependences of the SP maximum in polarized extinction spectra of soda-lime glass with spherical Ag nanoparticles on laser pulse intensity by irradiation at 400 nm. Red circles – s-polarization, blue solid circles – p-polarization, light gray area – region of the SP bleaching.

Copyright © 2010. Nova Science Publishers, Incorporated. All rights reserved.

If the number of pulses irradiated to one spot is further increased one observes that the maximum dichroism grows and is reached at lower peak pulse intensity [Figures 21(c-f); note the scales change from Figure 21(c) to 21(d)]. The crossing point of the curves for the p- and s-band, however, remains approximately constant around 2 TW/cm^2, while the region of beginning particle destruction comes down to lower intensity step by step to finally ~0.7 TW/cm^2 at 5000 pulses per spot [Figure 21(f)]. Thus, for 100 or more pulses per spot we can only observe the low intensity region of spectral changes with the corresponding dichroism, because further increase of intensity leads to destruction of nanoparticles and results in a bleaching of SP bands. The maximum dichroism recognized in our experiments was found in the case of 5000 pulses, where, at the pulse intensity of 0.65 TW/cm^2, the p- and s-bands are peaked at 525 nm and 390 nm, respectively. It should be mentioned here that even more than 5000 pulses per spot do not increase the induced dichroism further.

As was discussed previously and also shown in Refs. [14-17, 103], the principal persistent modifications induced by fs laser pulses do not only comprise the transformation of nanoparticle shapes, but also the generation of a surrounding region of small Ag particles ('halo'). While the first effect explains the splitting of the SP band (dichroism), the second one causes, in a first approximation, a modified matrix refractive index which may lead to isotropic spectral shift of the SP bands [104].

With this additional information, the above presented results on peak intensity and irradiation density (number of pulses per spot) of the fs laser pulses allow us the following general conclusions: independent of the number of pulses applied, there exist two special intensities $I_1 \approx 0.2$ TW/cm^2 and $I_2 \approx 2$ TW/cm^2. For intensities $I < I_1$ there is no spectral change at all, and at $I = I_2$ only spectral shift of the SP band to long wavelengths is observed. In the intensity region $I_1 < I < I_2$, dichroism is found with the larger red-shift for the p-polarized SP band, while for $I > I_2$ a reversed dichroism is seen. This indicates that the processes of shape transformation are controlled by the laser pulse intensity (energy density per pulse), while the number of pulses applied mainly accumulates the changes caused by each single pulse. Looking in more detail to the low-intensity region $I_1 < I < I_2$ first, the dichroism observed there is associated with a transformation of the original silver nano-spheres to prolate spheroids with their long axis oriented parallel to the laser polarization [104]. Anticipating volume conservation for the silver, Mie theory predicts for this case blue-(red-) shift of the SPR of the short (long) particle axis, the spectral spacing between the two bands being correlated to the aspect ratio of the nanoparticle. So the growth of dichroism with increasing number of pulses can be explained by successive increase of the particles' aspect ratio.

A red-shift of both bands however, as observed for 1 pulse for all intensities or at $I >$ 1.5 TW/cm^2 at 25 or 50 pulses, can only be explained by additional modification of the host matrix in the vicinity of the nanoparticle which was shown in Ref. [103, 104]. So it is obvious to assign the increasing general red-shift for higher pulse intensities to a growing influence of the halo. In the high-intensity region $I > I_2$, oblate spheroids with their symmetry axes (short axis) along the laser polarization are produced. Again the fact that both SP bands are red-shifted indicates significant modification of the particle surroundings, because otherwise the short axis should show a blue-shifted SP band.

To get an idea about the nanoscopic modifications in the region around $I_2 \approx 2$ TW/cm^2, and in the region of beginning particle destruction (where SP band extinction starts to

Copyright © 2010. Nova Science Publishers, Incorporated. All rights reserved.

decrease again), transmission electron microscopy is quite instructive. It should be mentioned however that it is not possible to assign exactly a local irradiation intensity to a special TEM image. Figure 22 shows two examples for particle shapes found after single-shot irradiation: Figure 22(a) refers to intermediate intensity (around I_2), Figure 22(b) to very high intensity (significantly above I_2). In the first case, a fairly spherical particle with a limited halo region is seen. In contrast, at very high intensity there is on one hand a non-spherical central Ag particle, but a much larger region of small silver fragments. Considering that this image was taken after one laser pulse only, it is quite plausible that after several pulses of sufficiently high intensity the particles are destroyed completely and the pertinent SPR band vanishes. In our experiments, total bleaching of the samples has been observed at intensities higher than 1.2 TW/cm^2 applying at least 5000 pulses per spot. We interpret this finding as complete destruction of the Ag nanoparticles into small fragments without distinct SPR.

On the low-intensity side, in particular if one irradiates the sample with many pulses only slightly above the modification threshold (0.2 - 0.3 TW/cm^2), the maximum spectral shift (and thus the maximum particle aspect ratio) achievable is limited [17], because due to successive particle deformation the SP band polarized along the laser polarization moves out of resonance decreasing the interaction with the laser pulses. In the next section we will discuss how this problem can be circumvented by proper selection of irradiation wavelengths.

Summarizing this section, we want to point out that laser induced shape transformation of silver nanoparticles embedded in glass using fs pulses requires a minimum peak pulse intensity of 0.2 TW/cm^2. Above this first threshold, linearly polarized pulses are able to create uniformly oriented, prolate spheroids with different aspect ratios depending on actual intensity and number of pulses per spot. Exceeding a second threshold of ~2 TW/cm^2, one observes a reversal of the observed dichroism, which can be explained by oblate spheroids being produced by the laser pulses. In both cases the symmetry axes of the spheroids is oriented along the linear laser polarization. It should be also mentioned here that although oblate spheroids are also being created for circular polarization, their symmetry axes are given by the laser propagation direction [105] and such shape transformation is only possible in low intensity, multi-shot mode. In all situations, too high intensity or too many applied pulses cause destruction of the particles into very small fragments, macroscopically observable by fading of the SP absorption bands.

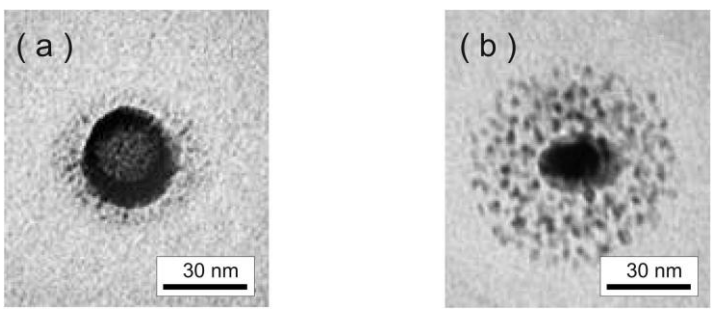

Figure 22. TEM of Ag nanoparticles in soda-lime glass after irradiation: (a) in the region around $I_2 \approx 2$ TW/cm^2, (b) partially destructed nanoparticle.

Copyright © 2010. Nova Science Publishers, Incorporated. All rights reserved.

5. "OFF-RESONANT" EXCITATION: IRRADIATION WAVELENGTH DEPENDENCE

In this section we will discuss the influence of various irradiation wavelengths on the dichroism achievable in soda lime glass with embedded silver nanoparticles. In the previous chapter we have seen that the position of p-polarized SP band can only be red-shifted by a limited amount (to a peak position of 530 nm when using fs laser pulses at 400nm). Any further increase of intensity or number of pulses applied to one sample position leads to bleaching of the SP bands, which can be explained by (partial) nanoparticle destruction. As many possible applications for optical elements prepared by the proposed technique require polarization contrast at larger wavelengths in the visible and near IR spectral range, it is attractive to look for ways to meet this needs.

We will show that tuning of the irradiation wavelength is a very powerful parameter for reshaping Ag nanoparticles to large aspect ratios. First, we have found that even rather strongly red-shifted excitation (with respect to the initial SP band) can, in spite of the low remaining SP absorption in this region, still very effectively induce a nanoparticle shape transformation to spheroids. In particular, such 'off-resonant' irradiation can create an even larger dichroism than resonant excitation. Second, we will demonstrate that subsequent irradiation by increasing laser wavelengths increases the particles' aspect ratio and thus the induced dichroism further, allowing to shift the p-polarized SP band down to the near infrared region. At the end, we will show the results of simultaneous irradiation of the sample by the pulses with different wavelengths, which results in a similar elongation of nanoparticles as it is obtained by subsequent irradiation.

5.1. Long Wavelength Irradiation

It should be mentioned here that all experimental results shown below have been conducted in the multi shot regime. Figure 23(a) gives a first example for "off-resonant" excitation. We will use this notion in the following to characterize a situation where the laser wavelength is considerably larger than the maximum of the SPR. The polarized extinction spectra in Figure 23(a) were measured on a sample containing Ag nanoparticles which was irradiated by 1000 pulses per spot at λ = 550 nm with a peak pulse intensity of 1.2 TW/cm^2. The effect of this irradiation is similar to the one obtained by resonance excitation, namely, the original SP band of the spherical Ag nanoparticles peaked at λ = 413 nm splits into two polarization dependent bands. However, in this case, the p-polarized SP band (seen with light polarized parallel to the laser polarization) is peaked at 620 nm, while the s-polarization (perpendicular to laser) is shifted to shorter wavelengths, overlapped by a small residual absorption at 413 nm (due to small not transformed particles [106]). This large spectral gap of p- and s-polarized bands leads to a good polarization contrast at 620 nm, i.e., low and high transmission for p- and s-polarization, respectively. In analogy to previous experiments, we can easily conclude that also in case of "off-resonant excitation" the nanoparticles are transformed into prolate spheroids. From the spectral gap between the maxima of polarized extinction bands being significantly larger than in case of resonant excitation, it is obvious that the aspect ratio of the reshaped nanoparticles is also larger than for resonant excitation.

Copyright © 2010. Nova Science Publishers, Incorporated. All rights reserved.

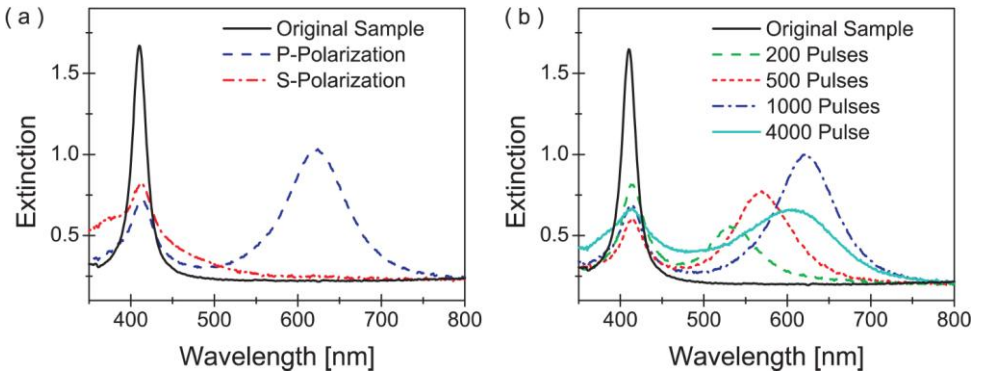

Figure 23. Polarized extinction spectra of samples with Ag nanoparticles irradiated at 550 nm in multi-shot regime. (a) 1000 pulses in single spot, peak pulse intensity 1.2 TW/cm^2. (b) P-Polarization, different number of pulses applied, peak pulse intensity 1.3 TW/cm^2.

Additionally, similar to the case of resonant irradiation, the particle elongation and the corresponding magnitude of induced dichroism can be tuned by variation of the peak pulse intensity and/or by number of pulses per spot. Figure 23(b) illustrates the effect of different writing densities for samples irradiated at 550 nm with peak pulse intensity of 1.3 TW/cm^2. Only the p-polarized extinction spectra are shown. It is clearly seen that, increasing the number of applied pulses from 200 to 1000, both peak wavelength and integrated extinction of the p-polarized band are increasing, while the absorption peak in s-polarization moves slightly to shorter wavelengths [not shown in Figure 23(b)]. For further increase of the writing density, however, the p-polarized SP band starts to shift back towards shorter wavelengths, accompanied by decrease of amplitude and increase of bandwidth. This bleaching due to partial destruction of the silver nanoparticles is clearly seen in the spectrum obtained after shining 4000 pulses per spot on the sample. Again the off-resonant irradiation behaves very similar to the resonant case: up to a certain amount of pulses per spot, the dichroism can be increased by applying a larger number of pulses to the sample, but beyond this value (in the range of 1000 pulses/spot) the maximal spectral shift is limited by beginning destruction of the nanoparticles.

The results discussed so far show that irradiation of the samples at λ = 550 nm with optimum laser intensity and number of pulses leads to a larger spectral gap between the SP bands than resonant excitation at λ = 400 nm can do. Therefore, one should expect a further increase of the induced dichroism when samples are being irradiated with even more off-resonant, longer wavelengths. We have also looked into this effect. Figure 24 shows three examples for extinction spectra of samples irradiated at different wavelengths, here λ = 490 nm, 560 nm, and 610 nm. The parameters of irradiation (laser intensity and number of pulses per spot) were chosen so that for each laser wavelength the maximal spectral shift was reached. It is clearly seen that in fact irradiation with the longer wavelengths leads to a larger spectral gap between polarized SP bands. However, moving the irradiation wavelength further beyond 610 nm, the efficiency of nanoparticle shape transformation decreases more and more, and finally the laser pulses do not evoke any measurable extinction changes anymore. For our samples this was the case for $\lambda \geq 670$ nm; for instance, even the very strong laser fundamental at 800 nm does not cause dichroism when irradiated on a sample with original, spherical Ag nanoparticles.

Copyright © 2010. Nova Science Publishers, Incorporated. All rights reserved.

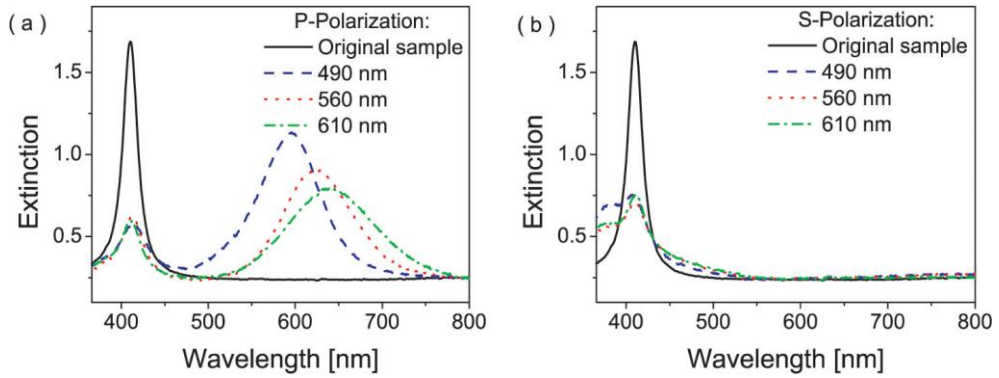

Figure 24. Polarized extinction spectra of original and irradiated sample with Ag nanoparticles by different wavelengths irradiation. Intensity and number of pulses are optimized to achieve the best dichroism. (a) P-Polarization; (b) S-Polarization.

The obvious conclusion from the above results is that there is a threshold in absorption efficiency, which limits the long wavelength irradiation. This and all other findings are in a good agreement with theory. As it was shown, the extinction efficiency decreases rapidly for wavelengths longer than SP resonance and at 800 nm it becomes almost zero (see for example Figure 15). At the same time, the E-field enhancement, which is present in the long wavelength region (Figure 15), increases the probability of direct electron emission and makes the shape transformation of nanoparticles possible even for off-resonant excitation. And, as long as absorption efficiency and laser intensity are high enough to emit ions from the particles and transform their shape at least a little bit after the first few pulses, the process is expected to work, because even very minor changes per pulse shift the p-polarized SP band closer to resonance with the irradiation wavelength and so, step by step, increase the efficiency of shape transformation for the next pulse. The process then will go on until the excitation wavelength is located considerably far in the blue wing of the p-polarized SP band. From then on the same mechanisms like in the case of resonant excitation lead to particle destruction and limit the spectral gap achievable by single-wavelength irradiation.

5.2. Subsequent Irradiation

As one could see in the previous section, the long wavelength irradiation leads to the higher elongation of nanoparticles. However, this type of irradiation has also the limit as in the case of resonance excitation. Nevertheless, we have found that this limitation can be overcome by multi-wavelength irradiation, i.e. subsequent irradiations of the same sample area by different laser wavelengths. If in particular after the first step the laser is tuned to another off-resonant position on the long-wavelength side of the already modified SP resonance, much larger dichroism compared to single-wavelength irradiation can be prepared. As an example, Figure 25(a) shows the extinction spectra of a sample which was first irradiated at 535 nm, then at 670 nm with polarization parallel to the long axis of the already modified particles. It is clearly seen that the p-polarized band shifts in the second step further from peak position 560 nm to 760 nm. At the same time, the absorption peak in s-polarization shifts to shorter wavelengths. This large spectral gap between s- and p-polarized bands

Copyright © 2010. Nova Science Publishers, Incorporated. All rights reserved.

corresponds to an aspect ratio of (a/c) > 3 of the nanoparticles, which is proven by the TEM image shown in Figure 25(b). Clearly, subsequent irradiation with increasing laser wavelength leads to very high dichroism, and because of the minimal losses for s-polarized light at 760 nm, the polarization contrast is also high. It should be mentioned here that further red-shift of the p-polarized SP band can be done by further irradiations with successively longer laser wavelengths at each step. We have performed preliminary experiments with a third irradiation at λ = 800 nm, which proved this idea. It is obvious that, by proper choice of the irradiation sequence and optimization of the pertinent laser parameters, the range of dichroism induced by this technique can be extended into the IR region.

5.3. Two Wavelengths Irradiation

If subsequent irradiation by different wavelengths can create larger aspect ratio of the nanoparticles embedded in glass, it is an obvious idea to save time and to try simultaneous irradiation. We have done this and found that, other than in the previous case where the pulse intensities of subsequent irradiation were roughly the same (around 0.5-1.5 TW/cm^2), it is sufficient to include a quite small portion of the larger wavelength. In Figure 26 we show the results of irradiating a sample simultaneously with 532 and 800 nm. The intensity of the green pulses was around 1.4 TW/cm^2, while the 800 nm pulses had an intensity which was lower by several orders of magnitude. Applying 1000 pulses (for every wavelength) leads to similar results as presented above for the case of long wavelength irradiation (Figure 26, dotted curve). The p-polarization band is peaked at ~570 nm, while the s-polarized SP band is shifted to the UV region (not shown). Increasing the number of pulses to the value of 2000 results in a bleaching (amplitude decrease) of the p-polarized SP band at ~570 nm and appearance of an additional band in the region of 750 nm (Figure 26, blue, short-dashed curve). Further increase of the writing density strengthens this trend: the amplitude of the band located in the yellow region is decreasing with simultaneous shift of the SP resonance to shorter wavelengths, while the band located in the red region is increasing and shift towards the IR region.

The obtained results can be explained in the following way: The first 1000 pulses lead to the transformation of initially spherical particles to prolate spheroids with aspect ratio varying in the region of 2-2.5. Then, increasing the number of pulses, some number of nanoparticles with the highest aspect ratio starts to elongate further. As a result, the sample contains lower (with respect to the case of 1000 pulses irradiation) number of particles with aspect ratio of 2.5 and additionally some number of nanoparticles, which have the higher elongation. Spectroscopically, we see the amplitude decrease of the band corresponding to the NPs with a/c ~ 2.5 and additional band for higher elongated particles. Further increase of the writing density leads to a decrease of the number of nanoparticles with aspect ratio of 2.5 (therefore, decrease in amplitude) and further rise of the amount of longer NPs with simultaneous increase of elongation (increase of amplitude and red-shift). The residual absorption at 550 nm for the case of irradiation by 4000 pulses is due to the NPs with the lowest aspect ratio, which can not be transformed further [similar to residual absorption at 413 nm in the case of off-resonant irradiation (e.g. Figures 23-24)].

Copyright © 2010. Nova Science Publishers, Incorporated. All rights reserved.

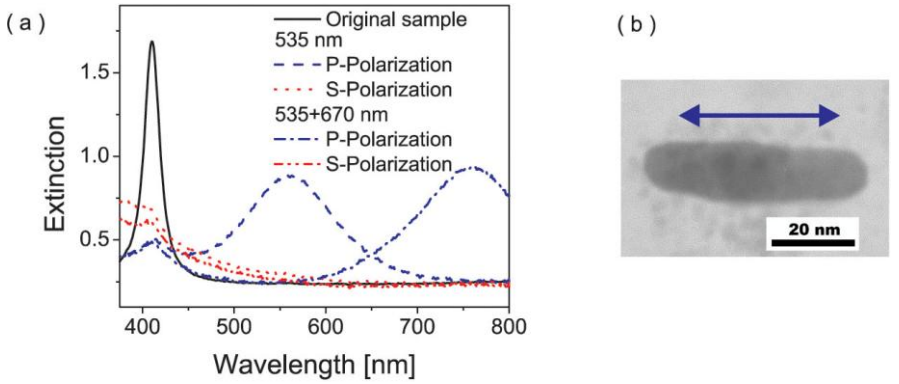

Figure 25. (a) Polarized extinction spectra of samples with Ag nanoparticles irradiated firstly at 535 nm and subsequently at 670 nm laser pulses, 1000 pulses per spot, peak pulse intensity was 1.5 TW/cm^2. (b) TEM image of transformed nanoparticles. Laser polarization is given as an arrow.

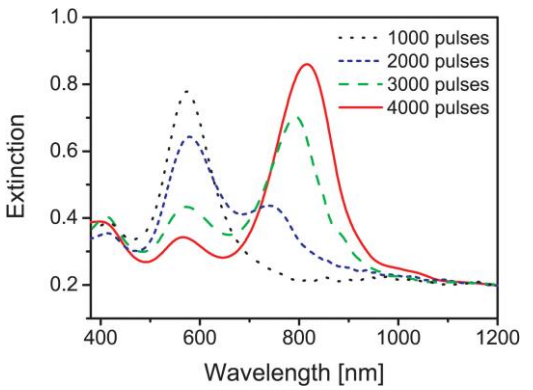

Figure 26. P-polarized extinction spectra of the sample with Ag nanoparticles irradiated simultaneously by the pulses at 532 and 800 nm.

However, the question “how is it possible?” is still open. One of the possible and most probable effects, which can explain the obtained results, is the electric field enhancement and its dependence on the wavelength. During the irradiation of the first 1000 pulses, the electric field enhancement created by the green pulses, enhances the directed photoionization of NP and the existed processes are similar to the ones occurring for ‘usual’ irradiation, while the enhancement for the 800 nm pulses is very weak. However, as the SP resonance band and the electric field enhancement factor are both shifted successively towards longer wavelengths, at some time after 1000 (or more) pulses we reach a situation where the electric field enhancement factor is weak for the green pulses, while its value is now quite high for the pulses at 800 nm. Thus, the pulses at 532 nm are not very efficient for directed photoionization, but they are strong enough to excite the electrons of nanoparticle. In turn, the weak pulses at 800 nm can not excite the nanoparticle, but the high EFE factor now enables directional ionization of still very hot (since being excited by the green pulses) nanoparticle. As a result, the NPs are elongated further. It is also obvious that increasing the intensity of the IR pulses to the modification threshold can lead to the over-excitation of NP, which will result in destruction of the last one. At the same time, if the intensities of both pulses will be lower than the modification threshold, the shape transformation will not be achieved.

Copyright © 2010. Nova Science Publishers, Incorporated. All rights reserved.

In summary, we have to state that laser induced shape transformation of Ag nanoparticles is strongly dependent on the wavelength of fs laser pulses used for irradiation. The proposed technique of subsequent (or simultaneous) multi-wavelength, off-resonant irradiation of metal-glass nanocomposites has a huge potential for preparing polarizing elements with high polarization contrast at any desired spectral position in the visible and near IR spectral range.

6. Effects of Temperature on the Laser Induced Modifications of Ag Nanoparticles

In the previous section we have investigated the influence of laser irradiation parameters on the nanoparticles' shape transformation. Now we focus on the effects of temperature on the reshaping processes. As discussed in section 3, upon absorbing the energy of the laser pulse, the NP and its surrounding matrix experience a strong temperature increase of several hundred degrees for a time window of some ten picoseconds to a few nanoseconds. The pertinent softening of the adjacent glass matrix is crucial for the NP to have some degrees of freedom for the necessary shape changes. On the other hand, it is known that heating the samples to temperatures above the glass transition temperature of soda-lime glass (~600°C) is restoring in any case the spherical shape of the modified Ag nanoparticles [17]. This allows us to assume that the fs laser assisted modification has to occur in the nearest shells where large transient, localized heating is present, while the further shells of surrounding glass should be cold enough to keep the anisotropic shape of nanoparticle.

In addition to these effects, it has also been shown [103], that annealing at moderate temperatures after fs irradiation may cause modification of the SPR bands (and thus also of NP shape and surrounding matrix). So, quite obviously the continuous global sample temperature as well as the transient local heating and cooling have considerable influence on the laser induced shape modification of metallic NPs embedded in glass. Therefore we will in the following discuss the influence of global heating of the samples as well as the local effects arising by heat accumulation in the focal volume of fs laser irradiation as a function of laser repetition rate.

We start our discussion with the effect of irradiating a sample in multi-shot regime with the typical laser parameters, but keeping the sample temperature at a considerably elevated level during irradiation. Figure 27(a) shows polarized extinction spectra of a sample irradiated by 300 pulses per spot with a peak pulse intensity I_p = 0.8 TW/cm^2 at the laser wavelength λ = 400 nm at room temperature. In this case, the p-polarized SP band is centered at 507 nm while the s-polarization band is peaked in the UV region at 383 nm. However, irradiation of a preheated sample using the same laser parameters changes the extinction spectra [Figure 27(b)]. At a temperature of 125ºC, both SP bands are a little shifted towards longer wavelength and, in particular, are broadened and show considerably decreased amplitudes. A further increase of the global sample temperature to 200ºC results in almost complete bleaching of the plasmon bands [short-dashed lines in Figure 27(b)]. Concomitantly, the residual SP bands are further broadened, nearly making the induced dichroism disappear. So the first important experimental finding is that already relatively low temperature increase (with respect to the glass transition temperature) dramatically changes the results of the laser-induced NP shape modification.

Copyright © 2010. Nova Science Publishers, Incorporated. All rights reserved.

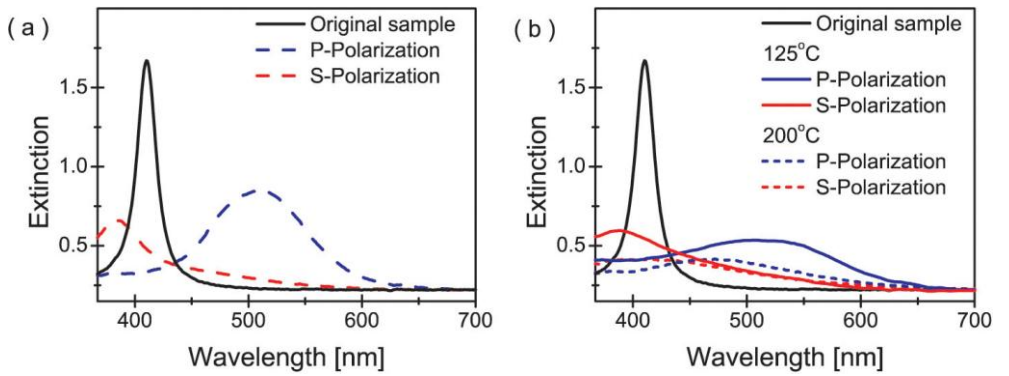

Figure 27. Polarized extinction spectra of original and irradiated samples (λ=400 nm, 300 pulses per spot, repetition rate 1 kHz, peak pulse intensity I_p = 0.8 TW/cm^2): (a) room temperature; (b) 125 and 200ºC.

To better understand the influence of temperature on the laser-induced modification of Ag NPs embedded in glass, we have measured the polarized spectra of samples irradiated at various temperatures from -100ºC to 170ºC in steps of 5-10ºC. The results in parametrized form are presented in Figure 28. The spectral gap between the maxima of the polarized SP bands can be used as an approximate measure of the NPs' aspect ratio. The changes of the band integrals, which include the changes of amplitudes and bandwidths, are directly proportional to the absorption changes of the system.

Looking at Figure 28(a) first, one can recognize three temperature intervals with different behavior of the SP band center positions. In the first interval from -100°C to +80ºC the positions of the bands are nearly constant at ≈ 508 nm and ≈ 384 nm for the p- and s-polarization bands, respectively. Then, towards higher temperature (here up to ≈ 130ºC), the p-polarized SP band occurs at a red-shifted position ($\Delta\lambda_{max}$ ≈ 20 nm), while almost no shift of the s-polarized band is seen. Further increase of the sample temperature leads to a blue-shift of the p-polarized band with respect to the low-temperature limit. The behavior of the band integrals is given in Figure 28(b). Here again almost no temperature dependence is observed in the above defined first interval (-100°C to +80ºC), similar to the behavior of the band centers. At higher temperatures >80ºC, however, the band integrals of p-polarized SP bands start to decrease very rapidly, mainly due to decreasing amplitude. The amplitudes of the s-polarization bands decrease very similarly, but at temperatures above ≈ 120°C this effect is partially compensated by spectral broadening (compare Figure 27), which results in no further decrease of the band integrals above this temperature.

It should be mentioned here that we have also done similar series of irradiations with modified laser parameters (intensity and number of pulses applied); the results were comparable to those given above, i.e. the temperature dependence does not depend on the actual irradiation conditions.

Interestingly, a quite similar behavior of the spectral changes discussed in Figure 28 has been observed in a series of totally different experiments: the sample was irradiated at room temperature by fs pulses of different temporal separation, which was achieved by varying the laser repetition rate. Figure 29 shows selected results in parametrized form, i.e. the band centers [Figure 29(a)] and the band integrals [Figure 29(b)] derived from the polarized extinction spectra band as a function of laser repetition rate. In Figure 29(a) it is clearly seen

Copyright © 2010. Nova Science Publishers, Incorporated. All rights reserved.

that increasing the laser repetition rate from 1 kHz to 10 kHz first leads to a small red shift of the p-polarized band, but for rates ≥20 kHz both polarized SP bands are shifting back towards the original band of spherical nanoparticles. The corresponding band integrals are decreasing monotonously with increasing repetition rates. At 100 kHz we have observed complete bleaching of the bands.

If we increased the writing density, i.e. the number of pulses applied on average per sample position, the observed decreases of absorption and spectral gap occurred already at lower repetition rates. For instance, doubling the writing density to 600 pulses per spot, already at ≈ 20 kHz repetition rate the bands were bleached so strongly that the analysis of SP bands was discouraged. Still, however, the spectra obtained by irradiation at 1 kHz were very similar to those observed for 300 pulses per spot.

Regarding the physical mechanism of NP shape transformation introduced above, we can conclude some novel details from the experimental findings shown in this chapter: first, for a globally increased matrix temperature the diffusion mobility of silver ions increases also, leading to an enlarged radius of the cationic shell arising by Ag^+ emission after absorbing the fs laser pulse. Accordingly, the concentration of silver cations in the immediate surroundings of a NP will decrease resulting in a lower precipitation rate. These processes are well-suited to understand the spectral changes observed when irradiating preheated samples.

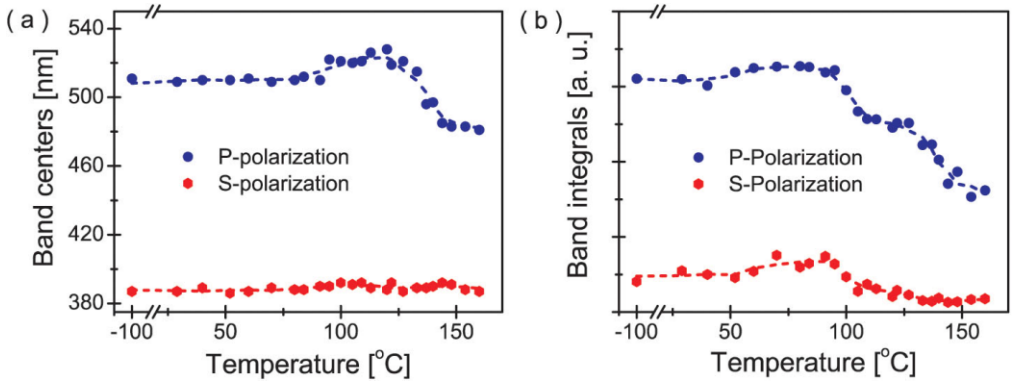

Figure 28. Temperature dependence of polarized extinction spectra (a) band centers; (b) band integrals.

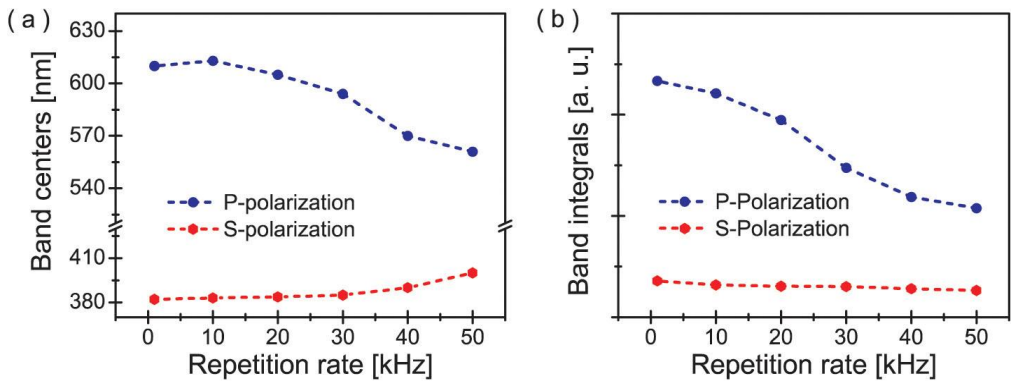

Figure 29. (a) Dependence of polarized extinction spectra band centers on repetition rate; (b) The corresponding dependence of band integrals.

Copyright © 2010. Nova Science Publishers, Incorporated. All rights reserved.

Apparently, in the temperature range from -100 to +80ºC the ionic mobility is too low to cause significant diffusion of the emitted ions. Therefore, both the produced shapes of the NPs [as an example see TEM image on Figure 30(a)] and the pertinent SP bands are fairly constant in this regime. At slightly higher temperature, i.e. in the range of 100-120ºC, the optical extinction spectra start to show characteristic changes: the more prominent effect is decrease of the band integrals. This can be understood assuming that now the mobility of Ag ions has increased so far that the radius of the cationic shell grows; then consequently the precipitation rate of Ag atoms or clusters to the main particle goes down, and the reduced volume of the resulting reshaped NP leads to smaller optical absorption. The second effect, moderate red shift of both polarized SPR bands, can in this case be attributed to those Ag cations which are a little further away from the main NP, but still close enough to each other to precipitate as small clusters. These clusters will form an extended halo region which, via increasing the effective refractive index around the NP, can explain the observed small red-shift. Rising the temperature further, the again increased mobility of the silver cations allows them to diffuse so far away from the nanoparticle that reduction and precipitation rates are diminished more and more. Concomitantly, partial and finally total dissolution of the Ag NPs will occur instead of shape transformation to prolate spheroids. Figure 30(b) proves this assumption and shows an example of partially dissolved NP. Additionally, this figure confirms that roughly 50% of the NP volume is dissolved by ion emissions after applying 300 laser pulses. These experimental findings urge us to consider the effect of ion emissions on the NP-glass system as it was introduced in section 3.5.

Considering the above given calculations on the dynamics of heat flow, we can conclude that transient heating and cooling within a shell of 5-10 nm around the NP are crucial for the question if shape change or dissolution occurs: the results of heat conduction calculations show that, starting from $T = 300$ K, the temperature in distances of $\geq$ 6-7 nm from the NP surface remains below 500 K at any time, while in the nearest shells of the matrix high temperatures up to >1000 K can be reached. Apparently this situation is required to promote the NP shape transformation on one hand, but protect the nanoparticles from total dissolution on the other hand. Any change of parameters extending the spatial range around the NPs where temperatures clearly above 500 K occur, at least transiently, seems to enable particle dissolution. This holds for the temperature-dependent studies as well as for experiments with considerably higher laser intensity, which also resulted in partial NPs dissolution.

If this picture is correct, it should also provide an explanation for the results observed by irradiation of NPs by laser pulses with different repetition rates, i.e. we have to look for a connection between the temporal separation of the laser pulses and the local sample temperature. The connection can be found considering the heat flow from the focal volume (which in beam direction is limited by the thickness of ≈ 2 µm of the layer containing NPs) to the cold parts of the sample. The total thickness of the glass substrate is 1 mm. Using these parameters and Eq. 21 (equation describing heat transfer), we have calculated the temperature accumulation in the focal volume as a function of pulse repetition rate and number of pulses applied. The pertinent temperature rise ΔT in the focal volume as a function of number of pulses is shown in Figure 31(a). It is clearly seen that every pulse increases the temperature in the focal volume. Applying 300 pulses to one spot with temporal separation of 1 ms (1 kHz repetition rate) results in a temperature rise of about 50-60 K, while the same number of pulses at 100 kHz repetition rate increases the temperature by more than 300 K. Figure 31(b) shows the dependence on the laser repetition rate of ΔT after 300 pulses.

Copyright © 2010. Nova Science Publishers, Incorporated. All rights reserved.

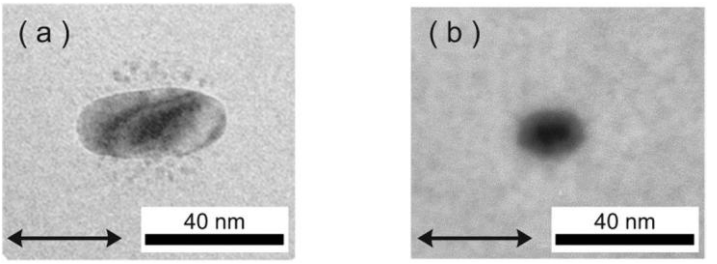

Figure 30. TEM images of nanoparticles irradiated: (a) at room temperature; (b) at 150 ºC. Polarization of laser light is show as an arrow.

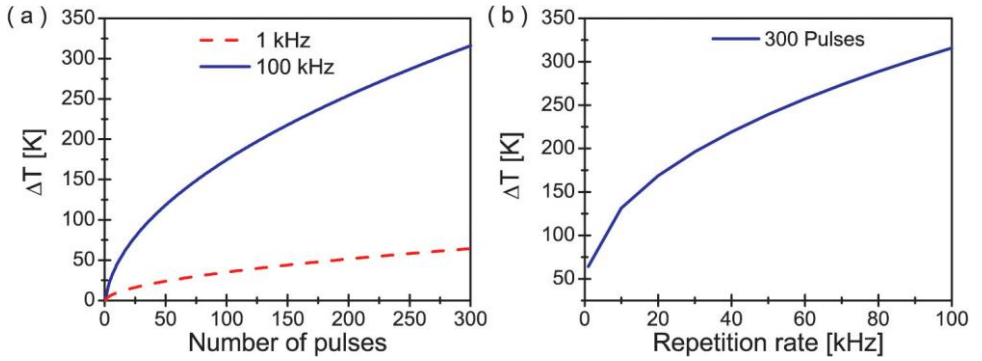

Figure 31. (a) Increase of the temperature in focal volume as a function of: (a) applied number of pulses for the cases of irradiation at 1 and 100 kHz; (b) repetition rate applying 300 pulses.

These simulations are in very good agreement with our experimental results: Figure 31(b) tells that irradiation of nanoparticles by 300 pulses at repetition rates below 10 kHz leads to relatively small increase of temperature in the focal volume (< 130 K for 300th pulse). As shown in Figure 28 this is typically the constant temperature where NP dissolution begins. For repetition rates above 10 kHz this region of $\Delta T > 100$K is reached increasingly earlier, which should cause a reduced spectral gap and higher degree of NP dissolution. Just this behavior is seen in the experimentally obtained dependence on the laser repetition rate shown in Figure 29. Finally, also the observation that a higher number of pulses lets the dissolution process appear already at lower repetition rates is nicely compatible with this calculations, since, e.g., in the case of 600 pulses the first 300 prepare a considerable temperature rise ΔT which enables dissolution by the 'second half' of the pulse train.

In conclusion, we have shown that the intended transformation of initially spherical NPs to prolate shapes with high aspect ratio by irradiation with a few hundred laser pulses requires a special spatio-temporal evolution of the matrix temperature: the heat-affected zone reaching transiently temperatures above ≈ 500 K around a nanoparticle should apparently be limited to a few nanometers. Then the increased mobility of emitted Ag ions enables the processes of shape transformation within that shell, while the cooler outer shells prevent the ions from drifting farther away from the NP. The latter obviously happens when the initial sample temperature lies above 100°C, which can also be reached by accumulation of the absorbed energy in the focal volume applying high laser repetition rates. In this case the emitted Ag cations seem to drift so far away from the NP that they can not diffuse back to a NP and recombine with it, but rather precipitate where they are, forming an enlarged halo region. This

Copyright © 2010. Nova Science Publishers, Incorporated. All rights reserved.

process readily explains the observed dissolution of the NPs after irradiation with some hundred fs laser pulses.

7. PREPARATION OF SUB-MICRON POLARIZING STRUCTURES

It was shown in the previous sections that the shapes of the initially spherical Ag NPs in glass can be permanently modified by femtosecond laser irradiation; that in turn leads to the optical dichroism induced in the composite glass. The amount of dichroism (spectral gap between the two polarized resonances), being correlated with the aspect ratio (ratio of long and short axis) of the NPs, depends on the irradiation parameters such as wavelength, peak intensity and number of laser pulses applied. Varying these parameters, quite different optical dichroism can be achieved, which lets this technique of ultrashort laser pulse irradiation appear as very attractive for the production of polarization and wavelength selective micro-devices. To achieve considerably high polarization contrast for such polarizing elements, the total extinction of the shape-transformed NPs must be correspondingly high. This obviously requires the initial nanocomposite materials to have high concentration of NPs. Under such conditions, it may become necessary to perform several successive irradiations to achieve the ultimatively desired spectral parameters, mostly interrupted by annealing times to remove color centers and other defects in the glass matrix. We have studied in previous work a number of these more technical points to set the framework for further optimization [109]. As this requires usually a complex interplay of finding the best combination of sample (NP sizes, their spatial distribution etc.) and irradiation parameters, we refrain from discussing here all the details of this optimization task. Instead, we will only give some instructive examples for polarizing optical micron structures which we already have achieved to demonstrate the huge application potential of this technique.

As a first example for micro-polarizing structures in the nanocomposite glass containing silver nanoparticles is shown in Figure 32. To achieve spots with sizes of a few micrometers requires focusing with sufficiently high numerical aperture. In this experiment the beam size was enlarged to 15 mm and then focused with lenses with 55 or 80 mm focal length, respectively. We have irradiated the sample by pulses at λ = 515 nm; the laser parameters were chosen so that the maximum dichroism is obtained. The matrix seen in Figure 32 consists of spots (modified area) with a size of around 3 μm and a distance of 15 μm between them. The spots are seen when polarization of the light (in microscope) is parallel to the laser polarization. If the light is polarized perpendicularly to the laser polarization, the spots disappear. The irradiated areas have a green color in p-polarisation because of extinction at around 600 nm.

The next example is shown in Figure 33. Here, again parameters of irradiation were the same for every spot. However, the pattern of the structure, in this case, consists of three irradiated and one non-irradiated spots and the laser polarization is rotated by 45° and 90° for every next irradiated spot in pattern. The four photos shown in Figure 33 were taken from the same area on the sample. The only difference is the polarization of light in the microscope, which for every case is shown as an arrow. The color of the spots is darker than in the previous case, because the irradiated sample had a higher filling factor, which leads to the broader extinction.

Copyright © 2010. Nova Science Publishers, Incorporated. All rights reserved.

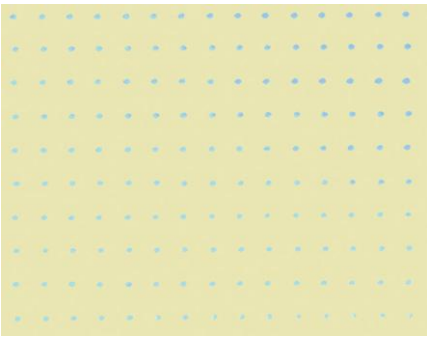

Figure 32. Polarized matrix made by laser irradiation of silver nanoparticles embedded in glass. Polarization of the light is parallel to the laser polarization. If the light is polarized perpendicularly to the laser polarization, the spots are disappearing. The size of one spot is around 3 μm.

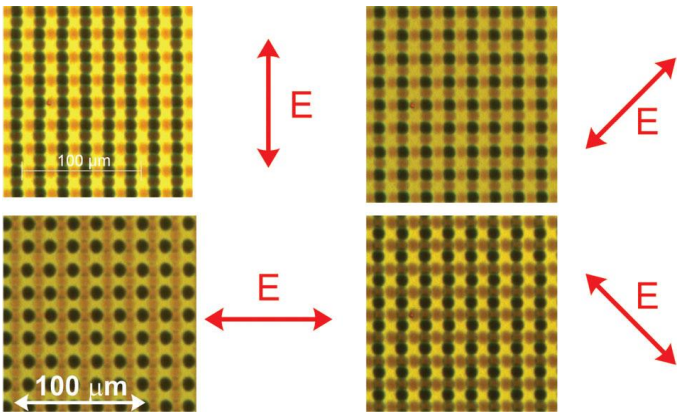

Figure 33. Polarized microstructure made by laser irradiation of silver nanoparticles embedded in glass. Parameters of irradiation (except laser polarization) are the same for every spot. Polarizations of the light in microscope are shown as red arrows.

The last example presented in Figure 34 shows similar structure as was shown in Figure 33. Again, the pattern consists of three irradiated and one non-irradiated spots and the laser polarization is rotated by 45° and 90° for every next irradiated spot in pattern. However, in this case parameters of irradiation for every spot were different. The rise in number of pulses leads to the red shift of p-polarized SP band and as a result the colour is changed from brown to green. On the other hand, rotation of the probe light polarization leads to the changes of spots' colours, so that the spot which has red colour in one polarization becomes yellow-brown for the light polarized in perpendicular direction.

In summary, we have managed to prepare several regular micro-patterns with tailored dichroism (with the spot size of about 3 μm) by laser irradiation of nanocomposite glass with embedded silver nanoparticles. These and any other microstructures are not subject to any mechanical limitations, which would be the case if similar polarization patterns have to produced by standard technology (cutting and pasting of large polarizers); only the diffraction limit sets a lower limit of few hundred nanometers for structures to be created. Insofar the technology is well-suited to produce polarization and wavelength selective micro-devices, allowing unprecedented features currently not achievable by any other method.

Copyright © 2010. Nova Science Publishers, Incorporated. All rights reserved.

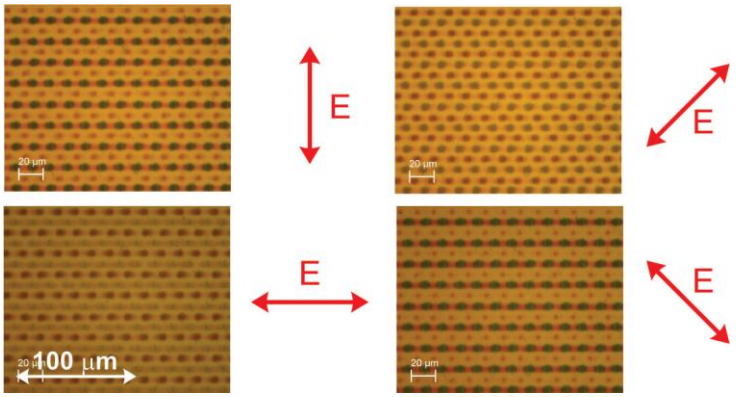

Figure 34. Polarized microstructure made by laser irradiation of silver nanoparticles embedded in glass. Parameters of irradiation are different for every spot in the pattern. Polarizations of the light in microscope are shown as red arrows.

CONCLUSION

The experimental results presented in this chapter are mostly concentrated on the investigation of the laser-induced shape modification of initially spherical silver nanoparticles incorporated in glass and the processes leading to the different NPs shapes. A detailed understanding of all these processes helps to optimize the technique of NPs shape transformation based on laser irradiation, and as a result, to modify the optical properties of composite glasses with metal nanoparticles as it is needed for every special application.

First, the dependence of the nanoparticle shapes on the laser polarization was discussed. It was found that irradiation of the NPs by the laser pulses with circular polarization leads to the transformation of initially spherical particles to oblate spheroids with the symmetry axis parallel to the propagation direction. In the case of linearly polarized light, however, the NPs shape can be modified to either prolate or oblate spheroid with their symmetry axes parallel to the laser polarization. The shape in this case is defined by the laser peak pulse intensity used for irradiation. Pulse intensities slightly above a first modification threshold lead to elongation of the silver nanoparticle parallel to the laser polarization (prolate spheroid). On the other hand, increase in the peak pulse intensity by one order of magnitude above a second threshold results in oblate spheroids, but in this case, with the short axis parallel to the laser polarization. These results allowed us to conclude that the main process responsible for the different NPs shape transformation is the directional photoionization.

We have also found that laser induced shape transformation of Ag nanoparticles is strongly dependent on the wavelength of fs laser pulses used for irradiation. The first striking observation is that, considerably off-resonant excitation [i.e. irradiation with a laser wavelength shifted more than 100 nm to the long wavelength side of the SP resonance absorption of spherical nanoparticles (at 413 nm)] can even more effectively transform the shapes of the nanoparticles to spheroids with large aspect ratios than near resonant interaction, in spite of the very weak coupling to the SPR in this region.

The fact that the laser assisted elongation of nanoparticles stops when the excitation wavelength is located considerably far in the blue wing of the p-polarized SP band together

Copyright © 2010. Nova Science Publishers, Incorporated. All rights reserved.

with results obtained in experiment with simultaneous irradiation of the sample by two wavelengths allowed us to conclude that the very weak electric field enhancement at a wavelength of irradiation can be the main factor limiting the laser-induced dichroism. This limit can be overcome by subsequent irradiation tuning the irradiation pulses to the longer wavelengths.

Taking into account the theoretical estimations and experimental results observed by the study on temperature dependence we can conclude that the intended transformation of initially spherical NPs to prolate shapes with high aspect ratio by irradiation with a few hundred laser pulses requires a special spatio-temporal evolution of the matrix temperature: the heat-affected zone reaching transiently temperatures above ≈ 500 K around a nanoparticle should apparently be limited to a few nanometers.

According to all acquired experimental results and calculations we also proposed the possible deformation mechanisms based on the transient phenomena which are controlled either directly by the electric field of the laser pulse or indirectly by the temperature rise induced by it. Formation of the prolate spheroids with the long axis parallel to the laser polarization in the low intensity range for multi-shot irradiation could be explained by combination of the photoionization and metal particle precipitation on the poles of the nanosphere. The intensity-dependent extension of the cationic shell around the nanoparticle and the photoelectron emission in direction of the laser polarization play a key role here. In the case of high intensities (above 2 TW/cm^2) and low number of pulses (less than 40), dense electron plasma formation at the poles of the sphere and following thermal expansion or even ablation of the glass matrix dominate, leading to transformation of nano-spheres to oblate spheroids.

All these findings allowed us to optimize the technique of laser-induced modification of optical properties of the nanocomposite glasses with silver nanoparticles and to show that this technique is a very good tool for production of (sub-)micro-polarizing structures (polarization and wavelength selective devices) with high polarization contrast and broad tunable range of dichroism.

Copyright © 2010. Nova Science Publishers, Incorporated. All rights reserved.

ACKNOWLEDGMENT

The authors are very gratefully to CODIXX AG for providing samples with Ag nanoparticles for the experiments. We also owe many thanks to Prof. Dr. W. Hergert, O. Kiriyenko and C. Matyssek for providing material on the Electric Field Enhancement and some calculations presented in this chapter. We would like to thank Dr. A. A. Unal, Dr. A. Podlipensky, Dr. A Abdolvand and Dr. M. Kaempfe for fruitful discussions and their contribution on previous stages of the work. We express our thanks to Dr. J. Lange, I. Otten and C. Seidel for the technical support. We extend our cordial thanks to F. Syrovatka (IWZ Materialwissenschaft, MLU Halle), Dr. P. Miclea (MLU, Halle) and Dr. H. Hofmeister (Max Planck Institute of Microstructure Physics-Halle) for help with the scanning electron microscopy and the transmission electron microscopy. Last but not least, financial support from the Deutsche Forschungsgemeinschaft (SFB 418), without which this work would not have been possible, is gratefully acknowledged.

REFERENCES

[1] Kreibig, U; Vollmer, M. *Optical Properties of Metal Clusters; Springer Series in Material Science*, 25, Springer: Berlin, DE, 1995.

[2] Shalaev, VM; Kawata, S. *Nanophotonics with surface plasmons; Advances in NANO-OPTICS AND NANO-PHOTONICS*, Elsevier, UK, 2007.

[3] Kelly, KL; Coronado, E; Zhao, LL; Schatz, GC. *J. Phys. Chem. B*, 2003, 107, 668-677.

[4] Jin, R; Cao, YC; Hao, E; Merraux, GS; Schatz, GC; Mirkin, CA. *Nature*, 2003, 425, 487-490.

[5] Gudiksen, MS; Lauhon, LJ; Wang, J; Smith, DC; Lieber, CM. *Nature*, 2002, 415, 617-620.

[6] Chakraborty, P. *J. Mat. Sci*., 1998, 33, 2235-2249.

[7] Gonella, F; Mazzoldi, P. *Handbook of Nanostructured Materials and Nanotechnology*, Vol. 4, Academic Press: San Diego, CA, 2000.

[8] Krenn, JR. *Nature Mater*, 2003, 2, 210-211.

[9] Maier, SA; G. Kik, PR; Atwater, HA; Meltzer, S; Harel, E; Koel, B; Requicha, AG. *Nature Mater*, 2003, 2, 229-232.

[10] Wenzel, T; Bosbach, J; Goldmann, A; Stietz, F; Trager, F. *Appl. Phys. B*, 1999, 69, 513-517.

[11] Stietz, F. *Appl. Phys. A*, 2001, 72, 381-394.

[12] Stepanov, AL; Hole, DE; Bukharaev, AA; Townsend, PD; Nurgazizov, NI. *Appl. Surf. Sci*., 1998, 136, 298-305.

[13] Shimotsuma, Y; Yuasa, T; Homma, H; Sakakura, M; Nakao, A; Miura, K; Hirao, K; Kawasaki, M; Qiu, J; Kazansky, PG. *Chem. Mater*, 2007, 19, 1206-1208.

[14] Kaempfe, M; Rainer, T; Berg, KJ; Seifert, G; Graener. H. *Appl. Phys. Lett*, 1999, 74, 1200-1202.

[15] Kaempfe, M; Seifert, G; Berg, KJ; Hofmeister, H; Graener. H. *Eur. Phys. J. D*, 2001, 16, 237-240.

[16] Seifert, G; Kaempfe, M; Berg, KJ; Graener. H. *Appl. Phys. B*, 2001, 73, 355-359.

[17] Podlipensky, A; Abdolvand, A; Seifert, G; Graener. H. *Appl. Phys. A*, 2005, 80, 1647-1652.

[18] Podlipensky, AV. *Laser assisted modification of optical and structural properties of composite glass with silver nanoparticles*. Ph.D. Thesis, Martin-Luther-Universität Halle-Wittenberg. http://sundoc.bibliothek.uni-halle.de/dissonline/05/05H084/t1.pdf 2005.

[19] Shalaev, VM. *Optical Properties of Nanostructured Random Media; Topics in Applied Physics*, 82, Springer: Berlin, DE, 2002.

[20] Mie, G. *Ann. Phys*., 1908, 25, 377-445.

[21] Brongersma, ML; Kik, PG. *Surface Plasmon Nanophotonics*, Springer Series in OPTICAL SCIENCES 131, Springer: Berlin, DE, 2007.

[22] Tominaga, J; Tsai, DP. Optical Nanotechnologies: The Manipulation of Surface and Local Plasmons; Topics in *Applied Physics* 88; Springer: Berlin, DE, 2003.

[23] Righini, M; Girard, C; Quidant, R. *J. Opt. A: Pure Appl. Opt*., 2008, 10**,** 093001.

[24] Wang, J; Blau, WJ. *J. Opt. A: Pure Appl. Opt*, 2009, 11**,** 024001.

Copyright © 2010. Nova Science Publishers, Incorporated. All rights reserved.

[25] Bohren, CF; Huffman, DR. *Absorption and Scattering by Small Particles*, Wiley: New York, NY, 1983.
[26] Maier, SA. *Plasmonics: Fundamentals and Applications*, Springer: Berlin, DE, 2007.
[27] Palick, ED. *Handbook of optical constants of solids*, Academic Press: Boston, MA, 1985.
[28] Kresin, VV. *Phys. Rev. B*, 1995, 51, 1844-1899.
[29] Berg, KJ; Berger, A; Hofmeister, H. *Z. Physik D*, 1991, 20, 309-311.
[30] Hilger, A; Tenfelde, M; Kreibig, U. *Appl. Phys. B*, 2001, 73, 361-372.
[31] Link, S; El-Sayed, M. A. *Ann. Rev. Phys. Chem*., 2003, 54, 331-366.
[32] Berciaud, S; Cognet, L; Tamarat, P; Lounis, B. *Nano Lett*, 2005, 5, 515-518.
[33] Seah, MP; Dench, WA. *Surf. Interface Anal*., 1979, 1, 2-11.
[34] Genzel, L; Martin, TP; Kreibig, U. *Z. Phys. B*, 1975, 21, 339-346.
[35] Kreibig, U; Genzel, L. *Surf. Science*, 1985, 156, 678-700.
[36] Amendola, V; Meneghetti, M. *J. Phys. Chem. C*, 2009, 113, 4277-4285.
[37] Postendorfer, J. Numerische Berechnung von Extinktions- und Streuspektren spharoidaler Metallpartikel beliebiger Größe in dielektrischer Matrix. *PhD thesis*, Martin-Luther University Halle-Wittenberg, 1997.
[38] Voshchinnikov, NV; Farafonov, VG. *Astrophys. Space Sci*., 1993, 204, 19-86.
[39] See for example the following link: http://www.codixx.de/
[40] Marton, JP; Lemon, JR. *Phys. Rev. B*, 1971, 4, 271-280.
[41] Xu, G; Tazawa, M; Jin, P; Nakao, S. *Appl. Phys. A*, 2005, 80, 1535-1540.
[42] Markel, VA; Muratov, LS; Stockman, MI; George, TF. *Phys. Rev. B*, 1991, 43, 8183-8195.
[43] Markel, VA; Shalaev, V; Stechel, EB; Kim, W; Armstrong, RL. *Phys. Rev. B*, 1996, 53, 2425-2436.
[44] Lamprecht, B; Leitner, A; Ausseneg, FG. *Appl. Phys. B*, 1997, 64, 269-272.
[45] Hofmeister, H; Drost, WG; Berger, A. *Nanostruct. Mater*, 1999, 12, 207-210.
[46] Gittleman, JI; Abeles, B. *Phys. Rev. B*, 1977, 15, 3273-3275.
[47] Bigot, JY; Halte, V; Merle, JC; Daunois, A. *Chem. Phys*., 2000, 251, 181-203.
[48] Link, S; El-Sayed, MA. *Int. Rev. Phys. Chem*., 2000, 19, 409-453.
[49] Arbouet, A; Voisin, C; Christofilos, D; Langot, P; Del Fatti, N; Vallee, F; Lerme, J; Celep, G; Cottancin, E; Gaudry, M; Pellarin, M; Broyer, M; Maillard, M; Pileni, MP; Treguer, M. *Phys. Rev. Lett*, 2003, 90, 177401.
[50] Voisin, C; Christofilos, D; Loukakos, PA; Del Fatti, N; Vallee, F; Lerme, J; Gaudry, M; Cottancin, E; Pellarin, M; Broyer, M. *Phys. Rev. B*, 2004, 69, 195416.
[51] Del Fatti, N; Voisin, C; Achermann, M; Tzortzakis, S; Christofilos, D; Vallee, F. *Phys. Rev. B*, 2000, 61, 16956.
[52] Del Fatti, N; Arbouet, A; Vallee, F. *Appl. Phys. B*, 2006, 84, 175-181.
[53] Kamat, P; Flumiani, M; Hartland, GV. *J. Phys. Chem. B*, 1998, 102, 3123-3128.
[54] Pfeiffer, W; Kennerknecht, C; Merschdorf, M. *Appl. Phys. A*, 2004, 78, 1011-1028.
[55] Calvayrac, F; Reinhard, PG; Suraud, E; Ullrich, CA. *Phys. Rep.*, 2000, 337, 493-578.
[56] Fann, WS; Storz, R; Tom, HWK; Bokor, J. *Phys. Rev. Lett*, 1992, 68, 2834-2837.
[57] Fann, WS; Storz, R; Tom, HWK; Bokor, J. *Phys. Rev. B*, 1992, 46,13592-13595.
[58] Perner, M; Bost, P; Lemmer, U; von Plessen, G; Feldmann, J; Becker, U; Mennig, M; Schmitt, M; Schmidt, H. *Phys. Rev. Lett*, 1997, 78, 2192-2195.

Copyright © 2010. Nova Science Publishers, Incorporated. All rights reserved.

[59] Aeschlimann, M; Bauer, M; Pawlik, S. *Chem. Phys*., 1996, 205, 127-141.
[60] Cao, J; Gao, Y; Elsayed-Ali, HE; Miller, RJD; Mantell, DA. *Phys. Rev. B*, 1998, 58, 10948-10952.
[61] Knoesel, E; Hotzel, A; Wolf, M. *Phys. Rev. B*, 1997, 57, 12812-12824.
[62] Ogawa, S; Nagano, H; Petek, H. *Phys. Rev. B*, 1997, 55, 10869-10877.
[63] Voisin, C; Christofilos, D; Del Fatti, N; Vallee, F; Prevel, B; Cottancin, E; Lerme, J; Pellarin, M; Broyer, M. *Phys. Rev. Lett*, 2000, 85, 2200-2203.
[64] Voisin, C; Del Fatti, N; Christofilos, D; Vallee, F. *J. Phys. Chem. B*, 2001, 105, 2264-2280.
[65] Hodak, J; Martini, I; Hartland, GV. *Chem. Phys. Lett*, 1998, 284, 135-141.
[66] Ahmadi, TS; Logunov, SL; El-Sayed, MA. *J. Phys. Chem*., 1996, 100, 8053-8056.
[67] Roberti, TW; Smith, BA; Zhang, JZ. *J. Chem. Phys*., 1995, 102, 3860-3866.
[68] Haus, JW; Kalyaniwalla, N; Inguva, R; Bloemer, M; Bowden, CM. *J. Opt. Soc. Am. B*, 1989, 6, 797-807.
[69] Uchida, K; Kaneko, S; Omi, S; Hata, C; Tanji, H; Asahara, Y; Ikushima, AJ; Tokizaki, T; Nakamara, A. *J. Opt. Soc. Am. B*, 1994, 11, 1236-1243.
[70] Stella, A; Nisoli, M; De Silvestri, S; Svelto, O; Lanzani, G; Cheyssac, O; Kofman, R. *Phys. Rev. B*, 1996, 53, 15497-15500.
[71] Kreibig, U; Bour, G; Hilger, A; Gartz, M. *Phys. Stat. Solid. A*, 1999, 175, 351-366.
[72] Bigot, JY; Merle, JC; Cregut, O; Daunois, A. *Phys. Rev. Lett*, 1995, 75, 4702-4705.
[73] Hodak, JH; Martini, I; Hartland, GV. *J. Phys. Chem. B* 1998, 102, 6958-6967.
[74] Anisimov, SI; Kapeliovich, BL; Perelman, TL. *Zh. Eksp. Teor. Fiz*., 1974, 66, 776.
[75] Muskens, OL; Del Fatti, N; Vallee, F. *Nano Lett*, 2006, 6, 552-556.
[76] Wang, XY; Riffe, DM; Lee, YS; Downer, MC. *Phys .Rev. B*, 1994, 50, 8016-8019.
[77] Lin, Z; Zhigilei, LV. *Proc. SPIE*, 2006, 6261, 62610U.
[78] Hultgren, R; Desai, PD; Hawkins, DT; Gleiser, M; Kelley, KK; Wagman, DD. *Selected Values of the Thermodynamic Properties of the Elements;* ASM: Metals Park, OH, 1973.
[79] Ashcroft, NW; Mermin, ND. *Solid State Physics;* HCP: Orlando, FL, 1976.
[80] Hamanaka, Y; Hayashi, N; Nakamura, A; Omi, S. *J. Lumin*, 1998, 76, 221-225.
[81] Lysenko, S; Jimenez, J; Zhang, G; Liu, H. *J. Elect. Mat*, 2006, 35, 1715-1721.
[82] Lin, Z; Zhigilei, LV; Celli, V. *Phys. Rev. B*, 2008, 77, 075133.
[83] Kresse, G; Hafner, J. *Phys. Rev. B*, 1993, 47, 558-561.
[84] Stalmashonak, A; Podlipensky, A; Seifert, G; Graener, H. *Appl. Phys. B*, 2009, 94, 459-465.
[85] Plech, A; Kotaidis, V; Gresillon, S; Dahmen, C; von Plessen, G. *Phys. Rev. B*, 2004, 70, 195423.
[86] Plech, A; Kotaidis, V; Lorenc, M; Boneberg, J. *Nature Physics*, 2006, 2, 44-47.
[87] Inouye, H; Tanaka, K; Tanahashi, I; Hirao, K. *Phys. Rev. B*, 1998, 57, 11334-11340.
[88] Plech, A; Kurbitz, S; Berg, K. J; Graener, H; Berg, G; Gresillon, S; Kaempfe, M; Feldmann, J; Wulff, M; von Plessen, GA. *Europhys. Lett*, 2003, 61, 762-768.
[89] Unal, AA; Stalmashonak, A; Graener, H; Seifert, G. *Phys. Rev. B*, 2009, 80, 115415.
[90] Schaffer, CB. Interaction of Femtosecond Laser Pulses with Transparent Materials. *PhD thesis*, Harvard University. http://mazur-www.harvard.edu/publications.php?function =display&rowid=123, 2001.

Copyright © 2010. Nova Science Publishers, Incorporated. All rights reserved.

[91] Busolt, U; Cottancin, E; Rohr, H; Socaciu, L; Leisner, T; Woste, L. *Eur. Phys. J D*, 1999, 9, 523-527.
[92] Fierz, M; Siegmann, K; Scharte, M; Aeschlimann, M. *Appl. Phys. B*, 1999, 68, 415-418.
[93] Ertel, K; Kohl, U; Lehmann, J; Merschdorf, M; Pfeiffer, W; Thon, A; Voll, S; Gerber, G. *Appl. Phys. B*, 1999, 68, 439-445.
[94] Koller, L; Schumacher, M; Kohn, J; Teuber, S; Tiggesbaumker, J; Meiwes-Broer, KH. *Phys. Rev. Lett*, 1999, 82, 3783-3786.
[95] Lehmann, J; Merschdorf, M; Pfeiffer, W; Thon, A; Voll, S; Gerber, G. *Phys. Rev. Lett*, 2000, 85, 2921-2924.
[96] J Lehmann, J; Merschdorf, M; Pfeiffer, W; Thon, A; Voll, S; Gerber, G. *J. Chem. Phys*., 2000, 112, 5428-5434.
[97] Merschdorf, M; Pfeiffer, W; Thon, A; Voll, S; Gerber, G. *Appl. Phys. A*, 2000, 71, 547-552.
[98] Akella, A; Honda, T; Liu, AY; Hesselink, L. *Opt. Lett*, 1997, 22, 967-969.
[99] Hao, E; Schatz, GC. *J. Chem. Phys*., 2004, 120, 357-366.
[100] Hao, E; Schatz, GC; Hupp, JT. *J. Fluoresc*, 2004, 14, 331-341.
[101] Unal, AA; Stalmashonak, A; Seifert, G; Graener, H. *Phys. Rev. B*, 2009, 79, 115411.
[102] Doppner, T; Fennel, T; Diederich, T; Tiggesbaumker, J; Meiwes-Broer, KH. *Phys. Rev. Lett*, 2005, 94, 013401.
[103] Podlipensky, AV; Grebenev, V; Seifert, G; Graener, H. *J. Lumin*, 2004, 109, 135-142.
[104] Stalmashonak, A; Seifert, G; Graener, H. *Opt. Lett*, 2007, 32, 3215-3217.
[105] Stalmashonak, A; Graener, H; Seifert, G. *Appl. Phys. Lett*, 2009, 94, 193111.
[106] Stalmashonak, A; Seifert, G; Graener, H. *J. Opt. A: Pure Appl. Opt*, 2009, 11, 065001.
[107] Stalmashonak, A; Unal, AA; Graener, H; Seifert, G. *J. Phys. Chem. C*, 2009, 113, 12028-12032.
[108] Melikyan, A; Minassian, H. *Appl. Phys. B*, 2004, 78, 453-455.
[109] Stalmashonak, A; Seifert, G; Unal, AA; Skrzypczak, U; Podlipensky, A; Abdolvand, A; Graener, H. *Appl. Opt*., 2009, 48, F37-F43.

Copyright © 2010. Nova Science Publishers, Incorporated. All rights reserved.

In: Silver Nanoparticles
Editor: Audrey E. Welles, pp. 169-219
ISBN: 978-1-61668-690-1
© 2010 Nova Science Publishers, Inc.

Chapter 4

ION-SYNTHESIS OF SILVER NANOPARTICLES AND THEIR OPTICAL PROPERTIES

Andrey L. Stepanov*

Kazan Physical-Technical Institute, Russian Academy of Sciences,
420029 Kazan, Russian Federation
Kazan State University, 420008 Kazan, Russian Federation

ABSTRACT

Recent results on ion-synthesis by low energy implantation and optical properties of silver nanoparticles in various dielectrics (glasses and polymers) and on the interaction of high power laser pulses with such composite materials are reviewed. One of the features of composites prepared by the low energy ion implantation is the growth of metal particles with a wide size distribution in the thin depth from the irradiated substrate surface. This leads to specific optical properties of implanted materials, partially to difference in reflection measured from implanted and rear face of samples. The excimer laser pulse modification of silver nanoparticles fabricated in silicate glasses are considered. Pulsed laser irradiation makes it possible to modify such composite layer, improving the uniformity in the size distribution of the nanoparticles. The optical absorption of silver nanoparticles fabricated in polymer is also analysed. Unusual weak and broad plasmon resonance spectra of the nanoparticles is studied in the frame of the carbonisation of ion-irradiated polymer. Based on the Mie theory, optical extinction spectra for metal particles in the polymer and carbon matrices are simulated and compared with partical spectra for complex silver core–carbon shell nanoparticles. A new experimental data on nonlinear optical properties of synthesised silver nanoparticles are also presented.

Copyright © 2010. Nova Science Publishers, Incorporated. All rights reserved.

* Corresponding author: e-mail: aanstep@gmail.com

INTRODUCTION

Nanomaterials are cornerstones of nanoscience and nanotechnology. The relevant feature size of nanomaterial components is on the order of a few to a few hundreds of nm. At the fundamental level, there is a real need to better understand the properties of materials on the nanoscale level. At the technological front, there is a strong demand to develop new techniques to fabricate and measure the properties of nanomaterials and relevant devices. Significant advancement was made over the last decades in both fronts. It was demonstrated that materials at the nanoscale have unique physical and chemical properties compared to their bulk counterparts and these properties are highly promising for a variety of technological applications. One of the most fascinating and useful aspects of nanomaterials is their optical properties. Applications based on optical properties of nanomaterials include optical detectors, laser, sensor, imaging, display, solar cell, photocatalysis, photoelectrochemistry and biomedicine [1]. Among a variety of nanomaterial the most fascinating ones are composite metamaterials containing metallic nanoparticles (MNPs) which are now considered as a basis for designing new photonic media for optoelectronics and nonlinear optics [2]. Simultaneously with the search for and development of modern technologies intended for nanoparticle synthesis, substantial practical attention was devoted to designing techniques for controlling the MNP size. This is caused by the fact that the properties of MNPs, such as the quantum size effect, single-electron conduction, etc., which are required for various applications, take place up to a certain MNP size. An example of their application in optoelectronics is a prototype of integrated electronic circuit—chip that combines metallic wires as conductors of electric signals with fibers as guides of optical signals. In practice, light guides are frequently made of synthetic sapphire or silicon oxide, which are deposited on or buried in semiconductor substrates. In this case, electrooptic emitters and those which accomplish electric-to-optic signal conversion are fabricated inside the dielectric layer. This light signal from a microlaser is focused in a light guide and then transmitted through the optoelectronic chip to a high-speed photodetector, which converts the photon flux to the flux of electrons. It is expected that light guides used instead of metallic conductors will improve the data rate by at least two orders of magnitude. Moreover, there is good reason to believe that optical guide elements will reduce the energy consumption and heat dissipation, since metallic or semiconductor components of the circuits may be replaced by dielectric ones in this case. Prototype optoelectronic chips currently available are capable of handling data streams with a rate of 1 Gbit/s, with improvement until 10 Gbit/s in the future. Key elements of dielectric waveguides used for light propagation are nonlinear optical switches, which must provide conversion of laser signal for pulse duration as short as pico- or femtoseconds. The nonlinear optical properties of MNP-containing dielectrics stem from the dependence of their refractive index and nonlinear absorption on incident light intensity [2, 3]. This effect is associated with MNPs, which exhibit an enhancement of local electromagnetic field in a composite and, as consequence, a high value of the third order nonlinear susceptibility when exposed to ultrashort laser pulses. Therefore, such MNP-containing dielectric materials may be used to advantage in integrated optoelectronic devices, for example, as shown in Figure 1.

Copyright © 2010. Nova Science Publishers, Incorporated. All rights reserved.

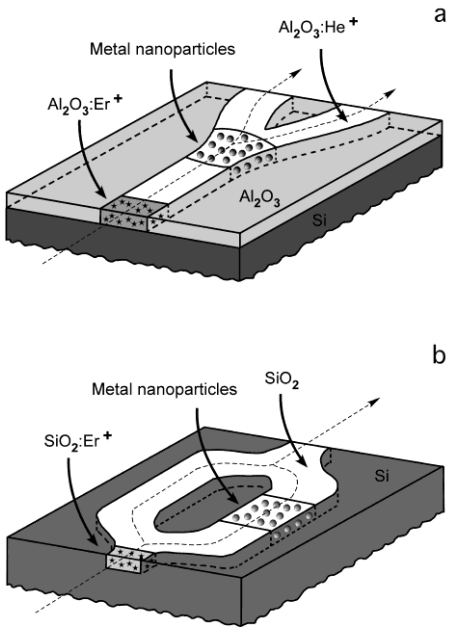

Figure 1. A prototypes of optoelectronic chip with a dielectric waveguide combined with silicone substrate. Ion implantation can be applied to fabricate selective area doped by rear metal ions (marked by stars) to work as microlaser and to illuminate in waveguide, created by rear-gas ion radiation with MNPs to form an optical switcher.

It is well known [4] that a local field enhancement in MNPs stimulates a strong linear optical absorption called surface plasmon resonance (SPR). The electron transitions responsible for plasmon absorption in MNPs cause also a generation of an optical nonlinearity of a composite in the same spectral range. As a result, the manifestation of nonlinear optical properties is most efficient for wavelengths near the position of a SPR maximum. In practice, to reach the strong linear absorption of a composite in the SPR spectral region, attempts are made to increase the concentration (filling factor) of MNPs. Systems with a higher filling factor offer a higher nonlinear susceptibility, with all other parameters of composites being the same. Usually noble metals and copper are used to fabricate nonlinear optical materials with high values of third order susceptibility. There are a variety ways to synthesize MNPs in dielectrics, such as magnetron sputtering, the convective method, ion exchange, sol–gel deposition, etc. One of the most promising enhanced fabrication methods is ion implantation [5-9] because it allows reaching a high metal filling factor in an irradiated matrix beyond the equilibrium limit of metal solubility and provides controllable synthesis of MNPs at various depths under the substrate surface. Nearly any metal–dielectric composition may be produced using ion implantation. This method allows for strict control of the doping ion beam position on the sample surface with implant dose as, for example, in the case of electron- and ion-beam lithography. Today, Ion implantation is widely used in industrial semiconductor chip fabrication. Therefore, the combination of MNP-containing dielectrics with semiconductor substrates by same technological approach as ion implantation could be reached quite effectively. Moreover, ion implantation can be

Copyright © 2010. Nova Science Publishers, Incorporated. All rights reserved.

applied for different steps in optoelectronic material fabrication such as creation of optical waveguides by implantation with rear gas ions (H^+, He^+ etc.) [9], a designing of electric-to-optic signal convectors and microlaser by irradiation of dialectics waveguides with rear metal ions (Er^+, Eu^+ etc.) [9, 10] and a synthesis of MNPs (Figure 1).

The history of MNP synthesis in dielectrics by ion implantation dates back to 1973, when a team of researchers at the Lyons University in France [11, 12] pioneered this method to create particles of various metals (sodium, calcium, etc.) in LiF and MgO ionic crystals. Later, ion-synthesis of noble nanoparticles was firstly done in study of Au- and Ag-irradiated lithia-alumina-silica glasses [13, 14]. Developments was expanded from the metal implants to the use of many ions and the active formation of compounds, including metal alloys and totally different composition precipitate inclusions. In ion implantation practice MNPs were fabricated in various materials, such as polymers, glass, artificial crystals, and minerals [15, 16]. By implantation, one can produce almost any metal–dielectric composite metamaterials, as follows from Table 1, which gives a comprehensive list of references of various dielectrics with implanted silver nanoparticles with conditions for their fabrications. This chapter focuses on recent advantages in fabrication of silver nanoparticles by low-energy in implantation in various inorganic matrixes [17-161]. Also some examples of nonlinear optical repose in such composites are presented and discussed.

Table 1. Types of dielectric inorganic matrix with silver nanoparticles synthesized by ion implantation combined in some cases with post-implantation heat treatment

Matrix type	Ion energy, keV	Ion dose, ion/cm^2	Current density, μA/см^2	Matrix temperature, °C	Post-implantation heat treatment	Methods of particle detection	Authors
Al_2O_3 crystal <1010>	50 360	$4.0\cdot10^{16}$ $5.0\cdot10^{16}$ $8.0\cdot10^{16}$	1-5	77 K 300	Annealing in air at 650°C, 30 min.	OA	Rahmani *et al.* 1988 [17] 1989 [18]
Al_2O_3 crystal <0001>	$1.8\cdot10^3$	$1.2\cdot10^{17}$		77 K	Annealing in air at 1100°C, 2 h	OA, DFWM	White *et al.* 1993 [19]
Al_2O_3 crystal	$1.5\cdot10^3$	$8.0\cdot10^{16}$	2<		Annealing in air at 500°C, 1 h	OA	Ila *et al.* 1998 [20]
Al_2O_3 crystal	25 30	$(0.2\text{-}2.0)\cdot10^{17}$				OA, OR, TEM	Steiner *et al.* 1998 [21]
Al_2O_3 crystal	30	$3.8\cdot10^{17}$	3, 6, 10	RT		OA RZ-scan	Ganeev *et al.* 2005 [22] 2006 [23]
Al_2O_3 crystal	160	$(0.1\text{-}1.0)\cdot10^{17}$				OA	Marques *et al.* 2006 [24]
ABSG, BPYR glass	270	$1.5\cdot10^{16}$				OA	Mazzoldi *et al.* 1993 [25]
MgO crystal (100)	180	$(0.5\text{-}1.0)\cdot10^{17}$	1	RT	Some samples annealed in vacuum at 25-1500°C	OA TEM	Abouchacra and Serughetti 1986 [26] Fuchs *et al.* 1988 [27]
MgO crystal (100)	$1.5\cdot10^3$	$1.2\cdot10^{17}$	2-3	27 C	Annealing in air at 550 and 1100°C	OA TEM	Qian *et al.* 1997 [28] Zimmerman *et al.* 1997 [29]
MgO crystal (100)	600	$1.0\cdot10^{16}$		RT	Annealing in air at 1200°C, 22 h	OA, XRD TEM-CS	van Huis *et al.* 2002 [30]

Copyright © 2010. Nova Science Publishers, Incorporated. All rights reserved.

Table 1. (Continued)

Matrix type	Ion energy, keV	Ion dose, ion/cm^2	Current density, μA/см^2	Matrix temperature, °C	Post-implantation heat treatment	Methods of particle detection	Authors
MgO crystal (100)	200	$2.0 \cdot 10^{17}$	2	RT	Some samples annealed in air, Ar, O_2 or 70%N_2 + 30%H_2, at 300-900°C, 1 h	OA, SAED TEM-CS	Xiao *et al.* 2008 [31]
$MgOP_2O_5$ glass	150	$(0.1\text{-}1.0) \cdot 10^{17}$	0.5-3	RT		OA	Matsunami and Hosono 1993 [32]
Lithia-alumina-silica glass	275-285	$1.0 \cdot 10^{16}$	1-2	300		OA	Arnold and Borders 1976 [14]
$LiNbO_3$ crystal	50 360	$(4.0\text{-}0.8) \cdot 10^{16}$	1-4	77 K 300	Annealing in air at 250-650°C, 30 min	OA	Rahmani *et al.* 1988 [17] 1989 [18]
$LiNbO_3$ crystal	20, 25 $3 \cdot 10^3$ $4.2 \cdot 10^3$	$(0.5\text{-}8.0) \cdot 10^{16}$		RT	Some samples annealed in air at 200-600°C, 1-3 h	OA OM X-ray	Deying *et al.* 1994 [33] Shang *et al.* 1996 [34] Saito and Kitahara 2000 [35] Fujita *et al.* 1994 [36]
$LiNbO_3$ crystal	160 $1.5 \cdot 10^3$	$2.0 \cdot 10^{16}$ $4.0 \cdot 10^{16}$ $1.7 \cdot 10^{17}$		RT 500	Some samples annealed in air at 500-800°C, 1 h	OA Z-scan TEM TEM-CS	Sarkisov *et al.* 1998 [27-40] 1999 [41] 2000 [42] Williams *et al.* 1998 [43, 44] 1999 [45]
$LiNbO_3$ crystal	$1.5 \cdot 10^3$	$2.0 \cdot 10^{16}$		300	Annealing in Ar gas at 100-1100°C, 30 min	OA TEM TEM-CS	Amolo *et al.* 2006 [46]
SiO_2 crystal	200	$(2.3\text{-}9.0) \cdot 10^{16}$	1-5	77 300	Annealing in air at 300-500°C, 30 min	OA	Rahmani and Townsend 1989 [18]
SiO_2	65 130 270	$(1.5\text{-}5.0) \cdot 10^{16}$	1 1.5	300	Some samples annealed in air or 4 % H_2 gas	OA TEM EXAFS	Mazzoldi *et al.* 1993 [47] Mazzoldi *et al.* 2005 [48] Mazzoldi *et al.* 2007 [49] Antonello *et al.* 1998 [50] Battaglin *et al.* 1998 [51] 2001 [52] Bertoncello *et al.* 1998 [53] Caccavale 1998 [54] Cattaruzza *et al.* 1999 [55] Gonella *et al.* 1999 [56]
SiO_2	150	$(0.1\text{-}6.0) \cdot 10^{17}$	1.5-14	300		TEM-CS, OA	Matsunami and Hosono 1993 [57]
SiO_2	305	$(3.0\text{-}9.0) \cdot \cdot 10^{16}$	2	0		OA TEM X-ray	Magruder III *et al.* 1995 [58] 1996 [59] 2009 [60]

Copyright © 2010. Nova Science Publishers, Incorporated. All rights reserved.

Table 1. (Continued)

Matrix type	Ion energy, keV	Ion dose, ion/cm^2	Current density, μA/см^2	Matrix temperature, °C	Post-implantation heat treatment	Methods of particle detection	Authors
							Anderson *et al.* 1996 [61] 1997 [62] 1998 [63] 2000 [64] Zuhr *et al.* 1998 [65]
SiO_2	20-58 130	(0.4-2.0)·10^{17}	0.6	300		AFM	Pham *et al.* 1997 [66]
SiO_2 crystal	200	(2.3-9.0)·10^{16}		300		OA TEM	Liu *et al.* 1998 [67-69]
SiO_2	1.5·10^3	2.0·10^{16} 4.0·10^{16} 1.4·10^{17}	2		Annealing in Ar gas at 500-1000°C, 1 h	OA Z-scan	Ila *et al.* 1998 [70]
SiO_2	65	5.0·10^{16}				X-ray EXAFS	D'Acapito and Zontone 1999 [71]
SiO_2	60	4.0·10^{16}	10	RT		OA, AFM	Stepanov *et al.* 2000 [72] 2003 [73]
SiO_2	43 90 150 200 300	(0.06-2.0)·10^{17}	0.8-2.5	300	Some samples annealed in air, Ar, O_2 or 70%N_2+ 30%H_2 at 300-800°C, 1 h	SAED OA, STEM TEM, EDS HRTEM TEM-CS Z-scan	Jiang *et al.* 2000 [74] Ren *et al.* 2004 [75, 76] 2005 [77-79] 2006 [80] 2007 [81] 2008 [82] 2009 [83] Liu *et al.* 2005 [84] Xiao *et al.* 2006 [85] 2007 [86, 87] Wang *et al.* 2007 [88] Wang *et al.* 2008 [89] Zhang *et al.* 2004 [90] Cai *et al.* 2008 [91] 2009 [92]
SiO_2 sol-gel film	5-100	(5.0-6.0)·10^{16}	1.5-2.5	330 K		TEM HR-TEM XRD SAED	Armelao *et al.* 2002 [93]
SiO_2 on Si	10 30 40	(1.0-5.0)·10^{15} (1.0-5.0)·10^{16} 1.0·10^{17}	2	-	Annealing in Ar gas at 500-900°C, 1 h	OR, OR TEM-CS R TEM HR-TEM	Ishikawa *et al.* 2002 [94] 2009 [95] Tsuji *et al.* 2002 [96, 97] 2003 [98] 2004 [99] 2005 [100] Arai *et al.* 2003 [101] 2005 [102] 2006 [103] 2007 [104, 105]
SiO_2	2.0·10^3	(0.4-1.0)·10^{17}	2	RT	Some samples annealed in 50%N_2 + 50%H_2 gas or in air at 230-800°C, 1 h	OA TEM HRTEM	Roiz *et al.* 2004 [106] Oliver *et al.* 2006 [107] Cheang-Wong *et al.* 2007 [108] Peña *et al.* 2007 [109] 2009 [110]

Copyright © 2010. Nova Science Publishers, Incorporated. All rights reserved.

Table 1. (Continued)

Matrix type	Ion energy, keV	Ion dose, ion/cm^2	Current density, μA/см^2	Matrix temperature, °C	Post-implantation heat treatment	Methods of particle detection	Authors
							Reyes-Esqueda *et al.* 2008 [111] 2009 [112] Rodrigues-Iglesias *et al.* 2008 [113] 2009 [114] Rangel-Rojo *et al.* 2009 [115]
SiO_2 on Si	40	$0.3 \cdot 10^{15}$		RT	Annealing in vacuum at 550°C, 20 min	TEM	Romanyuk *et al.* 2006 [116]
SiO_2	60	$(0.3\text{-}1.0) \cdot 10^{17}$	3	RT		OA Z-scan	Takeda *et al.* 2006 [117]
SiO_2	32-40 $1.7 \cdot 10^3$ $2.4 \cdot 10^3$	$(0.1\text{-}1.0) \cdot 10^{17}$	3-5	RT	Some samples annealed in air at 500°C, 1 h	OA TEM Z-scan	Joseph *et al.* 2007 [118, 119] Sahu *et al.* 2009 [120]
SiO_2	0.65 1.5 3 keV	$(1.2\text{-}4.7) \cdot 10^{15}$	3-5	RT		OA, OR TEM HRTEM TEM-CS	Carles *et al.* 2009 [121]
SiO_2	200	$(0.1\text{-}2.0) \cdot 10^{17}$	< 2.5	-		OA TEM TEM-CS Z-scan	Wang *et al.* 2009 [122, 123]
SiO_2+TiO	305	$6.0 \cdot 10^{16}$	7	-		OA TEM-CS	Magruder III *et al.* 2007 [124]
Si_3N_4	20 130	$4.0 \cdot 10^{16}$	0.6	300		AFM	Pham *et al.* 1997 [66]
BPYR glass	270	$1.5 \cdot 10^{16}$				OA	Mazzoldi *et al.* 1993 [25]
Soda-lime glass	60	$2.0 \cdot 10^{16}$ $4.0 \cdot 10^{16}$	-	300	-	OR TEM-CS	Nistor *et al.* 1993 [125] Wood *et al.* 1993 [1126]
Soda-lime glass	200	$(0.5\text{-}4.0) \cdot 10^{16}$	0.5-2	RT 77 K	-	TEM TEM-CS OA	Dubiel *et al.* 1997 [127] 2000 [128] 2003 [129] 2008 [130] Seifert *et al.* 2009 [131]
Soda-lime glass	200	$(0.5\text{-}4.0) \cdot 10^{16}$	0.5-2	RT 77 K	-	TEM TEM-CS OA	Stepanov *et al.* 1998 [132] 1999 [133-135] 2000 [136-139] 2001 [140-142] 2002 [143-146] 2003 [147-149] 2004 [150, 151] 2005 [152] 2008 [153, 154] 2009 [155]
Ta_2O_5	80-130	$6.0 \cdot 10^{16}$	0.6 – 6.4	300		AFM	Pham *et al.* 1997 [66]
TiO_2 crystal	50 65	$(0.3\text{-}1.0) \cdot 10^{17}$	2	-	Annealing in Ar gas at >400°C, 1 h	OA TEM-CS	Tsuji *et al.* 2002 [156] 2003 [157]

Copyright © 2010. Nova Science Publishers, Incorporated. All rights reserved.

Table 1. (Continued)

Matrix type	Ion energy, keV	Ion dose, ion/cm^2	Current density, μA/см^2	Matrix temperature, °C	Post-implantation heat treatment	Methods of particle detection	Authors
TiO_2 Sol-gel films	30 65	(0.1-0.5)·10^{17}	2	RT	Annealing in Ar gas at 300-600°C, 1 h	OA	Tsuji *et al.* 2005 [158] 2006 [159]
YSZ	20 1.5·10^3 3.0·10^3	(0.7-6.0)·10^{16}	2	RT	Some samples annealed in air at 500-1000°C	OA	Saito *et al.* 2003 [160] Fujita *et al.* 2007 [161]

Abbreviations – $2Ag_2O·3Na_2O·25ZnO·70TeO_2$ (ANZT glass), alkali-borosilicate glass (ABSG), borosilicate Pyrex glass (BPYR), soda-lime silicate glass (SLSG), yttria stabilized cubic zirconia (YSZ); optical reflection (OR), optical absorption (OA), transmission electron microscopy (TEM), TEM cross-section (TEM-CS), high resolution TEM (HRTEM), scanning transmission electron microscopy (STEM), conductivity measurements (CM), atom force microscopy (AFM), optical microscopy (OM), selected area electron diffraction (SAED), energy dispersive X-ray spectrometry (EDS), high-resolution X-ray diffraction (XRD), Z-scan, RZ-scan by reflection, degenerate four wave mixing (DFWM); room temperature (RT).

DEPTH DISTRIBUTION AND DIFFUSION OF SILVER IONS DURING IMPLANTATION

The formation of MNPs resulting from ion implantation into dielectric substrates is complex, since there are a large number of influencing factors. A simple ion range estimate of the silver concentration can be computed, but this is only a precursor of processes involving diffusion and clustering and so simple simulations of the entire process are extremely challenging. Thus, the process should be divided into subprocesses with a time scale that resolves implantation, diffusion and particle growth. The first step for consideration is the dependence the ion depth distribution caused by silver diffusion at different substrate temperatures. At simple consideration, during the irradiation implanted ions leads to a depth distribution in the substrate, which has approximately a Gaussian shape, as described by range algorithms such as TRIM [162]. The diffusion equation of ion-implanted impurities is assumed to be expressed as [163]:

$$\frac{\partial N(x,t)}{\partial t} = D \cdot \frac{\partial^2 N(x,t)}{\partial x^2} + n(x,t), \quad (1)$$

where $N(x,t)$ is the concentration of impurities, D is their diffusion coefficient, $n(x,t)$ is the generation rate of the impurities due to ion implantation, x is distance and t is a duration of implantation. The diffusion coefficient in Eq. 1 is assumed to be independent of the distance x in the following calculation. D will depend on the rate of vacancy formation and the pre-existing concentration of silver particles, which act as trapping sites. Initially the generation rate $n(x,t)$ is believed to be of a Gaussian form [9, 163] and is given by

Copyright © 2010. Nova Science Publishers, Incorporated. All rights reserved.

$$n(x,t) = \frac{\Phi}{\Delta R_p (2\pi)^{1/2}} \exp\left[-\frac{1}{2}\left(\frac{x - R_p}{\Delta R_p} \right)^2 \right], \quad (2)$$

where Φ is the dose rate per unit area of impurity ions, R_p is the projected range of an implanted ion, ΔR_p is the projected range straggling.

Let us consider, as example, the R_p and ΔR_p corresponding to Ag-implantation into SLSG for different energies calculated by TRIM (SRIM-2000) programme [162]. The concentration profiles for different implant temperatures of Ag ions in SLSG are given by solution of Eq.1 and 2 [164] as

$$N(x,t) = \Phi \sqrt{\frac{2Dt + \Delta R_p^2}{2\pi D^2}} \left(-\frac{\alpha^2}{4Dt + 2\Delta R_p^2} \right) - \Phi \sqrt{\frac{\Delta R_p^2}{2\pi D^2}}\, exp\left(\frac{\alpha^2}{2\Delta R_p^2} \right) + \frac{\alpha\Phi}{2D} \left(erfc \frac{\alpha}{\sqrt{4Dt + 2\Delta R_p^2}} - erfc \frac{\alpha}{\Delta R_p \sqrt{2}} \right) \quad (3)$$

where $\alpha = x - R_p$ and t is a duration of ion implantation. As seen from Eq.3, the diffusion coefficient, which is dependent on temperature, determines the shape of the concentration profile. For an estimate of the silver diffusion coefficient in SLSG the Arrhenius equation may be applied with values of 0.69 eV for the activation energy and 5.6 x 10^{-5} cm^2/sec for frequency factor [165]. If these values are suggested to be time independent for a fixed temperature, then the results of concentration profile calculations for an applied dose rate of $5.58 \cdot 10^{13}$ ion/cm^2 and a 360 second duration implantation, which correspond to a total dose of $2 \cdot 10^{16}$ ion/cm^2, are presented in Figure 2. As seen in the figure, increasing the temperature from 20 to 100°C and, consequently, increasing the Ag diffusion coefficient in the glass from $2.88 \cdot 10^{-17}$ to $2.66 \cdot 10^{-14}$ cm^2/s, leads to a broadening of the initial Gaussian concentration profile and a reduction of the concentration at the peak of the profile. This decreasing in concentration is most critical for samples implanted at low energy especially. Thus, the accumulation of implanted ions in the SLSG layer is strongly affected by the substrate temperature, and hence this in turn influences the rate and depth of the development of the conditions for reaching a sufficient impurity concentration for metal particle nucleation and growth. Obviously, if the Ag mobility is high, there is no possibility for nanoparticle nucleation during a reasonable implant time. Such an inhibiting effect had been clearly seen in earlier experiments which recorded depth profiles by RBS measurements of the similar type of float glass implanted with Ag ions at substrate temperatures higher than ~180°C [166]. Note also that for this calculations it is assumed that the bulk glass temperature, and the local temperature within the implanted layer, are the same. In practice the surface will be heated to a higher temperature than the bulk of the glass.

Figure 2 does not include the influence of diffusion limited by the appearance of metal particles in the implanted material. However, it was shown, both in an example of implantation of Ag ions into SiO_2 glass [57] that the impurity diffusion coefficient drops dramatically after metal particle formation which act as traps for mobile ions. This suggests

Copyright © 2010. Nova Science Publishers, Incorporated. All rights reserved.

that the critical time for control of the nanoparticle spacing and nucleation is at the beginning of the implant, and therefore both the substrate temperature and ion beam currents during this initial phase are crucial. After particle formation has commenced, any changes, such as increasing temperature from beam heating or increases in ion current, will presumably have effects on the particle sizes, but less influence on the depth profile of the distribution. High temperature conditions in the initial stages will increase the impurity diffusion and so reduce the supersaturation, which is required for particle nucleation, hence nanoparticles may not form. These conclusions are important as they emphasise that there is a need to control the temperature and ion beam current density throughout the implant. Many experimentalists fail to do this, but instead allow the temperature to rise from the beam heating. In some cases the initial dose is provided at a low current density in order to avoid surface charging, and hence changes in the ion beam energy. Once some implantation has occurred the surface conductivity is increased and hence the beam currents can be raised. The foregoing conclusions suggest both situations influence the nanoparticle sizes and their depth distributions.

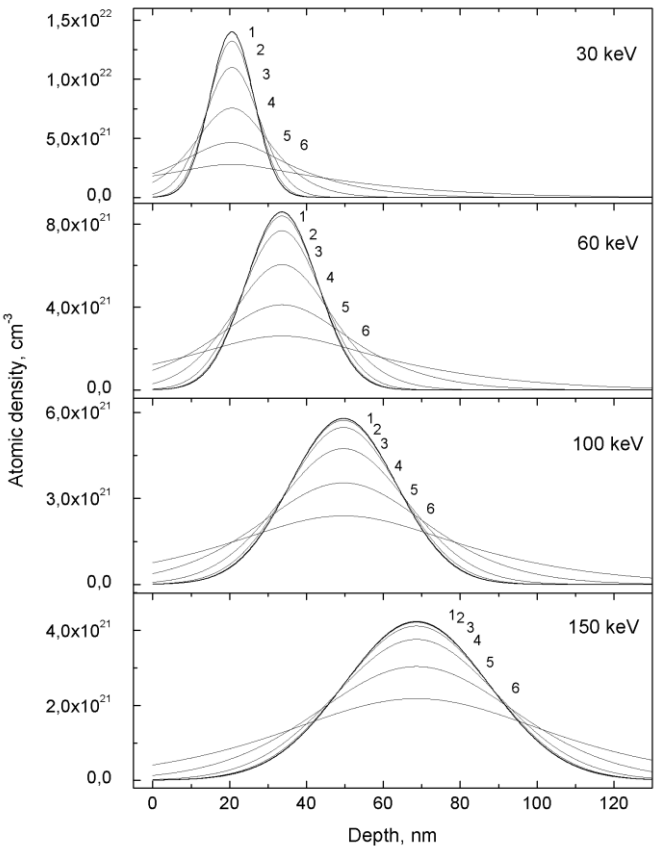

Figure 2. Calculated ion implanted silver distribution in SLSG as a function of energy, after taking into account the impurity diffusion in dependence on substrate temperature: 1.- TRIM distribution; 2.- 20; 3.-40; 4.- 60; 5.- 80; 6.-100°C. The concentration profiles correspond to the R_p and ΔR_p of 20.6 and 5.7 nm (30 keV), 33.6 and 9.3 nm (60 keV), 49.6 and 13.8 nm (100 keV), 68.6 and 18.8 nm (150 keV), respectively [134].

Copyright © 2010. Nova Science Publishers, Incorporated. All rights reserved.

DEPTH DISTRIBUTION OF SILVER IONS IN DEPENDENCE ON IRRADIATION ENERGY AND SURFACE SPUTTERING EFFECTS

As was noticed, in first approximation, implantation of ions leads to a depth distribution in the substrate which is approximately Gaussian as described by range algorithms such as TRIM [162]. However, the interaction of implanted ions with the substrate leads to ejection of ions and neutrals from the surface [9, 163]. This sputtering yield is a function of the incoming ion energy, dose and the masses of the ion and target atoms. Figures 3 and 4 show the calculated thickness of the sputtered layers for float glass, and the corresponding TRIM concentration profiles of the Ag-ion implantation [167]. Secondary features such as alterations in range with time dependent compositions after sputtering (and diffusion) was ignored. Nerveless, these figures demonstrate that for 60 keV Ag-implantation the depth concentration in the float glass differs from a Gaussian profile, and have a maximum concentration near the surface.

To take into account the alterations in range by dose effect changes in composition, new simulations, using a dynamic computer code DYNA [168, 169], based on binary collision approximations in intermixed layer formations and sputtering processes, were applied for Ag ion implantation into amorphous insulators: SiO_2, Al_2O_3 and SLSG [137]. To include a change of the near-surface layer composition due to cascade atom mixing into a concentration profile calculation, the volume of atoms has to be initially estimated, and was determined here, from the element densities or interatomic separations in the substrates. The sputtering yields at normal ion incidence are dependent on the energy of the metal-ion implantation and were separately calculated using the SRIM-2000 (TRIM) programme [162] with the corresponding binding, surface and lattice energies for amorphous SiO_2, Al_2O_3 and SLSG. The elemental concentrations for ion energies of 30, 60 and 100 keV have been obtained at doses of 0.1, 0.3, 0.6 and $1 \cdot 10^{16}$ ion/cm^2. The dose step in the calculations was $5 \cdot 10^{14}$ ion/cm^2.

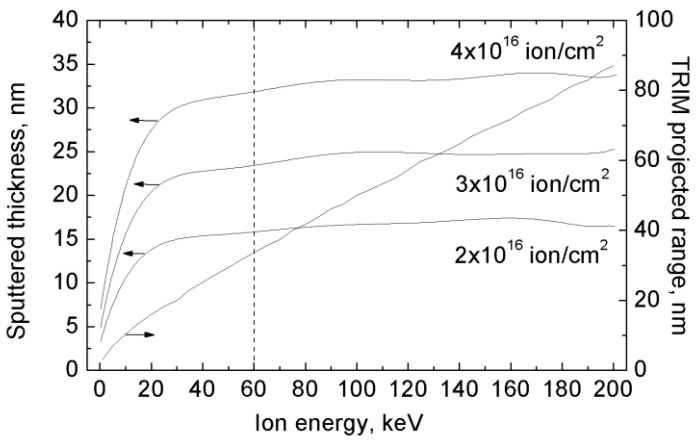

Figure 3. The calculated dependence of the Gaussian maximum in the depth, excluding sputtering (right hand scale), and thickness of the surface sputtered float glass layer (left hand scale) for Ag implanted into SLSG [167].

Copyright © 2010. Nova Science Publishers, Incorporated. All rights reserved.

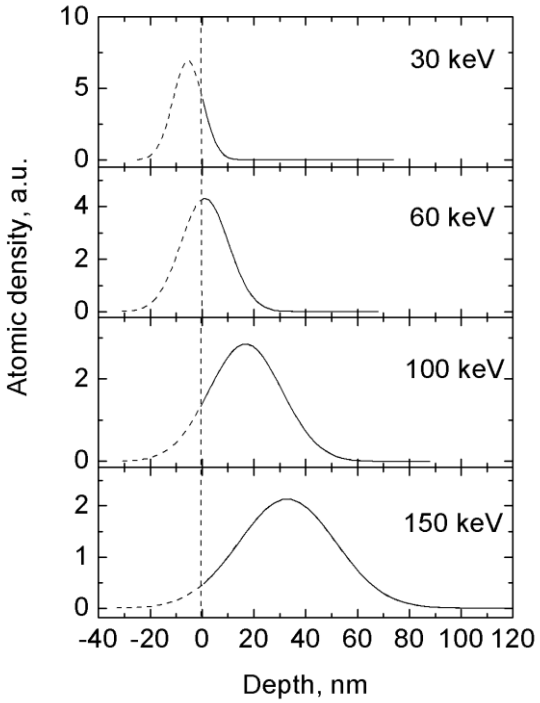

Figure 4. Calculated ion implanted silver distribution as a function of energy after taking into account the sputtering yield. The vertical dashed line indicates the final surface position, and the left part of the ion distribution from this point shows the sputtered ion portion [167].

The results of DYNA calculations for Ag ion implantation into different insulators are presented in Figure 5 [137]. Curves marked "TRIM" in these figures correspond to typical statistical TRIM calculations, which produce the Gaussian impurity distributions. Other curves 1-4 show the DYNA concentration profiles simulated for doses of 0.1, 0.3, 0.6 and $1 \cdot 10^{16}$ ion/cm^2. As shown here the peak position of the DYNA profiles appear closer to the implanted surface than the symmetrical TRIM curve. Also, the shapes of DYNA curves become asymmetrical, when the dose exceeds a critical value.

For the cases of higher energy (60 – 100 keV) implantation in it is possible to see a dynamic development of the concentration profile during the time of accumulation of implanted ions in the substrates. At the start of the implantation the impurity distribution matches the TRIM curve. As is known, high dose irradiation can, in principle, alter or limit the ultimate concentrations attainable, because of some competition between the sputtering process, and change of both the composition and density of the surface substrate layer by introduction of ions and intermixing with volume atoms. During ion implantation, the sputtering process removes both target and implanted ions. Eventually, an equilibrium condition (steady state) may be reached, where as many implanted atoms are removed by sputtering as are replenished by implantation. The depth distribution of implanted atoms under this condition typically has a maximum at the surface and falls off over a distance comparable to the initial ion range. As seen in Figure 5 this competition for the case of Ag ion implantation into dielectrics, leads to a shift of the concentration profile to the surface with increasing dose. Thus the profiles become very asymmetrical.

Copyright © 2010. Nova Science Publishers, Incorporated. All rights reserved.

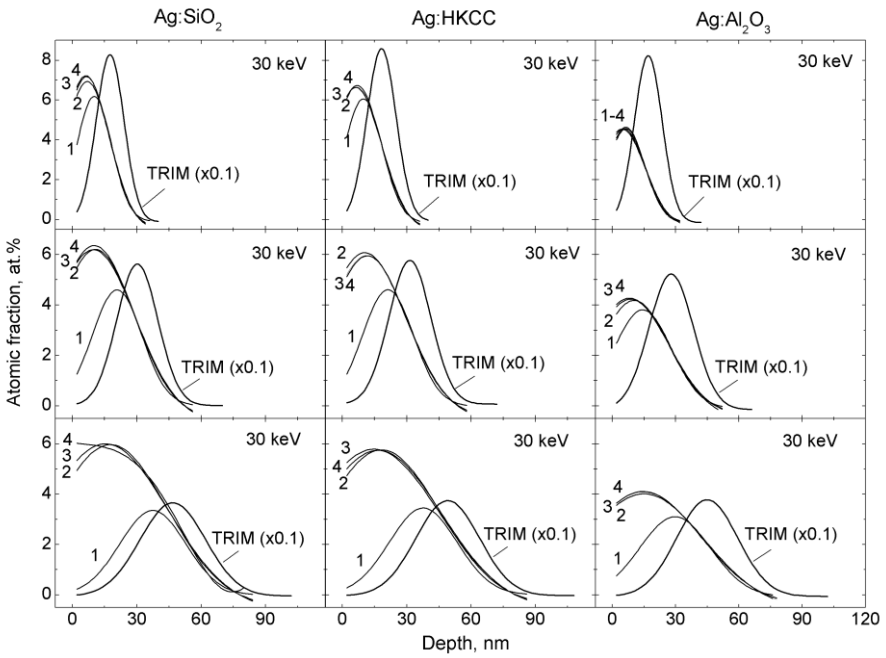

Figure 5. Calculated Ag-ion implanted depth distributions in amorphous insulators: SiO_2, Al_2O_3 and SLSG as a function of energy and dose: 1- 0.1·; 2- 0.3·; 3- 0.6· and 4- $1 \cdot 10^{16}$ ion/cm^2. There is also a profile corresponding to the TRIM simulations, which does not take into account sputtering and atom-target mixing effects [137].

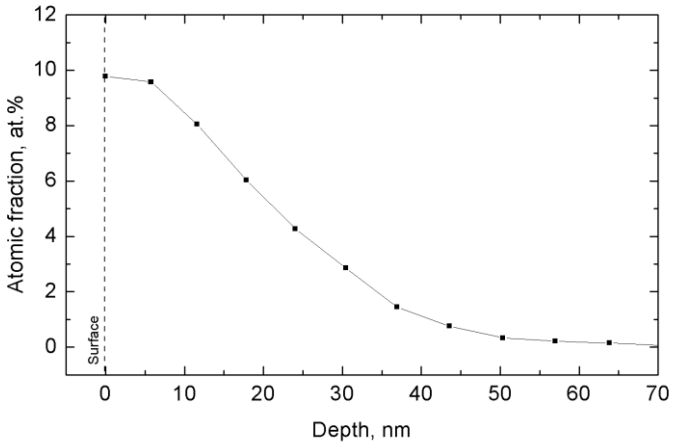

Figure 6. The depth distribution of silver derived from the RBS spectrum for ion dose of $7 \cdot 10^{16}$ ion/cm^2 at 60 keV into the SLSG [133].

All calculations were obtained at the dose simulations below 10^{16} ion/cm^2, because at higher dose implantation the increasing metal-ion concentration is above the solubility limit in these dielectrics [9]. This causes nucleation and growth of the MNPs that immediately alters the implanted ion penetration depth in the near-surface layer. Though it is impossible to calculate a correct DYNA ion-profile for high doses, nevertheless the metal distribution in

Copyright © 2010. Nova Science Publishers, Incorporated. All rights reserved.

implanted insulators for such cases may also be predicted from the present calculated data. Since both the increase of metal concentration in the depth profile and the sputtering yield depend on implantation time, then the metal particle nucleation and growth will also vary with time and depth. It is obvious that during implantation the size and growth of the particles with depth is *"proportional"* to the metal filling factor, because they are both determined by the ion concentration profile. Consequently, in accord with the calculated asymmetrical profiles for a dose of 10^{16} ion/cm^2 Figure 5, the large MNPs (or/and the higher filling factor) in the same insulators implanted with higher doses will be close to the implanted surface, with small ones in the interior of the implant zone. These predicted features for implanted MNPs are qualitatively confirmed by the silver depth concentration in the SLSG derived from experimental RBS [133] corresponds to present calculations (Figure 6).

SYNTHESIS OF SILVER NANOPARTICLES BY LOW ENERGY ION IMPLANTATION

Ion implantation is an effective technological tool for introducing single impurities into the surface layer of the substrate to a depth of several micrometers. The degree of surface modification of the materials depends on their individual chemical and structural properties, as well as on variations of implantation parameters, such as the type and energy of an implant, current density in ion beam, substrate temperature, etc. A most critical parameter is ion dose F_0, which determines the implant amount. Depending on the modification of dielectrics by irradiation, ion implantation can be conventionally divided into low-dose and high-dose processes.

In the case of low-dose irradiation ($\sim F_0 \leq 5.0 \cdot 10^{14}$ ion/cm^2), the Ag ions implanted, after stopping and thermalization, are dispersed throughout the volume of the dielectrics and are well separated from each other. The energy of the implant is transferred to the matrix via electron shell excitation (ionization) and nuclear collisions. This causes radiation-induced defects, which, in turn, may reversibly or irreversibly modify the material structure [9]. Various types of crystal structure damage have been observed in practice : extended and point defects, amorphization and local crystallization, precipitation of a new phase made up of host atoms or implanted ions, etc.

The range of high-dose implantation may be divided into two characteristic dose sub-ranges. In the range $10^{15} \leq \sim F_0 \leq 10^{17}$ ion/cm^2, the concentration of Ag ions exceeds the solubility limit of metal atoms in matrices and the system relaxes by nucleation and growth growth of MNPs (Figure 7), as illustrated in plane [121] and cross-section [81] TEM views of SiO_2 glass with ion-synthesized Ag particles (Figure 8 and 9). The threshold dose value (at which MNPs nucleate) depends on the type of the dielectric matrix and implant. For example, for 25-keV Ag+-ion implantation into $LiNbO_3$, the threshold dose was found to be $F_0 \sim 5.0 \cdot 10^{15}$ ion/cm^2 [33], for 30-keV silver ions embedded in epoxy resin, $F_0 \sim 10^{16}$ ion/cm^2 [170]. The next subrange of high-dose implantation, $\sim F_0 \geq 10^{17}$ ion/cm^2, leads to the coalescence of already existing MNPs with the formation of either MNP aggregates or thin quasi-continuous films at the dielectric surface. For instance, the irradiation of silicone polymer-glass by 30-keV Ag ions at higher-than threshold-nucleation doses favors the formation of aggregate structures (Figure 10) [171]. The MNP distribution established in the

Copyright © 2010. Nova Science Publishers, Incorporated. All rights reserved.

dielectrics after coalescence or Ostwald ripening may be dramatically disturbed by postimplantation thermal or laser annealing.

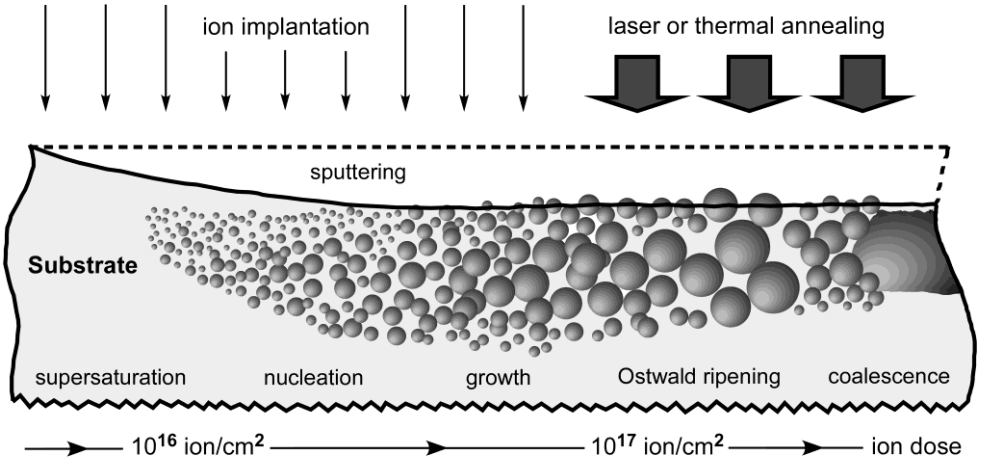

Figure 7. Basic physical processes (from left to right) involved in the formation of nanoparticle from an implant vs. the ion dose with regard to surface sputtering under irradiation.

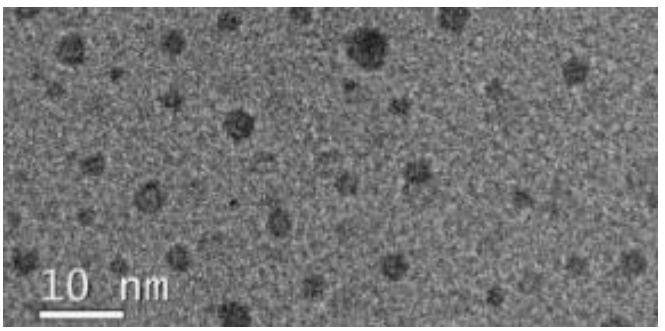

Figure 8. Plan-view TEM image of SiO_2 with Ag nanoparticles fabricated at a dose of $6.0 \cdot 10^{16}$ ion/cm^2 and an energy of 3 keV. Fragment of an image from [121].

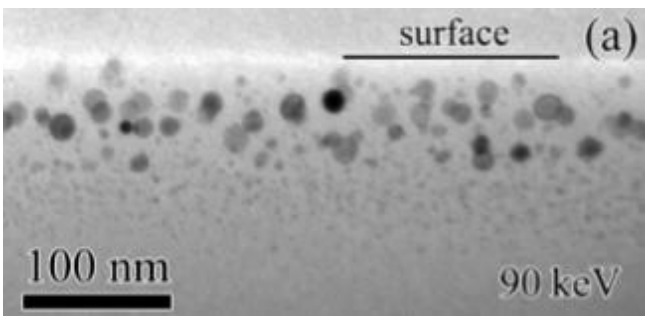

Figure 9. Cross-section TEM image of SiO_2 with Ag nanoparticles fabricated at a dose of $5.0 \cdot 10^{16}$ ion/cm^2 and an energy of 90 keV. Fragment of an image from [81].

Copyright © 2010. Nova Science Publishers, Incorporated. All rights reserved.

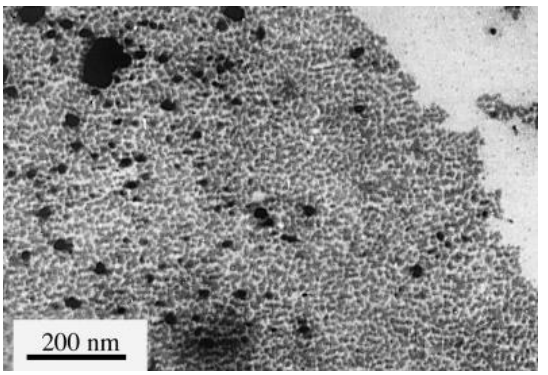

Figure 10. Plan-view TEM image of silicone polymer-glass with Ag nanoparticles fabricated at a dose of $3.0 \cdot 10^{16}$ ion/cm^2 and an energy of 30 keV [170].

ION SYNTHESIS OF SILVER NANOPARTICLES IN GLASS AT ROOM TEMPERATURE

Although the implantation is made with Ag ions, the dynamics within the ion beam trajectory in the glass and the fact that there is a large capture cross-section for electrons at low ion velocities, means that the Ag ion in SLSG will have a high probability of being in a neutral charge state (Ag^0) as it slows down. The mobility of the neutral atom is higher than that of the ion and additionally there are chemical reactions between the silver and the lattice ions. These are particularly difficult to assess in a target material such as SLSG as the surface chemistry of this multi-component glass is even more complicated than within the equilibrium conditions of the bulk material. Analyses of the surface show quite different depth distributions of the host elements, impurities and the tin dopants together with intrinsic structural defects (such as oxygen vacancy sites), and these as well as the dopant ions, exist in several valence states [172]. Within the glass medium there is competition between Ag and other ions for oxygen bond formation. However the differences in Gibbs free energies can lead to Ag-Ag bond formation and hence aggregation of several Ag atoms. As was discussed [173], in spite of the fact that the free energy of silver oxide, at -2.68 kcal/mol at 25°C, is lower then that for pure metallic silver (0 kcal/mol at 25°C), the free energy of formation of SiO_2 (~ -200 kcal/mol at 25°C) is even lower. Consequently there is dissociation of Ag-O bonds to form Si-O and Ag-Ag bonds as this reduces the total energy of the system. These same arguments suggest that the silver nanoparticles have a sharp boundary between the silver and the host glass. However, in some cases there is still evidence, which indicates that an outer silver oxide layer may act as an interface between the glass and the metal.

An excess of neutral Ag atoms in the glass, above the solubility limit, causes nucleation and growth of metal particles. If nucleation and particle growth result from attachment of neutral Ag atoms, then, if slow diffusion of substrate atoms is compared with the rate of incorporation of the implanted impurity species reaching the nucleation sites (diffusion limited growth), the attachment frequency is proportional to both the impurity diffusion coefficient and to the implant concentration [174]. Since the increase of Ag concentration in the depth profile depends on implantation time, then the metal particle nucleation will also

Copyright © 2010. Nova Science Publishers, Incorporated. All rights reserved.

vary with time and depth. In such a system the size of the growth particles with depth is partially determined by the ion concentration profile. As was shown above, for present condition of ion implantation the final Ag profile is characterized by a maximum concentration near the surface and differs from the theoretical symmetrical Gaussian distribution of the initial implantation. This implies the larger Ag nanoparticles are close to the implanted glass surface, with smaller particles in the interior of the implant zone. On the other hand, the concentration profile peak of implanted Ag ions moves during implantation, going deeper into the substrate as the sputtering, and hence, the nucleation and growth of metal particles is initiated at different depths, consistent with irradiation time and sputtering.

In practice, optical properties of Ag nanoparticles embedded into glasses are characterised by absorption and reflectance in the visible region. The intensity and spectral position of the peak depends on the concentration and size of the Ag particles, which in the case of spheres, are given by Mie theory predictions at longer wavelengths for large metal particles [175], and hence qualitative size estimates may be applied to the optical spectra. In Figure 11 the reflectance of Ag-implanted SLGT corresponding different stages (different doses) of implantation at 60 keV and at various temperature of substrate are presented. At an early stage of implantation ($2 \cdot 10^{16}$ ion/cm^2) the smallest Ag particles appear in the glass at a depth consistent with the Gaussian distribution prediction, and as seen in Figure 11a, there is no remarkable difference in the reflectance peak positions (~ 450 nm) between samples prepared at various substrate temperatures. Increasing the ion dose leads to the appearance of reflectance peaks at different wavelengths and overall changes in the shape of the reflectance curves. For a dose of $3 \cdot 10^{16}$ ion/cm^2 the peaks shifts monotonically to a longer wavelength between 470 nm for a 20°C and 500 nm for the 60°C case (Figure 11b). In these cases the Ag particles become larger, though at higher temperature there are many much smaller MNPs then at 20°C.

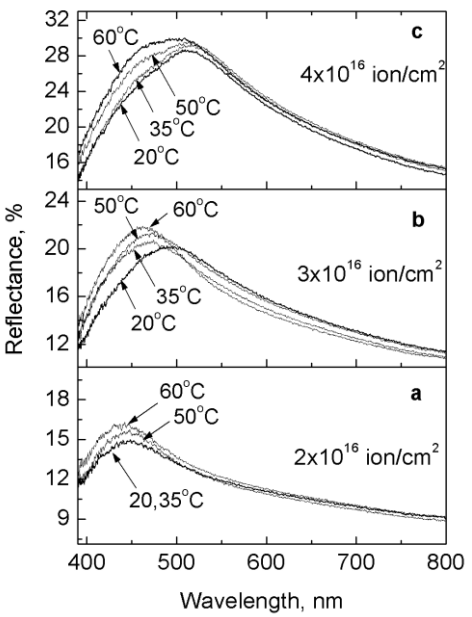

Figure 11. Reflectance of Ag-implanted SLSG at bulk-substrate temperatures of 20, 35, 50 and 60°C for various doses [146].

Copyright © 2010. Nova Science Publishers, Incorporated. All rights reserved.

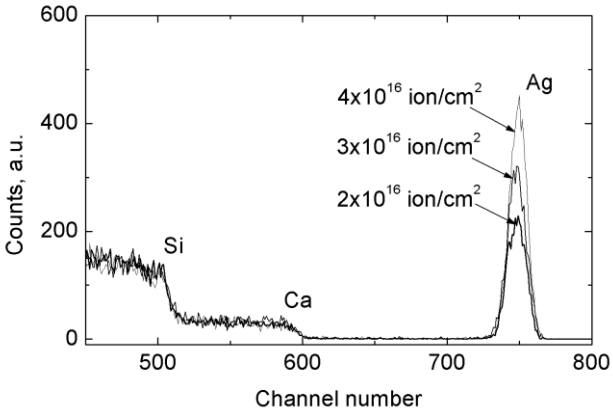

Figure 12. The RBS data for the Ag-implanted SLSG at a bulk-substrate temperature of 60ºC for various doses [148].

Greater changes in reflectance spectra were registered at the highest dose of $4 \cdot 10^{16}$ ion/cm^2. The samples prepared at temperature higher then 35°C are characterised by reflectivity consisting of overlapping spectral bands with two maxima, for example at 470 and 510 nm for 50°C implants as shown by vertical arrows in Figure 11c, and at least two distinct particle size ranges are favoured. However, in the cases of 20°C implantation there is evidence of only one broad reflectance peak, also near 510 nm. These differences in reflectance spectra in Figure 11c, and the corresponding models of the size of the Ag particles, cannot be described by variations in long-range Ag diffusion at 20 to 60°C (Figure 2) only, though some differences in diffusion values for these temperatures, of course, essential. The measured RBS data for samples prepared at the highest doses show that the width of the Ag depth penetration is approximately constant (Figure 12) [134]. Thus the formation of metal particles at high dose appears in the glass layer over the same thickness range for the temperatures between 20 and 60°C. The explanation of the appearance of a bimodal concentration dependence, which has mainly large particles in the outer region and mostly small particles in the deeper zone, may result because of the variations of the Ag ion concentration into the glass. It was suggested for the case of higher energy (> 150 keV) Ag-implants into glass [32], that one depth region is set by the penetration maximum of the Gaussian concentration profile, and the second is at maximum of glass damage where there are peaks in the vacancy concentration, displaced atoms, pint defects and broken bonds. Similar consideration was applied for the present case of low energy implantation. In Figure 13 the concentration profile calculated from the TRIM programme, and the corresponding vacancy profile, are presented for the case of 60 keV Ag implants into SLSG using the SRIM-2000 programme [162]. It is seen that the maximum of glass-damage profile is resolved from the Ag concentration peak, and is placed closer to the irradiated glass surface. Taking into account the enhanced Ag damage-related diffusion to the surface, which is effective at higher temperature (60°C), it is possible to explain the probabilities for accumulation of Ag atoms with the consequent growth of metal particles in the damage region. It should be noted, that damage profiles move from the irradiated substrate surface, consistent with sputtering. Overall the distributions of the impurity and damage profiles result in formation of bigger particles close to the glass surface, with a range of smaller particles deeper below the surface.

Copyright © 2010. Nova Science Publishers, Incorporated. All rights reserved.

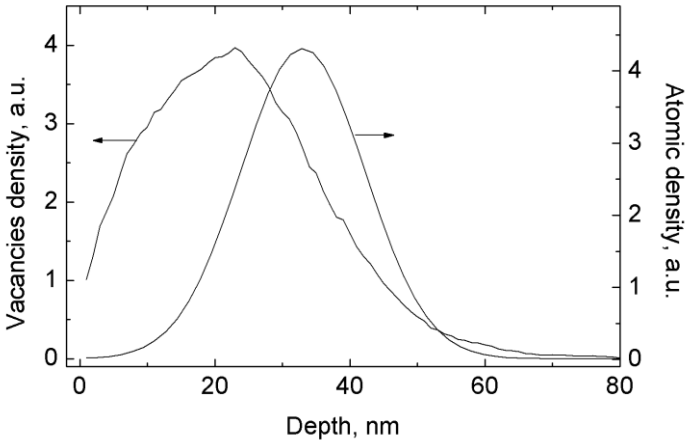

Figure 13. Calculated 60 keV implanted silver TRIM concentration profile in SLSG (right hand scale), and vacancy distributions (left hand scale), as characteristic of radiation glass damage without taking into account the sputtering process [210].

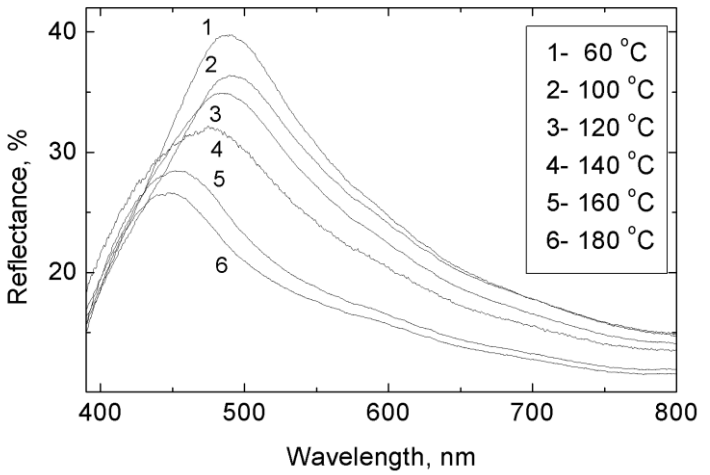

Figure 14. Reflectance of 60 keV Ag-implanted float glass for a dose of $4 \cdot 10^{16}$ ion/cm^2 at various SLSG temperatures [210].

The reflectance spectra for similar samples Ag-implanted at the different temperature of SLSG from 60 to 180ºC is presented in Figure 14 [167]. The net reflectance and average particle size both decrease with higher temperature implants. The reflectance peak moves from 490 (60°C) to 450 nm (180°C) and the intensity decreases by ~14%. This optical result is consistent with RBS data, which shows that the high temperature implants lower the local concentration, both by inward diffusion and by enhanced sputter losses RBS spectra are plotted in Figure 15 [167]. These indicate a sharp Ag peak at 60°C, but by 180°C, there is loss of Ag from the glass surface (~19 %) and Ag in-diffusion from the implanted layer. Thus the average Ag size decreases as seen by the reflectance data. Similar trends were exemplified in earlier RBS measurements [166] using implantation at the temberature from 250 to 600°C. For high-temperature Ag ion implantation into dielectrics, the diffusion coefficient drops

Copyright © 2010. Nova Science Publishers, Incorporated. All rights reserved.

dramatically after MNP formation. This means that the critical time for metal particle nucleation is the beginning of the implantation as it was suggested above from TRIM calculation for different temperatures of substrate, and therefore the substrate temperature during this initial phase. After particle nucleation has commenced, any changes, such as increasing temperature from beam heating or increases in ion current, will not interrupt the growth of metal particles. Conversely, high temperature conditions initially will increase the impurity diffusion and so reduce supersaturation and particle nucleation.

OPTICAL REFLECTANCE ION-SYNTHESISED SILVER NANOPARTICLES

Ion implantation gives the possibilities for the synthesis of metal nanoparticles in the volume of insulators with high values for the metal filling factor that lead to new perspectives for their opto-electronic applications. The optical properties of glasses containing implanted nanoparticles have been studied extensively by linear absorption spectroscopy, by the z-scan method or by direct measurements of the third-order optical susceptibility. The interpretation of experimental optical data is usually based on a restricted approximation in which the composite material acts as a dielectric medium containing equal-size metal nanoparticles, uniformly distributed in the total implanted volume. Moreover many authors assume that the absorption band is defined by measurements of transmission data only, which is incorrect [176]. To derive the absorption properties of a thin composite layer, one must separate effects of absorption from reflection in the measured transmission data. In a simplistic model of a uniform nanoparticle distribution throughout the bulk, there is no inconsistency, but this does not apply to the real ion-implanted material. One of the main features of the ion implantation process is a non-uniform statistical penetration of accelerated ions into the substrate that leads to the growth of metal particles with a very wide size distribution in the depth from the irradiated glass surface, as was shown by electron microscopy [57, 125]. Failure to include this non-uniformity causes considerable error in assessing the particle size distribution and in interpretation of optical properties. One of the possibilities for analysing of optical properties of dielectrics with non-uniform size distribution of refractive index over the depth, is the consideration of the composite as consisting of a number of layers with specific-size particles [176]. This approach could be also used for modelling and description of the optical reflectance of glass containing silver nanoparticles formed by ion implantation.

As was shown in Figure 6, low energy implantation of metal ions leads to a non-uniform distribution in the glass, which is different from the statistical Gaussian profile. Silver depth concentration in SLSG derived from experimental RBS spectra shows a maximum near the implanted surface of the sample with some penetration to about 60 nm. The large silver nanoparticles in the glass are close to the implanted surface with small ones in the interior of the implant zone.

Optical spectra of such implanted glass are presented in Figure 16. The transmittance spectrum is characterised by a deep minimum near 430 nm and the shape of spectral curve is almost symmetrical. The reflectance spectra are more complex and, although the transmission is the same whether the glass is viewed from the implanted or the reverse face, the shapes of the reflectivity curves differ. Overlapping peaks of reflectance spectra measured from the

Copyright © 2010. Nova Science Publishers, Incorporated. All rights reserved.

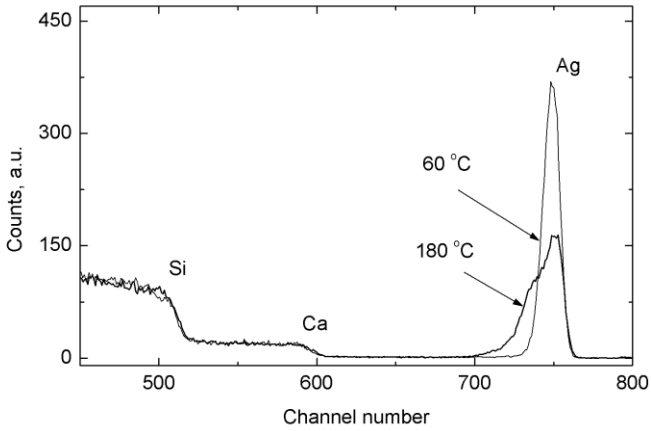

Figure 15. The RBS data for the 60 keV Ag-implanted float glass for a dose of $4 \cdot 10^{16}$ ion/cm^2 at surface-substrate temperatures of SLSG [167].

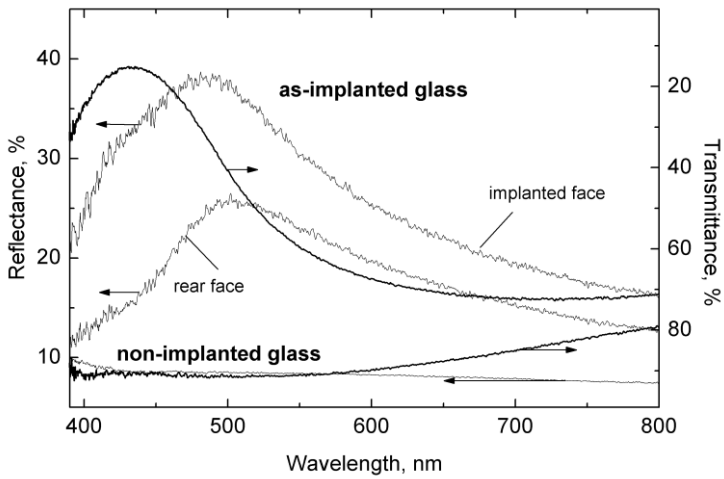

Figure 16. Optical transmittance and reflectance of the silver implanted SLSG and virgin glass with a dose of $7 \cdot 10^{16}$ ion/cm^2 and an energy of 60 keV.. Reflectance was measured from both the implanted and rear faces of the sample [132].

implant face of the samples exhibit a shoulder at about 430 nm, on the left side of a clearly determined maximum at 490 nm, whereas reflectivity from the rear face appears to have a simpler peak at longer wavelengths near 500 nm.

As the typical sizes of spherical metal particles formed by ion implantation are orders of magnitude smaller than the wavelengths of visible light [9] (Figure 8 - 10), composite optical properties can be treated in terms of an effective medium theory. Also the laws of geometric optics for light beam directions and the Fresnel formulae for the intensities can be applied. An effective dielectric permeability, ε_{eff}, provided for dispersions of spherical metal particles with complex dielectric constants, ε_{Ag}, and a filling factor, *f*, in a surrounding glass (ε_m) for implanted composite may be derived from the effective medium theory, for example Maxwell-Garnet equation [177, 178]. For reflectivity evaluation of the composite material

Copyright © 2010. Nova Science Publishers, Incorporated. All rights reserved.

with a metal distribution which is changing in depth, and hence with a changing ε_{eff}, the implanted sample was considered as consisting of thin homogeneous isotropic layers characterised with their own constant ε_{eff} and *f*. For calculation of the multilayer reflectance, a matrix method [176] using the complex Fresnel coefficients was applied in this study for the case of normal incidence of the light. The values of *f* and thicknesses of composite layers may be estimated at different depths in the sample from Figure 6. Assuming the surrounding glass to be a non-absorbing medium it should be noted that the refractive index of SLSG (1.54) increases after incorporation of dispersed silver ions in its volume [179].

Firstly, consider the case of reflectivity from a single absorbing layer with ε_{eff} on a transparent substrate. Using the symbolic expressions derived from the matrix method for reflectance of such a structure [176], it is possible to calculate the optical spectra of the surface layer. For trial values of: a refractive index ($n_1 = 1.9$) of the layer containing metal particles, thickness of 9 nm, *f* from 0.05 to 0.16 and a refractive index of SLSG substrate with silver atoms as $n_{sub} = 1.6$, the set of computed spectra are presented in Figure 17. The reflectance intensity increases and the position of the reflectivity peak shifts continuously toward longer wavelengths with increasing *f*, as expected for optical spectral bands when using the Maxwell-Garnet theory. is a single maximum corresponding to each *f* value. Hence such a consideration cannot describe the experimental reflectance spectra with at least two overlapping peaks shown in Figure 16, and modelling in terms of a single-layer structure with an average metal concentration (*f*) is not suitable. Proceeding to the next modelling case of two absorbing layers, each with a thickness of 9 nm on a transparent substrate, generates data of the form shown in Figure 18. Examples shown in Figure 18a are modelled for the case of reflectance from the implanted face of an implanted sample where the top medium has a very low refractive index ($n_0 = 1$), a high index first metal layer with refractive index of $n_1 = 1.9$, and a second layer with $n_2 = 1.7$. The value of the substrate refractive index was the same as in the previous system at $n_{sub} = 1.6$. Optical spectra in Figure 18a present the calculations when *f* in the surface layer is changed from 0.08 to 0.16, and the deeper layer has a constant $f = 0.05$. In Figure 18a all the examples predict reflectivity from the implanted sample face to be characterised by two peaks: one at 430 nm and another between 440 and 480 nm. The second peak corresponds to the surface layer, where the increasing silver concentration (*f*) shifts the peak position towards longer wavelengths. However, there are clear differences between the experimental reflectivity spectra from the implanted and the rear faces of the layers (Figure 16), and so calculated spectra for reflectivity from the substrate side of the same multilayer structure are presented in Figure 18b. Again there are two wavelength peaks, at somewhat different positions in the spectra, and the more intense reflectance band corresponds to the deeper layer, (from this viewing direction). Although the layer with a low value of *f* is effectively the outer layer, for rear face reflectivity, the intensity of the reflectance band at 430 nm corresponding to this layer is weaker than the reflectance for the same layer when measured from the implanted face (Figure 18a). The second essential feature is that the spectral peaks of the layers with high values of *f* appear at longer wavelengths for reflectance measured from the rear face. This calculation therefore predicts the pattern seen in the experimental reflectance data shown in Figure 16, that emphasises the differences between front and rear face reflectivity for non-uniform nanoparticle depth distributions and underlines the problem that simple analyses of the transmission and front face reflectivity data do not give all the information required to derive the optical absorption band shapes.

Copyright © 2010. Nova Science Publishers, Incorporated. All rights reserved.

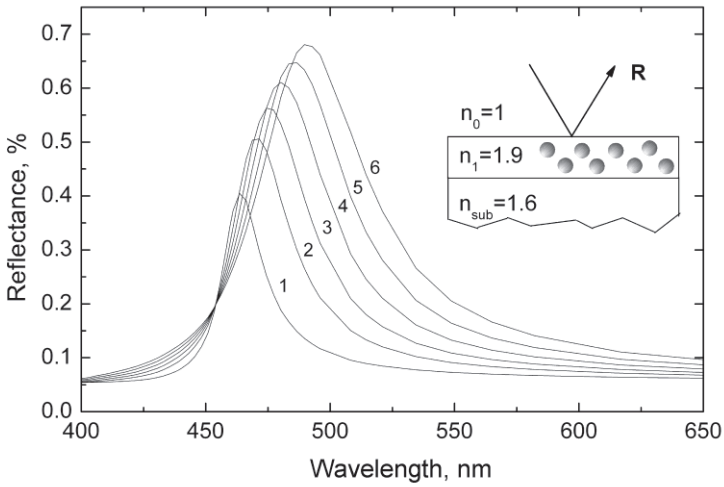

Figure 17. Calculated optical reflectance of the silver-glass composites. Spectral curves correspond to layers with a metal filling factor: (1) 0.05 , (2) 0.08 , (3) 0.1 , (4) 0.12 , (5) 0.14 , (6) 0.16 [136].

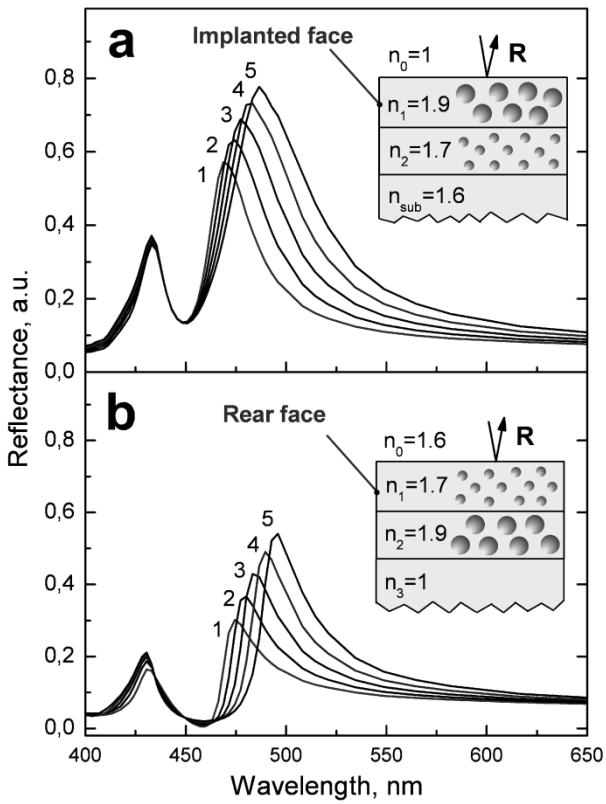

Figure 18. Calculated optical reflectance of the silver-glass composites. Spectral curves correspond to a layer a with refractive index of 1.9 and a metal filling factor: (1) 0.08 , (2) 0.1 , (3) 0.12 , (4) 0.14 , (5) 0.16. In the layer with refractive index of 1.7 the filling factor is 0.05. Figs. (a) and (b) correspond to implanted and rear face reflectivity, respectively [136].

Copyright © 2010. Nova Science Publishers, Incorporated. All rights reserved.

EFFECT OF SURFACE TEMPERATURE ON SILVER NANOPARTICLES FORMATION

Inevitably during ion implantation into an dielectrics, which is a poor thermal conductor, there is temperature gradient near the glass surface, as a nucleation and growth in the surface layer differ from those estimated by knowledge of the result of ion beam heating. Hence the effective temperature conditions for metal controlled substrate/holder temperature – bulk glass temperature. The measured parameter is therefore only a first step in the control process, although it can result in reproducible samples. To reveal the influence of the surface temperature gradient on the formation of metal nanoparticles in the glass implantation of thin (0.15 mm) and thick (3.1 mm) SLSG samples at the same temperature of 35°C were compared [142]. Both samples were fixed to watercooled sample holed during implantation by thermoglue. It was assumed the surface temperature of the thick sample should be higher than in the thinner one and hence identical implant conditions will result in appearance of differences in the size of Ag nanoparticles, and their optical characteristics. Measurements of the transmittance and reflectance from both the implanted and rear face of the samples were made, and corresponding spectra are presented in Figure 19. As seen from the figure there are no remarkable spectral differences between the transmittance curves from Ag nanoparticles into the samples near 425 nm, but some minor changes in the near-red transmittance. However, there are clear differences in the reflectance data. In previous paragraph the contrast between the information available from transmission and reflectivity has been stressed, and the changes are recognized as coming from the growth of Ag-implanted nanoparticles, which vary with depth into the glass surface.

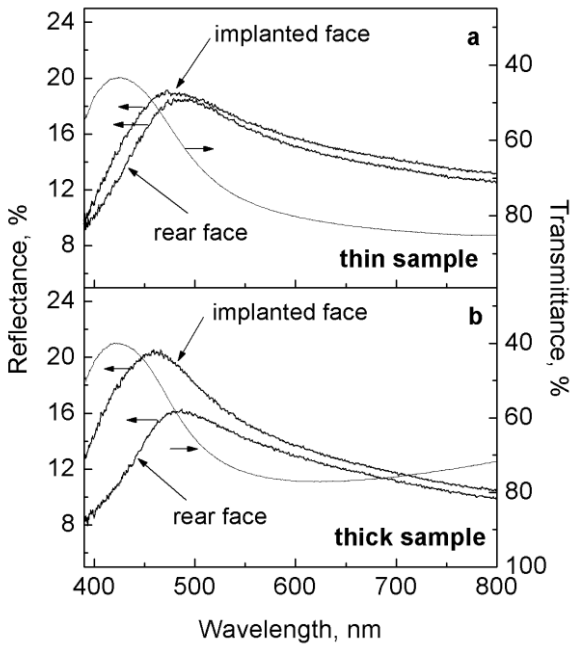

Figure 19. Comparison of the transmission (right hand scale) and reflectance (left hand scale) of 60 keV Ag-implanted SLSG with dose of $3 \cdot 10^{16}$ ion/cm^2 and at bulk-substrate (target holder) temperatures of 35°C for various thicknesses of irradiated substrate: a.- this sample of 0.15 mm; b.- thick sample of 3.1 mm. All the samples were measured from the implanted and rear faces [142].

Copyright © 2010. Nova Science Publishers, Incorporated. All rights reserved.

The differences between implanted and rear face reflectivity of a thick sample, which contain peaks near 450 and 475 nm, (Figure 19b), immediately emphasise that the distribution of particle sizes vary with depth beneath the implant surface. Although the transmission is the same whether the glass is viewed from the implanted or the reverse face, the shapes of the reflectivity curves differ. Whilst the reflectance differences from implanted and rear faces are monitoring an asymmetry of the nanoparticle size distribution and concentration of the particles with depth into the sample, the precise distributions cannot be determined. As already mentioned, particles of larger size are concentrated near the implanted glass surface, whereas small ones occur throughout the ion range. The reflectances from thin and thick samples are very different in spectral shape, although the RBS data for samples in both cases show an approximately constant width for the Ag distribution profile. Moreover, the reflectance from implanted and rear faces of thin samples, with peaks near 470 and 480 nm, are very similar in shape and intensity to each other (Figure 19a). This suggests that the smaller temperature gradient across the glass results in a more symmetrical particle size distribution with depth. Moreover, the position of reflectance peaks of the thin sample are at longer wavelengths than in thick samples, indicating formation of a more uniform distribution of large particles.

Quite clearly the reason for differences in reflectance between thick and thin samples results from the different temperature gradient at the irradiated surface, and as seen from data in Figure 19 suggests that for thin samples there is closer control to the base temperature of 35 °C. For thin samples a more uniform particle size-depth distribution was produced than for thick glass targets. Since such temperature gradients and average temperature differences exist relatively close to room temperature, it is worth noting that this is contrary to some of the early models for describing the nanoparticle formation in insulators by ion implantation which are based on thermal spike considerations, as these assume the local temperature inside an ion trajectory within a silicate glass to be ~ 3,000 K [180]. Such mechanisms would not respond in the way described here. Modeling suggests that radiation damage enhanced Ag diffusion in glass is important, as are the temperature gradients, which develop in the surface of the insulator during implantation. Overall the initial beam and temperature conditions have a major influence on the resulting nanoparticle generation.

SILVER NANOPARTICLES FORMATION AT DIFFERENT CURRENT DENSITIES

The fabrication of silver nanoparticles in a dielectric matrix by ion implantation is a complex process which depends on a number of factors. The conditions of metal nanoparticle synthesis can be varied depending on the ion implantation parameters such as ion energy, dose, ion current, target temperature etc. In previous paragraphs it was that temperature of the irradiated glass is a significant factor for size control of the MNPs. Unfortunately, the target temperature is often ignored in experiments. Let us now to consider an influence of the ion current density and concomitant thermal effects on the silver nanoparticle formation and surface modification under the low-energy ion implantation of silicate glass (SiO_2).

Copyright © 2010. Nova Science Publishers, Incorporated. All rights reserved.

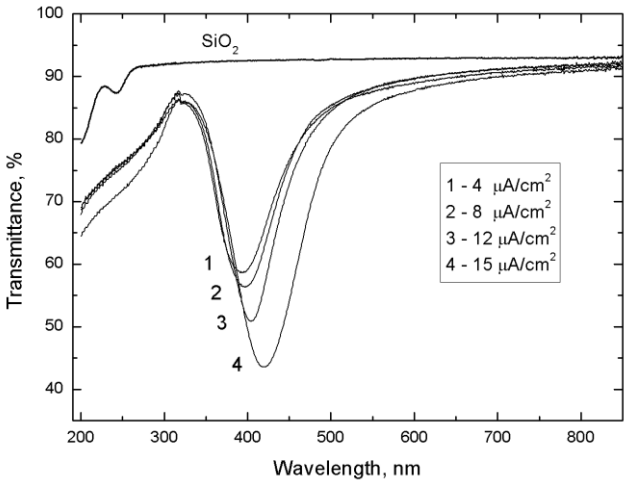

Figure 20. Transmittance spectra of SiO_2 samples after Ag^+ ion implantation with dose of $5 \cdot 10^{16}$ ion/cm^2 at various ion current densities [151].

Formation of the Ag nanoparticles in the implanted SiO_2 was estimated by the optical transmittance measurements showing an appearance of the characteristic band of SPR absorption. It was observed [151] that the increase of the ion current density monotonically shifts the absorption band to longer wavelengths indicating the rise of the nanoparticle sizes (Figure 20).

AFM image of the virgin glass surface, which is relatively smooth, is shown in Figure 21. AFM images in Figure 22 show the glass surface morphology produced by the Ag^+ ion implantation at different current densities in the beam [151]. Compared to Figure 21, formation of semi-spherical hillocks is observed for all implanted samples. This surface structure is explained by the sputtering of glass layer resulted in partial towering of the spherical-shaped metal nanoparticles nucleated in the near-surface layer of the substrate. Similar morphology was earlier detected by AFM for different metal nanoparticles synthesised in various dielectrics by low-energy implantation, for example: Ag ions into Ta_2O_5, SiO_2, Si_3N_4 [21, 66]. It is seen from the images of Figure 22 that the hillock size (or particle sizes) increases with the ion current density. This result is in good correlation with the observed optical dependences (Figure 20).

The formation of bigger particles at higher ion current densities, when the dose is constant, may be explained by an increase in Ag atom mobility and faster particle nucleation. The increase in the diffusion mobility is expected due to the substrate heating by the implantation at high dose rate. The numerical estimation presented in shown that the coefficient of diffusion of silver atoms in the glass increased for two orders of magnitude with the substrate temperature rise from 20 to 100°C (Figure 2). At the beginning of implantation all samples in our case were at the same room temperature but, it is obvious, that by the moment of collection of the ion dose the substrate implanted at higher ion current density has higher temperature. Thus, the change in ion current density under implantation of metal ions into dielectric considerably affects the formation of metal nanoparticles. This method can be used for control of particle size to synthesise the metal/dielectric composites with desirable parameters.

Copyright © 2010. Nova Science Publishers, Incorporated. All rights reserved.

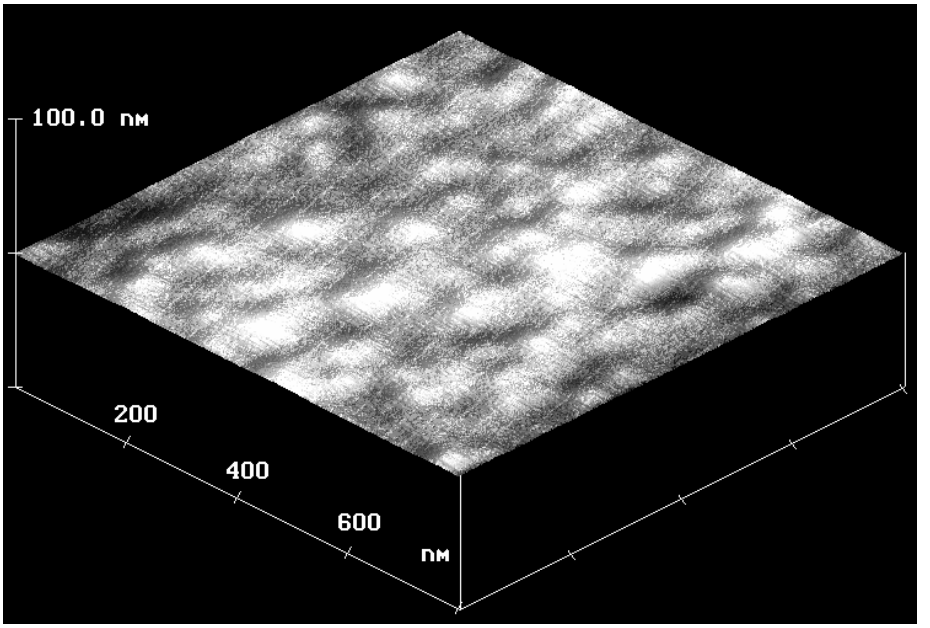

Figure 21. AFM image of SiO_2 surface before ion implantation [151].

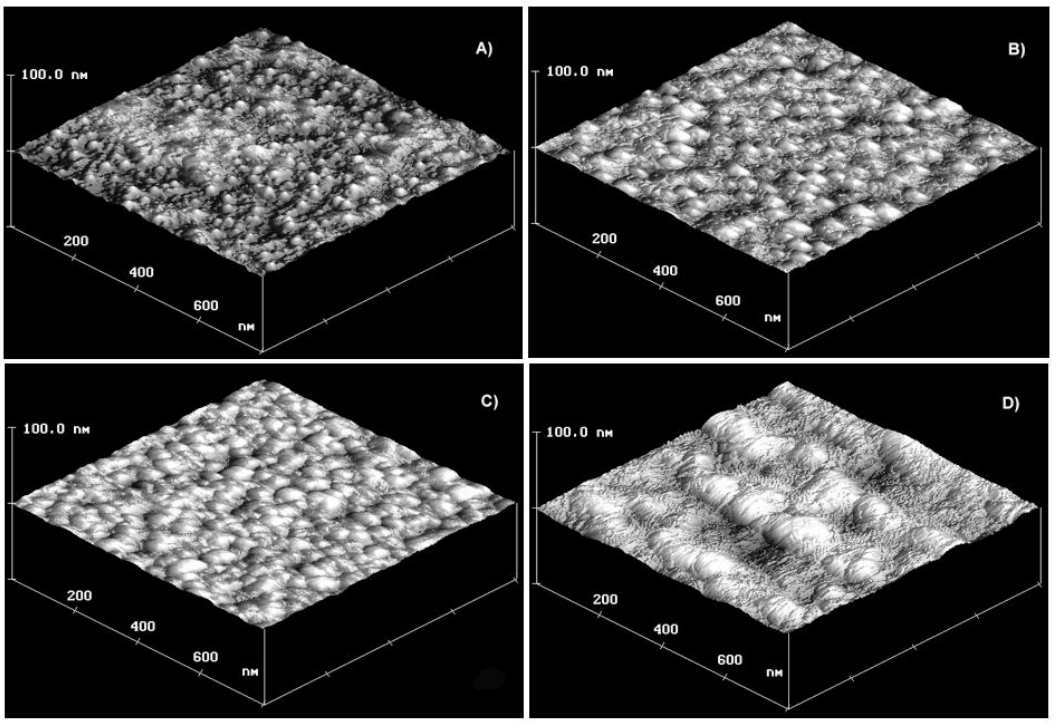

Figure 22. AFM images of SiO_2 surfaces implanted at different ion current densities: a) 4; b) 8; c) 12; d) 15 $\mu A/cm^2$ [151].

Copyright © 2010. Nova Science Publishers, Incorporated. All rights reserved.

THERMAL ANNEALING OF DIELECTRICS WITH IMPLANTED SILVER NANOPARTICLES

Ion implantation and diffusion of metals into insulators can lead to an excess of the metal which is unstable in the form of atomically dispersed particles. The systems relax into precipitates of metal nanoparticles. As was considered, one problem is that, as formed, there is invariably a wide distribution in the sample depth in terms of nanoparticle size. Many features, such as the optical response, are size dependent, hence for any potential application, variations in size degrade the performance, or confuse the interpretation of the fundamental processes. Consider the possibility of the furnace annealing for modification of metal nanoparticles in implanted dielectrics. Again, as in previous case, the size distribution of metal particles is monitored by optical transmittance and reflectance from both the implant and rear face of the samples. The difference between the data indicates the asymmetry in the size distribution with depth.

For the Ag ion implantation of SLSG at 60 keV and the dose of $7 \cdot 10^{16}$ ion/cm^2 is characterised by optical transmission, maximised near 430 nm, with a long wavelength tail extending across the entire visible range (Figure 23a) [135]. Reflectance spectra measured from the implant face of such samples partially resolve overlapping peals, as a clearly determined maximum at 490 nm and the 430 nm shoulder. Where reflectivity from the rear face is peaked more obviously at 500 nm. Note that there are major differences shown in Figure 23a between assessments of the peak optical changes, and widths, for transmission, and front and rear face reflectivity.

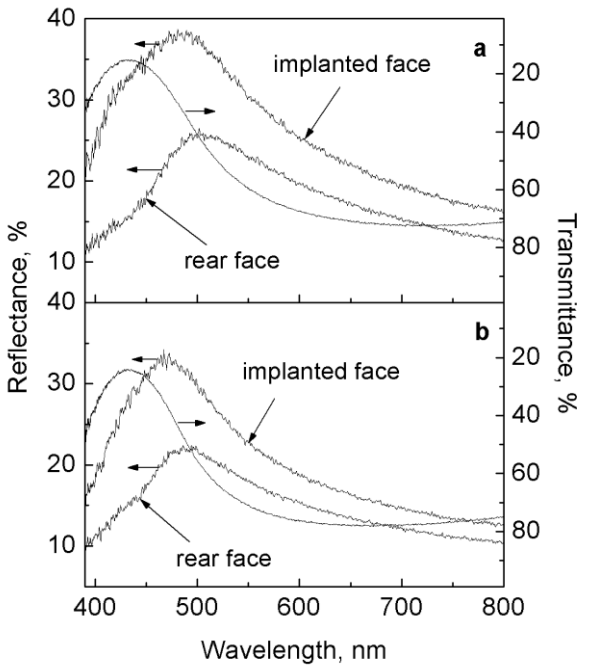

Figure 23. Comparisons of the transmission and reflectivity spectra of ion implanted silver in SLSG: (a) for the sample after implantation; (b) the spectra after a furnace annealing at a temperature of 350ºC for 3 h in atmosphere [135].

Copyright © 2010. Nova Science Publishers, Incorporated. All rights reserved.

The simplest method of altering the structure and distribution of the metal nanoparticles is to use a furnace annealing. The treatment can allow a mixture of diffusion, dissolution of the large clusters, or growth from small particles. These competing factors are strongly temperature dependent, but for the present purposes, the example from only a single temperature heating, of 350ºC, are presented in Figure 23b [135]. For studies of nanoparticles it is essential to note that the results can be influenced by the rate of cooling from the high temperature. The magnitude of the signals, and their wavelength maxima , are markedly different for front and rear face reflectance measurements as in the case of as-implanted samples. In another words, there is the contrast between reflection spectra, which demonstrates the wide size distribution of nanoparticles in the depth. Ideally, a narrow size distribution would introduce the symmetrical reflectance bands.

NONLINEAR OPTICAL ABSORPTION OF ION-SYNTHESISED SILVER NANOPARTICLES

The Ag nanoparticles doped in different dielectrics demonstrate variable nonlinear optical properties [181]. The interest on such structures is based on the prospects of the elaboration of optical switchers with ultrafast response, optical limiters, and intracavity elements for mode locking. Ag nanoparticles have an advantage over another metal nanoparticles (i.e., gold and copper) from the point of view that the surface plasmon resonance energy of Ag is far from the interband transition energy. So, in the silver nanoparticle system it is possible to investigate the nonlinear optical processes caused solely by SPP contribution. It should be noted that previous studies of nonlinear optical parameters of silver nanoparticles-doped glasses were mostly focused on determination of third-order nonlinear susceptibility $\chi^{(3)}$. It was previously predicted that silver-doped glasses possess by saturated absorption. The spectral dispersion of the imaginary part of third-order susceptibility $\mathrm{Im}\chi^{(3)}$ of silver-doped glass matrices was analyzed and it was shown that $\mathrm{Im}\chi^{(3)}$ was negative in the spectral range of 385 – 436 nm [182]. The nonlinear absorption coefficient β is also negative in the case of saturated absorption. The saturated absorption in silicate glasses doped with Ag nanoparticles at wavelength of 532 nm and their dependence on laser radiation intensity are considered at present paragraph.

The Ag nanoparticles ion-synthesized in SLSG (Ag:SLSG) and (Ag:SiO_2) demonstrate the SPP band with minimum transmission in the range of 410–440 nm (Figure 24) [183]. The normalized transmittance dependences of Ag:SLSG and Ag:SiO_2 samples measured using open aperture Z-scan scheme at laser radiation intensity of $I_0 = 2.5 \cdot 10^9$ W/cm^2 and pulse duration of 55 ps is presented in Figure 25 [184]. The transmission of samples was increased due to saturated absorption as they approached close to the focal plane. After fitting of experimental data the β are $-6.7 \cdot 10^{-5}$ cm/W in Ag:SLSG and $-3.6 \cdot 10^{-5}$ cm/W in Ag:SiO_2. Coefficient β can be presented as $\beta = \alpha / I_s$ where is I_s saturated intensity. The values of I_s are $1.1 \cdot 10^9$ and $1.4 \cdot 10^9$ W/cm^{-2}, also the $\mathrm{Im}\chi^{(3)}$ are $-2.4 \cdot 10^{-8}$ and $-1.3 \cdot 10^{-8}$ esu in Ag:SLSG and Ag:SiO_2, respectively. In Figures 26 and 27 values of β in dependence of laser intensity varied from 10^9 to $2 \cdot 10^{10}$ W/cm^2 are presented [184]. As seen from the figures there are a decrease β of for higher intensities. In particularly, a 21- and 12-fold decrease of β was

Copyright © 2010. Nova Science Publishers, Incorporated. All rights reserved.

measured at $I_0 = 1.15 \cdot 10^{10}$ W/cm^2 for Ag:SLSG and Ag:SG, respectively, compared to β detected at $I_0 = 1 \cdot 10^9$ W/cm^2.

The variations of transmission in similar MNP structures were attributed in some cases to the fragmentation [185-187], or fusion [188] of nanoparticles following the photothermal melting. It was reported about the alteration of the sign of nonlinear refractive index of small Ag clusters embedded in SLSG [189]. They noted that thermal effects could change the properties of nanoclusters. The transparency in these samples was associated with oxidation of Ag nanoparticles. However, no irreversible changes of transmittance were observed in present experiments.

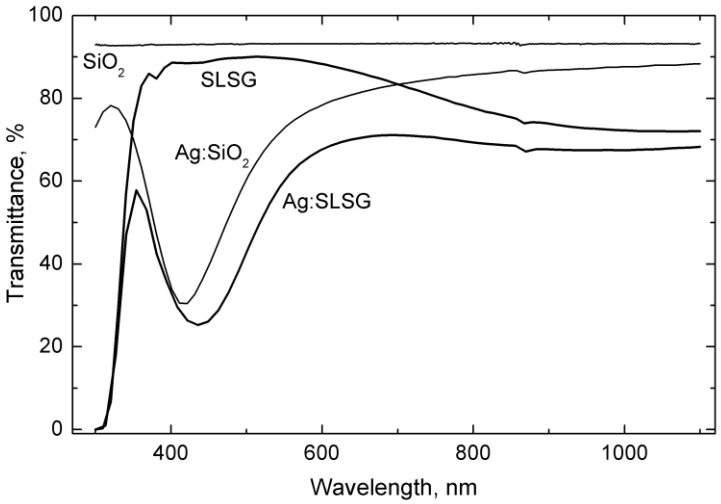

Figure 24. Optical transmittance of the Ag nanoparticles formed in SLSG and SiO_2 by implantation with a dose of $4 \cdot 10^{16}$ ion/cm^2 and an energy of 60 keV [183].

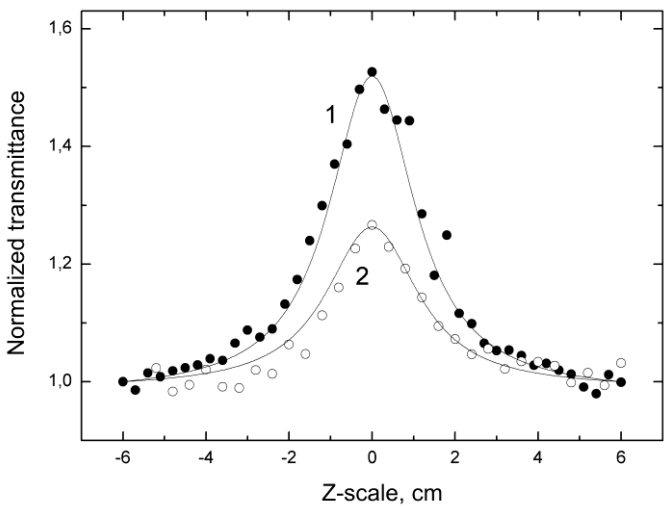

Figure 25. Normalised transmittance Ag:SLSG (1) and Ag:SiO_2 (2) samples at laser radiation intensity of $I_0 = 2.5 \cdot 10^9$ W/cm^2. Solis lines show theoretical fittings [184].

Copyright © 2010. Nova Science Publishers, Incorporated. All rights reserved.

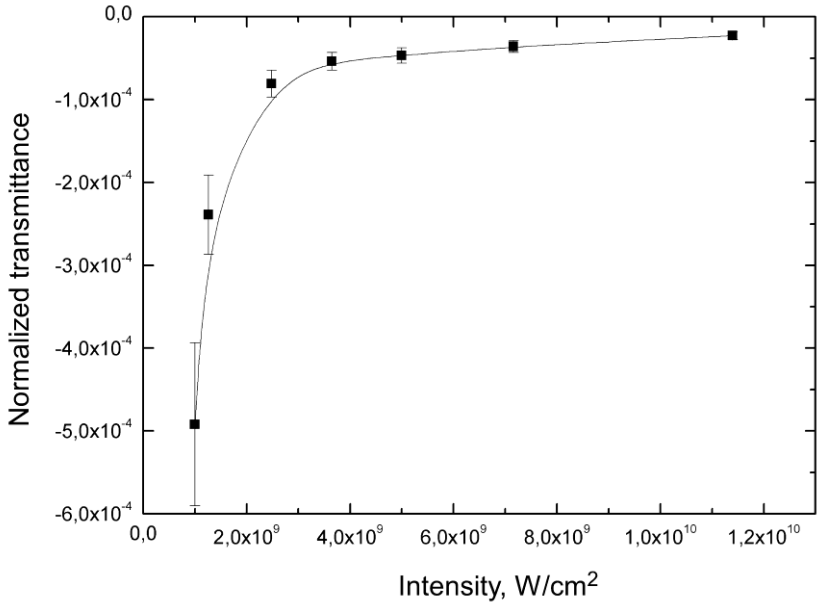

Figure 26. Coefficient β of Ag:SLSG in dependence of laser intensity [184].

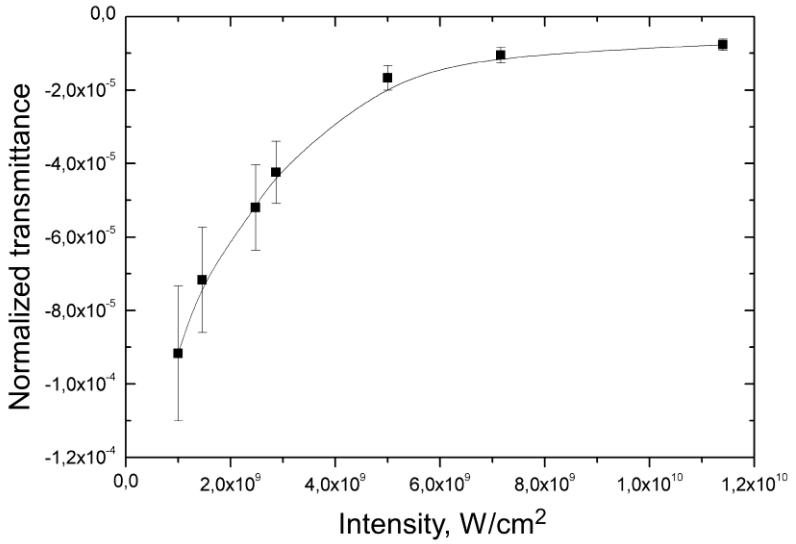

Figure 27. Coefficient β of Ag:SiO_2 in dependence of laser intensity [184].

The reverse saturated absorption can be responsible for the decrease of negative nonlinear absorption of Ag nanoparticles and it could be assume that in the case of picosecond pulses the reverse saturated absorption starting to play an important role in the overall dynamics of nonlinear optical transmittance of metal nanoparticles contained compounds, taking into account the saturation of intermediate transitions responsible for saturated absorption. Thus, saturated absorption in Ag:SLSG and Ag:SiO_2 was dominated at small intensities and

Copyright © 2010. Nova Science Publishers, Incorporated. All rights reserved.

decreased with the growth of intensity due to influence of competing effects, whereas the selfdefocusing at low intensities was changed to self-focusing at high intensities. The possible mechanism of the decrease of $\mathrm{Im}\chi^{(3)}$ is the influence of nonlinear optical processes with opposite dependences on laser intensity, also such as two-photon absorption [181]. The wavelength range corresponded to the interband transitions in Ag is located below 320 nm, so the two-photon absorption connected with interband transitions can be involved in the case of 532 nm radiation. The possibility of two-photon absorption due to interband transition of photoexcited electrons was previously demonstrated for Ag particles [58]. The three-photon absorption connected with interband transition for Ag nanoparticles was analysed in [190]. Thus, saturated absorption in Ag:SLSG and Ag:SiO_2 was dominated at small intensities and decreased with the growth of intensity due to influence of competing effects, whereas the selfdefocusing at low intensities was changed to self-focusing at high intensities.

LASER ANNEALING OF GLASSES WITH ION-SYNTHESISED SILVER NANOPARTICLES

Despite advantages the use of ion implantation for nanoparticle synthesis there have not yet emerged clear mechanisms which allow precisely controlled particles sizes and depth distributions. Latter has a certain drawback, which is the statistically nonuniform depth of penetration of implanted ions into a material. As was shown in previous paragraphs this leads to a wide size distribution of synthesized nanoparticles not only in the plane parallel to the irradiated surface but to a great extent also over the depth of the sample. Dispersion of nanoparticles with respect to sizes leads to a broadening of the SPR optical absorption band accompanied by a decrease it in the intensity [4]. This is also attributable to the dependence of the SPR spectral position on the particle size, i.e. the absorption spectrum in real sample is a superposition of several overlapping less intense bands that corresponding to particles of various sizes. The concern of the modern task is to increase the uniformity of the size distribution of MNPs synthesized by ion implantation using an approach of high-power pulse laser annealing with sequential furnace one. Experience gained from using the laser annealing techniques for various purposes allowed MNPs to be modified in various dielectrics. The main feature most of all the experiments with laser annealing of composites with MNPs is that the laser light was applied directly into the spectral region of the transparency of the dielectric matrix, and consequently, the intense laser pulses were primarily absorbed by the metal particles. Contrary to that, a new approach for annealing was demonstrated, when soda-lime silicate glass (SLSG) with Ag particles was irradiated by a laser light at wavelengths of glass absorption in the ultraviolet region [126]. When applying high-power excimer ArF (193 nm) laser pulses, a decrease of the reflectance intensity of composite samples was observed. It was suggested that the implanted silver particles in glass can be dissolved and the glass matrix can be modified to be a silver rich metastable new glass phase. If this is correct then the new phase will be the potential to be destabilized to precipitate out the new silver particles in a controlled fashion by furnace.

Copyright © 2010. Nova Science Publishers, Incorporated. All rights reserved.

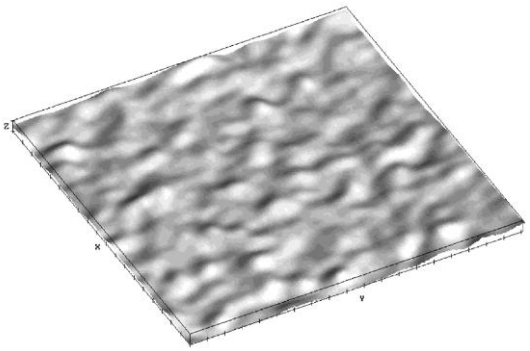

Figure 28. An AFM image as a top view under lateral illumination of the surface of SLSG Ag-implanted with a dose of $7 \cdot 10^{16}$ ion/cm^2 and an energy of 60 keV. The step along the X and Y axes is 100 nm, and the step along the Z axis is 3 nm [132].

As was shown in this chapter the large ion-synthesised silver in the glass are close to the implanted surface with small ones in the interior of the implant zone. These features can be recognized in optical spectra of dielectrics with implanted nanoparticles (Figure 16) [132]. The atomic force microscope images implanted surfaces of this sample shown in Figure 28 [132]. As seen from the figure the implanted surface is smoother (roughness) and there are many hemispherical hills on this surface with an average diameter of approximately 100-150 nm. There are no such protrusions on the unimplanted sample. The reason for the existence of surface hills is assumed to be from a sputtering of irradiated glass during implantation, which leads to unequal ejection of ions of different elements from the surface, exposing the synthesized nanoparticles in the sub-surface glass. The sputtered glass thickness is typically of the order of tens of nanometers for the present ion dose [167], and hence, the synthesized buried MNPs appear near to the glass surface in the implanted sample.

Consequences of the excimer laser pulse with nanosecond pulse width and high beam intensity are heating, melting and/or vaporisation (ablation) of material on a time scale of nanoseconds to microseconds. The excimer laser treatment has been applied to many glasses, but there is less information on high-power pulse laser interaction with dielectrics containing metal nanoparticles. In the present case the energy density is lower than the value of the ablation threshold for the SLSG, which was determined to be about 5 J/cm^2 [191]. Also, the excimer laser is characterised by a UV-wavelength, which is much longer than the typical sizes of the nanoparticles formed by ion implantation. Hence, present metal/glass composites may be considered similar to be a homogeneous material for light propagation [4]. This is a simplification, which is true generally for low intensity light, but it gives an estimate of the optical penetration depth as (α^{-1}) of the laser pulses into the composite material, where α is the linear absorption coefficient. An intense laser pulse is absorbed and relaxed into heat into the surface SLSG layer of a thickness of α^{-1}, which is several microns [192], i.e., deeper than the thickness of the implanted layer (Figure 6).

The optical spectral result of pulse laser treatment by 5 pulses of a KrF excimer laser with pulse length of 25 ns full-width at half-maximum at a wavelength of 248 nm with the total released energy of 0.2 J/cm^2 on the optical spectra of the Ag-implanted glass is presented in Figure 29 [148]. Applied laser pulses did not change the reflectance and transmittance spectra of the non-implanted SLSG, but for implanted sample the location of the transmittance

Copyright © 2010. Nova Science Publishers, Incorporated. All rights reserved.

minimum shifts slightly towards shorter wavelengths, and the transmittance in peak position increases from 16 to 23% (Figure 29a). Remarkable change was found in the reflectance spectra, where in the case of the implanted surface, the peak of the overlapping bands shifts continuously from 490 to 450 nm with modifications in the shape of the envelope of the bands, which become narrower (Figure 29b). The reflectance intensity falls from 38 to 27 %. However, for reflectance from the rear face of the same sample (Figure 29c) there is only a decrease of the intensity to a 13 % maximum, which is at the same initial wavelength as in the implanted sample. As presented in Figure 30, (note an increased magnification of ten times in the direction perpendicular to plane of the figure), it is seen that there are a lot of clearly defined hills (believed to be silver particles) on the glass surface whose size is one order smaller in contrast to large hills on the implanted glass surface in Figure 28 [132]. The MNPs accumulate effect on the laser irradiated surface of glass is result of melting implanted composite layer and some desorption of glass material under the laser pulses, which exposes the melted metal particles after their solidification. Hence, the first of the conclusions from the present data on excimer laser treatment of implanted glass is the reduction of the size of the silver nanoparticles, and second is the existence of some asymmetry in their depth distribution (Figure 29b, c). To recognize the mechanisms by which the changes occur for strongly absorbed excimer laser pulses the thermal propagation after the laser-irradiation must be considered. The laser heating is traditionally characterized by the heat diffusion length, $l(t) = (D \cdot t)^{1/2}$, where D is the heat diffusivity, and t is the laser pulse duration. In the present experiment with laser pulses of 25 ns, the heat propagation is approximately $l(t) = 115$ nm, that is shorter than the α^{-1}, i.e., the temperature rise is no longer controlled by the diffusion of the heat. However, the $l(t)$ surpasses the depth of the implanted Ag nanoparticles. As was estimated earlier [192], the temperature at the surface of laser treated SLSG reaches values exceeding ~700°C, which is equivalent to the SLSG melting temperature. Under these temperature conditions there is also a possibility for melting small silver particles, because their melting temperature is drastically decreased, for example, to ~400°C for sizes < 30 nm, compared with the bulk melting temperature of 960°C [193]. The time scale of electronic relaxation and energy transfer to the lattice vibrations in the metal particles is several orders faster than in the surrounding glass medium. Therefore, during the interaction of the excimer laser pulse with the metal/glass composite, the Ag nanoparticles are heated and melted more quickly than solidification of the melted glass can occur. Atomically dispersed Ag released from nanoparticles enters into the glass melt, and immediately diffuse throughout all the heated thickness of the laser treated substrate. In principle in time this could lead to a uniform metal distribution, where the silver atom concentration exceeds the solubility value in the solid glass. However, following glass solidification spreading from the depth to the surface, as heat from the laser pulse penetrates into the depth of the sample, the cooling part of the annealing cycle will stimulate new nucleation and regrowth of metal particles. In this case, the possibility of regrowth of metal particles will depend on competition between regrowth and the cooling speed of the moving solidification front, resulting in a new non-uniform size distribution of new MNPs over a depth scale similar to that after ion implantation. Obviously, under some conditions the metal particles may be dispersed into separate metal ions and/or into such small units that they cannot display nanoparticle type optical properties. As shown here, subsequent high power excimer laser pulse treatments of the ion implanted layer may be used to melt, and/or regrow, the MNPs within the insulator medium. Overall this results in a

Copyright © 2010. Nova Science Publishers, Incorporated. All rights reserved.

tighter distribution of small particles. The laser treatments have slightly reduced, but not completely removed evidence for a non-symmetric depth distribution of the silver particles. The Ag-insulator composite material is complex, and so a much wider range of laser pulse conditions, and more data on the cooling rates are required to fully model the changes in the size distributions, which can occur.

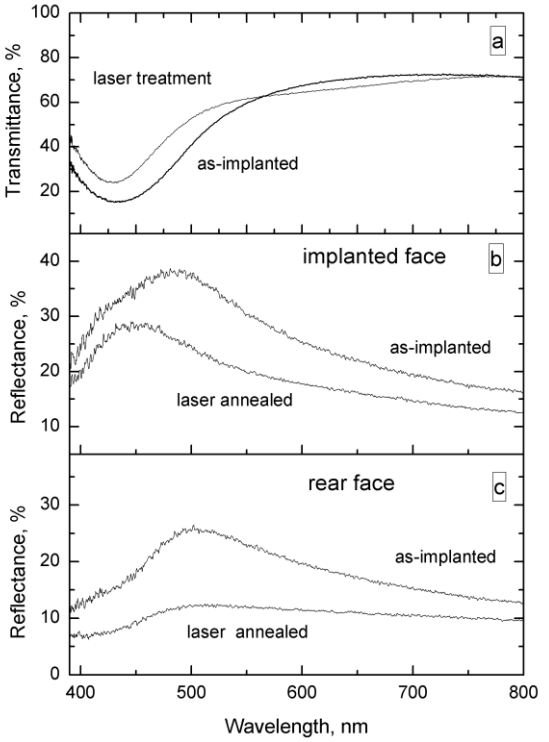

Figure 29. Optical spectra of the SLSG after silver implantation as in Figure 7 and the implantation followed with laser treatment (0.2 J/cm^2): (a) transmittance; (b) reflectance measured from the implanted face; (c) reflectance measured from rear faces of the sample [148].

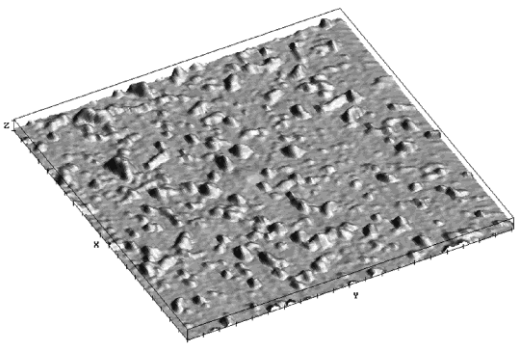

Figure 30. An AFM image as a top view under lateral illumination of the surface of SLSG Ag-implanted with a dose of $7 \cdot 10^{16}$ ion/cm^2 and an energy of 60 keV followed with irradiation with an excimer laser (0.2 J/cm^2). The step along the X and Y axes id 100 nm, and the step along the Z axis is 40 nm [132].

Copyright © 2010. Nova Science Publishers, Incorporated. All rights reserved.

ION SYNTHESIS OF SILVER NANOPARTICLES IN POLYMER MATRIX

The task of designing new polymer-based composite materials containing MNPs is of current interest. nanoparticles may be embedded in a polymer matrix in a variety of ways. These are such techniques as chemical synthesis in an organic solvent [1], vacuum deposition on viscous polymers [194], plasma polymerization combined with metal evaporation [195], etc. However, they all suffer from disadvantages, such as a low filling factor or a large distribution in size and shape of nanoparticles, which offsets the good optical properties of composites. Ion implantation is a promising method. Despite the intensive study of MNP synthesis by ion implantation in dielectrics, such as non-organic glasses and crystals, the formation of nanoparticles in organic matrices was realized only at the beginning of the eighties by Koon *et al*. in their experiments on implantation of Fe ions into polymers in 1984 [196]. A first publication on ion-synthesis of noble metal nanoparticles in polymer was realised in 1995 when silver particles were created in PMMA [197]. In Table 2 a comprehensive list of publications on ion synthesis of silver nanoparticles [197-215] with preparation conditions is presented.

Table 2. Types of organic matrix with silver nanoparticles synthesized by ion implantation

Matrix type	Ion energy, keV	Ion dose, ion/cm^2	Current density, μA/см^2	Matrix temperature, °C	Methods of particle detection	Authors
Epoxy	30	(0.1-1.8)·10^{17}	4	RT	OA, TEM	Stepanov *et al.* 1995 [198] 1997 [199] 2009 [200] Khaibullin I. *et al.* 1997 [201]
PC	60	3.0·10^{17}	3	-	OA, TEM	Boldyryeva *et al.* 2004 [202]
PET	40	(0.1-2.0)·10^{17}	4.5	-	CM TEM	Wu *et al.* 2000 [203] 2001 [204, 205] 2002 [206]
PI	130	(0.1-5.0)·10^{17}	1-3	< 350	TEM	Kobayashi *et al.* 2001 [207]
PMMA	30	(0.1-7.5)·10^{16}	4	RT	OA, TEM	Stepanov *et al.* 1994 [197] 2000 [208] 2002 [209] 2004 [210] Bazarov *et al.* 1995 [211]
PMMA	60	(0.1-3.0)·10^{17}	3	-	OA, TEM	Boldyryeva *et al.* 2005 [212]
Silicone resin	30	(0.1-1.8)·10^{17}	4	RT	OA TEM	Khaibullin R. *et al.* 1998 [213] 1999 [214] Stepanov *et al.* 1995 [215]

Abbreviations – Polycarbonate (PC), Poly(ethyleneterephthalate (PET), Polyimide (PI), Polymethylmethacrylate (PMMA); Phenylmethyl-silane resin with tin diethyldicaprilate (Silicone resin); optical absorption (OA), transmission electron microscopy (TEM), conductivity measurements (CM); room temperature (RT).

Copyright © 2010. Nova Science Publishers, Incorporated. All rights reserved.

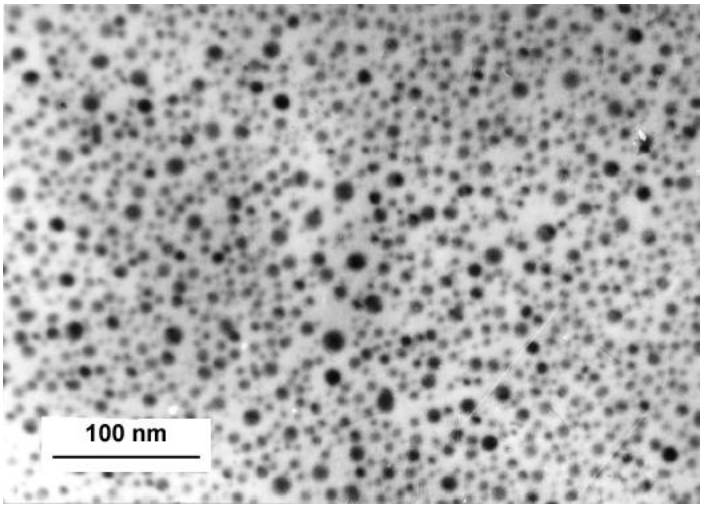

Figure 31. TEM image of silver nanoparticles fabricated in PMMA by Ag-ion implantation [208].

The aim of this paragraph is to observe the SPR-related optical absorption of MNPS with an example as silver nanoparticles introduced into polymethylmethacrylate (PMMA) by ion implantation. As substrates, 1.2-mm-thick, which are optically transparent in a wide spectral range (400–1000 nm), were used. PMMA plates were implanted by 30 keV Ag^+ ions with doses in the range from $3.1 \cdot 10^{15}$ to $7.5 \cdot 10^{16}$ ion/cm^2 at ion current density of 4 μA/cm^2. Optical spectra of spherical MNPs embedded in various dielectric media were simulated in terms of the Mie electromagnetic theory [175], which allows one to estimate the extinction cross section σ_{ext} for a light wave incident on a particle. This value is related to the intensity loss ΔI_{ext} of an incident light beam I_0 passes through a transparent particle-containing dielectric medium due to absorption σ_{abs} and elastic scattering σ_{sca}, where $\sigma_{ext} = \sigma_{abs} + \sigma_{sca}$. Following the Lambert-Beer law

$$\Delta I_{ext} = I_0 \left(1 - e^{-\#\sigma ext\, h}\right), \tag{4}$$

where h is the thickness of the optical layer and # - the density of nanoparticles in a sample. The extinction cross section is connected to the extinction constant γ as $\gamma = \#\sigma_{ext}$. Experimental spectral dependencies of optical density (OD) are given by

$$OD = -\lg(I/I_0) = \gamma \cdot \lg(e) h, \tag{5}$$

hence, for samples with electromagnetically non-interacting nanoparticles, it possible to put $OD \sim \sigma_{ext}$. Therefore, experimental OD spectra are compared with modeled spectral dependences that are expressed through σ_{ext} calculated by the Mie theory.

As follows from TEM, Ag-ion implantation results in the formation of silver nanoparticles. As example, the micrograph in Figure 31 shows spherical nanoparticles synthesized in PMMA at a dose of $5.0 \cdot 10^{16}$ ion/cm^2 [208]. Microdiffraction patterns of the composite samples demonstrate that the MNPs have the fcc structure of metallic silver. The diffraction image consists of very thin rings (corresponding to polycrystalline nanoparticles) imposed on wide diffuse faint rings from the amorphous polymer matrix. By comparing the

Copyright © 2010. Nova Science Publishers, Incorporated. All rights reserved.

experimental diffraction patterns with standard ASTM data, it possible to conclude that implantation does not form any chemical compounds involving silver ions.

Optical absorption spectra of PMMA irradiated by xenon and silver ions at various doses are shown in Figure 32 [208]. As seen in Figure 32a, when the xenon ion dose increases, the absorption of the polymer in the visible (especially in the close-to-UV) range also increases monotonically. This indicates the presence of radiation-induced structure defects in the PMMA. The implantation by silver ions not only generates radiation defects but also causes the nucleation and growth of MNPs. Therefore, along with the absorption intensity variation as in Figure 32a, a selected absorption band associated with silver nanoparticles is observed (Figure 32b). For the lowest ion dose, the maximum of this band is near 420 nm and shifts to red spectral area (up to ~600 nm) with dose increasing, simultaneously with the band broadening. The maximum of this band is not sharp, although it is definitely related to the SPR effect in the silver nanoparticles. Such broad SPR absorption is untypical for silver nanoparticles in PMMA. When silver particles were synthesized in PMMA by the convection melting technique [216], the SPR band was very sharp, unlike present experiment. Figure 32 shows the *OD* spectrum for inorganic silica glass irradiated by silver ions under the implantation conditions as here. Particle size distributions in the SiO_2 and PMMA are nearly the same. SiO_2 has the refractive index close to that of PMMA. However, the absorption of Ag nanoparticles in the glass (Figure 32b) is much more narrow and intense than the absorption of the MNPs in the polymer.

The attenuation (extinction) of an optical wave propagating in a medium with MNPs depends on the SPR absorption and the light scattering efficiency. The wavelength of optical radiation, the particle size, and the properties of the environment are governing factors in this process. Within the framework of classical electrodynamics (the Maxwell equations), the problem of interaction between a plane electromagnetic wave and a single spherical particle was exactly solved in terms of optical constants of the selected materials by Mie [175]. The complex value of the optical constant ε_{Ag} [217] and ε_{PMMA} [218] in the visible range was used The extinction was calculated for particles of size between 1 and 10 nm to be in consistence with experimental sizes (Figure 31).

As a first step of simulation, consider the simplest case where Ag nanoparticles are incorporated into the PMMA. Simulated extinction spectra of Ag nanoparticles embedded in a polymer matrix shown in Figure 33 [210]. The extinction feature is a very wide band, which covers the entire spectral range. In the given range of particle sizes, the position of the SPR absorption maximum (near 440 nm) is almost independent of the particle size. In same time, the extinction band intensity grows while the band itself somewhat narrows with increasing particle size. Comparing the modeled and experimental spectra, it is seen that Figure 33 refers to the situation where PMMA is implanted by silver ions with doses between $0.33 \cdot 10^{16}$ and $2.5 \cdot 10^{16}$ ion/cm^2 (Figure 32b, curves *1–3*). This dose range corresponds to the early stage of MNP nucleation and growth in the *OD* spectral band with a maximum between 420 and 440 nm. Thus, it is possible to conclude that ion implantation in this dose range results in the formation of Ag nanoparticles, as also revealed by TEM. However, at higher implantation doses, the measured *OD* spectra and the modeled spectra shown in Figure 33 diverge.

Copyright © 2010. Nova Science Publishers, Incorporated. All rights reserved.

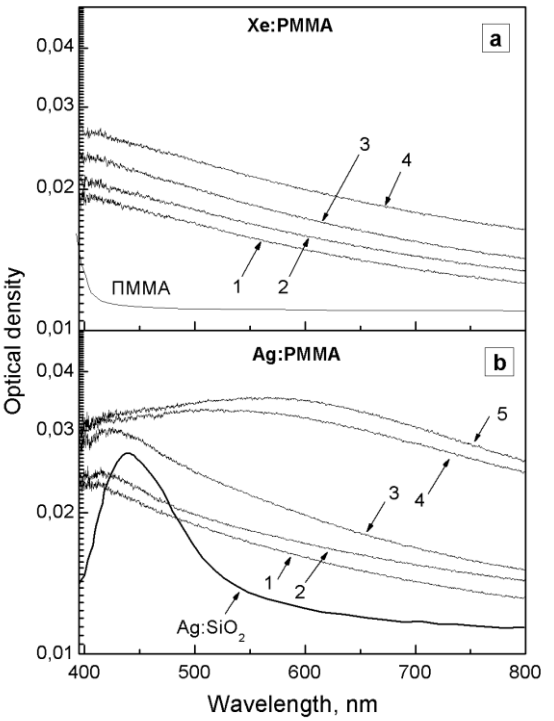

Figure 32. Optical density spectra from PMMA irradiated by (a) xenon and (b) silver ions for doses of (1) $0.3 \cdot 10^{16}$, (2) $0.6 \cdot 10^{16}$, (3) $2.5 \cdot 10^{16}$, (4) $5.0 \cdot 10^{16}$, and (5) $7.5 \cdot 10^{16}$ ion/cm^2. The spectrum taken of SiO_2 implanted by silver ions ($5.0 \cdot 10^{16}$ ion/cm^2) [209].

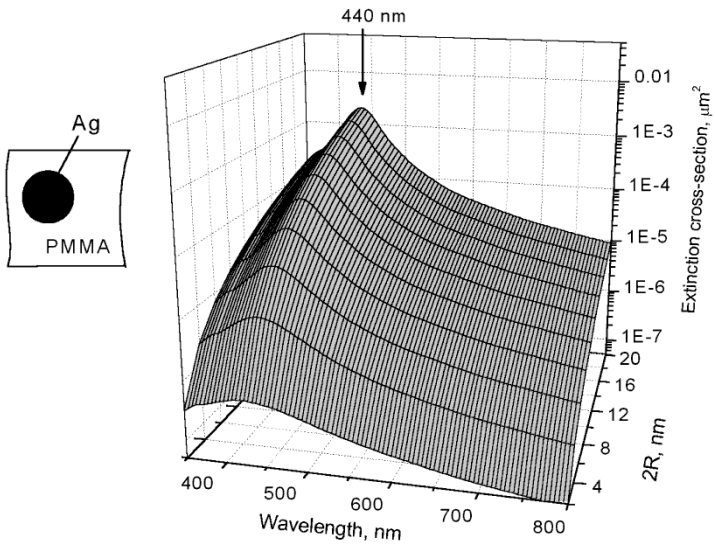

Figure 33. Simulated optical extinction spectra for silver nanoparticles embedded in PMMA vs. particle size [210].

Copyright © 2010. Nova Science Publishers, Incorporated. All rights reserved.

To explain the experimental dependences corresponding to high-dose silver implantation into PMMA, it should be consider a difference between implantation into polymers and inorganic materials (silicate glasses, crystals, etc.). The most important distinction is that, as the dose increases, so does the number of dangling chemical bonds of polymer along the track of an accelerated ions. Because of this, gaseous hydrogen, low-molecular hydrocarbons (e.g., acetylene), CO, and CO_2 evolve from the matrix [219]. In particular, ion-irradiated PMMA loses HCOOCH3 methoxy groups [220]. The evolution of several organic fractions leads to the accumulation of carbon in the irradiated polymer layer, and radiation-induced chemical processes may cause chain linking. Eventually, an amorphous hydrogenated carbon layer is produced.

To take into account the specific phase structure of the irradiated polymer, it is of interest to analyse the optical properties (extinction) of Ag nanoparticles embedded in the amorphous carbon matrix (C-matrix). For this system, the extinction cross section spectra vs. particle size dependence was simulated (Figure 34) in the same way as for the MNP–PMMA using complex optical constants ε_C for amorphous carbon [221]. As before (Figure 33), throughout the particle size interval, the extinction spectra exhibit a single broad band, which covers the visible range, but with a maximum at longer wavelength (~510 nm). This wavelength position of the maximum, which is observed upon changing the matrix, may be assigned to a longer wavelength *OD* band in the experimental spectra for the PMMA, which arises when the Ag ion dose exceeds $2.5 \cdot 10^{16}$ ion/cm^2 (Figure 33b; curves *3*, *4*). It seems that this spectral shift may be associated with the fact that the pure polymeric environment of the Ag nanoparticles turns into the amorphous carbon as the implantation dose rises. The broader extinction bands in the C-matrix (Figure 34) compared with the PMMA (Figure 33) also count in favor of this supposition, since the broadening of the extinction bands is observed in the experiments as well (Figure 32b). In a number of experiments, however, the carbonization of the polymer surface layer depended on the type of the organic material and accelerated ions, as well as on the implantation parameters, and completed at doses of $(0.5–5.0) \cdot 10^{16}$ ion/cm^2 but the entire material was not carbonized. The carbon fragments may reach several tens of nanometers in size [219]. Thus, the assumption that the polymer irradiated is completely carbonized, which was used in the simulation (Figure 34), does not completely correspond to the real situation. Therefore, extinction spectra for nanoparticles represented as a silver core covered by a carbon shell in an insulating matrix (PMMA) will be analyzed in terms of the Mie relationships for shelled cores [222].

Optical extinction spectra for a Ag nanoparticle with a fixed size of the core (4 nm) and a varying thickness of the carbon shell (from 0 to 5 nm) are shown in Figure 35. The maximum of the SPR bands of the particles is seen to shift from 410 nm (uncovered particle, Figure 35) to approximately 510 nm. Simultaneously, the SPR band intensity decreases, while the UV absorption increases, so that the absorption intensity at 300 nm and a shell thickness of 5 nm exceeds the SPR absorption of the particles. Both effects (namely, the shift of the SPR band to longer wavelengths and the increased absorption in the near ultraviolet) agree qualitatively with the variation of the experimental *OD* spectra (Figure 34b) when the implantation dose exceeds $2.5 \cdot 10^{16}$ ion/cm^2. Thus, our assumption that the increase in the carbonized phase fraction with implantation dose and the variation of the *OD* spectra (Figure 32b) go in parallel is sustained by the simulation of the extinction for complex particles (Figure 35).

Copyright © 2010. Nova Science Publishers, Incorporated. All rights reserved.

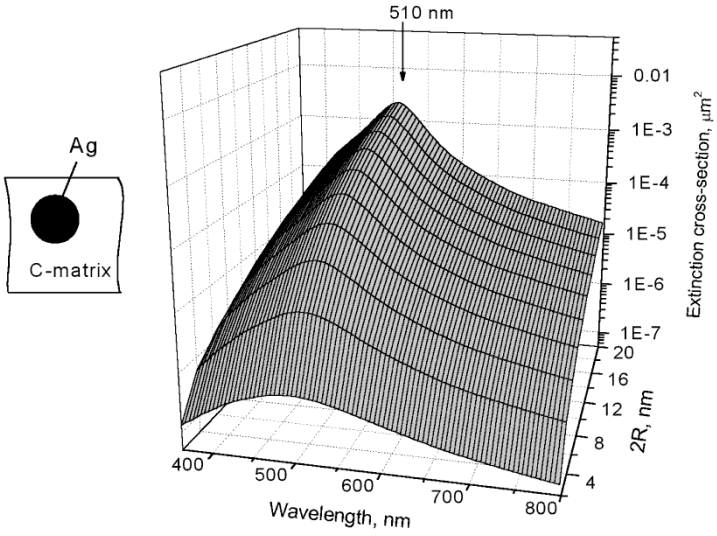

Figure 34. Simulated optical extinction spectra for silver nanoparticles embedded in the C-matrix vs. particle size [210].

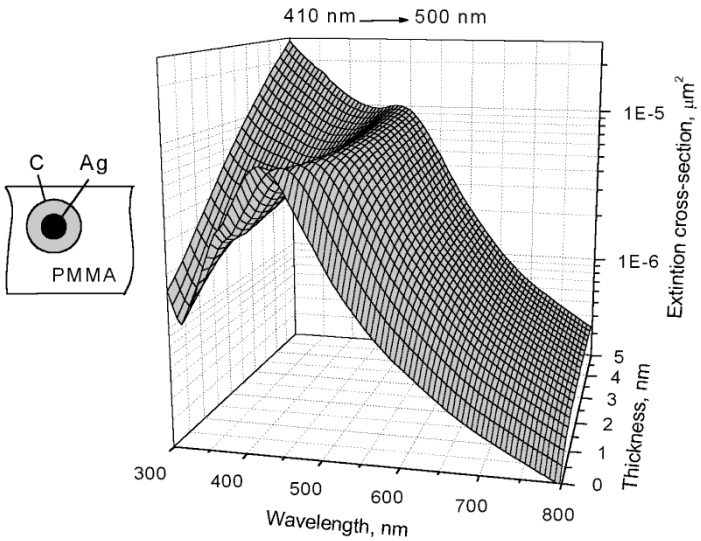

Figure 35. Simulated optical extinction spectra for 4-nm silver nanoparticles with the carbon shell that are placed in the PMMA matrix vs. sheath thickness [210].

When analyzing the optical properties of nanoparticles embedded in a medium, it should be taking into account effects arising at the particle–matrix interface, such as the static and dynamic redistributions of charges between electronic states in the particles and the environment in view of their chemical constitution [221]. Consider first the charge static redistribution. If an atom is deposited (adsorbed) on the MNP surface, the energy levels of this atom change his positions compared with this in the free state [222].When the number of

Copyright © 2010. Nova Science Publishers, Incorporated. All rights reserved.

the adsorbed matrix atoms becomes significant, their contact generates a wide distribution of density of states. Additionally, the adsorbed atoms are separated from surface atoms of the metal by a tunnel barrier. The gap between the energy positions of the adsorbed atoms and the Fermi level of the particles depends on the type of the adsorbate. The overlap between the energy positions of the matrix atoms and the energy positions of the silver surface atoms depends on the rate with which the electrons tunnel through the barrier. Accordingly, the conduction electron density in the particles embedded will change compared with that in the particles placed in a vacuum (without adsorbates): it decreases if the electrons tunnel toward the adsorbed atoms or increases when the electrons tunnel in the reverse direction. Eventually, equilibrium between the particle and the matrix sets in; i.e., a constant electrical charge (Coulomb barrier) forms at the nanoparticle surface.

Such a charge static redistribution due to the deposition of an adsorbate on the particle surface and the respective change in the electron concentration in the MNPs could also observed in the SPR absorption spectra [4]. The incorporation of Ag nanoparticles into the carbon matrix of C_{60} fullerene (or the deposition of carbon on the nanoparticle surface) reduces the concentration of 5*sp* electrons in the particle roughly by 20%, since they are trapped by matrix molecules [221]. It was shown that the decrease of electrons shifts the MNP extinction spectrum toward longer wavelength. This shift of the SPR extinction band to the longer wavelength with increasing of implantation dose in present experiment (Figure 32) may also be explained by the formation of a carbon shell around silver nanoparticles, which traps conduction electrons.

The charge dynamic variation in time at the particle–matrix interface causes the electron concentration in the particle to fluctuate. Fluctuation influences directly to the SPR relaxation. The lifetime of excited conduction electrons in the particle defines the SPR spectral width. Here, the contribution from electron scattering by the interface (because of restrictions imposed on the electron free path [4]) adds up with the charge dynamic variation at the interface. Thus, the temporal capture of conduction electrons from the particle broadens the SPR-related extinction spectra. Such effect was demonstrated with silver nanoparticles embedded in the C_{60} matrix [221]. Silver nanoparticles in the carbon matrix exhibit the much broader SPR band than in free space. We may therefore suppose that, as the dose rises, the charge dynamic redistribution may broaden the SPR spectra of silver nanoparticles synthesized by ion implantation in PMMA. This is because implantation carbonizes the irradiated layer with increasing absorbed dose and raises the amount of acceptor levels on the MNP surface, which change the relaxation time of electrons excited.

ACKNOWLEDGMENT

I wish to thank my partners and co-authors D. Hole, P.D. Townsend, I.B. Khaibullin, V.I. Nuzhdin, V.F. Valeev, R.I. Khaibullin, V.N. Bazarov, Yu.N. Osin, S.N. Abdullin, V.A. Zikharev, I.A. Faizrakhmanov, A.A. Bukharaev, V.N. Popok, U. Kreibig, A.I. Ryasnyansky, R.A. Ganeev, E. Alves. Also, I am grateful to the Alexander von Humboldt Foundation in Germany, Austrian Scientific Foundation in the frame of Lisa Meitner Fellowship and the Royal Society in UK for financial support. This work was partly supported by Russian State Grant № 02.740.11.0797.

Copyright © 2010. Nova Science Publishers, Incorporated. All rights reserved.

REFERENCES

[1] Zhang, JZ. *Optical properties and spectroscopy of nanomaterial*s, World Sci. Pub.: London, 2009.

[2] Sarychev, A; Shalaev, V. *Electrodynamics of metamaterials*, World Sci. Pub.: New York, 2007.

[3] Flytzanis, C; Hache, F; Klein, MC; Ricard, D; Rousignol, P. *Nonlinear Optics in Composite Materials*, (Elsevier Sci.: Amsterdam, 1991.

[4] Kreibig, U; Vollmer, M. *Optical Properties of Metal Clusters*, Springer: Berlin, 1995.

[5] Stepanov, AL; Khaibullin, IB; Townsend, PD; Hole, DE; Bukharaev, AA. *Rus. Feder. Patent*, No. 2156490, 2000.

[6] Townsend, PD; Massarelli, L. *US Patent*, No. 5102736, 1992.

[7] Hampikian, JM; Hunt, EM. *US Patent*, No. 6294223, 2001.

[8] Kishimoto, N; Takeda, Y; Okubo, S; Jap. *Patent*, No. JP2004091817, 2004.

[9] Townsend, PT; Chandler, PJ; Zhang, L. *Optical Effects of Ion Implantation*, Cambridge Univ. Press: Cambridge, 1994.

[10] Polman, AJ. *Appl. Phys*., 1997, 82, 1-39.

[11] Davenas, J; Perez, A; Thevenard, P; Dupuy, CHS. *Phys. Stat. Sol. A*, 1973, 19, 679-686.

[12] Treilleux, M; Thevenard, P; Ghassagne, G; Hobbs, LH. *Phys. Stat. Sol. A*, 1978, 48, 425-430.

[13] Arnold, GW. *J. Appl. Phys*., 1975, 46, 4466-4473.

[14] Arnold, GW; Borders, JA. *J. Appl. Phys*., 1977, 48, 1488-1496.

[15] Stepanov, AL. *In Metal-Polymer Nanocomposites*, L; Nicolais, G. Carotenuto, Eds., John Wiley & Sons Publ: London, 2004, 241-263.

[16] Stepanov, AL. In *High-power and femtosecond lasers*, PH; Barret, M; Palmer, Eds., NOVA Sci. Publ. Inc.: New York, 2009, 27-70.

[17] Rahmani, M; Abu-Hassan, LH; Townsend, PD; Wilson, IH; Destefanis GL. *Nucl. Inst. Meth. Phys. Res. B*, 1988, 32, 56-60.

[18] Rahmani, M; Townsend, PD. *Vacuum*, 1989, 39, 1157-1162.

[19] White, CW; Thomas, DK; Hensley, DK; McCallum, JC; Pogany, A; Haglund, Jr., RF; Magruder, RH; Yang, L. *Nanostruc. Mat*, 1993, 3, 447-457.

[20] Ila, D; Williams, EK; Sarkisov, S; Poker, DB; Hensley, DK. Mat. *Res. Soc. Symp. Proc*., 1998, 504, 381- 385.

[21] Steiner, G; Pham, MT; Kuhne, Ch; Salzer, R. *Fresenius J Anal Chem*., 1998, 362, 9-14.

[22] Ganeev, RA; Ryasnyanskii, AI; Stepanov, AL; Marques, C; da Silva, RC; Alves, E. *Opt. Comm*., 2005, 253, 205-213.

[23] Ganeev, RA; Ryasnyanskii, AI; Stepanov, AL; Usmanov, T; Marques, C; da Silva, R. C; Alves E. *Optics and Spectroscopy*, 2006, 101, 615-622.

[24] Marques, C; da Silva, RC; Wemans, A; Maneira, MJP; Kozanecki, A; Alves, E. *Nucl. Inst. Meth. Phys. Res. B*, 2006, 242, 104-108.

[25] Mazzoldi, P; Tramontin, I; Boscolo-Boscoletto, A; Battaglin, G; Arnold GW. *Nucl. Inst. Meth. Phys. Res. B*, 1993, 80-81, 1192-1196.

[26] Abouchacra, G; Serughetti, *J. Nucl. Inst. Meth. Phys. Res. B*, 1986, 14, 282-289.

Copyright © 2010. Nova Science Publishers, Incorporated. All rights reserved.

[27] Fuchs, G; Abouchacra, G; Treilleux, M; Thevenard, P; Serughetti, *J. Nucl. Inst. Meth. Phys. Res. B*, 1988, 32, 100-103.
[28] Qian, Y; Ila, D; Zimmerman, RL; Poker, DB; Boatner, LA; Hensley, DK. *Nucl. Inst. Meth. Phys. Res. B*, 1997, 127, 524-527.
[29] Zimmerman, RL; Muntele, CI; Ila, D. *Surf. Coat. Technol*., 2005, 196, 85-88.
[30] van Huis, MA; Fedorov, AV; van Veen, A; Falub, CV; Eijt, SWH; Kooi, BJ; De Hosson, J. Th. M; Hibma, T; Zimmerman, RL. *Nucl. Inst. Meth. Phys. Res. B*, 2002, 191, 442-446.
[31] Xiao, XH; Xu, JX; Ren, F; Liu, C; Jiang, CZ. *Physica E*, 2008, 40, 705-708.
[32] Matsunami, N; Hosono, H. *Nucl. Inst. Meth. Phys. Res. B*, 1993, 80, 1233-1236.
[33] Deying, S; Saito, Y; Suganomata S. *Jpn. J. Appl. Phys*., 1994, 33, L966-L969.
[34] Shang, DY; Saito, Kittaka, YR; Taniguchi, S; Kitahara, A. *J. Appl. Phys*., 1996, 80, 6651-6654.
[35] Saito, Y; Kitahara, A. *J. Appl. Phys*., 2000, 87, 1276-1279.
[36] Fujita, T; Ijima, K; Mitsui, N; Mochiduki, K; Ho, A. Yi-J; Saito, Y. *Jap. J. Appl. Phys*., 2008, 47, 7224-7229.
[37] Sarkisov, SS; Williams, EK; Curley, MJ; Smith, CC; Ila, D; Venkateswarlu, P; Poker, DB; Hensley, DK. *Mat. Res. Soc. Symp. Proc*., 1998, 504, 357- 362.
[38] Sarkisov, SS; Williams, EK; Curley, MJ; Ila, D; Venkateswarlu, P; Poker, DB; Hensley, DK. *Nucl. Inst. Meth. Phys. Res. B*, 1998, 141, 294-298.
[39] Sarkisov, SS; Williams, EK; Curley, MJ; Smith, CC; Ila, D; Poker, DB; Hensley, DK; Banks, C; Penn, B. *Proc. SPIE*, 1998, 3283, 942-948.
[40] Sarkisov, SS; Williams, EK; Curley, MJ; Ila, D; Svetchnikov, VL; Pan, VM; Poker, DB; Hensley, DK; Banks, C; Penn, B; Wang JW. *Proc. SPIE*, 1998, 3413, 98-110.
[41] Sarkisov, SS; Curley, MJ; Williams, EK; Ila, D; Svetchnikov, VL; Zandbergen, HW; Zykov, GA; Poker, DB; Hensley, DK. *Proc. SPIE*, 1999, 3790, 43-55.
[42] Sarkisov, SS; Curley, MJ; Williams, EK; Ila, D; Svetchnikov, VL; Zandbergen, HW; Zykov, GA; Banks, C; Wang, JC; Poker, DB; Hensley, DK. *Nucl. Inst. Meth. Phys. Res. B*, 2000, 166-167, 750-757.
[43] Williams, EK; Ila, D; Sarkisov, SS; Curley, MJ; Poker, DB; Hensley, DK; Borel, C. *Mat. Res. Soc. Symp. Proc*., 1998, 504, 363-369.
[44] Williams, EK; Ila, D; Sarkisov, SS; Curley, MJ; Cochrane, JC; Poker, DB; Hensley, DK; Borel, C. *Nucl. Inst. Meth. Phys. Res. B*, 1998, 141, 268-273.
[45] Williams, EK; Ila, D; Darwish, A; Poker, DB; Sarkisov, SS; Curley, MJ; Wang, JC; Svetchnikov, VL; Zandbergen, HW. *Nucl. Inst. Meth. Phys. Res. B*, 1999, 148, 1074-1078.
[46] Amolo, GO; Comins, JD; Naidoo, SR; Connell, SH; Witcomb, MJ; Derry, TE. *Nucl. Inst. Meth. Phys. Res. B*, 1999, 250, 233-237.
[47] Mazzoldi, P; Tramontin, L; Boscolo-Boscoletto, A; Battaglin, G; Arnold, GW. *Nucl. Inst. Meth. Phys. Res. B*, 1993, 80-81, 233-237.
[48] Mazzoldi, P; Mattei, G. *Rivista del nuovo cimento*, 2005, 28, 1-69.
[49] Mazzoldi, P; Mattei, G. *Phys. Stat. Sol. A*, 2007, 204, 621-630.
[50] Antonello, M; Arnold, GW; Battaglin, G; Bertoncello, R; Cattaruzza, E; Colombo, P; Mattei, G; Mazzoldi, P; Trivillin F. *J. Mater. Chem*., 1998, 8, 457-461.
[51] Battaglin, G; Cattaruzza, E; D'Acapito, F; Gonella, F; Mazzoldi, P; Mobilio, S; Priolo, F. *Nucl. Inst. Meth. Phys. Res. B*, 1998, 141, 252-255.

Copyright © 2010. Nova Science Publishers, Incorporated. All rights reserved.

[52] Battaglin, G; Catalano, M; Cattaruzza, E; D'Acapito, F; De Julian Fernandez, C; De Marchi, G; Gonella, F; Mattei, G; Maurizio, C; Mazzoldi, P; Miotello, A; Sada, C. *Nucl. Inst. Meth. Phys. Res. B*, 2001, 178, 176-179.
[53] Bertoncello, R; Gross, S; Trivillin, F; Cattaruzza, E; Mattei, G; Caccavale, F; Mazzoldi, P; Battaglin G. *J. Mater. Res*., 1999, 14, 2449-2457.
[54] Caccavale, F. Pramana - *J. Phys*., 1998, 50, 653-668.
[55] Cattaruzza, E; Battaglin, G; Polloni, R; Cesca, T; Gonella, F; Mattei, G; Maurizio, C; Mazzoldi, P; D'Acapito, F; Zontone, F; Bertoncello, R. *Nucl. Inst. Meth. Phys. Res. B*, 1990, 148, 1007-1011.
[56] Gonella, F; Mattei, G; Mazzoldi, P; Sada, C; Battaglin, G; Cattaruzza, E. *Appl. Phys. Lett*, 1999, 75, 55-57.
[57] Matsunami, N; Hosono H. *Appl. Phys. Lett*, 1993, 63, 2050-2053.
[58] Magruder III, RH; Zuhr, RA; Osborne, Jr. DH. *Nucl. Inst. Meth. Phys. Res. B*, 1995, 99, 590-593.
[59] Magruder III, RH; Anderson, TS; Zuhr, RA; Thomas, DK. *Nucl. Inst. Meth. Phys. Res. B*, 1996, 108, 305-312.
[60] Magruder III, RH; Robinson, SJ; Smith, C; Meldrum, A; Halabica, A; Haglund, Jr., RH. *J. Appl. Phys*., 2009, 105, 24303-8.
[61] Anderson, TS; Magruder III, RH; Zuhr, RA; Wittig, JE. *J. Electronic Mater*, 1996, 25, 27-35.
[62] Anderson, TS; Magruder III, RH; Kinser, DL; Zuhr, RA; Thomas, DK. *Nucl. Inst. Meth. Phys. Res. B*, 1997, 124, 40-46.
[63] Anderson, TS; Magruder III, RH; Kinser, DL; Wittig, JE; Zuhr, RA; Thomas, DK. *J. Non.-Cryst. Sol*., 1998, 224, 299-306.
[64] Anderson, TS; Magruder III, RH; Wittig, JE; Kinser, DL; Zuhr, RA. *Nucl. Inst. Meth. Phys. Res. B*, 2000, 171, 401-405.
[65] Zuhr, RA; Magruder III, RH; Anderson, TS. Surf. Coat. *Technol*., 1998, 101, 401-408.
[66] Pham, MT; Matz, W; Seifarth, H. *Anal. Chim. Acta*, 1997, 350, 209-220.
[67] Liu, Z; Wang, H; Li, H; Wang X. Appl. *Phys. Lett*, 1998, 72, 1823-1825.
[68] Liu, Z; Li, H; Feng, X; Ren, S; Liu, Z; Lu, B. *J. Appl. Phys*., 1998, 84, 1913-1917.
[69] Liu, Z; Li, H; Wang, H; Shen, D; Wang, X; Alkemade, PFA. *J. Mater. Res*., 2000, 15, 1245-1247.
[70] Ila, D; Williams, EK; Sarkisov, S; Smith, CC; Poker, DB; Hensley, DK. *Nucl. Inst. Meth. Phys. Res. B*, 1998, 141, 289-293.
[71] D'Acapito, F; Zontone, F. *J. Appl. Cryst*., 1999, 32, 234-240.
[72] Stepanov, AL; Hole, DE; Townsend, PD. *Nucl. Inst. Meth. Phys. Res. B*, 2000, 166-167, 882-886.
[73] Stepanov, AL. Rev. *Adv. Mater. Sci*., 2003, 4, 45-60.
[74] Jiang, CZ; Fan, XJ. Surf. Coat. *Technol*., 2000, 131, 330-333.
[75] Ren, F; Jiang, CZ; Chen, HB; Shi, Y; Liu, C; Wang, JB. *Physics B*, 2004, 353, 92-97.
[76] Ren, F; Jiang, CZ; Zhang, L; Shi, Y; Wang, JB; Wang, RH. *Micron*, 2004, 35, 489-493.
[77] Ren, F; Jiang, CZ; Liu, C; Shi, Y. *J. Kor. Phys. Soc*., 2005, 46, S43-S47.
[78] Ren, F; Jiang, CZ; Fu, DJ; Ru, Q. Jap. *J. Appl. Phys*., 2005, 44, 8512-8514.
[79] Ren, F; Jiang, CZ; Liu, C; Fu, D; Shi, Y. *Solid State Comm*., 2005, 135, 268-272.
[80] Ren, F; Jiang, CZ; Liu, C; Wang, J; Oku, T. *Phys. Rev. Lett*, 2006, 97, 165501-1 -4.

Copyright © 2010. Nova Science Publishers, Incorporated. All rights reserved.

[81] Ren, F; Jiang, CZ; Cai, GX; Fu, Q; Shi, Y. Nucl. Inst. *Meth. Phys. Res. B*, 2007, 262, 201-204.
[82] Ren, F; Cai, GX; Xiao, XH; Fan, LX; Liu, C; Fu, DJ; Wang, JB; Jiang, CZ. *J. Appl. Phys*., 2008, 103, 843308-1 -5.
[83] Ren, F; Xiao, XH; Cai, GX; Wang, JB; Jiang, CZ. *Appl. Phys. A*, 2009, 96, 317-325.
[84] Liu, XF; Jiang, CZ; Feng, R; Fu, Q. *Acta Phys. Sinca*, 2005, 54, 4633-4637.
[85] Xiao, XH; Jiang, CZ; Ren, F; Wang, J; Shi Y. *Solid State Comm*., 2006, 137, 362-365.
[86] Xiao, XH; Ren, F; Wang, JB; Liu, C; Jiang, CZ. *Mater. Lett*, 2007, 61, 4435-4437.
[87] Xiao, XH; Guo, LP; Ren, F; Wang, JB; Fu, DJ; Chen, DL; Wu, ZY; Jia, QJ; Liu, C; Jang, CZ. *Appl. Phys. A*, 2007, 89, 681-684.
[88] Wang, YH; Jiang, CZ; Ren, F; Wang, QQ; Chen, DJ; Fu DJ. *J. Mater. Sci*., 2007, 42, 7294-7298.
[89] Wang, YH; Jiang, CZ; Xiao, XH; Chen, D. *J. Physica B*, 2008, 403, 2143-2147.
[90] Zhang, L; Jiang, CZ; Ren, F; Chen, HB; Shi, Y; Fu, Q. *Acta Phys. Sinica*, 2004, 53, 2910-2914.
[91] Cai, GX; Ren, F; Xiao, XH; Fan, LX; Jiang, CZ. Nucl. Inst. Meth. *Phys. Res. B*, 2008, 266, 889-893.
[92] Cai, GX; Ren, F; Xiao, XH; Fan, LX; Zhou, XD; Jiang, CZ. *J. Mater. Sci. Technol*. 2009, 25, 669-672.
[93] Armelao, L; Bertoncello, R; Cattaruzza, E; Gialanella, S; Gross, S; Mattei, G; Mazzoldi, P; Tondello, E. *J. Mater. Chem*., 2002, 12, 2401-2407.
[94] Ishikawa, J; Tsuji, H; Motono, M; Gotoh, Y; Arai, N; Adachi, K; Kotaki, H. *IEEE*, 2002, 12, 690-693.
[95] Ishikawa, J; Tsuji, H; Motono, M; Gotoh, Y. *Surf. Coat. Technol*., 2009, 203, 2351-2356.
[96] Tsuji, H; Kurita, K; Gotoh, Y; Kishimoto, N; Ishikawa, *J. Nucl. Inst. Meth. Phys. Res. B*, 2002, 195, 315-319.
[97] Tsuji, H; Kurita, K; Motono, M. *J. Vac. Soc. Jap*, 2002, 45, 528-532.
[98] Tsuji, H; Arai, N; Motono, M; Gotoh, Y; Abachi, K; Kotaki, H; Ishikawa, *J. Nucl. Inst. Meth. Phys. Res. B*, 2003, 206, 615-619.
[99] Tsuji, H; Arai, N; Matsumoto, T; Ueno, K; Gotoh, Y; Abachi, K; Kotaki, H; Ishikawa, *J. Appl. Surf. Sci*., 2004, 238, 132-137.
[100] Tsuji, H; Arai, N; Matsumoto, T; Ueno, K; Abachi, K; Kotaki, H; Gotoh, Y; Ishikawa, *J. Surf. Coat. Technol*., 2005, 196, 39-43.
[101] Arai, N; Tsuji, H; Motono, M; Goto, Y; Adachi, K; Kotaki, H; Ishikawa, J. *Nucl. Inst. Meth. Phys. Res. B*, 2003, 206, 629-633.
[102] Arai, N; Tsuji, H; Ueno, K; Matsumoto, T; Gotoh, Y; Abachi, K; Kotaki, H; Ishikawa, J. Surf. Coat. *Technol*., 2005, 196, 44-49.
[103] Arai, N; Tsuji, H; Ueno, K; Matsumoto, T; Gotoh, Y; Abachi, K; Kotaki, H; Gotoh, Y; Ishikawa, J. *Nucl. Inst. Meth. Phys. Res. B*, 2006, 242, 217-220.
[104] Arai, N; Tsuji, H; Abachi, K; Kotaki, H; Gotoh, Y; Ishikawa, J. *Jap. J. Appl. Phys*., 2007, 46, 6260-6266.
[105] Arai, N; Tsuji, H; Gotoh, N; Matsumoto, T; Ishibashi, T; Adachi, K; Kotaki, H; Gotoh, Y; Ishikawa, J. *J. Phys*., Conf. Ser. 2007, 61, 41-45.
[106] Roiz, J; Oliver, A; Munoz, E; Rodríguez-Fernández, L; Hernandez, JM; Cheang-Wong JC. *J. App. Phys*., 2004, 95, 1783-1791.

Copyright © 2010. Nova Science Publishers, Incorporated. All rights reserved.

[107] Oliver, A; Reyes-Esqueda, JA; Cheang-Wong, JC; Román-Velázquez, CE; Crespo-Sosa, A; Rodríguez-Fernández, L; Seman, JA; Noguez, C. *Phys. Rev. B*, 2006, 74, 245425-1- 6.
[108] Cheang-Wong, JC; Oliver, A; Rodríguez-Fernández, L; Arenas-Alatorre, J; Peña, O; Crespo-Sosa A. *Revista Mexicana de Física S*, 2007, 53, 49-54.
[109] Peña, O; Cheang-Wong, JC; Rodríguez-Fernández, L; Arenas-Alatorre, J; Crespo-Sosa, A; Rodríguez -Iglesias, V; Oliver, A. *Nucl. Inst. Meth. Phys. Res. B*, 2007, 257, 99-103.
[110] Peña, O; Pal, U; Rodríguez-Fernández, L; Silva-Pereyra, HG; Rodríguez -Iglesias, V; Cheang-Wong, JC; Arenas-Alatorre, J; Oliver, A. *J. Phys. Chem*., 2009, 113, 2296-2300.
[111] Reyes-Esqueda, JA; Torres-Torres, C; Cheang-Wong, JC; Crespo-Sosa, A; Rodríguez-Fernández, L; Noguez, C; Oliver, A. *Opt. Express*, 2008, 16, 710-713.
[112] Reyes-Esqueda, JA; Rodríguez -Iglesias, V; Silva-Pereyra, HG; Torres-Torres, C; Santiago-Ramirez, AL; Cheang-Wong, JC; Crespo-Sosa, A; Rodríguez-Fernández, L; Lopez-Suarez, A; Oliver, A. *Opt. Express*, 2009, 17, 12849-12868.
[113] Rodríguez -Iglesias, V; Silva-Pereyra, HG; Cheang-Wong, JC; Reyes-Esqueda, JA; Rodríguez-Fernández, L; Crespo-Sosa, A; Kellerman, G; Oliver, A. *Nucl. Inst. Meth. Phys. Res. B*, 2008, 266, 3138-3142.
[114] Rodríguez -Iglesias, V; Silva-Pereyra, HG; Torres-Torres, C; Reyes-Esqueda, JA; Cheang-Wong, JC; Crespo-Sosa, A; Rodríguez-Fernández, L; López-Suárez, A; Oliver, A. *Opt. Comm*., 2009, 282, 4157-4161.
[115] Rangel-Rojo, R; McCarthy, J; Bookey, HT; Kar, AK; Rodríguez-Fernández, L; Cheang-Wong, JC; Crespo-Sosa, A; Lopez-Sosa, A; Oliver, A; Rodríguez -Iglesias, V; Silva-Pereyra, HG *C. Opt.omm*., 2009, 282, 1909-1912.
[116] Romanyuk, A; Spassov, V; Melnik, V. *J. Appl. Phys*., 2006, 99, 034314-1 - 4.
[117] Takeda, Y; Plaksin, OA; Lu, J; Kishimoto, N. *Vacuum*, 2006, 80, 776-779.
[118] Joseph, B; Suchan Sandeep, CS; Sekhar, BR; Mahapatra, DP; Philip, R. *Nucl. Inst. Meth. Phys. Res. B*, 2007, 265, 631-636.
[119] Joseph, B; Lenka, HP; Kuiri, PK; Mahapatra, DP; Kesavamoorthy, R. *Intern. J. Nanoscience*, 2007, 6, 423-430.
[120] Sahu, G; Rath, SK; Joseph, B; Roy, GS; Mahapatra, DP. *Vacuum*, 2009, 83, 836-840.
[121] Carles, R; Farcãu, C; Bonafos, C; Benassayag, G; Pécassou, B; Zwick, A. *Nanotechnol*. 2009, 20, 1-6.
[122] Wang, YH; Peng, SJ; Lu, JD; Wang, RW; Mao, YI; Chen, YG. *Vacuum*, 2009, 83, 408-411.
[123] Wang, YH; Peng, SJ; Lu, JD; Wang, RW; Chen, YG; Mao, YI. *Vacuum*, 2009, 83, 412-415.
[124] Magruder III, RH; Meldrum, A. J. Non.-Cryst. *Solids*, 2007, 353, 4813-4818.
[125] Nistor, LC; von Landuyt, J; Barton, JB; Hole, DE; Skelland, ND; Townsend, PD. J. Non.-Cryst. *Solids*, 1993, 162, 217-224.
[126] Wood, RA; Townsend, PD; Skelland, ND; Hole, DE; Barton, J; Afonso, CN. *J. Appl. Phys*., 1993, 74, 5754-5756.
[127] Dubiel, M; Hofmeister, H; Schurig, E. *Phys. Stat. Sol. B*, 1997, 203, R5-R6.
[128] Dubiel, M; Hofmeister, H; Schurig, E; Wendler, E; Wesch, W. *Nucl. Inst. Meth. Phys. Res. B*, 2000, 166-167, 871-876.

Copyright © 2010. Nova Science Publishers, Incorporated. All rights reserved.

[129] Dubiel, M; Hofmeister, H; Tan, GL; Schicke, KD; Wendler, E. *Eur. Phys. J. D*, 2003, 24, 361-364.
[130] Dubiel, M; Hofmeister, H; Wendler, E. *J. Non.-Cryst. Solids*, 2008, 354, 607-611.
[131] Seifert, G; Stalmashonak, S; Hofmeister, H; Haug, J; Dubiel M. *Nanoscale Res. Lett*, 2009, 4, 1380-1383.
[132] Stepanov, AL; Hole, DE; Bukharaev, AA; Townsend, PD; Nurgazizov, NI. *Appl. Surf. Sci*., 1998, 136, 298-305.
[133] Stepanov, AL; Hole, DE; Townsend, PD. *J. Non.-Cryst. Solids*, 1999, 224, 275-279.
[134] Stepanov, AL; Hole, DE; Townsend, PD. *J. Non.-Cryst. Solids*, 1999, 260, 67-74.
[135] Stepanov, AL; Hole, DE; Townsend, PD. *Nucl. Inst. Meth. Phys. Res. B*, 1999, 149, 89-98.
[136] Stepanov, AL; Hole, DE; Townsend, PD. *Nucl. Inst. Meth. Phys. Res. B*, 2000, 161-163, 913-916.
[137] Stepanov, AL; Zhikharev, VA; Hole, DE; Townsend, PD; Khaibullin, IB. *Nucl. Inst. Meth. Phys. Res. B*, 2000, 166-167, 26-30.
[138] Stepanov, AL; Hole, DE; Townsend, PD. *Nucl. Inst. Meth. Phys. Res. B*, 2000, 166-167, 882-886.
[139] Stepanov, AL. *Optics and Spectroscopy*, 2000, 89, 408-412.
[140] Stepanov, AL; Popok, VN; Hole, DE; Bukharaev, AA. *Physics of Solid State*, 2001, 43, 2192-2198.
[141] Stepanov, AL; Popok, VN. *J. Appl. Spectr*, 2001, 68, 164-169
[142] Stepanov, AL; Hole, DE; Popok, VN. Tech. *Phys. Lett*, 2001, 27, 554-556.
[143] Stepanov, AL; Hole, DE; Bukharaev, AA. *Vacuum*, 2002, 64, 169-177.
[144] Stepanov, AL; Hole, DE; Popok, VN. Glass *Phys. Chem*., 2002, 28, 90-95.
[145] Stepanov, AL; Hole DE. *Phil. Mag. Lett*, 2002, 82, 149-155.
[146] Stepanov AL. In Recent research development in applied physics; SG. Pandalai, Ed; *Transworld Res*., Network: Kerala, 2002, 5, 1-25.
[147] Stepanov, AL; Popok, VN. *Tech. Phys. Lette*, 2003, 29, 977-979.
[148] Stepanov, AL. *Rev. Adv. Mater. Sci*., 2003, 4, 45-60.
[149] Stepanov, AL. In Recent research development in non.-crystalline solids; SG. Pandalai, Ed; *Transworld Res*. Network: Kerala, 2003, 3, 177-193.
[150] Stepanov, AL; Popok, VN. Surf. Coat. *Thechnol*, 2004, 185, 30-37.
[151] Stepanov, AL; Popok, VN. *Surf. Sci*., 2004, 566-568, 1250-1254.
[152] Stepanov, AL; Popok, VN. *J. Appl. Spectr*, 2005, 72, 229-234.
[153] Stepanov, AL; Chichkov, BN; Valeev, VF; Faizrakhmanov, IA. *Tech. Phys. Lett*, 2008, 34, 184-186.
[154] Stepanov, AL; Valeev, VF; Faizrakhmanov, IA; Chichkov, BN. *Tech. Phys. Lett*, 2008, 34, 1014-1017.
[155] Stepanov, AL; Valeev, VF; Bazarov, VV; Faizrakhmanov, IA. Excimer laser-assisted annealing of silicate glass with ion-synthesised silver nanoparticles *Tech. Phys*., 2009, 54, 1504-1510.
[156] Tsuji, H; Sugahara, H; Gotoh, Y; Ishikawa J. *Surf. Coat. Technol*, 2002, 158-159, 208-213.
[157] Tsuji, H; Sugahara, H; Gotoh, Y; Ishikawa, J. *Nucl. Inst. Meth. Phys. Res. B*, 2003, 206, 249-253.

Copyright © 2010. Nova Science Publishers, Incorporated. All rights reserved.

[158] Tsuji, H; Sakai, N; Sugahara, H; Gotoh, Y; Ishikawa J. *Nucl. Inst. Meth. Phys. Res. B*, 2005, 237, 433-437.
[159] Tsuji, H; Sakai, N; Gotoh, Y; Ishikawa, J. *Nucl. Inst. Meth. Phys. Res. B*, 2006, 242, 129-132.
[160] Saito, Y; Imamura, Y; Kitahara, A. *Nucl. Inst. Meth. Phys. Res. B*, 2003, 205, 272-276.
[161] Fujita, T; Ijima, K; Mitsui, N; Mochiduki, K; Saito, Y. *Jap. J. Appl. Phys*., 2007, 46, 7362-7364.
[162] Ziegler, JF; Biersack, JP; Littmark, U. *The stopping and range of ions in solids*, Pergamon Press: New York, 1996.
[163] Nastasi, M; Mayer, JW; Hiroven, JK. Ion-solid interactions: *Fundamentals and applications*, Cambridge Univ. Press: Cambridge, 1996.
[164] Namba, S; Masuda, K; Gamo, K; Doi, A; Ishinara, S; Kimura, I. *Ion implantation*. Proc. Of conf. on ion implantation in semiconductors; FD; Eisen, LT. Chadderton, Eds; Cordon and Breach Sci., Publ.: London, 1971, 231-236.
[165] Berger, A. J. *Non.-Cryst. Solids*, 1992, 151, 88-94.
[166] Skelland, ND; Townsend, PD. J. *Non.-Cryst. Solids*, 1995, 188, 243-253.
[167] Hole, DE; Stepanov, AL; Townsend, PD. *Nucl. Inst. Meth. Phys. Res. B*, 1999, 148, 1054-1058.
[168] Konoplev, VM. *Radiat. Eff. Lett*, 1986, 87, 207-214.
[169] Konoplev, VM; Vicanek, M; Gras-Martí, A. *Nucl. Inst. Meth. Phys. Res. B*, 1992, 67, 574-579.
[170] Stepanov, AL; Abdullin, SN; Khaibullin, RI; Valeev, VF; Osin, Yu. N; Bazarov, VV; Khaibullin, IB. *Mat. Res. Soc. Proc*., 1995, 392, 267-272.
[171] Khaibullin, RI; Osin, Yu. N; Stepanov, AL; Khaibullin, IB. *Nucl. Inst. Meth. Phys. Res. B*, 1999, 148, 1023-1028.
[172] Townsend, PD; Can, N; Chandler, PJ; Farmery, BW; Lopez-Heredero, R; Peto, A; Salvin, L; Underdown, D; Yang, B. *J. Non.-Cryst. Solids*, 1998, 223, 73-85.
[173] Wang, PW. *Appl. Surf.. Sci*., 1997, 120, 291-298.
[174] Bartels, J; Lembke, U; Pascova, R; Schmelzer, J; Gustzow, I. *J. Non.-Cryst. Solids*, 1991, 136, 181-197.
[175] Mie, G. *Ann. Phys.*, 1908, 25, 377-445.
[176] Heavens, OS. *Optical properties of thin solid films*, Butterworths Sci. Pub.: London, 1955.
[177] Maxwell Garnet, JC. *Philos. Trans. R. Soc. Lond*, 1904, 203, 385-420.
[178] Maxwell Garnet, JC. *Philos. Trans. R. Soc. Lond*, 1906, 205, 237-288.
[179] Faik, A; Allen, L; Eicher, C; Gagola, A; Townsend, PD; Pitt, CW. *J. Appl. Phys*., 1983, 54, 2597-2601.
[180] Hosono, H. Jpn. *J. Appl. Phys*., 1993, 32, 3892-3894.
[181] Palpant, B. In *Non-linear optical properties of matte;* MG; Papadopoulos, Ed; Springer: Berlin, 2006, 461-508.
[182] Hamanaka, Y; Hayashi, N; Nakamura, A; Omi, S. J. *Lumines*, 2000, 87-89, 859-861.
[183] Ganeev, RA; Ryasnyanskii, AI; Stepanov, AL; Kondirov, MK; Usmanov, T. *Optics and Spectroscopy*, 2003, 95, 1034-1042.
[184] Ganeev, RA; Ryasnyanskii, AI; Stepanov, AL; Usmanov, T. *Opt. Quant. Electr*., 2004, 36, 949-960.
[185] Kurata, H; Takami, A; Koda, S. *Appl. Phys. Lett*, 1998, 72, 789-791.

Copyright © 2010. Nova Science Publishers, Incorporated. All rights reserved.

[186] Link, S; Burda, C; Mohamed, MB; Nikoobakht, B; El-Sayed, MA. *J. Phys. Chem. A*, 1999, 103, 1165-1170.
[187] Mafune, F; Kohno, J; Takeda, Y; Kondow, T. *J. Phys. Chem. B*, 2002, 106, 8555-8561.
[188] Chandrasekharan, N; Kamat, PV; Hu, J; Jones, II, G. *J. Phys. Chem. B*, 2000, 104, 11103-11109.
[189] Osborne, Jr., DH; Haglund, Jr., RF; Gonella, F; Garrido, F. *Appl. Phys. B*, 1998, 66, 517-521.
[190] Kyoung, M; Lee, M. *Opt. Comm*., 1999, 171, 145-148.
[191] Buerhop, C; Blumenthal, B; Weissmann, R. *Appl. Surf. Sci*., 1999, 46, 653-668.
[192] Townsend, PN; Olivares, J. *Appl. Surf. Sci.*, 1997, 109-110, 275-282.
[193] Castro, T; Reifenberger, R; Choi, T; Andres, PP. *Phys. Rev. B*, 1990, 42, 8549-8556.
[194] Stepanov, AL; Valeev, VF; Osin, Yu. N; Nuzhdin, VI; Faizrakhmanov, IA. *Tech. Phys*., 2009, 54, 997-1001.
[195] Heilmann, A. *Polymer films with embedded metal nanoparticles*, Springer: Berlin, 2003.
[196] Koon, NC; Weber, D; Pehrsson, P; Sindler, A. I. Mater. Res. Soc. *Proc*., 1984, 27, 445-449.
[197] Stepanov, AL; Abdullin, SN; Khaibullin, RI; Osin, Yu. N; Khaibullin, I. B. Proc. *Royal Micr. Sci*., 1994, 29, 226.
[198] Stepanov, AL; Abdullin, SN; Khaibullin, RI; Valeev, VF; Osin, Yu. N; Bazarov, VV; Khaibullin, IB. *Mat. Res. Soc. Proc*., 1995, 392, 267-272.
[199] Stepanov, AL; Abdullin, SN; Khaibullin, RI; Khaibullin, IB. *Patent PF*, 109708, 1997.
[200] Stepanov, AL; Khaibullin, RI; Valeev, VF; Osin, Yu. N; Nuzhdin, VI; Faizrakhmanov, IA. *Tech. Phys*., 2009, 54, 1162-1167.
[201] Khaibullin, IB; Khaibullin, RI; Abdullin, SN; Stepanov, AL; Osin, Yu. N; Bazarov, VV; Kurzin, SP. Nucl. Inst. Meth. *Phys. Res. B*, 1997, 127-128, 685-690.
[202] Boldyryeva, H; Kishimoto, N; Umeda, N; Kono, K; Plaksin, OA; Takeda, Y. *Nucl. Inst. Meth. Phys. Res. B*, 2004, 219-220, 953-958.
[203] Wu, Y; Zhang, T; Zhang, H; Zhang, X; Deng, Z; Zhou, G. *Nucl. Inst. Meth. Phys. Res. B*, 2000, 169, 89-93.
[204] Wu, Y; Zhang, T; Zhang, Y; Zhang, H; Zhang, X; Zhou, G. Nucl. *Inst. Meth. Phys. Res. B*, 2001, 173, 292-298.
[205] Wu, Y; Zhang, T; Zhang, Y; Zhang, H; Zhang, X; Zhou, G. *Science in China E*, 2001, 44, 493-498.
[206] Wu, Y; Zhang, T; Liu, A; Zhou, Gu. *Surf. Coat. Technol*., 2002, 157, 262-266.
[207] Kobayashi, T; Iwata, T; Doi, Y; Iwaki, M. *Nucl. Inst. Meth. Phys. Res. B*, 2001, 175-177, 548-553.
[208] Stepanov, AL; Abdullin, SN; Petukhov, VYu; Osin, YuN; Khaibullin, RI; Khaibullin, IB. *Philos. Mag. B*, 2000, 80, 23-28.
[209] Stepanov, AL; Popok, VN; Khaibullin, IB; Kreibig, U. *Nucl. Inst. Meth. Phys. Res. B*, 2002, 191, 473-477.
[210] Stepanov, AL. *Tech. Phys*., 2004, 49, 143-153.
[211] Bazarov, VV; Petukhov, V. Yu; Zhikharev, VA; Khaibullin, IB. *Mater. Res. Soc. Proc*., 1995, 388, 417-422.
[212] Boldyryeva, H; Umeda, N; Plaksin, OA; Takeda, Y; Kishimoto, N. *Surf. Coat. Technol*., 2005, 196, 373-377.

Copyright © 2010. Nova Science Publishers, Incorporated. All rights reserved.

[213] Khaibullin, RI; Osin, YN; Stepanov, AL; Khaibullin, IB. *Vacuum*, 1998, 51, 289-294.
[214] Khaibullin, RI; Osin, YN; Stepanov, AL; Khaibullin, IB. *Nucl. Inst. Meth. Phys. Res. B*, 1999, 148, 1023-1028.
[215] Stepanov, AL; Khaibullin, RI; Khaibullin, IB. *Philos. Mag. Lett*, 1998, 77, 261-266.
[216] Scheunemann, W; Jäger, HZ. *Phys*., 1973, 265, 441-454.
[217] Quinten, MZ. *Phys. B*, 196, 101, 211-217.
[218] Khashan, MA; Nassif, AY. *Opt. Comm*., 2001, 188, 129-139.
[219] Sviridov, DV. Russian *Chem. Rev*., 2002, 71, 315-327.
[220] Pignataro, B; Fragala, ME; Puglisi, O. *Nucl. Instr. Meth. Phys. Res. B*, 1997, 131, 141-148.
[221] Palik, ED. *Handbook of optical constants of solids*, Academic: London, 1997.
[222] Sinzig, J; Quinten, M. *Appl. Phys. A*, 1994, 58, 157-162.
[223] Kreibig, U; Gartz, M; Hilger, A. Ber. Bunssenges. *Phys. Chem*., 1997, 101, 1593-1601.
[224] Hölzl, J; Schulte, F; Wagner, H. *Solid surface physics*, Springer: Berlin, 1979.

Copyright © 2010. Nova Science Publishers, Incorporated. All rights reserved.

Copyright © 2010. Nova Science Publishers, Incorporated. All rights reserved.

In: Silver Nanoparticles
Editors: Audrey E. Welles, pp. 221-258
ISBN: 978-1-61668-690-1
©2010 Nova Science Publishers, Inc.

Chapter 5

BIOLOGICAL EFFECTS OF SILVER NANOPARTICLES

Elena M. Egorova*
Russian Academy of Medical Sciences, Moscow, Russia

ABSTRACT

Silver nanoparticles are widely used now for the creation and production of modified materials with special properties. However, the mode of their action on the living organisms and the conditions providing the safety of their applications for humans and other living beings remain poorly understood. Therefore, of particular interest are studies allowing to reveal the effects of nanoparticles' parameters on various functions of the biological systems and, in particular, to determine the concentration limits within which the nanoparticles are not toxic for a given plant, animal or human organism..

This chapter presents a review on the biological effects of silver nanoparticles observed in experiments on the living organisms of various types. The nanoparticles used in these studies were obtained by the original method of biochemical synthesis, based on the reduction of metal ions by natural plant pigments (flavonoids) in reverse micelles formed by the anionic surfactant. From micellar solutions of nanoparticles in organic solvent water dispersions are prepared according to the special procedure. Optical spectra and TEM micrographs of silver nanoparticles in solutions are presented. Both water solutions containing silver nanoparticles and solid or polymer materials modified by the nanoparticles are considered. The antimicrobial properties and toxic action of the nanoparticles on slim mold, alga, plant seeds and animals are described. The results are compared with those reported in similar studies using silver nanoparticles obtained by the other methods.

Copyright © 2010. Nova Science Publishers, Incorporated. All rights reserved.

1. INTRODUCTION

One of the most prominent features of modern development in the field of science and technologies is the rapid growth of researches dealing with nanosized objects and their

* The laboratory of nanopathology, Institute of general pathology and pathophysiology, Russian Academy of Medical Sciences, Baltijskaya st., 8, Moscow, Russia,emenano@mail.ru

applications. Judging from both the theoretical grounds and known examples of successful use of nanotechnology-based products it seems quite possible to suppose that further development of nanoscience and nanotechnologies may give the effective tools for solving a lot of problems which faces the humanity nowadays and will probably meet in future. It is clear, however, that, as "each picture has its dark side" so each new stage of scientific and technical progress, apart from obvious advantages possess also its opposite side, resulting in new problems and dangers. With respect to nanotechnologies, one of the dangers more or less clearly realized today is poor knowledge of the influence of nanoparticles and nanoparticles-containing materials on the living organisms, including humans. This danger is the more significant, the bigger is the extent of penetration of the corresponding methods and products into science, technology and everyday life. Thus the problem arises of elaboration of the adequate safety standards for the use of nanotechnology-based products, the point which is discussed both by scientists and official organizations responsible for the public health [1-5]. It is strongly emphasized that unique properties of nanoparticles, such as very small size, large surface area and high reactivity, which open great perspectives of their practical application, at the same time may be responsible for the risks for health which one can hardly escape without thorough investigation of their action on the living organisms.

In the last decade these general considerations were confirmed by the results of studies of the biological effects of nanoparticles of different origin, made from metals, metal oxides, polymers, silicon and other materials (e.g.[5-8]). In these studies, much attention was paid to the metal nanoparticles, since, on the one hand, they are one of the most popular and promising objects of applied researches in chemistry, technics and medicine and, on the other hand, they found already a great number of practical applications – in production of various means for medical purposes (wound dressings, antimicrobial coatings, cancer detection agents et al) and consumer goods (cosmetics, clothes, domestic devices, toys et al.). Studies on the possibilities of use of metal nanoparticles in diagnostics and healing of various (including oncological) deceases as well as in immunochemical researches form now a new field of experimental medicine (e.g. [9-13]).

At the same time it is well documented that metal nanoparticles may cause serious disorders (nanopathologies) in the living organisms, including humans. It is established that these nanoparticles can enter a human organism by three main ways: (1) through the inhalation of air containing nanoparticles resulting from the industrial activities or military operations, (2) during the use of consumer goods containing metal nanoparticles and (3) in the course of medical treatment or with drugs (e.g. colloidal silver). Elucidation of the causes of *nanopathologies* and searching for the ways of their medical treatment are now the subjects of another new trend in experimental medicine.

So it is possible to assert that determination of the ways and modes of the action of nanoparticles on a living organism is a very important and actual task, necessary, *first*, for both the improvement of the remedies and medical treatment now in use and creation of new ones, i.e. for nanomedecine, *second*, for finding the causes of deceases provoked by the nanoparticles and *third*, for the substantiation of permissible concentrations and sizes of nanoparticles in air, water and various materials in contact with people.

Although studies on the biological effects of metal ions on cells and higher organisms were started rather long ago (e.g.[14-17]), similar data on the biological action of nanoparticles or metal sols appeared mainly in the last decade. Up to the end of ninetieth, the majority of publications were devoted to the studies of biosorption and biomineralization of metals by bacteria cells

Copyright © 2010. Nova Science Publishers, Incorporated. All rights reserved.

[15,16], the processes underlying extraction of gern (Au, Ag) or several metals used in technics (Cu, Fe, Ni et al) from soil waters or industry scraps. Some data on the action of metal ions and sols were obtained also on unicellular algae [17]. Basing on these results, various events underlying cell membrane – nanoparticles interaction were considered, pertaining mainly to bacteria cells. It was supposed, that the interaction under question includes processes of at least three kinds: (1) adhesion of colloid metal particles to the cell surface driven by electrostatic and chemisorption forces, (2) cell reaction to the adhesion of metal particle, expressed as particle "dissolution" by means of oxidation of metal atoms constituting a particle and subsequent formation of new, bigger metal particles through the association of atoms and ions and (3) aggregation of microbial cells at the sites of nanoparticles adhesion. Besides it was elucidated that interaction of metal nanoparticles with living and dead cells proceeds in substantially different ways, and that cell surface charge which may differ on various parts of cell membrane, plays a noticeable role in this interaction [16]. The role of surface charge was emphasized also in studies of the interaction of Ag^+ , Cu^{2+} and Au^{3+} ions with unicellular algae [17].

In the last several years a noticeable "jump" in the number of publications is observed, resulting mainly from the necessity of providing safety of use for the products of nanotechnology, as mentioned above. The majority deal with bacteria-nanoparticle interactions ([8, 18-23] and references herein); the nanoparticles effects on virus [22], mammalian cultured cells [24-27], fishes and animals [28-33] are also described. It was shown that various nanoparticles, including metallic ones, provoke membrane damage of bacteria cells [8]. The mechanism of this damage currently discussed [8] is lipid peroxidation induced by the formation of reactive oxygen species (ROS), such as superoxide anion (O_2^-) and hydroxyl radical (OH^{-*}); the idea issued from the studies of interaction of TiO_2 nanoparticles with eucaryotic cells and was further supported by the fact that two enzymes which catalyse the O_2^- transformation into inactive species (H_2O and O_2), when added to solutions of Ag/Al_2O_3 nanoparticles significantly reduce the damage of E.coli membranes. However, toxic effect of metal ions released from the nanoparticles into the aqueous phase is also considered. The role of surface charge of both nanoparticles (first of all, of their stabilizing shell) and cell membrane is emphasized as a main driving force for the formation of nanoparticle-cell contact [8], necessary for the subsequent membrane damage.

In these recent studies much attention is paid to the effects of silver nanoparticles (AgNP), partly because of the diversity of products containing them, partly due to the fact that silver nanoparticles seem to be the most simple to obtain, in many cases are stable enough and can be properly investigated and characterized by optical properties, size and sometimes charge. Therefore for the time being, studies on the biological effects of silver nanoparticles give the most extensive information about the processes taking place during the interaction of metal nanoparticles with biological objects, and also about the difference between biological action of nanoparticles and the corresponding metal ions. It is now well documented that AgNP are toxic for bacteria [8,18,20-22], animal cultured cells [24-26], fish embryos [28] and animal organisms [29,30, 33].

Some early studies on the mechanism of the toxic action of colloidal silver on bacteria E.coli allowed to suggest [14,15] that suppression of the living functions of bacteria cells is connected mainly with release of silver ions and their subsequent binding with SH-groups of proteins on cell membrane or (at higher metal concentrations) in the inner cell structures and the resultant block of important cell functions. In the more recent work on E.coli [20] it was found that 1) toxic effect depended on the particle size (9 nm nanoparticles were more effective than 62 nm) and 2) toxicity of AgNP may result from the presence of Ag^+ ions on their surface due to the oxidation. However, the adhesion of AgNP to the cell membrane was not recorded, so it remained unclear how the Ag^+ ions were delivered from the particle surface to the cell membrane, the process which is thought to

Copyright © 2010. Nova Science Publishers, Incorporated. All rights reserved.

be necessary for realization of their antibacterial activity. In the other work on E.coli it was revealed [21], that toxic action of AgNP depends on their form: triangular particles were more active than spherical ones. It was shown also that toxicity depends on the particle size and the effect of AgNP exceeds that of Ag^+ ions in equivalent concentrations.

In studies of AgNP with HIV-I [23] it was shown that 1-10 nm nanoparticles bind to the definite sites on the virus surface, presumably to the glycoprotein knobs responsible for the viral activity towards host cells. Thus it is possible that AgNP can serve as a means which prevents the virus from invasion into mammalian cells.

In vitro studies on germline stem cells [24] revealed that 15 nm AgNP exert the concentration-dependent toxic effect; in particular, they suppress the functions of mitochondrial enzymes, while Ag^+ ions introduced as soluble salt had no influence on cell functions. Experiments on fish embryos [28] testify to the strong toxic action of AgNP (5-20 nm) on the early embryonic development. Control additions of Ag^+ ions in equivalent concentrations had practically no toxic effect.

By contrast, studies of the effect of AgNP (average size 60 nm) on rats in vivo [29] did not reveal noticeable changes in body weight or hematology and blood biochemical values after the NPs inhalation. After oral administration [30] AgNP of the same size did not induce the DNA damage or exerted toxic action on bone marrow cells. However, the 28-days of repeated oral doses did induce liver toxicity and did have a coagulation effect on peripheral blood. Electron microscopy studies revealed the accumulation of AgNP in liver and kidneys.

In summary, it was found that AgNP exert negative (toxic) influence on the functions of living organisms on various levels – from microorganisms to animals. The toxic effects are concentration-dependent; the corresponding concentrations of silver ions introduced as soluble salt have no significant influence on the same object. The extent of toxic effect depends on the particle size, form and mode of preparation; the latter often determines the nanoparticles stability and size distribution, as well as the width, surface charge and chemical properties of their stabilizing shell which plays a noticeable role in their biological activity [23].

As to the general strategy of research, it seems clear that, to obtain the reliable conclusions on the regularities working in the biological activity of metal nanoparticles, it is necessary to combine two main lines of development: *horizontal* - studies on one object or one definite level of biological organization (microbes, plant or animal cells, tissues, multicellular organisms of definite type) using nanoparticles of a given metal, having different sizes and forms, prepared by different ways, and *vertical* – studies on different objects or levels of organization using one definite type of nanoparticles of a given size, form and mode of preparation. The horizontal line allows to distinguish the effects resulting from variation of the particle parameters; the vertical line makes possible to reveal the effects caused by specific properties of biological objects. In reality, each research group works with the objects and nanoparticles available, thus making contributions either to the horizontal, or to the vertical line. As follows from literature, at present the majority of studies move along the horizontal line, using various nanoparticles in studies of one biological object or several objects on one organization level (e.g. different bacteria strains). The idea underlying our investigations was to start the movement along the vertical line, namely, to use the nanoparticles with a given set of parameters, obtained in one and the same way, for studies of different biological objects both within the same level and on various levels of complexity.

Such an attempt was undertaken in our studies of the biological effects of AgNP obtained by means of the original method of biochemical synthesis [34, 35]. The method is based on the reduction of metal ions in reverse micelles by the non-traditional reducing agents – natural

Copyright © 2010. Nova Science Publishers, Incorporated. All rights reserved.

plant pigments from the group of flavonoids - first of all, quercetin and rutin. These two flavonoids are well-known bioactive compounds used in medicine because of their anti-inflammatory, antioxidant and radioprotector properties [36-38]. In the last years much attention is paid to the studies of their interaction with mammalian cells in vitro [39], which open the possibilities to use them as hepatoprotectors as well as in the treatment of oncological and some other deceases. The use of such substances as reducing agents is based on their ability to form stable complexes with metal ions; in some cases the complexation leads to the reduction of metal ion to the smaller oxidation extent [40,41]. The combination of this ability of flavonoids with reverse micelles as microreactors for the synthesis of nanoparticles ([42-44], see also section.2 below) provides several advantages important for the practical application of nanoparticles [45]. As noted recently also conformably to the reduction with other natural substances (extracts from certain plants) [46] here synthesis takes place in relatively mild conditions and there is no danger of pollution of the environment with toxic products inevitable with conventionally used chemical reductants, such as hydrazine or sodium borohydride and their oxidation products. However, our method can not be related to the separate group of biochemical methods in one of the modern classifications [46], because in our case, in contrast to this group, the nanoparticles are synthesized not in water solution, but in reverse micelles, the fact that leads to essential difference in the process of particle formation. Also the other advantages should be mentioned, namely, it is possible to prepare small metal particles (less than 30 nm in size) on air, stable in solution for a long time (from several months to several years) using a comparatively simple procedure, with significant yield (the extent of transformation of metal ions into nanoparticles), that allows to obtain in some cases rather high concentrations of metal in the form of nanoparticles.

From micellar solutions stable water solutions of nanoparticles are prepared by specially developed procedures [47]. Thus we obtain metal nanoparticles of the same size, form, structure and surface charge both in organic and water solution, that makes it possible to study their properties and to develop various ways of their practical application, both in native solutions and in combinations with various materials. The most extensive studies were made with AgNP in directions connected with their use as antimicrobial means; also the toxic effects on other living organisms were investigated, with the aim to determine the range of their safe concentrations.

In this review we report some data obtained in our studies of the biological action of silver nanoparticles of definite size (9-10 ±4 nm) on the objects staying on various levels of organization. We give first a brief account of the preparation of silver nanoparticles by the biochemical synthesis; optical spectra and sizes obtained by TEM and PCS are also presented. Then follow the experimental tests on the biological action of AgNP in solutions as well as of various liquid-phase and solid nanoparticles-containing materials. Where possible, our data are compared with those present in literature. The main results are summarized in Conclusion.

Copyright © 2010. Nova Science Publishers, Incorporated. All rights reserved.

2. SILVER NANOPARTICLES OBTAINED BY THE BIOCHEMICAL SYNTHESIS

Metal nanoparticles are formed in the ternary system $Me^{n+}(H_2O)$/AOT/ liquid hydrocarbon. Here $Me^{n+}(H_2O)$ – metal ions in water solution, solubilized in liquid hydrocarbon by aerosol-OT (AOT), an anionic surface active substance (SAS) widely used for the formation of reverse micelles. Schematic presentation of a reverse micelle is given in Fig.1. Reduction of metal ions to atoms and subsequent formation of nanoparticles takes place in the water core at small hydration extent $w = [H_2O]/[AOT]$, [mole]/[mole]. For $w < 4$ commonly used for synthesis of AgNP all the internal water is "binded", i.e. hardly structuralized and its properties differ significantly from those of free water in molecular solution. Liquid hydrocarbon most often used is isooctane, but n-heptane, n-octane and n-decane are also applicable.

It is known that synthesis of metal nanoparticles in reverse micelles has several advantages in comparison with molecular solution [42,43]. *First*, here the nanoparticles aggregate, as a rule, more slowly so their lifetime in reverse micelles (further referred to as micellar solution) is substantially greater than that in molecular solution. *Second*, varying parameters of micellar solution (in particular, diameter of the water core) it is possible to control sizes of nanoparticles. Therefore, synthesis in reverse micelles allows to obtain nanoparticles with relatively narrow size distribution, what is important for the studies of their properties, including "size effects", the peculiar property of "true" nanoparticles [48,49].

Flavonoids applied for the reduction of metal ions are polyphenolic substances composed of two aromatic rings (A and B) connected by the heterocycle (C); as an example, structure of flavonoid quercetin (Qr) most often used in our work is shown in Fig.2.

2.1. General Scheme and Methods

Two possible ways of synthesis are presented in Fig.1 conformably to silver nanoparticles: (I) mixing of preliminary prepared micellar solutions of flavonoid and metal salt and (II) introduction of metal salt water solution directly into the flavonoid micellar solution. In the first case, for the preparation of flavonoid micellar solution its concentrated solution in ethanol or propanol is added to the AOT/isooctane solution, In the second case flavonoid taken as powder is solubilized in AOT/isooctane solution. In both cases the final products are nanoparticles and oxidized flavonoid in reverse micelles. The proper choice of system composition (concentrations of reagents, hydration extent, metal salt, solvent) allows to provide the high enough rate of synthesis, stability and yield of nanoparticles. The rate of process was usually higher in the case (II), so this way is commonly used for the synthesis, including that of silver nanoparticles.

As silver salt we used either silver nitrate (analytical grade) or silver ammonium nitrate, prepared by adding ammonium hydroxide to silver nitrate water solution until silver hydroxide sediment was fully dissolved with creation of $Ag(NH_3)_2^+$ ions. Metal salt solutions were made on deionized water (no less than 10 MΩ) from either Millipore-Q system or its high-quality Russian analogue called "Vodoley". AOT, sodium bis(2-dioctyl)sulphosuccinate, was purchased from Aldrich or Acros, flavonoids – from Merck.

Copyright © 2010. Nova Science Publishers, Incorporated. All rights reserved.

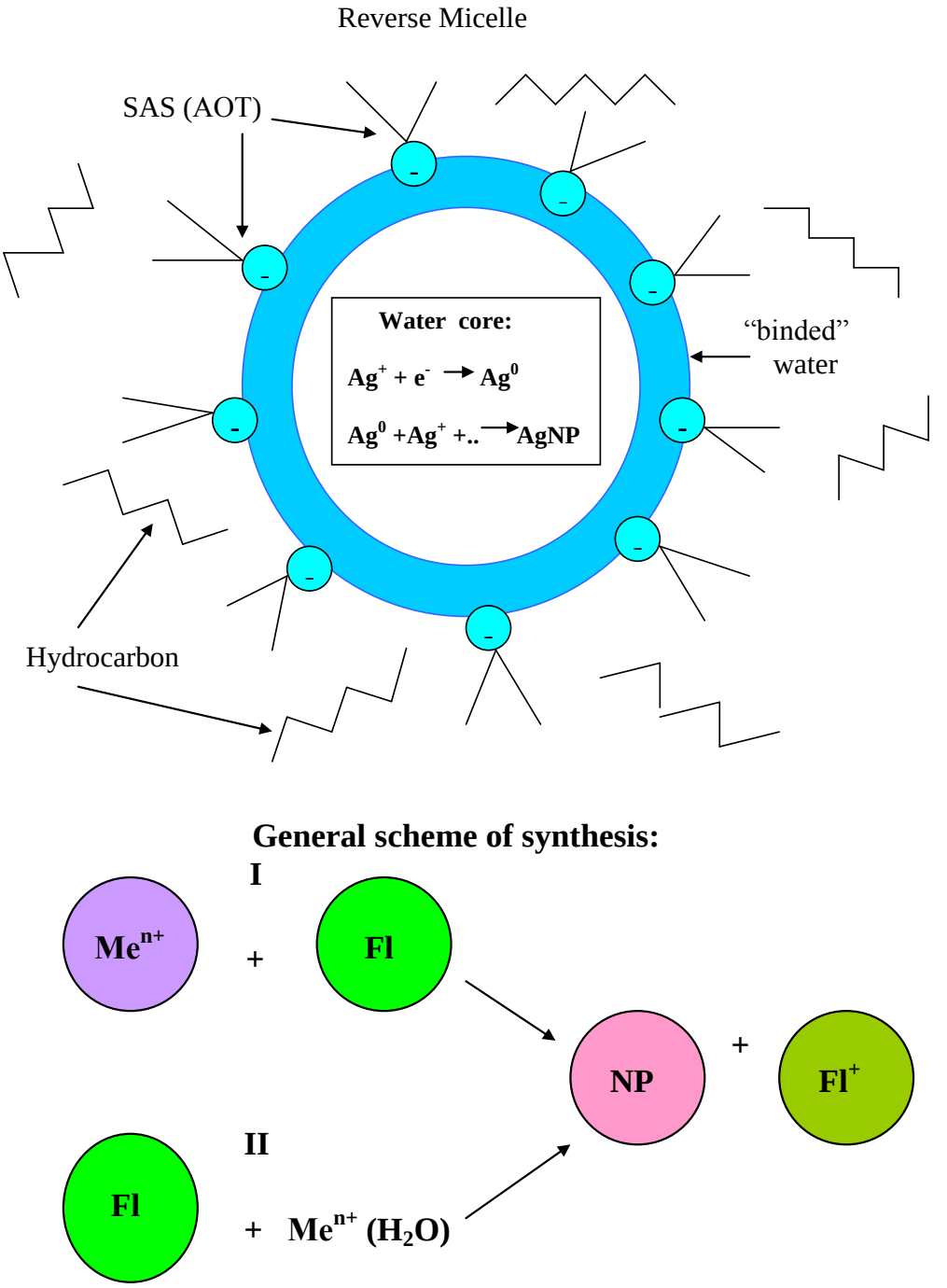

Figure 1. Structure of a reverse micelle and general scheme of biochemical synthesis. SAS – surface active substance. Fl and Fl^+ - flavonoid in molecular and oxidized form, respectively. NP - nanoparticle. See text for details.

Copyright © 2010. Nova Science Publishers, Incorporated. All rights reserved.

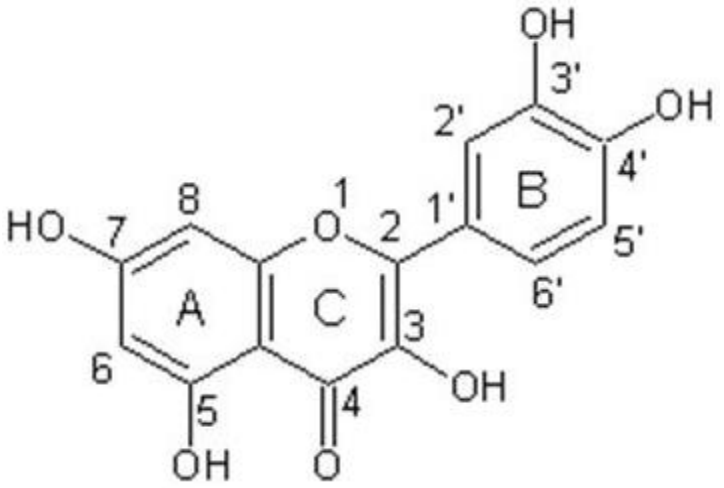

Figure 2. Structure of the flavonoid quercetine commonly used as reducing agent in the biochemical synthesis.

To obtain silver nanoparticles, Qr micellar solution was first prepared according to the procedure described in detail elsewhere [50, 51]. In a typical experiment, water $AgNO_3$ or $Ag(NH_3)_2NO_3$ solution (the «initial» salt solution) was introduced into the Qr micellar solution to the hydration extent, w = 2-4. Silver salt concentration in reverse micelles was varied by changing the concentration of the initial salt solution. After shaking for several minutes, almost colorless Qr solution acquired the intense red-brown coloration that indicated to the appearance of nanoparticles. Further changes in the system were followed by measuring optical absorption spectra. The AgNP concentration in micellar and water solutions was determined from the measured optical densities in absorption band maximum and the extinction coefficient ($\varepsilon = 1.03 * 10^4$ l/mol *sm) found by us as described in [51].

Water solutions of silver nanoparticles were obtained from their micellar solutions by either centrifugation of the two-phase system or mixing of micellar solution with equal volume of distilled water and subsequent treatment allowing to remove the organic solvent and excess of surfactant; the details of preparation are given in [47]. Control of pH and residual concentration of silver ions was carried out by means of potentiometric measurements. The AOT concentration was estimated according to the state standard procedure accepted in Russia for the determination of anionic surfactants in drinking water.

The absorption spectra of micellar or water solutions were recorded on spectrophotometer Helios-α (Thermo Electronics, GB) in 1 mm quartz cell in the range 230-700 nm at room temperature. Either isooctane or distilled water was used as reference solution.

Particle sizes in micellar or water solution were determined by transmission electron microscopy on LEO912 AB OMEGA microscope (production of Carl Zeiss, Germany) at 120 kV accelerating voltage. From electron micrographs particle size distributions were found for no less than 300 particles. Additional control of sizes was made by photon correlation spectroscopy (PCS) technique on Horiba LB-550 (production of Horiba, Japan) and Zetasizer Nano ZS (production of Malvern Instruments, GB). The latter device was used also for the estimation of zeta potential of the external surface of the stabilizing shell (in water solution).

Copyright © 2010. Nova Science Publishers, Incorporated. All rights reserved.

2.2. Optical Spectra and Sizes

According to the standard procedure developed in our studies of the biochemical synthesis, addition of silver salt water solution into the flavonoid micellar solution, after shaking for 1-3 min results in the quick changes of color and absorption spectrum. Typical picture observed with Qr is shown in Fig.3. Instead of the two-band spectrum in the UV region characteristic for flavonoids [40,41,50,51] a new absorption band appears with λ_{max} = 420-440 nm, lying in the range characteristic for silver nanoparticles in reverse micelles at low hydration extent [46,52,53]. The nanoparticles absorption band (the optical density at λ_{max}, i.e. D_{max}) grows with time, showing to the increase of particles concentration. As seen from Fig.3, with silver ammonium nitrate the process is almost fully accomplished within several hours, when D_{max} reaches its stationary value. With silver nitrate it takes about 1-4 days; possible reasons for this difference in the rate of synthesis are considered in [54]. After the stationary state is established, only small changes of optical density take place, not exceeding 10% of the D_{max} value. Such stationary solution has a more or less deep red-brown color, depending on the concentration of nanoparticles; the color remains unchanged for a long time (up to several years), showing to the presence of nanoparticles. The concentration of nanoparticles, C(AgNP), in standard micellar solution lies in the range 0.3-0.6 mgAg/ml.

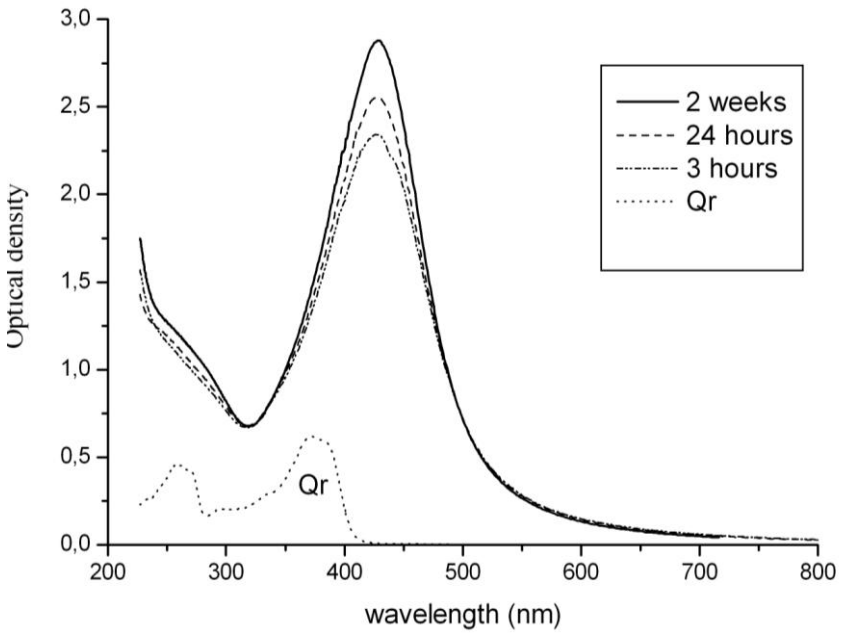

Figure 3. Formation of Ag nanoparticles from silver ammonium nitrate. Absorption spectra of Qr micellar solution at various time intervals after the addition of $Ag(NH_3)_2NO_3$ water solution, the hydration extent w = 3.7. Concentrations of reagents in micellar solution: C(Qr) = 0.236 mM, C(Ag) = 3 mM. Dashed line – spectrum of the initial Qr/AOT/isooctane system.

Copyright © 2010. Nova Science Publishers, Incorporated. All rights reserved.

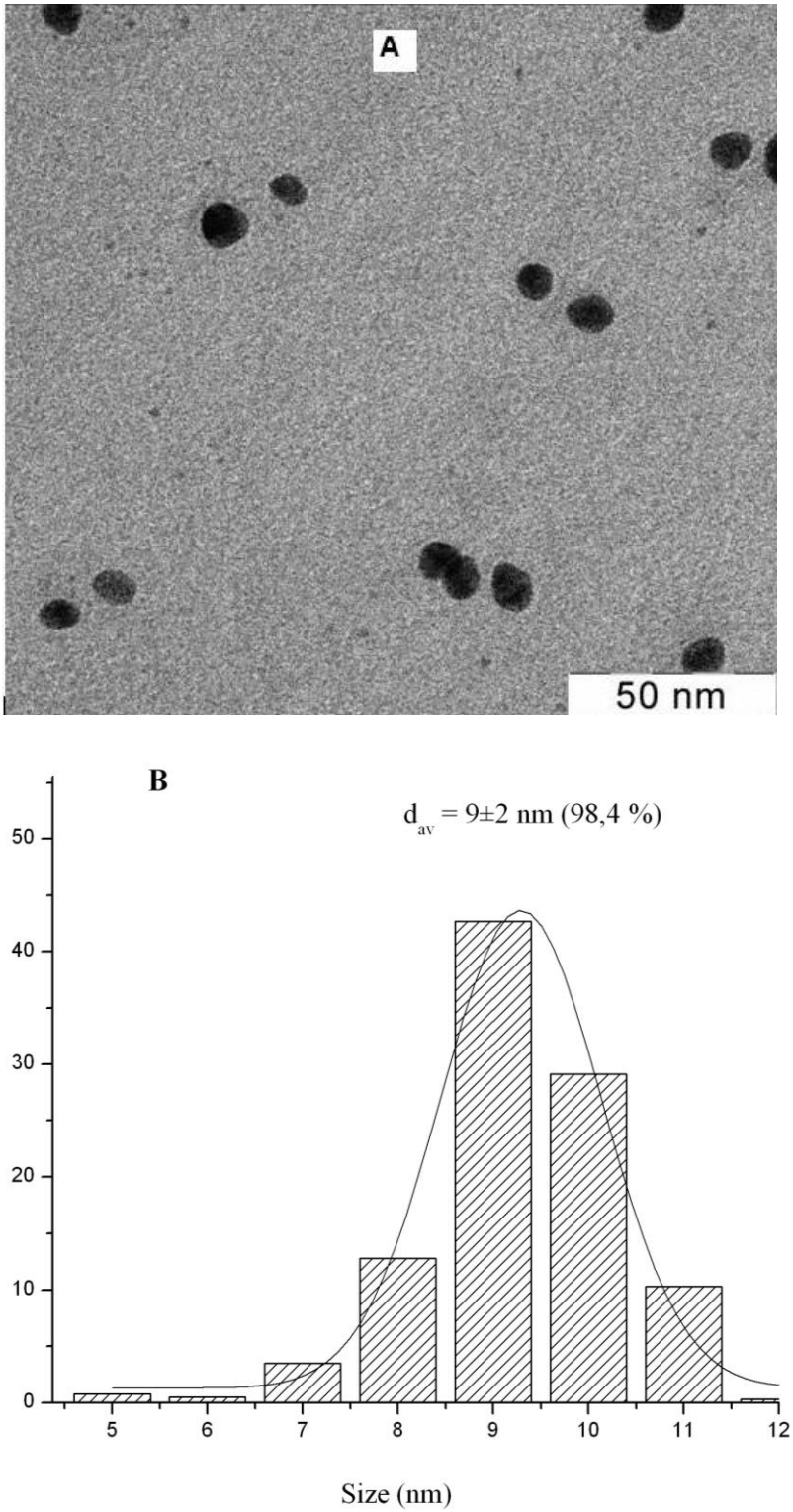

Figure 4. TEM image (A) and size distribution (B) of Ag nanoparticles in standard micellar solution. One week in the stationary state.

Copyright © 2010. Nova Science Publishers, Incorporated. All rights reserved.

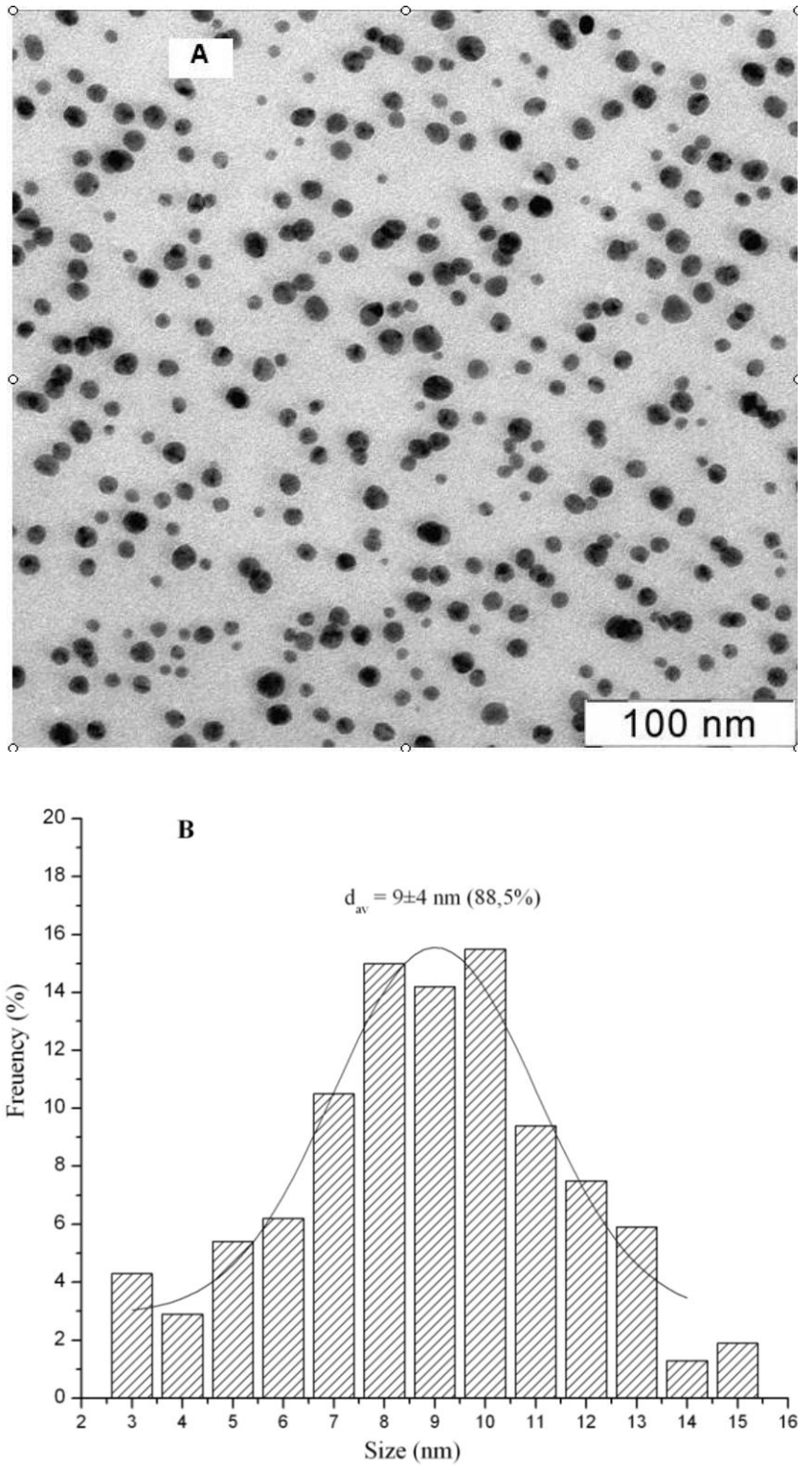

Figure 5. TEM image and size distribution of Ag nanoparticles in standard micellar solution. Six months in the stationary state.

Copyright © 2010. Nova Science Publishers, Incorporated. All rights reserved.

Size measurements in micellar solutions and preparation of water solutions were carried out at the stationary stage, usually no sooner than a week after the beginning of synthesis. As revealed by TEM studies, for the definite set of parameters used for the biochemical synthesis of AgNP, it is possible to obtain nanoparticles with reproducible characteristics: the particles are approximately spherical, the hystograms are almost symmetrical; Gauss approximation gives average particle sizes from 8 to 10 nm with deviation 2-4 nm. Solutions of this kind are referred to as standard micellar solutions. Two examples of electron micrographs and the corresponding hystograms of silver nanoparticles in the standard micellar solution are shown in Figs 4,5. The deviation is small for the relatively "young" (1-2 week old) preparations (Fig.4) and may become bigger with time, presumably because of the slowly going processes of aggregation-dissociation (Fig.5). As follows from electron diffraction patterns, in all cases the nanoparticles have crystal structure similar to that of gold standard.

Measurements by PCS technique in most cases give monomodal distribution with average sizes somewhat bigger then those found by TEM. Typical result given by Horiba LB-550 for a "young" AgNP micellar solution is given in Fig.6; the average size is approximately by 1.5 times bigger than found from the TEM measurements (Fig.4B). The increase in average size can be even more significant: for standard micellar solution one may obtain d_{av} = 24-26 nm; example of such kind is shown in Fig.9A. Similar enlargement of the average size compared to the electron microscopy data was observed for the particles of different origin – for latexes, liposomes, metal and metal oxide nanoparticles in water solutions [55]. This was assumed to be connected with one of the disadvantages inherent to PCS technique, namely with its high sensitivity to the presence of the bigger particles, because they scatter light considerably more intensively than the smaller ones.

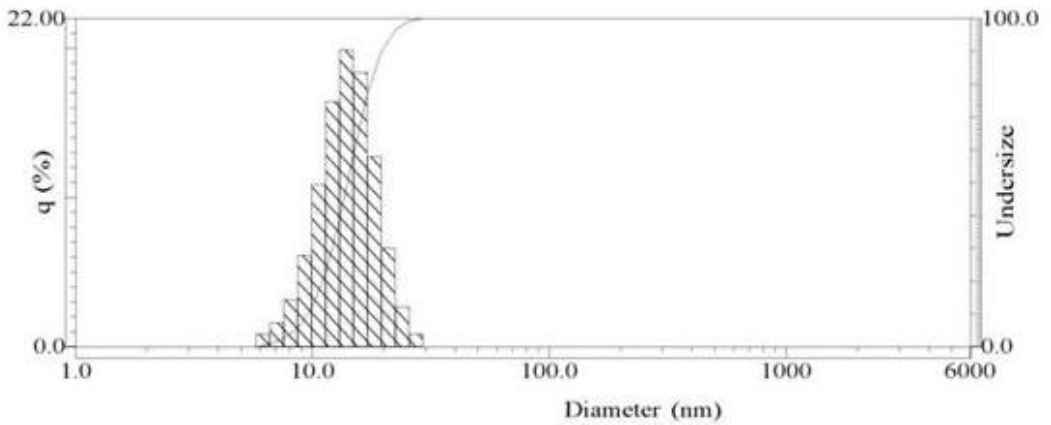

Figure 6. Particle size distribution in standard micellar solution obtained by PCS technique (Horiba LB-550). One week in the stationary state. Average size 14.1 nm.

Transfer of nanoparticles to the water phase leads to the blue shift of absorption band (Fig.6). This shift is assumed to be conditioned by the change of the medium in contact with the particle surface, similarly to what is usually observed for the fluorescent probes upon their transfer between polar and apolar phase. In water solution λ_{max} lies between 400 and 415 nm, in accordance with absorption band position observed in many cases for silver nanoparticles in water

Copyright © 2010. Nova Science Publishers, Incorporated. All rights reserved.

solutions (e.g.[46, 57]). Depending on the procedure used for the preparation of AgNP water solution, the D_{max} values may be smaller or slightly bigger then those achieved in micellar solution. In standard water solutions C(AgNP) lies in the range 0,2-0,6 mg/ml, with pH 7.6 – 8.5 and AOT concentration between 15 and 35 mM, .

Comparison of the TEM micrographs and hystograms for water solution (Fig.8) and the corresponding micellar solution (Fig.5) shows that there is almost no change both of average size and size distribution. The same conclusion issues from the results given by the PCS technique (Fig.9): neither average size nor size distribution suffers changes upon the transfer of nanoparticles to the water phase.

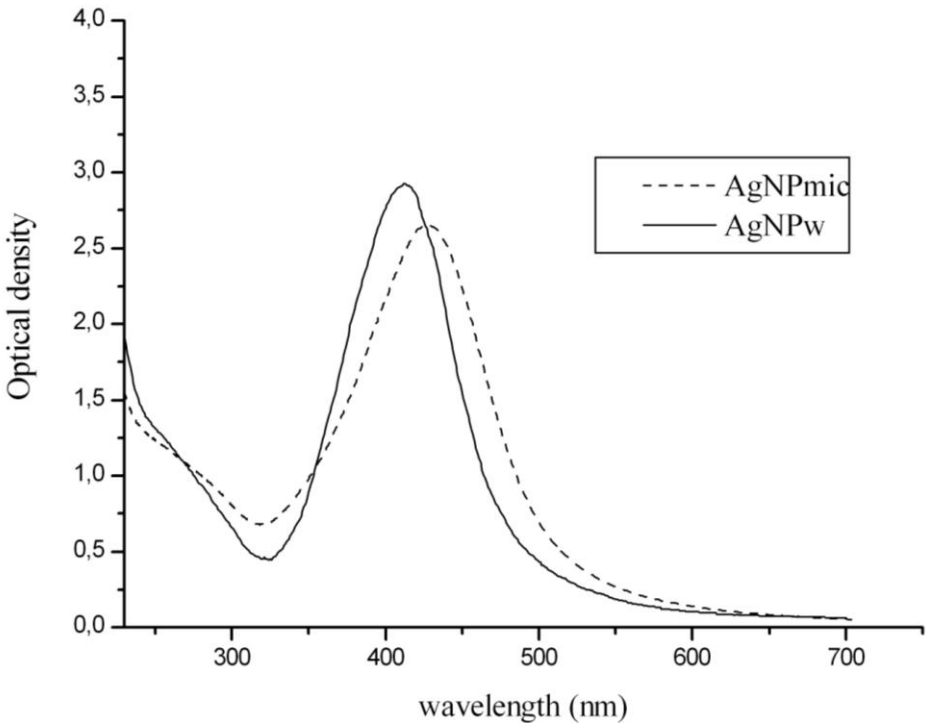

Figure 7. Typical change of the optical spectra at the transfer of silver nanoparticles from organic (standard micellar solution) to water phase in the process of preparation of AgNP water solution.

Using the PCS technique, it was possible to estimate also the zeta potential of silver nanoparticles in water solutions. Taking into account that here the nanoparticles exist in a shell formed from the bilayer of AOT molecules, with external monolayer negatively charged due to the dissociation of its acidic groups, one could expect to obtain negative zeta potential. Indeed, it was found that, at ionic strength lower than 10^{-4} M, the electrophoretic mobility values are negative and zeta potential of the nanoparticles lies in the range -80 – -100 mV. In principle, from the measured mobilities it is possible to find the surface charge of external monolayer, but our experience in this field (see e.g. [58]) allows to suggest that the task is not a simple one, since the small particle size and low ionic strength require taking into account the relaxation effects; this, in its turn, suggests the use of the more general equations from the theory of electrophoresis than those commonly applied in the programs installed in the devices available from Malvern.

Copyright © 2010. Nova Science Publishers, Incorporated. All rights reserved.

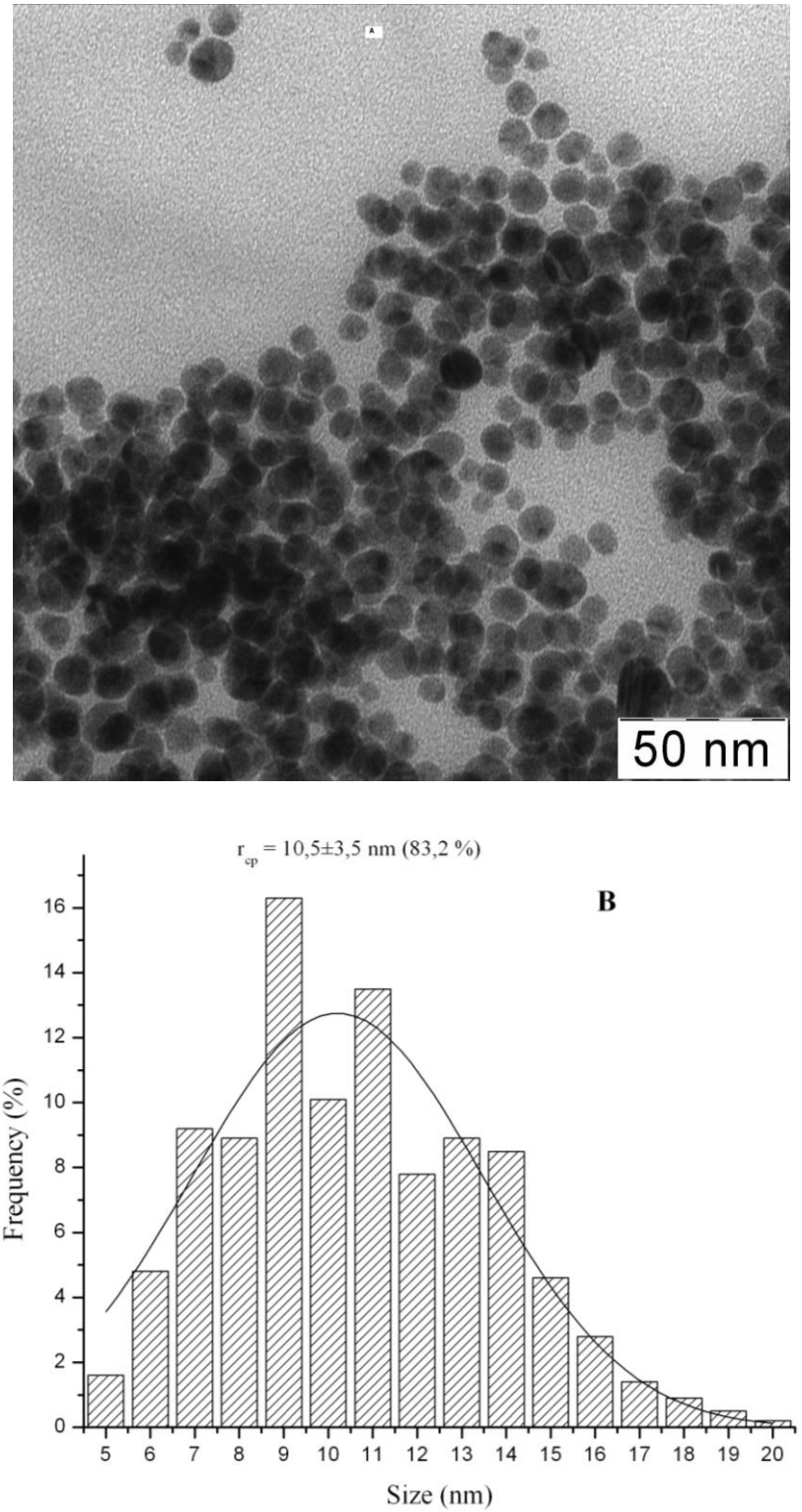

Figure 8. TEM image (A) and size distribution (B) of silver nanoparticles in standard water solution.

Copyright © 2010. Nova Science Publishers, Incorporated. All rights reserved.

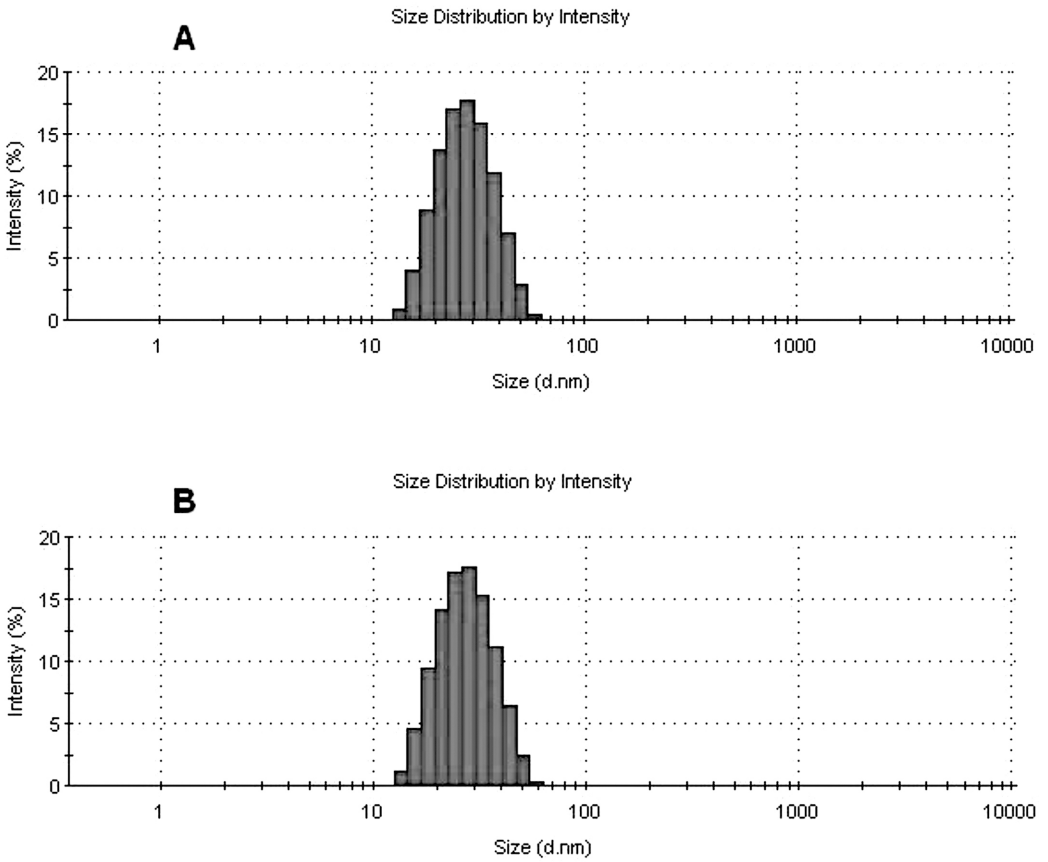

Figure 9. Particle size distribution in standard micellar solution (A) and in water solution (B) prepared from this micellar solution. Average sizes are 26.1 nm (A) and 25.7 nm (B). The hystograms obtained by PCS technique (Zetasizer Nano ZS).

2.3. Modification of Liquid and Solid Materials

As follows from the results of our preliminary studies, AgNP can be used directly as micellar or water solutions and also for the modification of various liquid and solid materials in order to impart to them the special properties required.

Water solutions are used directly in studies of the antimicrobial effects of AgNP in aqueous medium as well as for the determination of the toxic concentrations of AgNP for the other living organisms *in vitro* and *in vivo*. Besides, water solutions may be applied for the modification of water-based paints, cosmetics, water-soluble polymers, also for the creation of carbon materials and polymer membranes covered with AgNP for the use in filtering equipment for water purification from bacterial contaminations [59].

Micellar solutions may be applied as small additions to the liquid-phase materials (e.g. varnish-paint materials based on organic solvents) or for the deposition of nanoparticles on solid surfaces for the creation of modified materials with antimicrobial properties. In such a way paints and cloths with biocidal activity were obtained.

Copyright © 2010. Nova Science Publishers, Incorporated. All rights reserved.

Modification of solid materials with nanoparticles is carried out by means of adsorption from liquid solution onto a specimen surface. For each kind of material the conditions are chosen providing the high enough adsorption rate and density of coverage with nanoparticles and also stability of the coverage in supposed conditions of exploitation. The type of solution used for the deposition of AgNP depends on the properties of the specimen surface. Micellar solutions are used for the treatment of glasses, metals, cloths, metal oxide powders, silica gel and other materials with polar groups on the surface. Water solutions are used for the modification of activated carbon, carbon cloths, polyamide membranes and other materials with mainly hydrophobic groups on the surface. The adsorption rate is controlled by measuring the changes of nanoparticles concentration in solution from the changes of optical density in the absorption band maximum. At the end of adsorption, a modified solid material is washed several times with the proper solvents for the removal of adsorbed AOT and weakly bound nanoparticles; the quantity of desorbed nanoparticles in the washing liquids is estimated from the measured optical spectra. The quantity of the adsorbed nanoparticles is evaluated in the quantity of deposited metal, mgAg/g or (for the known specific surface of material) in $mgAg/m^2$.

Examples of the biological effects of silver nanoparticles solutions as well as of the materials modified with nanoparticles are given in section 3.

3. BIOLOGICAL EFFECTS

Here we give a brief account of our results obtained in studies of the biological effects of silver nanoparticles 9-10 ± 4 nm in size obtained as standard micellar or water solution with parameters given in section 2.2. The whole pool of data is divided into two parts: (1) aintimicrobial properties and (2) toxic effects towards the other biological objects.

3.1. Antimicrobial Properties of AgNP

Tests on the antimicrobial activity of AgNP were fulfilled in several State institutions of Russian academy of medical sciences (RAMS), also in the Institute for genetics and selection of industrial microorganisms of State Scientific Center (IGS SSC) and in Moscow Disinfection Center(MDC). Experiments were made both with nanoparticles in solutions and with modified materials. The results were presented on the international conferences and exhibitions (e.g.[60, 61]) and reported in several publications [45, 62-68]. First we describe the data obtained on AgNP water solutions in the aqueous media, then follow the effects observed for varnish-paint materials modified with AgNP water or micellar solutions, then the results found for polymer films with small additions of AgNP, and finally, for various cloths and filtering materials containing these nanoparticles.

3.1.1. Water Solutions

Water solutions of AgNP were tested in aqueous media containing various concentrations of pathogen bacteria species. The nanoparticles were introduced into the cell suspensions as small aliquots of the initial AgNP solution; the extent of dilution of the initial AgNP solution varied from 3 to 100, depending on the initial AgNP concentration and that required in a cell suspension

Copyright © 2010. Nova Science Publishers, Incorporated. All rights reserved.

for a given study. After incubation for a definite time the AgNP activity was quenched by the addition of calcium nitrate solution to the concentration providing full sedimentation of the nanoparticles. Then the treated cells were spread on the agar in Petri dishes and cultivated in standard conditions. The effect of nanoparticles was estimated from the comparison of the found CFU (colonies forming units) number with that obtained for the control cell suspensions without AgNP. In all cases studied it was revealed that AgNP solutions possessed a high antibacterial activity [45,60,68]. Here we give three examples of the data obtained in experiments carried out in various institutions.

Fig.10 shows the results observed in the tests on E.coli in water suspension. It is seen that, at the high initial concentration of bacteria cells ($3* 10^8$ CFU/ml) the high level of inactivation (> 90%) is achieved after incubation for 30 min in the whole range of AgNP concentrations (3 – 30 μg/ml). Beginning from 5 μg/ml, total death of bacteria (100 % inactivation) is registered.

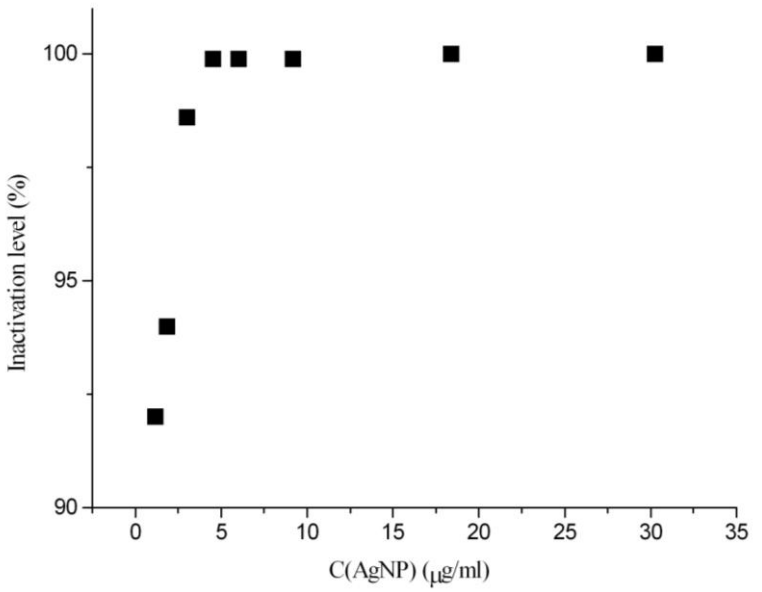

Figure 10. The effect of AgNP on inactivation level of E.coli cells in water suspension. The AgNP concentration in suspension was varied by means of dilution of the initial AgNP water solution. Initial concentrations of AgNP – 60.5 μg/ml, AOT – 20 mM. At each AgNP concentration the suspension was incubated for 30 min before quenching the AgNP activity. Initial concentration of bacteria cells – $3* 10^8$ CFU/ml. Data from the IGS SSC.

In similar experiments in the Sysin Institute for human ecology and hygiene of the environment RAMS the antibacterial and antiviral activity of AgNP was compared to that of Ag^+ ions introduced as water solution of silver nitrate [68]. Water suspensions containing the known concentrations of E.coli cells or coliphage MS-2 particles were prepared, and then each of them was incubated with either AgNP or equivalent concentration of silver nitrate. For three chosen AgNP concentrations (10.8, 6.5 and 3.2 μg/ml) it was found that AgNP were more effective than Ag^+ ions. Fig. 11 shows the results for C(AgNP) = 6.5 μg/ml obtained with E.coli (A) and phage MS-2 (B). For E.coli the stronger effect of AgNP was clearly expressed after 30 min incubation, less noticeable after 1 hour and practically indistinguishable from that of ions after 2-4 hours, where 100% of inactivation was obtained in both cases. For MS-2 the AgNP were significantly

Copyright © 2010. Nova Science Publishers, Incorporated. All rights reserved.

more active than Ag^+ ions, though the highest level of inactivation achieved (98.2%) was still less than 100%, showing that virus is more stable towards the nanoparticles than bacteria cells. In the tests fulfilled in MDC on E.coli and S.aureus, cell suspensions with $2*10^5$ CFU/ml were incubated with various concentrations of AgNP (0.27 - 6.5 μg/ml) obtained by dilution of the initial AgNP water solution (by 800 - 33.3 times, respectively). It was found that both bacteria species were fully destroyed beginning from 2.88 μg/ml after 30 min of incubation (see Table 1). From the results of the abovementioned and other similar tests it was concluded that AgNP water solutions possess a high antimicrobial activity and can be considered as basic solutions for the creation of disinfectants of a new type, effective and less dangerous for users than those containing chlorine and its derivatives or amino compounds.

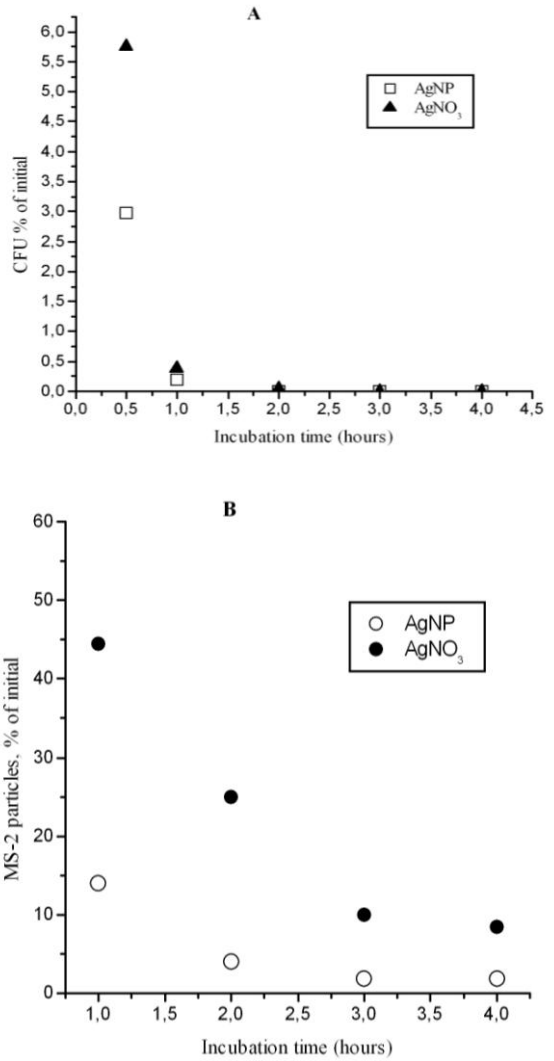

Figure 11. Dynamics of E.coli (A) and phage MS-2 (B) inactivation in water suspension by the addition of either AgNP or equivalent concentration of $AgNO_3$ as water solutions. The AgNP concentration – 6.5 μg/ml. Initial concentrations of E.coli - (3.2 – 3.5) * 10^5 CFU/ml, MS-2 particles - 50000/ml (AgNP) and 59000/ml ($AgNO_3$). Data from the Sysin Institute (RAMS).

Copyright © 2010. Nova Science Publishers, Incorporated. All rights reserved.

Table 1. Action of AgNP water solution on the bacteria species Esherichia coli 1257 and Staphyllococcus aureus 906 in aqueous medium. Initial concentration of nanoparticles in water solution C(AgNP) = 216 μg/ml; C(AOT) = 30 mM. Initial concentration of bacteria cells – 2*105 CFU/ml. Tests of the antibacterial activity were carried out by means of incubation of bacteria with silver nanoparticles at various dilutions of AgNP initial water solution. (-) – absence and (+) – presence of bacterial growth. The data obtained by Moscow Disinfection Center (MDC)

Microorganism	Exposition (hours)	Bacteria growth at various C(AgNP). Upper row - % of initial AgNP concentration, lower row – AgNP concentration in the medium (μg/ml)							
		3 (6,5)	2 (4,32)	1,5 (2,88)	1.0 (2,16)	0,75 (1,44)	0,5 (1,08)	0,25 (0,54)	0,125 (0,27)
E.coli 1257	0,5	-	-	-	+	+	+	+	+
	1,0	-	-	-	+	+	+	+	+
	2,0	-	-	-	+	+	+	+	+
	24,0	-	-	-	-	-	+	+	+
S.aureus 906	0,5	-	-	-	+	+	+	+	+
	1,0	-	-	-	+	+	+	+	+
	2,0	-	-	-	+	+	+	+	+
	24,0	-	-	-	-	-	+	+	+

It should be noted that our studies were aimed mainly to test the antimicrobial activity of AgNP preparations and to determine the concentrations of nanoparticles providing the effect strong enough for the practical applications; elucidation of the mechanism of AgNP-bacteria interaction is supposed to be the goal of future experiments. Therefore at present it seems untimely to undertake thorough comparison of our results with those reported in the papers devoted to the comprehensive consideration of the factors affecting the antibacterial and antiviral action of silver nanoparticles. It may be useful however, to make some preliminary observations in order to find out whether or not our data correlate with those known from literature, in cases when the particle parameters and the mode of investigation allow the correct comparison.

Judging from the data available, it turns out that the range of particle concentrations where their antimicrobial activity is clearly expressed, found in our experiments, coincides with that determined in similar studies on E.coli by the other authors [8, 18,20-22]. In all cases the bacteria cells are killed effectively at silver concentrations beginning from one to several tenth μg/ml; in our studies – from 2-3 to 33 μg/ml. For silver nanoparticles of the same size as in our work (9.2 ± 2 nm [20]) minimum inhibitory concentration was reported to be 5.4 μg/ml, what is practically equal to that registered in one of our experiments as the minimum concentration necessary for 100% inactivation of E.coli (5 μg/ml, Fig.10). Since the nanoparticles used in [20] were stabilized by either citrate or BSA, they had the protecting shells different from AOT bilayer used in our work. One may infer therefore that nature of the capping agent is not of primary importance for the antibacterial action, at least for the case of E.coli. Hence follows also that the toxicity of AOT itself does not play a role in the antibacterial effect of AgNP water solutions at the dilutions used in our studies.

Copyright © 2010. Nova Science Publishers, Incorporated. All rights reserved.

3.1.2. Varnish-Paint Materials with AgNP

Varnish-paint materials were modified by small additions (0.5 – 2 % by volume) of AgNP micellar or water solutions to organic solvent-based or water-based compositions, respectively. In laboratory studies, specimens of wood or other materials were painted with modified compositions. Bacteria suspensions were placed on the dried surfaces and, after definite time periods, the microflora was washed off, resuspended in the appropriate medium and analyzed for the presence of active bacteria cells according to the standard procedures. It was found that paints with silver nanoparticles manifest strongly expressed biocidal action towards a number of pathogen flora species; the effect was considerably more expressed than that observed for control paints without nanoparticles. Example of the results obtained on water-based paint is given in Table 2. It is seen that the inactivation level after a given time of exposition is higher for the AgNP modified paint both for bacterium (E.coli) and virus (phage MS-2). The effect is more significant on the short times (0.5 – 2 hours). Apart from E.coli, strong bactericidal effect on short times of exposition was registered for other bacteria widely distributed in everyday life (Table 3).

Table 2. Biocidal action of enamel and water-based paints modified by silver nanoparticles (AgNP). Concentration of the nanoparticles was 1,62 μgAg per ml of paint. The data obtained in the Sysin Institute of human ecology and hygiene of the environment RAMS

Microflora	Time of Exposition	Enamel (organic solvent)		Water-based paint	
		% inactivation		% inactivation	
		Control	+AgNP	Control	+AgNP
E.coli	0,5h	0	0	24,08	84,63
	1h	14,29	31,83	18,85	98,22
	3h	100	100	99,71	99,07
	24h	100	100	99,99	99,90
Phage MS-2	2h	92,4	99,9	0,44	53,62
	24h	99,5	99,99	59,08	91,42
	3day	100	100	100	100
	7days	100	100	100	100

Basing on the results of laboratory experiments, it was possible to create the compositions for industrial tests in schools, hospitals and in one of the prisons in Moscow. Here we present the results obtained for the prison [62] (Table 4). In the two cells several internal elements (walls, ceiling et al) were painted with the same paints; in one of the cells the paints were modified with nanoparticles, the other cell was used as control. In both cells the microflora was washed off periodically and analyzed for the presence of various microorganisms. It is seen that addition of AgNP leads to the noticeable decrease of the GMN value, that is, of the overall microbial contamination of the chamber on a painted surface. The effect is more manifested for bacteria and coliphages and less expressed for fungi and spores, in accordance with similar results obtained in laboratory tests; also the activity of modified

Copyright © 2010. Nova Science Publishers, Incorporated. All rights reserved.

paints depends on the sampling point considered. So it was established that paints modified with AgNP exert quite noticeable effect on the microorganisms in a prison cell, where high microbial contamination should be expected.

Table 3. Dynamics of bactericidal action of AgNP added to the water-based paint on the bacteria strains: E.coli ATCC 25922, Salmonella typhimurium TMLR 66, Salmonella typhi Ty 2, Shigella flexneri 516, Staphilococcus aureus Wood-46, Enterococcus faecalis CG 110, Listeria monocyntogenes EGD, Pseudomonas aeruginosa 508. Data for the paint containing 1 vol.% of AgNP water solution (2,1 μgAg per ml of paint) obtained from the Gamaleya Institute of epidemiology and microbiology (RAMS)

Bacteria strain	Control culture (-) and paint with AgNP (+)	Log of the number of living bacteria on the painted surface at a given time 9HOURS0 after the deposition of bacteria culture			
		0	1,0	2,0	4,0
E.coli	-	**6,2±0,1**	**6,2±0,1**	**6,2±0,1**	**6,2±0,2**
	+	**4,8±0,2**	**0**	**0**	**0**
S.typhimurium	+	**5,1±0,2**	**0**	**0**	**0**
S.typhi Ty2	-	**6,0±0,1**	**6,1±0,2**	**6,0±0,1**	**6,0±0,1**
	+	**4,6±0,1**	**0**	**0**	**0**
S.Flexneri 516	-	**6,2±0,2**	**6,2±0,2**	**6,2±0,2**	**6,1±0,1**
	+	**4,5±0,1**	**0**	**0**	**0**
S.Aureus	-	**6,0±0,1**	**6,0±0,2**	**6,0±0,1**	**6,0±0,1**
	+	**5,4±0,1**	**0**	**0**	**0**
E.faecalis	-	**6,1±0,1**	**6,1±0,1**	**6,1±0,1**	**6,1±0,1**
	+	**4,9±0,1**	**0**	**0**	**0**
L.monocytogenes	-	**6,2±0,2**	**6,2±0,2**	**6,2±0,1**	**6,1±0,1**
	+	**4,6±0,1**	**0**	**0**	**0**
P.aeruginosa	-	**6,1±0,1**	**6,1±0,1**	**6,0±0,1**	**6,0±0,1**
	+	**5,6±0,2**	**3,4±0,1**	**1,2±0,1**	**0**

It is worth noting also that, in contrast to the majority of other biocidal additions used conventionally in the paint industry, the AgNP are essentially less toxic for people and environment, as confirmed by the corresponding certificates of sanitary-hygienic services. Therefore paints and coatings containing silver nanoparticles have good perspectives for the application in public meal enterprises, medical and sports institutions, and in all other places where the enhanced level of infection may be suggested.

Copyright © 2010. Nova Science Publishers, Incorporated. All rights reserved.

Table 4. Surface concentration of microorganisms (cells/100 cm^2) on various painted surfaces of a chamber in prison. The data obtained a week after the chambers were painted. The nanoparticles concentration was 6,4 μgAg per ml of paint. More detailed description is given in [62]. Data obtained from the Sysin Insitute of human ecology and hygiene of the environment RAMS (in collaboration with the paints manufacturer ASCT "Lakma-IMEX"; Moscow, Russia)

Object	Sampling point	Indicators									
		GMN *	E.coli	Staphyllococcs		Fungi			Spores	Viruses	Coliphages
				Overall number	golden	Overall number	Mold	yeast-like			
1	2	3	4	5	6	7	8	9	10	11	12
Control	Door	500	0	3000	0	6500	5000	1500	10	-	150
	Toilet	2200	30	6600	20	12000	6000	6000	100	+	400
	Wall	100	0	100	0	4000	3000	1000	20	-	100
	Ceiling	200	0	500	0	5000	3000	2000	10	-	150
AgNP	Door	10	0	100	0	3000	1000	2000	20	-	20
	Toilet	200	15	2300	10	6500	2500	4000	100	+	50
	Wall	10	0	100	0	1200	200	1000	0	-	20
	Ceiling	20	0	300	0	4000	3000	1000	0	-	30

* General microbial number

As for the working concentrations of nanoparticles in paints, they were found to be in the range 5 – 40 μgAg per ml of paint, depending on the type of paint, the type and concentration of microbial species studied and the time required for 100% death of microorganisms. For one and the same AgNP concentration, their activity in paints is somewhat lower than in the water solutions described above. This is not surprising because in paints the activity of nanoparticles may by affected by the other components of a composition used. That means, in particular, that here to elucidate the mechanism of the AgNP biocidal activity is even more difficult than in the aqueous media.

3.1.3. Biodegradable Polymer Films

Polymer films with silver nanoparticles were obtained by mixing of the AgNP water solution with that of biodegradable polymer (caboxymethyl chitin); details of the film preparation are given in [65]. Such films were tested on antimicrobial activity against *Staphillococcus aureus and Salmonella typhimurium.* The result is shown in Table 5. It is seen that the films containing small additions of AgNP possess a high antimicrobial activity towards the bacteria studied, at high concentrations of bacteria cells in the films (doses 10^4 and 10^6 CFU are equivalent to $\approx 4* 10^5$ and $4*10^7$ CFU/cm^3, respectively). It is seen also that this activity is significantly higher than that observed for the control films made from carboxymethyl chitin without nanoparticles. The level of bactericidal action increases with the increase of the AgNP concentration in the film. For the film with 0.06 wt% of AgNP 100 % total death of bacteria was registered already after I hour of contact. The results obtained testify to the strong bactericidal effect of the films. It is possible to suppose that such polymer material can be applied in medicine, for example, in the treatment of skin injuries.

Estimate of the working AgNP concentrations shows that in this case they are about an order of magnitude higher than in paints and even more than that in water solution. This is

Copyright © 2010. Nova Science Publishers, Incorporated. All rights reserved.

presumably connected with the capping action of polymer which may form thick layers around the nanoparticles thus decreasing their bactericidal activity.

Table 5. Dynamics of the interaction of bacteria strains with polymer films made from carboxymethyl chitin with or without AgNP. Bacterial culture was introduced into the segment (1/4) of polymer film (d=50 mm, thickness 50 μ). After incubation for a given time films were resuspended in the nutrient broth and the CFU number was calculated after cultivation in the standard conditions. Data obtained from the Gamaleya Institute of epidemiology and microbiology (RAMS)

Bacteria species, Dose	Films without (control) and with various concentrations of AgNP	Log of the number of living cells in the films after the time periods (hours)			
		1	3,0	6,0	24,0
Salmonella typhimurium TMLR66 10^6 KOE	Initial bacteria culture	6,0	6,0	6,0	6,0
	Chit - 10. A (control)	6,0	5,8	5,5	3,0
	Chit – 10. B (0,03wt% Ag)	5,1	4,2	3,0	0
	Chit – 10.C (0,06 wt% Ag)	0	0	0	0
Staphylococcus aureus 10^6 KOE	Initial bacteria culture	6,0	6,0	6,0	6,0
	Chit - 10. A (control)	6,0	5,7	5,3	3,5
	Chit – 10. B (0,03wt% Ag)	5,2	4,4	3,2	0
	Chit – 10.C (0,06 wt% Ag)	0	0	0	0

3.1.4. Cloths with AgNP

Wool, cotton, flax and other cloths with adsorbed AgNP were introduced into the aqueous medium containing E.coli strains or placed in Petry dishes on the surface of culture medium (agar gel) containing the same bacteria (data from IGS SSC). The antimicrobial action of the cloths was estimated from the comparison of the extent of suppression of bacteria growth after various periods of incubation with and without the nanoparticles. It was shown that in experiments both in water medium and in Petry dishes the cloths with AgNP exert strong suppressive influence on bacteria growth. Example of the results obtained with wool in Petry dishes is given in Fig.12. Three wool specimens with nanoparticles (50 mgAg/g, colored ones) and two control (uncolored) were placed on the surface of agar gel containing E.coli cells. Two specimens with AgNP and one control were removed from the surface after 24 hours of incubation (Fig.12). It is seen that the agar gel remained transparent under the wool with AgNP, testifying to the absence of bacteria growth, while the rest of agar surface (including that under one of the control specimens) is covered by the even “lawn” of bacteria colonies, as confirmed by the microscopic investigation. Around the specimens containing nanoparticles a kind of “halo” is observed, showing to the avoidance reaction of bacteria. After a week incubation of the Petry dish shown in Fig.12, sizes of the "transparent" segments under the removed test specimens remained nearly the same, which shows the preservation of the biocidal activity though the cloth was absent. At the same time, significant increase in the number of colonies was observed in the segment under the removed control specimen. Similar results were obtained with the other cloths studied. It was found also that certain cloths with AgNP may be washed without the decrease of the initial density of coverage with nanoparticles. Hence it is clear that working in this direction it is possible to

Copyright © 2010. Nova Science Publishers, Incorporated. All rights reserved.

obtain clothwares for the applications in medicine or in the other fields where the antimicrobial cloths are required.

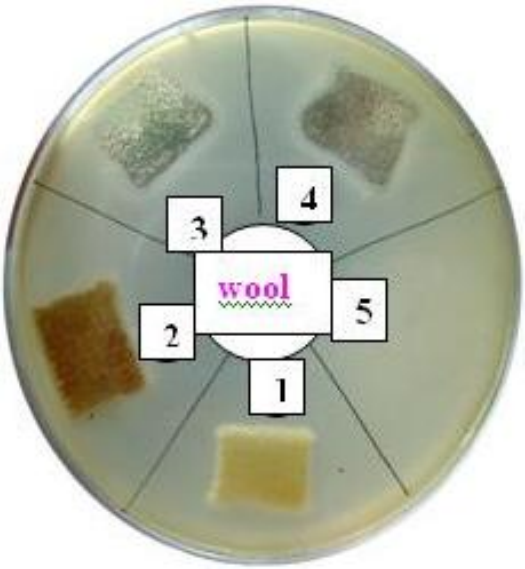

Figure 12. Testing of the biocidal properties of the woolen cloth specimens modified with Ag nanoparticles. 24 hours after placing the cloth specimens on the agar with freshly introduced E.coli cells. 1 – control cloth (not modified). 2 – test cloth with AgNP. 3, 4 – "transparent" segments (no bacteria growth) in the medium after the removal of specimens with AgNP. 5 – dense "lawn" of the grown E.coli colonies after the removal of control specimen.

3.1.5. Filtering Materials: Activated Carbon and Polyamide Membranes

Activated Carbon with Silver Nanoparticles

Adsorption of AgNP fron water solutions on the surface of activated carbon allows to obtain the carbon with enhanced biocidal activity [59]. In the tests carried out in the A.N.Sysin Institute, water from the water pipe with bacteria (E.coli) or viruses (coliphage MS-2) added to the concentrations exceeding the accepted standard for the drinking water was spilled through the column with activated carbon modified with AgNP (30 mgAg/g). In parallel the same water with added microflora was spilled through the column with the same carbon without nanoparticles. The spilling was carried out uninterruptedly during a week; probes from the outlet water were taken twice a day for the determination of the concentration of living microorganisms. It was established that water after the carbon modified with nanoparticles contains much less living bacteria cells or virus particles than that spilled through the unmodified carbon. For example, for water with initial bacteria concentration 3-5 * 10^2 CFU/ml, after the AgNP-modified and control carbon the decrease in bacteria concentration was found to be 50% and 20%, respectively. It is noteworthy that the decrease in the concentration of microorganisms was stable during the whole time of experiment, showing that silver nanoparticles are not washed out of the carbon with water flow. This gives

Copyright © 2010. Nova Science Publishers, Incorporated. All rights reserved.

grounds to believe that activated carbon modified with Ag nanoparticles as filtering element for water purification may serve much longer than carbon impregnated with silver salts, since the latter are relatively quickly washed out with water flow (e.g. [69]).

Polyamide Membranes with Silver Nanoparticles

Adsorption of AgNP from water solution gives also the possibility to create technical polymer membranes with biocidal activity. As example of such kind we present here the results obtained on polyamide membranes used for microfiltration of water and some other liquids in medicine and experimental biology. The membranes modified with nanoparticles showed positive results in the microbiological tests. The antimicrobial activity of membranes was evaluated from the number and type of colonies grown on a membrane at various time after the filtration of water from the water-pipe. Typical result is given in Table 6. For comparison the result obtained for standard Millipore membranes in similar conditions is also presented. As seen from the table, on three membranes modified with silver nanoparticles, at first two days after filtration no bacteria colonies are detected; at the third day no more than 10 colonies are observed. It may be inferred that AgNP-modified membranes possess a high antimicrobial activity, exceeding that observed with Millipore membranes.

Table 6. Microbiological tests of polyamide membranes covered with silver nanoparticles. Water from the water-pipe was filtered through the membranes (with pore size 0.22 mcm) and then the type*) and number of bacteria colonies on the membranes were determined after 1,2 and 3 days of incubation. The results obtained from Science-Technology Company "Technofilter" (Vladimir, RF)

Specimen N	Membrane type and density of coverage with AgNP	Time spent for filtration of water (50 ml), min	Number of colonies: 1 day after filtration	Number of colonies: 2 days after filtration	Number (type) of colonies: 3 days after filtration
1	$MMPA^+$ - 0.2 0,33 mgAg/g	4	0	0	5 (I) 10 (II)
2	$MMPA^+$-0.2 1,16 mgAg/g	2,5	0	0	5 (I), 7 (II)
3	$MMPA^+$ -0.2 2,22 mgAg/g	3,5	0	0	3 (I), 10 (II)
4	Millipore membrane (d = 0,45 mcm)	0,5	27 (I)	49 (I)	55 (I), 3-5 (II)

*) Type I – yellow, round, salient, with even boundaries; type II – lustrless, colorless, diffuse.

To sum up, studies of the antimicrobial properties of AgNP in different media show that these nanoparticles manifest antibacterial and antiviral activity both in the liquid phase - in water solution or in the liquid composite materials, such as paints and polymer films - and on the solid surfaces. Since in water solution the nanoparticles exist in AOT bilayer shell which is absent in the case of solid surfaces (see section 2.3.), one may deduce that this stabilizing shell does not play a significant role in the effects considered. Similar conclusion follows from the comparison of working AgNP concentrations in water solution and water-based paints. As noted above (section 3.1.1), the unimportance of the nature of capping shell followed also from the comparison of the working AgNP-concentrations in antimicrobial tests reported by the other authors with those found in our studies in water solutions.

Copyright © 2010. Nova Science Publishers, Incorporated. All rights reserved.

3.2. Toxic Effects on the Other Living Organisms

Apart from the antimicrobial properties of silver nanoparticles we studied also their interaction with several biological objects of other kinds. For the time being, the results are obtained for plasmodium of the slim mold Physarum polycephalum, unicellular alga, plant seeds and mammalians organisms (mice). In experiments of all kinds the required concentration of AgNP was achieved by dilution of the initial standard AgNP water solution with C(AgNP) in the millimolar range; the working AOT concentration was determined by dividing its known concentration in the initial AgNP solution (see section 2.2.) by the extent of dilution. The effect of AgNP water solution was compared with those of the AOT and Ag^+ ions, both taken in the same concentrations as introduced with AgNP solution into the medium under study. In such a way it was possible (1) to distinguish the effect of nanoparticles in the total action of AgNP and AOT and (2) to clear out whether or not the effect of AgNP is conditioned by Ag^+ ions, the question important for the elucidation of the mechanism of nanoparticles action. The main results are briefly described below.

3.2.1. Slim Mold Physarum Polycephalum

This work was fulfilled in collaboration with the Institute for theoretical and experimental biophysics of Russian Academy of Sciences (ITEB RAS). Plasmodium of the *Physarum polycephalum* **(**referred to below as Plasmodium**)** is a known popular object used in studies of chemotactic phenomena. Its structure and main properties, as well as some of the effects of AgNP water solutions are described in [63,64]. In short, Plasmodium represents a multinuclear protoplasm surrounded by the mutual membrane and capable of unrestrictable growth and amoeboid movement. The aim of our experiments was to determine the effect of AgNP on the Plasmodium motive activity and growth. The oppressive action (characterizing the toxicity) of AgNP water solutions was compared with that of AOT and Ag^+ ions. The AgNP solutions were introduced as small additions to the medium in contact with Plasmodium; in control measurements, the corresponding concentrations of AOT and silver nitrate were introduced as their water solutions in the appropriate dilutions. Experiments were made in the aqueous medium (the motive activity level of Plasmodium strands) and on the plates or Perty dishes with nutrient medium (the Plasmodium growth). Example of the experiment on the plates is presented in Fig.13. The germ was placed on the boundary between two plates; one of them (right) contained the added small concentration of AgNP. It was revealed that Plasmodium demonstrates quite obvious asymmetry of development, namely the avoidance of the plate with AgNP.

In several series of experiments on Petry dishes it was shown that, first, the AgNP concentrations $\geq 10^{-4}$ M (10.8 μg/ml) cause the quick death of Plasmodium and second, at AgNP concentrations which do not provoke the death of Plasmodium ($\leq 10^{-5}$ M or 1.08 μg/ml) the nanoparticles are more toxic than AOT, Ag^+ ions or AOT + Ag^+ mixture in the concentrations equal to those introduced with AgNP water solution. This is exemplified in Fig.14. It is seen that, at C(AgNP) = 10^{-4} M there no growth is observed in all cases. At C(AgNP) = 10^{-5} M, there is a marked difference in Plasmodium growth in the medium containing the nanoparticles and in three media containing silver nitrate, AOT and their mixture in the relevant concentrations. It is clear also that the "pure" control without any

Copyright © 2010. Nova Science Publishers, Incorporated. All rights reserved.

additions is practically indistinguishable from the case with $AgNO_3$, and only slightly different from the other two cases containing AOT. The data obtained allowed to work out the following row of effectiveness: $AgNO_3$ << AOT< $AgNO_3$ +AOT << AgNP. These results indicate that, in the case of nanoparticles, toxic action is substantially amplified, and the amplification effect can not be reduced to the destabilizing action of the AOT protective shell or AOT molecules present in the initial solution, or to the release of Ag^+ ions from the surface of silver nanoparticles.

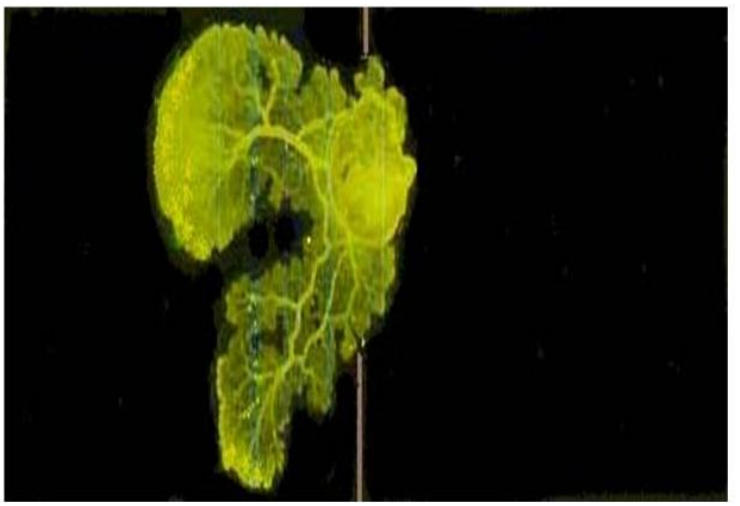

Figure 13. The effect of AgNP on Plasmodium growth. Test on the plates with agar gel. Control (left) and gel with AgNP (equivalent to $\approx 10^{-5}$ g-ionAg^+/l). The avoidance of the right plate is clearly expressed.

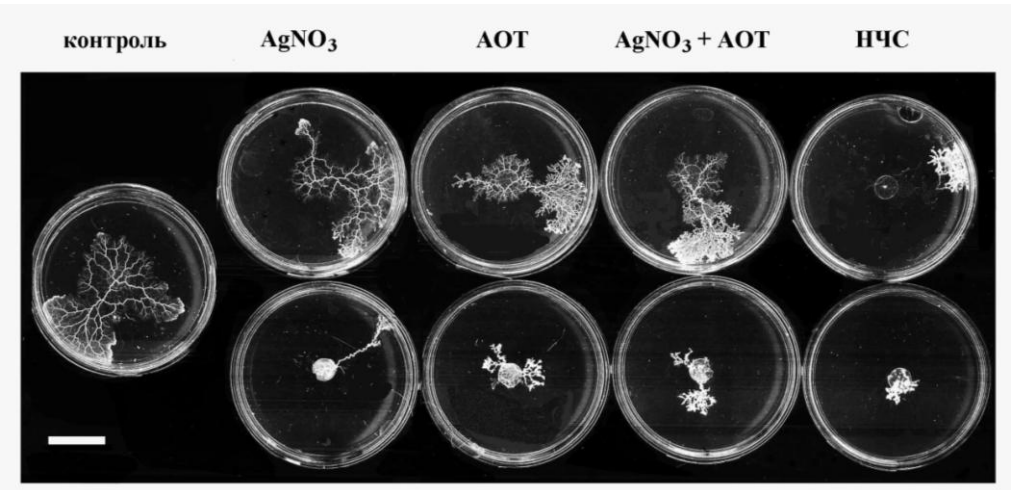

Figure 14. Spreading of Plasmodia on agar substrate in 6h. AgNP, AOT and Ag^+ concentrations are, respectively, 10^{-5} g-ion/l (1,08 μgAg/ml), $2*10^{-3}$ M and 10^{-5} M (upper row) and ten times higher (lower row). Scale bar, 1 cm. Reproduced from [63] with permission from Springer.

Copyright © 2010. Nova Science Publishers, Incorporated. All rights reserved.

Further efforts have been undertaken in order to find out the relation between the size and toxicity of AgNP. For this purpose AgNP water solutions were studied with nanoparticles of two different sizes both below 15 nm. The results will be presented in our paper to be submitted for publication in the nearest future [70].

At present it seems useful to compare our results on Plasmodium with those obtained in similar conditions (incubation with silver nanoparticles in the water medium) on some other biological objects surrounded by the biological membranes – on cultured cells in vitro [24,71].

On mammalian germline stem cells [24] the toxic effect of 15 nm silver nanoparticles expressed in reduction of the mitochondrial function was recorded at 2.50 – 8.75 μg/ml, depending on the cell type studied. On HT-1080 and A431 cells [71] it was established that, upon exposure to the 7-20 nm nanoparticles at concentration 6.25 μg/ml, clear signs of oxidative stress took place, as well as the increased lipid peroxidation. When the apoptotic thresholds of silver nanoparticles were monitored with caspase-3 assay, the concentrations required for the onset of apoptosis were found to be much lower (0.78 μg/ml in HT-1080, 1.56 μg/mL in A431) than the necrotic concentration (12.5 μg/ml in both cell types). With Plasmodium the first stages of the toxic action are observed at C(AgNP) ≤ 1.08 μg/ml (beginning approximately from 0.3 – 0.6 μg/ml), and death is registrered at 10.8 μg/ml. One can note the remarkable closeness of the AgNP concentrations which cause the toxic effect, with the beginning in the range ≈0.3 – 2 μg/ml, and deadly concentrations around 10-12 μg/ml.

In the three cases mentioned, silver nanoparticles were obtained in different ways and protected with different capping agents. However, in all cases exposure to the nanoparticles of similar size range was realized in similar conditions. So it seems that, at least for the nanoparticles with sizes below 20 nm the inhibition of cell functions in vitro as well as of the viability of Plasmodium is affected mainly by the particle concentration and does not depend significantly on the mode of their preparation and stabilizing agents used.

3.2.2. Alga Chlorella Vulgaris

Toxic effects of AgNP on microalga *Chlorella vulgaris* were studied by means of microelectrophoresis in collaboration with laboratory for biotesting of the Ministry of Natural Resources (Izhevsk, RF). The use of microelectrophoresis technique for the estimation of toxicity of various agents towards algae is based on the fact that the viability of living cells is closely connected with surface charge of their plasma membrane. Therefore the decrease in viability reflecting the toxicity of a given agent may be estimated from the decrease in membrane surface charge which, in its turn, is determined by measuring the changes in the amplitude of cell vibration in the alternative electric field.

In the typical experiment, initial AgNP water solution (initial concentrations: C(AgNP) =2.2* 10^{-3} M or ≈238 μg/ml, C(AOT) = 1.5 10^{-2} M) was added to the suspension of test Chlorella cells (2-5 mcm in size) in distilled water to the concentrations, C(AgNP) = 10^{-8} – 10^{-4} M equivalent to 0.00108 – 10.8 μgAg/ml. The whole system was mixed and incubated for 25 min. Then aliquote of the suspension was placed into the electrophoretic cell of the research complex where the alternative voltage was applied and the cell response was registered by means of the digital video camera in combination with microscope and

Copyright © 2010. Nova Science Publishers, Incorporated. All rights reserved.

automatic registration system. The results were compared with those obtained for the control chlorella cells in distilled water.

Toxic effect was found as undimensional index $T = (A_c - A_{cell})/A_c$ where A_c and A_{cell} are the average amplitudes of vibration found for the control and experimental cell suspension, respectively. Apart from AgNP, toxic effects of Ag^+ ions and mixture AOT+Ag^+ were estimated independently. For comparison, toxicity of the AgNP was determined also for E.coli cells from measurements of the change in luminescence of bacteria cells containing luminescent probes. The toxic effect on bacteria was characterized by index $T = (I_c - I_{exp})/I_c$, where I_c and I_{exp} – the intensity of luminescence registered for control cell suspension and experimental one, respectively.

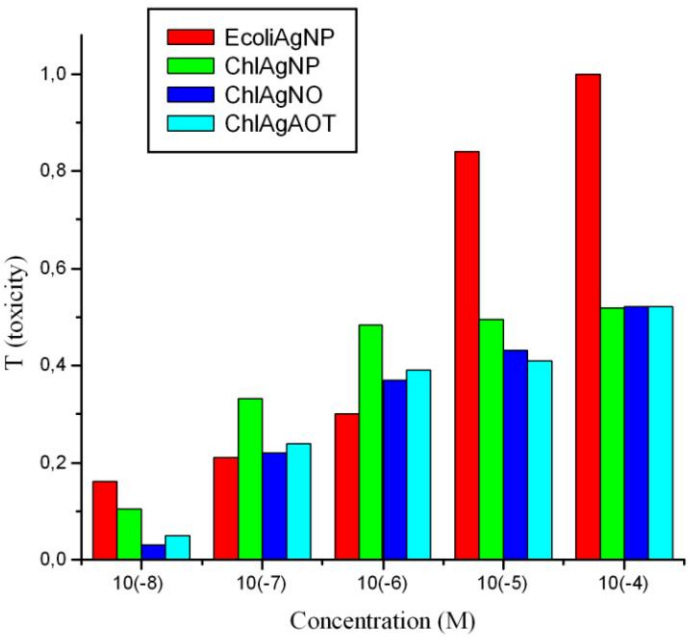

Figure 15. The effect of AgNP, Ag^+ ions and mixture Ag^+ + AOT on the viability of Chlorella vulgaris. The agents studied were added to the distilled water with alga cells to the concentration indicated and incubated for 25 min. The toxic action is characterized by the toxicity index T determined from the comparison of the data of microelectrophoretic measurements for control and test specimens. The toxicity of AgNP for E.coli from the measurements of luminescence changes is also shown. See text for details.

The results are summarized in Fig.15. It is seen that the toxicity of AgNP for chlorella increases with AgNP concentration and then remains constant at C(AgNP) from 0.108 μg/ml (10^{-6} M) to 10.8 μg/ml (10^{-4} M), the achieved level of toxicity being equal to approximately half of the maximal (T = 1). At almost all concentrations studied (excluding 10^{-4} M) the AgNP are more toxic for chlorella than Ag^+ ions or Ag^+ + AOT mixture added to the same total concentrations as those introduced with nanoparticles. Hence here the toxic action of AgNP is unlikely to be caused by only Ag^+ ions released from the nanoparticles surface or by the combined effect of Ag^+ ions and AOT molecules present in the nanoparticles solution.

Copyright © 2010. Nova Science Publishers, Incorporated. All rights reserved.

This is in accordance with observations made on Physarum and (for Ag^+ ions) in studies of AgNP antimicrobial activity on E.coli (section 3.1.1., Fig.11). At the highest concentration (10^{-4} M), the equal toxicity of all three agents studied is, most likely, the result of the cell death or near death state, similar to that observed for Plasmodium at the same concentration (Fig.14).

Comparison with the data on the AgNP effect on E.coli obtained from the measurements of luminescence shows that, first, with chlorella the maximal toxic effect is achieved at the lower AgNP concentration and second, this maximal effect is one/half of that observed for E.coli. This means, probably, that chlorella is less sensitive to AgNP than E.coli. Besides it is possible to assume different mechanism of the AgNP interaction with alga and bacteria cells: the three-layer cell wall present in this alga [17] may protect it from the penetration of nanoparticles to the inner part of a cell, while the bacteria membrane is more permeable for the nanoparticles and hence bacteria cells may be more strongly affected. It is worth noting also that the results for E.coli demonstrate the obvious increase in toxic effect at 1.08 μg/ml and total death at 10.8 μg/ml, in agreement with the working AgNP concentrations against this bacterium in water solutions both reported in literature [18, 20-22] and found in our measurements described above (section 3.1.1.).

3.2.3. Plant Seeds

The effect of AgNP on the germination of seeds was studied on arabidopsis (*Arabidopsis thaliana*) and soy-bean **(** *Glycine max*). The data were obtained in Vavilov Institute of general genetics (RAS). Both plants are the known test objects used for investigations of the effects of various factors on genetic characteristics of the plant organisms. The effect of AgNP was considered here as the first stage of research, which allows to determine the extent of toxicity of AgNP water solution, the estimate important for the choice of working AgNP concentrations in the further experiments. The influence of AgNP water solution (initial concentrations: C(AgNP) = $5*10^{-3}$ M or 540 μg/ml, C(AOT) = 1.5 10^{-2} M) was compared to that of AOT and $AgNO_3$ water solutions with initial concentrations $1.5*10^{-2}$ M and $5*10^{-3}$ M, respectively. The required AgNP, AOT or $AgNO_3$ concentrations were achieved by dilution of the initial solutions.

The results for arabidopsis are presented in Fig.15. As issues from these data, in the wide range of concentrations ($5*10^{-7}$ - $1*10^{-3}$ M) the nanoparticles in water solution are not toxic for the seeds studied. A decrease in germination was observed only for C(AgNP) > $1*10^{-3}$ M (108 μg/ml); for the lower concentrations there was no change in comparison with control seeds without added nanoparticles. This shows that the AgNP solution may be used for the treatment of seeds in order to protect them from infection by the pathogen bacteria. Besides, it turned out that AOT exerted practically no influence on the germination, i.e., the cytolytic effect was absent in the whole range of concentrations studied.

It is seen also that, at the highest concentrations studied (C(AgNP) > $1* 10^{-3}$ M) the AgNP water solution is clearly more toxic than AOT in the corresponding concentrations (C(AOT) > $4 *10^{-3}$ M). The higher toxicity of AgNP compared to AOT agrees qualitatively with what was found for Plasmodium and alga; however, for the seeds the relative toxicity of AgNP and AOT changes with their concentration in the opposite way. Namely, for the seeds the difference in toxicity becomes noticeable with the increase in concentration, while for the previous two objects it becomes apparent at low concentrations and practically

Copyright © 2010. Nova Science Publishers, Incorporated. All rights reserved.

indistinguishable at the higher concentrations studied, when the cessation of life functions is registered. This observation, in combination with the concentration range where the effect of AgNP on seeds is found (> 108 μg/ml) allows to suggest that seeds, surrounded by the rigid protective shell, are less sensitive to the action of nanoparticles than unicellular alga or Plasmodium surrounded by the plasma membrane. This probably indicates again to the role of external shell of biological objects – the more strongly built is external shell, the less sensitive to nanoparticles is the object.

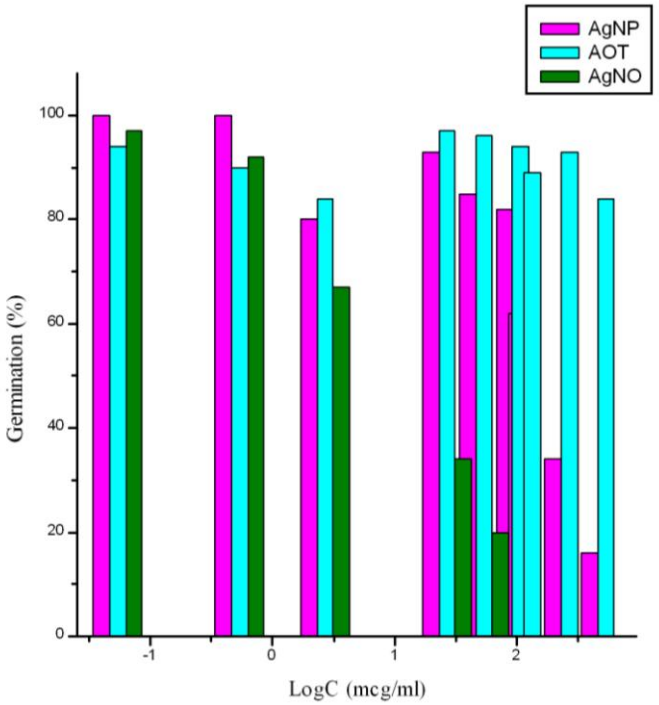

Figure 16. The effect of AgNP, Ag^+ ions and AOT water solutions on the germination of plant seeds (*Arabidopsis thaliana*). The required concentration of the three agents studied was achieved by dilution of their initial solutions. The seeds were soaked in distilled water for 24 hours, then washed and placed into Petry dishes with AgNP, AOT or $AgNO_3$ water solution for another 24 hours. Afterwards the seeds were washed with distilled water and placed for germination in the standard conditions.

In experiments with silver nitrate water solutions it was revealed that, in contrast to the results obtained on Plasmodium and alga, Ag^+ ions exert strong toxic effect on the seeds, the total block of germination was observed at $C(AgNO_3) \geq 1$ mM (dilution of initial solution by 5); for lower concentrations, noticeable decrease of germination was registered up to the dilution by 200 (2.7 μ g/ml). The reason for such an effect remains to be established.

3.2.4. Animals (Mice)

The effect of AgNP water solutions on the lifetime of mice was studied in Vavilov Institute of general genetics RAS on the same AgNP preparation as that used in experiments

Copyright © 2010. Nova Science Publishers, Incorporated. All rights reserved.

on plant seeds (see previous section); a detailed description is given in [61,66]. The study was fulfilled on 3-4 month mice of the BALB line (weight 35-37 g); one dose (0.2 ml) of AgNP water solution in various dilutions was introduced by intraperitoneal injections. Maximal and minimal AgNP concentration in the injected solutions was $5* 10^{-3}$ M (540 μg/ml, undiluted initial AgNP solution) and $0.05 * 10^{-3}$ M (5.4 μg/ml, dilution by 100), respectively. The aim was to determine, first, the percent of survived mice as a function of AgNP concentration and second, the dose leading to 50% death of animals 30 days after the injection (LD50/30). The effect of AgNP solution was compared to those of AOT and $AgNO_3$ solutions in equivalent concentrations (introduced with AgNP solution). The extent of survival was determined according to the standard method during the 30 day period after injections. Analysis of the data obtained shows that the percent of death was higher in the group with injected AgNP than in that with injected AOT. The LD(50/30) values for AgNP and AOT were, respectively, $2. 75 \pm 0.66 *10^{-3}$ M (or 297± 71.3 μg/ml) and $32.6 \pm 17.1 *10^{-3}$ M. The results indicate to the strong and concentration-dependent lethal effect of AgNP solution, independently on the sex of animals. The significant difference in the LD(50/30) values for AgNP and AOT testifies also to the lower toxicity of AOT compared to the AgNP, in agreement with the results for Plasmodium and plant seeds described above. Injection of silver nitrate did not cause death or any noticeable decrease in life functions of the animals at all concentrations studied (from 0.05 to $5.4 * 10^{-3}$ M). Hence follows that (1) Ag^+ ions are substantially less toxic than nanoparticles and (2) toxic effect of the nanoparticles can not be reduced to the action of Ag^+ ions.

It is interesting to compare our results with those obtained in experiments with silver nanoparticles on rats in vivo [30]. In these studies oral toxicity of 52.7 – 70.9 nm (average 60 nm) silver nanoparticles coated with carboxymethylcellulose (CMC) was tested on eight week old rats with doses 30 mg/kg, 300 mg/kg and 1000 mg/kg. The rats were exposed to the AgNP by oral administration; after 28 days of exposure all animals were alive and even no significant changes in body weight were observed. For the larger doses there were only signs of the slight liver damage; also accumulation of silver in kidneys was noted. Taking into account that for rats the doses of AgNP were significantly higher than in our studies on mice (the highest dose we used was 3 mg/kg), it is clear that in our case the AgNP are obviously more toxic. This may be due to the difference in (1) the particle size (our 9 nm versus 60 nm with rats), (2) the capping agent (AOT versus CMC), (3) the way of introduction (intraperitoneal versus peroral) and (4) the natural properties of the organisms (mice versus rats). Which of these reasons plays a dominant role remains to be elucidated. To our view, the capping agent can hardly be responsible, since both in experiments with mice and in all other cases studied it was found that AOT was noticeably less toxic for the living organisms than AgNP. Most likely, the amplification of toxicity in our case is conditioned by either small particle size or introduction directly into blood vessels (omitting the stomach and abdomen), or both.

Copyright © 2010. Nova Science Publishers, Incorporated. All rights reserved.

4. CONCLUSION

Viewed as a whole, the results of our studies of the biological effects of AgNP obtained by the biochemical synthesis and stabilized by anionic surface active substance (AOT) allow to make conclusions outlined below.

First, it is clear that AgNP of the chosen sizes (9±4 nm) act as a strong toxic agent, which can suppress the viability of various microorganisms as well as the life functions of the other living systems, including mammalian organisms. The toxic action of the nanoparticles towards microorganisms is registered both in the water medium (for AgNP added as water solutions) and for the AgNP-modified liquid-phase or solid materials.

The extent of toxicity of AgNP water solutions depends on the concentration of nanoparticles in the aqueous medium. For microorganisms in the water phase the toxic action of AgNP becomes noticeable from C(AgNP) ~ 1-3 μg/ml, and total death is observed in the range 5-10 μg/ml, in agreement with the results reported in [20] for the same bacteria species (E.coli) and for silver nanoparticles of the same size.

As follows from our experiments on the other objects, manifestation of the AgNP toxicity may be connected with the properties of external surface of the object under study: the plant seeds with the most rigid external shell are the less sensitive to the toxic action of the nanoparticles. This indicates to the role of adsorption of the nanoparticles in their biological action.

Second, our capping agent, AOT, also exerts toxic action on the biological objects studied, excluding the plant seeds; therefore, to determine the "pure" effect of nanoparticles it is necessary (a) to minimize the AOT content in AgNP water solution and (b) to make control experiments with AOT water solutions. However, comparison of the toxic action of AgNP and AOT in concentrations equal to those introduced with AgNP water solutions shows that, in all cases studied, the effect of AgNP exceeds that of AOT. Therefore, it was possible to find the range of AgNP concentrations where the AOT toxicity could be neglected and the biological effect observed was related only with the action of nanoparticles. For example, with Plasmodium the toxic action of AOT is negligible at AgNP concentrations ≤ 1.08 μ g/ml (10^{-5}M), while the effect of AgNP is clearly expressed. The AgNP concentration range providing the negligible AOT effect was determined also in similar experiments with human cultured cells (data obtained by Moskovtzev A.A. and co-workers, to be published).

Nevertheless, change of the capping agent is certainly not excluded; the work is now in progress on the modification of biochemical synthesis allowing to obtain silver nanoparticles capped with natural phospholipid. Comparison of the results found with different capping agents for the AgNP of similar size and mode of preparation is supposed to throw more light on the role of stabilizing shell in the biological activities of silver nanoparticles.

Third, it is found that, in the majority of cases studied the effect of silver nanoparticles exceeds significantly that of Ag^+ ions in equivalent concentrations. Similar conclusion was made in studies of AgNP interaction with bacteria [8,21,71] and fish embryos [28]. Therefore there are grounds to assume that the biological action of silver nanoparticles can be realized through the mechanism different from that of Ag^+ ions.

Fourth, antimicrobial effect of AgNP is clearly expressed not only in water medium, where the nanoparticles are introduced in the AOT bilayer shell, but also in studies of solid materials with nanoparticles deprived of their protective shell. Hence follows that, at least the

Copyright © 2010. Nova Science Publishers, Incorporated. All rights reserved.

bactericidal action of nanoparticles is conditioned by their own nature and does not depend significantly on the existence of protective shell. The same inference issues from the fact that, as follows from our data and those present in literature, the toxic action of silver nanoparticles with sizes below 20 nm becomes apparent at their close concentrations in the water medium for several different biological objects - bacteria, plasmodium, mammalian cultured cells – irrespectively of the capping shell and mode of the particles preparation. Certainly, at the present stage this may not be regarded as the general regularity, but rather as indication to the complexity of the phenomena taking place between the nanoparticles and living systems.

The most general conclusion which one can draw from our results is that silver nanoparticles possess a high biological activity towards various living systems, the fact that testifies, once and again, to the importance of the thorough investigation of the mechanism of their action. In spite of the extensive studies undertaken in the last years, it seems that many points here still remain unclear. Meanwhile, without the distinct understanding of the processes underlying the biological effects of silver or other metal nanoparticles one can hardly hope to give the well-grounded recommendations for the safe application of silver nanoparticles both in native solutions and as components of various liquid or solid materials.

REFERENCES

[1] Mossman, B.T.; Borm, P.J.; Castranova, V. et al. Mechanisms of action of inhaled fibers, particles and nanoparticles in lung and cardiovascular deseases. *Particle and Fibre Toxicology*, 2007 May 30, available from: *http//www.particleandfibretoxicology.com/content/4/1/4.*

[2] Oberdorster, G.; Maynard, A.; Donaldson, K. et al. Principles for characterizing the potential human health effects from exposure to nanomaterials: elements of a screening strategy. *Particle and Fibre Toxicology*, 2005, V.2, N8.

[3] Donaldson, K.; Tran, L.; Jimenez, L.A. et al. Combustion-derived nanoparticles: a review of their toxicology following inhalation exposure. *Particle and Fibre Toxicology*, 2005, V.2, N10.

[4] Elder, A.; Gelein, R.; Silva, V. et al. Translocation of inhaled ultrafine manganese oxide particles to the central nervous system. *Environmental Health Perspectives*, 2006, v.114, p.1172-1178.

[5] Stratmeyer, M.E.; Goering, P.L; Hitchins, V.M. et al. What we know and do not know about the bioeffects of nanoparticles: developing experimental approaches for safety assessment. *Biomed. Microdevices*, 2008, DOI 10.1007/s10544-008-9261-9.

[6] Takenaka, S.; Karg, E.; Roth, C. et al. Pulmonary and systemic distribution of inhaled ultrafine silver particles in rats. *Environmental Health perspectives*, 2001, v.109, p.547-551.

[7] Geiser, M.; Rothen-Rutishauser, B.; Kapp, N. et al. Ultrafine particles cross cellular membranes by nonphagocytic mechanisms in lungs and cultured cells. *Environmental Health Perspectives*, 2005, V.113, N11, p.1555-1560.

[8] Neal, A.L. What can be inferred from bacterium-nanoparticle interactions about the potential consequences of environmental exposure to nanoparticles? *Ecotoxicology*, 2008, v.17, p.362-371.

Copyright © 2010. Nova Science Publishers, Incorporated. All rights reserved.

[9] Salata, O.V. Aplications of nanoparticles in biology and medicine. *Journal of nanobiotechnology*, 2004, 2:3 doi:10.1186/1477-3155-2-3.
[10] Pissman, D.; Valenzuella, S.M.; Cortie, M.B. Therapeutic possibilities of plasmonically heated gold nanoparticles. *Trends Biotechnol*., 2006, v.24, p.62-67.
[11] Mukerjee, P.; Bhattacharya, R.; Bone, N. et al. Potential thereapeutic application of gold nanoparticles in B-chronic lymphocytic leukemia (BCLL): enhancing apoptosis. *Journal of Nanobiotechnology*, 2007, **5**:4 doi:10.1186/1477-3155-5-4.
[12] Soloviev, M. Nanobiotechnology today: focus on nanoparticles. *Journal of Nanobiotechnology, 2007*, 5:11 doi:10.1186/1477-3155-5-11.
[13] Sigha, S.; Bhattacharya, J.; Datta, H. et al. Anti-glycation activity of gold nanoparticles. *Nanomedecine: nanotechnology, biology and medicine*, 2009, v.5, p.21-29.
[14] Koulsky, L.A. *Silver Water* (Russian). Kiev: Naukova Dumka; 1987.
[15] Lopanov, A.N. Silver. (Russian*). SPb: Agat*; 2005.
[16] Karamushka, V.I.; Gadd, D.M.; Grusina, T.G.; Ulberg, Z.R. The use of colloid-biochemical parameters of microbial cells for the estimation of toxicity of heavy metals. *Colloid journal* (Russian), 1998, v.60, p.775-779.
[17] Ulberg, Z.R.; Marochko, L.G.; Sawkin, A.G.; Pertzov, N.V.. Chemical interactions during metal sorption by microorganisms. *Colloid journal* (Russian), 1998, v.60, p.836-842.
[18] Sondi, I.; Salopek-Sondi, B. Silver nanoparticles as antimicrobial agent: a case study on E,coli as a model for Gram-negative bacteria. *J. Colloid Interface Sci.*, 2004, v.275, p.177-185.
[19] Williams, D.N.; Ehrman, S.H.; Holoman, P. Evaluation of the microbial growth response to inorganic nanoparticles. *Journal of nanobiotechnology*, 2006, **4**:3 doi:10.1186/1477-3155-4-3.
[20] Lok, C.-N.; Ho, C.-M.; Chen, R. et al. Silver nanoparticles: partial oxidation and antibacterial activities. *J.Biol.Inorg.Chem*., 2007, v.12, p.527-534.
[21] Pal, S.; Tak, Y.K.; Song, J.M. Does the antibacterial activity of silver nanoparticles depend upon the shape of the nanoparticles? *Applied and Environmental Microbiology*. 2007. V. 73. № 6. P. 1712.
[22] Kim, J.S.; Kuk, E.; Yu, K.N. et al**.** Antimicrobial effects of silver nanoparticles**.** *Nanomedecine: nanotechnology, biology and medicine*, 2007, v.2, p.95-101.
[23] Elechiguerra, J.L.; Burt, J.L. ; Morones, J.R. et al. Interaction of silver nanoparticles with HIV-I. *Journal of nanobiotechnology*, 2005, 3:6 doi:10.1186/1477-3155-3-6.
[24] Braydich-Stolle, L.; Hussain, S.; Schlager, J.J.; Hofmann, M.-C. In vitro cytotoxicity of nanoparticles in mammalian germline stem cells. *Toxicological sciences*, 2005, v.88, p.412-419.
[25] Hussain, S.; Hess, K.; Gearhart, J. et al. In vitro toxicity of nanoparticles in BRL3A rat liver cells. *Toxicological sciences*, 2006, v.92, p.456-462.
[26] Sheikpranbabu, S.; Kalishwaralal, K; Venkataraman, D. et al**.** Silver nanoparticles inhibit VEGF-and IL-1β-induced vascular permeability via Src dependent pathway in porcine retinal endothelial cells. *Journal of nanobiotechnology*, 2009, **7**:8 doi:10.1186/1477-3155-7-8.

Copyright © 2010. Nova Science Publishers, Incorporated. All rights reserved.

[27] Kwon, Y.M.; Xia, Z.; Glyn-Jones, S. et al. Dose-dependent cytotoxicity of clinically relevant cobalt nanoparticles and ions on macrophages in vitro. *Biomed. Mater*. 2009, v.4(2), p.25018.

[28] Asharani, P.V.; Wu, Y.L.; Gong, Z.; Valivaveettil, S. Toxicity of silver nanoparticles in zebrafish models. *Nanotechnology*. 2008, v. 19, p.255102.

[29] Ji, J.H,; Jung, J.H.; Kim, S.S. et al. A twenty-eight-day inhalation toxicity study of silver nanoparticles in Sprague-Dawley rats. *Inhalation toxicology*, 2008, v.19, p.857-871.

[30] Kim, Y.S., Kim, J.S.; Cho, H.S. et al. Twenty-eight-day oral toxicity, genotoxicity and gender-related tissue distribution of silver nanoparticles in Sprague-Dawley rats. *Inhalation toxicology*, 2008, v.20, p.575-583.

[31] Zhang, G.; Yang, Z.; Lu, W. et al. Influence of anchoring ligands and particle size on the colloidal stability and in vivo biodistribution of polyethylene glycol-coated gold nanoparticles in tumor-xenografted mice. *Biomaterials*, 2009 v.30, p.1928-1936.

[32] Sonavane, G.; Tomoda, K.; Makino, K. Biodistribution of colloidal gold nanoparticles after intravenous administration: effect of particle size. *Colloids Surfaces B*, 2009, v.15, p.274-280.

[33] Rahman, M.F.; Wang, J.; Patterson, T.A. Expression of genes related to oxidative stress in the mouse brain after exposure to silver-25 nanoparticles. *Toxicology letters*, 2009, v.187, p.15-21.

[34] Egorova, E.M.; Revina, A.A.; Kondratieva, V.S. *The mode of preparation of nanosized metallic particles*. Patent RF N 2147487, priority from 01.07.1999.

[35] Egorova, E.M., Revina, A.A. Synthesis of metallic nanoparticles in reverse micelles in the presence of quercetin. *Colloids Surfaces A*, 2000, v. 168, p.87-96.

[36] Afanas'ev, I.B.; Dorozhko, A.I.; Brodskii, A.V. et al. Chelating and free radical scavenging mechanisms of inhibitory action of rutin and guercetin in lipid peroxidation. *Biochemical Pharmacology*, 1989, v.38, p.1763-1769.

[37] De Whalley, C.V.; Rankin, S.M.; Hoult, J.R.S. et al. Flavonoids inhibit the oxidative modification of low density lipoproteins by macrophages. *Biochemical Pharmacology*, 1990, v.39, p.1743-1750.

[38] *Flavonoids: chemistry, biochemistry and applications*. (O.M.Andersn, ed.) C.H.I.P.S., 2005.

[39] Middleton, E., Jr.; Kandaswami, C.; Theoharides, T.C. The Effects of Plant Flavonoids on Mammalian Cells: Implications for Inflammation, Heart Disease, and Cancer. *Pharmacological Reviews*, 2000, v. 52, p.673- 751.

[40] El Hajji, H.; ; Nkhili, E.; Valerie Tomao, V.; Olivier Dangles, O. Interactions of quercetin with iron and copper ions: complexation and autoxidation. *Free Radical Research*, 2006, v.40, p.303 — 320.

[41] Mira, L.; Fernandez, M.T.; Santos, M. Interactions of Flavonoids with Iron and Copper Ions: A Mechanism for their Antioxidant Activity. *Free Rad. Research*, 2002, v.36, p.1199.

[42] Robinson, B.H.; Khan-Lodhi, A.N.; Towey, T. *Microparticle synthesis and characterization in reverse micelles*. In: M-P.Plileni (Ed.) Structure and Reactivity in Reverse Micelles, Elsevier, Amserdam, 1989, p.199-219.

[43] Pileni, M.-P. Nanosized particles in colloidal assemblies. *Langmuir*, 1997, v.13, p.3266-3276.

Copyright © 2010. Nova Science Publishers, Incorporated. All rights reserved.

[44] Wilcoxon, P.; Abrams, B.L. Synthesis, structure and properties of metal nanoclusters. *Chemical Society Reviews*, 2006, v.35, p.1162-1194.
[45] Egorova, E.M. Metal nanoparticles in solutions: biochemical synthesis and applications. *Nanotechnics* (Russian), 2004, N1, p.15-26.
[46] Zhang, W.; Quaio, X.; Chen, J. Synthesis of silver nanoparticles – effects of concerned parameters in water/oil microemulsion. *Materials Science and Engineering B*, 2007, v.142 p.1-15.
[47] Egorova, E.M.; Revina, A.A.; Rumyantzev, B.V. et al. Stable silver nanoparticles in water dispersions obtained from micellar solutions. *J. Applied Chem*. (Russian), 2002, v.75, p.1620-1625.
[48] Sergeev, G.B. *Nanochemistry*. Moscow: Publishing House of Moscow State University; 2003.
[49] Suzdalev, I.P. *Nanotechnology. Physico-chemistry of nanoclusters, nanostructures and nanomaterials.* Moscow: KomKniga; 2005.
[50] Egorova, E.M.; Revina, A.A. Optical properties and sizes of silver nanoparticles in micellar solutions. *Colloid Journal* (Russian), 2002, v.64, p.334-345.
[51] Egorova, E.M.; Revina, A.A. *Mechanism of the interaction of quercetin with silver ions in reverse micelles.*
[52] Petit, C.; Lixon, P.; Pileni, M.-P. In situ synthesis of silver nanocluster in AOT reverse micelles, *J.Phys.Chem*., 1993, v. 97, p.12974-12983.
[53] Brichkin, S.B.; Rasumov, V.F.; Spirin, M.V. Formation of silver clusters by the photostimulated chemical reduction of AgBr nanocrystals in reverse micelles, *Colloid Journal* (Russia), 2000, v. 62, p. 12-17.
[54] Egorova, E.M. Metal nanoparticles in solutions: biochemical synthesis, properties and applications (a review). In: *Nanobiotechnology and nanosafety*. Moscow: Nauka, 2010 (in press).
[55] Van der Meeren, P.; Van Laethem, M.; Vanderdeelen, J.; Baert, L. Particle sizing of liposomal dispersions: a critical evaluation of some quasi-elastic light-scattering data-analysis software programs. *Journal of Liposome Research*, 1992, v.2, p.23-42.
[56] Dahneke, B.E. *Measurements of Suspended Particles by Quasi-elastic Light Scattering.* New York: Wiley; 1983.
[57] Shen, X.; Yuan, Qi; Liang, H. et al. Hysteresis effects of the interaction between serum albumins and silver nanoparticles. *Science in China B*, 2003, v.46, p.387-398.
[58] Egorova, E.M. Some applications of the Dukhin theory in studies of lipid membranes. *Colloids Surfaces* A, 2001, v.192, p.317-330.
[59] Egorova, E.M.; Revina, A.A.; Shishkov, D.I. et al. *The mode of creation of silver nanoparticles-modified carbon material with biocidal properties*. Patent RF N 2202400. priority from 5.07.2002.
[60] Proceedings of the I and II All-Russian (International) Conference *" Nanotechnology for Industry"*, Fryazino - 2004, 2005; Moscow, 2004, p.54-62; Moscow, 2006, p.26-32; (2) abstracts of the XVIII Mendeleev Congress for General and Applied Chemistry, Moscow, 2007, v.2, p.236; (3) Proceedings of the Fifth International Congress *"Biotechnology: state of the art and prospects of development*", Moscow, 2009, part I, p.471, 487; I and II Nanotechnology International Exhibition "Rusnanotech - 08, 09" II Nanotechnology International Forum Rusnanotech - 09.

Copyright © 2010. Nova Science Publishers, Incorporated. All rights reserved.

[61] Ordchonikidze, C.G.; Ramayya, L.K.; Egorova, E.M.; Rubanovich, A.V. Toxical and genotoxical effects of silver nanoparticles on mice in vivo. Abstracts of the 4-th *International Conference Environmental effects of nanoparticles and nanomaterials.* Vienna, 6-9th September, 2009

[62] Kudryavtzev, B.B.; Figovsky, O.; Egorova, E.M. et al. The use of nanotechnology in production of bioactive paints and coatings. *The Journal "Scientific Israel – Technological Advantages",* 2003, v.5, p.209-212.

[63] Matveeva, N.B.; Egorova, E.M.; Beylina, S.I.; Lednev, V.V. Chemotactic assay for biological effects of silver nanoparticles. *Biophysics*, 2006, v.51, p.758-763.

[64] Matveeva, N.B.; Egorova, E.M.; Beylina, S.I. Chemotactic assay is capable to reveal the difference in efficiency of nanosized silver particles. In: *"Biologocal motility: achievements and perspectives"* (Eds. Z.A.Podlubnaya and S.I.Malyshev). 2008, v.2, p.240-242.

[65] Shirokova, L.N., Alexandrova, V.A., Egorova, E.M.; Vihoreva, G.A. Macromolecular systems and bactericidal films based on chitin derivatives and silver nanoparticles. *Applied biochemistry and microbiology*, 2009

[66] Ordzhonikidze, C.G., Ramaiyya, L.K., Egorova, E.M., Rubanovich, A.V. Toxical and genotoxical effects of silver nanoparticles on mice in vivo. *Acta Naturae*, 2009, N3. p.

[67] Egorova, E.M., Revina, A.A., Ristovschikova, T.N., Kiseleva, O.I. Bactericidal and catalytic properties of stable metallic nanoparticles. *Vestnik of MSU, ser.2 Chimia*, 2002, v.42, p.332-338.

[68] Egorova, E.M.; Revina, A.A.; Rumyantzev, B.V. Preparation and antimicrobial properties of water dispersions of silver nanoparticles. Proceedings of the VI All-Russian (International) conference *"Physico-chemistry of ultradisperse (nano-) systems"* Moscow, 2003, p.149-152.

[69] Park, S.-J.; Jang, Y.-S. Preparation and characterization of activated carbon fibers supported with silver metal for antibacterial behavior. *J. Coll. Interf. Sci*., 2003, v.261, p.238-243.

[70] Beylina, S.I.; Matveeva, N.B.; Egorova, E.M. Chemotaxis-based Assay for the Biological Action of Silver Nanoparticles. Paper to be submitted for the book *"Chemotaxis: Types, Clinical Significance and Mathematical Models".* Novascience, 2010.

[71] Arora, S.; Jain, J.; Rajwade, J.M.; Paknikar, K.M**.** Cellular responses induced by silver nanoparticles: *In vitro* studies. *Toxicology letters*, 2008, v.179, p.93-100.

Copyright © 2010. Nova Science Publishers, Incorporated. All rights reserved.

In: Silver Nanoparticles
Editor: Audrey E. Welles, pp. 259-290
ISBN: 978-1-61668-690-1
© 2010 Nova Science Publishers, Inc.

Chapter 6

THE STUDY OF SILVER NANOPARTICLES APPLIED ON THE PHOTONICS MATERIALS BASED ON THE SURFACE PLASMON RESONANCE

You Yi Sun
Research Center for Engineering Technology of Polymeric
Composites of Shanxi Province, North University of China

1. INTRODUCTION

Recent theoretical progress in understanding the application of silver nanoparticles on the photonics materials based on the surface plasmon resonance (SPR) has been discussed in this chapter. In the first, a novel procedure to enhance the luminescence from Europium complexbased on the surface-enhanced fluorescence of silver nanoparticles, was described. It shows that the noble metal nanoparticles act as enhancer and quencher of Europium complex fluorescence. And then the both interactions strongly depend on noble metal particle diameter, concentration and surrounding medium, the systematic studies have been carried out. Secondly, recent studies about third order nonlinear optical properties of noble metal nanocomposite film were also discussed. It shows that a nonlinear optical response in copper, silver and gold nanocomposite materials with an enhanced third order nonlinear susceptibility, which is particularly useful in their applications as optical switchers with ultrashort time response and optical limiters of intense laser radiation. The crystallite size and concentration of nanoparticles on their nonlinear properties of such systems are discussed. Particularly, the synthesis method of the silver nanocomposite film is also described. Thirdly, the influence of silver nanoparticles on the phase behavior of liquid crystalline polymers was also conclued. A series of polymer films containing liquid crystalline groups and silver nanoparticles were prepared. Local electromagnetic fields near the particle can be many orders of magnitude higher than the incident fields due to hat light at the surface plasmon resonance frequency interacts strongly with metal particles and excites a collective electron motion, or plasmon. As a result, photo-induced reorientation of liquid crystalline polymers

Copyright © 2010. Nova Science Publishers, Incorporated. All rights reserved.

was affected by silver nanoparticles. The effect of liquid crystalline polymers structure, size and concentration of silver nanoparticles, polarized light on the photo-induced reorientation of the liquid crystalline group films was systemic studied.

Despite all the studies done so far in this field, the application of silver nanoparticles on the photonics materials here is a relative new physical process first described about 10 years ago. So it is quite usual that most of the work done so far was devoted to the development and optimization of the effect than to a deeper understanding of the mechanism of the physical process. The scope of this chapter is to discuss some mechanistic aspects of the physical process between noble metallic nanoparticles on the photonics materials, which are plausible and in line with earlier and new findings of our group, and to compare them with results of other groups. It may be a help for further discussions and the development of better optical materials based on SPR of noble nanoparticles.

2. FUNDAMENTAL CONCEPTS

2.1. Surface Plasmon Resonance

Surface plasmon resonance (SPR) of silver nanoparticles is a surface bound electromagnetic wave propagating at the interface between free electron silver and a dielectric layer[1]. The propagation constant (k_{SP}) of the surface plasmon (SP) is dependent on the effective refractive index of the dielectric layer(n_a), which denote the sensing medium. At resonance, i.e. at a specific angle of incidence, θ_{SP} of a monochromatic beam of light, the propagation constant of the light parallel to the surface, k_x , is matched to the real part of the propagation constant of the surface plasmon, k_{SP}*[2]*:

$$k_x = (2\pi / \lambda) n_p \sin\theta_{SP} = \mathrm{Re}(k_{sp})$$

$$\approx (2\pi / \lambda)\,\mathrm{Re}[(\varepsilon_m n_a{}^2)^{1/2} / (\varepsilon_m + n_a{}^2)^{1/2}]$$

$$\mathrm{P}=Kx\times 10^{\,np}\times P_0$$

where P_o and P is the intensity of input laser and surface bound electromagnetic feild, respectively; λ is the wavelength in free space; n_p is the refractive index of the prism; ε_m is the relative permittivity of the silver and Re denotes the real part of the expression. Owing to the damping of the SP caused by absorption of the light in the silver film, angles close to the resonance condition can also excite a SP. This means that a dark band, denoted the SPR dip, is projected onto a detector, as shown in Figure 1.

2.2. Surface-Enhanced Luminescence

A procedure to enhance the fluorescence from Eu complex based on the surface-enhanced fluorescence (SEF) of noble nanoparticles has been developing[3-9]. The surface-

Copyright © 2010. Nova Science Publishers, Incorporated. All rights reserved.

enhanced fluorescence is attributed to the large electromagnetic field arising from the excitation of surface plasmon polariton (SPP) of silver nanoparticles. The mold of enhancement fluorescence is shown in Figure 2. According to the mold and Mie theory [10], the enhancement factor is calculated by the following equation:

$$E_1 = \left(2\frac{\varepsilon_2\varepsilon_a - \varepsilon_3\varepsilon_b}{\varepsilon_2\varepsilon_a + 2\varepsilon_3\varepsilon_b}\frac{r_2^3}{r^3} + 1\right)E_0 COS(\theta)e_r + \left(\frac{\varepsilon_2\varepsilon_a - \varepsilon_3\varepsilon_b}{\varepsilon_2\varepsilon_a + 2\varepsilon_3\varepsilon_b}\frac{r_2^3}{r^3} - 1\right)E_0 SIN(\theta)e_\theta$$

The E_1 is amplified incident field around silver metallic surface. The ε and P is presented in following equations:

$$\varepsilon_a = \varepsilon_1(3-2P) + 2\varepsilon_2 P$$
$$\varepsilon_b = \varepsilon_2(3-P) + \varepsilon_1 P$$
$$P = 1 - \left(r_1/r_2\right)^3$$

Where ε_1 and ε_2 are electrical constant of silver metal and medium around silver metal, respectively. r_1 and r_2 is radius of pure silver nanoparticles and silver metal complexes, respectively. When the θ is supposed to be 0, the enhancing factor is shown in following equation:

$$\alpha = \left|2\times 10^3 \bullet \frac{\varepsilon_1 - 7}{\varepsilon_1 + 14}\frac{1}{r^3} + 1\right|^2$$

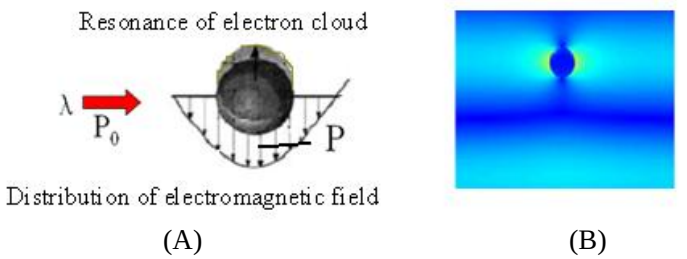

(A) (B)

Figure 1. (A) The SPR configuration and SPR photo graph of silver nanoparticles.

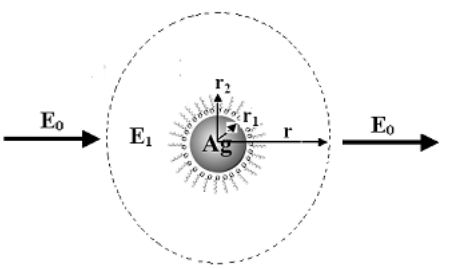

Figure 2. The representation of the amplified incident field around metallic surface and nonradiative relaxation due to damping of the dipole oscillators by the silver metallic surface.

Copyright © 2010. Nova Science Publishers, Incorporated. All rights reserved.

In the Drude mode, there are several assumptions as shown in following: (1) the particles are spherical; (2) the organic materials adsorbed on surface of particles are ignored; (3) the interaction between particles is not considered. It is easy to be observed from the equation (1) that the SEF strongly depend on particle size, particles shape, concentration, the distance between Lanthanon complexes and particle, and surrounding medium.

2.3 Photo-Induced Rate

As well-known, the photo-induced rate and stabilization of LC polymers are an important parameter with regard to their potential use as the optical materials[11]. Generally, the photo-induced rate can be improved in the presence of silver nanoparticlesm, which is also attributed to the surface plasmon resonance[12]. The light of linear polalrized laser at the surface plasmon resonance frequency interacts strongly with silver particles and excites a collective electron motion, or plasmon. As a result, local electromagnetic fields near the particle can be many orders of magnitude higher than the incident fields. So, the intensity of light interacting with LC polymers can be improved, resulting in the increase of photo-induced rate. Although the mechanism has not been understood completely, total enhancement is generally believed to be a result of combination of electromagnetic and chemical effects between the adsorbed molecules and the surface. Surface plasmon resonance, which is associated with collective electron resonance induced by incident light on a rough metal surface, is similar to the SERS phenomenon[13].

2.4. Third-Order Nonlinear Optical Response

Materials exhibiting large third-order nonlinear optical response accompanied by low losses (e.g. at the wavelength of interest), good optical quality, mechanical stability and processability are generally considered as promising candidates for use in optoelectronic devices and potential photonic applications[14]. Silver has inherently very large optical nonlinearities based on the surface plasmon resonance. The Maxwell-Garnett theory has been successfully applied to the calculation of nonlinear optical properties by the following equation[15].

The silver metal core is assumed to have a displacement **D**-local electric field **E** response of the form:

$$\mathrm{D}=\varepsilon_{\mathrm{c}}(E)E=\varepsilon_{\mathrm{c}}^{(0)}E+\chi_{c}^{(3)}\mid E\mid^{2}E\,, \tag{1}$$

where $\varepsilon_c^{(0)}$ is the linear dielectric function and $\chi_c^{(3)}$ is the third-order nonlinear susceptibility. Here, the second-order susceptibility $\chi_c^{(2)}$ vanishes in the present case. Thus, silver particles have nonvanishing linear dielectric function and third-order susceptibility.

Such cubic nonlinearity is the lowest-order nonlinearity appearing in the material with inversion symmetry or macroscopic isotropy. we can obtain explicit expressions for $\varepsilon_c^{(0)}$ and $\chi_c^{(3)}$

Copyright © 2010. Nova Science Publishers, Incorporated. All rights reserved.

$$\varepsilon_e^{(0)} = \varepsilon_m + 3f\varepsilon_m \frac{\varepsilon_c^{(0)} + (\frac{2I}{a\varepsilon_m} - 1)\varepsilon_m}{P} \tag{2}$$

and

$$\chi_e^{(3)} = f\chi_c^{(3)} \left(\frac{3\varepsilon_m}{P}\right)^2 \left|\frac{3\varepsilon_m}{P}\right|^2 . \tag{3}$$

It is known that the effective nonlinearity $\chi_c^{(3)}$ of the composite can be strongly enhanced by the embedding of nonlinear small silver particles in the matrix. The enhancement of $\chi_c^{(3)}$ is believed to stem from two essential elements[16]. One is the large nonlinear susceptibility of metal particles $\chi_c^{(3)}$ and the other is surface plasmon excitation. Three mechanisms, including interband transitions between the *d* band and the conduction band, intraband transitions in the quantum-confined conduction band, and hot electron effects, can contribute to $\chi_c^{(3)}$. Each of these mechanisms depends on the electronic description of metal particles. $\chi_c^{(3)}$ can also be enhanced due to the enhancement of the local field near the surface plasmon resonant frequency. The surface plasmon resonant frequency depends on the linear dielectric function $\varepsilon_c^{(0)}$, which is also determined by the electronic description of silver particles. From Eqs. (2) and (3), we can find, due to local field enhancement (3 ε_m/P is called linear local-field enhancement factor), both $\varepsilon_c^{(0)}$ and $\chi_c^{(3)}$ show resonance behavior. However, the surface plasmon resonant effect on $\chi_c^{(3)}$ is much pronounced. The above considerations high light *n* the dependence of $\varepsilon_c^{(0)}$ and $\chi_c^{(3)}$ on the electronic properties of silver particles.

It is known that, for some noble metal, the linear dielectric function of metal $\varepsilon_c^{(0)}$ can be characterized by the Drude free-electron model in combination with the Lorentz oscillator model for the bound-electron contributions. The linear dielectric function is written as

$$\varepsilon_c^{(0)} = 1 - \frac{\omega_{pf}^2}{\omega^2 + i\frac{\omega}{\tau_f}} + \frac{\omega_{pb}^2}{\omega_0^2 - \omega^2 - i\frac{\omega}{\tau_b}} \tag{4}$$

where ω_{pf}, ω_0 are the plasmon frequency and the boundelectron resonant frequency, respectively, τ_b is the bound electron decay time, and τ_f is the free electron scattering time and is found particle-size dependent.

$$\frac{1}{\tau_f} = \frac{1}{\tau_0} + \frac{V_f}{a}, \tag{5}$$

where τ_0 is the scattering time in the bulk metal, and v_f denotes the Fermi velocity. So far, we have formulated the dependence of $\varepsilon_c^{(0)}$ and $\chi_c^{(3)}$ on the mean radius of metal particles via a simple model by introducing an interfacial factor *I*. The effective linear dielectric function $\varepsilon_c^{(0)}$ and cubic nonlinear optical susceptibility $\chi_c^{(3)}$ can be readily solved as a function of particle-size *a* by substituting Eqs.(4) And (5) into Eqs. (2) and (3).

Copyright © 2010. Nova Science Publishers, Incorporated. All rights reserved.

For wavelengths near the SPR, the local electromagnetic field inside the particles is enhanced leading to a strong amplification of the third order nonlinear optical (NLO) properties of the nanocomposite as first reported by Ricard et al. According to this model, for small metal volume concentration p, the nanoconposite third order susceptibility $\chi^{(3)}$ is a function of the metal concentration, the bulk metal third order susceptibility $\chi_m^{(3)}$, the local field factor $f(\omega)$ and the incident light angular frequency p as related by the following equation:

$$\chi^{(3)} = pf(\omega)^2 \mid f(\omega)\mid^2 \chi_m^{(3)}.$$

For independent spherical particles, the local field factor is defined by

$$f(\omega) = \frac{3\varepsilon_d}{\varepsilon_m + 2\varepsilon_d},$$

where ε_m and ε_d are, respectively, the metal and matrix dielectric permittivities. It turns out that the NLO properties of nanocomposite materials are strongly dependent on the nanostructure of the films. Indeed, the metal dielectric permittivity is strongly correlated with the SPR spectral position that in turn depends on the particle size and shape. Therefore, in order to fabricate high performance NLO nanocomposite, a high number of structural parameters needs to be precisely controlled.

3. SYNTHESIS OF OPTICAL MATERIALS CONTAINING THE SILVER NANOPARTICLES

3.1. The Synthesis of Silver/Lanthanon Complex Nanocomposite Materials

3.1.1. The synthesis of silver/lanthanon complex composite nanoparticles

(1) Lanthanon ion grafted to silver nanoparticles

Here, the synthesis of silver/lanthanon complex composite nanoparticles was synthesized by more than two steps as shown in Figure 3A. Firstly, the silver/functional molecule composite particles are prepared by in-situ method, in which the silver nanoparticles are formed in the presence of functional molecule. The functional molecule must contain the groups (-NH-, -S-, -OH, -COOH and so on) that can form physical or chemical interaction with silver nanoparticles and Lanthanon ion, such as poly(vinylpyrrolidone), Trifluorothenoyl-acetone, pyridine-3, 5-dicarboxylic acid and dipicolinic acid[3-5]. Secondly, the Lanthanon ion is added into the silver colloidal solution, and then the Lanthanon ion is adsorbed on surface of silver by the interaction between functional groups and lanthanon ion.

However, the fluorescence efficiency and intensity of the silver/lanthanon ion composite nanoparticles is low, which restrict their applications on optical materials. So the lanthanon complexes replacing with lanthanon ion is added into silver colloidal solution and a novel silver/lanthanon complex composite nanoparticles is formed[17], which obtain high

Copyright © 2010. Nova Science Publishers, Incorporated. All rights reserved.

fluorescence efficiency and intensity due the fluorescence efficiency and intensity of the lanthanon complex as shown in Figure 3B.

(2) Lanthanon ion grafted from silver nanoparticles

The silver nanoparticles was prepared in the presence of lanthanon complex as shown in Figure 4[8,17], in which the lanthanon complex contains the functional group that has strong interaction with silver. The literatures reporting the synthesis process are relatively few and only lanthanon complex $Eu(TTA)_3 \cdot 2H_2O$ as stabilizer was reported. However, the quenching fluorescence was observed due to the distance between lanthanon ion and silver metallic surface to be close zero. A novel macromolecule ligand-Lanthanon complex was used as stabilizer, in which the fluorescence quenching was restricted due the long chain of polymer and the process has been studying by our group.

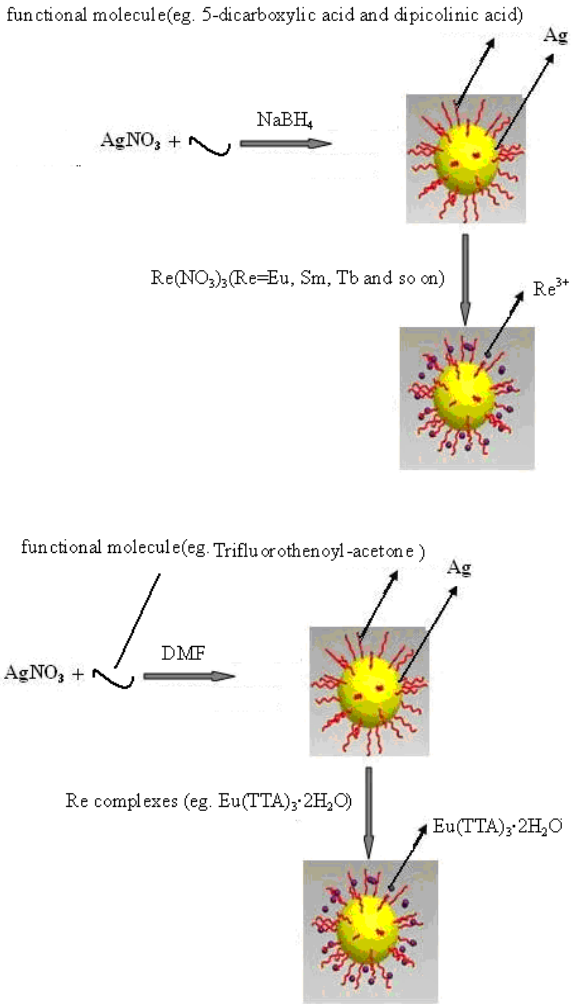

Figure 3. Synthesis of silver/lanthanon complex composite nanoparticles.

Copyright © 2010. Nova Science Publishers, Incorporated. All rights reserved.

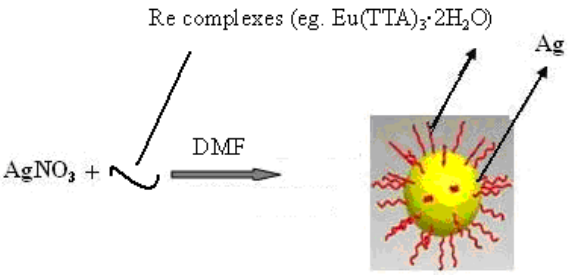

Figure 4. Synthesis of silver/lanthanon complex composite nanoparticles.

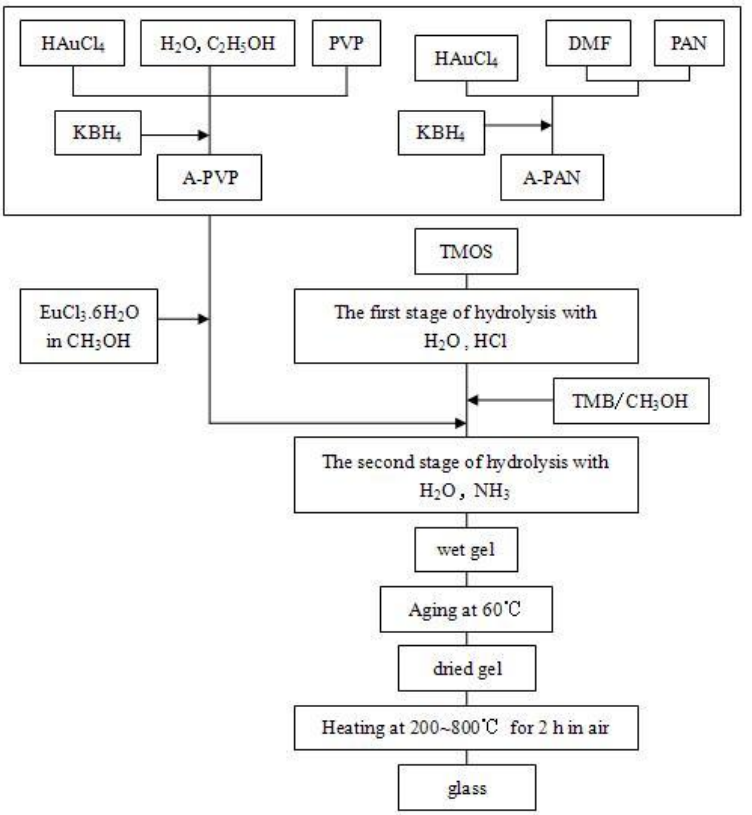

Figure 5. Synthesis of silver/lanthanon complex doped solid materials.

3.1.2. The synthesis silver/Lanthanon complex composite nanoparticles doped solid materials

Generally, the silver/Lanthanon complex composite nanoparticles doped inoriganic solid materials were prepared by sol-gel route. In one case[9], the synthesis of $10B_2O_3$-$90SiO_2$ solid materials were prepared by the sol-gel route as shown in Figure 5. Firstly, the nanometer-sized Ag colloids was synthesized by reducing $AgNO_3$ with KBH_4 in the aqeuous solution containing PVP (or other funcational polymer). Secondly, the Ag collodial solution

Copyright © 2010. Nova Science Publishers, Incorporated. All rights reserved.

was coperated into $10B_2O_3$-$90SiO_2$ solid materials together with Lanthanon ion. At first, TMOS was added dropwise to distilled water that included a small amount of HCl, and stirred. TMB in methanol ($C_3H_9BO_3/CH_3OH$) was added dropwise with further stirring. The polymer-protected Ag sol was mixed with methanol dissolving $EuCl_3$, and added to the B_2O_3-SiO_2 sol. And then, distilled water including NH_3 was added with stirring. It took several days to obtain a stiff gel.

The composites of silver/Lanthanon complex composite nanoparticles doped polymer were also prepared either through melting extrusion and solution cast or through polymerization of lanthanide–monomer complexes. But there are few works reporting the synthesis process and the systmic study is required. As above discussions, during the synthesis process of silver/Lanthanon complex composite nanoparticles doped solid materials, the good dispersion of the complex nanoparticles on the solid matrix is a challenge and very important to obtain enhancement fluorescence.

3.2. The Synthesis of LC Polymer/Metal Nanocomposites

Lots of attentions were paid to some LC polymer systsiems that are usually used as templates for the preparation and stabilization of inorganic nanoparticles[18-19]. However, the role of nanoparticles in the mesophase formation, as well as their influence on liquid crystal properties, was yet to be understood. Especially, the synthesis and properties of LC polymer/silver nanopartics nanocomposites, there are only three literatures reporting the physical process as shown in following.

3.2.1. The in-situ method

The silver/polymer LC complex composite nanoparticles or complex film was synthesized by more than two steps as shown in Figure 6[20-21]. Firstly, the LC functional polymer is prepared, in which the functional molecule must contain the functional group (-NH-, -S-, -OH, -COOH, CN and so on) that form physical or chemical interaction with silver nanoparticles, such as poly(6-[4-(4-cyanophenylazo)phenoxy]x-methylene methacrylate), polyimide and so on. Secondly, the silver/polymer LC complex composite nanoparticles are prepared by in-situ method, in which the silver nanoparticles are formed in the presence of functional molecule. Generally, the LC polymer dose not dissolved in aqueous solution. So, the reaction is carried out in DMF or DMF/water mixing solution, in which the $NaBH_4$ or DMF solution acts as the reducer of Ag ion. In addtion, in order to obtain the silver/polymer complex composite film, the concentration of LC polymer is high during the synthesis process. And then, the nanocomposite film containing LC polymer can be formed by the spin-coating technique.

The excellence of the synthesis method is that the silver nanoparticles can been well dispersed in LC polymer matrix and there are few aggregate of silver nanoparticles. Furthermore, the group of polymer can be located close to surface of silver nanoparticles. There are very important to enhance the photo-induced rate of LC polymer based on the SPR of silver nanoparticles. However. There are two disadvantages. Firstly, the concentration of silver doped in LC polymer is difficult to be controlled. Secondly, if the LC group has strong interaction with silver metal, the photo-induced rate will be reduced.

Copyright © 2010. Nova Science Publishers, Incorporated. All rights reserved.

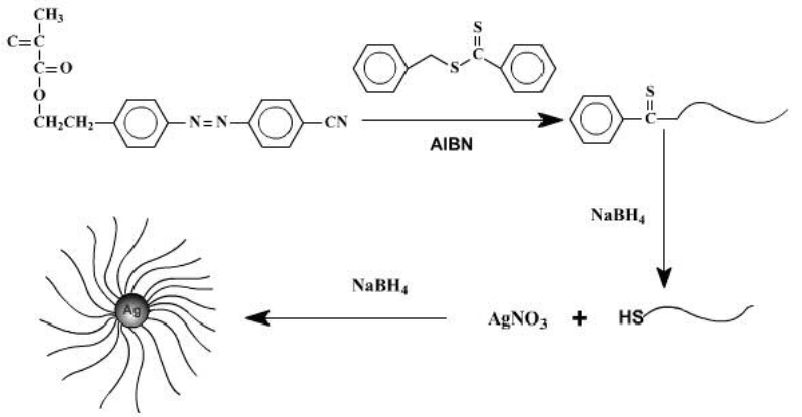

Figure 6. Synthesis of silver/LC polymer complex film.

3.2.2. The mixing method

Here, the silver/polymer composite nanoparticles were also synthesized by mixing method[12]. Firstly, the silver colloidal solution is prepared by in-situ method. Secondly, the LC polymer is added into the silver colloidal solution, and then the mixing solution can also form film by the spin-coating technique. Here, the concentration and size of silver doped in LC polymer is easy to be controlled. At the same time, the strong interaction between LC group and silver metal is averted, which is benefit to enhance the photo-induced rate. However, the poor dispersion of silver nanoparticles in LC polymer matrix decrease photo-induced rate.

3.3. The Synthesis of Third-Order Nonlinear Optical Materials

Although there are lots of works reporting the synthesis of noble metal doping solid materials[22-24], the effect of noble metal nanoparticles on third order nonlinear optical properties of these nancomposites is few consideration. The reason is that the high dispersion of sliver nanoparticles in solid materials is very important for study of third order nonlinear optical properties, which is difficult to be obtained.

3.3.1. Synthesis of Ag nanocomposite polymer films

(1) The in-situ method

Geneally, silver metal nanocomposite polymer film was prepared by in-siut synthesis technique as shown in Figure 7, in which the silver nanoparticles was well dispersed in polymer matrix[25]. The synthesis techniques is required with a functional group for the polymer, which can be interacted with noble metal, i.e. cyano (-CN) groups, thiol (-SH) group, and so on.

However, most of polymers do not contain the functional group, for example poly(methyl methacrylate) (PMMA). As a polymer matrix, the PMMA has attracted particular interests for its low optical absorption, refractive index tailorability with molecular weight, simple

Copyright © 2010. Nova Science Publishers, Incorporated. All rights reserved.

synthesis and its low cost. These characteristics make it suitable as a host material for investigation and application in optical materials.

The functional sulfur end group of PMMA was introduced by Reversible addition-fragmentation transfer (RAFT) polymerization. In following, Ag nanocomposite PMMA film can be prepared by in-situ synthesis technique as shown in Figure 7. Compared to conventional synthesis procedure, it will be better for meeting two advantages: (1) it is suit to lots of monomers, which can be polymerized by RAFT to produce a polymer with such a functional group at the chain end of the polymer; (2) molecular weight and its distribution of the polymer can be controlled at the same time, providing an opportunity to investigate the effects of molecular weight and its distribution on nonlinear optical properties of nanocomposite polymer film;(3) the difference is that part of the PMMA is adsorbed on the surface of Ag nanoparticles with one end group of polymer as soon as Ag nanoparticles formed.

(2) Self-assembly method

Noble metal nanocomposite polymer film was also prepared by the self-assembly method, by which the high dispersion polymer film was obtained as shown in Figure 8[26]. In one case, PAH/PSS/Ag bilayer film was prepared by the method as shown in following. Firstly, the $AgNO_3$ solution and tannic acid solution were added to water while stirring continuously. The resulting colloid was yellow-brownish and could be stable for several weeks. Secondly, single crystal Si(111) and glass slide were used as the substrates, which were cleaned with a concentrated sulfuric acid/hydrogen peroxide solution. After rinsing with plenty of water, the cleaned substrates were then placed into a dilute aqueous solution of PEI and held. Then rinsing with water and flushing with N_2 flow, a thin layer of PEI was formed on the substrate. Prior to the construction of the Ag/PAH multilayered coating systems, two-cycle PAH/PSS bilayers were deposited on the PEI modified substrate to promote the combinability between the surface and the first monolayer of Ag film. The two-cycle PAH/PSS bilayer film architecture was achieved by alternately depositing PSS and PAH from their aqueous solutions.

As above discussions, the synthesis is very complex, which is difficult to be controlled. At the same time, few polymers as matrix are suit to the synthesis process. Addtionally, the mechnical properties of polymer film is bad, which is difficult to be applied on optical materials.

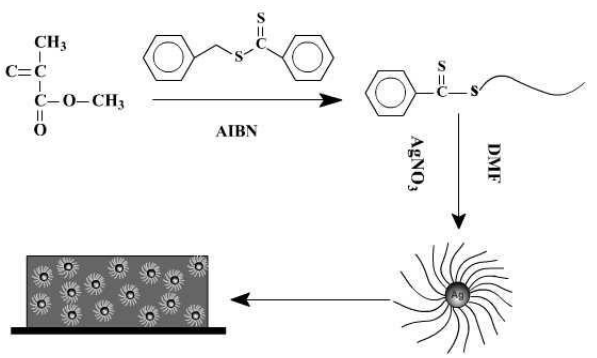

Figure 7. Synthesis of silver nanoparticles doped composite film by the in-siut method.

Copyright © 2010. Nova Science Publishers, Incorporated. All rights reserved.

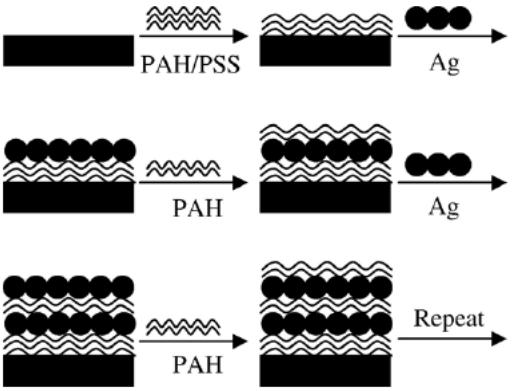

Figure 8. Synthesis of silver nanoparticles doped composite film by the self-assembly method.

(3) Others

As well-known, the good dispersion of silver in polymer matrix is very important to study the third order nonlinear properties of nancomposite. There is one work reporting the synthesis of nancomposite with high dispersion as shown in Figure 9[27]. Moreover, the present method shows an easy processing and the synthesis process is easily controlled. Aqueous solutions of silver nitrate and PVA were mixed and stirred; the solution mixture was spin-coated either directly on quartz or on glass substrates previously coated with a PS layer. Silver nanoparticles were generated by heating the solid films in a hot air oven under ambient atmosphere. PVA acts simultaneously as the reducing agent, stabilizer for the nanoparticles, and the matrix for homogeneous distribution and immobilization. But, the third order nonlinear properties of the composite film prepared by the method are not understood. There are requested for lots of works studying synthesis and third order nonlinear properties of the polymer nanocomposite in the future.

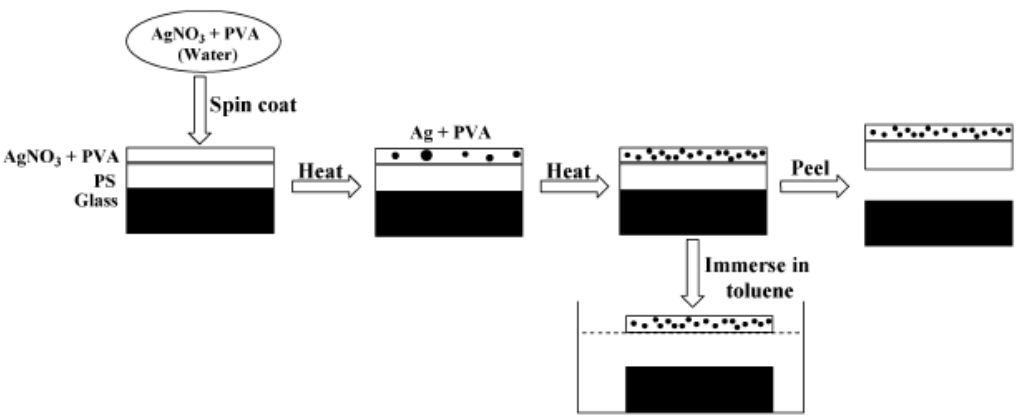

Figure 9. Synthesis of silver nanoparticles doped composite film by the new method.

Copyright © 2010. Nova Science Publishers, Incorporated. All rights reserved.

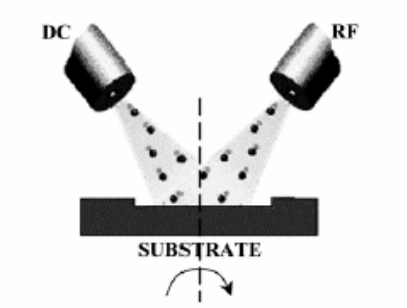

Figure 10. The Scheme of RF-Dc Co-sputtering system.

3.3.2. Synthesis of Ag nanocomposite inoriganic films

(1) Multitarget magnetron sputtering method

Some Ag nanocomposite inoriganic films (eg. Ag:Bi_2O_3 composite films) were prepared by co-sputtering of Ag and BiO onto the fused silica substrate and using the multi-target magnetron sputtering system[28]. As shown in Figure 10, the Ag and BiO targets were diagonally mounted on two target holders with a distance separation between them and at an inclined angle related to the surface normal of the substrate. The Ag and BiO target was sputtered by the DC and RF. power supply, respectively. The sputtering power on the target was controlled to achieve a variation of the Ag concentration in the film over a wider range. In the film depositing process, the sample holder was rotated to improve the uniformity of composition distribution of the film. As above discussions, the synthesis is very complex. Especially, it needs special equipment.

(2) Hybrid deposition technique

The Ag nanocomposite inoriganic films were also prepared by a hybrid process simultaneously combining PECVD and pulsed DC sputtering as shown in Figure 11[29]. The substrates (c-Si and fused silica) were placed on an RF-powered substrate holder electrode on which negative substrate bias voltage V_B develops. The working gas flow consisted of Ar, O_2, and SiH_4, while the total pressure was maintain. Ag was simultaneously sputtered from a gold target installed on a magnetron head located at a 15cm distance from the substrate. The Ag concentration was controlled by the total power delivered to the target from a pulsed DC power supply using a pulse frequency.

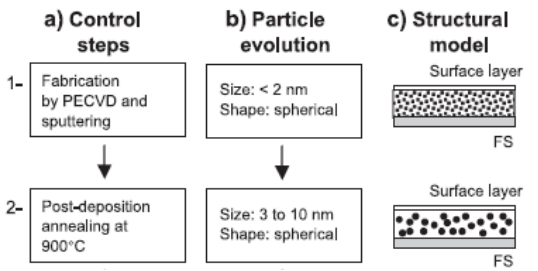

Figure 11. Illustration of the film preparation steps, evolution of the particle size and shape, and corresponding microstructural models.

Copyright © 2010. Nova Science Publishers, Incorporated. All rights reserved.

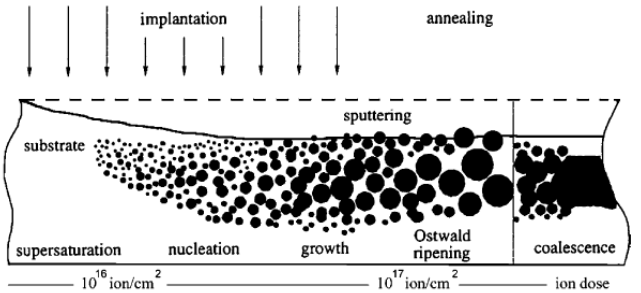

Figure 12. Scheme of major physical stages under metal ion implantation with dose increase.

(3) Ion implantation

The Ag nanocomposite inoriganic films were also prepared by ion implantation as shown in Figure 12[30-31]. The silicate glasses (SG) were prepared as plates with the thickness of 1mm. The accelerate energies used for implantation were 30 keV-60 keV at a dose. The concentration of silver and thickness of the composite film is controlled by the accelerate energies, the dose and implantation times. It is very convenience to synthesis Ag doped inoriganic films. However, the distribution and size in matrix is difficult to be controlled. In the other way, it needs special equipment.

4. CHARACTERIZATIONS OF OPTICAL METRIALS

4.1. Fluorescence Properties

As well-known, the fluorescence intensity, efficiency and lifetime of luminescent materials are very important with regard to their potential use as the optical materials [32], which are studied and analysis by RF-5301PC spectrofluorometer and lifetime spectrofluormeter (Fluorolog-3-TAU), respectivly.

(1) Fluorescence intensity

The fluorescence intensity can be obtained accroding to the emssion speactrum as shown in Figure 13, in which the value of longitudinal coordinates show the fluorescence intensity. In one case, five emission peaks centered at 580, 592, 616, 650, and 698 nm, assigned to $^5D_0 \rightarrow {}^7F_0$, $^5D_0 \rightarrow {}^7F_1$, $^5D_0 \rightarrow {}^7F_2$, $^5D_0 \rightarrow {}^7F_3$, and $^5D_0 \rightarrow {}^7F_4$ transition of Eu ion, respectively, were observed[33]. The result indicate that the effect of silver colloids on the energy level of Eu ion is slight. However, it can see the increase in intensity by the presence of Ag colloids, while the emission wavelength remains unchanged. Of course, the fluorescence intensity can be compared under identical instrumental conditions.

(2) Quantum yields and fluorescence lifetime

The quantum yields (*qx*) have been determined by absolute measurements(RF-5301PC spectrofluorometer) and is thus determined as follows[34]:

Copyright © 2010. Nova Science Publishers, Incorporated. All rights reserved.

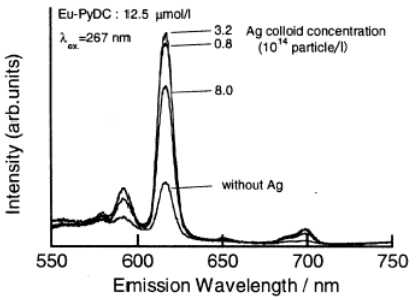

Figure 13. Emssion speactrum of Eu ion complexe with various silver colloidal solution.

$$q_x = \left\{\frac{1-R_{st}}{1-R_x}\right\}\left\{\frac{\Delta\varphi_{st}}{\Delta\varphi_s}\right\}q_{st} \tag{1}$$

where *R*st and *Rx* are the amount exciting radiation reflected by the standard and by the sample, respectively, and *q*st is the quantum yield of the standard phosphor. The terms $\triangle\varphi$st and $\triangle\varphi$s give the integrated photo flux (photons s^{-1}) for the sample and the standard phosphors, respectively. Generally, the stand was sodium salicylate, which has a broad emission band with the maximum at 616 nm and q = 60% at room temperature [35].

The values of $R_{ST,}$ $R_{s,}$ $\Delta\Phi$,and $\Delta\Phi_{ST}$ must be obtained for the same excitation wavelength, geometry and instrumental conditions.Unmost care was taken to ensure a constant and reproducible position for the sample/standard holder and unchanged instrumental conditions throughout the measurement.The samples and standards were thoroughly ground to a fine powder into an agate mortar in order to minimize grain size difference.All measurements were carried out using a compacted powder layer to prevent insufficient absorption and back scattering of the exciting radiation.

The values of $\Delta\Phi$,and $\Delta\Phi_{ST}$ are determined by integrating the emission intensity over the total spectral range in the emission spectra plotted as quanta per wavelength interval (photons $s^{-1}nm^{-1}$) versus wavelength(mm). The emission spectra must be previously corrected for the spectral dependencies of the photomultiplier response and the grating reflectivity.

The reflection coeffocients are established by scanning the emission monochromator through the excitation wavelength region and integrating the intensities of the spectra thus obtained.In order to have absolute values.

The fluorescence lifetime can be obtained accroding to the fluorescence decay curve of Eu complex solution as shown in Figure 14. The experiment data satisfied very well the monoexponential Eq. (2)[36]:

$$I(t) = I_1 \exp(-t/t_1),$$

where I(t) was the fluorescence intensity varying with t and t_1 is lifetime.

Copyright © 2010. Nova Science Publishers, Incorporated. All rights reserved.

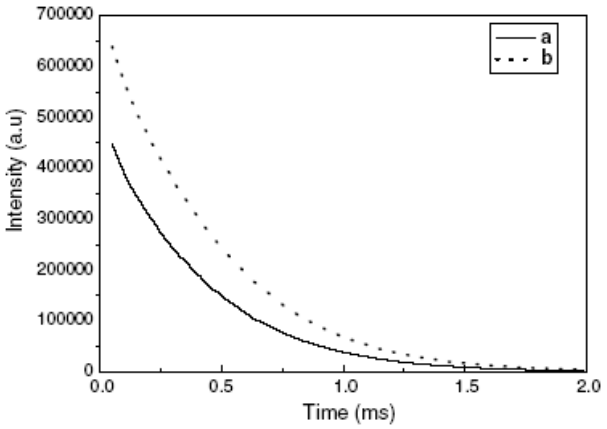

Figure 14. Fluorescence decay curve of Eu ion complexe.

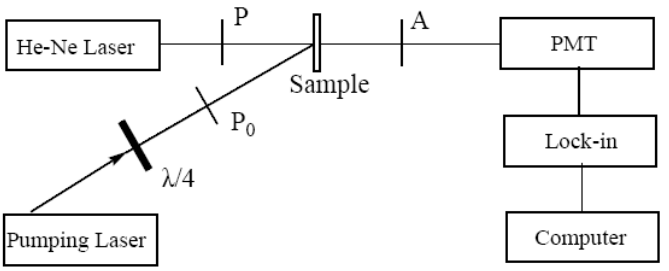

Figure 15. Schematic of experimental arrangement for optimizing photo-induced molecular reorientation by using two polarized actinic beams of two colors.

4.2. Photo-Induced Molecular Reorientation

The LC polymer can be oriented in solid matrices by polarized light due to the accompanying process of trans–cis–trans isomerization [37]. The trans-LC polymer are stable with an elongated molecular form and the cis-LC polymer are photo-induced isomers with a bent form and revert back to trans form thermally or by light.

The experiment of photo-induced anisotropy is performed by use of polarized exciting beams of two colors to investigate the features of optimization of reorientation of the LC polymer molecules. Figure 15 shows the experimental arrangement. The sample is placed between two crossed polarizers (vertical P and horizontal P0) and a weak He–Ne 633 nm beam is used to probe the photo-anisotropy of the sample. Initially no light reaches the detector due to the random distribution of the azobenzene molecules. When an exciting beam polarized at 45^{o} to the vertical from a 442nm He–Cd laser, 533nm Nd-YAG or 488nm Ar+ irradiates the sample, the analyzer transmits some 633nm light. This photoinduced anisotropy is due to the reorientation of LC polymer molecules induced by the pupming light. The LC chian transition moment lies along the molecular axis and only the molecules with their

Copyright © 2010. Nova Science Publishers, Incorporated. All rights reserved.

orientation parallel to the electric vector absorb light. The repeated trans–cis–trans isomerization results in the alignment of LC polymer molecules in the direction perpendicular to the polarization of the exciting beam.

4.3. Third-Order Nonlinear Optical Properties

The third-order nonlinear optical properties have been investigated using the Z-scan technique in the nanosecond regime[26, 38]. The experimental setup used in this work is schematically shown in Figure 16. Z-scan measurements were performed using a Q-switched Nd-YAG laser emitting at 442nm, 533nm, 488nm or 1064 nm. Laser pulses were converted in second harmonic pulses resulting in the final 532 nm wavelength. A low wavelength pass filter was used to remove any remaining power. Generally, the sample measurements were performed using a 10Hz repetition rate in order to minimize the nonlinear thermal effect and sample damaging.

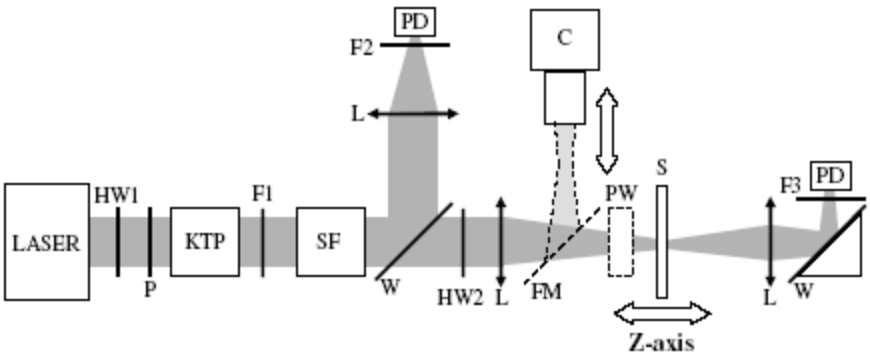

Figure 16. Experimental setup for P-scan and Z-scan measurements. Laser. HW1: half-wave plate (1064 nm). P: polarizer, KTP frequency doubling crystal. F1: absorbing filter for 1064 nm, SF: spatial filter, W: wedge, L: lenses, F2 and F3: attenuators, FM: mirror on a flip mount, C: camera mounted on translation axis, HW2: half-wave plate (532 nm), PW: pyrometer, S: sample mounted on a translation stage, PD: photodiode.

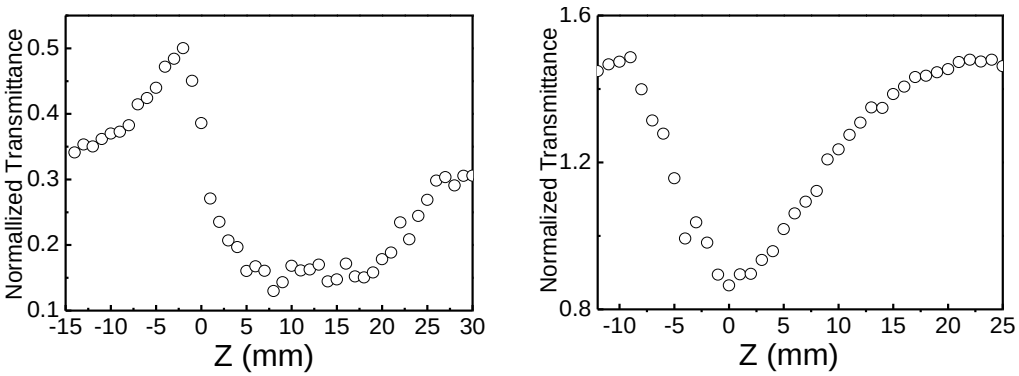

Figure 17. The dependences of the normalized transmittance in the close-aperture and open-aperture.

Copyright © 2010. Nova Science Publishers, Incorporated. All rights reserved.

The laser beam was spatially-filtered and focused by a 100mm focal lens to obtain a beam radius at the beam waist. The beam profile was measured using a CCD camera. The laser beam was separated into a reference arm and a sample measurement arm using a silica wedge. A wedge was used instead of a beam splitter in other to avoid interferences in the focal volume. The intensities of the reference and signal beams were measured using standard photodiodes linked to a digital oscilloscope with a reduced 20MHz bandwidth. Special attention was taken to set-up reference and signal arms as similar as possible. Thus, optical paths of the reference line and the sample line were kept close to each other in order to minimize the measurement delay between pulses. Furthermore, incoming powers were set at similar values in order to obtain as identical photodiode responses as possible. Finally, the sample was mounted on a motorized translation stage.

Figure 17 presents the results of Z-scan experiment for the nanocomposite film[25]. the third-order susceptibility can be considered as a complex value

$$\chi^{(3)}=\mathrm{Re}\chi^{(3)}+i\ \mathrm{Im}\chi^{(3)}$$

Where the real part ($\mathrm{Re}\chi^{(3)}$) is connected with the nonlinear refraction and the imaginary part ($\mathrm{Im}\chi^{(3)}$) is connected with the nonlinear absorption as shown follow equation(1) and (2). The nonlinear refraction and nonlinear absorption of pure PMMA was negligible:

$$\mathrm{Re}\chi^{(3)}= n_2\cdot n_0/3\pi \quad (1)$$

$$\mathrm{Im}\chi^{(3)}= \beta\cdot n_0\cdot\varepsilon_0\cdot c^2/\omega \quad (2)$$

For the calculations of nonlinear refractive indices (n_2) and nonlinear absorption(β) of the samples we used the equations (3) and (4),respectively. Where ω is the laser radiation frequency and ε_0 is the electric permittivity of free space.

$$n_2 =\Delta T_{p-v}/[0.406\ (1-S)^{0.25}\cdot|(2\pi/\lambda)\ I_0\ L_{\mathrm{eff}}|] \quad (3)$$

$$T(z) =(\beta I(z)\ L_{\mathrm{eff}})^{-1}\ \ln(1+\beta I(z)\ L_{\mathrm{eff}}) \quad (4)$$

where ΔT_{p-v} is the peak-to-valley transmission difference in the Fig.4A, $T(z)$ is dependence in open-aperture scheme as shown in Fig.4B, I_0 is the radiation intensity at the focal point, S is the transmission of the aperture and Leff is the sample's effective length.

5. The Effects of Silver Nanoparticles on Optical Materials

5.1. The Effect of Silver Nanoparticles' Concentration

5.1.1. Fluorescence

The enhancement fluorescence and the quenching fluorescence all depend on the concentration of silver nanoparticles[3-5]. Firstly, silver colloids have one of surface-

Copyright © 2010. Nova Science Publishers, Incorporated. All rights reserved.

enhanced phenomena based on the large electromagnetic field arising from the excitation of surface plasmon polariton (SPP). Furthermore, the enhancement field around silver metallic nanostructures is strongly enhanced when two or more particles come into close proximity with each other as shown in Figure 18 [39]. When silver nanoparticles is irradiated by light in its range of resonant frequency, the resonance plasmon of particle occurrs and make local electromagnetic fields near the particle many orders of magnitude higher than the incident fields of single particle. So the enhancement factor increases with increasing in concentration of silver nanoparticle. On the other way, the quenching effect of silver nanoparticle also increases with increasing in concentration of nanoparticles, resulting from the re-absorption of surface plasmon resonance (SPR) and silver nanoparticles scattering. So, generally the enhancement factor firstly increases with increasing in silver colloidal concentration and decreases rapidly with further increasing in concentration.

5.1.2. Photo-induced re-orientation rate

As well-known, silver colloids have one of surface-enhanced phenomena based on the large electromagnetic field arising from the excitation of surface plasmon polariton (SPP). And, surface plasmon polariton (SPP) around LC polymer is strongly enhanced when two or more silver nanoparticles come into close proximity with each other. On the other hand, exciting the plasmon resonance of the particles would lead to light absorption and local heating, which clearly makes it easier for the molecules to re-orientate. The above two aspects both promote the photo-induced reorientation of LC groups especially for the fast growth progress that was thought to depend on the quantum yield of the isomerization reaction, the isomerization rate and the local mobility of the LC polymer molecule. So, it is clearly seen that the re-orientation rate rapidly increases with the increase of the silver content as shown in Figure 19. On the other way, however as the sliver content increased further, the enhancement effect began to reduce. The result is attributed that the silver as filler on the polymer matrix reduce the free volume of polymer chian, which effective inhibit the movement of LC of polymer[12]. Eventually, the reorientation rate of the doped sample was even lower than that of the undoped sample. So, generally the reorientation rate at least for “fast” progress can be largely enhanced when using an appropriate dopant content of silver nanoparticles.

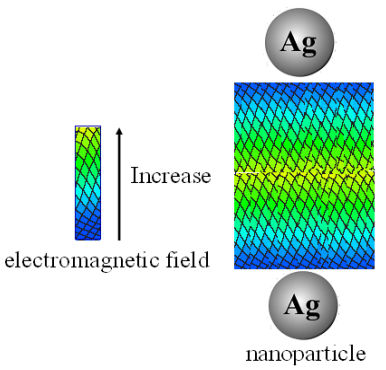

Figure 18. The representation of the large electromagnetic field between silver nanoparticles.

Copyright © 2010. Nova Science Publishers, Incorporated. All rights reserved.

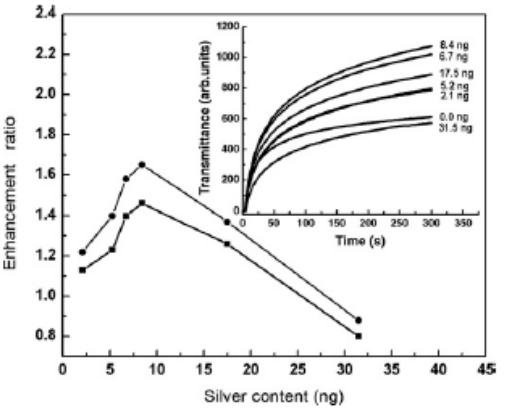

Figure 19. The re-orientation rate of LC polymer depended on the concentration of silver nanoparticles.

5.1.3. Third-order nonliner optical property

The third-order nonliner optical property is also strongly depended on the silver content [25, 28]. As well-known, the the intensity of large electromagnetic field increases with increase in silver content. So, generally, the third-order nonlinear susceptibility incerases with with increase in silver content, whereas neither dissolved in normal solvents nor doped in polymer film. But there should be one assumption that the particle is well dispersion in solid mterials and the interaction between particles is not considered.

YY. Sun has reported the preparation and nonlinear optical properties of Ag doped in PMMA film[25]. The result shows that the third-order nonlinear susceptibility increases with the increasing in the concentration of Ag doped in PMMA film. When the concentration of Ag doped in PMMA is 2.4%, the third-order nonlinear susceptibility is 6.22×10^{-9} esu, which close to the largest value (10^{-7} esu) of noble metallic nanoparticles embedded in inorganic materials. Here it can point out important effects for the enhancement third-order nonlinear susceptibility due to good distribution.

At the same reason, there are particle coalescence or percolation, the third-order nonlinear susceptibility will decrease. In one case, the nonlinear optical properties of Ag:Bi_2O_3 films is also measured for with different Ag concentration are plotted in Figure 20[28]. It can be seen that the value of third-order nonlinear susceptibility is enhanced with increasing Ag concentration up to 35.7%, and then rapidly decreases. There are two factors determining the enhancement of effective nonlinearity for metal-dielectric composites: the nanoparticle density [40] and the local filed near and inside particle [41]. For Ag:Bi_2O_3 films with relatively low Ag concentration (<35.7%), the increase of Ag concentration mainly results in an increase of particle density and decrease of interparticle spacing that enhances the multiple particle electromagnetic interaction as above-mentioned discussion about the SPR absorption, leading to an enhancement of the local field. Both effects can enhance the effective third-order nonlinear susceptibility. At higher Ag concentration, due to particle coalescence or percolation, the local field will be averaged out [42], leading to the significant weakening of the enhancement effect.

Copyright © 2010. Nova Science Publishers, Incorporated. All rights reserved.

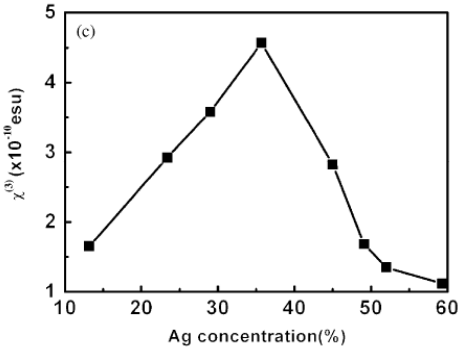

Figure 20. The third-order nonliner optical property of LC polymer depended on the concentration of silver nanoparticles.

5.2. The Effect of Nanoparticles' Size

5.2.1. Fluorescence

The enhancement and the quenching fluorescence are all mainly attributed to the SPR absorption of silver particles [3-5]. And the SPR absorption of silver nanoparticles strongly depends on their size [43]. It is obviously seen from the Table 1 that the enhancement factor decreases with increasing in size and size distribution of silver nanoparticles[3-7]. The obtained maximum enhancement factor for each sample is thus regarded as the result of a delicate balance between the enhancing and the quenching effect. The SPR absorption peak is red shift with increasing in size of silver nanoparticles. So, the resonant energy level (350nm) between ligand and Lanthanon ion is far from absorbing region of Ag colloids and the intensity of located electromagnetic field decreases with increasing in size of particles, resulting in a decrease of enhancement factor.

Since the kind of small silver colloid shows characteristic absorption band in Uv-visible region, the decrease of enhancement factor is also due to re-absorption of surface plasmon resonance (SPR) of silver colloids as shown in Table 1. The absorption bands of particles are 320nm-500nm, 320nm-700nm and 320nm-800nm corresponding to the size of 9.7nm, 15.7nm and 27.1nm, respectively. The emission photon of Lanthanon complexes (wavelength of 615nm) is re-absorption and scattered by the particles with size of 15.7nm and 27.1nm. Contrarily, the quenching effect due to re-absorption of surface plasmon resonance is almost ignoring at the size of 9.7nm. Therefore, SPR re-absorption of Ag colloids must be taken into consideration in order to improve the enhancement factor.

Table 1. The effect of the particle size on the enhancement factor and C_{max}

Size(nm)	Absorption peak (absorption band)	Enhancement factor	C_{max}
9.7	400nm(320nm-500nm)	>1.35	>1.5 ×10^{-9} mol/L
15.9	420nm(320nm-700nm)	1.35	6.0×10^{-10} mol/L
27.1	460nm(320nm-800nm)	1.15	8.0×10^{-11}mol/L

Copyright © 2010. Nova Science Publishers, Incorporated. All rights reserved.

And each sample shows a different particle concentration at which the enhancement factor reaches the maximum (C_{max}) as shown in Table 1. The enhancement C_{max} is strongly determined by the size of the silver nanoparticles, too. The decreasing tendency in C_{max} values with increase in the particle size further indicates the increase in the quenching effect arising from the two interactions(re-absorption and scattering).

In summary, the observed fluorescence intensity is thus regarded as the result of the delicate balance between enhancing and quenching effect of the silver nanoparticles, which are all strongly dependent of the particle size. Generally, smaller particles had larger enhancement factor and the higher particle concentration region (C_{max}). Finally, it is pointed out that the observed changes in the fluorescence properties are attributed to the formation of the particle aggregates in the solution. It should also be noted that the enhancement fluorescence was observed despite the off-resonant condition between the excitation wavelength (276 nm) and the surface plasmon (ca.400nm), and these findings suggest that the improvement of enhancement factor is expected even in the solution phase by optimizing the design of both nanoparticles and Lanthanon complexes.

5.2.2. Photo-induced re-orientation rate

The enhancement of reorientation rate also depends mainly on size of silver particles. But, there are few works reporting the effect of silver nanoparticles' size on the reorientation rate.

For approving the above mechanism, the polymer films containing LC groups and silver nanoparticles were prepared[12]. Photo-induced reorientation was performed on the films under polarized light with wavelength at 442nm, 532nm and 365nm, respectively. The influence of silver nanoparticles on the photo-induced reorientation of the films was studied, in which the SPR bands is at 450nm. It is obviously seen that the largest enhancement was obtained when film samples were irradiated with 442nm light that is identical to the maximum absorbance wavelength of silver nanoparticles at 450nm wavelength. The enhancement was weaker when irradiating with light at 532nm because a weaker absorption can be detected at about 532nm wavelength in sliver nanoparticles' absorption spectrum. Moreover, the enhancement disappeared when induced by 365nm wavelength light for no plasmon resonance absorption of Ag nanoparticles at 365nm wavelength. The above results provide a strong evidence for resonance plasmon effect of silver nanoparticles on reorientation enhancement of LC groups.

At the same mechanism, when the wavelength of pumping laser is 442nm, the SPR bands are closer to the wavelength and the larger enhancement is obtained, in which the SPR band is controlled by the size and surface property of silver nanopartilces.

5.2.3. Third-order nonlinear optical properties

There are few works and mechanism reporting the effect of silver nanoparticles' size on the third-order nonlinear susceptibility. For approving the mechanism that the enhancement nonlinear optical absorption also deepens on their size, the nonlinear optical absorption in silver nanosol was discussed at selected wavelengths using open aperture Z-scan technique[44]. The SPR band of doped noble nanoparticles is about 550nm. The third-order nonlinear susceptibility at different wavelengths around the plasmon peak is presented in Figure 21. The NLO parameters of metallic nanoparticles embedded in an inert dielectric

Copyright © 2010. Nova Science Publishers, Incorporated. All rights reserved.

matrix system can be predicted using the Maxwell±Garnett theory. This theory predicts strong enhancement of the NLO properties near the surface plasmon resonance. Considering the wavelength variation of the surface plasmon enhancement factor as the most important term in governing the optical properties, a simple estimate gives a scaling of third-order nonlinear susceptibility with the square of the absorption coefficient.

The above results also provide a strong evidence for resonance plasmon effect of silver nanoparticles on third-order nonlinear susceptibility, which is also generally adjusted by the size and surface property of silver nanoparticles.

5.3. The Effect of Solid Phase

5.3.1. Fluorescence

The use of silver nanostructures in solid phase as fluorescence enhancers is an attractive challenge and has been studied [9, 45-51]. Enhancement fluorescence from Lanthanon ion owing to surface plasma oscillation of silver particles in solid sphase, such as $10B_2O_3$-$90SiO_2$, TeO_2-PbO-GeO_2, SiO_2 and TeO_2-PbO-GeO_2 glass were easily observed. Even if the Lanthanon ion and bare silver nanoparticles were distributed in matrix of SiO_2 glass, in which the protecting molecule or functional molecule was not used. As above discussion in solution phase, the quenching fluorescence was observed in the absence of protecting molecule or functional molecule due to Lanthanon ion being far from silver nanoparticles. Here, the Lanthanon ion can be close proximity to the silver metallic surface with the help of the solid phase. So, here it can point out important effects for the enhancement fluorescence of Lanthanon ions due to surface plasma oscillation of silver particles in solid sphase : (1) the particle sizes and their distribution, (2) the volume fraction, and (3) energy matching between the surface plasmon frequency of a particle and the excitation energy of Lanthanon ions.

In some cases, a sol-gel method was also used to prepare GeO_2-Eu_2O_3-Ag films, in which the luminescence efficiency of Eu ions during UV excitation was comparable to that in films activated by organic Lanthanon complexes. It was found to be complex Eu-Ag centers with a high quantum yield of the intracenter transfer of excitations to the rare-earth activator from silver ions and Ag oligomer clusters located on the surface of silver nanoparticles.

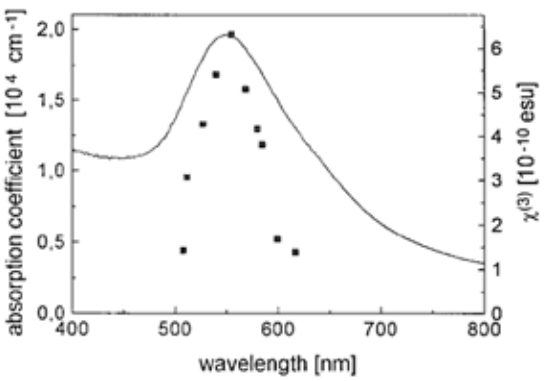

Figure 21. The third-order nonliner optical property of composite film depended on the wavelength of laser.

Copyright © 2010. Nova Science Publishers, Incorporated. All rights reserved.

Additionally, enhancement and quenching fluorescence from samarium (Sm) ions owing to surface plasma oscillation of silver particles in "Aerosil" silica glasses was also investigated. The introduction of silver into the Sm-containing silica glasses prepared by the original sol-gel method leads to the formation of complex optical centers involving Sm ions and simple and/or complex silver ions. The formation of Sm-Ag centers was accompanied by an increase in the concentration of non-bridging oxygen ions, which prevent the reduction of silver ions by hydrogen. Silver nanoparticles formed in small amounts upon this reduction were effective luminescence quenchers from the corresponding excited states of Sm ions. However, the SEF of Sm ion in the solution system is few studies. So, systematic studies are required to elaborate the relation between SEF and SPR in solution with respect to the condition of silver nanoparticles for further application.

5.3.2. Photo-induced re-orientation rate

The enhancement of re-orientation rate stronghly depends on the structure of matrix LC polymer. When the LC group of the polymer has strong interaction with the silver nanoparticles, the movement of LC chain is difficult, resulting in decrease of reorientation rate. Eventually, the reorientation rate of the doped sample was even lower than that of the undoped sample. So the LC polymers structure is very important to obtain the enhancement of reorientation rate [12, 20-21]. In one case**,** the different structure of molecules (P1 and P2) is shown in Figure 22, in which LC chain of P1 has strongh interaction with silver metallic spheroids. So, the formation of nanoparticles in nematic polymer matrix P1 leads to a rapid increase of the glass transition and a less-significant decrease of the clearing temperature as shown in Table 2. As a result, the overall mesophase stability is rapidly decreasing.

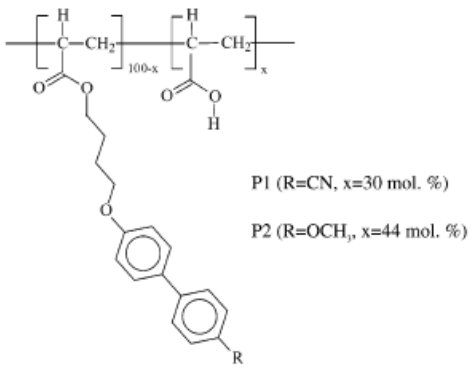

Figure 22. The Scheme of different structure of LC polymer.

Table 2. The glass transition and clearing temperature of LC polymer containing silver nanoparticles

	concentration	melt		glass	
		orign	after	orign	after
P1	2%	98	90	35	58
P2	2%	135	130	54	54
P3	50%	168	168	126	126

Copyright © 2010. Nova Science Publishers, Incorporated. All rights reserved.

It shows that nanocomposites P2-Ag are able to form an LC phase, in which the movement of LC chain is not affected by the silver nanoparticles due to no interaction between P2 and silver nanoparticles.

Thses indicate that, as in P1-Ag, silver nanoparticles influence negatively the mesophase stability. However, due to the different chemical structure, P2 is less sensitive to this influence.

The data on the phase behavior and structure of the nanocomposites P1-Ag and P2-Ag discussed above let us make the first important conclusion. Nanoparticles are not passive elements of the mesomorphic polymer matrix. On the contrary, they are able to influence significantly the temperature interval of LC phase. It is of evident interest to understand the nature and mechanisms of such influence, as well as its interconnection with the chemical structure of polymer matrix. So, in oder to obtain the enhancement of reorientation rate funtions, the polymer LC should contain the funcational group that has strongh interaction with silver nanoparticles, and at the same time, the LC group has no interaction with silver nanoparticles. Generally, the polymer LC is copolymer as shown in Figure 21, and the LC chian can not contian the funtional group -CN, $-NH_2$ and so on. In the other way, the unit of copolymer contains the functional group.

However, there are lots of LC polymer, in which the LC group contain the -CN, $-NO_2$, $-NH_2$ and so on that have strong interaction with silver nanoparticles. Here, the enhancement of re-orientation rate is difficult to be observed due to the interaction inhibiting the movement of LC chain. Taking this into consideration, here a new synthetic approach to mesomorphous nanocomposite polymer system has been developed[20]. The key is that -S- groups were introduced to terminus of LC polymer by RAFT polymerization as shown in following Figure 23. It is expected to efficiently avoid the interaction between LC units and Ag because the thiol groups tend to form preferentially complexes comparing with other groups (-CN, $-NH_2$ and so on) of LC units on Ag nanoparticles[52]. As shown in Table 2, the glass and metal temperature of P3 is same with that of the P3 adsorped on silver nanoparticles. Which effectively indicate the conclusion. It will provide an opportunity to obtian enhancement of reorientation rate.

5.3.3. Third-order nonlinear optical properties

Let us consider a nonlinear random composite in which nonlinear spherical metal particles with concentric coating shell are randomly embedded in a linear matrix[53]. The radii of the core and the shell are a and $a+t$ (t is the thickness of interfacial layer). Dielectric constants of the linear shell and dielectric matrix are given as ε_s and ε_m, respectively. It is known that the nonlinearity $\chi_e^{(3)}$ of the composite can strongly depended on the embedding nonlinear small metal particles and the matrix as follows:

$$\chi_e^{(3)} = f\chi_c^{(3)}\left(\frac{3\varepsilon_m}{p}\right)^2\left|\frac{3\varepsilon_m}{p}\right|^2$$

where $\chi_c^{(3)}$ is the third-order nonlinear susceptibility of nonlinear small metal particles ; ε_m is the Dielectric constants of the linear dielectric matrix ; f is the volume fraction of metal particles.

Copyright © 2010. Nova Science Publishers, Incorporated. All rights reserved.

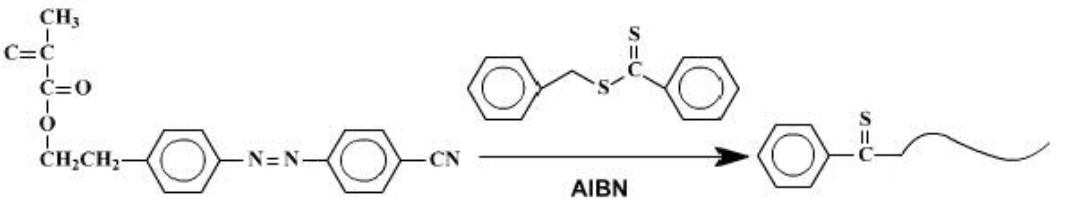

Figure 23. Schematic representation of P3 prepared by RAFT.

$$P \equiv \varepsilon_c^{(0)}(1-f)+[2(1+I/a\varepsilon_m)-f(2I/a\varepsilon_m-1)]\varepsilon_m$$

where where $\varepsilon_c^{(0)}$ is the linear dielectric function. when I=0 (corresponding to sharp and smooth interface).

According to the above Equations, The $\chi_e^{(3)}$ is determined on the $\varepsilon_e^{(0)}$and $\chi_e^{(3)}$ of silver particles, and the dielectric properties. When the dielectric constants of the linear dielectric matrix is larger, the he $\chi_e^{(3)}$ is larger. So, for a nonlinear random composite, the property of matrix also affact the third-order nonlinear optical properties.

In some case[25], when the silver nanoparticles is doped into polymer film with the concentration of 2.4%, the composite film shows high third-order nonlinear susceptibility of 6.22×10^{-9} esu. However, the third-order nonlinear susceptibility of the silver collodial solution was measured to 1.22×10^{-11} esu, in which the Ag particles and its content were same with nancomposite polymer film. The difference is attributed to the various matrix for the silver nanoparticles, in which the dielectric constants (ca. 2.8) of the linear dielectric PMMA matrix is lower than that of DMF solution(ca.70).

Additional[19], the ultrafast nonlinear optical properties of co-sputtered silver/bismuth oxide (eg. Ag:Bi_2O_3) nanocomposite films with different Ag concentration (13.2–59.3 at%) were also investigated by femtosecond (fs) pump–probe and fs optical Kerr effect techniques. The result of the femtosecond OKE measurements showed that the third-order susceptibilities of Ag:Bi_2O_3 films have a maximum of 4.1×10^{-10} esu at Ag concentration of 35.7%.

Furthermore, nonlinear optical response of silver nanoparticles synthesized by ion implantation in silicate glasses (ε_m=1.6) was investigated in ultraviolet range 354.7 nm and laser radiation 1064 nm[30-31]. It was shown that $\chi^{(3)}$ in ultraviolet range (354.7 nm) of Sg :Ag was calculated to be 6.1×10^{-8}esu. It is considered that the Sg :Ag composite materials as effective homogeneous media. The legitimacy of this approach proves to be true by the fact that the sizes of MN are much smaller than the wavelength used in experiment. For an effective homogeneous medium described by the presence of resonant transitions one can apply the standard two-level model. In addtion to this, The variations of the sign of the nonlinear refractive in Nd :YAG laser radiation (λ = 1064 nm) indices depending on matrix properties are analyzed. The SG:Ag and SLSG:Ag was calculated to be 1.5×10^{-8} esu and -3.5×10–8 esu, respectively.

Here it can point out important effects for the enhancement nonlinear optical response due to surface plasma oscillation of noble particles in glass: (1) the particle sizes and their distribution, (2) the volume fraction, (3) the particle' distribution in solid matrix, and (4) the dielectric constants of the linear dielectric matrix.

Copyright © 2010. Nova Science Publishers, Incorporated. All rights reserved.

6. APPLICATION

6.1. Optical Limiting Behavior Based on Third-Order Nonlinear Optical Properties

The advent of high power lasers, in both civilian and military applications, makes the search for efficient optical limiters for a wide range of personnel and equipment (e.g., sensor) protection the highest priority[54]. An ideal optical limiter exhibits a high, linear transmission below a certain "limiting" threshold, but its intensity is greatly attenuated (opaque with constant, low, and nonlinear transmittance) above the threshold. Among many promising optical limiting materials, organometallic, metallophthalocyanines, metalloporphrins, and metal clusters containing a small number of metal atoms have attracted considerable attention. Compared to organic optical limiting materials, these compounds have the advantage of multiple electronic transitions such as metal-ligand charge transfers. However, these systems often suffer from low damage threshold and inefficient optical limiting.

So, the nonlinear optical properties of silver nanoparticles are currently being explored with great interest, which is expected to suffer from high damage threshold and inefficient optical limiting. It shows that in either solid film or in solution, structurally well-defined Ag nanoparticles can achieve nearly 2 orders of magnitude of attenuation of highintensity laser power. More importantly, it opens the door to a new class of highly promising optical limiting materials based on nanosized metal clusters. In one case[55], the silver colloidal solutions were prepared by in-situ synthesis technique in the presence of the PMMA, which was polymerized by Reversible addition-fragmentation transfer. The average size of sphere silver nanoparticles is about 10nm. It shows the optical limiting properties at 532 nm as shown in Figure 24. The energy transmittance decreases when the input energy increases. The limiting threshold was about 161J/cm^2. The limiting characteristics result from the RSA effect of the sample, which is one of nonlinear absorption mechanisms. Optical limiters have many applications, including eye and sensor protection[56], optical information processing [57] and optical communications [58].

Copyright © 2010. Nova Science Publishers, Incorporated. All rights reserved.

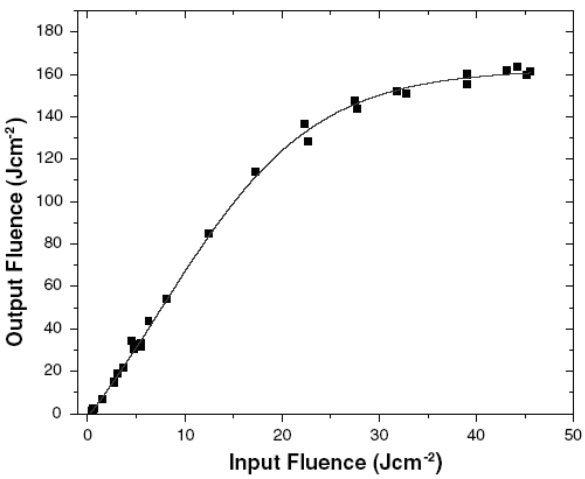

Figure 24. Optical limiting curve of the silver colloidal solution at 532nm.

In conclusion, the Ag nanomaterials in stabilized suspensions are potent optical limiters toward nanosecond laser pulses in the green, and the optical limiting properties are stable and insensitive to changes in the nanoparticle-related parameters. The optical limiting responses in the nanomaterial are likely dominated by a nonlinear absorption mechanism, though the details remain to be explored in further investigations. In addition to this, the works are in progress to design and fabricate new optical limiters based on nanosized metal clusters and to understand their optical limiting mechanism.

6.2. Optical Switching Based on Third-Order Nonlinear Optical Properties

Recent years have witnessed dramatic progress in the design of all-optical switching devices for ultrafast high band width optical communication and computing. Optical switching which enables routing of optical data signals regardless of data rate and data protocol has the advantage on conventional electrical switches to redirect the information without the expensive and power consuming optical–electrical–optical conversion. Thus, optical switching allows treatment of future data rate upgrades [59-61]. Applications of optical switching include protection and restoration in optical networks, bandwidth provisioning, wavelength routing and network monitoring.

Current interest has focused on molecular devices that offer advantages of small size and weight, extremely low propagation delay, high intrinsic speed and ability to tailor properties to suit the specific device configurations

Recently, all-optical switching based on nonlinear excited-state absorption has been demonstrated in different molecular configurations such as liquid crystals, rubidium vapor, organometallic phthalocyanines, polydiacetylene, poly(methyl methacrylate), PVK and azobenzene dyes, polymethine dye, 2-(20-hydroxyphenyl) benzoxazole, fullerene C60 and naturally occurring retinal protein bacteriorhodopsin[62-64].Organometallic compounds are prospective nonlinear materials, as they exhibit large optical nonlinearities. Organometallic compounds have a number of advantages over organic compounds. But, these systems often suffer from low intrinsic speed and ability to tailor properties. So, the silver nanoparticles are currently being explored with great interest for application on optical switching based on third-order nonlinear optical effects, which is expected to suffer from high intrinsic speed and ability to tailor properties

In one case[25], The $\chi^{(3)}$ of the Ag nanoparticles doped PMMA film was obtained by Z-Scan technique and increased with increase in concentration of Ag doped in PMMA. When the concentration of Ag doped in PMMA is 2.4%, the $\chi^{(3)}$ is 6.22×10^{-9} esu.

The possibilities of materials' applications as optical switching elements are further analyzed. The critical parameter that applies for estimation of optical switching effectiveness is the ratio between nonlinear absorption coefficient and nonlinear refractive index at the investigated wavelength[65].

$$K = \beta\lambda/n_2$$

Where n_2 is the nonlinear refractive index in SI units. In the case of Ag nanocomposite materials, the K is 8.48, 0.26 and 1.25 corresponding to concentration of 0.3%, 0.8% and

Copyright © 2010. Nova Science Publishers, Incorporated. All rights reserved.

2.4%, respectively. The materials at concentration of 0.8% lead to $K< 1$, and therefore makes the material the prospective ones for optical switching applications at the wavelength of 532 nm.

It is expected that the homo-size Ag nanopaticles can be obtained and controlled if amphiphilic copolymer with surfer end group is further introduced in the technique, and corresponding investigations on synthesis and optical properties are currently in progress.

7. CONCLUSIONS

Surface-enhanced optical properties based on the surface plasmon resonance (SPR) of silver metal nanoparticles has been dicusssed on improving fluorescence properties of Lanthanon complexes, nonlinear optical properties of composite and reorientation rate of LC polymer. At the same time, the observed quenching fluorescence is attributed to the re-absorption of SPR and photon scattering by silver metal nanoparticles, interaction between optical materials and silver nanoparticles. And then the enhancing and quenching effect strongly depend on silver metal particle size and concentration.There are lots of problemes to be investigated in the future. In some cases, the effect of distance between Lanthanon complexes and silver nanoparticles on SEF has few considerations, resulting in being relatively low enhancement factor (<10). Furthermore, it has few reports on optical memory polymer materials, nonlinear optical polymers materials and polymer optical fiber perform based on the surface-enhanced fluorescence and enhancement of photo-induced re-orientation rate. In addition, the effec of silver particles size and shape on mechanism and physical process of third-order nonlinear optical properties and enhancement of photo-induced re-orientation rate have been fewly reporting. The chapter discussions are very value to further improve overall enhancement factor and C_{max}, which are key to be applied in optical materials for the surface-enhanced optical properties phenomenon of silver nanoparticles.

Copyright © 2010. Nova Science Publishers, Incorporated. All rights reserved.

REFERENCES

[1] Knut Johansen, Ralph Stålberg, Ingemar Lundstr ¨om, Bo Liedberg, Meas. *Sci. Technol*., 2000, 11, 1630.
[2] Kretschmann, E. *Z. Phys*., 1971, 241, 313.
[3] Yuehui Wang, Ji Zhou, Ting Wang, *Materials Letters*, 2008, 62, 1937.
[4] Nabika, H; Dekia, S. *Eur. Phys. J. D*, 2003, 24, 369.
[5] Yuehui Wang, Xinran Zhou, Ting Wang, Ji Zhou, *Materials Letters*, 2008, 62, 3582.
[6] *J. Phys. Chem. B*, 2003, 107, 9162.
[7] Youyi Sun, Zhi Zheng, Qing Yan, Jiangang Gao, Hongfang Jiu, Qijin Zhang, *Materials Letters*, 2006, 60, 2756.
[8] Youyi Sun, Hongfang Jiu, Douguo Zhang, Jiangang Gao, Bin Guo, Qijin Zhang, *Chemical Physics Letters*, 2005, 410, 204.
[9] Tomokatsu Hayakawa, Kazunori Furuhashi, Masayuki Nogami, *J. Phys. Chem. B*, 2004, 108, 11301.
[10] Wang, DS; Kerk er, M. *Physical review B*, 1981, 24, 1777.

[11] Tawa, K; Kiyohara, K; Kamada, K; Ohta, K; Sekkat, Z; Kawata, S. *Macromolecules*, 2001, 34, 8232.
[12] Jingli Zhou, Jianjun Yang, Youyi Sun , Douguo Zhang, Jing Shen,Qijin Zhang, Keyi Wang, *Thin Solid Films*, 2007, 515, 7242.
[13] Mengtao Sun, Lixin Xia, Maodu Chen. *Spectrochimica Acta Part A: Molecular and Biomolecular Spectroscopy*, 2009, 74, 509.
[14] Guang Yang, Dongyi Guan, Weitian Wang, Weidong Wu, Zhenghao Chen, *Optical Materials*, 2004, 25, 439.
[15] Barrera, RG; Monsivais, G; Mochan, WL; Del Castillo, M. *Physica A: Statistical Mechanics and its Applications*, 1989, 157, 369.
[16] Unnikrishnan, KP; Nampoori1, VPN; Ramakrishnan, V; Umadevi, M; Vallabhan, CPG. *J. Phys. D: Appl. Phys.*, 2003, 36 , 1242.
[17] Si Wu, Youyi Sun, Xin Wang, Wenxuan Wu, Xiujie Tian, Qing Yan, Yanhua Luo, Qijin Zhang, *Journal of Photochemistry and Photobiology A: Chemistry*, 2007, 191, 97.
[18] Bouchama, F; Thathagar, MB; Rothenberg, G; Turkenburg, DH; Eiser, E. *Langmuir*, 2004, 20, 477.
[19] Andersson, M; Alfredsson, V; Kjellin, P; Palmqvist, AEC. *Nano Lett*, 2002, 2, 1403.
[20] Evgenii, B; Barmatov, Dmitry, A; Pebalk, Marina, V. Barmatova, *Langmuir*, 2004, 20, 10868.
[21] Jiangang Gao, Youyi Sun, Jingli Zhou, Zhi Zheng, Hongwei Chen, Wei Su, Qijin Zhang, *Journal of Polymer Science Part A: Polymer Chemistry*, 2007, 45, 5380.
[22] Sensors and Actuators B: *Chemical*, 2006, 117, 367.
[23] Jin-Woong Kim, Jung-Eun Lee, Su-Jin Kim, Jong-Suk Lee, Jee-Hyun Ryu, Junoh Kim, Sang-Hoon Han, Ih-Seop Chang, Kyung-Do Suh, *Polymer*, 2004, 45, 4741.
[24] Heilmann, A; Hamann, C; Kampfrath, G; Hopfe, V. *Vacuum*, 1990, 41, 1472.
[25] Youyi Sun, Yaqing Liu, Guizhe zhao, Xing Zhou, Qijin Zhang, Yan Deng, *Materials Chemistry and Physics*, 2008, 111, 301.
[26] Fredrick, W; Vance, Robert, C; Johnson, Buford, I; Lemon, Joseph, T; Hupp, Daniel, L. Feldheim, *J. Am. Chem. Soc*., 2000, 122, 12029.
[27] Shatabdi Porel, Shashi Singh, S. Sree Harsha, D. Narayana Rao, T. P. Radhakrishnan, *Chem. Mater*, 2005, 17, 9.
[28] Guanjun Youa, Peng Zhou, Chunfeng Zhanga, Zhiwei Donga,Liangyao Chen, Shixiong Qian, *Journal of Luminescence*, 2006, 119-120 , 370.
[29] Jean-Michel Lamarre, Franck Billard, Chahineze Harkati Kerboua , Michel Lequime , Sjoerd Roorda, Ludvik Martinu, *Optics Communications*, 2008, 281, 331.
[30] Ganeev1, RA; Ryasnyansky, AI; Stepanov, AL; Usmanov, T. *phys. stat. sol*., (b). 2003, 238, 5.
[31] Ganeev, RA; Ryasnyansky, AI; Stepanov, AL; Usmanov, T. *phys. stat. sol*., (b). 2004, 41, 935.
[32] Hongfang Jiu, Youyi Sun et.al, *Journal of Non-Crystalline Solids*, 2006, 352, 197.
[33] Youyi Sun, Qijin Zhang et.al, Spectrochimica Acta Part A: *Molecular and Bimolecular Spectroscopy*, 2006, 64, 977.
[34] Malta, OL; Brito, HF; Menezes, JFS; Goncalves esilva, FR; de Mello Donega, C; Alves Jr, S. *Chemical Physicas Letters*, 1998, 282, 233.
[35] Bril, A; De Jager-Veenis, AW. *J. Electrochem. Soc*., 1976, 123, 396.

Copyright © 2010. Nova Science Publishers, Incorporated. All rights reserved.

[36] Ren-Jie Zhanga, Kong-Zhang Yanga,*, An-Chi Yub, Xin-Sheng Zhao, *Thin Solid Films*, 2000, 363 , 275.
[37] Pengfei Wu , DVGLN. Rao, *Optical Materials*, 2002, 21, 295.
[38] Minjoung Kyoung, Minyung Lee, *Optics Communications*, 1999, 171, 145.
[39] Chen, YL; Fang, Y. *Spectrochimica Acta Part A: Molecular and Biomolecular Spectroscopy*, 2008, 69, 733.
[40] Pincon, N; Palpant, B; Prot, D; Charron, E; Debrus, S. *Eur. Phys. J. D*, 2002, 19, 395.
[41] Ma, HR; Sheng, P; Wong, GKL. *Topics Appl. Phys*., 2002, 82, 41.
[42] Liao, HB; Xiao, RF; Wang, H; Wong, KS; Wong, GKL. *Appl. Phys. Lett*, 1998, 72 , 1817.
[43] Senoy Thomas, Saritha K Nair, E Muhammad Abdul Jamal, S H Al-Harthi, Manoj Raama Varma, M R Anantharaman. *Nanotechnology*, 2008, 19, 1.
[44] Georg Maxein, Harald Keller, Bruce, M. Novak, Rudolf Zentel, *Adv. Mater*, 1998, 3, 338.
[45] Hayakawa, T; Selvan, ST; Nogami, M. *Journal of Non-Crystalline Solids*, 1999, 259, 16.
[46] Almeida, Rd; da Silva, Davinson, M; Kassab, Luciana, RP; de Arau′ jo, Cid, B. *Optics Communications*, 2008, 281, 108.
[47] Petit, L; Griffin, J; Carlie, N; Jubera, V; García, M; Hernández, FE; Richardson, K. *Materials Letters*, 2007, 61, 2879.
[48] Geddes, Chris, D; Cao, Haishi, I; Gryczynski, Z; Fang, JY; Lakowicz, JR. *J. Phys. Chem. A* , 2003, 107, 3443.
[49] Malashkevich, GE; Shevchenko, GP; Serezhkina, SV; Pershukevich, PP; Semkova, GI; Glushonok, GK. *Physics of the solid state*, 2007, 49, 1891.
[50] Malashkevich, GE; Semchenko, AV; Sukhodola, AA; Stupak, AP; Sukhodolov, AV; Plyushch, BV; Sidski, VV; Denisenko, GA. Physics of the Solid State. 50(2008)1464.
[51] J.A. Jime′nez, S. Lysenko, H. Liu, *Journal of Luminescence*, 2008, 128, 831.
[52] Evgenii, BP; Dmitry, AB; Marina, V. *Langmuir*, 2004, 20, 10868.
[53] Jean-Michel Lamarre, Franck Billard, Chahineze Harkati Kerboua, Michel Lequime, Sjoerd Roorda, Ludvik Martinu, *Optics Communications*, 2008, 281, 331.
[54] Tutt, LW; Boggess, TF. Prog. *Quantum Electron*, 1993, 17, 299.
[55] Yan Deng, Youyi Sun, Pei Wang, Douguo Zhang, Xiaojin Jiao, Hai Ming, Qijing Zhang, Yang Jiao, Xiaoquan Sun, *Current Applied Physics*, 2008, 8, 13.
[56] Shi, S; Ji, W; Tang, SH; Lang, JP; Xin, XQ. *J. Am. Chem. Soc*., 1994, 116, 3615.
[57] Koch, SW; Peyghambarian, W; Gibbs, HM. *J. Appl. Phys*., 1988, 63, 1.
[58] Russ, DM. Proc. *SPIE*, 1986, 630, 161.
[59] Papadimitriou, GI; Papazoglou, C; Pomportsis. AS. J. *Light wave Technol*., 2003, 21, 384.
[60] Wu, B. A comparison of optical switches and their applications, in: NFOEC *Tech. Proc*., Baltimore, MD, USA, 2001, 8-12, 255.
[61] Chaires, D. *All-optical switching, in: NFOEC Tech. Proc., Dallas*, TX, USA, 2002, 15-19, 1868.
[62] Chen, SH; Chen, HMP; Geng, Y; Jacobs, SD; Marshall, KL; Blanton, TN. *Adv. Mater*, 2003, 15, 1061.
[63] Dawes, AMC; Illing, L; Clark, SM; D. J. Gauthier, *Science*, 2005, 308, 672.
[64] Erlacher, A; Miller, H; Ullrich, B. *J. Appl. Phys*., 2004, 95, 2927.

Copyright © 2010. Nova Science Publishers, Incorporated. All rights reserved.

[65] Mizrahi, V; DeLong, KD; Stegeman, GI; Saifi, MA; M. *J. Andrejco, Opt. Lett*, 1989, 14, 1140.

Copyright © 2010. Nova Science Publishers, Incorporated. All rights reserved.

In: Silver Nanoparticles
Editor: Audrey E. Welles, pp. 291-308
ISBN: 978-1-61668-690-1
© 2010 Nova Science Publishers, Inc.

Chapter 7

A BIOMOLECULAR APPROACH ON THE FUNCTIONALIZATION OF SILVER NANOPARTICLES

Aswathy Ravindran[1], M. Ashok Raichur[2], N. Chandrasekaran[1] and Amitava Mukherjee[1*]
[1]Nanobio-medicine Research Group, School of Bio Sciences & Technology, VIT University, Vellore, India
[2]Department of Materials Engineering, Indian Institute of Science, Bangalore, India

ABSTRACT

Nanotechnology involves the production, manipulation and use of materials (nanoparticles) usually in the size range of 1 to 100 nm. Silver nanoparticles offer unusual optical, electronic, and chemical properties due to their ability to effectively interact with photons by virtue of the surface plasmon resonance. Owing to this property, silver nanoparticles are potentially attractive as building blocks for the development of photonic and surface plasmon devices. Silver nanoparticles also exhibit bioactivity and antibacterial properties, which make them attractive for medical and agricultural applications. Moreover the development of nanoparticles for the delivery of therapeutic agents has introduced new opportunities for the improvement of medical treatment. Despite having excellent physical and chemical bulk properties, nanoparticles do not posses suitable surface properties for specific applications like Biomolecular imaging, drug delivery etc. The surface chemistry of the nanoparticles plays a critical role in retaining the biological function of the biomolecules conjugated to nanoparticles. Currently available synthetic methodologies, however, are not satisfactory at providing the appropriate surface chemical properties like water-solubility, biocompatibility and biostability of nanoparticles. There arises the need for surface modification or Biofunctionalization of the nanoparticle where in we attach suitable organic groups to the nanoparticles. It is a process that also stabilizes the nanoparticles against agglomeration and enables their self-organization. Recent efforts have focused on developing targeted nanoparticles, which are formulated by (for therapeutic delivery) functionalizing nanoparticle surfaces with targeting molecules, such as antibodies, peptides, small

Copyright © 2010. Nova Science Publishers, Incorporated. All rights reserved.

molecules and oligonucleotides. Phospholipids derivatives containing disulfide groups were used to modify silver nanoparticle surfaces. The surface modified silver nanoparticles have proved to have improved biocompatibility and intracellular uptake for drug delivery. The biomolecules conjugated with nanoparticles have received the most attention in the field of clinical diagnosis and drug delivery because of their high stability, good biocompatibility and high affinity for biomolecule.

1. AN OVERVIEW ON NANOTECHNOLOGY

Silver is a metal that came into use even before Neolithic revolution and its first recorded medicinal use was reported during 8th century (Moyer,1965).Until the recent past, silver was known only as a metal but with the coming of the nano era people started to believe that silver could even be produced at the nanoscale. The intrigue of nanotechnology came from the ability to control the material properties of such materials by assembling them at the nanoscale. The term nanotechnology came into existence in 1974 when Norio Taniguchi, a researcher at the University of Tokyo, Japan coined the term "nanotechnology" while engineering the materials precisely at the nanometer level (Taniguchi, 1974).It is a field which emphasizes on the control of matter on an atomic and molecular scale. Generally nanotechnology deals with structures of the size 100 nanometers or smaller, and involves developing materials or devices within that size. This definition includes:

Type	Nature	Size range
Nanoclusters	Amorphous or semi crystalline structures	At least one dimension between 1-10nm
Nanopowders	Agglomeration of non crystalline nano structural subunits	At least one dimension less than 100nm
Nanocrystals	Single crystalline nanomaterials	At least one dimension less than or equal to100nm

Nanoparticles (NP) for example take advantage of their dramatically increased surface area to volume ratio. Their optical properties, e.g. fluorescence, become a function of the particle diameter. NPs are of great scientific interest as they form an effective bridge between bulk and atomic or molecular structures. Metal or metal oxide nanoparticles possess many unique properties when compared to matter of the same chemical composition on a larger scale. The synthesis and physical characterization of metal nanoparticles are currently very active fields of research due to their unique electronic, optical and catalytic properties (Tang *et al.*, 2005) originating from their quantum-scale dimensions (Alivisatos *et al.*, 1996).

This review attempts to create an insight into silver nanoparticles, where we shall discuss the importance, the functionalization of silver nanoparticles, various biofunctionalizing techniques involved and the possible applications of both functionalized and non functionalized silver nanoparticles.

This review is divided into four sections. The first section emphasizes the importance of silver nanoparticles and its applications in various fields. The various techniques involved in the synthesis and characterization of silver nanoparticles will be discussed in the second

Copyright © 2010. Nova Science Publishers, Incorporated. All rights reserved.

section followed by the various concepts and techniques involved in the functionalization of silver nanoparticles using biomolecules. And the last section focuses on the applications of the functionalized nanoparticles

2. PROPERTIES AND APPLICATIONS OF SILVER NANOPARTICLES

2.1. Optical Properties of Silver Nanoparticles

Silver nanoparticles have been known for excellent optoelectronic properties (Nie *et al.*, 1997). Optical properties of silver nanoparticle strongly depend on the size, shape, structure, composition and the presence of adsorption layers and their environment including the spatial ordering of particles (Henglein *et al.*,1993*).*Optical properties of silver nanoparticles has received much attention due to their potential in advanced photonic and sensor applications.

The absorption and scattering spectra of metal nanoparticle with sizes above 2 nm is governed by the presence of an intense and broad band in the visible range or in the adjacent near-IR and -UV ranges. This band is referred to as the surface plasmon resonance (SPR) band or, more frequently, the Mie resonance. Silver exhibits the highest extinction ratio in the SPR band peak among not only metals, but also the other known materials that absorb in the same spectral range.

The frequency of the surface plasmon resonance is governed by various factors like shape, size, and dielectric properties of the particle environment, interparticle interactions and the electron density in the metal. This frequency can either be blue- or red-shifted depending on injection or withdrawal of electrons from the nanoparticles by varying the applied potential in an electrochemical environment [Foss *et al.,* 1999 and Mulvaney *et al.,* 1997].

2.2. Silver Nanoparticles as a Catalyst

A major application of silver nanoparticles is its use as a catalyst. Jiang *et al.*, (2004) reported the catalytic properties of silver nanoparticles supported on silica spheres. The silica sphere immobilized silver nanoparticles were tested for their ability to catalyze the reduction of dyes by sodium borohydride. Catalysis of dyes was chosen because it is easy to detect a change in color when the dyes are reduced. The sample remained stationary showing very little or no reduction of the dyes in the absence of silver nanoparticles.

2.3. Nanosilver in Diagnosis and Imaging

With the advent of Nanotechnology, the uses and the availability of silver in the nanoparticle form has allowed the use of pure silver in medical practices. As one of the most popular Surface Enhancement Raman scattering (SERS) active substrates, silver nanoparticles have been used to obtain million fold enhancements in Raman scattering, which provides a high sensitive tool for trace analysis, and even for probing single molecules. As the current antibody based techniques lack the sensitivity to detect the low level detection of virus

Copyright © 2010. Nova Science Publishers, Incorporated. All rights reserved.

particles, SERS has emerged as a powerful analytical tool which extends its possibilities in vibrational spectroscopy. In a recent work done by Huang *et al.,* (2008) substrates which were composed of silver nanorods were used to determine the Raman Spectra of respiratory syncytial virus (RSV) making use of SERS. Silver nanoparticles has also proved its role in matrix-assisted laser desorption/ionization (MALDI), which is a powerful ionization technique for the detection of peptides, proteins, pharmaceuticals, and imaging studies (Shrivas *et al.,*2008).Novel applications of silver nanoparticles is that they have significant potential for single molecule labeling based biological assays because of their non-bleaching properties. They are also being employed for their usage in biosensors (Schultz *et al.,* 2000).

2.4. Antimicrobial Properties of Nano Silver

Among the noble metals, silver nanoparticle has raised considerable interest in biomedical applications due to its excellent biocompatibility and antibacterial properties. (Nair *et al.,* 2007). The use of silver nanoparticles ranges from the fields like antiseptics, disinfectants, effective antimicrobial agents, medical surgery, air purifiers, vacuum cleaners, washing powders, air conditioners, refrigerators etc.

2.4.1. Nano silver as a potent bactericidal agent

Another area where silver nanoparticles have proved its role is in its ability to control and suppress bacterial growth. Tripathy *et al*.,(2009) reported the antibacterial applications of the silver nanoparticles synthesized using the aqueous extract of neem leaves. The nanoparticles were coated on cotton disks and their bactericidal effect was studied against *E.coli*. Duran *et al*., (2007) reported the significant antibacterial activities of the silver nanoparticles synthesized using *Fusarium oxysporum*. The biologically synthesized silver nanoparticles could be of immense use in medical textiles for their efficient antimicrobial function (Vigneshwaran *et al.,* 2006). Silver nanoparticles have shown promise against gram positive *S. aureus.* Nanoparticles have also been incorporated in cloth which has shown promise to be sterile and thus helping in minimizing infections. Metal nanoparticle embedded paints have been synthesized using vegetable oils and have been found to have good antibacterial activity (Kumar *et al*., 2008).

2.4.2. Nano silver in anti fungal therapy

Silver nanoparticles have also proved its role in anti fungal therapy. Fungal infections have become more common in the recent years. In particular, fungal infections are more frequent in patients who are immunocompromised because of cancer chemotherapy, or organ or human immunodeficiency virus infections (Groll *et al.,* 1996). There are many reports showing the anti microbial effects of silver nanoparticles but the anti fungal effects of silver nanoparticles remain un explored. In a recent study Kim *et al.,* (2009) reported the mode of action and the antifungal effects of silver nanoparticles on Candida albicans. Their studies showed that nano silver showed anti fungal effects on fungi tested with low hemolytic effects with human erythrocytes. Their results suggest that the silver nanoparticles may exert an anti fungal activity by disrupting the structure of cell membrane and inhibiting the normal budding process due to the destruction of the membrane integrity.

Copyright © 2010. Nova Science Publishers, Incorporated. All rights reserved.

3. SYNTHESIS AND CHARACTERIZATION OF SILVER NANOPARTICLES

During the past few decades many different methods have been proposed for the preparation of metal nanostructured substrates valid for Surface Enhanced Resonance Scattering (SERS) (Hu *et al* ., 2002) Among these substrates, colloidal nanoscale particles have been the most frequently used (Aroca *et al.*, 2005). Silver is the most universal substrate due to its broad plasmon resonance in the visible–near infrared region, high stability, and easy preparation (Sanchez-Cortez *et al.*, 1994).

3.1. Conventional Synthesis of Silver Nanoparticles

Among the preparation methods of Ag nanoparticles (AgNPs), the most employed ones are chemical reduction (Sanchez-Cortez *et al.*, 1994) or laser ablation (Neddersen *et al*., 1993). Chemical reduction methods are usually performed using silver nitrate as the starting Ag salt, which is reduced by a chemical reducing agent to produce colloidal suspensions integrated by nanoparticles. In general, the use of a chemical reducing agent has the advantage of the feasibility and rapid preparation of the colloidal suspension, although the stability of the suspended nanoparticles is sometimes poor. The most commonly employed method for chemical synthesis of nanoparticles is citrate reduction method and sodium borohydride reduction method.

Laser ablation method, is another commonly used technique where silver colloids were prepared by the extraction of metallic nanoparticles from an Ag plate induced by high intensity laser pulses (Neddersen *et al*., 1993).Some advantages of this method are the absence of chemical reagents or ions in the suspension. It is also possible to control the size of the nanoparticles by changing the ablation conditions (Monti *et al*., 2004).This method allows the nanofabrication of AgNPs in the desired point, by using a microscope to focus the laser beam (Canamares *et al.*, 2007). The immobilization of the resulting nanoparticles is the main advantage of this method, as no flocculation process takes place, leading to long term stable nanoparticles.

Silver colloids were prepared by reduction of silver nitrate with two different reducing agents: trisodium citrate dihydrate and hydroxylamine hydrochloride.

3.1.1. Ag-citrate colloid (SC)

In this method, silver citrate colloid was obtained according to the method described by Lee and Meisel (1982). A total of 1ml of a 1% (w/v) trisodium citrate aqueous solution was added to 50 mL of a boiling 10−3 M silver nitrate aqueous solution, and boiling was continued for 1 h. The colloid obtained showed a turbid gray aspect and had a final pH of 6.5.

3.1.2. Ag-hydroxylamine colloid (SH)

The method described by Leopold and Lendl (1982) is used for the preparation of silver hydroxylamine colloid. A total of 4.5 mL of a sodium hydroxide solution (0.1 M) was added to 5 mL of a 6×10^{-2} M hydroxylamine hydrochloride solution. Then, the mixture was added rapidly to 90 ml of a 1.11×10^{-3} M silver nitrate aqueous solution, and the resulting mixture

Copyright © 2010. Nova Science Publishers, Incorporated. All rights reserved.

was shaken until a homogeneous mixture was obtained. The resulting colloid showed a milky gray color. The stability of the colloid prepared in this way was lower than that of the SC colloid, due to the formation of nitrogen oxides as a consequence of the reduction process of silver nitrate. Because of the reaction of these oxides with water, the pH of the Ag-hydroxylamine colloids tends to slightly decrease with time. Therefore, aqueous NaOH was added to the suspension in order to set the pH to 6.5.

3.1.3. Ag-ablation colloid (SA)

These Ag nanoparticles were prepared by laser ablation of an Ag plate. The 1064 nm line of an Nd: YAG laser with different pulse energies (16.7, 29.2 and 40.0 mJ) was used as the irradiation source. The laser beam was focused with a quartz lens of either 4 or 10 cm of focal distance on the plate contained in a beaker and suspended in 10 mL of triply distilled water. The ablation was continued for 50 min. The resulting colloid showed a yellowish color, with an absorption maximum at 400 nm.

3.1.4. Ag-photo reduction films (SP)

These Ag nanoparticles were obtained by photo reduction of a 10−3 M silver nitrate aqueous solution by means of the 514.5 nm line of an Ar+ laser and a confocal optical microscope.(Canamares *et al.*,2007). In this work a 100× objective was used, together with a laser power of 3 mW and an irradiation time of 25 and 30 min.

3.2. Biosynthesis of Silver Nanoparticles

The need for biosynthesis of nanoparticles rose as the physical and chemical processes were costly. So in the search for cheaper pathways, scientists used microbes and then plant extracts for synthesis. The microbial enzymes or the plant phytochemicals with anti oxidant or reducing properties are usually responsible for reduction of metal compounds into their respective nanoparticles.

Often chemical synthesis methods lead to the presence of some toxic chemical species adsorbed on the surface that may have adverse effects in medical applications (Parashar *et al.*, 2009). This is not an issue when it comes to biosynthesized nanoparticles as they are eco friendly and biocompatible for pharmaceutical applications.

The use of microbial cells for the synthesis of nanosized materials has emerged as a novel approach for the synthesis of metal nanoparticles. Although the efforts directed towards the biosynthesis of nanomaterials are recent, the interactions between microbes and metals have been well documented (Gericke & Pinches, 2006). Thermophilic bacteria have also been used for the synthesis of metal oxide Nanoparticles and the process has been patented (US Patent 7060473, filed by ORNL). Though there are many studies reporting the biosynthesis of various nanoparticles, there is very little information available regarding the mechanistic aspects of nanoparticle production.

Recently CdS nanoparticles have been biosynthesized using the photosynthetic bacteria, Rhodopseudomonas palustris. Reasonably monodisperse spherical nanoparticles were obtained. The work indicated that C-S lyase could control crystal growth (Bai *et al.,* 2009).

Copyright © 2010. Nova Science Publishers, Incorporated. All rights reserved.

Fungi have been widely used for the biosynthesis of nanoparticles as more amounts of nanoparticles can be produced compared to bacteria (Mohanpuria *et al.*, 2008).

Mycelia free medium of the fungus, Cladosporium cladosporioides was used to synthesize silver nanoparticles extracellularly. It was hypothesized that proteins, polysaccharides and organic acids released by the fungus were able to differentiate different crystal shapes and were able to direct their growth into extended spherical crystals (Balaji *et al.*, 2009). Fusarium oxysporum has been reported to synthesize silver nanoparticles extracellularly by means of a nitrate reductase. Titanium dioxide Nanoparticles have been synthesized from F. oxysporum and the process has been patented by NCL, Pune (United States Patent Application 20050214916).

The advantage of using plants over other organisms is that they are easily available, safe to handle and possess a broad variability of metabolites that may aid in reduction.

Recently much work has been done with regard to plant assisted reduction of metal nanoparticles and the respective role of phytochemicals. The main phytochemicals responsible have been identified as terpenoids, flavones, ketones, aldehydes, amides and carboxylic acids. The phytochemicals present in Bryophyllum sp. (Xerophytes), Cyprus sp. (Mesophytes) and Hydrilla sp. (Hydrophytes) were studied for their role in the synthesis of silver nanoparticles. The phytochemicals responsible for bioreduction were identified as anthraquinones and benzoquinones (Jha *et al.*, 2009). Recently, scientists in India have reported the synthesis of silver nanoparticles using the leaves of Parthenium hysterophorus. The use of this noxious weed has an added advantage in that it can be used by nanotechnology processing industries (Parashar *et al.*, 2009). Azadirachta indica leaf extract has also been used for the synthesis of silver, gold and bimetallic (silver and gold) nanoparticles. Studies indicated that the reducing phytochemicals in the neem leaf consisted mainly of terpenoids. The major chemical constituents in the extract were identified as nimbin and quercetin (Shankar *et al.*,(2004) Tripathy *et al.*,). The latex of Jatropha curcas has also been used for the synthesis of silver nanoparticles. Some of the major components responsible for bioreduction were identified as curcain, curacycline A and curacycline B (Bar *et al.*, 2009).

Li *et al*.,(2007) synthesized silver nanoparticles using the Capsicum annum L. extract. Capsicum annum L. extract is known to contain a number of biomolecules such as proteins, enzymes, polysaccharides, amino acids and vitamins. These biomolecules could be used as bioreductants to react with metal ions and they could also be used as scaffolds to direct the formation of nanoparticles in solution.

While fungi and bacteria require a comparatively longer incubation time for the reduction of metal ions, water soluble phytochemicals do it in a much lesser time. Therefore compared to bacteria and fungi, plants are better candidates for the synthesis of nanoparticles. Taking use of plant tissue culture techniques and downstream processing procedures, it is possible to synthesize metallic as well as oxide nanoparticles on an industrial scale once issues like the metabolic status of the plant etc. are properly addressed.

Though there is no dearth in information regarding the biosynthesis of Nanoparticles, more research needs to be done regarding the actual mechanism of nanoparticle formation. Understanding the mechanistics of nanoparticle formation and more detailed studies on the process variables could eventually lead to fine tuning of the process leading to the production of monodisperse particles.

Copyright © 2010. Nova Science Publishers, Incorporated. All rights reserved.

3.3. Characterization Techniques

The size, shape, and optical properties determine the functional role of nanoparticles in various fields. So characterization is a primary criterion in materials research. Spectroscopic studies, microscopic analysis (SEM and TEM), dynamic light scattering, XRD, Fourier transform infra red spectroscopy (FTIR) etc are some of the commonly employed techniques.

Recently Murawala and co workers (2009) has worked on the insitu synthesis and cytocompatibility studies of water dispersible bovine serum albumin coated gold and silver nanoparticles .The optical characterization of the synthesized particles were carried out using UV-visible spectroscopy. TEM was also performed and the size of the Au-BSA nanoparticles were of 15nm in size, whereas the Ag-BSA nanoparticles were in the size range of 25-45nm. The bending and stretching vibrations which depicts the secondary structure of proteins were monitored using FTIR spectroscopy. In pure BSA amide I and amide II were the prominent peaks observed and it was observed that there was no change in the peak position in case of Au-BSA and Ag-BSA. This confirms the secondary structure of BSA and its coverage onto the surface of the nanoparticle.

In another set of work done on the hysteresis effects of silver nanoparticles on serum albumins, Xing can and his co workers (2000) carried out the synthesis and characterization of the silver nanoparticles. The size and shape of the particles were characterized by means of TEM and it was found to be 50-70nm.The HSA molecules formed darkish floccules on the surface of silver nanoparticles indicating the complete coverage of HSA on the surface of the particle. According to the authors the HSA molecules formed a stable coating on the surface of the nanoparticle there by stabilizing it. To determine the adsorption of the molecules on the surface of the particle, UV visible absorption studies were carried out and the plasmon peak for silver nanoparticles were obtained at 415nm.The plasmon bands were found to decrease with increasing concentration of HSA.

4. SURFACE MODIFICATION OF NANOPARTICLES

Biofunctionalization or Surface modification is an important and predominant technique for obtaining biofunction and biocompatibility in metals for its biomedical applications. One of the key issues is that the interaction mechanisms and the nanoscale effects about nanoparticles and bio-macromolecules have not been well understood. Although many nanoparticles possess excellent physical and chemical properties they do not possess suitable surface properties for specific applications. There arises the need for modifying the surface of such materials. (Ruckenstein *et al.,* 2005).

The surface modification of nanoparticles with biomolecules in a controlled way changes the surface composition, structure and morphology of a material, leaving the bulk mechanical properties intact. This process also takes the advantage of introducing chemical functional groups to a surface. A novel approach to this technique is the immobilization of biofunctional molecules to the metal surface.

The controlled interaction of biomolecules with various types of nanoparticles is becoming increasingly important for applications in modern bioelectronics and life sciences. Functional nanoparticles are being developed at the crossroads of nanotechnology and

Copyright © 2010. Nova Science Publishers, Incorporated. All rights reserved.

biology. The properties of these nanoparticles are tuned towards a number of biological applications such as biosensing, imaging and hyperthermia treatment. The process creates an interface that is compatible with the environments of real biological systems.

4.1. Interaction of Silver Nanoparticles with Biomolecules

Metal nanoparticles can be made useful for biological applications by engineering the inorganic properties of the nanoparticles and there by creating optimal biological interfaces. Nanoparticles also require suitable surface functional groups for conjugating with biomolecule. Most biomolecules have carboxylic acid, primary amine, alcohol, phosphate, or thiol groups on their surfaces. The nanoparticles that are functionalized with primary amines, carboxylic acids and thiol surface groups can be covalently conjugated with biomolecules via amide, disulfide and ester bonds. Labeling proteins with nanoparticles has been used for many applications but often the characterization of the structure of the protein in the conjugate is not done. In addition, site-specific labeling of the protein with a nanoparticle has been achieved for only a limited set of proteins and nanoparticles. Any number of molecules can be attached to the nanoparticle surface to make the surface of the metal nanoparticle functional. The most commonly used attachment group is a thiol group, which has a strong affinity for both gold and silver surfaces, and a huge research effort has succeeded in adding a large range of biological molecules to nanoparticles.

The possible potential applications of silver nanoparticles have already been described; however, there are some concerned problems about how to apply them safely and effectively in biological systems. The literature on noble metal nanoparticles is very dense, with gold nanoparticles being well investigated. For example, gold nanoparticles are good vehicles for tracers, and silver nanoparticles are very strong light absorbers and light scatterers. A number of outstanding studies already dealt with this rapidly increasing research area highlighting their promising application in materials science and molecular biotechnology (Mirkin *et al.*, 2000). Especially, biomolecules conjugated with Au nanoparticles have received the most attention because of their high stability, good biocompatibility and high affinity for biomolecules (Mandal *et al.*, 2001). Mirkin group exploited the colorimetric detection technology of DNA utilizing the aggregation of the oligonucleotide-modified Au nanoparticles which were prepared through the thiol interaction. Proteins or small biomolecules containing the thiol group were also widely employed to modify the Au nanoparticles (Zhang *et al.*, 2002). The functionalization of silver nanoparticles is not explored too much but due to its SERS and other properties there arises a need for the Biofunctionalization of silver nanoparticles for its better applications in various fields.

Given below are some selected examples used for functionalizing silver nanoparticles. Selected examples will be provided in the following sections.

4.2. Biomolecule-Directed Nanoparticle Organization

Many approaches are available now which enables the formation, modification and organization of semiconductor nanoparticles. Incorporation of the particles onto glassy

Copyright © 2010. Nova Science Publishers, Incorporated. All rights reserved.

surfaces, using biomolecules as linker molecules, the use of bivalent linker compounds, the deposition of the particles on structured surfaces are the most commonly employed methods.

4.2.1. Protein based recognition systems

Conjugation of proteins to nanoparticles has numerous applications in sensing, imaging, delivery, catalysis, therapy and control of protein structure and activity. Therefore, characterizing the nanoparticle–protein interface is of great importance. A variety of covalent and non-covalent linking chemistries have been reported for nanoparticle attachment. Site-specific labeling is desirable in order to control the protein orientation on the nanoparticle, which is crucial in many applications such as fluorescence resonance energy transfer.

There are a number of reports which suggests the functionalization of gold nanoparticles with proteins and amino acids. For example, an extensive study carried out by Yoo and his co workers (2008) suggests the flocculation behavior of colloidal gold nanoparticles modified with various biomolecules. In their study gold nanoparticles of different sizes were produced and were modified with various amino acids like arginine, lysine and cysteine and proteins like bovine serum albumin, horse serum albumin etc. The flocculation behaviors of the modified gold nanoparticles were studied by observing their colorimetric and morphological changes. Their studies conclude that the flocculation behavior varied depending on the size of the gold nanoparticle and also with the nature of the biomolecules used.

Shenton *et al*., (1999) functionalized gold and silver nanoparticles with immunoglobulins of class G and E (IgG and IgE, respectively), which had a specificity directed against either the d-biotin or the dinitrophenyl (DNP) group.

However the functionalization of silver nanoparticles with proteins and amino acids still needs an intensive study. However the exact mechanism of the interaction between these biomacromolecules with nanoparticles is yet to be well understood.

In another group of experiments Kathiravan and his co workers (2005) studied the interaction between colloidal $AgTiO_2$ nanoparticles and Bovine serum albumin by various spectroscopic measurements. Their results clearly indicated that colloidal $AgTiO_2$ nanoparticles quench the fluorescence of BSA through a static mechanism. The binding constants, quenching rate constants and the number of binding sites were also calculated. From the synchronous fluorescence data it was confirmed that the conformational change of BSA was induced by the interaction of colloidal $AgTiO_2$ nanoparticles with the tyrosine moiety of BSA. This study would be of importance to study the interaction of BSA with metal nanoparticles especially in the filed of pharmacy, pharmacology and biochemistry.

4.2.2. DNA based nanoparticle aggregates

The great mechanical rigidity of the double helices and the high physicochemical stability that DNA possesses makes it the most suitable biomolecule for modifying the surface of nanoparticles. Metal DNA and metal nucleotide interactions are of great importance and have been an intensive area of study. Even though many reports are available on the functionalization of gold nanoparticles with DNA for biomedical applications, very limited literature discusses the interaction of Silver nanoparticles with DNA.

The metal ions act as counter ions and may interact with DNA noncovalently or covalently. Metal ions may interact with DNA noncovalently as counter ions to balance the negative charge of the phosphate backbone. It can also interact with DNA covalently at a

Copyright © 2010. Nova Science Publishers, Incorporated. All rights reserved.

number of different binding sites including the nitrogen centres in nucleobases, sugars and the phosphates.

Based on DNA melt studies, Eichorn (1973), proposed that Ag^{+} ion binds more strongly with nucleobases than phosphates

4.3. Biotemplating

The synthesis and assembly of organic and inorganic compounds can be made possible through the derived supramolecular complexes of bio macromolecules and their electrostatic and topographic properties. In this approach the proteins which are produced by bacteria, components of nucleic acids, and hollow biological compartments like virus particles are employed.

4.3.1. Bacterial and fungal surface layers

Bacteria are known to produce inorganic materials either intra cellularly or extra cellularly. Microorganisms are considered as a potential biofactory for the synthesis of nanoparticles like gold, silver and cadmium sulphide. Some well known examples of bacteria synthesizing inorganic materials include magnetotactic bacteria (synthesizing magnetic nanoparticles) and S layer bacteria which produce gypsum and calcium carbonate layers (Shankar *et al*., 2004).

Silver nanoparticles in the size range of 10- 15 nm were produced by treating dried cells of *Corynebacterium sp* with diamine silver complex. The ionized carboxyl group of amino acid residues and the amide of peptide chains were the main groups trapping ($Ag(NH3)^{2+}$) onto the cell wall and some reducing groups such as aldehyde and ketone were involved in subsequent bioreduction. But it was found that the reaction progressed slowly and could be accelerated in the presence of OH- (Fu *et al*., 2006).

Extracellular secretion of the microorganisms which are free from other cellular proteins associated with the organism serves as one of the best templates for the synthesis of nanoparticles. Mycelia free spent medium of the fungus, *Cladosporium cladosporioides* was used to synthesize silver nanoparticles extracellularly. It was hypothesized that proteins, polysaccharides and organic acids released by the fungus were able to differentiate different crystal shapes and were able to direct their growth into extended spherical crystals (Balaji *et al*., 2009)

4.3.2. DNA templated assembly

The electrostatic and topographic properties of bio macromolecules make them the ideal agents for the synthesis and assembly of organic and inorganic components. In the process of biological templating two dimensional lattices of bacterial cell surface proteins, nano and micrometer- sized nucleic acid components as well as hollow biomolecular compartments like virus particles can be used for the generation and modification of nanoparticles. Sun *et al.,* (2006) reported about the Fabrication of Silver nanoparticle ring by Plasmid DNA.. The study reported the electrostatic assembling of 4-aminothiophenol (4-ATP) capped silver nanoparticles on predefined extended circular plasmid pBR322 DNA. The resulting silver nanoparticles ring was about 1.5 mm in length, and about 2.2 nm in height. In addition to its

Copyright © 2010. Nova Science Publishers, Incorporated. All rights reserved.

use as a nanotemplate, DNA can also be employed to produce micrometer-scaled elements that are useful in microelectronics. Braun *et al*,.(1998) described, an example in which a 16-mm l-DNA molecule, which contained two cohesive ends, was used to bridge the 12 ± 16 mm distance between two gold microelectrodes, prepared by standard photolithography. Successful interconnection of the electrodes was confirmed by optical microscopy of the fluorescent labeled λ- DNA. Next, the sodium ions bound to the phosphate backbone of the λ -DNA were exchanged with Ag ions, and the latter were chemically reduced by hydroquinone. The small sized silver formed along the DNA backbone was then used as catalysts for further reductive deposition of silver, eventually leading to the formation of a silver nanowire.

In another study Zheng and his co workers (2005) have reported on the interaction of Silver nanoparticles and Nucleic acids in the presence of cetyltrimethylammonium chloride. The silver nanoparticles were synthesized using citrate reduction method and the resulting silver nanoparticles were allowed to interact with DNA in the presence of CTMAB. The interaction mechanism was studied using Transmission electron spectroscopy (TEM), circular dichroism (CD), fluorometry and UV spectrometry. The fresh silver nanoparticles were adopted as RLS probes for the determination of nucleic acids at nanogram levels. The produced probe showed high selectivity and sensitivity towards the detection of nucleic acid.

5. APPLICATIONS OF THE FUNCTIONALIZED SILVER NANOPARTICLE

In recent years, a wide variety of analytical techniques has been developed based on changes associated with the SPR of gold and silver nanoparticles and thin films. The SPR is a consequence of the collective oscillations of metal valence electrons resulting in a strong absorption peak that can be used to monitor changes in the surrounding medium such as biomolecule adsorption events at the metal surface, or nanoparticle aggregation.

Surface Enhanced Raman Spectroscopy has served the purpose as an important tool in analytical and biological applications due to the wealth of information on molecular structures, surface processes, and interface reactions that can be obtained from the experimental data.

Wie *et al.*, (2007) has done a significant work by functionalizing the surface of silver nanoparticles using adenine and exploring its application in Surface Enhanced Raman Spectroscopy. Their work reports the coating of silver nanoparticles using adenine during the in situ synthesis of silver nanoparticles using silver nitrate and sodium borohydride in an aqueous medium at room temperature. The characterization studies of the as prepared silver nanoparticles were carried out using TEM, UV-Visible spectroscopy etc. Due to electrostatic interactions silver nanoparticles easily interacted with polyelectrolyte poly (sodium 4-styrenesulfonate) (PSS), and this was fabricated onto mercaptopropyltrimethoxysilane/AgNP functionalized indium tin oxide (ITO) substrate via the layer-by-layer self-assembly technique. Furthermore using a probe molecule like *p*-aminothiophenol, the ITO substrates which were coated with multilayers of different thickness were investigated as Surface Enhanced Raman scattering (SERS) active substrates.

Copyright © 2010. Nova Science Publishers, Incorporated. All rights reserved.

Surface Enhanced Resonance Raman Scattering (SERRS) has also shown its role in the quantitative detection of dye labelled DNA. SERRS is said to be generally three orders of magnitude more sensitive than fluorescence for the detection of dye labelled oligonucleotide.

In an investigation carried out by Faulds and his co workers (2005), the detection of dye labeled DNA was possible using Surface Enhanced Resonance Raman Scattering from silver nanoparticles. The dye used for the study was commercially available and not used before as an SERRS dye. In the study they reported the SERRS detection limit for four dye labelled oligonucleotide at two excitation frequencies. The obtained results were proved to be consistent and it also showed that a range of labels for use in quantitative DNA detection has been expanded.

In another set of studies, Allain and his co-workers (2002) used a silver/PVA surface to detect labelled DNA corresponding to a gene which was responsible of breast cancer. In these studies the dye used was Rhodamine B.

Fang *et al*.,(2004) developed a novel method for the determination of proteins in aqueous solution based on the enhancement of resonance light scattering (RLS) of Ag nanoparticles in the presence of proteins.

Shan *et al.*,(2006) reported the synthesis and antibacterial effects of Norvancomycin capped silver nanoparticles. The authors report that such kind of nanobiocomposites can be used as novel bactericidal methods.

Ling *et al.*, (2008) developed a colorimetric analytical method for the detection of Berberine hydrochloride using citrate stabilized silver nanoparticles. The negatively charged citrate capped silver nanoparticles tend to repel each other due to the strong electrostatic repulsion between the particles. On adding the positively charged beberine hydrochloride to the nanoparticle dispersion the particle tends to aggregate resulting in a change in the color of the silver colloid from yellow to green and then to blue based on the degree or extent of aggregation. Hence this method allows the detection of beberine hydrochloride from 0.05μM to 0.4μM visually based on the color alteration of the solution.

A few other reports by Wu and his coworkers (2009) stated about the selective colorimetric detection of the amino acid cysteine using triangular silver nanoprisms (TSN). Cysteine interacts with the triangular silver nanoprisms through Ag-S covalent bonds. Eighteen different amino acids were tested separately for their reaction with cysteine. A color change was noticed when the cysteine nanoparticles interacted with Ag nanoparticles which was absent in all the other cases. Thus this method has proved to be a selective and sensitive method for the colorimetric detection of cysteine.

In a similar study, Shang *et al.*, (2009) reported the application of a novel water soluble fluorescent Ag cluster in fluorescent sensors for detecting cysteine. Simple mixing of silver salt and polymethacrylic acid followed by photo reduction resulted in the fluorescent silver clusters that are capable of detecting cysteine even at low concentrations with a specific response.

Coupled with silver nanoparticles, the gold nanoparticle probes have been used to analyze the combinatorial DNA arrays, and both its selectivity and sensitivity exceed those of the fluorescence method (Taton *et al.*, 2000). Silver Nano (Silver Nano Health System) is a trademark name of an antibacterial technology which uses silver nanoparticles in washing machines, refrigerators, air conditioners, air purifiers and vacuum cleaners introduced by Samsung in April 2003.

Copyright © 2010. Nova Science Publishers, Incorporated. All rights reserved.

Elechiguerra *et al.,* (2005) studied metal nanoparticle interactions with the human immunodeficiency virus-1 (HIV-1), and silver nanoparticles of the size 1– 10 nm were attached to HIV-1, and this prevented the virus from binding to host cells.

The surface modified silver nanoparticles have proved to have improved biocompatibility and intracellular uptake for drug delivery. The biomolecules conjugated with nanoparticles have received the most attention in the field of clinical diagnosis and drug delivery because of their high stability, good biocompatibility and high affinity for biomolecule.

REFERENCE

[1] Alivisatos, A. P. (1996). Semiconductor Clusters, Nanocrystals, and Quantum Dots. *Science*, *271*, 933-937.

[2] Allain, L. R., & Vo-Dinh, T. (2002). Surface-enhanced Raman scattering detection of the breast cancer susceptibility gene BRCA1 using a silver-coated microarray platform, *Analytica Chimica Acta*, *469*, 149-154.

[3] Aroca, R. F., Alvarez-Puebla, R. A., Pieczonka, N., Sanchez-Cortez, S. & Garcia-Ramos, J. V. (2005). Surface-enhanced Raman scattering on colloidal nanostructures. *Advances in Colloid and Interface Science*, *116*, 45-61.

[4] Bai, H. J., Zhang, Z. M., Guo, Y. & Yang, G. E. (2009). Biosynthesis of cadmium sulfide nanoparticles by photosynthetic bacteria Rhodopseudomonas palustris. Colloids and surfaces B: *Biointerfaces*, *70*, 142-146.

[5] Balaji, D. S., Basavaraja, S., Deshpande, R., Mahesh, D.B., Prabhakar, B. K. & Venkataraman, A. (2009). Extracellular biosynthesis of functionalized silver nanoparticles by strains of *Cladosporium cladosporioides* fungus. Colloids and surfaces B: *Biointerfaces*, *68*, 88- 92.

[6] Bar, H., Bhui, D. K., Sahoo, G. P., Sarkar, P., De, S. P. & Misra, A. (2009). Green synthesis of silver nanoparticles using latex of Jatropha curcas. Colloids and surfaces A: *Physicochemical and engineering aspects*, *339*, 134- 139.

[7] Braun, E., Eichen, Y., Sivan, U. & Ben-Yoseph, G. (1998). DNA Templated Self-Assembly of a Conductive Wire Connecting Two Electrodes. *Nature*, *391*, 775 -778.

[8] Canamares, M. V., Garcia-Ramos, J. V., Gomez-Varga, J. D., Domingo, C. & Sanchez-Cortes, S. (2007). Ag Nanoparticles Prepared by Laser Photo reduction as Substrates for in Situ Surface-Enhanced Raman Scattering Analysis of Dyes. *Langmuir*, *23*, 5210-5215.

[9] Duran, N., Marcato, P. D., De, S., Gabriel, I. H., Alves, O. L. & Esposito, E. (2007). Antibacterial effect of silver nanoparticles produced by fungal process on textile fabrics and their effluent treatment. *Journal of Biomedical Nanotechnology*, *3*, 203- 208.

[10] Eichorn, G. L. (1973). *Metal ions in Genetic information transfer, Inorganic Biochemistry*, Elsevier /North Holland, New York, 34.

[11] Elechiguerra, J. L., Burt, J. L., Morones, J. R., Camacho-Bragado, A., Gao, X., Lara, H. H. & Yacaman, M. J. (2005). Interaction of silver nanoparticles with HIV-1. *Journal of Nanobiotechnology*, *3*, 6.

Copyright © 2010. Nova Science Publishers, Incorporated. All rights reserved.

[12] Fang, B., Gao, Y., Li, M., Wang, G. & Li, Y. (2004). Application of Functionalized Ag Nanoparticles for the Determination of Proteins at Nanogram Levels Using the Resonance Light Scattering Method. *Microchimica Acta*, *147*, 81-86

[13] Faulds, K., Stewart, L., Smith, W. & Graham, D. (2005). Quantitative detection of dye labelled DNA using surface enhanced resonance Raman scattering (SERRS) from silver nanoparticles. *Talanta*, *67*, 667-671.

[14] Foss, C. A. & Hussain, A. (1999). Electrochemically induced shifts in the plasmon resonance bands of nanoscopic gold particles adsorbed on transparent electrodes. *Journal of the Electrochemical Society*, *146*, 628-636.

[15] Fu, M., Li, Q., Sun, D., Lu, Y., He, N., Deng, X., Wang, H. & Huang, J. (2006). Rapid preparation process of silver nanoparticles by bioreduction and their characterizations. *Chinese Journal of Chemical Engineering*, *14*, 114-117.

[16] Gericke, M. & Pinches, A. (2006). Biological synthesis of metal nanoparticles. *Hydrometallurgy*, *83*, 132-140.

[17] Groll, A. H., Shah, P. M., Mentzel, C., Schneider, M., Just-Nuebling, G. & Huebner, K. (1996). Trends in the postmortem epidemiology of invasive fungal infections at a University Hospital. *Journal of infection*, *33*, 23-32.

[18] Henglein, A. (1993). Physicochemical properties of small metal particles in solution: microelectrode reactions, chemisorption, composite metal particles, and the atom-to-metal transition. *The Journal of Physical Chemistry*, *97*, 5457–5471.

[19] Hu, J., Zhao, B., Xu, W., Fan, Y., Li, B. & Ozaki, Y. (2002). Simple Method for Preparing Controllably Aggregated Silver Particle Films Used as Surface-Enhanced Raman Scattering Active Substrates. *Langmuir*, *18*, 6839-6844.

[20] Huang, Y. F., Chang, H. T. & Tan, W. H. (2008). Cancer cell targeting using multiple aptamers conjugated on nanorods. *Ananlytical Chemistry*, *80*, 567-72.

[21] Jha, A. K., Prasad, K., Prasad, K. & Kulkarni, A. R. (2009). Plant system: Nature's nanofactory. Colloids and Surfaces B: Biointerfaces (in press), doi: 10.1016/j.colsurfb.2009.05.018.

[22] Jiang, Z. J., Liu, C. Y. & Sun, L. W. (2004). Catalytic properties of silver nanoparticles supported on silica spheres. American Chemical Society. *The Journal of Physical Chemistry B*, *109*, 1730-1735.

[23] Kathiravan, A., Renganathan, R. & Anandan, S. (2005). Interaction of colloidal AgTiO2 nanoparticles with bovine serum albumin. *Polyhedron*, *28*, 157-161.

[24] Kim , K. J., Sung , W. S., Suh, B. K., Moon , S. K., Choi , J. S., Kim , J. G. & Lee, D. G. (2009). Antifungal activity and mode of action of silver nanoparticles on Candida albicans. *Biometals*, 22, 235-242.

[25] Kumar, A., Kumar, P., Ajayan, M. P. & John, G. (2008). Silver nanoparticle embedded antimicrobial paints based on vegetable oil. *Nature Materials*, *7*, 236- 241.

[26] Lee, P. C. & Meisel, D. (1982). Adsorption and surface-enhanced Raman of dyes on silver and gold sols. *The Journal of Physical Chemistry*, *86*, 3391-3395.

[27] Leopold, N. & Lendl, B. (1982). A New Method for Fast Preparation of Highly Surface-Enhanced Raman Scattering (SERS) Active Silver Colloids at Room Temperature by Reduction of Silver Nitrate with Hydroxylamine Hydrochloride. The *Journal of Physical Chemistry B*, *107*, 5723-5727.

Copyright © 2010. Nova Science Publishers, Incorporated. All rights reserved.

[28] Li, S., Shen, Y., Xie, A., Yu, X., Qui, L., Zhang, L. & Zhang, Q. (2007). Green synthesis of silver nanoparticles using Capsicum annum L. extract. *Green Chemistry*, *9*, 852-858.

[29] Ling, J., Sang, Y. & Huang, C. Z .(2008). Visual colorimetric detection of berberine hydrochloride with silver nanoparticles. *Journal of Pharmaceutical and Biomedical Analysis*, *47*, 860-864.

[30] Mandal, S., Gole, A., Lala, N., Gonnade, R., Ganvir, V. & Sastry, M. (2001). Studies on the Reversible Aggregation of Cysteine-Capped Colloidal Silver Particles Interconnected via Hydrogen Bonds. *Langmuir*, *17*, 6262-6268.

[31] Mirkin, C. A. & Taton, T. A. (2000). Materials chemistry: Semiconductors meet biology. *Nature*, *405*, 626-627.

[32] Mohanpuria, P., Rana, K. N. & Yadav, S. K. (2008). Biosynthesis of nanoparticles: technological concepts and future applications. *Journal of Nanoparticle Research*, *10*, 507-517.

[33] Monti, O., Fourkas, J. T. & Nesbitt, D. J. (2004). Diffraction-Limited Photo generation and Characterization of Silver Nanoparticles. *The Journal of Physical Chemistry B*, *108*, 1604-1612.

[34] Moyer, C A. (1965). Treatment of burns, Trans. Stud. Coll. Physicians, *Philadelphia*, *33*, 53-103.

[35] Mulvaney, P., Ung, T., Giersig, M. & Dunstan, D. (1997). Spectroelectrochemistry of Colloidal silver. *Langmuir*, *13*, 1773-1782.

[36] Murawala, P., Phadnis, S. M., Bhonde, R. R. & Prasad, B. L. V. (2009). In situ synthesis of water dispersible bovine serum albumin capped gold and silver nanoparticles and their cytocompatibility studies. Colloids and Surfaces B: *Biointerfaces*, *73*, 224-228.

[37] Nair, L. S. & Laurencin, C. T. (2007). Silver Nanoparticles: Synthesis and Therapeutic Applications. *Journal of Biomedical Nanotechnology*, *3*, 301-316.

[38] Neddersen, J., Chumanov, G. & Cotton, T. M. (1993). Laser Ablation of Metals: A New Method for Preparing SERS Active Colloids. *Applied Spectroscopy*, *47*, 1959-1964.

[39] Nie, S**.** & Emory, S. R. (1997). Probing Single Molecules and Single Nanoparticles by Surface-Enhanced Raman Scattering. *Science*, *275*, 1102-1106.

[40] Parashar, V., Prashar, R., Sharma, B. & Pandey, A. C. (2009). Parthenium leaf extract mediated synthesis of silver nanoparticles: a novel approach towards weed utilization. *Digest journal of nanomaterials and biostructures*, *4*, 45-50.

[41] Ruckenstein, E. & Li, Z. F. (2005). Surface modification and functionalization through the self-assembled monolayer and graft polymerization. *Advances in Colloid and Interface Science*, *113*, 43-63.

[42] Sanchez-Cortes, S., Garcia-Ramos, J. V. & Morcillo, G. (1994). Morphological Study of Metal Colloids Employed as Substrate in the SERS Spectroscopy. *Journal of Colloid and Interface Science*, *167*, 428-436.

[43] Schultz, S., Smith, D. R., Mock, J. J. & Schultz, D. A. (2000). Applications of silver nanoparticles in biosensors. *Proceedings of the National Academy of Sciences*, U.S.A., *97*, 996.

Copyright © 2010. Nova Science Publishers, Incorporated. All rights reserved.

[44] Shan, W, Q., Jian J., Hong, F. J. & Cong, S. J. (2006).Norvancomycin-capped silver nanoparticles: Synthesis and antibacterial activities against *E.coli*. *Science in China Series*: *B*, *50*, 418-424.

[45] Shang, L. & Dong, S. (2009). Sensitive detection of cysteine based on fluorescent silver clusters. *Biosensors and Bioelectronics*, *24*, 1569-1573.

[46] Shankar, S. S., Rai, A., Ahmad, A. & Sastry, M. (2004). Rapid synthesis of Au, Ag and bimetallic Au core- Ag shell nanoparticles using neem (*Azadirachta indica*) leaf broth. *Journal of colloid and interface science*, *275*, 496-502.

[47] Shenton, W., Davies, S. A. & Mann, S. (1999). Directed Self-Assembly of Nanoparticles into Macroscopic Materials Using Antibody-Antigen Recognition. *Advanced Materials*, *11*, 449-452.

[48] Shrivas, K. & Wu, H. F. (2008). Modified silver nanoparticle as a hydrophobic affinity probe for analysis of peptides and proteins in biological samples by using liquid liquid micro extraction coupled to AP-MALDI-Ion trap and MALDI-TOF mass spectroscopy. *Analytical chemistry*, *80*, 2583-2589.

[49] Sun, L., Wei, G., Song, Y., Liu, Z., Wang, L. & Li, Z. (2006). Fabrication of silver nanoparticles ring templated by plasmid DNA. *Applied Surface Science*, *252*, 4969-4974.

[50] Tang, Z., Wang, Y., Sun, K. & Kotov, N. A. (2005). Spontaneous Transformation of Stabilizer-Depleted Binary Semiconductor Nanoparticles into Selenium and Tellurium Nanowires. *Advanced Materials*, *17*, 358-363.

[51] Taniguchi N. (1974). Proc. *of International Conference on Precision Engineering (ICPE)*, Tokyo, Japan, 18-23.

[52] Taton, T. A., Mirkin, C. A. & Letsinger, R. L. (2000). Scanometric DNA Array Detection with Nanoparticle Probes. *Science*, *289*, 1757-1760.

[53] Tripathy, A., Chandrasekaran, N., Raichur, A. M. & Mukherjee, A. (2009). Antibacterial Applications of Silver Nanoparticles Synthesized by Aqueous Extracts of Azadirachta indica (Neem) leaves. *Journal of Biomedical Nanotechnology*, *5*, 93-98.

[54] Tripathy, A., Raichur, A. M., Chandrasekaran, N., Prathna, T. C. & Mukherjee, A. (2009). Process variables in biomimetic synthesis of silver nanoparticles by aqueous extract of *Azadirachta indica* (Neem) leaves. *Journal of Nanoparticle Research*. Article in press, DOI 10.1007/s11051-009-9602-5.

[55] Vigneshwaran, N., Kathe, A. A., Varadarajan, P. V., Nachane, P. R. & Balasubramanya R. H. (2006). Biomimetics of silver nanoparticles by white rot fungus, Phaenerochaete chrysosporium. *Colloids and Surfaces B: Biointerfaces*, *53*, 55-9.

[56] Wei, H., Li, J., Wang, Y. & Wang, E. (2007). Silver nanoparticles coated with adenine: preparation, self-assembly and application in surface-enhanced Raman scattering**.** *Nanotechnology*, *18*, 610-615.

[57] Wu, T., Li, Y. F. & Huang, C. Z. (2009). Selectively colorimetric detection of cysteine with triangular silver nanoprisms. *Chinese Chemical Letters*, *20*, 611-614.

[58] Xingcan, S., Qi, Y., Hong, L., Haigang, Y. & Xiwen, H. (2000). Hysteresis effects of the interaction between serum albumins and silver nanoparticles. *Science in China (Series B)*, *46*, 387-398.

[59] Yoo, E. J., Li, T., Park, H. G. & Chang, Y. K. (2008). Size-dependent flocculation behavior of colloidal Au nanoparticles modified with various biomolecules. *Ultramicroscopy*, *108*, 1273-1277.

Copyright © 2010. Nova Science Publishers, Incorporated. All rights reserved.

[60] Zhang, F. X., Han, L., Israel, L. B., Daras, J. G., Maye, M. M., Ly, N. K. & Zhong, C. J. (2002). Colorimetric Detection of Thiol-Containing Amino Acids Using Gold Nanoparticles. *Analyst*, *127*, 462-465.

[61] Zheng, G., Patolsky, F., Cui, Y., Wang, W. U. & Lieber, C. M. (2005). Multiplexed delectrical of cancer markers with nanowire sensor arrays, Nature Biotechnology, 23, 1294-1301.

Copyright © 2010. Nova Science Publishers, Incorporated. All rights reserved.

In: Silver Nanoparticles
Editor: Audrey E. Welles, pp. 309-325
ISBN: 978-1-61668-690-1
© 2010 Nova Science Publishers, Inc.

Chapter 8

APPLICATIONS OF SILVER NANOPARTICLES' SURFACE PLASMON RESONANCE EFFECT IN THE FIELD OF NONLINEAR OPTICAL MATERIALS

Xin Chen[1], Gang Zou[1]*, Jun Tao[2] and Yan Deng[2]

[1]Department of Polymer Science and Engineering, Joint Laboratory of Polymer Thin Films and Solution, Key Laboratory of Optoelectronic Science and Technology in Anhui Province, University of Science and Technology of China, Hefei, Anhui 230026, P. R. China

[2]Department of Physics, University of Science and Technology of China, Hefei, Anhui 230026, P. R. China

Copyright © 2010. Nova Science Publishers, Incorporated. All rights reserved.

ABSTRACT

This Account describes a new strategy for the preparation of nonlinear optical devices based on the silver nanoparticles and the conjugated polymer, polydiacetylene (PDA), owing to the surface plasmon resonance of silver nanoparticles. It is worth nothing that nano metal exhibited the enhancement of NLO properties induced by quantum confinement effect. The large picosecond optical nonlinear of Au and Ag colloids surrounded by water or glass have been reported. For the most part, however, inorganic nonlinear materials are different to modify compared with organic nonlinear materials. So, characteristic interactions between exciton, plasmon and their resonance effect in the hybridized systems between organic microcrystals and inorganic nano fine particles would make it possible to exhibit novel optical properties. In the course of developing composite nonlinear materials, we discovered that nearly seven times enhancement was observed as a result of localized field enhancement under the surface plasmon resonance of silver nanoparticles at the interface of PDA vesicles. The most importance is that the NLO properties of this PDA/Ag nanocomposite system can be further significantly enhanced and flexibly modulated by three strategies which can tune the surface plasmon resonance of silver nanoparticles: (1) changing the size of Ag nanoparticles (which based on the mediation of a size-dependent light-confinement effect and a size-dependent dielectric constant of Ag particles), (2) varying the array of Ag nanoparticles (which based on the coupling effect of local field between neighboring Ag

nanoparticles), (3) altering the concentration of Ag nanoparticles (this based on the particle clusters phenomenon which would reduce the local field). The facile preparation and modulation of nonlinear optical devices based on the Ag nanoparticles and PDA make a new way for the development of organic/inorganic composite nonlinear optical materials.

1. THE OPTICAL PROPERTIES OF METAL NANOPARTICLES

1.1. Localied Surface Plasmons (LSPs) of Metal Nanoparticles

In recent years, preparation, characterization and unique optical properties of controllable metal nanoparticles are of current interest [1], especially in the field of nonlinear optics, surface-enhanced Raman scattering and single-molecule detection [2, 3]. The optical properties of metal nanoparticles are closely linked with size, shape, dielectric of environment and other factors. As early as the middle ages, the optical properties of metal nanoparticles has attracted people's attention, gold nanoparticles were used to make stained glass because of the specific absorption of visible light. However its surface plasma resonance effect didn't be investigated intensively until the 20th century. We know that free-vibrational electron in the surface of metal can form wave transmiting along the metal surface when interacting with photon, which is the so-called surface plasmon (SPs). Compared with the SPs which exists in the interface of infinite metal medium [4, 5], there is another pattern called localized surface plasmons (LSPs) [6, 7], which plays a dominant role in different type of metal particles. Surface plasmon and local surface plasma both have local characteristics. However, they are two completely different excited states because of their different dispersion relations. SPs is a transmission mode (parallel to the interface). LSPs is a non-transmission mode, localized in a variety of different morphologies of the surface, and its dispersion relations is closely related with the morphology to local mediain in general. such high spatial locality can significantly enhance the electromagnetic field around the particles, this effect is closely linked with many physical phenomena and thus a number of research works were carried out, such as surface-enhanced Raman scattering, second-harmonic, the enhancement of third-order nonlinear effects, dynamic photonic devices and so on [8-10].

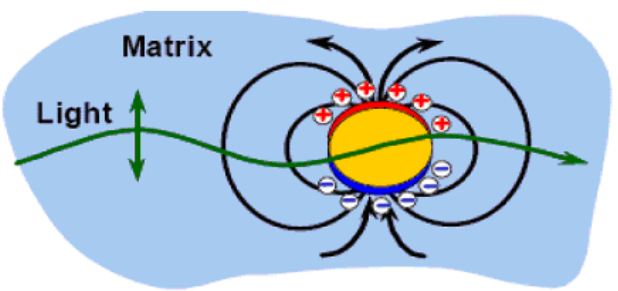

Figure 1-1. Schematic view of the excitation of a particle plasmon oscillation in a metal nanoparticle by an external light field [11].

Copyright © 2010. Nova Science Publishers, Incorporated. All rights reserved.

As shown in Figure 1-1, since the diameter of a nanoparticle is on the order of the penetration depth of electromagnetic waves in metals, the excitation light is able to penetrate the particle. The field inside the particle shifts the conduction electrons collectively with respect to the fixed positive charge of the lattice ions. The electrons build up a charge on the surface at one side of the particle. The attraction of this negative charge and the positive charge of the remaining lattice ions on the opposite side results in for a restoring force. If the frequency of the excitation light field is in resonance with the eigenfrequency of this collective oscillation, even a small exciting field leads to a strong oscillation. The magnitude of the oscillation depends only on the damping involved, which can be both radiative and nonradiative. The resonance frequency is mainly determined by the strength of the restoring force. This force depends on the separation of the surface charges, i.e. the particle size, and the polarizability of the medium between and around the charges, which depends on the embedding medium and the polarizability of the core electrons of the metal particle. The alternating surface charges effectively form an oscillating dipole, which radiates electromagnetic waves.

1.2. Optical Properties of Single Silver Nanoparticles

The optical properties of metal nanoparticles primarily depend on the localized surface plasmon. When there is the local surface plasmon resonance between metal nanoparticles, the surface plasma resonance absorption peak will occur in the spectrum, it is strongly subject to particle size, particle shape, and the dielectric of environment. Figure 1-2 (a) analyzes the spectrum of silver particles with different size in the medium of polymethyl methacrylate (PMMA) (refractive index is 1.49). The radius of silver particles are 9nm, 20nm and 30nm respectively, the incident wavelength range from 300nm to 550nm, and the characteristic peaks are located at 422nm, 441nm and 473nm. For the metal particles whose size is much smaller than incident wavelength, the extinction coefficient mainly depends on dipole moment and less depends on the multipolar effect. With the increasing of particle size, the intensity of absorption peaks change gradually, and the location of characteristic peaks shifted to long-wavelength. This is mainly due to that the energy difference is inversely proportional to the square of the radius of potential well. For the spherical silver particles, there will be dipole plasmon resonance when meetting $Re\varepsilon_{metal}=-2\varepsilon_h$.

When there is LSPs resonance, the energy of incident light is coupled around the metal nanoparticles, so the extinction efficiency will increase. At this time, there is a strong local field on the surface of these particles. This field enhancement effect can be effectively used for nonlinear optical (NLO), surface-enhanced Raman scattering (SERS), surface second harmonic generation (SHG) and fluorescence enhancement [8, 9]. In order to directly observe the field enhancement effect, we simulate the field distribution around the silver particles (radius is 9nm) by discrete dipole approximation (DDA) (As shown in Figure 1-2(b)).The wavelength of incident we selected was 442nm which is the same as the peak in extinction spectrum. In this figure we can find that the light field is localized around the particles, and the intensity of light field can be enhanced up to 15 times.

Copyright © 2010. Nova Science Publishers, Incorporated. All rights reserved.

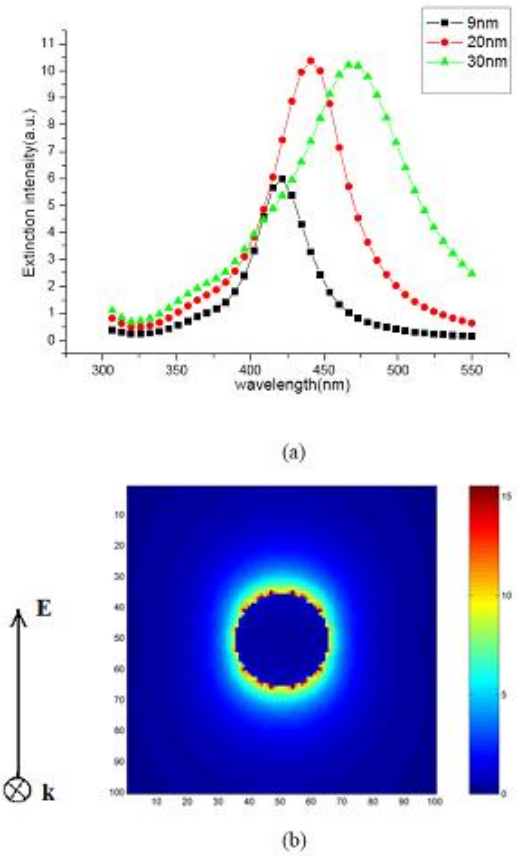

Figure 1-2. (a) extinction spectrum of silver nanoparticles with different size, (b) the field distribution around the silver particles (radius is 9nm).

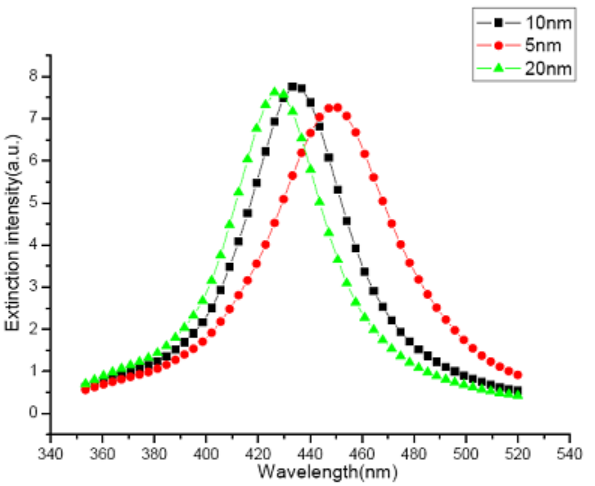

Figure 1-3. the extinction spectrum of silver particles (9nm) with the space between are 23nm, 28nm and 33nm respectively.

Copyright © 2010. Nova Science Publishers, Incorporated. All rights reserved.

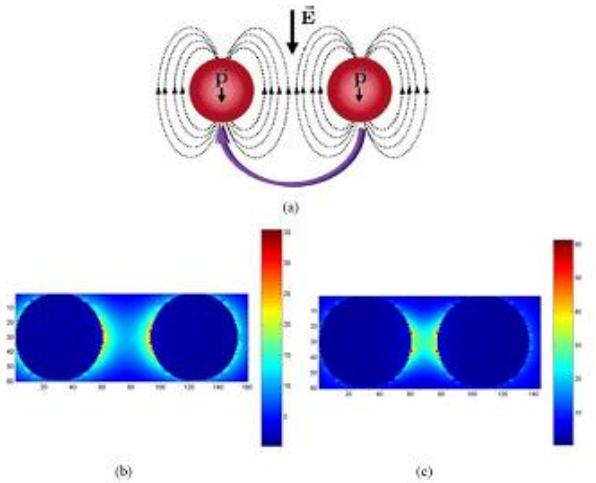

Figure 1-4. (a) Schematic diagram of the interaction between two Ag nanoparticles, field distribution of silver nanoparticles with the radius is (b) 28nm and (c) 23nm.

1.3. Optical Properties of the System Containing Multiple Silver Nanoparticles

It is very difficult to prepare system with completely dispersed silver nanoparticles, so it is important to research the optical properties of multiple silver nanoparticles. Figure 1-3 shows the extinction spectrum of silver particles (9nm) with the space between are 23nm, 28nm and 33nm respectively. The surrounding refractive index we selected is 1.49. It is obvious that the characteristic peaks of Ag nanoparticles woth different space are 452nm, 433nm and 425nm, there is a evident red-shift when the space between particles become smaller and smaller. Each silver particle can be seen as a dipole, if a spherical dipole is oscillating driven by incident field, its radiation field will interact with the another dipole, as shown in Figure 1-4 (a). If the two particles are very close, the dipole field of one particle will destroy the other one, and reduce the force between free electrons, thereby reducing the resonant frequency, the red-shift will occur.

Figure 1-4 (b) and 1-4 (c) show the electric field distribution near the two spherical silver particles simulated by DDA method. The radius of particles is 9nm, the space between particles are 28nm and 23nm, the wavelength of incident wave are 451nm and 433nm respectively, which are the same as the the peak of their extinction spectrum. As can be seen from the figure, the interaction between localized fields is weak when the space of two particles is 28nm, and the local field mainly localized in the surface of Ag nanoparticles. When the particle distance is reduced to 23nm, the coupling effects will markedly enhance the local field, and thus the local field is mainly. located between the two particles, maximum intensity of local field is up to 60 times stronger than the incident light. With the further decreasing of the distance between particles, particle clusters phenomenons occur, which will reduce the local field, so there is an optimal distance between the particles to furthest enhances the local field. When the volume fraction of metal particles is small, namely the space between particleis are large, the interactions between local fields can be negligible.

Copyright © 2010. Nova Science Publishers, Incorporated. All rights reserved.

However, with the enhancement of volume fraction, the distance between particles decreases, then we must take the interaction between particles into account. The contributing field is not only the original incident field, but also the scattered field of other particles.

2. Optical Properties of the Metal Nanoparticles Composite Materials

Nano-metal composite materials have a number of unique optical properties compared with traditional materials, these materials have extensive application prospects in the field of nano-photonics [12, 13]. When light interacts with the free electronsand in nano-metal composite structure, surface plasmon resonance effect (SPR) and localized surface plasmon resonance effect (LSPR) will occur. The SPR properties of metal surfaces can be successfully controlled by changing its carrier-metal nano structure. The LSPR characteristics Of metal nanoparticles are extremely sensitive to the particle size, shape, spacing and the environmental dielectric which mainly due to the enhancement of local field within and around metal particles, so it is possible to control the LSPR characteristics of mental nanoparticles by changing these factors to meet different application requirements, such as the near-field enhanced second-harmonic, surface-enhanced Raman scattering, third-order nonlinear optics and so on. Especially, metal nano-composite structure will show the enhanced third-order nonlinear optical properties under surface plasma resonance. At this time, this composite structure have large nonlinear optical properties and fast response characteristics which greatly reduce the size of all-optical devices, thus it has great application prospects in high-speed optical switch, optical modulator, optical waveguide devices and optical limiting devices [14, 15]. Therefore, the research of linear and nonlinear optical properties of nano-metal composite structure has an important guiding significance for the development of nano photonic devices.

2.1. Development of Nano-Metal Particles Composites Nonlinear Optical

During the past decade, much significant research has been directed toward understanding organic nonlinear optical (NLO) materials and their application in information processing due to their large NLO response and short response time. [16] In particular, organic third-order NLO materials, such as π-conjugated polymers, are powerful candidates for developing photonics devices, due to the high speed NLO response and easy chemical modification in comparison with inorganic systems. Many theoretical and experimental efforts have been made to improve effective third-order NLO susceptibility $\chi^{(3)}(\omega)$, however, the effective third-order NLO susceptibility Re $\chi^{(3)}$ is still not sufficient for device applications. One effective approach is to fabricate nanocomposites with well-defined shape holding improved NLO properties. As we know the particle size reached the nanometer scale not only is the surface-to-volume ratio drastically changed but a transition from metal to insulator also occurs and effects resulting from quantum confinement may be observed [17]. It is worth nothing that nano precious metal fine particles (Ag, Au nanoparticles) exhibited the enhancement of NLO properties induced by quantum confinement effect. [18]

Copyright © 2010. Nova Science Publishers, Incorporated. All rights reserved.

The surface plasma resonance (SPR), which results from collective electronic excitation at the interface between metal nanoparticles and dielectric matrix, not only is responsible for the linear optical properties but also governs nonlinear optical phenomena [19]. According to the local field enhancement under the surface plasmon resonance condition, the large picosecond optical nonlinear of Au and Ag colloids surrounded by water or glass was firstly reported by Rechard et al. [20] Now, characteristic interactions between exciton, plasmon and their resonance effect in the hybridized systems between organic microcrystals and inorganic nano fine particles would make it possible to exhibit novel optical properties. As predicted theoretically, [21, 22] the NLO property would be enhanced in organic microcrystals coated with metal thin layer. By incorporating metal nanoparticles into a organic NLO materials matrix, the nanocomposite films have attractive mechanical and electronic properties that facilitate the use in the practical devices and have been regarded as the potential materials for all-optical communication.

2.2. Synthesis and Nonlinear Optical Properties of Nanometer-Size Silver-Coated Polydiacetylene Composite Vesicles

Organic third-order NLO materials, such as π-conjugated polymers, are powerful candidates for developing photonic devices, due to the high speed NLO response and easy chemical modification in comparison with inorganic systems [23]. Among these organic NLO materials, polydiacetylene (PDA), classified as a one-dimensional π-conjugated polymer, possesses excellent third-order NLO response properties in the range of femtoseconds to subpicoseconds, which is attributed to delocalized π-conjugated electrons along the main chain backbone [24]. Also PDA can be chemically tailored by means of a polymerization reaction in the solid phase of a substituted mono diacetylene. However, the magnitude of the effective third-order NLO susceptibility $\chi(3)$ for PDA is still not sufficient for device applications. So these new organic/inorganic composite nonlinear optics materials with huge effective third-order NLO susceptibility are urgent required. Recently we report the fabrication of PDA/Ag nanocomposite vesicles and first experimentally demonstrated the enhancement of third-order NLO properties as a result of the surface plasmon resonance of silver nanoparticles at the interface. Also these PDA/Ag nanocomposite vesicles were expected to be good candidates for new optical and nonlinear devices. A schematic representation of the procedure employed for this purpose is given in Figure 2-1. Two novel kinds of PDA/Ag nanocomposite vesicles were designed and fabricated. One was that Ag colloidal nanoparticles were coated both onto the outer and inner surfaces of PDA vesicles (I), the other was that Ag colloidal nanoparticles were coated only onto the outer surface of PDA vesicles (II). As a reference sample, the mixing solution of Ag colloidal nanoparticles and PDA vesicles (Ag colloidal nanoparticles had not been coated onto the surface of PDA vesicles in this case) was prepared to evaluate the effect of Ag colloidal particles coating on the third-order NLO properties of PDA vesicles. TEM and HRTEM images of these nanocomposite vesicles are shown in Figure 2-2. These photos show that the metal silver-particle-coated PDA composite vesicles had a vesicle shell structure about 150 nm in diameter. The metal silver particles had wide dispersive sizes of 5–30 nm which is not a perfect silver crystalline layer film, and the plane distance is about 5 A°. All these above

Copyright © 2010. Nova Science Publishers, Incorporated. All rights reserved.

results indicated that PDA/Ag nanocomposite vesicles that Ag nanoparticles coated on the surface of PDA vesicles were prepared successfully.

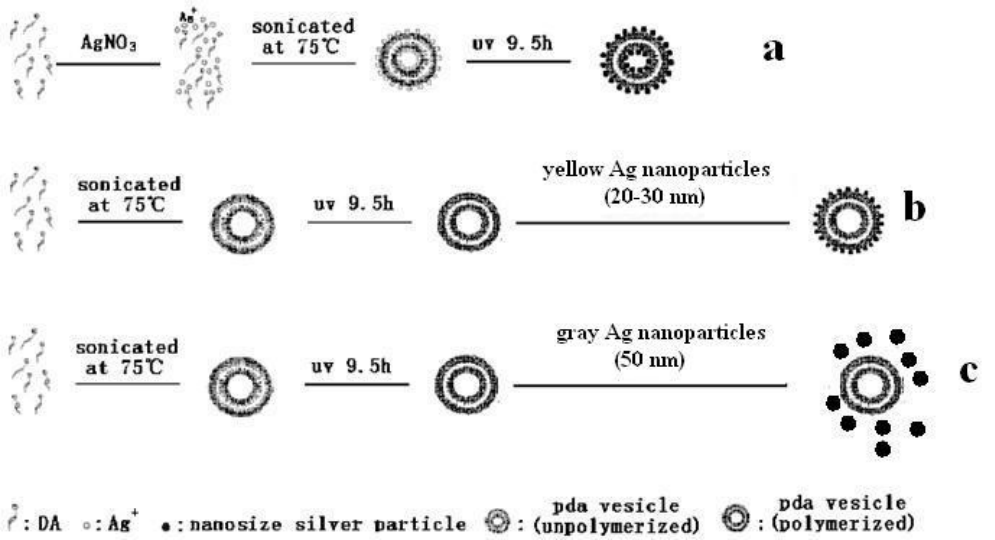

Figure 2-1. Preparation sequence of (a) PDA/Ag composite vesicles that Ag nanoparticles coated both on the outer and inner surface of PDA vesicles, (b) PDA/Ag composite vesicles that yellow Ag nanoparticles coated on the outer surface of PDA vesicles and (c) the mixing solution of gray Ag colloidal nanoparticles and PDA vesicles (Ag colloidal nanoparticles had not been coated onto the surface of PDA vesicles in this case) [25].

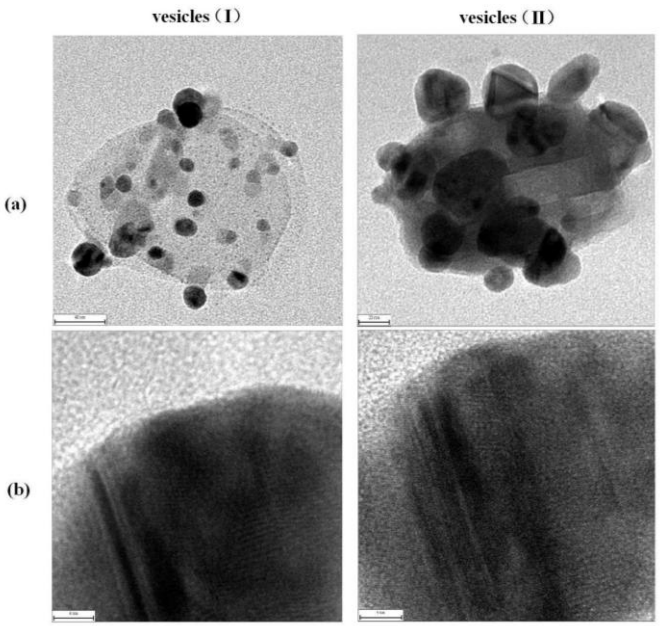

Figure 2-2. (a) The TEM images of Ag/PDA composite vesicles and (b) HRTEM images of coated Ag nanoparticles (the scale bar is 4 nm).

Copyright © 2010. Nova Science Publishers, Incorporated. All rights reserved.

Table 2-1. Nonlinear refractive index n_2, $\chi^{(3)}$ and nonlinear absorption coefficient for different PDA/Ag nanocomposite vesicles

Sample	Illumination	n_2 ($\times 10^{-14}$ cm^2/W)	Re $^{(3)}$ ($\times 10^{-12}$ esu)	β ($\times 10^{-11}$m/W)
PDA/Ag composite vesicles (a)	Pure PDA vesicles	1.2	0.4	6.7
	Ag colloidal nanoparticles attached both onto the outer and inner surface of PDA vesicles (I)	2.7	1.0	6.1
PDA/Ag composite vesicles (b)	Pure PDA vesicles	1.2	0.4	6.7
	Yellow Ag colloidal nanoparticles	2.0	0.8	6.6
	Yellow Ag colloidal nanoparticles only attached onto outer surface of PDA vesicles (II)	7.3	2.8	9.0
the mixing solution of gray Ag colloidal nanoparticles and PDA vesicles (c)	Pure PDA vesicles	1.2	0.4	6.7
	Gray Ag colloidal nanoparticles	1.9	0.7	6.0
	Gray Ag colloidal nanoparticles mixing with PDA vesicles	2.1	0.8	6.8

In Table 2-1 are displayed the effective third-order NLO susceptibility $\chi^{(3)}(\omega)$ of different PDA/Ag nanocomposite vesicles. Compared with pure PDA vesicles, the Ag colloidal nanoparticles coating leaded to the obvious enhancement of NLO properties for PDA vesicles. It is obvious that nearly 7 times improvement is observed as a result of local field enhancement under the surface plasmon resonance of silver nanoparticles at the interface.

2.3. Modulations of the NLO Properties of PDA/Ag Nanocomposite System

2.3.1. Size effect of nano silver – a significant factor to the NLO properties of PDA/Ag nanocomposite system

Localized surface plasmons (LSPs) have attracted considerable attention with the progress in optical nanotechnology. It is known that electric and magnetic fields associated with the LSPs excited in metal spheres penetrate into the outside of the spheres in the order of the sphere size. Moreover, such fields are strongly enhanced, compared with the incident field. As a consequence, LSPs can play a significant role in the development of nanosize optical devices, e.g., optical switches and optical bistable devices, and also a variety of nanosensors [26–28], nanoprocessing devices [29, 30], and near-field scanning optical microscopes [28,31]. The LSPs have been discussed by Fuchs and Kliewer in 1968 [32], using the so-called Mie theory. In applying the theory, the most significant issue is to determine an appropriate dielectric constant of metal spheres. Namely, the dielectric constant of small-size metal spheres indicates a strong size dependence and thus we should be very careful in choosing the corresponding dielectric constant. As we know, the dielectric constant is a significant parameter of the effective third-order nonlinear optical susceptibility $\chi^{(3)}(\omega)$. So it is obvious that the effective third-order nonlinear optical susceptibility $\chi^{(3)}(\omega)$ of nano metal spheres/organic nanocomposite system is closely connected with the size of metal

Copyright © 2010. Nova Science Publishers, Incorporated. All rights reserved.

spheres. When the optical intensity enhancement associated with LSPs is utilized, we need to know the relationship between the two parameters. This should be solved promptly.

Different size (20nm, 50nm and 80nm) Ag colloidal nanoparticles were coated onto the outer surface of polydiacetylene (PDA) vesicles to form PDA/Ag nanocomposite vesicles [33]. As shown in Figure 2-3, nearly 13 times enhancement in the effective third-order NLO susceptibility $X^{(3)}(\omega)$ was observed for PDA/Ag (50 nm) composite vesicles, however, only 7 times and 9 times enhancement were observed for PDA/Ag (20 and 80 nm) composite vesicles compared with PDA pure vesicles, respectively. This NLO properties enhancement was contributed to the local field enhancement under the surface plasmon resonance of silver nanoparticles at the interface. And the formation of core-shell-type structure consisting of a PDA vesicle core and an Ag nanoshell (Ag colloidal nanoparticles were coated onto PDA vesicles, not simply mixing) was proven to be essential for this remarkable NLO properties enhancement [25]. All above results were in agreement with the theoretical prediction of Neeves [34] and our previous experimental results [25]. Obvious, PDA/Ag (50 nm) composite vesicles showed maximum NLO properties enhancement effect and this size-dependent enhancement effect of Ag colloidal nanoparticles should be attributed to mediation effect of a size-dependent light-confinement and a size-dependent dielectric constant of Ag spheres. This size-dependent enhancement effect of Ag nanoparticles in PDA/Ag nanocomposite vesicles was also in accordance with theoretical calculation [21].

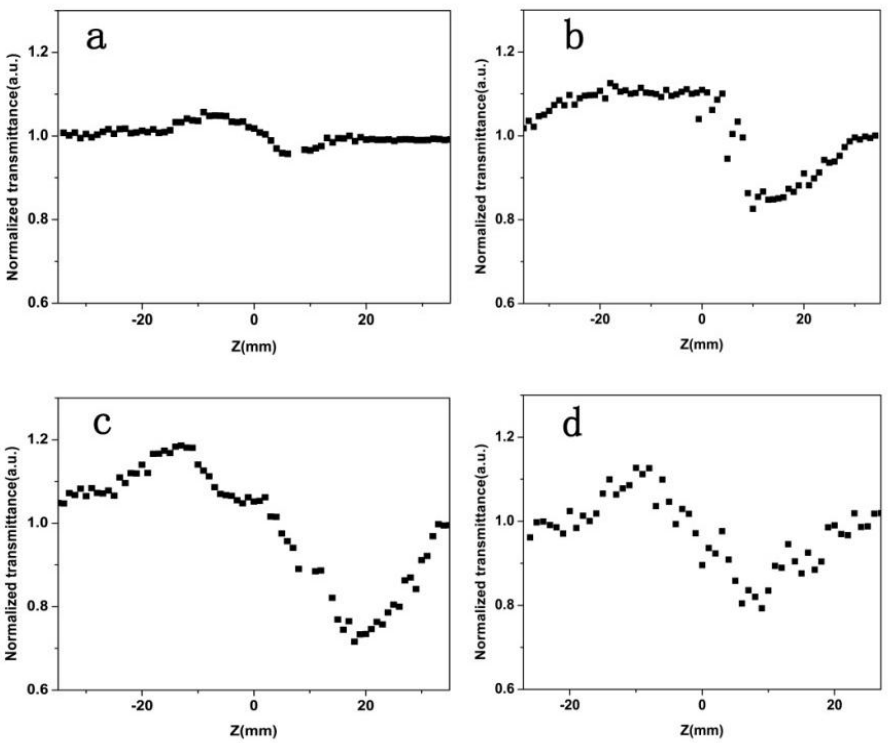

Figure 2-3. Measured Z-scan normalized transmittance curves of (a) pure PDA vesicles solution , (b) PDA/Ag (20 nm) composite vesicles solution, (c) PDA/Ag (50 nm) composite vesicles solution and (d) PDA/Ag (80 nm) composite vesicles solution.

Copyright © 2010. Nova Science Publishers, Incorporated. All rights reserved.

2.3.2. Coupling effect of silver nanoparticles in PDA/Ag nanocomposite system

Although the size-dependent NLO properties enhancement effect of Ag nanoparticles has been investigated, it is by no means for us to ignore another influencing factor of the NLO properties—the coupling effect. In order to research the influence of coupling effect to the NLO properties in metal spheres/organic nanocomposite system, Ag nanoparticles with different concentration were added to PDA system to prepare nanocomposite films [35]. Third-order nonlinear optical susceptibility Re $\chi^{(3)}$ increased unceasingly when the volume fraction of silver nanoparticles changed from 0 to 58%, and the maximum appeared when the volume fraction of silver nanoparticles reached 58%. When the volume fraction of silver nanoparticles increased over 58%, Re $\chi^{(3)}$ was observed to decrease contrarily (see Figure 2-4). Obviously, Re $\chi^{(3)}$ reached maximum when the the volume fraction of silver nanoparticles in PNADA/Ag composite films was 58% .This concentration-dependent enhancement effect of Ag colloidal nanoparticles should be attributed to the effect of localized field coupling among Ag nanoparticles. When the volume fraction of silver nanoparticles in the composite films is lower (the distance between Ag nanoparticles was far), the interaction between localized fields was relatively weak, and the electric field mainly localized in the surface of Ag nanoparticles. With the concentration of Ag nanoparticles increasing, the distance between nanoparticles gradually decreased. When the particle distance was reduced to a certain degree, the coupling effects will markedly enhance the local field, and thus the local field was mainly distributed between the two particles. With the distance between particles further decreasing, particle clusters phenomenon would occur, which would reduce the local field [36]. TEM images of different films clearly show the particle agglomeration when the volume fraction of silver nanoparticles was out of 50%, however, the silver nanoparticles were uniform and dispersive well when the volume fraction of silver nanoparticles was under 50%.

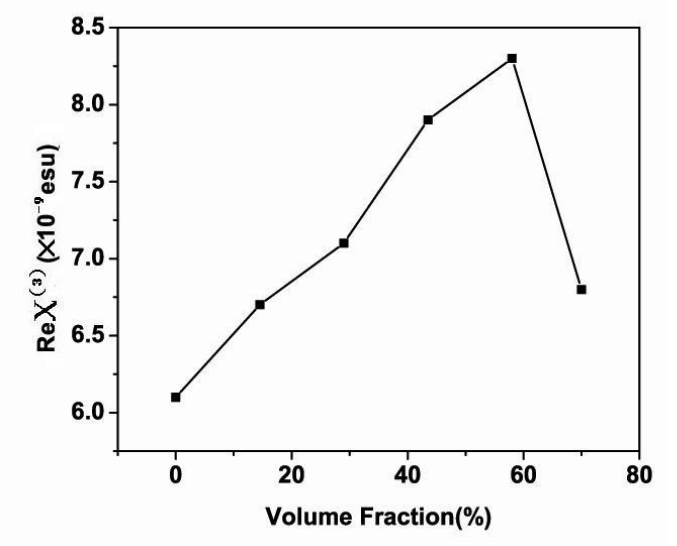

Figure 2-4. Figure caption. The variation of third-order nonlinear optical susceptibility Re $\chi^{(3)}$ versus different volume fraction of Ag nanoparticles for PDA/Ag composite films.

Copyright © 2010. Nova Science Publishers, Incorporated. All rights reserved.

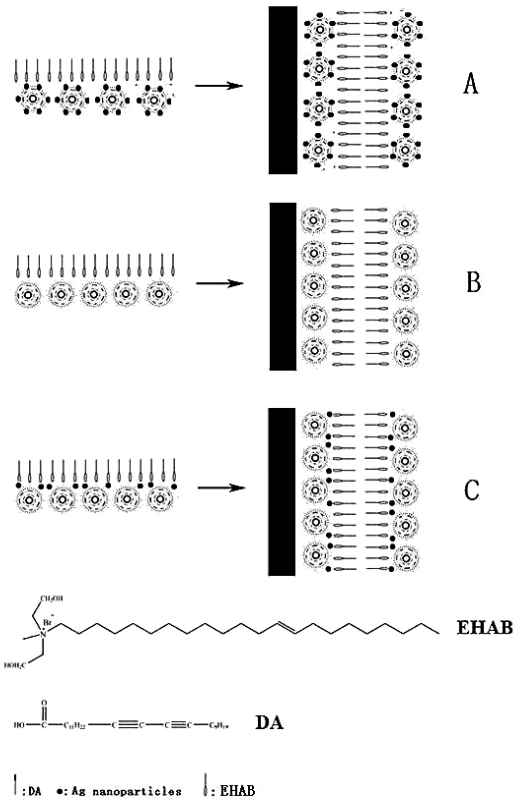

Figure 2-5. (a) Schematic preparation of PDA/Ag nanocomposite vesicles LB films of (a) EHAB and PDA/Ag nanocomposite vesicles (reference sample), (b) EHAB and pure PDA vesicles, (c) EHAB, Ag nanoparticles (Negative charge) and pure PDA vesicles.

Simulation of the effective third-order nonlinear optical properties of composite films with different volume fraction of spherical Ag nanoparticles was shown in Figure 2-5. This concentration-dependent enhancement effect of Ag colloidal nanoparticles was validated by Maxwell-Garnett model [37]. As shown in this Figure, P = 0.58 is the best volume fraction for the Ag nanoparticles doping, the maximum of third-order non-linear enhancement factor ($\chi^{(3)}_e/\chi^{(3)}_i$) was 24,178, and the third-order nonlinear was 10^4 times larger than that of metal particles in theory. All above simulation results were almost consistent with the results of our experiment (the volume fraction of metal particles was 58% when the composite film containing 80μg Ag nanoparticles). There is a certain value of p to keep an optimum distance between the particles with which the largest local field enhancement will occur. Thus the nonlinear properties of these Ag nanoparticles/organic matter composite films can be easily modulated by varying the concentration of Ag nanoparticles and the strategy described would be useful in the development of organic-inorganic hybrid linear optical and NLO devices.

2.3.3. Intended modulation of the distance between silver nanoparticles to control the NLO properties of nano silver / organic composites system

Modulation of the distance between silver nanoparticles to control the NLO properties is very attractive since it can be used to prepare materials with special third-order NLO

Copyright © 2010. Nova Science Publishers, Incorporated. All rights reserved.

susceptibility and can enhance the NLO properties furthest. Although the approach of modulation is in the initial phase of exploration, LB technology gives us some inspiration. In order for the modulation of the distance between silver nanoparticles, we immobilized these PDA/Ag composite vesicles onto the solid substrate by Langmuir-Blodgette (LB) method with special surface pressure to insure the silver nanoparticles outside PDA vesicles with special distance [33]. A schematic representation of the LB procedure employed for this purpose is given in Figure 2-5. An N,N-bis(2-hydroxyethyl)-N-methyl-N-(Z-13-docosyl) quaternary ammonium bromide (EHAB) solution in chloroform was used as the spreading solution. The aqueous solution of PDA vesicles, PDA/Ag composite vesicles or PDA vesicles mixed with negative charged Ag nanoparticles were respectively used as sub phase and the temperature was maintained at 22 ◦C. After evaporation for 20 min, the surface was compressed slowly to record the pressure–area isotherm. A compression rate of 5 mm/min was used for studying the pressure–area isotherm. When the desired surface pressure was attained, the monolayers were transferred from the air–water interface to a solid substrate (glass slides) by LB method. A surface pressure of 25 mN/m was maintained for deposition of LB films and eighty monolayers were deposited. Dipping and raising speed was fixed at 5 mm/min and a waiting time of 10 min was given between dips to dry the LB film.

The X-ray diffraction studies indicated that the preparation of this LB films as described above with PDA/Ag (50 nm) composite vesicles subphase was successful (as shown in Figure 2-6). The appearance of five equidistant Bragg diffraction peaks in the range $2\theta = 1.2° \sim 10°$ indicated the presence of a regular, periodic structure in the LB film. The average spacing in the LB film on glass slide could be calculated to be about 7 nm. In general, vesicles change their aggregate morphology by collapse and fusion in contact with solid surfaces to form supported membranes. The formation of supported membranes relative to that of vesicles depends on competition between the adhesive energy and the vesicle bending energy [38]. AFM image of this composite film, fabricated using the LB procedure, are shown in Figure 2-7. A remarkably rough surface was observed and the non-regular approximate spherical particles, whose sizes are approximately 150–300 nm, were clearly seen in the AFM images. However, the thickness of above non-regular particles is about 10 nm, which is in accordance with the results of XRD. It should be ascribed to the collapse and shrinkage of PDA/Ag nanocomposite vesicles after immobilization and drying. All above results indicated that despite there are a certain degree of collapse, PDA/Ag nanocomposite vesicles retained their microstructure and shape after immobilization.

In order to testify whether this film prepared by LB method can greatly enhance the third-order NLO susceptibility or not, Z-scan technique was used to evaluate the NLO properties of NLO properties of LB films of PDA/Ag nanocomposite vesicles, pure PDA vesicles and PDA vesicles mixed with negative charged Ag nanoparticles (see Figure 2-8). LB films of PDA/Ag composite vesicles promoted NLO properties enhancement. Compare to that of pure PDA vesicles LB films, the resulting $X^{(3)}(\omega)$ of LB films of PDA vesicles mixed with negatively charged nano-silver particles showed nearly 2.5 times enhancement, which should be ascribed to the local field enhancement effect of loading of Ag nano particles. However, the resulting $X^{(3)}(\omega)$ of PDA/Ag (50 nm) nanocomposite vesicles LB films showed nearly 8 times enhancement compared to pure PDA vesicles LB films, and nearly 5000 times enhancement compare to that of pure PDA vesicles solution. This stupendous enhancement can be explained as follow: the spacing and relative position of the neighboring PDA/Ag composite vesicles in LB films were closer than those in solution, which would cause remarkable

Copyright © 2010. Nova Science Publishers, Incorporated. All rights reserved.

enhancement in NLO properties due to coupling effect. The resulting $X^{(3)}(\omega)$ of PDA/Ag (50 nm) nanocomposite vesicles LB films was about 2.3 times larger than the value of LB films of PDA vesicles mixed with negatively charged nano-silver particles, which indicated that the optical nonlinearity is enhanced in the assemble of PDA/Ag core-shell microstructure due to the local-field enhancement effect. The local field could be concentrated in both the core and shell region of the nanocomposite vesicles at the surface-mediated plasma resonance, this increased field is then utilized for self-enhancements of the optical nonlinearity from each component of the composite films [21, 39]. We anticipate that the control of suitable immobilization spacing and relative position of the neighboring PDA/Ag composite vesicles in LB films should lead to more stupendous enhancements in third-order NLO response.

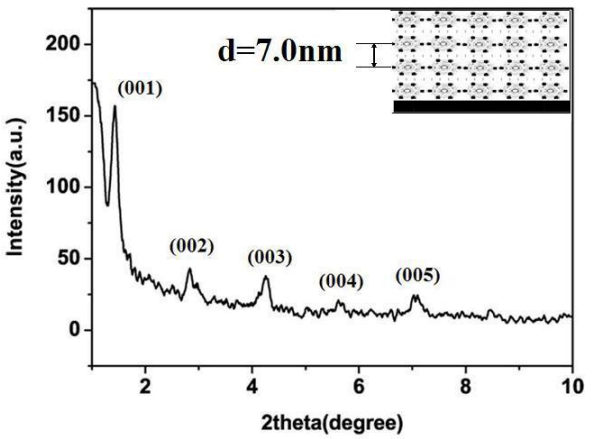

Figure 2-6. X-ray diffraction spectra of LB film composed of PDA/Ag (50 nm, positive charge) composite vesicles. The inset shows the schematic illustration of the structure of this LB film.

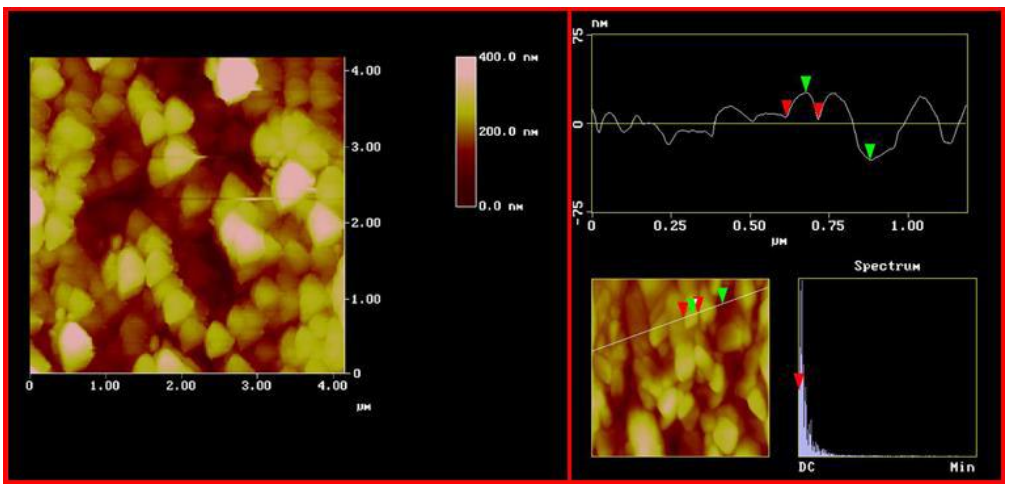

Figure 2-7. AFM images showing the topography and the roughness profile along the white line indicated by the green and red arrows of LB films prepared from PDA/Ag (50 nm, positive charge) composite vesicles on glass substrate.

Copyright © 2010. Nova Science Publishers, Incorporated. All rights reserved.

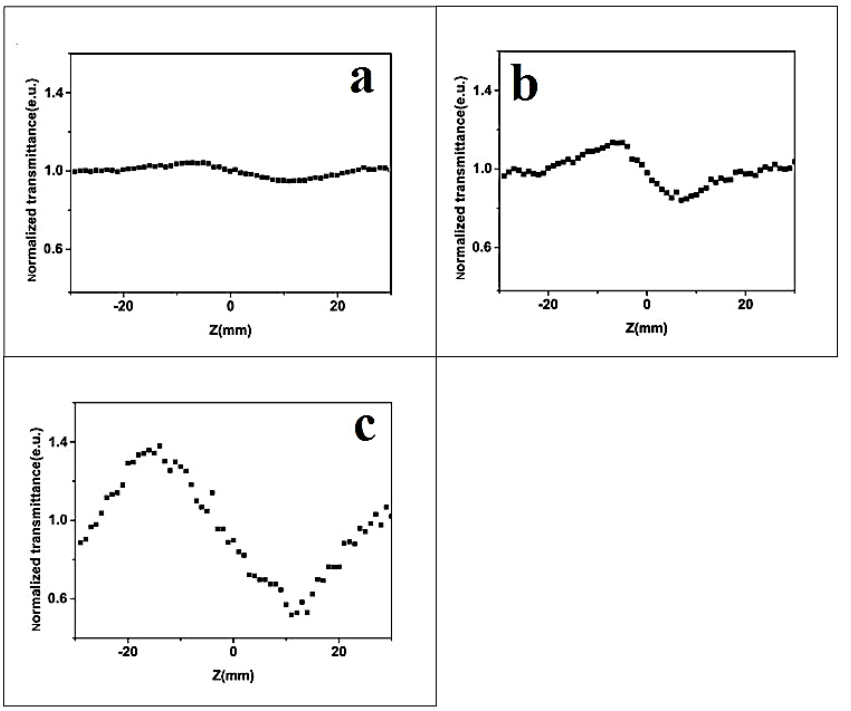

Figure 2-8. Measured Z-scan normalized transmittance curves of (a) pure PDA vesicles LB films (100 layers), (b) PDA vesicles maxed with Ag nanoparticles (50nm, negative charge) LB films (100 layers), (c) PDA/Ag (50nm, positive charge) nanocomposite vesicles LB films (100 layers).

3. CONCLUSIONS

Owing to the local field enhancement caused by surface plasmon resonance, Organic/metal nanoparticles nano-composite structure has larger third-order NLO susceptibility. Two kinds of PDA/Ag nanocomposite vesicles were fabricated successfully through simple physicochemical processes. Compared with pure PDA vesicles, the Ag colloidal nanoparticles coating led to the obvious enhancement of NLO properties for PDA vesicles. The obtained nonlinear refractive index for pure PDA vesicles and PDA/Ag composite vesicles with Ag nanoparticles coated on the outer surface of PDA vesicles was 1.2 × 10−14 cm^2 W^{-1} and 7.3 × 10−14 cm^2 W^{-1}, respectively. The nearly seven times improvement is observed as a result of local field enhancement under the surface plasmon resonance of silver nanoparticles at the interface.

Several methodologies were developed for the modulations of the NLO properties of PDA/Ag nanocomposite system. Then, our investigations became focused on modulating the size, concentration and array of Ag nanoparticles in PDA/Ag nanocomposite system to control the surface plasmon resonance, even to control the NLO properties. Several interesting results were obtained. Firstly, the NLO properties of PDA/Ag nanocomposite system are size-dependent. PDA/Ag composite vesicles with 50nm Ag particles showed

Copyright © 2010. Nova Science Publishers, Incorporated. All rights reserved.

maximum NLO properties enhancement effect (nearly 13 times compared pure PDA vesicles). Then the third-order nonlinear optical susceptibility Re $\chi^{(3)}$ shows remarkably concentration-dependence which increased unceasingly when the volume fraction of silver nanoparticles changed from 0 to 58%, and the maximum appeared when the volume fraction of silver nanoparticles reached 58%. Importantly, immobilization of PDA/Ag nanocomposite vesicles into thin films with special distance between Ag nanoparticles could promote NLO properties enhancement. Control of suitable immobilization spacing and relative position of the neighboring PDA/Ag composite vesicles in LB films in future implementations of this concept should lead to stupendous enhancements in third-order NLO response. The authors believe that these strategy described in this article would be useful in the development of PDA-based optical and NLO devices.

REFERENCE

[1] Hu, JQ; Chen, Q; Xie, ZX. et al. *Adv.Funct.Mater*, 2004, 14, 183.
[2] Gu, Z; Horie, R; Kubo, S. *Angew. Chem. Int. Ed*, 2002, 41, 1153.
[3] Tian, ZQ; Ren, B; Wu, DY. *J. Phys. Chem. B*, 2002, 106, 9463.
[4] Agranovich, VM. *Surface Polaritons*. Amsterdam: North-Holland, 1982.
[5] Raether, H. *Surface Plasmons*. Berlin: Springer, 1988.
[6] Boardman, AD. *Electromagnetic Surface Modes*. New York: Wiley, 1982.
[7] Kreibig, U. et al. *Optical Properties of Metal Clusters*. Berlin: Springer, 1995.
[8] Zayats, AV. *Opt. Commun*, 1999, 161, 156.
[9] Mills, DL. *Phys. Rev. B*, 2002, 65, 125419.
[10] Smolyaninov, II; Zayats, AV; Gungor, A; Davis, CC. *Phys. Rev. Lett*, 2002, 88, 187402.
[11] Dissertation der Fakultat fur Physik der Ludwig-Maximilians-Universit at Munchen, vorgelegt von Carsten S¨onnichsen aus Hamburg. *Munchen*, 20 June, 2001.
[12] Gans, R; Ann. *Phys*., (N.Y.), 1915, 47, 270.
[13] Link, S; El-Sayed, MA. *J. Phys. Chem. B*, 1999, 103, 8410.
[14] Zynio, SA; Samoylov, AV; Surovtseva, ER; Mirsky, VM; Shirsov, YM. *Sensors*, 2002, 2, 62.
[15] Sharma, AK; Gupta, BD. 2005, Opt. *Commun*, 245, 159.
[16] Park, S; Pelton, M; Liu, M; Guyot-Sionnest, P; Scherer, NF. *J. Phys. Chem. C*, 2007, 111, 116-123.
[17] Kou, X; Zhang, S; Yang, Z; Tsung, CK; Stucky, GD; Sun, L; Wang, J; Yan, C. *J. Am. Chem. Soc*., 2007, 129, 6402-6404.
[18] Ekimov, AI; Efros, AL. *Sov. Phys. Semicond*, 1982, 16(7), 775.
[19] van Dijk, MA; Lippitz, M; Orrit, M. *Acc. Chem. Res*., 2005, 38, 594-601.
[20] Richard, D; Roussignol, P; Flytzanis, C. *Opt. Lett*, 1985**,** 10, 51.
[21] Neeves, AE; Birnboim, MH. *J. Opt. Soc. Am. B*, 1989, 6, 787.
[22] Haus, JW; Zhou, HS; Takami, S; Hirasawa, M; Homma, I; Komiya, H. *J. Appl. Phys*., 1993**,** 73(3), 1043-1048.

Copyright © 2010. Nova Science Publishers, Incorporated. All rights reserved.

[23] Bosshard, C. h; Sutter, K; Prˆetre, P. h; Hulliger, J; Fl¨orsheimer, M; Kaatz, P; G¨unter, P. *Organic Nonlinear OpticalMaterials* (*Advances in Nonlinear Optics* vol 1), 1995, Kajzar, F; Garito, AF. (London: Gordon and Breach) chapter 6, 89.
[24] Sarkar, A; Okada, S; Matsuzawa, H; Matsuda, H; Nakanishi, H. *J. Mater. Chem*., 2000, 10, 819.
[25] Chen, X; Zou, G; Deng, Y; Zhang, Q. J. *Nanotechnologl*, 2008, 19, 195703.
[26] Inouye, Y; Hayazawa, N; Hayashi, K; Sekkat, X. and Kawata, S. *Proc. Spie*, 1999, 3791, 40.
[27] Liu, Y; Liu, C; Zhang, Z; Wang, C. *Spectrochim. Acta A*, 2001, 57, 35.
[28] Futamata, M; Bruckbauer, A. *Jpn. J. Appl. Phys*., 2001, 40, 4423.
[29] Krenn, JR; Salerno, M; Felidj, N; Lamprecht, B; Schider, G; Leitner, A; Aussenegg, F. R; Weeber, JC; Dereux, A; Goudonnet, JP. *J. Microsc*, 2000, 202, 122.
[30] Brongersma, ML; Hartman, JW; Atwater, HA. *Phys. Rev. B*, 2000, 62, R16356.
[31] Okamoto, T; Yamaguchi, I. *J. Microsc*, 2001, 202, 100.
[32] Fuchs, R; Kliewer, KL. *J. Opt. Soc. Am*, 1968, 58, 319.
[33] Chen, X; Tao, J; Zou, G; Su, W; Zhang, QJ; Liu, SY; Wang, P. *Physical Chemistry Chemical Physics*, submitted.
[34] Okamoto, T; Haraguchi, M; Fukui, M. *Japan. J. Appl. Phys*., 2004, 43(9), 6507-6512.
[35] Chen, X; Jiang, H; Wang, YL; Zou, G; Su, W; Zhang, Q. J. *New Journal of Chemistry*, submitted.
[36] Ryasnyanskiy, AI; Palpant, B; Debrus, S; Pal, U; Stepanov, A. *Journal of Luminescenc*, 2007, 127, 181-185.
[37] Giovanni Piredda; David, D. Smith; Bettina Wendling; Robert W. Boyd. *J. Opt. Soc. Am. B*, 2008, 25, 6.
[38] Su, YL; J. *Colloid Interface. Sci*., 2005, 292, 271-276.
[39] Yang, Y; Hori, M; Hayakawa, T; nogami, M. *Surface Science*, 2005, 579, 215-224.

Copyright © 2010. Nova Science Publishers, Incorporated. All rights reserved.

Copyright © 2010. Nova Science Publishers, Incorporated. All rights reserved.

In: Silver Nanoparticles
Editor: Audrey E. Welles, pp. 327-339
ISBN: 978-1-61668-690-1
© 2010 Nova Science Publishers, Inc.

Chapter 9

ANTIBACTERIAL APPLICATIONS OF SILVER NANOPARTICLES: BENEFITS AND HUMAN HEALTH RISKS

Renat R. Khaydarov[1], Rashid A. Khaydarov[1], Yuri Estrin[2], Svetlana Evgrafova[3], Seung Y. Cho[4] and Stefanie Wagner[5]

[1] Institute of Nuclear Physics, Tashkent, Uzbekistan
[2] ARC Centre of Excellence for Design in Light Metals, Department of Materials Engineering, Monash University and CSIRO Division of Process Science and Engineering, Clayton, Victoria, Australia
[3] V.N. Sukachev Institute of Forest SB RAS, Krasnoyarsk, Russia
[4] Dept. of Environmental Engineering, Yonsei University, Wonju, South Korea
[5] Institute of Technical Chemistry, Gottfried-Wilhelm-Leibniz University, Germany

Copyright © 2010. Nova Science Publishers, Incorporated. All rights reserved.

ABSTRACT

The minimum inhibitory concentrations (MICs) assays conducted for *E. coli*, *S. aureus*, *B. subtilis* and *P. phoeniceum* have shown that the antimicrobial activity of silver ions was superior to that of silver nanoparticles. As silver nanoparticles can be more suitable in some bactericidal applications than silver ions, the efficacy of nanosilver as an antimicrobial agent against a range of microbes on the surface of water paints and cotton fabrics has been studied. The cytotoxicity of silver nanoparticles has been studied using NIH-3T3, HEP-G2, A-549, PC-12, and Colo-320 cells via the MTT ((3-(4,5-dimethylthiazol-2-yl)-2,5-diphenyl-tetrazolium-bromid) test. The MTT test results obtained have shown that silver nanoparticles in concentrations of ~1-10 ppm entering the body from air or liquid suspensions can present a potential risk to human health. However, silver nanoparticles as a commercially viable addition to be used in paint and textile industry are unlikely to present a direct health risk.

Keywords: silver, nanoparticle, silver ion, cytotoxicity, Eucaryota, health risk

INTRODUCTION

Silver has been well known for its antimicrobial properties since antiquity. In ancient Greece and Rome, silver was widely used to control infections and spoilage. Since 20th century silver and its compounds have been used extensively in many bactericidal applications including wound healing, water treatment, flower preservatives, etc. (Klasen 2000). Over the last decades silver nanoparticles, defined as structures up to 100 nm in size, have been extensively investigated and have found applications in catalysis (Lewis 1993), optics (Murphy et al. 2005), electronics (Li et al. 2005) and other areas of science and technology (Niemeyer 2001) due to their unique size-dependent optical, electrical and magnetic properties. Currently, most of silver nanoparticles applications are connected with their usage as antibacterial/antifungal agents (Buzea et al. 2007). According to a recent market research report (http://www.bourneresearch.com), nanosilver is "one of the fastest growing product categories in the nanotechnology industry", For instance, there is a growing interest in preparation of bactericidal cotton fibers containing silver nanoparticles for textile industry (Lee and Jeong 2004, Lee and Jeong 2005). Indeed, owing to their ability to retain moisture ordinary cotton fabrics provide an excellent environment for microorganisms to thrive (Chen and Chiang 2008). There is also a promising trend to impregnate commercially available paints with silver nanoparticles. For example, nanosilver-based wall paint would prevent the formation of mould inside buildings and the growth of algae on outside walls (Revina et al. 2001).

The lack of knowledge on the mechanism of the bactericidal effects of silver nanoparticles in combination with the significant growth of applications of nanosilver in various branches of industry over the last years has caused new concerns that silver nanoparticles may have a toxic effect on human health. In the 20^{th} century a popular belief was that except for causing argyria, silver was relatively non-toxic to mammalian cells (Chen and Schluesener 2008). However the studies conducted over the last decade (Soto 2005, Braydich-Stolle et al. 2005, Hussain et al. 2005, Grodzik and Sawosz 2006) have shown that reaching nanoscale, silver-based materials can exhibit significant toxicity to animal and human cells. A recent review cautioned: "these are questions that need to be imperatively answered before people rush to indulge into the nanosilver boom" (Chen and Schluesener 2008).

The purpose of our study was a) to quantitatively estimate antimicrobial effect of silver nanoparticles comparing it with that of silver ions; b) to check the efficacy of nanosilver as antimicrobial agent against a range of microbes on the surface of paints and 100% cotton fabrics, c) to quantify cytotoxicity of silver nanoparticles using standard colorimetric MTT assay.

MATERIALS AND METHODS

Preparation of Ag Ions and Nanoparticles

The silver ions used in the bacterial susceptibility tests were released from pure silver electrodes via 12 V battery-operated constant current generators. The apparatus used for

Copyright © 2010. Nova Science Publishers, Incorporated. All rights reserved.

silver ions generation was described previously (Khaydarov et al. 2004). The water-based silver colloidal solution was obtained by our recently reported three-stage process based on the electroreduction of silver ions in water (Khaydarov et al. 2008). he nanosilver particles produced were spherical with diameter of 7 ± 3 nm (cf. Figure 1).

The concentration of silver nanoparticles and ions in solutions was determined by neutron activation analysis (NAA) (Soete et al. 1972). Samples were irradiated in the nuclear reactor of the Institute of Nuclear Physics (Tashkent, Uzbekistan). The product of nuclear reaction $^{109}Ag(n,\gamma) \rightarrow {}^{110m}Ag$ has the half-life $T_{1/2}$ = 253 days. The silver concentration was determined through measurements of the intensity of gamma radiation with the energy of 0.657 MeV and 0.884 MeV emitted by ^{110m}Ag. A Ge(Li) detector with a resolution of about 1.9 keV at 1.33 MeV and a 6144-channel analyser were used for recording gamma-ray quanta.

The morphology of silver nanopartilces on the surface of cotton and paint samples was observed by field emission scanning electron microscopy (FE-SEM; JSM-6700F, JEOL, Japan). The size and shape of the nanoparticles in solution were determined by transmission electron microscopy (TEM) (LEO-912-OMEGA, Carl Zeiss, Germany).

Antimicrobial Activity Assay

To evaluate the antibacterial and fungicidal properties of silver particles *Escherichia coli* was used as a representative Gram-negative bacterium; *Staphylococcus aureus* and *Bacillus subtilis* were used as Gram-positive bacteria; *Aspergillus niger, Aureobasidium pullulans* and *Penicillium phoeniceum* were used to represent cosmopolitan saprotrophic fungi. The minimum inhibitory concentrations (MICs) of solutions for various microbes were determined using the macrodilution broth susceptibility test. Nutrient broth used in the macrodilution method contained peptic digest of animal tissue 50.00 g/L; beef extract 1.5 g/L; sodium chloride 5.00 g/L; glucose 5 g/L; pH 7.4 ± 0.2. A standardized suspension of approximately 10^6 CFU/mL density was obtained by inoculating the culture in nutrient broth (Hi-Media) and incubating the tubes at 37°C for 3 h. A serial dilution of the dispersion of Ag ions and the dispersion of silver nanoparticles were prepared within a desired range. 10 mL of the standardized culture suspension was then inoculated and tubes were incubated at 37°C for 24 h. MIC was defined as the lowest concentration of the inhibiting agent that completely inhibited bacterial growth, the unit for MIC was chosen as mg(Ag)/L. MIC was examined visually, by checking the turbidity of the tubes.

Antimicrobial Finishing of Cotton and Paint Samples

Common household acrylic paint widely used for renovating and decorating purposes has been investigated. Silver nanoparticle-containing acrylic paint was obtained by diluting the initial paint sample with the Ag colloidal solution in such a way as to get the desired value of nanosilver concentration within the desirable testing range of 2-50 ppm. For the antibacterial tests a 22 mm x 22 mm pasteboard was covered with silver nanoparticle-containing acrylic paint.

Copyright © 2010. Nova Science Publishers, Incorporated. All rights reserved.

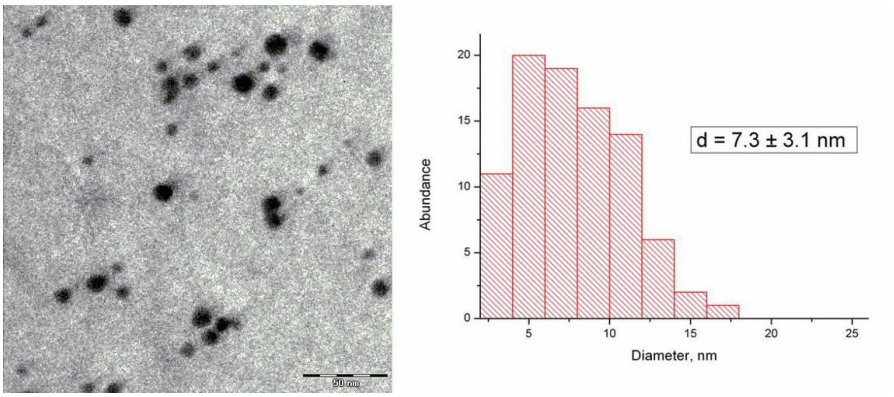

Figure 1. Typical TEM micrograph (scale of 50 nm) and size distribution histogram for silver nanoparticles prepared by the electrochemical method (adapted with permission from Khaydarov et al. 2008).

The bleached woven cotton fabric weighing 98 g/m^2 was cut into equal-size square pieces measuring 15 mm x 15 mm. The samples were immersed in a colloidal solution bath for 1 minute and squeezed thoroughly with further drying at 60°C for 5 minutes.

To evaluate the antibacterial and fungicidal properties of Ag nanoparticles added to a cotton fabric and an acrylic paint, samples with different Ag nanoparticle content as well as control samples were immersed in a thin layer of beef-extract agar. 1 mL of suspension with approximately 10^5 CFU/mL density of the microorganisms to be tested was distributed uniformly on agar surface and incubated at 28 °C (CFU = colony forming units). Antimicrobial activity was evaluated according to the presence or absence of microbial growth just above the sample after a 24-h incubation for bacteria and a 72-h incubation for fungi. All microbiological tests were performed in triplicate.

Materials for Cytotoxicity Assay

All solutions were prepared with deionised water (Arium, SARTORIUS, Göttingen, Germany). Dulbecco´s Modified Eagles Medium (DMEM) was purchased from Sigma-Aldrich (Steinheim, Germany) and foetal calf serum (FCS) and newborn calf serum (NCS) from PAA (Cölbe, Germany). Horse serum (HOS) was purchased from Invitrogen (Karlsruhe, Germany). Buffers, salts, antibiotics and other reagents were purchased from Fluka (Buchs, Switzerland) and Sigma-Aldrich (Steinheim, Germany) and are of *per analysi* quality.

The NIH-3T3 cells (Swiss mouse embryo) were cultivated in DMEM containing 10 % NCS and antibiotics (penicillin and streptomycin) at 37° C /5% CO_2.

The HEP-G2 (human hepatocellular carcinoma) cells were cultivated in DMEM containing 10 % FCS and antibiotics (penicillin and streptomycin) at 37 °C /5% CO_2.

The A-549 (human lung carcinoma) cells were cultivated in DMEM containing 10 % FCS and antibiotics (penicillin and streptomycin) at 37 °C /5% CO_2.

The PC-12 cells (rat adrenal pheochromocytoma) were cultivated in a PLL coated T-75-flask in DMEM containing 10 % HOS, 5 % NCS, 1% sodiumpyruvate, 1% L-glutamine and antibiotics (penicillin and streptomycin) at 37 °C /5% CO_2.

Copyright © 2010. Nova Science Publishers, Incorporated. All rights reserved.

The Colo-320 cells (human colon adenocarcinoma) were cultivated in Roswell Park Memorial Institute 1640 medium (RPMI 1640) containing 10 % FCS and antibiotics (penicillin and streptomycin) at 37 °C /5% CO_2.

All cell lines had grown to confluence after 3-4 days and were then detached with trypsin and cultured in a new flask.

Cultivation and Cell Viability

To test the effect of silver nanoparticles, 96-well plates were seeded with a defined number of cells. The plates were incubated for 4 days (37 °C/5% CO_2). On day 5 the suspensions of particles in the culture medium in different concentrations or just water in the highest concentration in the medium were added to the cells. On day 7 the viability of the cells was determined via MTT-test.

	NIH-3T3	HEP-G2	A-549	PC-12	Colo-320
Number of cells per well	6.000	10.000	8.000	10.000	10.000

The viability of the cells was analysed by the MTT ((3-(4,5-dimethylthiazol-2-yl)-2,5-diphenyl-tetrazolium-bromid) test (Sigma-Aldrich, Steinheim, Germany). This assay is based on the hydrolysis of a tetrazoium ring by mitochondrial dehydrogenase enzymes to an insoluble blue reaction product. To perform the MTT test the medium of each well was removed and 100 µL of fresh medium and 10 µL of MTT solution (5mg/mL PBS, sterile) were added to each well, followed by incubation for 4 h at 37°C/ 5 % CO_2. Subsequently, 100 µL of 10 % SDS in 0.01M HCl was added and the plates were further incubated for 24 h. The absorbance of solutions at the the wave lengths of 570-630 nm was determined using a microplate reader (Bio-Rad, München, Germany).

RESULTS AND DISCUSSION

MIC Assays

The minimum inhibitory concentration (MIC) assays were conducted for electrically generated silver ions and silver nanoparticles using Gram-negative bacterium *E. coli*, Gram-positive bacteria *S. aureus* and *B. subtilis* and fungus *P. phoeniceum* (see Table 1). For an adequate interpretation of the results obtained one needs to consider that in the case of silver nanoparticles, we deal with a combination of effects: (i) the one associated with Ag ions released from the nanoparticles and (ii) direct interaction of cells with nanoparticles (Mitragotri 2009). The purpose of our nanosilver MIC assay (Khaydarov et al. 2010) was not to reveal which of the effects prevails, but to quantitatively estimate the combined antimicrobial efficiency of nanosilver. Thus in order to inhibit the growth of gram-positive and gram-negative bacteria and fungi represented in Table 1 it was necessary to apply higher concentrations of nanosilver as compared to the concentration of electrically generated silver ions.

In spite of the pronounced antimicrobial effect, silver ions have only limited use as an antimicrobial agent in applications such as medical products, clothing, and household articles.

Copyright © 2010. Nova Science Publishers, Incorporated. All rights reserved.

This is due to their rapid bounding or inactivation by various substances present in a medium. This limitation can be overcome by using silver nanoparticles as an antimicrobial agent owing to continuous release of Ag ions they provide (Kim et al. 2007).

Modified Water Paint

We have impregnated water paints with our nanosized silver colloids. As one can see from Figure 2, most of initial silver nanoparticles had agglomerated into clusters up to 200 nm in size because of attractive interaction forces between them.

Table 1. Results of minimum inhibitory concentration (MIC) assay for silver nanoparticles and silver ions for some microbial species

Microbe	Electrically generated silver ions MIC (mg(Ag)/L)	Silver nanoparticles (average particle size of 7 nm) MIC (mg(Ag)/L)
E. coli	1	5
S. aureus	0.6	3
P. phoeniceum	0.5	2
B. subtilis	2.4	29

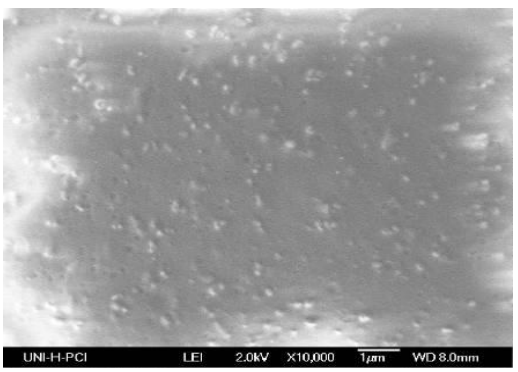

Figure 2. Sample of water paint with immobilized silver nanoparticles.

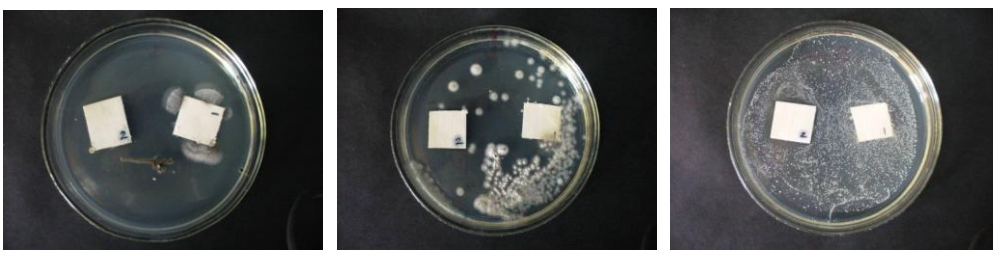

Figure 3. Growth of *A. pullulans* (left) *P. phoeniceum* (middle) and *S. aureus* (right) cultures on pasteboard samples modified by silver nanoparticles. (Note the white spots corresponding to microbial colonies). Sample #1 is a control sample, i.e. it was covered with non-modified paint; sample #2 was covered with the paint modified by silver nanoparticles of 0.8 μg/cm^2 density.

Copyright © 2010. Nova Science Publishers, Incorporated. All rights reserved.

Table 2. Antimicrobial effect of samples of water paint

Microbe species	Type of paint	
	Sample #1 (Non-treated paint)	Sample #2 (Nanosliver-modified paint, 0.8 μg/cm^2)
Aspergillus niger	+	-
Penicillium phoeniceum	+	-
Aureobasidium pullulans	+	-
Staphylococcus aureus	+	-
Bacillus subtilis	+	+
Escherichia coli	+	+
Control (samples on beef-extract agar)	+	-

The photographs in Figure 3 show growth of *A. pullulans*, *P. phoeniceum* and *S. aureus* cultures on pasteboard samples modified by silver nanoparticles.

The test results on antibacterial and antifungal effect of nanosilver-based water paint are summarized in Table 2, where a plus sign indicates the occurrence of microbial growth and a minus sign corresponds to the absence of visible growth.

Increase of the concentration of nanosilver in water paint to 5-6 μg/cm^2 lead to the suppression of growth of *B. subtilis* and *E. coli* as well. It should be noted that larger concentrations of nanosilver can potentially lead to undesirable color shift of the water paint with time. We observed an outside wall of a house painted (Tashkent, Uzbekistan) with nanosilver-modified (0.8 μg/cm^2) paint. The NAA tests conducted over a period of eight months (March-October, 2008) showed that no significant loss of silver nanoparticles in the wall paint occured. We suggest that silver nanoparticles may be a commercially viable addition for use in the paint industry. Microbes can come into contact with walls in a number of ways: by deposition of dust and fine aerosols, by human skin contact, and by splashes from liquids. The nanosilver-based wall paint can potentially prevent the formation of mould inside buildings and, by conjecture, the growth of algae on outside walls.

Modified Cotton Fabric

We have also impregnated 100% cotton fabrics with nanosized silver colloids synthesized by the electrochemical technique (Khaydarov et al. 2008). The particles had reasonably good dispersibility on the surface of a modified cotton spread. However, agglomeration of silver nanoparticles into larger clusters (up to 200 nm in size) was also observed (cf. Figure 4).

As shown previously (Khaydarov et al. 2009), a cotton fabric with immobilized silver nanoparticles (mean particle size of 15 nm) with the concentrations of 5 μg/cm^2, 3 μg/cm^2 and 1 μg/cm^2 can inhibit the growth of *A. niger*, *P. phoeniceum* and *S. aureus* cultures, respectively, on beef extract agar. In the present study we used aqueous dispersion of 7±3 nm silver nanoparticles during the finishing process. It allowed reducing sizes of silver particles

Copyright © 2010. Nova Science Publishers, Incorporated. All rights reserved.

on the surface of the 100% cotton fabric from the micron size (as in our previous work) down to ~100 nm (cf. Figure 4).

As a result, the antifungal/antibacterial effect for *A. niger, P. phoeniceum* and *S. aureus* was confirmed even for nanosilver concentration on the surface of the cotton fabric as low as 1 μg/cm^2. The same experiments conducted for *E. coli, B. subtilis* and *A. pullulans* cultures also demonstrated a pronounced antimicrobial effect for concentrations of nanosilver of 7 μg/cm^2, 5 μg/cm^2 and 3 μg/cm^2 respectively. In order to estimate the durability of the bacteriostasis of the silver-treated cotton fabric with respect to laundering, we have compared the surface concentration of silver particles on fabrics before washing to the particles on them after 2, 5 and 10 washes.

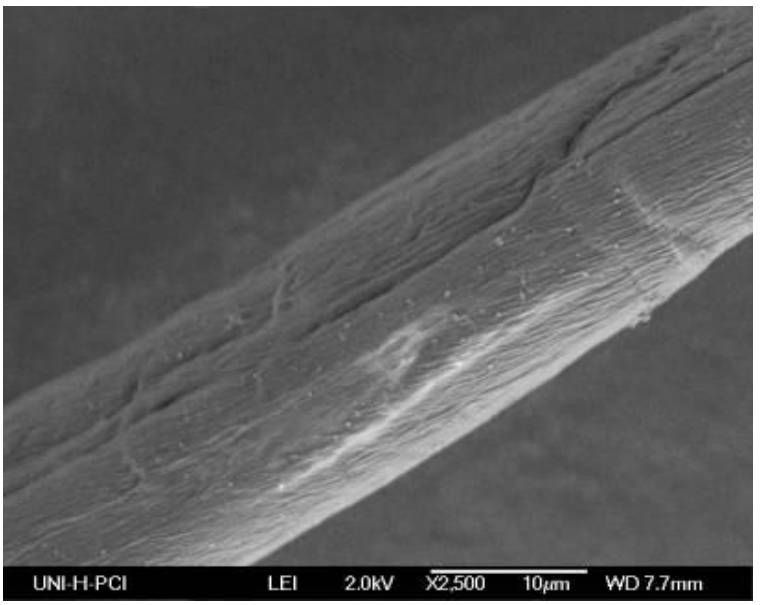

Figure 4. Sample of 100% cotton with immobilized silver nanoparticles.

Table 3. Laundering durability of silver nanoparticles on modified cotton fabric samples

	Ag concentration (μg/cm^2)
Before washing	5
After 2 cycles	3.5
After 5 cycles	1.8
After 10 cycles	1

The results indicate that silver particles were sufficiently bonded to the cotton fabric, which gave rise to a good bacteriostasis even after 10 cycles of washing. These are encouraging results suggesting that nanosilver-based textile materials give promise in various areas, for example in prevention of wound contamination with microorganisms, in particular fungi and bacteria, in hospitals.

Copyright © 2010. Nova Science Publishers, Incorporated. All rights reserved.

Nanosilver Cytotoxicity

Although the toxicity of silver particles in the µm size range has been established reliably (Donaldson et al., 2000; Donaldson et al., 2001; Donaldson et al., 2002), there is still a lack of information on the toxicity of nano-size silver particles, particularly on their biological interactions with cells including cellular proteins. Nanomaterials can enter human tissues through several ports: via the lungs after inhalation (Oberdorster et al. 2002), through the digestive system (Jani et al. 1990), and possibly through the skin (Lademann et al., 1999). The major toxicological concern derives from the fact that nanoparticles can penetrate the cell membranes and interact with the mitochondria (Braydich-Stolle et al. 2005).

We have studied the cytotoxicity of silver nanoparticles by the MTT test that measures cell activity through the mitochondrial cleavage of a molecule that exhibits a change of color that can be measured spectrophotometrically. NIH-3T3, HEP-G2, A-549, PC-12, and Colo-320 cells have been chosen in order to study all possible absorption paths of silver nanoparticles into the organism and various areas of particle accumulation in the body. Figure 5 shows the effect of silver nanoparticles on the aforementioned cells. The results of the MTT tests presented in the bar diagrams on Fig. 5 reveal a significant decrease of the viability of the Colo-320 cells and the NIH-3T3 cells when exposed to 5 ppm nanosilver. A-549 and HEP-G2 showed more resistance, a significant decrease of the viability being observed for higher concentrations ~ 10 ppm. As for PC-12 cells, even 1 ppm nanosilver caused a certain decrease in their viability.

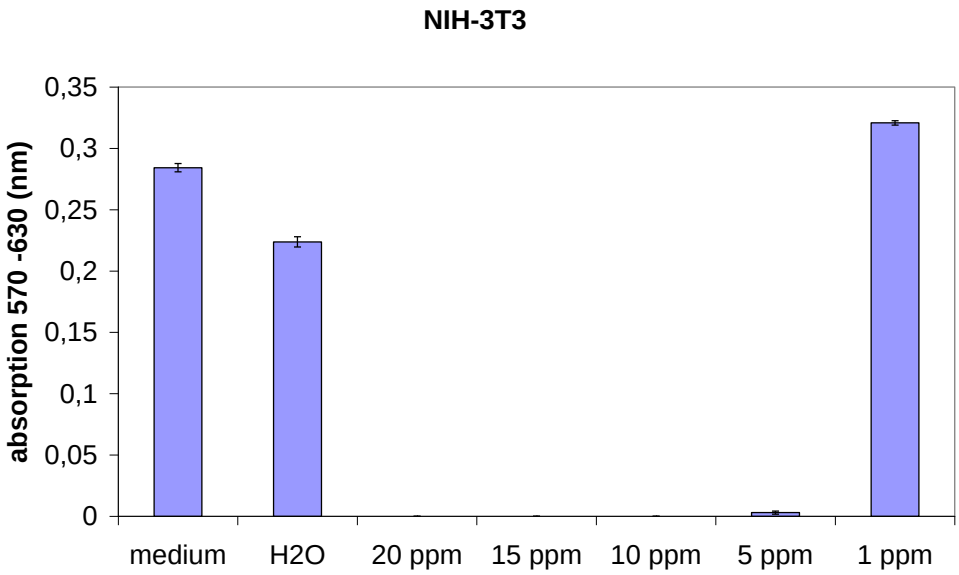

Figure 5. (Continued).

Copyright © 2010. Nova Science Publishers, Incorporated. All rights reserved.

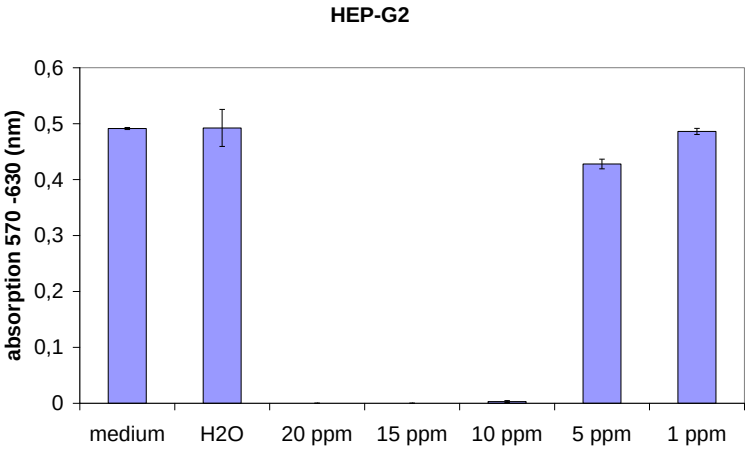

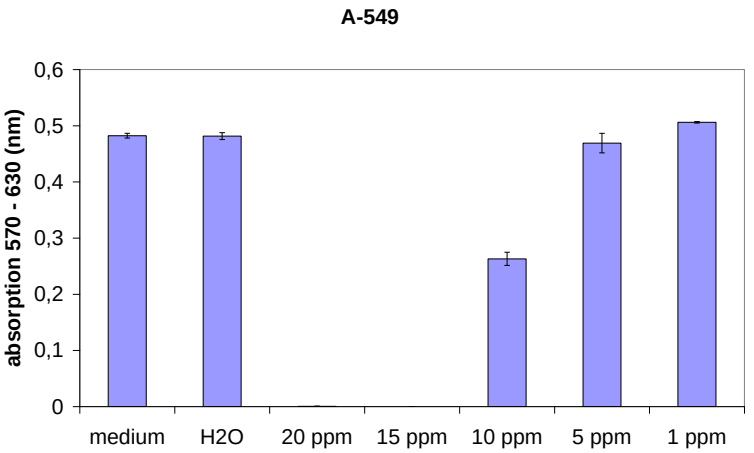

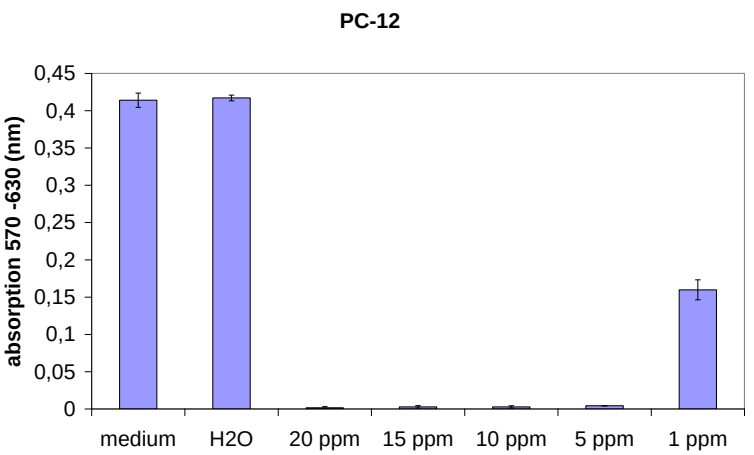

Figure 5. (Continued).

Copyright © 2010. Nova Science Publishers, Incorporated. All rights reserved.

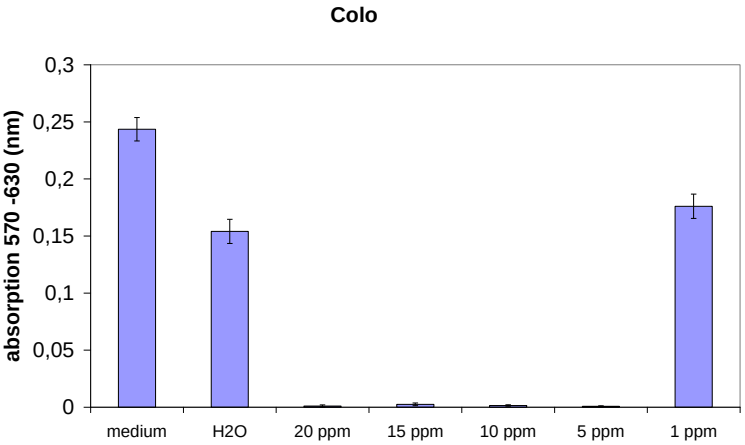

Figure 5. Results of MTT test for NIH-3T3, HEP-G2, A-549, PC-12, and Colo-320 cells.

The present MTT test results suggest that silver nanoparticles with concentrations of ~1-10 ppm entering the body from air or liquid suspensions can present a potential risk to human health. By contrast, silver nanoparticles in textiles or paints described above can be considered as minor constituents bound within potential consumer producsts. Therefore they are unlikely to present a direct health hazard to humans. Still, if due to unforeseen circumstances such silver-based materials enter the human body, their potential toxicity cannot be ruled out and caution with dealing with nanosilver-containing products is a must.

CONCLUSION

Silver nanoparticles synthesized by the cost-effective three-stage electrochemical technique (Khaydarov et al. 2008) were proven to be very promising as antimicrobial agents. MIC assays showed that quantitatively nanosilver was less effective against *E. coli*, *S. aureus*, *B. subtilis* and *P. phoeniceum* than silver ions. However, due to their capability to continuously release Ag ions in sufficient concentration, silver nanoparticles may be a better option in some bactericidal applications than silver ions. The tests conducted demonstrated that synthesized silver nanoparticles added to water paints or cotton fabrics show a pronounced antibacterial/antifungal effect, despite the fact that they tend to be agglomerated into clusters. The MTT test results showed that silver nanoparticles with concentrations of ~1-10 ppm entering the body from air or liquid suspensions can present a potential health hazard. However, nanosilver-treated textiles and paints described in this paper are believed not to present a *direct* health hazard, as owing to sufficient bonding of silver nanoparticles to the material the potential for excessive exposure to Ag ions or nanoparticles will be low. Intentional or inadvertent intake of materials modified by silver nanoparticles may be hazardous, though.

Copyright © 2010. Nova Science Publishers, Incorporated. All rights reserved.

REFERENCES

Braydich-Stolle, L., Hussain S., Schlager J. & Hofmann M. C. (2005). In vitro cytotoxicity of nanoparticles in mammalian germline stem cells, *Toxicological Sciences, 88(2),* 412-419.

Buzea, C., Pacheco, II. & Robbie, K. (2007). Nanomaterials and nanoparticles: Sources and toxicity. *Biointerphases, 2(4),* MR17-MR71

Chen, C. Y. & Chiang, C. L. (2008). Preparation of cotton fibers with antibacterial silver nanoparticles, *Mater. Lett.* doi:10.1016/j.matlet.2008.04.008

Chen, X. & Schluesener, H. J. (2008). Nanosilver: A nanoproduct in medical application, *Toxicology Letters, 176,* 1-12.

Donaldson, K., Stone, V., Gilmour, P. S., Brown, D. M. & MacNee, W. (2000). Ultrafine particles: mechanisms of lung injury. *Phil. Trans. R. Soc. Lond, A,* 2741-2749.

Donaldson, K., Brown, D., Clouter, A., Duffin, R., MacNee, W., Renwick, L., Tran, L. & Stone, V. (2002). The pulmonary toxicology of ultrafine particles. *J. Aerosol Med, 2,* 213-220.

Donaldson, K., Stone, V., Clouter, A., Renwick, L. & MacNee, W. (2001). Ultrafine particles. *Occup. Environ. Med, 3,* 211-6, 199.

Grodzik, M. & Sawosz, E. (2006). The influence of silver nanoparticles on chicken embryo development and bursa of Fabricius morphology, *Journal of Animal and Feed Sciences, 15(Suppl 1),* 111-114.

Hussain, S. M., Hess, K. L., Gearhart, J. M., Geiss, K. T. & Schlager, J. J. (2005). In vitro toxicity of nanoparticles in BRL 3A rat liver cells, *Toxicology in Vitro, 19,* 975-983.

Jani, P., Halbert, G. W., Langridge, J. & Florence, A. T. (1990). Nanoparticle uptake by the rat gastrointestinal mucosa: quantitation and particle size dependency. *J. Pharm. Pharmacol, 42,* 821-826.

Kim J. S., et al. (2007). Antimicrobial effects of silver nanoparticles, *Nanomedicine: Nanotechnology, Biology, and Medicine, 3,* 95- 101

Khaydarov, R. A., Khaydarov, R. R., Olsen, R. L. & Rogers, S. E. (2004). Water disinfection using electrolytically generated silver, copper and gold ions, *Journal of Water Supply RT-Aqua, 53,* 567-572.

Khaydarov, R A., Khaydarov, R R., Gapurova, O., Estrin, Y. & Scheper, T. (2008). Electrochemical method of synthesis of silver nanoparticles. *J Nanopart Res.*, Doi:10.1007/s11051-008-9513-x

Khaydarov, R. A., Khaydarov, R. R., Estrin, Y., Evgrafova, S., Cho, S., Scheper, T. & Endres, C. (2009). "Silver nanoparticles: Environmental and human health impacts", in Book: "Nanomaterials: *Risk and Benefits*", 2009, Springer, Netherlands, 287-299.

Khaydarov, R A., Khaydarov, R R., Gapurova, O. & Estrin, Y. (2010). A novel method of continuous fabrication of aqueous dispersions of silver nanoparticles. *Int. J. Nanoparticles, 3,* 77-91.

Klasen, H. J (2000). Historical review of the use of silver in the treatment of burns. I. *Early uses Burns, 26,* 117-130.

Lademann, J., Weigmann, H., Rickmeyer, C., Barthelmes, H., Schaefer, H., Mueller, G. & Sterry, W. (1999). Penetration of titanium dioxide microparticles in a sunscreen formulation into the horny layer and the follicular orifice. *Skin Pharmacol. Appl. Skin Physiol, 12,* 247-256.

Copyright © 2010. Nova Science Publishers, Incorporated. All rights reserved.

Lee, H. J. & Jeong, S H. (2004). Bacteriostasis of nanosized colloidal silver on polyester nonwovens. *Textile Research Journal*, *74*, 442-447.

Lee, H. J. & Jeong, S. H. (2005). Bacteriostasis and skin innoxiousness of nanosize silver colloids on textile fabrics. *Textile Research Journal*, *75*, 551-556.

Lewis, L N. (1993). Chemical catalysis by colloids and clusters, *Chem Rev*., *93*, 2693-2730 .

Li, Y., Wu, X. & Ong, B. S. (2005). Facile synthesis of silver nanoparticles useful for fabrication of high-conductivity elements for printed electronics. *J Am Chem Soc*., *127*, 3266-3267.

Lok, C. N. et al., (2007). *J Biol Inorg Chem*., *12*, 527-534.

Morones, J. R., Elechiguerra, J. L. & Camacho, A. et al (2005). The bactericidal effect of silver nanoparticles. *Nanotechnology*, *16*, 2346-2353.

Murphy, C. J., Sau, T. K. & Gole, A. M. et al (2005). Anisotropic metal nanoparticles: synthesis, assembly, and optical applications. *J Phys Chem B*, *109*, 13857-13870.

Oberdorster, G., Oberdorster, E. & Oberdorster, J. (2005). Nanotoxicology: an emerging discipline evolving from studies of ultrafine particles. *Environ. Health Perspect*, *113*, 823-839.

Revina, A. A. et al. (2001). *Himicheskaya Promyshlennost'*, *4*, 28-32.

Soto, K. F. et al., (2005). *Journal of Nanoparticle Research*, *7*, 145-169.

Copyright © 2010. Nova Science Publishers, Incorporated. All rights reserved.

Copyright © 2010. Nova Science Publishers, Incorporated. All rights reserved.

In: Silver Nanoparticles
Editor: Audrey E. Welles, pp. 341-360
ISBN: 978-1-61668-690-1
© 2010 Nova Science Publishers, Inc.

Chapter 10

MASS SPECTROMETRY EVALUATION OF THE IMPROVEMENT OF DLC FILM LIFETIME USING SILVER NANOPARTICLES FOR APPLICATION ON SPACE DEVICES: MATERIAL REVIEW AND ETCHING EXPERIMENTS

F.R. Marciano[1,2], L.F. Bonetti[3], R.S. Pessoa[2], J.S. Marcuzzo[2], M. Massi[2], L.V. Santos[1], E.J. Corat[1] and V.J. Trava-Airoldi[1]

[1]National Institute of Space Research (INPE), Av. dos Astronautas 1758, C.P. 515, São José dos Campos/SP, 12245-970, Brazil.
[2]Technological Institute of Aeronautics (ITA-CTA), São José dos Campos/SP, 12228-900, Brazil
[3]Clorovale Diamantes Indústria e Comércio Ltda, São José dos Campos/SP, 12229-390, Brazil

Copyright © 2010. Nova Science Publishers, Incorporated. All rights reserved.

ABSTRACT

In this chapter, a review of current literature on the improvement of diamond-like carbon (DLC) films lifetime using nanoparticles, in particular, silver nanoparticles, will be presented. Studies carried out in our laboratories will also show the results of incorporating silver nanoparticles in DLC films to improve the solid lubricant's lifetime when submitted atomic oxygen bombardment. For this, etching experiments were performed in oxygen plasma operated at low pressure. The DLC films were deposited on different metallic substrates and on silicon (100) wafer with thin amorphous silicon interlayer by using a pulsed directly current plasma enhanced chemical vapor deposition discharge. During etching experiments, the films were submitted to oxygen ions with energy of ~70 eV in order to evaluate the wear process of the surface in a short period. This evaluation was conducted during and after the etching process through the quadruple mass spectrometry and profilometry techniques, respectively. With the mass spectrometry analysis was possible to monitor in real time the gas effluents during etching process as well as the main volatile compounds resultants of reactions of oxygen

with the DLC film surface like atomic carbon, carbon monoxide and carbon dioxide. The results indicate a considerably reduction of the volatile species during the etching process for samples with more concentration of silver nanoparticles. This fact is confirmed by the offline etching profile measurement which indicates a decrease in DLC etching. These results confirm that the DLC films become more wear resistant when silver nanoparticles are incorporated in the film bulk.

INTRODUCTION

Diamond-like carbon (DLC) films have a lot of technological applications due to their physic-chemical properties, such as high mechanical hardness, chemical inertness, optical transparency and wide band gap. DLC films can be produced hydrogen free named a-C, or hydrogenated named a-C:H. These films are used as protective coatings for magnetic recording media, antireflective layer for silicon solar cells and solid lubricant coating for vacuum applications. Particularly in the microelectronic industry, this material can be used as gate dielectric, inter-metal dielectric layer because of its appropriate electrical resistivity and dielectric constant. Coatings on micro machine devices are another interesting application due to low friction coefficients. As a solid lubricant coating, DLC represents an important area of investigation related to space device mechanisms, where high vacuum and atomic oxygen environments are required. The degradation of lubricants and excessive wear limit satellites and space born systems, having a number of moveable mechanical parts. Spacecraft surfaces in Low Earth Orbit (LEO), with altitudes of 200-600 km, suffer the bombardment with atomic oxygen, which is the dominant atmospheric element. Since many space systems are designed to remain active in space for 10 to 30 years, the LEO environmental presents new challenges for materials research in the development of oxidation-resistant thin-film coatings.

SOLID LUBRICANTS

Solid lubricant coatings for vacuum and space mechanisms are widely used when conventional liquid is not efficient, either when the operating conditions become too severe (aggressive etching or ultrahigh vacuum) or when a clean environment is required [1]. Liquids are used when tribo-assembly can be sealed from the outside environment. In other cases, solid lubrication is preferred [2]. Solid films may be used over a larger temperature range, but they are limited to relatively short distances of travel, less than ten million passes for rolling or sliding contacts, and relatively low speed [1].

Satellites and space-born systems have a number of moveable mechanical parts, whose reliability is severely limited by degradation of lubricants and excessive wear [2]. Satellites designed for the high vacuum of space can be exposed to moisture during assembly, ground tests, or launching, and contact atomic oxygen in LEO [2]. These extreme operating conditions are coupled with an extended service life expectancy, which could be as long as 30 years for an unattended satellite operation [2].

The mechanical, environmental, and endurance requirements of space applications exceed the available lubrication and wear reduction technologies, demanding novel materials and advanced technologies [2].

Copyright © 2010. Nova Science Publishers, Incorporated. All rights reserved.

These systems are frequently tested on the ground and stored for many years under controlled environments before launching [2]. Space mechanisms are required to function in vacuum, but also during the assembly, test and storage phases which are often performed in the ambient atmosphere [1,3]. In addition, reliable data based on experimental investigations on the vibrational effects during the launching, the air-to-vacuum transition from ground to orbit, the effect of periodic temperature variations, and the action of molecular or atomic beams and particles are not completely take in account [1].

A coating can change the space-born surface (both chemistry and structure) to self-adjust to the environment and achieve long durability [2]. From the various kinds of solid lubricant coatings, it has been shown that diamond-like carbon (DLC) coatings may exhibit ultralow friction in high vacuum conditions [1,4]. DLC provide superior mechanical hardness and performance in space/terrestrial environmental cycles [2] and have been studied as potential candidate for a wear resistant material with low friction in vacuum conditions [1].

DIAMOND-LIKE CARBON

DLC is a metastable form of amorphous carbon containing a significant fraction of sp^3 bonds [5]. Carbon forms a great variety of crystalline and disordered structures because it is able to exist in three hybridizations, sp^3, sp^2 and sp^1 [5]. According to Robertson [5], in sp^3 configuration, as in diamond, a carbon atom's four valence electrons are each assigned to a tetrahedrally directed sp^3 orbital, which makes a strong σ bond to an adjacent atom; and in the three-fold coordinated sp^2 configuration, as in graphite, three of the four valence electrons enter trigonally directed sp^2 orbitals, which form σ bonds in a plane. The fourth electron of the sp^2 atom lies in a π orbital, which lies normal to the σ bonding plane [5]. The π orbital forms a weaker π bond with a π orbital on one or more neighbouring atoms [5]. The lubricant characteristic came from the π bonds between the graphitic/diamond layer. This kind of structure (typical of graphite) confer solid lubricant characteristic to DLC.

The extreme physical properties of diamond derive from its strong, directional σ bonds [5-6]. The sp^3 bonding of DLC confers on it many of the beneficial properties of diamond itself, such as hardness, elastic modulus and chemical inertness, but these are achieved in an isotropic disordered thin film with no grain boundaries [5]. DLC consists not only of the amorphous carbons (a-C) but also of the hydrogenated alloys (a-C:H) [5].

There is a range of DLC produce methods, such as physical or chemical process. The methods can be categorized as to whether they are most suitable for laboratory studies or industrial production [5]. On a physical process, DLC film is condensed from a beam containing medium energy (~100 eV) carbon or hydrocarbon ions and it is the impact of these ions on the growing film that induces the sp^3 bonding [5]. This method contrasts with the chemical process in which stabilizes the sp^3 bonding [5]. On Table 1 are presenting the main features of different DLC deposition methods.

DLC films are mostly obtained by plasma decomposition of a hydrocarbon-rich atmosphere [20]. It is usually accepted that surface chemisorption of carbon carrying neutral radicals is the main channel for the film growth [20-21]. In DLC films deposited by methane decomposition, the structure is composed of sp^2 hybridized clusters interconnected by sp^3 hybridized carbon atoms. Furthermore, the mechanical properties (e.g. hardness, Young's

Copyright © 2010. Nova Science Publishers, Incorporated. All rights reserved.

modulus, adhesion to the substrate, internal stresses) as well as important electronic properties (e.g. optical infrared gap, photoluminescence, conduction behavior) may be pre-determined to certain extent by varying the sp^3/sp^2 bonding ratio [5, 20].

DLC films also present low-friction coefficient, low wear rate and excellent tribological properties, as well as etching resistance [22-24]. Due to the mechanical, electrical, optical and chemical properties of these films, the use of DLC coatings in mechanical and electrical fields has increased with recent applications in food, beverage and medical application [22].

Table 1. Main features of the different DLC deposition methods

Deposition methods	Features	Advantages	Disadvantages	References
Ion beam	Carbon ions are produced by sputtering of graphite.	Give a controllable deposition species and energy, a filtering out of non-energetic species, and the ability to dope by switching the ion species.	High cost and size of the apparatus.	[5,7-9]
Sputtering	Uses the DC or RF sputtering of a graphite electrode by na Ar plasma.	Versatility, widespread use to sputter many materials and easy of scale up.	Expensive and low growth rate.	[1,5,10-11]
Cathodic arc	An arc is initiated in a high vacuum by touching the graphite cathode with a small carbon striker electrode and withdrawing the striker.	Produce a highly ionized plasma with an energetic species, a fairly narrow ion energy distribution, and high grow rate for a low capital costs.	The filtering is not sufficient for some applications, and the cathode spot is unstable.	[5,12-14]
Pulsed laser deposition	Pulsed excimer laser such as ArF give very short, intense energy pulses, which can be used to vaporize materials as an intense plasma.	Versatile laboratory scale method, which can be used to deposit many materials, from high temperature superconductors to hard coatings.	It's not possible to scale in an industrial proportion.	[5,15-17]
Plasma enhanced chemical vapor deposition	The reactor consists of two electrodes of different area. The power supply is usually coupled on the smallest electrode on which the substrate is mounted, and the other electrode is grounded.	Versatility to use different precursor gases, facility to deposition in samples with different size and shape, low cost production.	It's not possible to have independent control of the ion current and the ion energy, as they both vary with the power supply energy.	[5,9,18-20]

Copyright © 2010. Nova Science Publishers, Incorporated. All rights reserved.

In long duration, heavily loaded, and/or high sliding speed applications, the use of DLC leads to its graphitization and associated increase of friction coefficient in the high vacuum environment [2-25]. A hydrogenated DLC phase increases life through hydrogen termination of active carbon bonds, but not for long durations due to hydrogen depletion after about 10^4 cycles [2, 26-27]. An alternative approach is the incorporation of silver nanoparticles (SNP), which is also considered as a solid lubricant, into DLC films.

Diamond-Like Carbon with Silver Nanoparticles

Metal doping in DLC films prepared by chemical/physical vapor deposition techniques had been the issue of obtaining a new class of materials [28-32] but dispersing the metal particles homogeneously in the DLC matrix by the techniques used by the researches was found to be difficult [32]. The key issue was to reduce the internal stresses in DLC films via incorporation of silver nanoparticles.

In a pure carbon system, the total energy increased substantially as the bond angle deviated from the equilibrium angle of the tetrahedral sp^3 bonds, which would be the reason for the high residual compressive stress of amorphous carbon films [8]. However, the increase in the total energy was significantly reduced by the addition of noble metals as well as transition metals [8]. Choi et al suggested that both noble metals and transition metals dispersed in the amorphous carbon matrix may play the role of a pivotal site, resulting in the reduction of the residual stress in the amorphous carbon network from distortion of the bond angle [8].

Silver is known to have low shear strength, a good transfer forming tendency, etching resistance, high electrical and thermal conductibility [7,33-34]. Furthermore, silver films produce fewer wear particles and outgas than any other material for solid lubricant while being used in a vacuum condition [7]. DLC-silver nanocomposites (Ag-DLC) have also been show to posse antimicrobial and anticorrosion properties [8,32].

Since DLC films are large band gap material, metal inclusion in nanocrystalline form should also reveal interesting optical properties like surface plasmon resonance in this class of composite materials [32].

The Low Earth Orbit

The energetic atomic oxygen reaction with materials used in the exterior of a spacecraft operated in LEO is one of the key issues in future long-life spacecraft [18, 35]. LEO presents new challenges for materials research in the development of oxidation-resistant thin-film coatings [36]. A spacecraft in LEO environment, with altitudes of 200-600 km, suffer the bombardment by an atmosphere whose predominant species is neutral, ground-state, atomic oxygen [37-38].

The reaction of atomic oxygen with carbon,

$$C + O_g \rightarrow CO_g \qquad \Delta H^0 = -357 kJ/mol \qquad \text{(Eq. 1)}$$

Copyright © 2010. Nova Science Publishers, Incorporated. All rights reserved.

has been described as an important process both in combustion and reentry systems [38-41]. Some researchers have been observed the removal of carbon from surfaces exposed to the atmosphere in LEO on various flights of the Space Shuttle [38, 42]. The relative kinetic energy of the atomic oxygen bombardment is approximately 5 eV which is caused by the spacecraft's orbital velocity of 400 km/h (8 km/s), and flux ranged between 10^{17}-10^{19} atoms/m^2s [43]. The high chemical reactivity of the atomic oxygen flux has been shown by the material processing experiments flown on the space shuttle [43]. Tagawa et al. reported that a pronounced glow and serious chemical etching of the surface exposed normal had been detected to the direction of flight (ram surface) [43-44]. These phenomena have been correlated with atomic oxygen density, and thickness losses over 1 μm/day in ram surface have been observed for organic materials [43, 45-48]. These experimental data may indicate that exterior coatings used in large space structures are necessary and endurance tests against the atomic oxygen bombardments of the uncoated parts such as solid lubricants are needed [43].

Studies of the reaction of the lubricants with atomic oxygen in ground-based laboratories thus are essential to space station technologies [43]. The LEO environmental is commonly simulated in laboratory by using a standard semiconductor plasma reactor with as atmosphere of either air or pure oxygen gas [36].

The Synthesis Procedure of DLC Films with SNP

A SNP solution with about ~60 nm diameter particle was used to produce Ag-DLC films. The SNP colloidal production and nanoparticle characterization can be found in a paper previously published [49].

Silicon (100) and 316L stainless steel were the substrates. The stainless steel was polished by using up 0.25 μm diamond powder. All the substrates cleaned ultrasonically in an acetone bath for 15 min. were mounted on a water-cooled 10 cm diameter cathode fed by a 25 KHz and 50% duty cycle pulsed directly current plasma enhanced chemical vapor deposition (DC-PECVD) power supply.

It was used two different kind of methodology to produce Ag-DLC films. On the first, SNP was interpolated into DLC in layers. On the second, SNP solution in different concentrations was pulsed during the DLC deposition process. In both cases, it was used the DC-PECVD power supply.

Ag-DLC Film Production in Layers

DLC films were deposited on silicon (100) and 316L stainless steel using a pulsed DC-PECVD methane discharge from methane (1 sccm gas flow at 85 mTorr for 10 min and -700 V). After that, the samples were divided in 5 groups. Group 1 was composed of samples with only DLC films. For the other groups, an aqueous solution with SNP was pulverized over DLC film for 2 minutes, and after this, another thin DLC layer (25 nm) was deposited to fix the nanoparticles. This procedure was carried out 4, 6, 8 and 10 times respectively for the groups 2, 3, 4 and 5.

Copyright © 2010. Nova Science Publishers, Incorporated. All rights reserved.

Ag-DLC Film Production from SNP Hexane Solution

The SNP from the aqueous solution (~55 nm average size) [49] were transferred from water to hexane by centrifugation process [50]. It was obtained different concentrations of hexane SNP solutions.

The DLC films started to be deposited using methane as the feed gas to a thickness of ~150 nm (1 sccm gas flow at 85 mTorr for 10 min and -700 V). So, with the methane plasma on, hexane intermittent spray was pulsed (1 min pulse frequency and 300 μs pulse on) inside the chamber for 25 min. The voltage (-700 V) was kept constant and the pressure inside the chamber varied from 85 to 130 mTorr during the pulse interval.

To produce Ag-DLC films, 10.0, 50.0 and 100.0 g/L hexane SNP solutions replaced the pure hexane during the deposition.

Ag-DLC Film Characterization

The morphology of SNP in DLC films was shown by scanning electron microscopy (SEM) in Figures 1-2 and by atomic force microscopy (AFM), Figure 3-4. SEM images were acquired by using JEOL LEO-440, with 20.0 kV; and field emission gun scanning electron microscopy (FEG-SEM), JEOL JSM-6330F, with 30.0 kV, respectively. The AFM images were acquired by using the dynamic tip mode of a Shimadzu SPM9500J3 and VEECO 920006101 AFM, respectively.

The nanoparticle size is in good agreement with the SNP size in solution. Different sizes and shapes of SNP are also shown. As illustrated in Figure 1-2, it was possible to reach a satisfactory density of nanoparticles with the adopted methodology. The images reveal that SNP are not dispersed absolutely homogeneously. One may observe that two or more nanoparticles may be representing a large particle.

AFM images (Figures 3-4) confirmed SNP were really incorporated in DLC films. The nanoparticles had a tendency to form aggregates on the surface during the deposition process [51] (as shown on top right side of Figure 3a). Secondly, Figure 3b shows some nanoparticle completely immersed in DLC films and others partially immersed in DLC surface. SEM and AFM images shows the tendency of the inter-particle distances became smaller with the increase in number density of particles culminating in some clusters coming closer to one another.

On Ag-DLC films produced from SNP hexane solution (Figure 4), the agglomerate problem becomes more evident. This can be seen in Figure 4b (DLC from 50.0 g/L SNP hexane solution) which has not only more SNP, but also more agglomerates than on Figure 4a (DLC from 10.0 g/L SNP hexane solution). In the case of Figure 4, the SNP are bigger and form more aggregates on DLC surface, which can mislead the SNP real sizes. However, DLC films growth from hexane have higher growth rates, it means this methodology is more applicable when industrial scaling up is taking in account.

Copyright © 2010. Nova Science Publishers, Incorporated. All rights reserved.

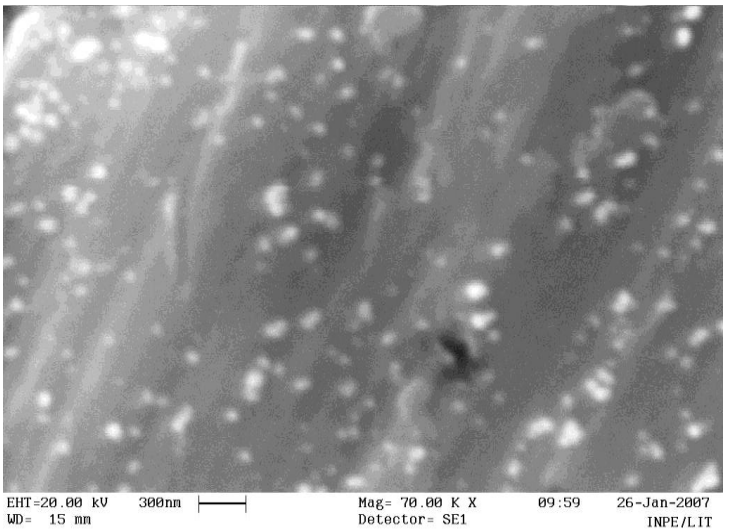

Figure 1. SEM image of a 10-layer-Ag-DLC film.

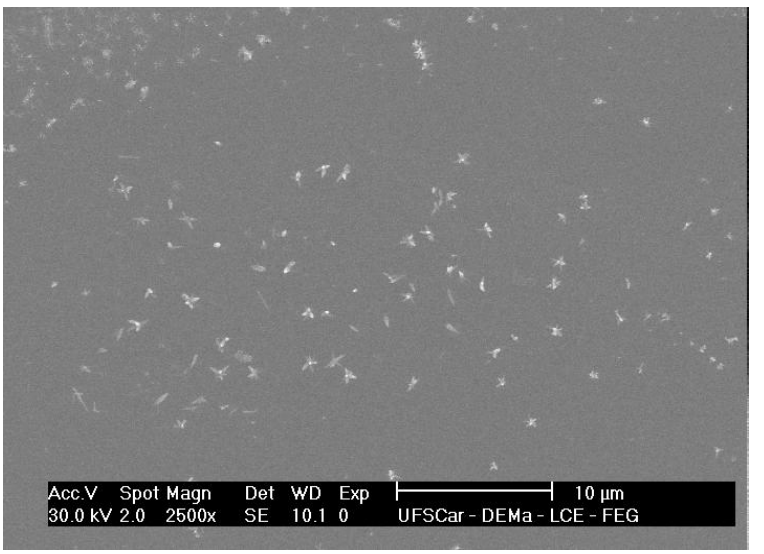

Figure 2. SEM image of Ag-DLC film produced from a 10.0 g/L SNP hexane solution.

The atomic arrangement of the Ag-DLC films was analyzed by Raman scattering spectroscopy in order to verify if the incorporation of SNP in DLC changed its arrangement using a Renishaw 2000 system with an Ar^+-ion laser (λ = 514 nm) in backscattering geometry. The laser power on the sample was ~0.6 mW and the laser spot had 2.5 µm diameter. The Raman shift was calibrated in relation to the diamond peak at 1332 cm^{-1}. All measurements were carried out in air at room temperature.

Copyright © 2010. Nova Science Publishers, Incorporated. All rights reserved.

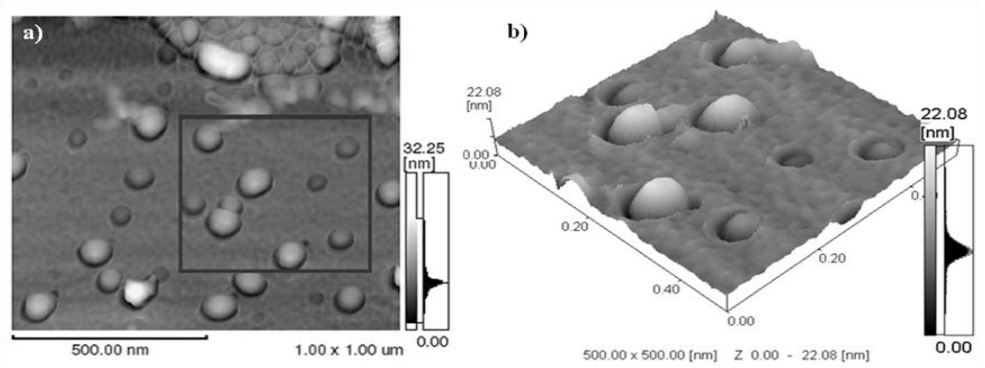

Figure 3. 10-layer-Ag-DLC film AFM image: a) 2D AFM using the dynamic tip mode in 500×500 nm^2 area and 22.08 nm depth. b) 3D enlargement of the squared region delineated in (a).

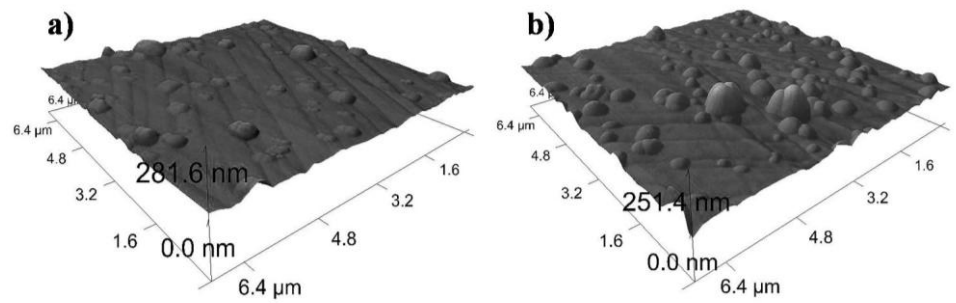

Figure 4. AFM image of Ag-DLC film produced from (a) 10.0 g/L and (b) 50.0 g/L SNP hexane solution.

Figure 5 shows Raman spectra of a pure DLC film and a 10-layer-Ag-DLC film. The two spectra are very similar. Presenting two overlapping bands known as the *D* and *G* bands [52], these spectra were fitted using two Gaussian lines. The integrated intensity ratio of the *D* and *G* peaks (I_D/I_G) has been correlated with the sp^3/sp^2 bonding ratio [53-54]. $I(D)/I(G)$ falls as the number of rings per cluster and the fraction of chain groups rise [55]. The measured I_D/I_G ratios for these quality DLC films ranged between 1.0 and 1.2 and these values do not change according with the Ag quantity tested. They are common values for DLC films [55] and these parameters are empirically correlated to quantities directly related to structural disorder, such as the Young's modulus, the hardness, hydrogen content, and atomic density [56]. Choi et al (2008) show I_D/I_G ratio increases as the Ag contents in the DLC film increases. In that case, Ag-DLC films were produced from a hybrid deposition system composed of an end-Hall-type hydrocarbon ion gun and a silver DC magnetron sputter source [57]. From these results, it is noticeable the quality of DLC films do not suffer any variation with the incorporation of SNP, independent of both used methodology.

Copyright © 2010. Nova Science Publishers, Incorporated. All rights reserved.

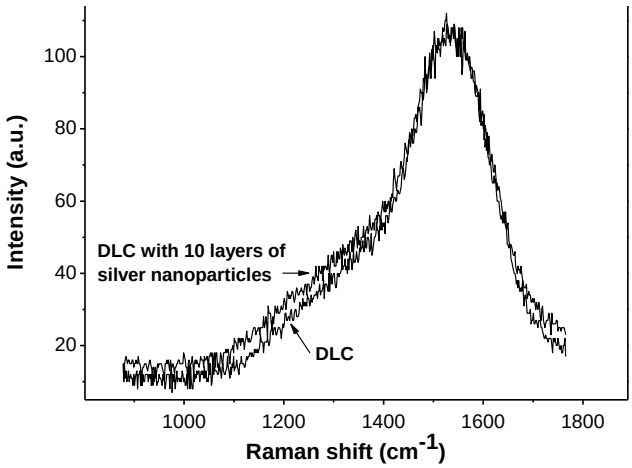

Figure 5. A comparison between Raman spectra from DLC without and with 10 layers of SNP.

Some authors [8,32] reported the stress reduction via nanoparticle incorporation in DLC bulk. Total stress was determined by measuring the substrate curvature before and after the DLC film deposition with a stylus profilometer and by analyzing the results with the well-known Stoney's equation [58-59].

Figure 6 shows the total compressive stress of the DLC films measured according to the layers. The zero point corresponds to the pure DLC film without any layer. The stresses of the films with SNP were decreasing with the number of silver layers whilst in the films with no silver, the stresses remain constant independently of the number of layers. SNP in DLC bulk also relieve the stresses between the substrate and DLC films. Lower total stress observed when nanoparticles are present in the DLC films are related to the defects in the films structure and multi-layer of the DLC films.

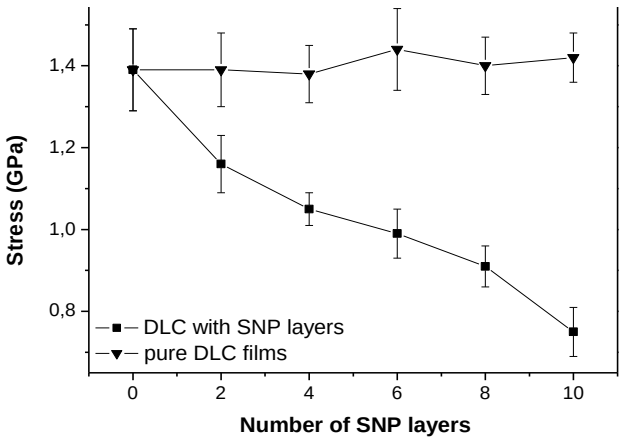

Figure 6. Total compressive stress as a function of the number of SNP layers. The zero point corresponds to the pure DLC film without any layer.

Copyright © 2010. Nova Science Publishers, Incorporated. All rights reserved.

Table 2. DLC and Ag-DLC hardness values (in GPa)

Production method	DLC	Ag-DLC
In layers	18-22	11-16
From hexane solution	18-20	11-14

Oxygen Plasma Etching of DLC and Ag-DLC Samples: Plasma Reactor and Discharge Parameters

Nanohardness was measured by the instrumented hardness test which was carried out using Fischerscope HV100 equipment with a Vickers indenter. The maximum load applied was 45 mN and at least 10 valid measurements were made for each sample. The hardness mean value was considered as the resultant hardness. The depth achieved was less than 20% of total film thickness in order to avoid substrate influence during the measurements. The load-unload cycles and hardness values were performed according to ISO 14577 [60] and the Oliver-Pharr method [61].

The DLC and Ag-DLC hardness values are presented on Table 2, according to the deposition method (in layers or from the hexane solution). When SNP are incorporated, DLC hardness also present a slightly decrease, because it was added a lot of defects in DLC structure. This decrease in hardness is counterbalanced with the increase of other properties of these films such as lower stress [49]. The difference in hardness among the films with SNP was not significantly different.

The etching of carbon based materials, like DLC films, can be done with discharges operating at two regions of pressure: atmospheric and low pressure oxygen plasmas. The atmospheric plasma generator proposed by Marcuzzo et al [62] consists in the use of dielectric barrier discharge (BDB) in oxygen gas at high pressure (600 Torr) and high gas flux (3 L/min). Despite this method can produce reactive oxygen, it was not used because the high gas flux and pressure not represent the LEO conditions.

Under low pressure (< 1 Torr) of reactive gases such as oxygen is common the use of techniques that use 13.56 MHz radio-frequency (RF) power sources to excite the plasma generation such as reactive ion etching (RIE), inductively coupled plasma (ICP) and electron cyclotron reactor (ECR) [63]. In this work we used the RIE system due to simplicity of construction and ability to generate oxygen plasma at pressures that simulate the LEO conditions. A schematic diagram of the experimental apparatus is shown in Figure 7. This apparatus consists of a capacitively coupled parallel plate reactor operating in RIE mode with 2 L volume and 50 mm electrode gap. The lower RF powered electrode has 150 mm in diameter while the upper electrode is connected with the reactor walls and grounded. Prior to gas feed the vacuum chamber is pumped down to pressure below 0.1 mTorr using a combination of a roots and a mechanical pump, providing both an effective pumping speed of approximately 110 L/s. Subsequently, the O_2 was inserted into the chamber.

For the etching experiments the DLC or Ag-DLC films were placed on the lower electrode since this enables the control of the flow and energy of species such as ions and charged electron on the sample through the modulation of process parameters such as pressure and RF power. All data were taken at an optimized condition of 20 mTorr total

Copyright © 2010. Nova Science Publishers, Incorporated. All rights reserved.

pressure (12 sccm gas flow) and 10 W of RF power. Under these conditions the established cathode fall potential (V_{dc}) is of the order of 70 V, which is equivalent to an energy gained by oxygen ions of 70 eV. In LEO simulator studies, the particle energies involved are about 5 eV, which promotes a slow etching process [38]. In our experiments, the high energy was chosen purposely in order to maximize the etching process quickly. Etching experiments were carried out through on masked DLC samples for 4 min, and part of them was covered with a mechanical mask to produce a step between the etched and non-etched regions. This step was measured by a profilometer (Alpha-Step 500), and the etching rates were determined.

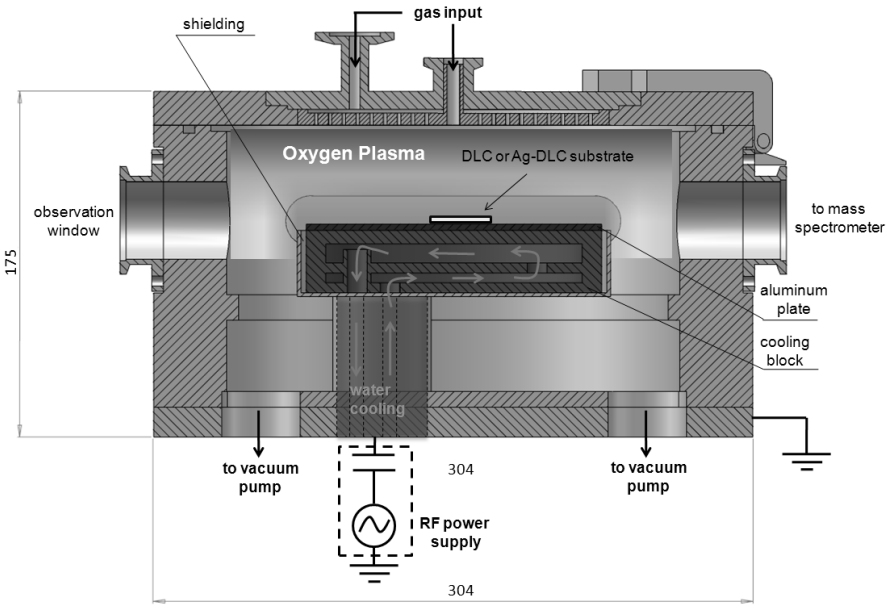

Figure 7. Schematic illustration of the reactive ion etching reactor. The reactor dimensions are in mm.

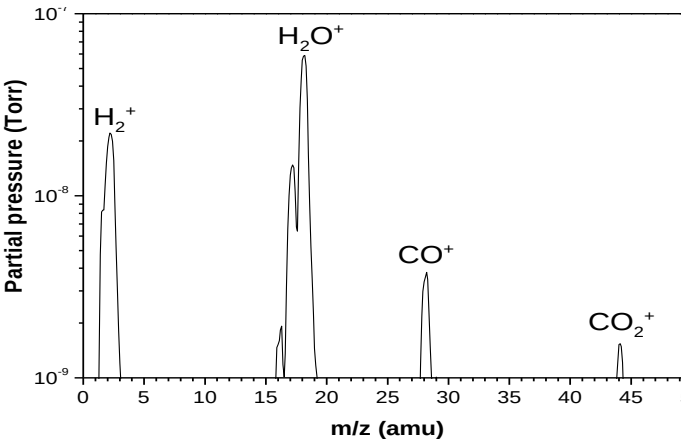

Figure 8. Mass spectrum of the RIE chamber obtained on background condition.

Copyright © 2010. Nova Science Publishers, Incorporated. All rights reserved.

In Situ Plasma Etching Analysis: The Mass Spectrometry Technique

The mass spectrometry is a powerful analytical technique that is used to identify unknown compounds, to quantify known materials, and to elucidate the structural and chemical properties of molecules. The detection of compounds can be achieved, even in very small quantities (partial pressures of up to 10^{-10} Torr). Because of this, the mass spectrometry provides valuable information for a wide range of professionals: physicians, engineers, chemists, biologists and astronomers, to name a few.

One method that uses frequently the mass spectrometry to perform their diagnosis is the processing of materials by cold plasma. However, determining the chemical composition of plasma is a very difficult task, due to the large amount of components and radicals present. In reactive plasmas such as O_2, SF_6 or CF_4, for example, the knowledge of the absolute concentrations of chemical species involved is extremely complicated, why, in many cases, only magnitudes are measures relating experimentally. In a reactive discharge, the energy is distributed among the various constituents, namely: stable neutral, electrons, molecular fragments (radicals), negative and positive ions and neutral excited. These, in turn, are in a chemical "soup" of large applications in various branches of technology. Of these components, it should be emphasized that the role of electrons, because of its greater mobility, are responsible for the electrical conductivity of plasma and the processes of formation of radicals, neutral and excited ions, important for the reactivity of the plasma.

In this scope, in the field of plasma etching of materials, particularly, etching of carbon-based materials, the use of mass spectrometry allows the monitoring of neutral effluents like atomic carbon, carbon monoxide and carbon dioxide that are generated during the reaction of oxygen plasma species with the substrate. The knowledge of these species allowed us to this work not only investigates the process kinetics but also evaluate the wear resistance of each material.

Copyright © 2010. Nova Science Publishers, Incorporated. All rights reserved.

Quadrupole Mass Spectrometer System

The analysis of the relative concentration of species extracted from the plasma was performed by using a quadrupole mass spectrometer AccuQuad 200D – Kurt J. Lesker Company, which allows to analyze mass up to 200 atomic mass unit (amu) with a resolution 1 amu, adapted to the vacuum chamber through a drifting tube. The plasma species were sampled through a micro orifice located at the mass spectrometer's entrance, undergoing subsequent electron impact ionization at constant electron energy of 70 eV. This energy is sufficient to ionize the neutral gas species that enter through the quadrupole RF mass filter that thus, is detected and classified as a function of their mass-to-charge ratio. The typical operation pressure within the mass spectrometer was 0.1 mTorr.

Mass Spectra Analysis Procedure

The first instance of a mass spectrometry analysis in cold plasma reactors is an inspection of the residual species inside the reactor in order to avoid these from the species of gas to be

inserted. These species are illustrated in the spectrum shown in Figure 8. In this spectrum we can see that the reactor was clean, i.e., without the presence of etching gas at a background pressure of approximately 0.1 mTorr. The species that can be observed in spectrum probably are contaminants that may be associated with small leaks in the reactor and because polypropylene pipelines that are used as drivers of gas, and yet there is the presence of water (mass 18) that probably should be constituent of the ambient air. This procedure has been taken aimed at determining the background conditions for subsequent analysis.

Once the subtraction of the background spectrum was made, we conducted the online monitoring of the etching process of DLC and Ag-DLC materials. Figure 9 illustrates an example of the spectra obtained for 3 different samples: DLC, Ag-DLC with 1 layer and Ag-DLC with 2 layers. We observed the following main species in these spectra: O^+ (mass 16) and O_2^+ (mass 32), from the oxygen gas and C^+ (mass 12), H_2O^+ (mass 18) and CO^+ (mass 28), from the reaction of oxygen species with the surface of the DLC substrate. The atomic carbon observes in gas phase derives from the reactive sputtering effect in the material surface due to bombardment by oxygen ions with energies of up to 84 eV. This effect decreases when the silver layers in the film bulk increases. Also, it was observed from these spectra a decrease in the partial pressure of CO^+ and CO_2^+ species which allows us to conclude that the reaction rates to formation of these species in gas phase are diminishing because the capture of oxygen by silver nanoparticles.

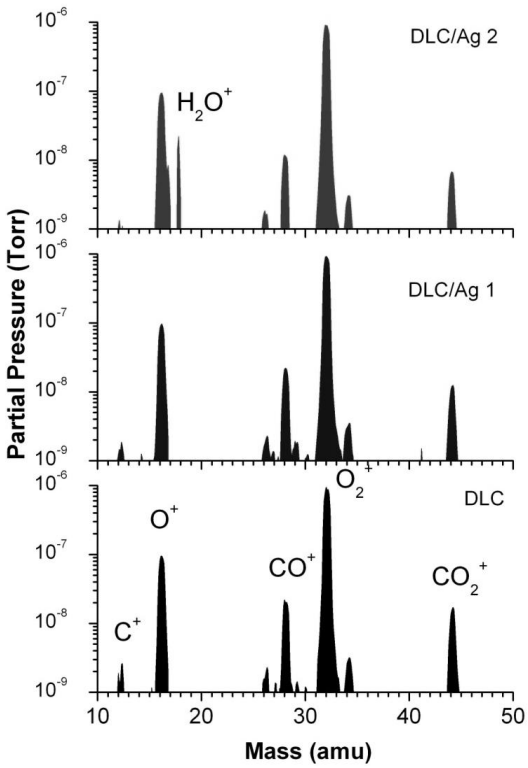

Figure 9. Mass spectra of the effluent from the reactor during etching of DLC and Ag-DLC films.

Copyright © 2010. Nova Science Publishers, Incorporated. All rights reserved.

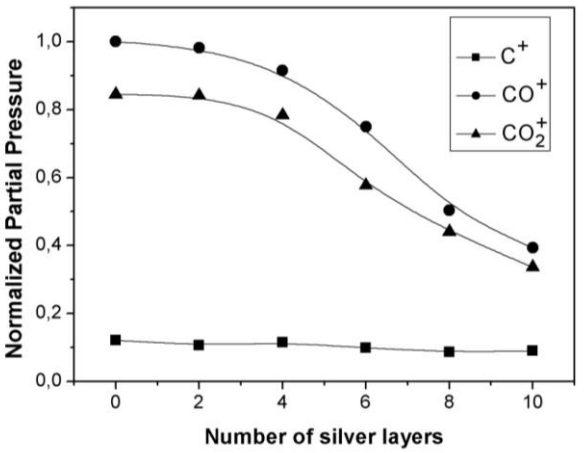

Figure 10. Normalized partial pressure of C^+, CO^+ and CO_2^+ species as a function of the number of SNP in DLC film. Partial pressures are normalized to 1 at the maximum value.

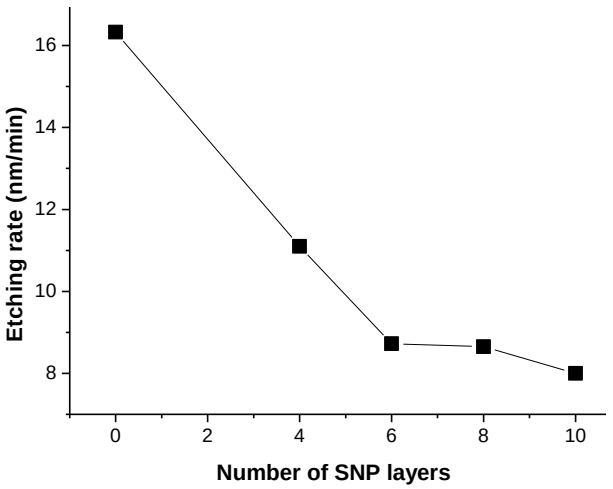

Figure 11. Etching rate as function the number of SNP layers in DLC films.

Etching Results for Ag-DLC Film in Layers

In order to verify the effect of the number of SNP layers on the generation of C^+, CO^+ and CO_2^+ species, experiments were done varying the number of layers from 0 to 10. Figure 10 shows the normalized partial pressure of C^+, CO^+ and CO_2^+ species as a function of the number of SNP layers. It noted a signal value strong decrease for the films with more than 4 SNP layers, where the signals decrease to 2 times up for the case of 10 SNP layers.

The mass spectrometry results observed during the etching process were corroborated by measuring of the etching step formed by a mask placed over a small area of the substrate. The height of these steps were measured after the process by a profilometer and so were determined the etching rates for each condition. The results are shown in Figure 11, the

Copyright © 2010. Nova Science Publishers, Incorporated. All rights reserved.

obtained etching rates are presented as function of the number of SNP in DLC film. In Figures 10-11, the zero point corresponds to the DLC film without any layer of SNP. As can be observed from Figure 11, a decrease in the etching rate up to 2 times occurs for value of 10 SNP layers. This fact shows the effectiveness of the mass spectrometry technique to evaluate the wear resistance of Ag-DLC material to the oxygen etching process.

Etching Results for Ag-DLC Film from SNP Hexane Solution

Figure 12 shows the obtained etching rates as function of SNP concentration in hexane solution. The etching shows that with an addition of 10.0 g/L of SNP in hexane, the etching rate suffers a decrease of more than 2 times of initial value, reaching a decrease of up to 3.5 times to a maximum hexane solution concentration of 100 g/L.

Also for this case, we have made the process monitoring by mass spectrometry, but with one difference, the main etching species CO^+ and CO_2^+ are monitored in real time at an interval range of 1 second between each detection. This permitted us to see how the signals of the species varies during all etching process, allowing a better evaluation of the effect of the silver concentration on the wear of the film. In Figure 13, the time evolution of CO^+ and CO_2^+ species is presented during the oxygen plasma degradation for DLC samples produced for (a) pure hexane, (b) 10.0 g/L SNP hexane solution, (c) 50.0 g/L SNP hexane solution and (b) 100.0 g/L SNP hexane solution. In this figure, on point 1, oxygen gas had started to be inserting in the chamber, point 2, plasma (10 W) had been on, and, point 3, plasma and oxygen had been off. We can see that when the discharge is on, a significant increase in the partial pressure of CO^+ and CO_2^+ species can be observed, indicating the reaction of oxygen species with the substrate material. After the discharge ignition the signals tends to decrease rapidly with time indicating a constant decrease in etching rate. This fact shows to be more prominent for higher silver concentrations.

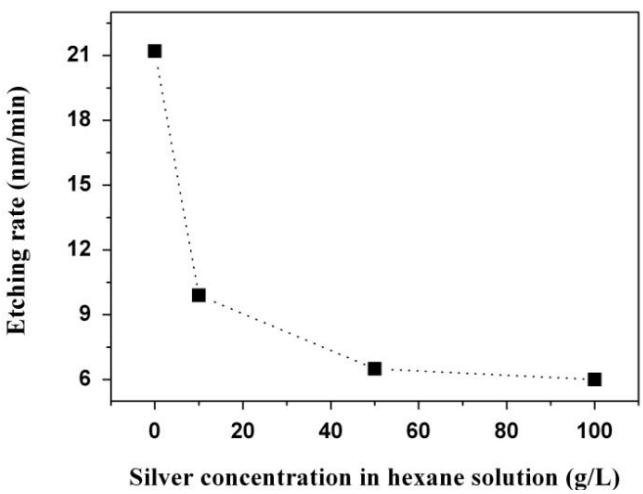

Figure 12. Etching rate as function of SNP concentration in hexane solution.

Copyright © 2010. Nova Science Publishers, Incorporated. All rights reserved.

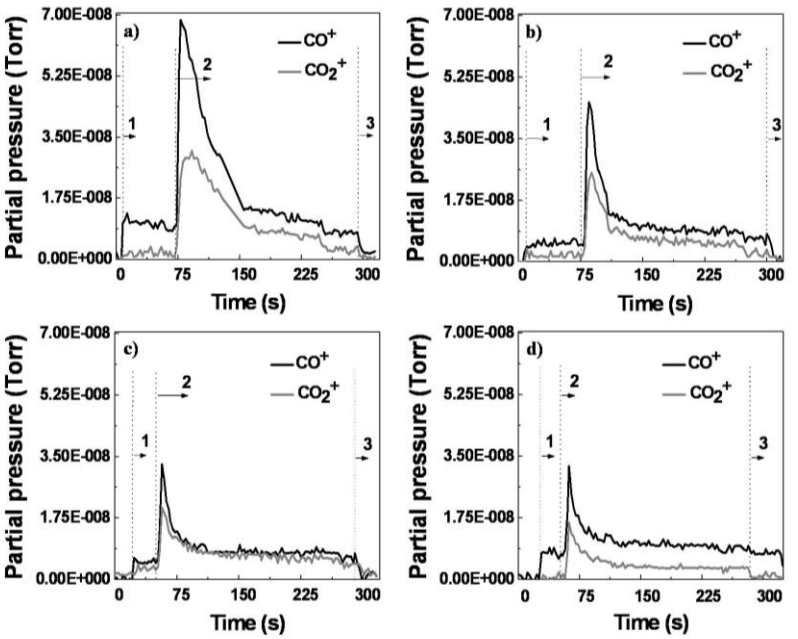

Figure 13. Temporal evolution of CO^+ e CO_2^+ species during the etching process of the DLC films produced from (a) pure hexane, (b) 10.0 g/L SNP hexane solution, (c) 50.0 g/L SNP hexane solution, and (d) 100.0 g/L SNP hexane solution. On point 1, oxygen gas had started to be inserting in the chamber, point 2, plasma (10 W) had been on, and, point 3, plasma and oxygen had been off.

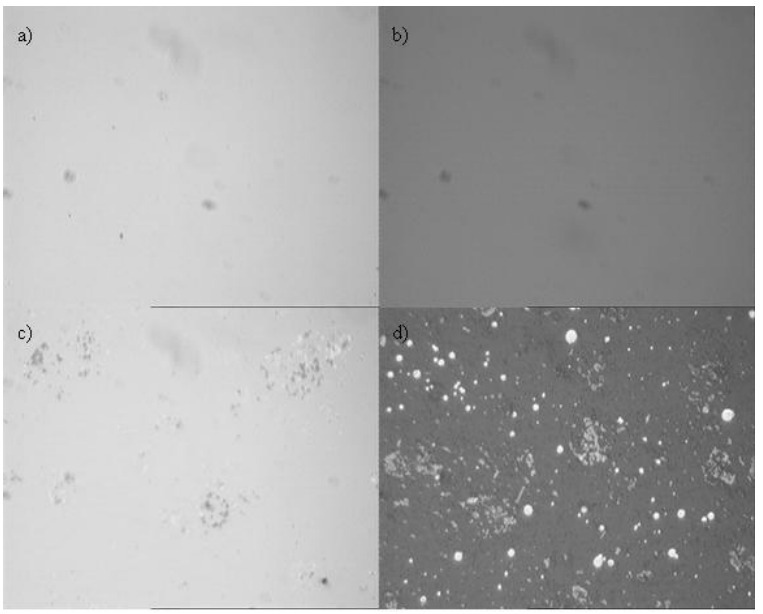

Figure 14. Optical microscopy of some samples before and after the etching process: a) DLC film before the etching, b) DLC film after the etching, c) 8-layer-Ag-DLC film before the etching, d) 8-layer-Ag-DLC film after the etching. All the figures are in the amplification of 1000x.

Copyright © 2010. Nova Science Publishers, Incorporated. All rights reserved.

It is known from the literature, that the etching process of the DLC material by cold plasmas is performed with the use of oxygen gas [64]. This, due to reaction with carbon, promotes the generation of volatile products CO and CO_2 that are pumped out by the vacuum system. With the insertion of SNP in the film volume, independent of the used method, the etching process of the film becomes slower, since silver has a higher reaction affinity with oxygen atoms forming a silver oxide layer on DLC surface owing to the irradiation of oxygen plasma. Oxygen atoms react preferentially with silver preventing the reaction of oxygen with carbon from the DLC films. The result of this experiment can be seen in Figures 11 and 12. Here, the obtained etching rate decreases with the increase of SNP in DLC bulk. The increase of SNP in the film proved to be very efficient in reducing the reaction of oxygen with carbon. This result was also verified by the analysis of etching environment with mass spectrometer (see Figures 10 and 13). The partial pressure of CO^+ and CO_2^+ showed a decreased with the increase of SNP, indicating that the film etching decreases with the increase of SNP. This decrease in the etching rate is due to the fact of rising silver agglomerates on the film surface as we can see in images of optical microscopy of Figure 14. One can note on the etched samples, that the silver nanoparticles become more evident, having resisted the etching process. In such case, the DLC films with silver nanoparticles become more resistant to the etching process allowing an increase of DLC permanency at the space atmosphere.

CONCLUSION

The SNP incorporation technique in DLC bulk presented in this chapter shows high quality Ag-DLC films produced. Raman scattering spectra shows DLC quality does not suffer any significant variation with the SNP incorporation. Also demonstrated that DLC films are more wear resistant against etching when the films have more SNP. It is clear the amount of CO_2 and CO produced by oxygen ion attack decreases with the increase of SNP in DLC bulk. We are convinced SNP react with oxygen, absorbing the oxygen atoms close to the DLC films surface. The mass spectrometry analysis was an indispensable technique to identify and to quantify the compounds etched by the oxygen plasma.

This chapter is part of initial studies to understanding this kind of etching process. Therefore, more experiments are need in order to further investigation the SNP behavior in DLC films and its effect on the etching process, as a function of SNP size and density.

REFERENCES

[1] Donnet, C; Fontaine, J; Le Mogne, T; Belin, M; Héau, C; Terrat, JP; Vaux, F; Pont, G. *Surf. Coat. Techol.*, 1999, 120-121, 548-554.
[2] Voevodin, AA; Zabinski, JS. *Compos. Sci. Technol.*, 2005, 65, 741-748.
[3] Rountree, RA. *J. Mech. Eng.*, 1988, 35, 28-32.
[4] Donnet, C; Grill, A. *Surf. Coat. Techol.* 1997, 94-95, 456-462.
[5] Robertson, J. *Mater. Sci. Eng. R*, 2002, 37, 129-281.
[6] Angus, JC; Hayman, CC. *Science*, 1988, 241, 913-921.
[7] Lee, KH; Takai, O; Lee, MH. *Surf. Coat. Techol.*, 2003, 169-170, 695-698.

Copyright © 2010. Nova Science Publishers, Incorporated. All rights reserved.

[8] Leger, LJ. et al. AIAA paper no. 83-2631 1983.
[9] Choi, HW; Choi, JH; Lee, KR; Ahn, JP; Oh, KH. *Thin Solid Films*, 2007, 516, 248-251.
[10] Trava-Airoldi, VJ; Bonetti, LF; Capote, G; Santos, LV; Corat, E. *J. Surf. Coat. Techol.*, 2007, 202, 549-554.
[11] Lu, ZG; Chung, CY. *Diamond Relat. Mater*., 2008, 17, 1871-1876.
[12] Ji, L; Li, H; Zhao, F; Chen, J; Zhou, H. *Diamond Relat. Mater*., 2008, 17, 1949-1954.
[13] Zhong, M; Zhang, C; Luo, J. *Appl. Surf. Sci*., 2008, 254, 6742-6748.
[14] Wu, JB; Chen, CY; Shin, CT; Li, MY; Leu, MS; Li, AK. *Thin Solid Films*, 2008, 517, 1141-1145.
[15] Liu, E; Kwek, HW. *Thin Solid Films*, 2008, 516, 5201-5205.
[16] Itoh, M; Suda, Y; Bratescu, MA; Sakai, Y. *Thin Solid Films*, 2006, 506-507, 96-100.
[17] Yap, SS; Tou, TY. *Vacuum*, 2008, 82, 1449-1451.
[18] Hu, A; Rybachuk, M; Lu, QB; Duley, WW. *Diamond Relat. Mater*., 2008, 17, 1643-1646.
[19] Tagawa, M; Yokota, K; Matsumoto, K; Suzuki, M; Teraoka, Y; Kitamura, A; Belin, M; Fontaine, J; Martin, JM. *Surf. Coat. Techol.*, 2007, 202, 1003-1010.
[20] Trava-Airoldi, VJ; Bonetti, LF; Capote, G; Fernandes, JA; Blando, E; Hubler, R; Radi, PA; Santos, LV; Corat, EJ. *Thin Solid Films*, 2007, 516, 272-276.
[21] Capote, G; Bonetti, LF; Santos, LV; Trava-Airoldi, VJ; Corat, EJ. *Thin Solid Films*, 2008, 516, 4011-4017.
[22] Jacob, W. *Thin Solid Films*, 1998, 326, 1-42.
[23] Shirakura, A; Nakaya, M; Koga, Y; Kodama, H; Hasebe, T; Suzuki, T. *Thin Solid Films*, 2006, 494, 84-91.
[24] Dearnaley, G. *Clin. Mater*., 1993, 12, 237-244.
[25] Thomson, LA; Law, FC; Rushton, N; Franks, J. *Biomaterials*, 1991, 12, 37-40.
[26] Voevodin, AA; Phelps, AW; Donley, MS; Zabinski, JS. *Diamond Relat. Mater*., 1996, 5, 1264-1269.
[27] Zaidi, H; Le, Huu; Paulmier, D. *Diamond Relat. Mater*., 1994, 3, 787-790.
[28] Miyoshi, K; Pohlchuck, B; Street, KW; Zabinski, JS; Sanders, JH; Voevodin, AA; Wu, RLC. *Wear*, 1999, 225-229, 65-73.
[29] Schiffmann, KI; Fryda, M; Goerigk, G; Laure, R; Hinze, P; Bulack, A. *Thin Solid Films*, 1999, 347, 60-71.
[30] Chan, KK; Silva, SRP; Amaratunga, GAJ. *Thin Solid Films*, 1992, 212, 232-239.
[31] Gehards, I; Ronning, C; Hofsass, H; Seibt, M; Gibhard, H. *J. Appl. Phys*., 2003, 93 1203-1207.
[32] Lau, SP; Li, YJ; Tay, BK; Sun, Z; Chen, GY; Ding, XZ. *Diamond Relat. Mater*., 2001, 10, 1727-1731.
[33] Hussain, S; Roy, PK; Pal, AK. *Mater. Chem. Phys*., 2006, 99, 375-381.
[34] El-Sherbiny, M; Salem, F. *Tribol. Trans*., 1985, 29, 223-228.
[35] Roy, R; Sen, SK. *Thin Solid Fil*ms, 1993, 223, 189-195.
[36] Minton, TK; Garton, DJ. In *Chemical Dynamics in Extreme Environments*, Dressler, R; 978-981-02-4177-3; World Scientific, Singapore, SP, 2001, Vol. 11, 1-632.
[37] Synowki, RA; Hale, JS; Woollam, JA. *J. Spacecraft Rockets*, 1993, 30, 116-119.
[38] Hedin, AE; Heber, CA; Newton, GP; Spencer, NW; Brinton, HC; Mayr, HG. *J. Geophys. Res-Space*, 1977, 82, 2148-2156.
[39] Arnold, GS; Peplinski, DR. *AIAA Journal*, 1986, 24, 673-677.

Copyright © 2010. Nova Science Publishers, Incorporated. All rights reserved.

[40] Park, C. *AIAA Journal*, 1976, 14, 1640-1642.
[41] Rosner, DE; Allendorf, HD. *AIAA Journal*, 1965, 3, 1522-1523.
[42] Rosner, DE; Allendorf, HD. *Carbon*, 1965, 3, 153-156.
[43] Peters, PN; Linton, RC; Miller, ER. *Geophys. Res. Lett*., 1983, 10, 569-571.
[44] Tagawa, M; Umeno, M; Ohmae, N. Influence of 5eV atomic oxygen on surface properties of Ag films and graphite. *AIAA paper*, 1990, 90-0728.
[45] Garret, HB; Chutjian, A; Gabriel, S. *J. Spacecraft Rockets*, 1988, 25, 321-340.
[46] Leger, LJ; Spiker, IK; Kuminecz, JF; Visentine, JT. *AIAA paper*, 1983, 83-2631.
[47] Leger, LJ; Visentine, JT; Kuminecz, JF. *AIAA paper*, 1984, 84-0548.
[48] Whitaker, AF. *AAIA paper*, 1983, 83-2632.
[49] Fraundorf, P; Lindstrom, D; Pailer, N; Sandford, S; Swan, P; Walker, R; Zinner, E. AIAA paper, 1983, 83-2636.
[50] Marciano, FR; Bonetti, LF; Pessoa, RS; Marcuzzo, JS; Massi, M; Santos, LV; Trava-Airoldi, VJ. *Diamond Relat. Mater*., 2008, 17, 1674-1679.
[51] Zhao, SY; Chen, SH; Li. DG; Ma, HY. *Colloids Surf. A*, 2004, 242, 145-149.
[52] Sileikaite, A; Prosycevas, I; Puiso, J; Juratis, A; Guobiene, A. *Mat. Sci*., 2006, 12, 287-291.
[53] Tuinstra, F; Koening, JF. *J. Chem. Phys*., 1970, 53, 1126-1130.
[54] Dillon, O; Woollam, J; Katkanant, V. *Phys. Rev. B*, 1984, 29, 3482-3529.
[55] Beeman, D; Silvermann, J; Lynds, R; Anderson, MR. *Phys. Rev. B*, 1984, 30, 870-945.
[56] Tamorn, MA; Vassell, WC. *J. Appl. Phys*., 1994, 76, 3823-3828.
[57] Casiraghi, C; Ferrari, AC; Robertson, J. *Phys. Rev. B*, 2005, 72, 385-401.
[58] Choi, HW; Dauskardt, RH; Lee, SC; Lee, KR; Oh, KH. *Diamond Relat. Mater*., 2008, 17, 252-257.
[59] Stoney, GG. *Proc. R. Soc. London, Ser*., 1909, A 82, 172-175.
[60] Jacobsohn, LG; Freire Jr, FL. *J. Vac. Sci. Technol*., *A*, 1999, 17, 2841-2850.
[61] ISO 14577, *Metallic Materials – Instrumented indentation test for hardness and materials parameters*. Part 1: Test method, 2002.
[62] Oliver, WC; Pharr, GM. *J. Mater. Res*., 1992, 7, 1564-1583.
[63] Marcuzzo, JS; Urruchi, WI; Massi, M; Grigorov, K; Maciel, HS. *J. Electrochem. Soc*., 2006, 4, 545-552.
[64] Lieberman, MA; Lichtenberg, AJ. *Principles of Plasma Discharges and Materials Processing*; 0471720011; John Wiley & Sons: New York, NY, 2005, Vol. 1, 1-721.
[65] Yun, DY; Choi, WS; Park, YS; Hong, B. *Applied Surface Science* 2008, 254, 7925-7928.

Copyright © 2010. Nova Science Publishers, Incorporated. All rights reserved.

In: Silver Nanoparticles
Editor: Audrey E. Welles, pp. 361-370
ISBN: 978-1-61668-690-1
© 2010 Nova Science Publishers, Inc.

Chapter 11

ELECTROSPUN GELATIN NANOFIBERS FUNCTIONALIZED WITH SILVER NANOPARTICLES

Florentina Tofoleanu, Tudorel Balau Mindru[1], Florin Brinza, Nicolae Sulitanu, Ioan-Gabriel Sandu[2], Dan Raileanu[3], Viorel Floristean[4], Bogdan Alexandru Hagiu[4], Cezar Ionescu[5], Ion Sandu[6] and Vasile Tura

Faculty of Physics, Al. I. Cuza University[1], Iasi, Romania
[1] Textiles and Leather Engineering, Gh. Asachi Technical University[2], Iasi, Romania
[2] Materials Science and Engineering, Gh. Asachi Technical University,
Str. Dimitrie Mangeron nr. 63, 700050[3], Iasi, Romania
[3] Biology, Al. I. Cuza University[4], Iasi, Romania
[4] Veterinary Medicine, Ion Ionescu de la Brad University of Agricultural Science and Veterinary Medicine[5], Iasi, Romania
[5] Medicine, Gr. T. Popa University of Medicine and Pharmacy[6], Iasi, Romania
[6] Orthodox Theology, Al. I. Cuza University of Iasi,[7] Romania

Copyright © 2010. Nova Science Publishers, Incorporated. All rights reserved.

ABSTRACT

The present chapter deals with gelatin nanofibres functionalized with silver nanoparticles, prepared by electrospinning using solutions of gelatin mixed with silver nitrate. As a common solvent for gelatin and AgNO3 was selected a mixture of formic acid and acetic acid in volume ratio 4:1. In this system, formic acid was used as a solvent

[1] Blvd. Carol I nr. 11A, 700506, Iasi, Romania.
[2] Str. Dimitrie Mangeron nr. 53, Corp TEX1, 700050, Iasi, Romania.
[3] Str. Dimitrie Mangeron nr. 63, 700050, Iasi, Romania.
[4] Blvd. Carol I nr. 11A, 700506, Iasi, Romania
[5] Aleea Mihail Sadoveanu nr. 3, Iasi, 700490, Romania.
[6] Str.Universitatii nr.16, 700115, Iasi, Romania.
[7] Bd. Carol I, nr. 11A, 700506, Romania.

of gelatine, but also as reducing agent for silver ions in solution. Silver nanoparticles were stabilized through a mechanism that involves an interaction with oxygen atoms of carbonyl groups of gelatin. The gelatin nanofibres functionalised with silver nanoparticles were characterized by transmission electron microscopy (TEM), scanning electron microscopy (SEM), X-ray diffraction (XRD) and antimicrobial test. The results of investigations by TEM and XRD confirmed the presence of silver nanoparticles with diameters less than 20 nm, uniformly distributed over the surface of smooth nanofibres with an average diameter of 70 nm. The tests demonstrated that gelatin/Ag nanofibers have a good antimicrobial activity against Escherichia coli.

Keywords: Electrospinning; Gelatin; Silver; Nanofibers; Nanoparticles.

1. INTRODUCTION

One of the very important tissues for human health is the skin, which plays the role of an interface between body and environment, and acts as a protective barrier against physical, chemical and biological aggressions. The skin is actually a complex system involved in the processes of absorption and excretion, showing a selective permeability for some important substances in human metabolism [1].

The currently increasing incidence of skin diseases caused a significant demand for skin replacement materials which in many cases can not be assured from natural sources. It also increased the demand for skin regrowth substrates used in treating skin lesions, which stimulated tissue engineering to develop new biodegradable materials which can promote adhesion, development and migration of fibroblasts, necessary for a good quality reepithelization [2]. Skin substitutes used today are expensive and have limitations concerning the biocompatibility, making their use sometimes risky [3].

There have been developed various technologies to produce biomaterials used for skin lesions treatment of wound dressings. One of the very interesting nanotechnologies investigated now is polymer solutions spinning in electrostatic field (electrospinning), which can be applied to solutions of various natural and synthetic polymers such as gelatine, collagen, chitosan, fibrinogen, silk, polylactic acid, hyaluronic acid, obtaining non-woven nanofibres membrane with thicknesses in a range that goes from a few tens of nanometers to over one thousand nanometers [4-6]. This type of three-dimensional structure of nanofibres prepared by electrospinning resembles very well with the human extracellular matrix, which explains the great interest manifested today for this nano-technology.

The biopolymers have high viscosity and very low solubility in common organic solvents, which makes them difficult to process by solution spinning in electrostatic field. Natural polymers dissolve well in 1,1,1,3,3,3-hexafluoro-2-propanol and trifluoroacetic acid [7], which are toxic and expensive solvents, features that limit their use in applications on an industrial scale [8-11].

Gelatin is a biopolymer widely used in pharmaceutical industry and for medical device applications. As a result of the growing interest for regenerative medicine, in the recent past gelatin has begun to be studied also as a candidate material for obtaining scaffolds with similar qualities of natural media for a wide range of tissues [12-16].

Copyright © 2010. Nova Science Publishers, Incorporated. All rights reserved.

In a previous study we reported the preparation of nanofibres with superior mechanical and biological characteristics, by electrospinning of gelatin solutions with concentrations up to 30% (w/v) [17]. In the present paper we investigated the possibility to improve the properties and extend the applicability of gelatin nanofibers by adding silver nanoparticles which are known to have a positive effect in wounds healing and skin regeneration.

2. EXPERIMENTAL

2.1. Gelatin/Agno$_3$ Solutions

The electrospinnable solutions used in our experiments were prepared using gelatin (Fisher HealthCare, MP Biomedicals), formic acid (98 +100%, Scharlau Chemie SA), acetic acid (99.5%, Chemical Company SA), silver nitrate (99.5% Chemical Company SA) and distilled deionised water. The reagents were used as received from the manufacturer.

In the beginning, a solution of 27% (w/v) gelatin in a mixture of formic acid with acetic acid in the volumetric ratio 4:1 was prepared. The solution was subjected to stirring at room temperature for 3h, after which the impurities and undissolved parts were eliminated using a stainless steel filter.

The silver precursor solution was prepared by dissolving 5% (w/v) $AgNO_3$ in 66% (v/v) acetic acid in distilled deionised water.

The electrospinnable solution was prepared by adding dropwise the $AgNO_3$ solution to the gelatin solution, under continuous stirring for 20 minutes.

The solutions viscosity was determined at room temperature using a Nahita Rotary Viscometer, observing the rules ISO 3219/1993 [18].

2.2. Electrospinning

The equipment for spinning in electrostatic field was made of a 10 ml syringe filled with solution, actuated by a home-made syringe pump able to provide flow rates in the range 1.0-40.0 μL/min. The syringe was connected through a 40 cm Teflon tube of 0.5 mm inner diameter to a blunt needle placed 12 cm high above a collector covered with aluminium foil. Between the needle and collector high-voltages in the range 11.0-19.5 kV have been applied using a Brandenburg Alpha III Series HV Power Supply (30V-30kV). The optimum solution flow-rate for obtaining good quality nanofibers was 2.4μL/min.

2.3. Crosslinking with Glutaraldehyde

The water stability of the nanofibers was improved by crosslinking with glutaraldehyde vapours (25% solution) for 24 h, drying at room temperature for 2 h and heating in a thermostat at 70^{o}C for 2h. It is known that such a treatment promotes gelatin chains crosslinking by formation of Schiff bases type iminic groups [19,20].

Copyright © 2010. Nova Science Publishers, Incorporated. All rights reserved.

2.3. Structural Characterization

The morphology of the electrospun gelatin nanofibers was examined by scanning electron microscopy (SEM) using a Vega 2 Tescan (Czech Republic) microscope. The nanofibers diameter was estimated using Atlas Tescan software for image analysis.

The chemical structure of nanofibers was investigated by Fourier-transform infrared attenuated total reflectance spectroscopy (FTIR-ATR) using a DIGILAB – SCIMITAR Series FTS 2000 spectrometer with ZnSe crystal, working in the range 750-4000 cm^{-1}, with 4 cm^{-1} resolution.

Dimensional analysis and structural characterization of silver nanoparticles was carried out by transmission electron microscopy (TEM) using a Philips CM100 microscope, and by X-rays diffraction (XRD) using a DRON 2.0 diffractometer with Cu tube (Kα radiation).

2.4. Antimicrobial Activity Characterization

The antibacterial activity was tested on solid media by the disk diffusion method. The bacterium inocula were prepared from a culture of *Escherichia coli* ATCC 25922 overnight incubated at 37^{o}C in nutrient broth, by diluting with peptoned water to a 0.5 McFarland standard. Petri plates containing Mueller Hinton agar were innoculated by inundation with prepared microbial suspension. Two samples of the investigated material, one containing Ag nanoparticles and one without Ag nanoparticles (used as control) were placed on the surface of the inoculated media. The plates were incubated at 37^{o}C for 24 hours. Following incubation, plates were examined in order to identify zones of no growth (halos around the fragments) characteristic for antimicrobial activity.

3. RESULTS AND DISCUSSIONS

In case of electrospinning gelatine, its strong polar nature makes it difficult to solve in common solvents. The special solvents mentioned above are toxic and very expensive. Using the results of our previous study, in the present work we choosed as gelatin solvent a mixture of formic acid and acetic acid in volumetric ratio 4:1 that provided a better solution stability and a longer electrospinnability interval [17], due to the acetic acid which determined a dynamic rebuild of the hydrogen bonds involved in generating helicoidal structures of gelatin molecules.

In the present work, by electrospinning a solution of AgNO3 in gelatin, good quality nanofibers with smooth surface and without beads were obtained, as proved by the SEM images presented in Figures 1, 2.

The morphology of the nanofibers shown in Figure 2(a) suggest that adding 5% (w/w) silver nitrate to gelatin resulted in an increased solution conductivity and caused a slight decrease of fibers diameter. Moreover, the increased conductivity and decreased viscosity of the electrospun solution determined occasionally the formation of some auxiliary microjets which formed nanofibres with diameters less than 30 nm, intercalated among majority nanofibres with an average diameter of 190 nm.

Copyright © 2010. Nova Science Publishers, Incorporated. All rights reserved.

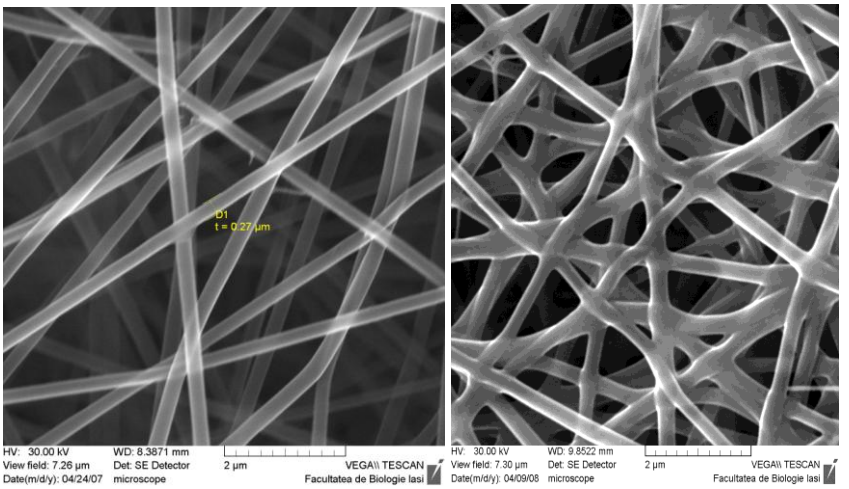

(a) (b)

Figure 1. SEM images of gelatin nanofibres prepared by electrospinning a solution of gelatin in formic acid and acetic acid: (a) as electrospun, (b)crosslinked in vapours of glutaraldehyde.

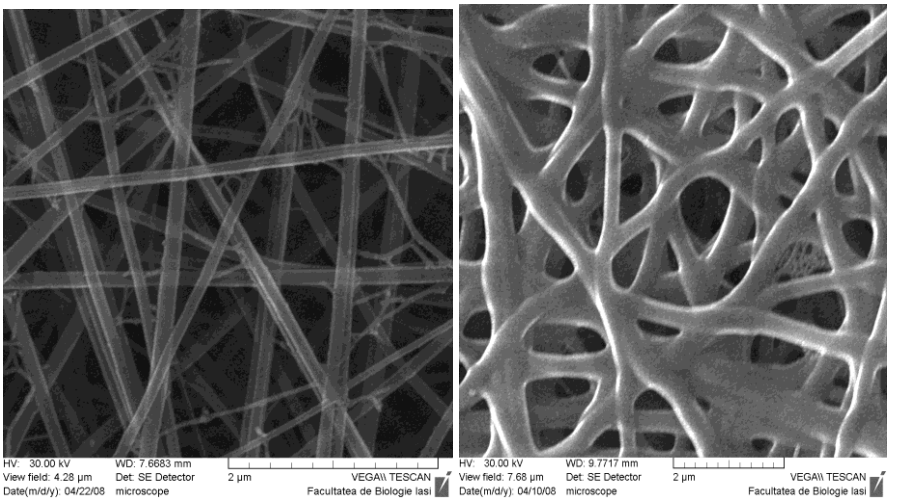

(a) (b)

Figure 2. SEM images of gelatin nanofibers functionalised with silver nanoparticles: (a) as electrospun, (b) crosslinked in vapours of glutaraldehyde.

Further treatment of gelatin or gelatin/Ag nanofibers with glutaraldehye vapours resulted in a slight increase of nanofibers diameter due to water removal and increase of material density (Figures 1b, 2b). The water removed during the crosslinking process accumulated on the nanofibers surface and caused a superficial dissolution and bonding of nanofibers at the contact points.

Copyright © 2010. Nova Science Publishers, Incorporated. All rights reserved.

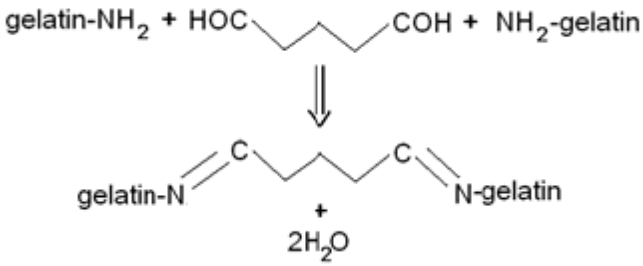

As compared with pure gelatin nanofibers in Figure 1b, the crosslinked gelatin/Ag nanofibers shown in Figure 2b appear to be more affected by water, probably because an increased hydrophylicity as a consequence of structural changes induced by silver nanoparticles surfaces.

Images obtained by TEM (Figure 3) show the presence of some nanoparticles on the surface and in the volume of gelatin nanofibers. The shape of nanoparticles is spherical, with diameters less than 20 nm.

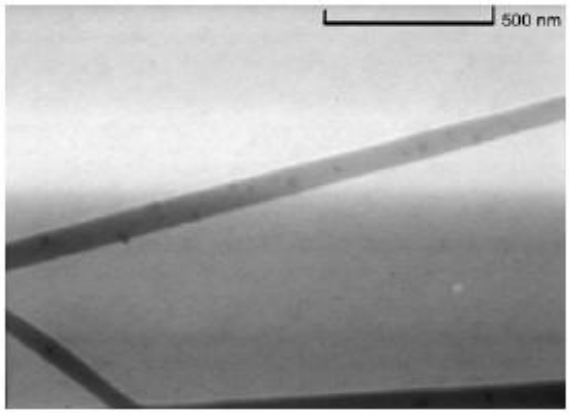

(a)

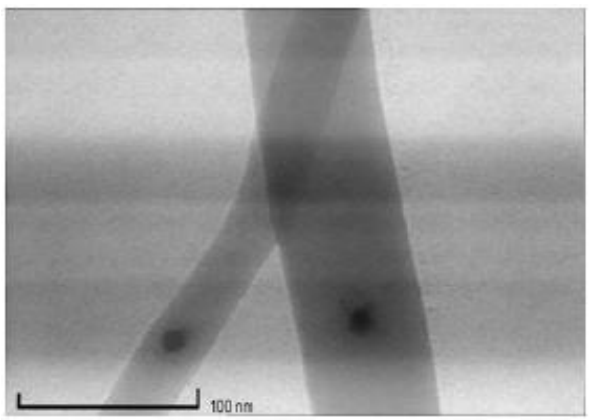

(b)

Figure 3. TEM images of silver nanoparticles on the surface (a), and inside (b) of electrospun gelatin nanofibers.

Copyright © 2010. Nova Science Publishers, Incorporated. All rights reserved.

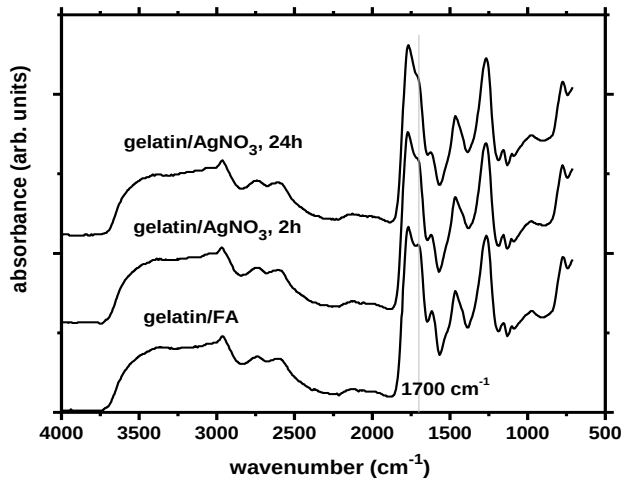

(a)

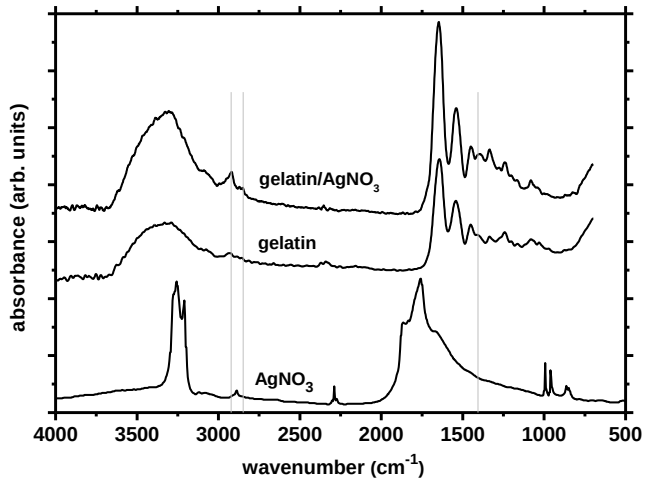

(b)

Figure 4. FT-IR spectra: (a) gelatin/AgNO3 solution, (b) electrospun gelatin nanofibers doped with silver nanoparticles.

3.3. Structural Characterization by FTIR and XRD

The infrared spectra showed in Figure 4 show that the spectrum of gelatine nanofibers is almost identical with the spectrum of gelatin/Ag nanofibers, with just two small differences. First, it can be observed a more intense absorption in the band at 1406 cm^{-1}, assigned to symmetrical stretching of the carboxyl group, -COOH. Second, the absorption peaks at 2922 cm^{-1} and 2848 cm^{-1}, suggest that the silver nanoparticles caused a reordering of gelatin chains by promoting the formation of peptide CH_2 links [21]. This restructuring effect is very similar to the effect reported in our previous paper [17], where the bands at 2922 cm^{-1} and 2848 cm^{-1} appeared in infrared spectra of films prepared from aqueous gelatin solutions and were not

Copyright © 2010. Nova Science Publishers, Incorporated. All rights reserved.

present in spectra of gelatin nanofibers. The high relative elongation of electrospun nanofibers and the fast solvent evaporation freezes an amorphous structure in pure gelatin nanofibers. By contrast, as the spectra from Figure4 prove, the presence of silver nanoparticles stimulates the restoration of local order of molecular chains and facilitates the formation of peptide links between them.

In the FTIR spectrum of the gelatin/$AgNO_3$ solution in Figure 4a, one can see a slight increase in the intensity of the absorption bands amide I and II, but without any new peaks that could be assigned to a possible unreacted phase of $AgNO_3$. On the basis of Figure 4a it can be assumed that the entire amount of silver nitrate reacted with the formic acid and silver is present in the gelatin/Ag nanofibers only in metal form. The presence of silver only in the form of well crystallised metal nanoparticles is certified by the X-ray difractogramme shown in Figure 5, where the peaks due metallic silver are clearly present.

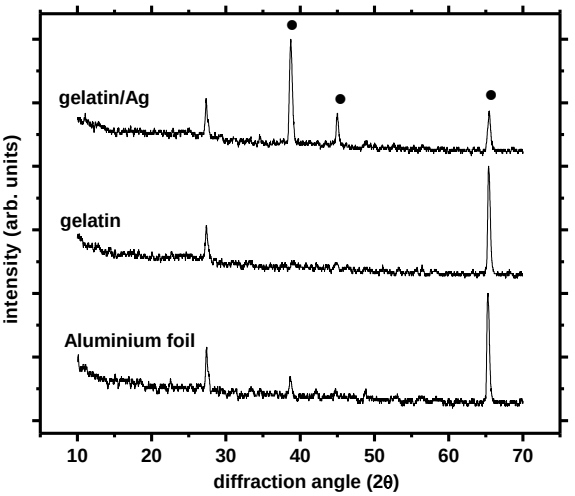

Figure 5. X-ray diffractograms of electrospun gelatin nanofibers functionalised with silver nanoparticles, crosslinked with glutaraldehyde.

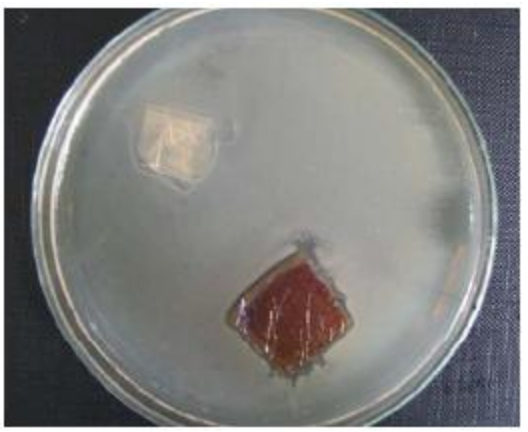

Figure 6. Antimicrobial activity of gelatin nanofibers against Escherichia coli ATCC 25922. Upper left – gelatin, bottom right - gelatin with silver nanoparticles.

Copyright © 2010. Nova Science Publishers, Incorporated. All rights reserved.

4. CONCLUSIONS

In the present work, there were prepared non-woven membranes made of gelatin nanofibers functionalized with silver nanoparticles with diameters less than 20 nm. After crosslinking with glutaraldehyde vapours, the nanofibers gained good water stability.

The structural analysis by infrared spectroscopy and X-ray diffractometry have shown that in the final nanofibers silver is present only in the form of well crystallised metal nanoparticles.

The presence of growth inhibition zones, i.e. halos around the samples of gelatin/Ag nanofibers proved the antimicrobial activity of the investigated material against *Escherichia coli* ATCC 25922.

The superior physical and chemical characteristics, along with a good biocompatibility and other improved properties as a lack of inflammatory reaction and relatively fast resorbtion, recommend the gelatin nanofibers functionalized with Ag nanoparticles as a good candidate material for the manufacture of wound dressings skin tissue scaffolds.

REFERENCES

[1] Shier, DN; Butler, JL; Lewis, R. Hole's Human Anatomy and Physiology, 11th edition, McGraw-Hill Higher *Education*, 2006.
[2] Langer, R; Vacanti, JP. *Science*, 1993, 260, 920.
[3] Damodaran, G; Syed, M; Leigh, I; Myers, S; Navsaria, H. *Expert Review of Dermatology*, 2008, 3(3), 345.
[4] Wen, X; Shi, D; Zhang, N. Applications of Nanotechnology in Tissue Engineering, in Handbook of Nanostructured Biomaterials and Their Applications in Nanobiotechnology, Ed. HS. Nalwa, *American Scientific Publishers*, 2005, 1.
[5] Zhang, Y; Ouyang, H; Lim, CT; Ramarkrishina, S; Huang, ZM. *J. Biomed. Mater. Res*., Part B: *Appl. Biomater*, 2005, 72B, 156.
[6] Kim, HW; Song, JH; Kim, HE. *Adv. Funct. Mater*, 2005, 15, 1988.
[7] Murugan, R; Ramakrishna, S. *Tissue Engineering*, 2006, 12(3), 435.
[8] Li, M; Mondrinos, MJ; Gandhi, MR; Ko, FK; Weiss, AS; Lelkes, PI. *Biomaterials*, 2005, 26, 5999.
[9] Wnek, GE; Carr, ME; Simpson, DG; Bowlin, GL. *Nano Lett*, 2003, 3, 213.
[10] Ohkawa, K; Cha, D; Kim, H; Nishida, A; Yamamoto, H. Macromol. *Rapid Commun*, 2004, 25, 1600.
[11] Matthews, JA; Wnek, GE; Simpson, DG; Bowlin, GL. *Biomacromolecules*, 2002, 3, 232.
[12] Li, M; Mondrinos, MJ; Gandhi, MR; Ko, FK; Weiss, AS; Lelkes, PI. *Biomaterials*, 2005, 26, 5999-6008.
[13] Liao, S; Bojun, L; Zuwei, M; Wei, H; Chan, C; Ramakrishna, S. *Biomed. Mater*, 2006, 1, R45.
[14] Langer, R; Tirrell, DA. *Nature*, 2004, 428, 487.
[15] Dankers, PYW; Harmsen, MC; Brouwer, LA; van Luyn, MJ; Meijer, EW. *Nature Mater*, 2005, 4, 568.

Copyright © 2010. Nova Science Publishers, Incorporated. All rights reserved.

[16] Huang, ZM; Zhang, YZ; Kotaki, M; Ramarkrishna, S. Compos. *Sci. Technol*, 2005, 63, 2223.
[17] Balau Mindru, T; Balau Mindru, I; Malutan, T; Tura, V. *Journal of Optoelectronics and Advanced Materials*, 2007, 9(11), 3633.
[18] ISO 3219:1993. Plastics - Polymers/resins in the liquid state or as emulsions or dispersions - Determination of viscosity using rotational viscometer with defined shear rate.
[19] Koyama, Y; Taniguchi, A. *J. Appl. Polym. Sci*., 1986, 31(6), 1951.
[20] Tual, C; Espuche, E; Escoubes, M; Domard, AJ. *Polym. Sci., Part B: Polym. Phys*., 2000, 38(11), 1521.
[21] Prystupa, DA; Donald, AM. *Polymer Gels and Networks*, 1996, 4, 87.

Copyright © 2010. Nova Science Publishers, Incorporated. All rights reserved.

INDEX

A

absorption spectra, 36, 37, 38, 39, 44, 45, 46, 47, 85, 86, 94, 98, 110, 111, 243, 248, 268
absorption spectroscopy, 36, 64, 83, 222
accuracy, 97
acetic acid, xv, 428, 429, 430, 432
acetone, 7, 311, 409
acid, xv, 7, 146, 147, 311, 317, 353, 356, 357, 358, 359, 428, 429, 430, 432, 436
activated carbon, 278, 287, 304
activation energy, 209
activity level, 290
additives, 20
adenine, 357, 363
adenocarcinoma, 389
adhesion, 113, 261, 262, 405, 428
adhesion properties, 113
adsorption, 277, 297, 345, 352, 357
aerosols, 392
agar, 279, 286, 287, 291, 389, 392, 393, 431
agent, xv, 428
agglomeration, xiii, 121, 344, 377, 393
aggregates, 4, 19, 29, 62, 100, 109, 162, 215, 329, 355, 410
aggregation, x, 4, 13, 25, 61, 63, 86, 94, 95, 97, 104, 110, 115, 116, 119, 217, 261, 273, 353, 357, 358
air, 403, 408, 412, 418
albumin, 354
alcohol, 52, 353
aldehydes, 350
algae, 261, 292, 386, 392
alloys, 23, 40, 202, 404
alternative, 406
alters, 214
aluminium, 430
aluminum, 98, 108
ambient air, 418
amide, 435
amines, 353
amino acids, 351, 354, 358
ammonia, 26
ammonium, 266, 269, 270
amoeboid, 290
amorphous carbon, 404, 407
amorphous silicon, xiv, 401
amplitude, 94, 159, 175, 178, 181, 292
anchoring, 301
anionic surfactants, 268
anisotropy, 20, 160, 163, 164, 323
annealing, 30, 146, 180, 186, 215, 231, 232, 236, 239, 255
annihilation, 165
antibacterial, 431
antibacterial properties, xiii, 343, 347
antibody, 346
antioxidant, 263
apoptosis, 292, 299
application, 402, 405
applied research, 260
aqueous solution, 409
aqueous suspension, 111
ARC, 385
arginine, 354
argon, 40, 100
argyria, 386
aromatic rings, 265
assessment, 299
assignment, 40
assumptions, 138, 308
asymmetry, 81, 227, 231, 238, 290
atmosphere, 403, 405, 408, 423
atomic force, 64, 98, 101, 237, 410
atomic force microscope, 98, 237
atomic force microscopy (AFM), 410

Copyright © 2010. Nova Science Publishers, Incorporated. All rights reserved.

ATP, 356
attachment, 9, 10, 11, 13, 14, 218, 353, 354
attenuated total reflectance, 431
authors, 190, 222, 249, 282, 289, 352, 358, 382, 413
availability, 107, 346
averaging, 68
avoidance, 287, 290, 291

B

background, 103, 138, 416, 418
backscattering, 411
bacterium, 282, 294, 299, 387, 390, 431
band gap, 402, 407
bandwidth, 88, 119, 124, 125, 129, 175, 324, 337
barrier, 415, 428
beams, 323, 324, 403
beef, 388, 389, 392, 393
behavior, xii, 69, 86, 90, 96, 126, 138, 159, 181, 185, 304, 305, 310, 333, 354, 363, 405, 424
behaviors, 354
bending, 351, 379
bias, 320
binding, 18, 29, 108, 162, 211, 262, 355, 359
binding energy, 18, 162
biochemistry, 2, 301, 303, 355
biocompatibility, xiii, 344, 347, 352, 353, 359, 428, 437
biodegradable, 428
biodegradable materials, 428
biological activity, 263, 298
biological systems, xi, 259, 353
biomaterials, 429
biomedical applications, 347, 352, 355
biopolymer, 429
biopolymers, 429
biosensors, 20, 346, 362
biostability, xiii, 344
biosynthesis, 349, 350, 351, 360
biotechnology, 353
biotin, 354
birth, 19
bismuth, 334
bleaching, 43, 44, 45, 170, 171, 172, 174, 175, 178, 180, 182, 346
blocks, 65, 128
blood, 263, 297
blood vessels, 297
body weight, 262, 296
bonding, 13, 25, 28, 397, 404, 405, 412, 433
bonds, 32, 33, 217, 220, 404, 406, 407, 432
bone, 15, 263
bone marrow, 263
brain, 301
branching, 11, 12, 13, 14, 22
breakdown, 68, 70, 90, 160, 164
breast cancer, 358, 359
broadband, 124
budding, 347
building blocks, xii, 15, 25, 343
bulk materials, 106, 109, 128
bursa, 398

C

cadmium, 356, 359
calcium, 202, 279, 356
calcium carbonate, 356
calibration, 112
cancer, 260, 347
candidates, 136, 309, 351, 371, 372
capital cost, 406
carbon atoms, 405
carbon dioxide, xiv, 402, 417
carbon film, 29, 120, 121, 407
carbon materials, 277
carbon monoxide, xiv, 402, 417
carbonization, 246
carbonyl groups, xv, 428
carboxyl, 435
carboxylic acids, 350, 353
carcinoma, 389
carrier, 160, 371
case study, 300
cast, 314
catalysis, 2, 11, 15, 20, 25, 354, 386, 398
catalyst, 14, 42, 44, 45, 46, 346
catalytic activity, 20, 43, 44, 45, 46
catalytic properties, ix, 2, 303, 345, 346
cathode, 406, 409, 415
cation, 163
cell death, 294
cell line, 389
cell lines, 389
cell membranes, 394
cell surface, 261, 356
central nervous system, 299
challenges, 25, 402, 407
channels, 148
character, 95, 138
chemical bonds, 28, 246
chemical etching, 408
chemical interaction, 311, 315
chemical properties, xii, 29, 200, 263, 343, 352, 402, 405, 417
chemical reactions, 25, 217

Copyright © 2010. Nova Science Publishers, Incorporated. All rights reserved.

chemical reactivity, 408
chemical vapor deposition, xiv, 402, 406, 409
chemisorption, 261, 361, 405
chemotherapy, 347
chicken, 397
chitin, 285, 286, 303
chitosan, 429
chlorine, 280
chloroform, 379
chronic lymphocytic leukemia, 299
clarity, 125
classical electrodynamics, 244
cleaning, 6
cleavage, 394
clinical diagnosis, xiii, 344, 359
cluster model, 28
clustering, 208
CO2, 246, 389, 390, 418, 419, 420, 421, 422, 423
coagulation, 4, 263
coal, 43
coatings, 15, 260, 284, 303, 403, 405, 406, 407, 408
cobalt, 53, 300
coherence, 149
collaboration, 130, 284, 289, 292
collagen, 429
collisions, 215
colon, 389
combined effect, 294
combustion, 408
communication, 336, 372
community, 136
competition, 213, 217, 239, 379
complexity, 37, 263, 298
components, 106, 115, 119, 166, 200, 285, 298, 351, 355, 356, 417
composites, ix, xi, 1, 25, 28, 29, 46, 47, 74, 81, 199, 202, 225, 226, 230, 236, 238, 241, 314, 327, 379
composition, ix, 1, 3, 202, 211, 213, 265, 285, 319, 345, 352, 417
comprehension, 137
compression, 379
computing, 336
concentrates, 87
condensation, 103, 116
conduction, 103, 138, 142, 153, 154, 158, 159, 160, 161, 162, 183, 200, 248, 310, 367, 405
conductivity, 150, 159, 208, 210, 242, 398, 417, 432
conductor, 226
conductors, 200
conference, 304
configuration, 87, 88, 89, 93, 116, 128, 308, 404
confinement, xiii, 93, 115, 128, 366, 371, 375
conjecture, 392
conservation, 157, 172
construction, 317, 415
consumer goods, 260, 261
consumption, 22
contaminants, 418
contamination, 7, 283, 394
conversion, x, 61, 63, 65, 99, 107, 112, 113, 116, 118, 119, 123, 124, 125, 128, 129, 200, 336
cooling, 103, 104, 148, 154, 155, 180, 183, 232, 239
cooling process, 154
copper, xii, 17, 21, 48, 62, 69, 78, 79, 84, 86, 101, 102, 120, 121, 141, 202, 233, 301, 305, 398
correlation, 45, 71, 77, 229, 269
cosmetics, 260, 277
cost, 3, 4, 6, 42, 62, 317, 397, 405, 406
cotton, xiv, 286, 347, 385, 386, 387, 388, 389, 392, 393, 394, 397
coupling, xiv, 25, 39, 40, 150, 152, 153, 154, 164, 189, 366, 370, 376, 380
covalent bond, 28, 358
covering, 30, 136
critical value, 213
crosslinking, 430, 433, 437
crystal growth, 2, 4, 13, 14, 19, 20, 350
crystal structure, 13, 215, 273
crystalline, xii, 8, 9, 10, 13, 22, 23, 33, 53, 255, 306, 344, 373, 404
crystalline solids, 255
crystallites, 12
crystallization, 6, 14, 15, 215
crystals, 6, 8, 27, 34, 49, 77, 202, 241, 246, 350, 356
CTA, 401
cultivation, 286
culture, 286, 351, 388, 390, 431
cycles, 26, 32, 66, 159, 393, 394, 404, 406, 414
cyclotron, 415
cytocompatibility, 351, 362
cytotoxicity, xiv, 300, 385, 386, 387, 394, 397

D

damping, 139, 159, 307, 308, 367
danger, 260, 264
data processing, 68
death, 279, 285, 290, 292, 294, 296, 297
decay, 149, 310, 322
decomposition, 103, 405
defects, 14, 71, 78, 186, 215, 220, 243, 413, 414
definition, 120, 344
deformation, 168, 173, 189
degenerate, 67, 69, 94, 208
degradation, 123, 402, 403, 421
dehydration, 29, 30

Copyright © 2010. Nova Science Publishers, Incorporated. All rights reserved.

delivery, xiii, 343, 354, 359
dendrites, ix, 1, 3, 6, 7, 8, 9, 10, 11, 12, 13, 14, 15, 20, 21, 22, 23, 24, 37, 40, 42, 44, 45, 46
depolarization, 143
deposits, 22, 24
depression, 22
derivatives, xiii, 280, 303, 344
desorption, 238, 346
destruction, 162, 163, 166, 170, 171, 172, 173, 174, 175, 177, 179, 347
detection, 2, 25, 203, 204, 206, 207, 241, 260, 346, 353, 357, 358, 359, 360, 361, 362, 363, 366, 417, 421
deviation, 273
diamond, xiv, 401, 403, 404, 409, 412
diamond-like carbon, xiv, 401, 403
dielectric constant, xiv, 69, 74, 82, 140, 141, 144, 145, 223, 334, 335, 366, 375, 402
dielectric permeability, 223
dielectric permittivity, 311
dielectrics, xi, 4, 25, 93, 136, 199, 201, 202, 213, 214, 215, 221, 222, 226, 229, 231, 233, 236, 237, 241
differential equations, 151
diffraction, xv, 8, 18, 22, 27, 34, 67, 187, 243, 379, 428, 431
diffusion rates, 23
diffusion time, 166
diffusivities, 154
diodes, 88
dipole moments, 72
direct measure, 222
directionality, 161
discharges, 415
discipline, 399
diseases, 428
disinfection, 398
dislocation, 13, 14
disorder, 412
dispersion, 7, 26, 34, 75, 77, 91, 97, 121, 145, 233, 315, 316, 317, 318, 327, 358, 366, 388, 393
displacement, 309
dissociation, 217, 273, 274
distilled water, 7, 268, 292, 293, 295, 314, 349
distribution function, 152
diversity, 262
DMF, 315, 334
DNA damage, 263
dominance, 93, 127
dopants, 217
doped, 435
doping, ix, 1, 35, 79, 202, 316, 378, 407
dressings, 260, 429, 437
drinking water, 268, 288
drug delivery, xiii, 343, 359
drugs, 261
drying, 110, 119, 379, 389, 430
durability, 393, 403
duration, x, 61, 64, 68, 70, 72, 75, 79, 81, 83, 90, 98, 102, 112, 118, 127, 201, 208, 209, 233, 238, 406
dyes, 76, 337, 346, 361
dynamics, 63, 64, 77, 83, 91, 94, 95, 96, 107, 123, 127, 148, 149, 150, 153, 183, 217, 235

E

E.coli, 262, 279, 281, 282, 283, 286, 287, 288, 293, 294, 297, 347, 362
earth, 331
ecology, 279, 283, 284
economy, 43
effluent, 360, 419
elaboration, 233, 260
electric charge, 36
electric field, 66, 74, 93, 138, 139, 157, 159, 160, 161, 164, 165, 166, 179, 189, 292, 309, 370, 376
electrical conductivity, 417
electrical fields, 405
electrochemical deposition, 15, 48
electrochemistry, 2, 6
electrodeposition, 57
electrodes, 6, 9, 26, 27, 356, 360, 387, 406
electrolyte, 8, 10, 11, 15, 26, 28, 33
electromagnetic, xii, 40, 65, 66, 137, 138, 140, 143, 148, 159, 201, 242, 244, 306, 307, 308, 310, 325, 326, 327, 328, 366, 367
electromagnetic field, xii, 40, 65, 138, 148, 159, 201, 306, 307, 308, 310, 325, 326, 327, 328, 366
electromagnetic fields, xii, 138, 306, 308, 326
electromagnetic waves, 137, 367
electron diffraction, 273
electron microscopy, xv, 208, 222, 273, 410, 428, 431
electron-phonon coupling, 150, 151, 152, 153
electro-optical properties, 2, 34
electrophoresis, 275
electroplating, 9, 55
electroreduction, 387
electrospinning, xv, 428, 429, 431, 432
elongation, 174, 175, 177, 178, 188, 189, 435
elucidation, 282, 289
embryo, 389, 397
emitters, 200
emulsions, 438
endothelial cells, 300
endurance, 403, 408

Copyright © 2010. Nova Science Publishers, Incorporated. All rights reserved.

energy consumption, 200
energy density, 96, 97, 120, 149, 150, 152, 154, 155, 172, 237
energy transfer, 79, 90, 149, 150, 151, 153, 154, 239, 354
engineering, 344, 353, 360, 428
enlargement, 79, 108, 273, 412
environment, 5, 42, 101, 139, 150, 151, 155, 244, 246, 248, 264, 279, 283, 284, 345, 346, 366, 367, 386, 403, 406, 408, 423, 428
enzymes, 262, 349, 351, 390
epidemiology, 284, 286, 360
epitaxial growth, 13
equality, 115
equilibrium, 6, 7, 11, 51, 149, 150, 202, 213, 217, 248, 407
equipment, 26, 32, 277, 319, 320, 335, 414, 430
erythrocytes, 347
ester, 353
ester bonds, 353
estimating, 80, 98
etching, xiv, 146, 147, 401, 403, 405, 407, 408, 415, 416, 417, 418, 419, 420, 421, 422, 423, 424
ethanol, 7, 26, 32, 83, 84, 85, 86, 87, 265
ethylene, 49, 83, 84, 86, 87
ethylene glycol, 49, 83, 84, 86, 87
evaporation, 99, 104, 111, 115, 154, 241, 379, 435
evolution, 10, 29, 30, 31, 32, 49, 124, 147, 151, 154, 155, 156, 157, 185, 189, 246, 320, 421, 422
excimer laser, xi, 199, 237, 238, 240, 406
exciton, xiii, 365, 372
exclusion, 68
excretion, 428
experimental condition, 72, 115
exploitation, 277
exploration, 4, 379
exposure, 164, 292, 296, 299, 301, 397
expulsion, 35
extracellular matrix, 429
extraction, 261, 348, 363
extrusion, 314

F

fabric, 388, 389, 393, 394
fabrication, 6, 65, 123, 129, 202, 228, 372, 398
Fermi level, 149, 152, 158, 161, 248
FFT, 3, 12, 13, 27
fiber, 98
fibers, 200, 299, 304, 386, 397, 432
fibrinogen, 429
fibroblasts, 428
field emission scanning electron microscopy, 387
film, xiv, 402, 403, 404, 405, 407, 409, 411, 412, 413, 414, 418, 419, 420, 421, 422, 423
film thickness, 414
filters, 68, 136
filtration, 288
financial support, 190, 249
fine tuning, 351
fish, 15, 262, 298
flavonoids, xi, 259, 263, 266, 269
flight, 408
float, 98, 100, 146, 209, 211, 212, 221, 223
flocculation, 348, 354, 363
flora, 282
flow, 409, 415, 430
flow rate, 430
fluctuations, 68
fluid, 4
fluorescence decay, 322
food, 7, 405
formula, 139
Fourier, 431
four-wave mixing, 69, 94
fractal cluster, 94
fractal dimension, 10
fragments, 162, 172, 173, 246, 417, 431
free energy, 217
free volume, 326
freedom, 180
frequencies, 40, 72, 93, 124, 358
frequency dependence, 139
Fresnel coefficients, 224
friction, 402, 404, 405, 406
FTIR, 33, 351, 431, 435
FTIR spectroscopy, 351
fullerene, 123, 248, 337
functionalization, 26, 345, 353, 354, 355, 362
fungal infection, 347, 361
fungi, 283, 347, 351, 388, 389, 390, 394
fungus, 350, 356, 360, 363, 390
fusion, 77, 90, 233, 379

G

gamma radiation, 387
gas, xiv, 402, 408, 409, 415, 418, 421, 422, 423
gas phase, 418
gases, 406, 415
gel, 49, 202, 207, 278, 286, 291, 314
gelatin, xv, 428, 429, 430, 431, 432, 433, 434, 435, 436, 437
gender, 301
gene, 358, 359
genes, 301

Copyright © 2010. Nova Science Publishers, Incorporated. All rights reserved.

genetics, 278, 294, 296
germination, 294, 295, 296
glass transition, 29, 157, 180, 332
glass transition temperature, 29, 157, 180
glucose, 54, 388
glutaraldehyde, 430, 432, 433, 436, 437
glycol, 86, 87, 301
government, iv
grain, 404
grain boundaries, 404
graph, 308
graphite, 122, 404, 405, 406, 425
gratings, 68, 136
grazing, 70, 112, 118
grids, 29, 120
ground-based, 408
group work, 263
growth inhibition, 437
growth modes, 3
growth rate, 20, 405, 410

H

half-life, 387
halos, 431, 437
hardness, 402, 404, 405, 413, 414, 426
healing, 260, 429
health, xiv, 260, 299, 386, 396, 397, 398, 428
health effects, 299
heat capacity, 150, 151, 152, 153, 154
heat conductivity, 151
heat transfer, 71, 96, 150, 154, 157, 165, 184
heavy metals, 300
height, 30, 356, 420
hematology, 262
hepatocellular carcinoma, 389
heptane, 265
hexane, 409, 410, 411, 412, 414, 421, 422
high pressure, 415
high temperature, 406
histogram, 388
HIV, 262, 300, 359, 360
homogeneity, 39
Honda, 193, 197
hospitals, 283, 394
host, 90, 113, 138, 141, 144, 158, 172, 215, 217, 262, 317, 359
hot spots, 35
human, 428, 429
human immunodeficiency virus, 347, 359
humidity, 29
hybrid, 68, 320, 378, 413
hydrazine, 264
hydrocarbon, 404, 405, 413
hydrocarbons, 246
hydrogen, 22, 43, 54, 119, 246, 317, 331, 402, 406, 413, 432
hydrogen bonds, 432
hydrogen peroxide, 317
hydrolysis, 390
hydroquinone, 357
hydrothermal synthesis, 32
hydroxide, 266
hydroxyl, 33, 261
hydroxyl groups, 33
hygiene, 279, 283, 284
hyperthermia, 352
hysteresis, 352

I

ideal, 335, 356
illumination, 237, 240
image analysis, 431
immersion, 34, 36
immobilization, 318, 348, 352, 379, 380, 382
immunocompromised, 347
immunoglobulins, 354
impacts, 398
implementation, 382
impurities, 14, 17, 27, 208, 214, 217, 430
in vitro, 263, 277, 292, 300
in vivo, 262, 277, 296, 301, 303
incidence, 70, 83, 112, 118, 145, 211, 224, 306, 428
inclusion, 100, 138, 158, 166, 407
incubation, 431
incubation time, 351
indentation, 426
India, 130, 343, 350
indication, 298
indices, 63, 335
indigenous, 105
indium, 124, 125, 129, 358
industrial, 404, 406, 410, 429
industrial production, 404
industry, xiv, 261, 284, 386, 392, 402, 429
inertness, 402, 404
infection, 284, 294, 361
infinite, 366
inflammatory, 437
information processing, 336, 371
infrared, 405, 431, 435, 437
infrared spectroscopy, 437
inhibition, 292, 437
injections, 296
insertion, 423

Copyright © 2010. Nova Science Publishers, Incorporated. All rights reserved.

insight, 345
inspection, 418
inspiration, 379
instability, 6, 68, 74
institutions, 278, 279, 284
insulators, 55, 211, 212, 213, 214, 221, 228, 231
integrity, 64, 104, 105, 115, 128, 347
intensity, 412
interaction process, 90
interactions, xii, xiii, 34, 37, 103, 144, 145, 148, 149, 255, 261, 299, 300, 305, 329, 346, 350, 355, 357, 359, 365, 370, 372, 394
interfacial layer, 333
interval, 154, 181, 246, 322, 333, 410, 421, 432
inversion, 118, 126, 309
ionic strength, 275
ionization, 68, 107, 109, 116, 157, 159, 162, 163, 166, 179, 215, 346, 417
iron, 57, 301
isolation, 43
isomerization, 323, 326
isomers, 323
isotropic, 404
issues, 136, 274, 294, 298, 351, 352, 407

K

ketones, 350
kidneys, 263, 296
kinetic energy, 408
kinetics, 3, 45, 151, 417

L

labeling, 346, 353, 354
laboratory studies, 404
laboratory tests, 283
lanthanide, 314
laser, 406, 411
llasers, 62, 67, 112, 250, 335
lattices, 356
laws, 223
leaks, 418
leisure, 45
lens, 68, 70, 83, 87, 90, 96, 112, 118, 125, 324, 349
life expectancy, 403
life sciences, 352
lifetime, xiv, 248, 265, 296, 321, 322, 401
ligand, 312, 328, 335
light beam, 223, 242
light scattering, 244, 351, 358
limitation, 177, 390
limitations, 428
linear dependence, 66, 72, 152
links, 435
lipid peroxidation, 261, 292, 301
lipoproteins, 301
liposomes, 273
liquid crystals, 337
liquid phase, 103, 289
liquids, 62, 64, 82, 83, 86, 92, 97, 127, 278, 288, 392
lithography, 202
liver, 263, 296, 300, 398
liver cells, 300, 398
liver damage, 296
local mobility, 164, 326
local order, 435
localization, 149
long distance, 115
losses, 408
lubricants, 402, 403, 408
lubrication, 403
luminescence, xii, 162, 293, 294, 305, 331
luminescence efficiency, 331
lying, 143, 163, 269
lysine, 354

M

macromolecules, 25, 352, 355, 356
macrophages, 300, 301
magnetic, 402
magnetic field, 4, 374
magnetic properties, 386
magnetron, 413
maintenance, 120
majority, 26, 261, 263, 284, 298, 432
manganese, 299
manipulation, xii, 136, 343
manufacturer, 285, 430
manufacturing, 143
market, 386
mask, 416, 420
mass spectrometry, xiv, 402, 417, 418, 420, 421, 423
material surface, 418
materials science, 353
measurement, xv, 66, 68, 322, 324, 402
measures, 394, 417
mechanical properties, 352, 405
mediation, xiii, 366, 375
melt, 146, 239, 332, 355
melting, 30, 32, 77, 90, 104, 113, 115, 153, 155, 164, 233, 237, 238, 243, 314
melting temperature, 32, 113, 155, 164, 238
membranes, 262, 277, 278, 288, 292, 299, 303, 379, 437

Copyright © 2010. Nova Science Publishers, Incorporated. All rights reserved.

memory, 104, 148, 338
Mendeleev, 303
metabolism, 428
metabolites, 350
metal oxides, 260
metallophthalocyanines, 335
metals, 3, 4, 25, 28, 88, 97, 98, 99, 113, 139, 150, 152, 202, 231, 260, 261, 277, 345, 350, 352, 367, 407
metamaterials, 200, 202, 249
methane, 405, 409
methanol, 121, 314
methodology, 409, 410, 413
mice, 289, 296, 297, 301, 303
micelles, xi, 259, 263, 265, 268, 269, 301, 302
microbial, 431
microbial cells, 261, 300, 350
microelectronics, 356
microemulsion, 302
micrometer, 57, 68, 136, 356
microscope, 29, 30, 84, 98, 121, 186, 187, 188, 269, 292, 348, 349, 431
microscopy, xv, 64, 96, 101, 208, 263, 410, 422, 423, 428, 431
microstructure, ix, 1, 3, 187, 188, 380
microstructures, ix, x, 1, 9, 135, 187
Mie theory, xi, 143, 172, 199, 218, 243, 307, 375
migration, 10, 428
military, 261, 335
minimum inhibitory concentrations, xiv, 385, 388
mitochondria, 394
mobility, 163, 182, 183, 185, 209, 217, 229, 275, 417
modeling, 137, 153
modelling, 222, 224
models, 10, 96, 151, 219, 228, 301, 320
modulation, 415
modulations, 382
modulus, 404, 405, 412
moisture, 386, 403
molar ratios, 38
mold, xi, 259, 289, 307
mole, 265
molecular reorientation, 323
molecular structure, 345, 357
molecular weight, 317
molybdenum, 53
monolayer, 55, 274, 317, 362
monomers, 18, 36, 317
motion, xii, 93, 306, 308
movement, 26, 68, 263, 290, 326, 332, 333
mucosa, 398
multicellular organisms, 263

N

nanocomposites, x, 135, 136, 137, 141, 157, 166, 179, 315, 332, 333, 371, 407
nanocrystalline, 407
nanocrystals, 302
nanodevices, 137
nanofabrication, 348
nanofibers, xv, 428, 429, 430, 431, 432, 433, 434, 435, 436, 437
nanomaterials, 99, 200, 249, 299, 302, 303, 336, 344, 350, 362
nanometer, 162, 314, 344, 371
nanometer scale, 371
nanometers, ix, 1, 108, 149, 157, 185, 187, 189, 237, 246, 344, 429
nanorods, 69, 346, 361
nanostructured materials, 104
nanostructures, ix, 1, 2, 3, 9, 20, 23, 34, 40, 42, 43, 44, 45, 46, 50, 55, 101, 108, 302, 325, 330, 359
nanotechnologies, 429
nanotechnology, 200, 260, 261, 300, 303, 344, 350, 352, 374, 386
nanowires, 90
natural, 428, 429
near-field scanning optical microscope, 375
network, 36, 337, 407
nitrate, xv, 428, 430, 432, 435
nitrogen, 349, 355
nitrogen oxides, 349
noble metals, 20, 139, 141, 202, 347, 407
noise, 18
nonequilibrium, 152
nonlinear optical response, x, xii, 61, 62, 80, 93, 94, 95, 104, 108, 109, 111, 114, 115, 137, 305, 309, 334, 335
nonlinear optics, 200, 366, 371, 372
normal, 404, 408
novel materials, 403
novelty, 3
nuclei, 4, 5, 17, 19, 24, 25, 26, 27, 28
nucleic acid, 355, 356, 357
nucleus, 14
numerical aperture, 186
nutrient, 431

O

observations, 65, 83, 86, 87, 88, 103, 107, 109, 127, 137, 282, 294
obstacles, 159
octane, 265
oil, 43, 98, 302, 430

Copyright © 2010. Nova Science Publishers, Incorporated. All rights reserved.

one dimension, 344
online, 418
opportunities, xiii, 2, 343
optical, 402, 405, 407, 423
optical communications, 336
optical density, 243, 269, 278
optical dichroism, x, 135, 136, 185
optical fiber, 338
optical limiters, xii, 69, 80, 233, 305, 335, 336
optical microscopy, 208, 356, 423
optical parameters, 63, 68, 74, 77, 81, 95, 97, 136, 233
optimization, xii, 2, 65, 118, 120, 129, 136, 177, 186, 306, 323
optoelectronic properties, 345
optoelectronics, 94, 104, 200
orbit, 403
organ, 335, 337, 347
organic, 408, 429
organic compounds, 337
organic matter, 378
organic solvent, 429
organic solvents, 277, 429
organism, xi, 259, 261, 356, 394
orientation, 20, 170, 323, 326, 327, 329, 332, 333, 338, 354
oscillation, 136, 148, 159, 161, 330, 331, 335, 367
oscillations, 137, 139, 140, 142, 143, 159, 164, 357
overlap, 22, 34, 248
oxidation, 45, 77, 234, 261, 262, 264, 300, 403, 407
oxidation products, 264
oxidative stress, 292, 301
oxide, 423
oxide nanoparticles, 273, 345, 351
oxides, 4, 349
oxygen, xiv, xv, 28, 29, 55, 217, 331, 401, 402, 403, 407, 408, 415, 417, 418, 420, 421, 422, 423, 425, 428
oxygen plasma, xiv, 401, 415, 417, 421, 423

P

paints, xiv, 277, 282, 283, 284, 285, 286, 289, 303, 347, 361, 385, 386, 387, 391, 396, 397
palladium, 54
paper, 408, 424, 425, 426
parallel, 8, 11, 13, 40, 41, 118, 143, 160, 164, 169, 170, 172, 174, 177, 186, 187, 188, 189, 236, 247, 288, 306, 323, 366, 415
parameter, 3, 4, 90, 93, 94, 96, 97, 165, 174, 215, 226, 308, 337, 375
particle nucleation, 209, 210, 214, 218, 221, 229
passive, 333
pathology, 259
pathophysiology, 259
pathways, 349
penicillin, 389
peptide, 435
peptide chain, 356
perchlorate, 26, 32
percolation, 327
performance, 231, 311, 404
periodic, 403
peripheral blood, 263
permeability, 300, 428
permittivity, 138, 139, 140, 307, 325
peroxide, 119
phage, 280, 281, 282
pharmaceutical, 429
pharmaceutical industry, 429
pharmaceuticals, 346
pharmacology, 355
phase behavior, xii, 306, 333
phase diagram, 103
phase transformation, 29
pheochromocytoma, 389
phonons, 148, 149, 150, 151
phosphates, 355
photocatalysis, 200
photoemission, 149, 157, 158, 161
photographs, 392
photo-induced reorientation, xii, 306, 326, 329
photolithography, 356
photoluminescence, 405
photonic crystals, 25
photonics, xi, xii, 136, 305, 306, 370, 371
photons, xii, 69, 86, 321, 322, 343
physical mechanisms, 80, 90, 96
physical properties, 404
physicians, 417
physics, 255, 257
pipelines, 418
plants, 264, 294, 350, 351
plasma membrane, 292, 295
plasmid, 356, 363
plasmodium, 289, 298
plasmon resonance spectra, xi, 199
platelets, 119, 120, 121
platform, 359
platinum, 40, 55
plausibility, 153
play, 407
point defects, 215
polar groups, 278
polarizability, 94, 124, 129, 138, 367
pollution, 264

Copyright © 2010. Nova Science Publishers, Incorporated. All rights reserved.

poly(methyl methacrylate), 317, 337
poly(vinylpyrrolidone), 311
polydiacetylene, xiii, 337, 365, 372, 375
polyimide, 315
polymer films, xii, 278, 286, 289, 306, 316, 329
polymer materials, xi, 259, 338
polymer matrix, 241, 243, 244, 315, 316, 317, 318, 326, 332, 333
polymer molecule, 323, 326
polymer solutions, 429
polymerization, 241, 314, 317, 333, 362, 372
polymers, xi, xii, 199, 202, 241, 246, 260, 306, 308, 317, 332, 338, 371, 372, 429
polymethylmethacrylate, 242
polypropylene, 418
polystyrene, 25
polyvinyl alcohol, 119
poor, 34, 226, 260, 316, 348
porosity, 103
ports, 394
powder, 409
precipitation, 165, 182, 183, 189, 215
prediction, 218, 375
pressure, xiv, 35, 103, 104, 120, 320, 379, 401, 410, 415, 418, 419, 420, 421, 423
prevention, 394
prisons, 283
probability, 107, 158, 160, 161, 176, 217
probe, x, 61, 104, 107, 187, 323, 334, 357, 358, 363
production, xi, xii, 3, 4, 42, 103, 123, 136, 168, 185, 189, 259, 260, 269, 303, 343, 350, 351, 404, 406, 408
program, 101
propagation, 87, 88, 90, 96, 99, 107, 112, 115, 143, 165, 173, 188, 201, 238, 306, 337
protective coating, 402
protein structure, 354
protocol, 336
protoplasm, 290
prototype, 200
prototypes, 201
public health, 260
pulse modification, xi, 199
pulses, 406
pumping, 415
pure water, 87, 92
purification, 109, 277, 288
purity, 3, 8, 17, 18

Q

quadrupole, 417
quanta, 322, 387
quantum confinement, xiii, 63, 99, 104, 109, 110, 114, 116, 365, 371
quantum dot, 7, 71
quantum dots, 7, 71
quantum yields, 321
quartz, 44, 268, 318, 349
quaternary ammonium, 379

R

radiation damage, 228
radicals, 5, 405, 417
radio, 415
radius, 29, 30, 67, 69, 72, 81, 90, 138, 142, 143, 149, 155, 156, 159, 160, 165, 182, 183, 307, 310, 324, 367, 368, 369, 370
Raman scattering, 411, 423
Raman scattering measurements, 40
Raman spectra, 42, 412, 413
random media, 138
reaction rate, 4, 6, 27, 418
reaction time, 22, 34, 35, 36, 43
reactions, xiv, 2, 3, 13, 26, 35, 43, 46, 54, 357, 361, 402
reactive ion, 415, 416
reactive oxygen, 261, 415
reactivity, 260, 408, 417
reagents, 6, 265, 270, 348, 389, 430
real time, xiv, 402, 421
reality, 263
reason, 41, 107, 116, 123, 152, 200, 228, 237, 296, 316, 327, 407
recall, 164
recognition, 354
recombination, 107, 108, 109, 123, 128
recommendations, iv, 298
red shift, 129, 145, 182, 183, 187, 328
redistribution, 151, 248, 249
reduction, xiv, 402, 403, 407, 413
reflectance spectra, 219, 221, 222, 224, 238
reflection, xi, 67, 71, 98, 100, 145, 199, 208, 222, 232, 322
reflectivity, 145, 219, 222, 223, 224, 226, 227, 232, 322
refraction index, 71
refractive indices, 63, 65, 66, 69, 70, 71, 94, 95, 325
regeneration, 429
regenerative medicine, 429
regrowth, 239, 428
relationship, 152, 375
relative toxicity, 295
relaxation, 103, 148, 149, 150, 151, 153, 162, 166, 239, 248, 275, 308

Copyright © 2010. Nova Science Publishers, Incorporated. All rights reserved.

relaxation process, 103
relaxation processes, 103
relaxation times, 153
reliability, 403
remediation, 55
reparation, 58
replacement, ix, 1, 3, 13, 17, 20, 21, 22, 54, 428
research, 402, 407
researchers, 408
residues, 356
resins, 438
resistance, 394, 405, 407, 417, 420
resistivity, 402
resolution, 3, 10, 12, 29, 40, 208, 387, 417, 431
respect, 45, 94, 96, 138, 152, 162, 164, 168, 170, 174, 178, 180, 181, 236, 260, 332, 367, 393
respiratory, 346
respiratory syncytial virus, 346
response time, 371
restructuring, 435
retention, 146
rings, 22, 27, 34, 243, 412
risk, xiv, 385, 386, 396
rods, 6, 15
rolling, 403
room temperature, 7, 98, 119, 152, 155, 156, 180, 181, 184, 208, 228, 230, 242, 268, 321, 357, 412, 430
roughness, 39, 41, 237, 381
routing, 336
rubidium, 337

S

safety, xi, 42, 259, 260, 261, 299
salt, 17, 119, 262, 263, 265, 266, 268, 269, 348, 359
salts, 97, 288, 389
samarium, 331
sample, 411, 414, 415
sampling, 88, 283
sapphire, 28, 57, 64, 68, 74, 83, 86, 98, 105, 111, 112, 118, 200
satellite, 403
satellites, 402
saturation, 77, 91, 107, 109, 115, 235
scaffolds, 429, 437
scaling, 129, 330, 410
scanning electron microscopy, xv, 3, 64, 110, 190, 410, 428, 431
scatter, 149, 273
school, 283
screening, 149, 299
search, 200, 335, 349
searching, 261
secretion, 356
sediment, 96, 266
sedimentation, 83, 85, 86, 279
seed, 14
seeding, 26, 48, 68, 83
selected area electron diffraction, 3, 208
selectivity, 357, 359
self-assembly, 317, 318, 358, 363
self-enhancement, 380
self-organization, xiii, 344
semiconductor, 76, 98, 200, 202, 354, 408
semiconductors, 255
sensing, 2, 306, 354
sensitivity, 273, 346, 357, 359
sensors, 11, 359
separation, 143, 182, 184, 319, 367
serum, 303, 351, 352, 354, 355, 361, 362, 363, 389
service life, 403
sex, 296
sharing, 150, 164
shear, 407, 438
shear strength, 407
short period, xiv, 402
signals, 68, 200, 232, 336, 420, 421
signs, 292, 296
silane, 242
silanol groups, 28, 30
silicon, xiv, 21, 98, 99, 101, 200, 260, 401, 402, 409
silk, 429
simulation, 244, 246, 247, 378
sintering, 29
skin, 285, 392, 394, 398, 428, 429, 437
skin diseases, 428
sodium, 42, 119, 202, 264, 266, 321, 346, 348, 349, 356, 357, 388
sodium hydroxide, 349
software, 4, 68, 302, 431
soil, 261
solar cell, 402
sol-gel, 205, 314, 331
solid matrix, 315, 335
solid phase, 330, 372
solid state, 340
solid surfaces, 106, 277, 289, 379
solidification, 238
solubility, xiii, 23, 70, 202, 214, 215, 218, 239, 344, 429
solvent, xv, 428, 432, 435
solvents, 35, 278, 327, 429, 431
sorption, 300
space, 4, 21, 30, 169, 249, 307, 325, 369, 370, 402, 403, 408, 423

Copyright © 2010. Nova Science Publishers, Incorporated. All rights reserved.

space shuttle, 408
space station, 408
specific heat, 96
specific surface, 278
speed, 200, 239, 337, 371, 372, 379, 403, 406, 415
spin, 315, 316, 318
sports, 284
sputtering, 405, 418
stability, x, xiii, 2, 28, 29, 34, 65, 118, 123, 263, 265, 277, 301, 309, 332, 333, 344, 348, 349, 353, 355, 359, 430, 432, 437
stabilization, 127, 308, 315
stabilizers, 4, 62
stained glass, 366
stainless steel, 409, 430
standards, 260, 322
stars, 201
steel, 409, 430
stem cells, 262, 292, 300, 397
sterile, 347, 390
stoichiometry, 103
stomach, 297
storage, 43, 403
strategies, xiii, 2, 4, 365
strategy, xiii, 263, 299, 365, 378, 382
strength, 8, 37, 57, 138, 155, 275, 367, 407
stress, 407, 413, 414, 415
stretching, 33, 40, 351, 435
strong interaction, 312, 315, 316, 332, 333
structural changes, 433
structural defects, 217
structuring, 136
substances, 428
substitutes, 428
subtraction, 418
sucrose, 32, 33
sulfur, 317
sulfuric acid, 317
superconductors, 406
superimposition, 147
supply, 44, 45, 319, 320, 406, 409
suppression, 88, 262, 286, 392
surface area, 3, 11, 26, 35, 260, 345
surface chemistry, xiii, 217, 343
surface energy, 20, 30
surface layer, 146, 211, 214, 224, 226, 229, 246, 356
surface modification, xiii, 214, 228, 344, 352
surface plasmon resonance, x, xi, xii, xiii, 2, 3, 61, 62, 94, 104, 135, 136, 137, 140, 141, 153, 201, 233, 305, 308, 309, 326, 328, 330, 338, 343, 345, 346, 365, 367, 370, 372, 374, 375, 382, 407
surface properties, xiii, 343, 352, 425
surface structure, 229
surface tension, 4, 32
surfactant, xi, 11, 36, 259, 268
surplus, 45
survival, 296
suspensions, xiv, 62, 110, 111, 278, 279, 282, 336, 348, 385, 390, 396, 397
switching, 68, 69, 79, 80, 104, 336, 337, 340, 405
symmetry, 65, 118, 126, 168, 170, 172, 173, 188, 309
synthetic polymers, 429
systems, 402, 403, 408

T

TCC, 283, 431, 437
technology, 417
temperature dependence, 152, 153, 181, 189
tension, 30, 79
testing, 388
textiles, 347, 396, 397
therapeutic agents, xiii, 343
therapy, 347, 354
thermal energy, 95, 162
thermal expansion, 189
thermal properties, 98
thermal stability, 2, 29, 31
thermalization, 149, 150, 158, 161, 164, 165, 215
thermodynamic equilibrium, 3, 6
thin film, 404
thin films, 64, 76, 357, 382
third-order susceptibility, 69, 72, 75, 93, 127, 233, 309, 325
three-dimensional, 429
threshold, 81, 113, 119, 153, 160, 163, 164, 168, 170, 173, 176, 179, 188, 215, 237, 335
thresholds, 68, 292
time, xiv, 402, 421
time periods, 282, 286
tin, 217, 242, 358
tin oxide, 358
tissue, 301, 351, 388, 428, 437
tissue engineering, 428
titanium, 398
total energy, 156, 217, 407
toxic, 429, 431
toxic effect, 262, 263, 264, 278, 292, 293, 294, 296, 386
toxic products, 264
toxicology, 299, 301, 397
toys, 260
trajectory, 217, 228
transfer, 407

Copyright © 2010. Nova Science Publishers, Incorporated. All rights reserved.

transition, 12, 13, 14, 32, 62, 72, 78, 95, 158, 168, 233, 236, 321, 323, 361, 371, 403, 407
transition metal, 407
transitions, 71, 77, 78, 79, 82, 124, 127, 139, 141, 201, 236, 309, 335
translation, 68, 70, 324, 325
transmission electron microscopy, ix, xv, 2, 3, 70, 110, 120, 162, 172, 190, 208, 242, 269, 387, 428, 431
transmits, 13, 323
transmittance spectra, 238
transparency, 77, 234, 236, 402
transport, 6, 10, 26
travel, 403
trends, 221
trial, 224
tribological, 405
trifluoroacetic acid, 429
triggers, 35
true fractal, 15
trypsin, 389
tumor, 301
twinning, 13, 14, 23
twins, 14
tyrosine, 355

U

ultrasound, ix, 1, 2, 6, 7, 9, 11, 26, 28, 33, 37, 38
ultraviolet range, x, 62, 80, 334
unforeseen circumstances, 396
uniform, 15, 22, 26, 34, 222, 225, 228, 239, 377

V

valence, 158, 217, 357, 404
values, 412, 414
vapor, xiv, 14, 97, 103, 337, 402, 406, 407, 409
variability, 62, 350
variables, 351, 363
variation, 413, 423
variations, 63, 71, 77, 78, 86, 87, 88, 90, 91, 94, 96, 127, 138, 214, 219, 231, 233, 335, 403
vector, 13, 323
vegetable oil, 347, 361
vehicles, 353
velocity, 66, 72, 90, 145, 310, 408
vesicle, 373, 375, 379
vibration, 7, 15, 26, 33, 292, 293
video, 292
viruses, 288
viscosity, 83, 86, 127, 429, 430, 432, 438
vitamins, 351

W

water, 409, 418, 430, 431, 433, 437
water-soluble polymers, 277
wave propagation, 90
waveguide, 201, 371
wealth, 357
wear, xiv, 402, 403, 404, 405, 407, 417, 420, 421, 423
weight ratio, 15, 42
wide band gap, 402
wires, 6, 48, 200
wood, 282
wool, 286
workers, 298, 351, 352, 354, 355, 357, 358
wound healing, 386
writing, 168, 175, 178, 182

X

xenon, 243, 245
XPS, 3, 18, 19
x-ray, xv, 3, 50, 70, 85, 154, 204, 205, 208, 379, 381, 428, 431, 436, 437
x-ray diffraction, xv, 3, 208, 379, 381, 428
x-rays, 431

Z

zirconia, 207

Copyright © 2010. Nova Science Publishers, Incorporated. All rights reserved.